Transactions of the ASME®

Journal of Heat Transfer

Published Quarterly by The American Society of Mechanical Engineers

VOLUME 119 • NUMBER 2 • MAY 1997

Transactions of the ASME, Journal of Heat Transfer (ISSN 0022-1481) is published quarterly (Feb., May, Aug., Nov.) for $220.00 per year by The American Society of Mechanical Engineers, 345 East 47th Street, New York, NY 10017. Periodicals postage paid at New York, NY and additional mailing offices. POSTMASTER: Send address changes to Transactions of the ASME, Journal of Heat Transfer, c/o THE AMERICAN SOCIETY OF MECHANICAL ENGINEERS, 22 Law Drive, Box 2300, Fairfield, NJ 07007-2300. **CHANGES OF ADDRESS** must be received at Society headquarters seven weeks before they are to be effective. Please send old label and new address. **PRICES:** To members, $40.00, annually; to nonmembers, $220.00. Add $30.00 for postage to countries outside the United States and Canada.

HEAT TRANSFER GALLERY

TECHNICAL PAPERS

Properties and Property Measurements

Conduction Heat Transfer

Forced Convection

Natural Convection

(Contents continued on Outside Back Cover)

(Contents continued)

Evaporation

Boiling and Nucleation

Heat Exchangers

TECHNICAL BRIEFS

(Contents continued on p. 362)

(Contents continued)

DISCUSSION

ANNOUNCEMENTS

Journal of Heat Transfer

Heat Transfer Gallery

C. T. Avedisian[1]. At the International Mechanical Engineering Congress and Exhibition (IMECE) in Atlanta last November, a technical session was offered entitled 'Heat Transfer Picture Gallery' (HTPG) at which photographs were displayed that depicted various processes occurring in the presence of temperature gradients. The turnout was notable for the attention it drew from spectators who browsed through the photo displays, like in an art gallery. The session attracted 25 photo displays and they were evaluated by a distinguished panel of engineers based on subjective judgments of the visual impact of the photographs and the original contribution they were thought to make to the understanding of a thermal process. Ten of the displays that received the highest ratings are published here in this special section of the ASME JOURNAL OF HEAT TRANSFER entitled 'Heat Transfer Gallery.'

The motivation for publishing these photographs is to draw attention to, and illustrate, the aesthetic qualities of thermal processes. The accompanying explanatory text for each photo display is kept to a minimum to focus attention on the visualization. The photographs include phenomena of natural and forced convection, boiling, and combustion. Reproductions in color are included to enhance the visualizations. It is hoped that the readership of the ASME JOURNAL OF HEAT TRANSFER enjoys browsing through this collection of color photographs.

The HTPG will again be offered at the upcoming IMECE to be held in Dallas in November 1997 (see an announcement in the February 1997 issue of the ASME JOURNAL OF HEAT TRANSFER. Furthermore, the opportunity may again be available for publication in the ASME JOURNAL OF HEAT TRANSFER of the best photographs displayed at the HTPG. There will be a strong preference for original contributions not previously published.

Publication of this 'Heat Transfer Gallery' would not have been possible without the strong support of the Senior Editor, Dr. Jack Howell. Additionally, Dr. Ray Viskanta (past editor) and the members of the Executive Committee of the Division of Heat Transfer, including Drs. Richard Buckius, Soung Cho, Ralph Greif, and Gus Plumb, who were instrumental in supporting the idea of this Heat Transfer Gallery for the ASME JOURNAL OF HEAT TRANSFER. Finally, thanks are due to ASME for defraying the cost of the color reproductions.

[1] Sibley School of Mechanical and Aerospace Engineering, Cornell University, Ithaca, New York, 14853-7501.

References

Ball, K. G., Song, M., Gomon, M., Silva, M. W., Taleff, E. M., Powers, B. M., and Bergman, T. L., 1996, "Canister Filling With a Molten Glass Jet," *Bulletin of the American Physical Society* Vol. 41, p. 1749.

Chyu, M. K., Ding, H., Downs, J. P., Van Sutendael, A., and Seochting, F. O., 1997, "Determination of Local Bulk Temperature for Heat Transfer Using Transient Liquid Crystals Technique," to be presented at the International Gas Turbine and Aeroengine Congress and Exposition, Orlando, June.

Dhir, V. K., 1972, "Viscous Hydrodynamic Instability Theory of the Peak and Minimum Pool Boiling Heat Fluxes," Ph.D thesis, University of Kentucky, Lexington, Kentucky.

Liakopoulous, A., Huang, X., Blythe, P. A., and Simpkins, P. G., 1991, "Buoyancy Driven Motions due to a Vertical Array of Heat Sources," HTD-Vol. 171, *Heat Transfer in Electronic Equipment,* A. Ortega et al., eds., p. 63.

Liu, Y. H., and Zumbrunnen, D. A., 1996, "Emergence of Fibrillar Composites Due to Chaotic Mixing of Molten Polymers," *Polymer Composites,* Vol. 17, pp. 187–197.

Presser, C., Gupta, A. K., Avedisian, C. T., and Semerjian, H. G., 1990, "Fuel Property Effects on the Structure of Spray Flames," *23rd Symposium (International) on Combustion,* The Combustion Institute, pp. 1361–1367.

Mukherjee, D. K., Prasad, V., Dutta, P., and Yuan, T., 1996, "Liquid Crystal Visualization of the Effects of Crucible and Crystal Rotation on Cz Melt Flow," *Journal of Crystal Growth,* Vol. 169, pp. 136–146.

Zumbrunnen, D. A., Miles, K. C., and Liu, Y. H., 1996, "Auto-Processing of Very Fine-Scale Composite Materials by Chaotic Mixing of Melts," *Composites: Part A,* Vol. 27A, pp. 37–47.

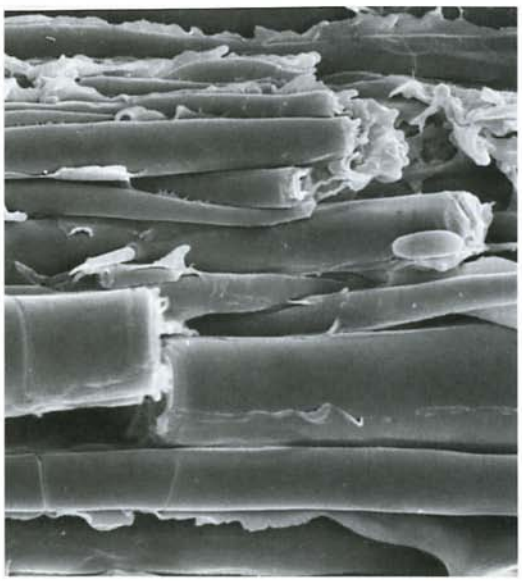

Solidification of Structured Melts, D. A. Zumbrunnen and Y. H. Liu, Laboratory for Materials Processing and Industrial Mixing, Department of Mechanical Engineering, Clemson University.

When melts are composed of immiscible substances, unique opportunities exist whereby extended fine-scale structures can be formed directly in the melt and subsequently captured by solidification. Such structures can have improved properties in comparison to unstructured materials of similar composition. In the upper photograph, recursive stretching and folding events of chaos were instilled within a mixing cavity to yield very rapid reductions in the sizes of melted thermoplastic minor phase bodies (Zumbrunnen et al., 1996). Lamellae of about 1 μm thickness appear in cross section as dark bands. Such structures can be especially effective as permeability barriers, for example. When interfacial tension is sufficient as in the scanning electron micrograph on the lower left, molten lamellae or thicker sheets eventually subdivide due to interfacial instabilities. The instabilities lead to the formation of interconnected fiber shafts of less than 10 μm diameter, as shown on the lower right, that may improve strength and toughness (Liu and Zumbrunnen, 1996). Since the microstructures are formed in the molten state and must be captured by solidification, heat transfer plays an important role in the formation of these novel materials. Both desirable and undesirable microstructural changes can occur upon application of temperature gradients. These effects must be understood so that effective manufacturing processes can be developed.

Figure 1
The central zone eddy
Gr = 1.26 x 10^5

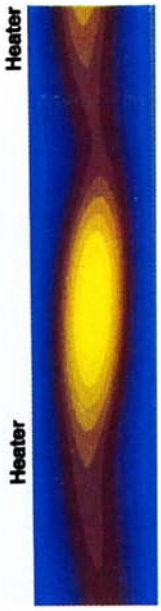

Figure 2
Computation for the
central zone eddy
Gr = 10^5

Figure 3
Top trailing corner vortex

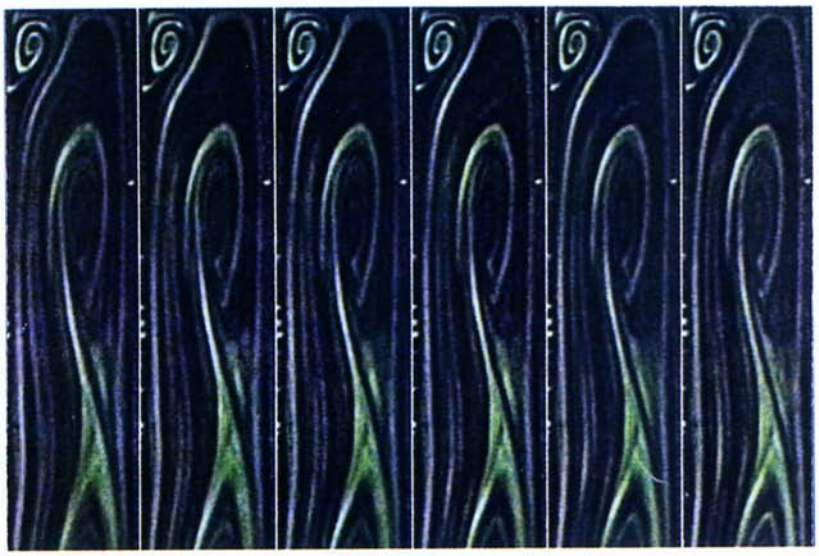

Figure 4. Mosaic of the top quandrant of the enclosure flow Gr = 1.8 x 10^5

EDDY STRUCTURES IN A SLOT WITH PERIODIC HEATING

P. G. Simpkins[1] and A. Liakopoulos[2]
[1]Bell Laboratories, Murray Hill, NJ
[2]Lehigh University, Bethlehem,PA

The photographs illustrate the buoyancy driven motion in an air-filled enclosure with a periodic heat flux along the left hand wall. Based on the cavity width l, the vertical aspect ratio is 20 and each heater is of length 2l. Figure 1 shows an eddy near the central zone of the cavity. The Grashof number is defined in terms of the applied heat flux.

A computational representation of the equivalent location is given in Figure 2, see Liakopoulos et al (1991). A close-up of the corner of the cavity is illustrated in Figure 3. Motion in the top corner of the cavity is illustrated as a mosaic in Figure 4. This image has been digitally enhanced using a three-frame averaging proceedure.

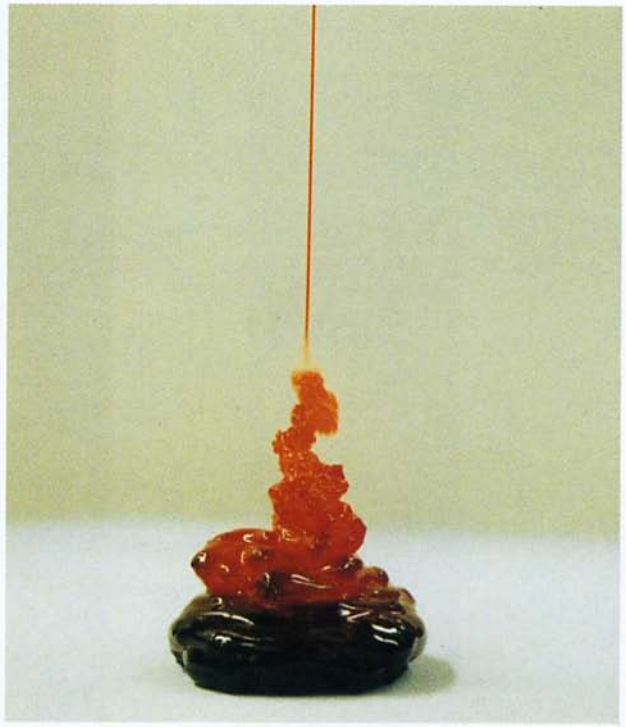

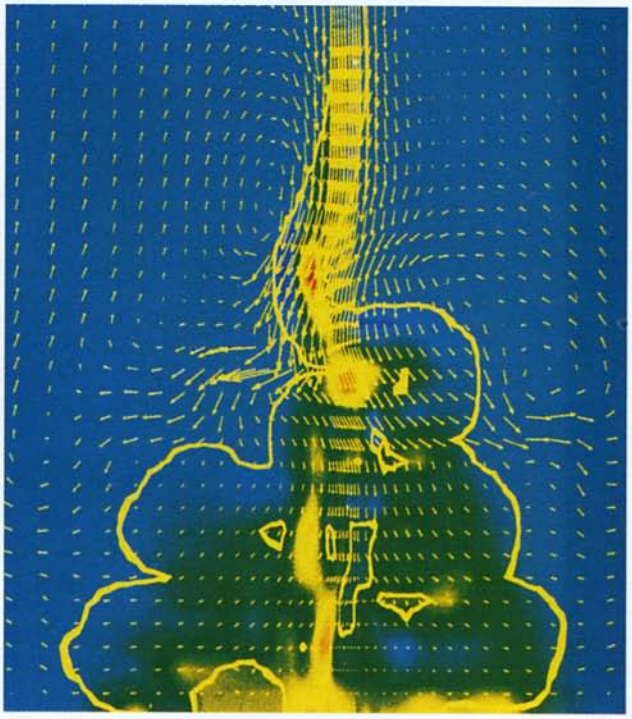

Canister Filling with a Molten Glass Jet

K. S. Ball, M. Song, M. Gomon, and M. W. Silva, Department of Mechanical Engineering,
E. L. Taleff and B. M. Powers, Department of Aerospace Engineering and Engineering Mechanics,
The University of Texas at Austin, Austin, TX 78712;
T. L. Bergman, Department of Mechanical Engineering, University of Connecticut, Storrs, CT 06269

Top row - high-temperature molten glass experiment (furnace temperature 1050 °C): (l) buckling of impinging jet, (r) bird's nest formation. Bottom row: (l) room-temperature analogous fluid experiment (corn syrup): pile-up after approximately 1 s, (r) finite element / volume of fluid simulation (FIDAP®) of analogous fluid experiment (velocity vectors and air/liquid interface location superimposed on pressure field; red indicates maximum compression). A description of the engineering application and research methodology can be found in Ball et al. (1996).

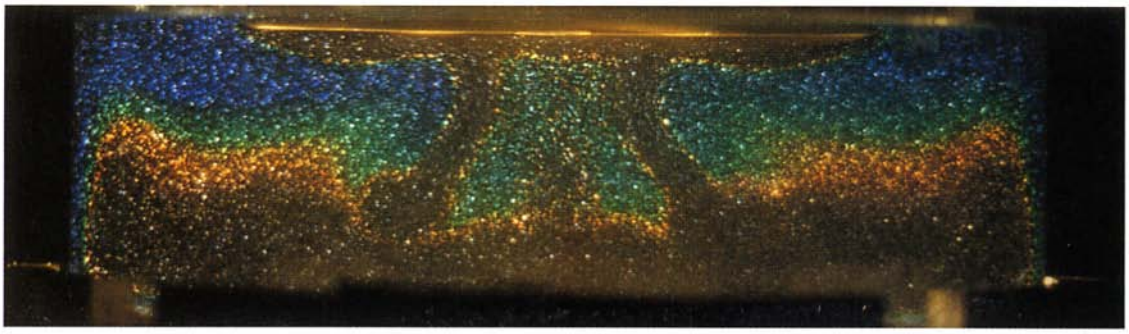

1(a)

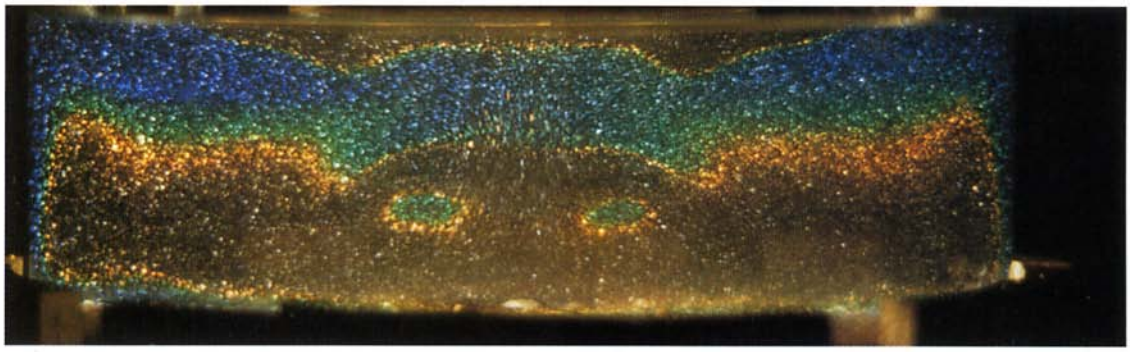

1(b)

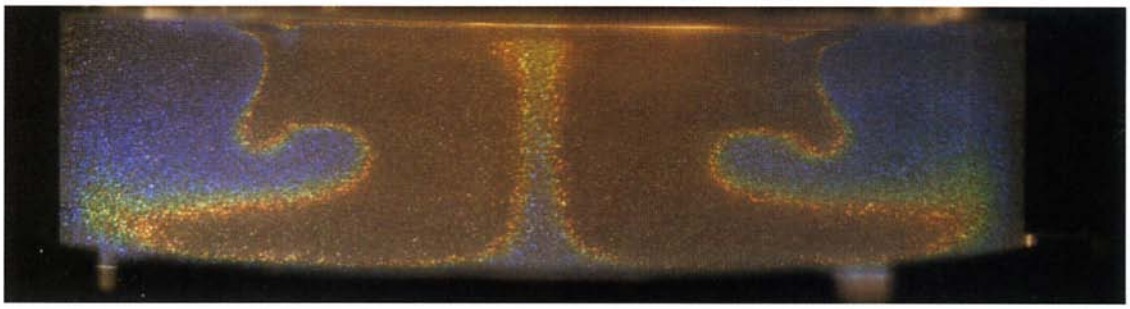

2(a)

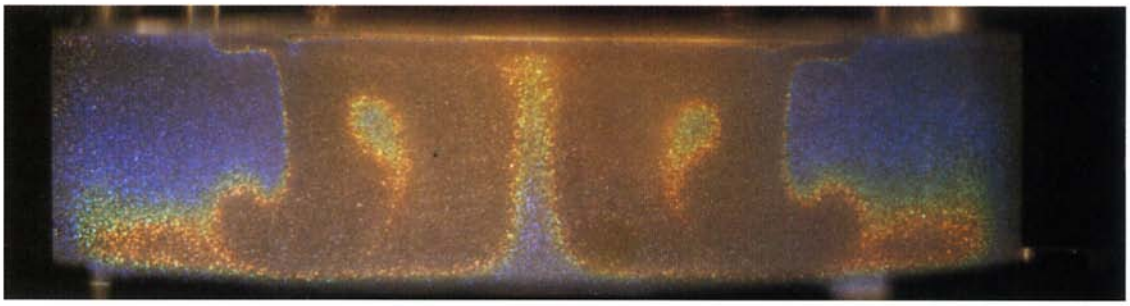

2(b)

Visualization of Transient Temperature Field in a Rotating System using Liquid Crystals

D.K. Mukherjee and V. Prasad
SUNY at Stony Brook, NY 11794-2300

The versatility of imaging transient thermal phenomena using liquid crystals is displayed above (Mukherjee et al., 1996). The first two photos (Figs. 1a-b) capture the oscillatory regime in a buoyancy driven flow ($Ra \approx 1.2 \times 10^5$, $Pr \approx 890$). The inner cylinder resting on the surface of the fluid is at 24 °C and the outer cylinder is at 36 °C. The progression from red (24 °C isotherm) to blue (36 °C isotherm) shows contributions from the buoyant and thermocapillary forces. The next two photos (Figs. 2a-b) portray a temporal behavior of (i) the competition between the buoyancy cum surface tension gradient driven flow toward the inner cylinder and the centrifugally pumped flow away from the inner cylinder ($Re \approx 4.41$, $Fr \approx 5.8 \times 10^{-3}$, $Gr/Re^2 \approx 6.4$), and (ii) the Ekman suction owing to the shear imposed at the fluid surface. The distinct change in contrast between the two sets of photos is attributed to the photographic parameters; ASA 25 (Kodak Ektar) with aperture at f/4 for 1a and 1b, and ASA 100 (Kodak Royal) with aperture at f/1.8 for the faster flow. An 85 mm Nikkor lens is used to minimize error due to angular imaging.

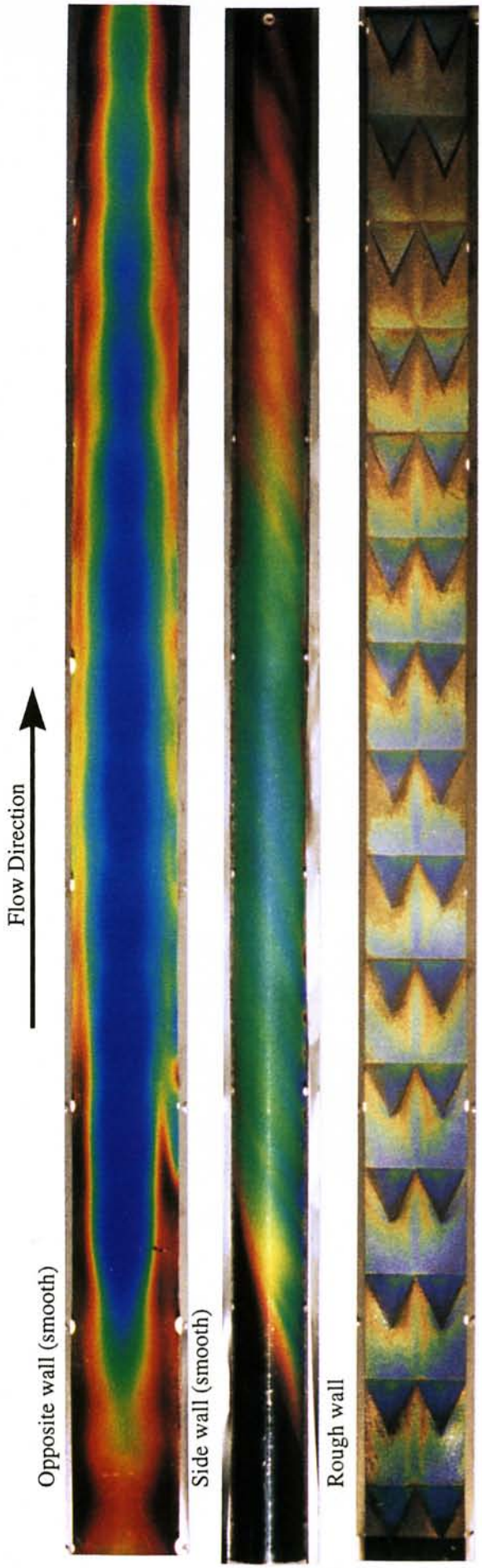

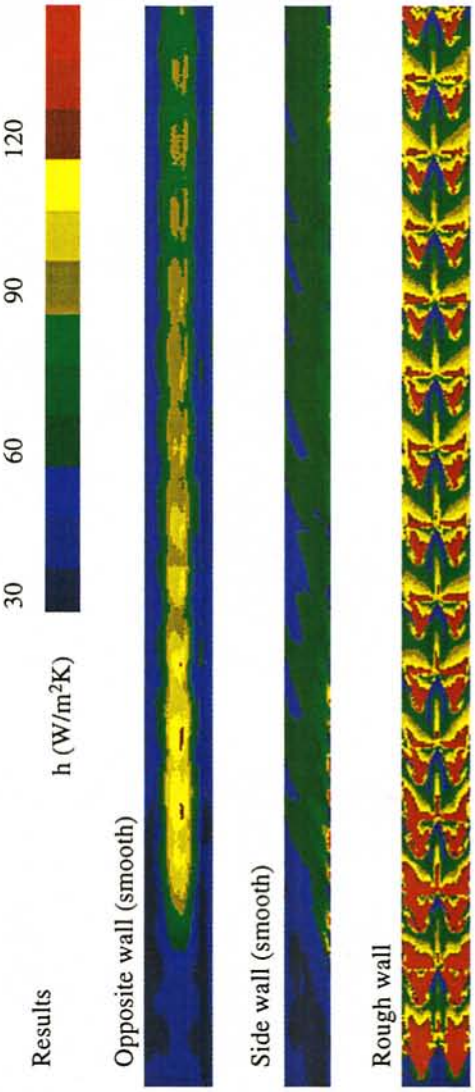

Heat Transfer in a Cooling Channel with Vortex Generators

Mingking K. Chyu and Hui Ding
Department of Mechanical Engineering
Carnegie Mellon University
Pittsburgh, Pennsylvania

The artwork shown consists of instantaneous photos of thermochromic liquid crystal (TLC) images on the surfaces of a model of an advanced airfoil internal cooling passage. Heat transfer enhancement over the entire passage results from the placement of delta-wing shaped vortex generators on one of the passage walls (Chyu et al., 1997). Sequential TLC images are transformed into distributions of heat transfer coefficients using a custom-developed, liquid crystal thermographic processing system. The average heat transfer coefficient over the entire periodic region can be as high as 5 times that in a smooth passage. Such a high level heat transfer enhancement has never been reported for internal passage cooling. The artwork indicates the swirling in the main passage flow; most evident on the sidewall photo.

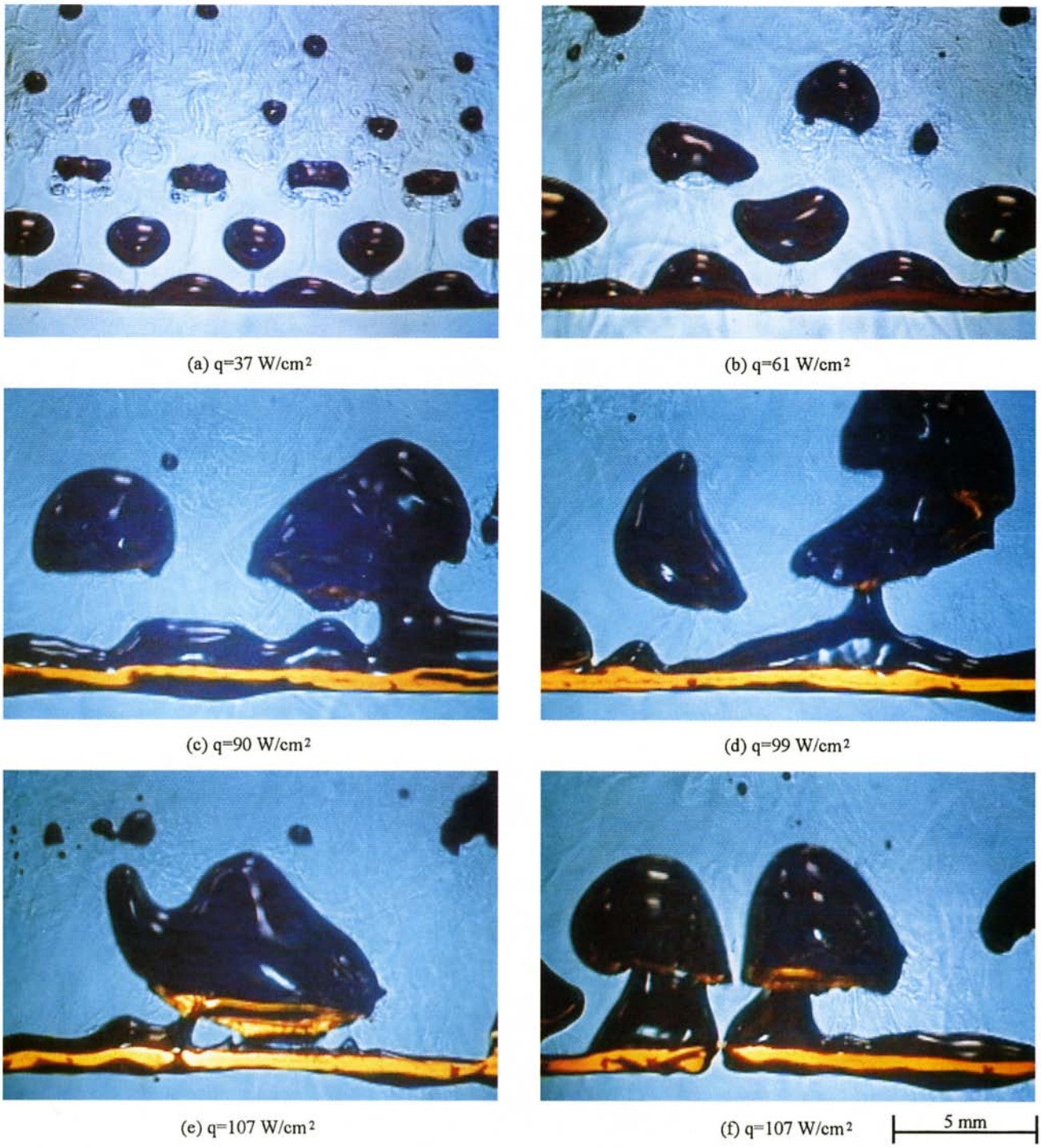

Ordered and Chaotic Bubble Departure Behavior During Film Boiling

Y.S. Hong, S.M. You, C.N. Ammerman and J.Y. Chang
Mechanical and Aerospace Engineering Department
The University of Texas at Arlington

Test Apparatus

A 510-μm-diameter, electrically heated Nichrome wire is immersed in gas-saturated FC-72 at 1 atm (T_{bulk}=25°C, T_{sat}=56°C).

Ordered Departure

In Fig.'s (a) and (b), the Taylor wavelength separating departing film-boiling bubbles is evident, and is increasing with heat flux (Dhir, 1972). Density gradients in the wake of condensing bubbles are visible.

Chaotic Departure

In Fig.'s (c) and (d), growing bubbles are merging laterally prior to departure, therefore a consistent departure pattern is not evident. The red glow of the wire indicates an increased surface temperature in this regime.

Burnout

Figures (e) and (f) show consecutive frames (0.067 second interval) at the moment of burnout. The melting point of Nichrome is approximately 1,400°C.

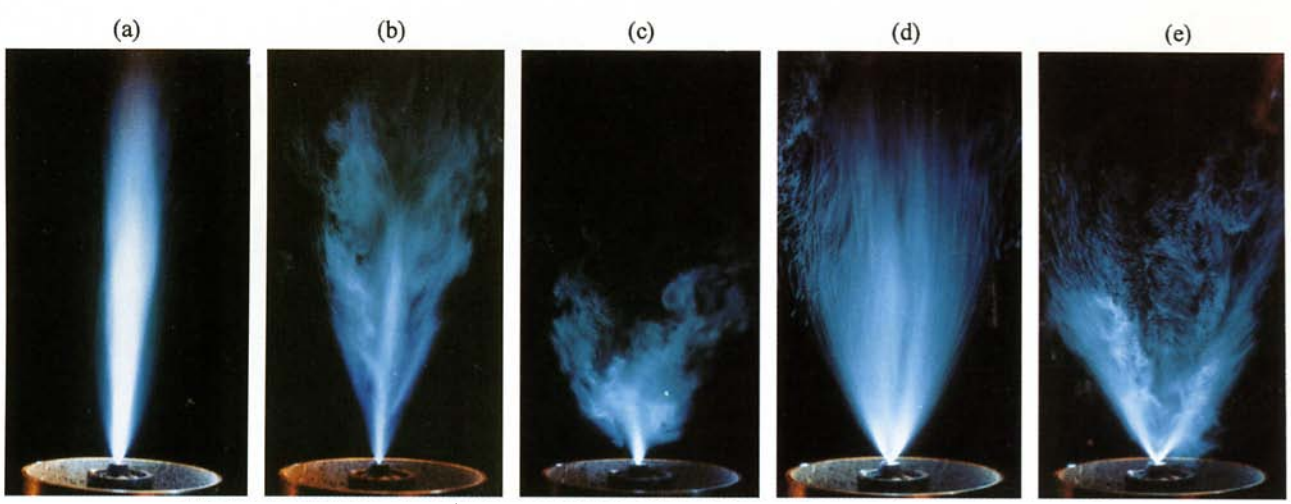

HEAT TRANSFER EFFECTS ON DROPLET VAPORIZATION BY AIR PREHEATING

A.K. Gupta, University of Maryland, C. Presser and C. Cook, National Institute of Standards and Technology, and C.T. Avedisian, Cornell University

These laser sheet beam photos show the effect of combustion air swirl at a vertical cross section (through the centerline) of vaporizing fuel sprays with surrounding coflowing air heated to about 430 K. The fuel spray was produced with a commercially available pressure-jet nozzle. Photos a, b, and c are for methanol while Photos d and e are for kerosene fuel under identical flow conditions. The structure of the spray changes significantly as the Swirl number is changed from 0 (Photos a and d) to 0.24 (Photo b) and to 0.46 (Photos c and e). Photo f shows donut-shaped horizontal spray structure for kerosene at a Swirl no. of 0.46. Increased droplet vaporization for the methanol spray yields a significantly different structure than for kerosene. The spray becomes significantly narrower for methanol as a result of enhanced droplet vaporization by the surrounding heated air. The development of this laser sheet beam technique is described in the paper by Presser et al. (1990).

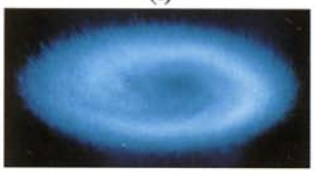

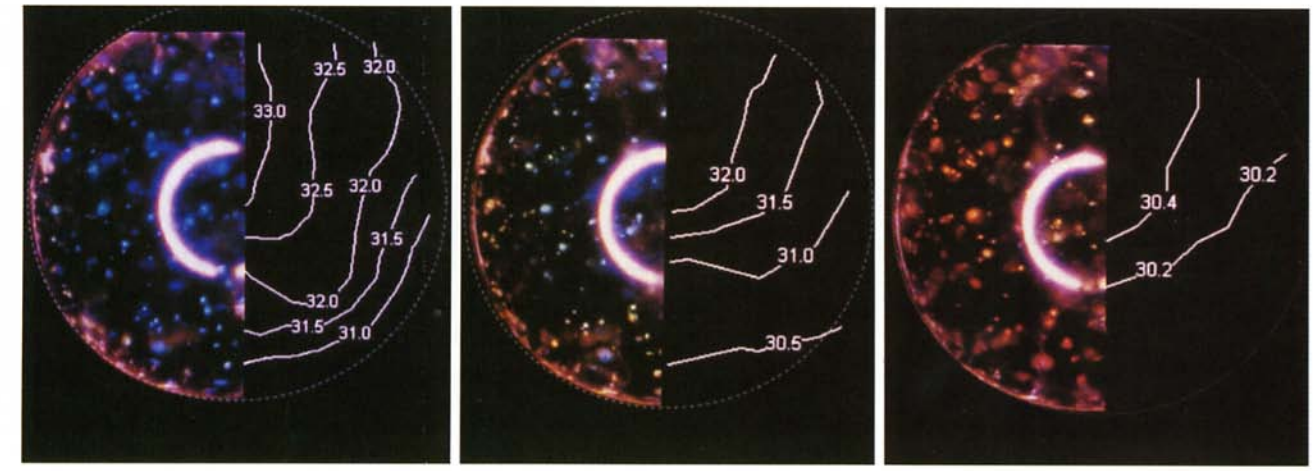

time = 0.000 s time = 0.133 s time = 0.267 s

C.D. Richards & R.F. Richards, School of Mechanical and Materials Engineering, Washington State University

Convective Cooling of a Suspended Water Droplet

The sequence of images, taken using a long-distance microscope and a color video camera framing at 30 Hz, shows the transient temperature history of a 960 μm water droplet as it cools in air. The small patches of color in the droplet are 10 μm beads of microencapsulated thermochromic liquid crystals (TLC). The colors of the beads change with temperature, giving a visible indication of the temperature field within the droplet. The contours of constant temperature, given in degrees C, on the right hand side of each image were determined by calibrating the hue of the microencapsulated TLC against temperature. The sequence of six images reveals the transient temperature field, in a slice through the center of the droplet.

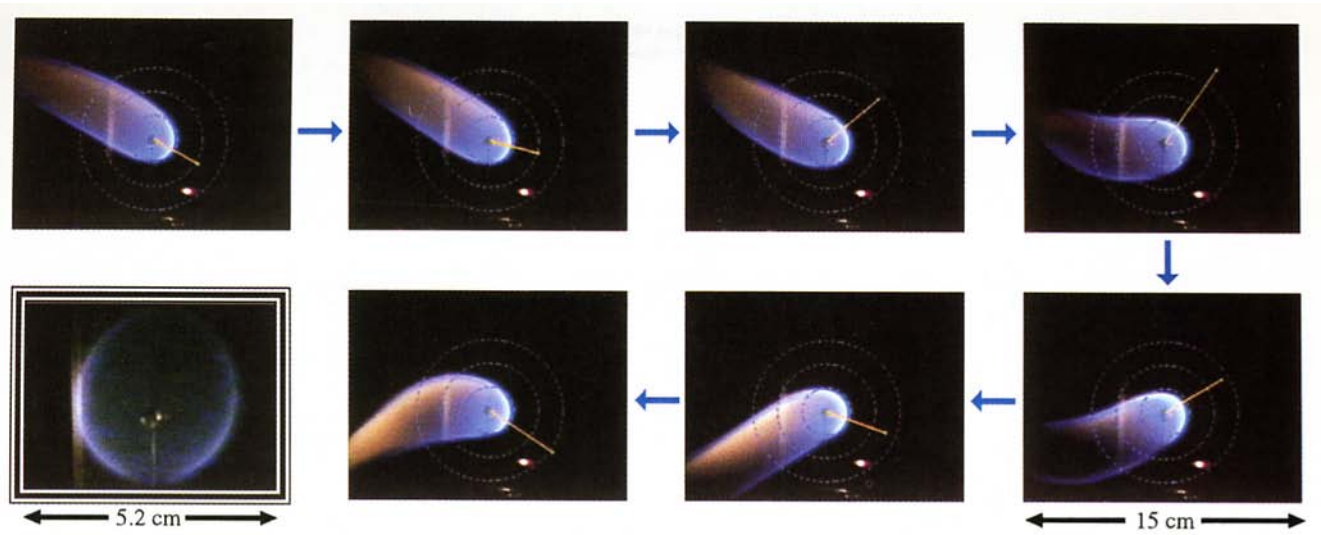

The Visualization of G-jitter Effects on a Burning Fuel Droplet in Reduced Gravity

P.M. Struk, J.S. T'ien, Case Western Reserve University
D.L. Dietrich, NASA Lewis Research Center

These flame images are from an experiment aboard NASA's reduced gravity research aircraft. The experiment studied the combustion of fuel droplets in reduced gravity. A constant size fuel droplet was simulated using a wetted porous sphere continuously supplied with fuel (n-decane). Instantaneous measurements of the acceleration were superimposed on the series of images showing the effect and time response of the flame. The variation of the gravity level (both magnitude and direction), or **g-jitter**, was due to aircraft acceleration–deceleration, vibrations, and atmospheric turbulence. The orange line is the acceleration vector originating at the center of the fuel droplet. Each graphically overlaid circle represents an acceleration magnitude of 10^{-2} normal (Earth's) gravity. Each frame is shown at 0.4 second intervals. This test was at .05 MPa pressure and a 15% oxygen 85% nitrogen ambient with a 5 mm diameter porous sphere. The last image shows a flame in 10^{-4} normal gravity. Here, at the lower gravity level and in the absence of g-jitter, the flame attained a near spherical shape.

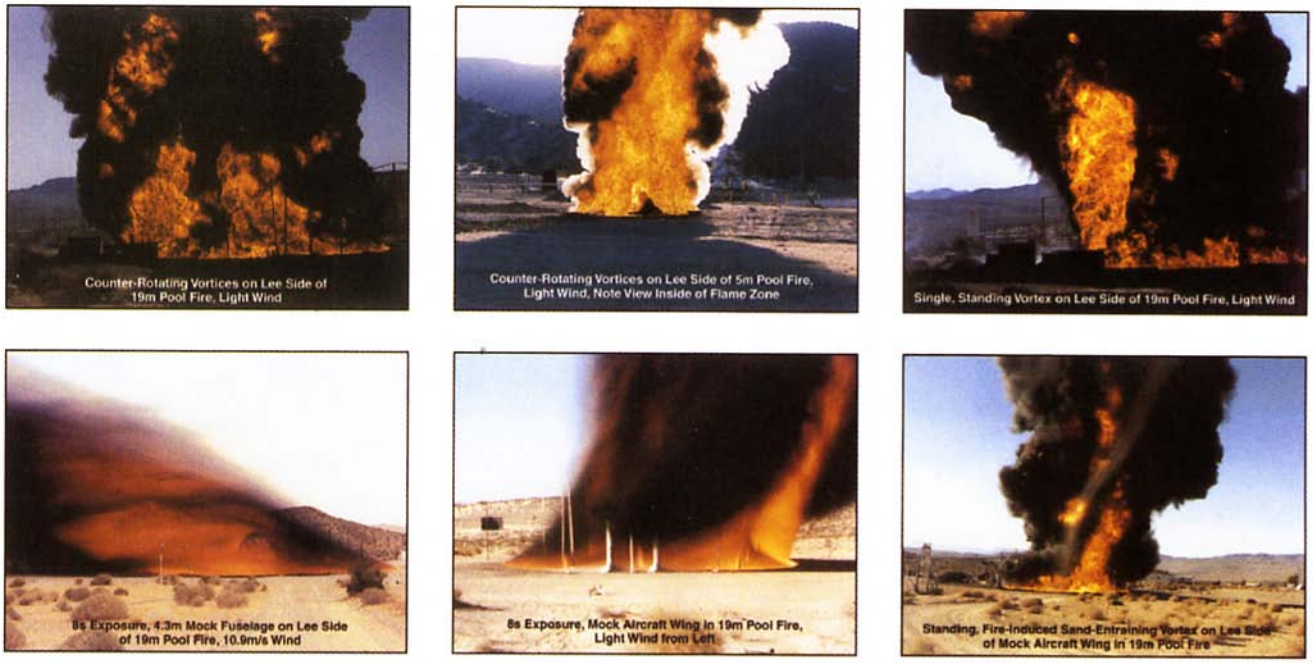

Flame Structure of Large, Hydrocarbon-Fueled Pool Fires

Louis A. Gritzo and Sheldon R. Tieszen, Sandia National Laboratories, Albuquerque, NM
Douglas Murray, Naval Air Warfare Center - Weapons Division, China Lake, CA.

These flame structures were observed during experiments performed to characterize the hazard posed by large fires, and to yield data, through the application of new and innovative diagnostics, required for the validation and further development of computational models which strive to predict this hazard.

These experiments were sponsored by the Defense Special Weapons Agency, and the Sandia Engineering Sciences Research Foundation. Work was performed in part at Sandia National Laboratories under United States Department of Energy contract DE AC04-94 AL8500.

Containerless Thermal Diffusivity Determination of High-Temperature Levitated Spherical Specimen by Extended Flash Methods: Theory and Experimental Validation

F. Shen[1]
Graduate Research Assistant
Assoc. Mem. ASME

J. M. Khodadadi
Associate Professor
Mem. ASME

M. C. Woods[2]
Graduate Research Assistant

Department of Mechanical Engineering,
Auburn University,
201 Ross Hall,
Auburn, AL 36849-5341

J. K. R. Weber
Director and Principal Scientist
Containerless Research, Inc.,
910 University Place,
Evanston, IL 60201-3149

B. Q. Li
Assistant Professor
Mem. ASME
Department of Mechanical Engineering,
Louisiana State University,
2513 A CEBA Building,
Baton Rouge, LA 70803-6413

In order to determine the thermal diffusivity of materials, especially solids and liquids at high temperatures, two extended containerless flash techniques that are applicable to levitated spherical specimen are proposed. The extended flash methods are modeled as an axisymmetric transient conduction heat transfer problem within the sphere. For the "single-step" method, analytic expressions for the temperature history on the surface of the sphere are obtained that are independent of the incident energy and the absorption layer thickness. It is shown that by knowing the sample diameter and recording the temperature transient history at least at two different points on the surface simultaneously, the thermal diffusivity can be determined. A detailed discussion of the effects of the various parameters is presented. For the "two-step" analysis the problem of nonlinearity of the radiative heat transfer boundary condition is overcome by replacing it with the measured time-dependent surface temperature data. Upon obtaining the temperature field the determination of the thermal diffusivity turns into a minimization problem. In performing the proposed two-step procedure there is a need to undertake a cool-down experiment. Results of an experimental study directed at determining the thermal diffusivity of high-temperature solid samples of pure Nickel and Inconel 718 superalloy near their melting temperatures using the single-step method are discussed. Based on close agreement with reliable data available in the literature, it is concluded that the proposed techniques can provide reliable thermal diffusivity data for high-temperature materials.

I Introduction

Thermal diffusivity is an important material thermophysical property that governs the time-dependent temperature distribution in materials during transient heat transfer processes. Thermal diffusivity of high-temperature liquid metals, alloys, and electronic materials is a crucial parameter in melting, solidification, crystal growth, casting, and welding processes where the temperature history and the associated heating/cooling requirements need to be known accurately. However, the thermal diffusivity data for high-temperature liquids are still far from complete even though a large amount of data is available on thermal diffusivity of solids over a wide range of temperatures (Touloukian et al., 1973). The main difficulties associated with the thermal diffusivity determination are due to the presence of convection within the molten material and the need for a container to hold the sample. Fortunately, the availability of levitation technology and space-related advances make it possible to solve these problems by levitating the specimen on the ground or in the microgravity environment of outer space.

II Literature Survey

There are several ways to measure the thermal diffusivity, among which the flash (or pulse) technique is the most popular one. This measurement method was introduced by Parker et al. (1961). The basic idea of the flash technique is simple, and the resulting ease of operation points to its popularity. The sample, a small disk-shaped specimen of uniform thickness which is initially at a constant temperature, receives a uniform high energy irradiation burst on the front surface. The temperature rise on the rear surface is then recorded as a function of time. The thermal diffusivity is then determined by comparing the recorded temperature with the theoretical expression obtained from the analytic solution of a one-dimensional transient heat conduction equation. The features of this technique were reviewed by Taylor and Maglic (1984) who reported that a survey of the literature in the early seventies showed that about 75 percent of the thermal diffusivity data reported within that period were obtained using the flash method. Using this technique, thermal diffusivity values in the range of 10^{-7} to 10^{-3} m^2/s have been reported in the temperature range of 100 to 3300 K. However, nearly all the different variations of the flash method up to now which account for radiation losses, multilayer specimen, finite pulse time, and large sample effects were developed to measure the thermal diffusivity of solids and low-temperature liquids. There are very few reports about the application of the flash method to high-temperature liquid materials (e.g., Schriempf, 1972) because of the complexity of the experimental set-up and the associated theoretical analysis. The main obstacle

[1] Currently with Adapco, Inc., Melville, NY.
[2] Currently with Applied Materials Company, Austin, TX.

Contributed by the Heat Transfer Division for publication in the JOURNAL OF HEAT TRANSFER. Manuscript received by the Heat Transfer Division May 10, 1996; revision received December 20, 1996; Keywords: Conduction, Liquid Metals, Measurement Techniques, Microgravity Heat Transfer, Radiation, Sprays/Droplets, Thermophysical Properties, Transient & Unsteady Heat Transfer. Associate Technical Editor: B. W. Webb.

is the corrosive nature of the high-temperature liquids and the inevitable container contamination. Consequently, a number of containerless thermal diffusivity measurement techniques have been proposed in recent years.

Bayazitoglu et al. (1990) proposed the theoretical foundation of a measurement method where two spherical samples are levitated. The diameter of the small sample is selected such that the Biot number is less than 0.1, and the sample is allowed to cool down starting at a uniform high temperature. This phase of the experiment is used to calculate the quantity $\epsilon_{\text{eff}} F/\rho c_p$, using a lumped parameter approach. Then, a bigger sample (Bi $\geq$ 0.1) is levitated and allowed to cool down similar to the small sample. It should be noted that due to the presence of a radiative surface, a curve-fit to the experimental surface temperature data is used in place of the original nonhomogeneous boundary condition. The temperature field as a function of time and the radial coordinate are then obtained analytically for various values of thermal diffusivity. The thermal diffusivity is then determined by minimizing a function that satisfies the heat balance at the surface. The main drawback associated with this method is that of the size of the big sample, which needs to meet the stringent requirement of the big-droplet experiment (i.e., Bi $\geq$ 0.1). For instance, for pure nickel at a temperature of 1700 K (melting point of 1728 K) the diameter of the sample has to be at least 20 cm. The minimum diameter values decrease as the initial temperature increases, but this rigid requirement calls for excessively big samples to be levitated, which might be physically impossible. Also, this method does not account for the multidimensionality of the initial temperature field that would result from the external heating device.

In this paper two extensions of the flash technique that are applicable to levitated high-temperature spherical samples are proposed. Due to high temperatures the radiative heat loss from the surface, which is dominant and behaves nonlinearly, is taken into account. In the presence of a surrounding medium, the effect of the participating medium on the radiation heat transfer can be accounted for by an effective emissivity of the sample (e.g., Bayazitoglu and Suryanarayana, 1990). For the *single-step* method upon linearization of the boundary condition, an analytic solution is obtained to predict the temperature history at any point. The thermal diffusivity is then determined by recording the temperature rise history at least at two different points on the surface simultaneously. The main advantage of the extended flash method presented here is that the necessity of knowing heat loss parameters, incident energy flux intensity, and absorption layer thickness are eliminated. The only parameters needed to determine the thermal diffusivity are the diameter of the sample and the temperature rise history at two different points on the surface. In comparison with the cooling method of Bayazitoglu et al. (1990), there is no size limitation which is required by this proposed approach.

For the proposed *two-step* method, the necessity of knowing the parameters associated with radiation heat transfer is eliminated by employing a cool-down experiment. This is followed by the pulse experiment that is applied to the same sample or another spherical sample. Once the transient measurements of the surface temperature are obtained, they are used as a substitute boundary condition, thus leading to an analytic expression or a computational solution of the temperature field. This is followed by a minimization method which leads to the thermal diffusivity value. The major advantages of the extended two-step flash method presented here are that in comparison with the cooling method of Bayazitoglu et al. (1990), there is no specimen size limitation and multidimensionality of the temperature field can be dealt with. The main drawback of the proposed technique is the great amount of experimental data that needs to be collected on the surface of the specimen. Finally, it should be noted that Murphy and Bayazitoglu (1992) have recently performed a computational study of the transient heat conduction in the same geometry considered here. A finite pulse time which resulted in a nonuniform temperature variation in the absorption layer was considered. The numerical solution option set forth in this paper is very similar to their work, and, therefore, that aspect of the problem will not be elaborated here.

A complementary study was also undertaken to experimentally validate the proposed technique. Samples of nickel and Inconel 718 superalloy were used, and their thermal diffusivity values were determined near their melting temperatures. The results obtained through applying the proposed method were then compared to previously published thermal diffusivity values.

III Overview of the Proposed Techniques

Regardless of the specific levitation method employed, the proposed techniques will utilize the components shown schematically in Fig. 1. The levitated sample is heated up to a uniform initial temperature (T_i) by an external heating device.

Nomenclature

Bi = Biot number, defined as $(4\epsilon_{\text{eff}}\sigma F T_{\text{sur}}^3 + h)R/k$
c_p = specific heat at constant pressure, J/kg·K
F = radiation view factor
h = convection heat transfer coefficient, W/m²·K
k = thermal conductivity, W/m·K
Q = incident energy flux, J/m²
Q_M = peak value of Q at the center of the beam, J/m²
r = radial coordinate within the sphere, m
r_b = radial distance from the center of the beam, m
r^* = dimensionless radial coordinate, defined as r/R
R = radius of the spherical sample, m
t = time, s
$t_{1/4}$ = rise time to quarter-maximum temperature, s
$t_{1/2}$ = rise time to half-maximum temperature, s
$t_{3/4}$ = rise time to three quarter-maximum temperature, s
t^* = dimensionless time, defined as $\alpha t/R^2$
T = temperature, K
T_i = initial temperature, K
T_{sur} = temperature of the surroundings, K
w_b = e^{-2} radius of the beam, m

Greek Symbols

α = thermal diffusivity, defined as $k/\rho c_p$, m²/s
ϵ_{eff} = effective hemispherical emissivity of the sample
θ = polar angle in the sphere
θ_0 = incidence angle of the beam, defined as $\sin^{-1}(w_b/R)$
Θ = temperature difference, defined as $(T - T_{\text{sur}})$, K
Θ^* = dimensionless temperature, defined as $\Theta/(Q_M/\rho c_p R)$
$\Theta^*_{\max}$ = maximum dimensionless temperature
$[\Theta^*]_{\infty G}$ = spatially uniform value of the dimensionless temperature at $t \to \infty$, when Bi = 0, for case of the Gaussian distribution incident energy
$[\Theta^*]_{\infty U}$ = spatially uniform value of the dimensionless temperature as $t \to \infty$, when Bi = 0, for case of the uniform incident energy
μ = transformed θ coordinate, defined as $\cos\theta$
μ_0 = $\cos\theta_0$
μ_m = the location of the measurement point on the surface of the sphere
ρ = density of the sample, kg/m³
σ = Stefan-Boltzmann constant

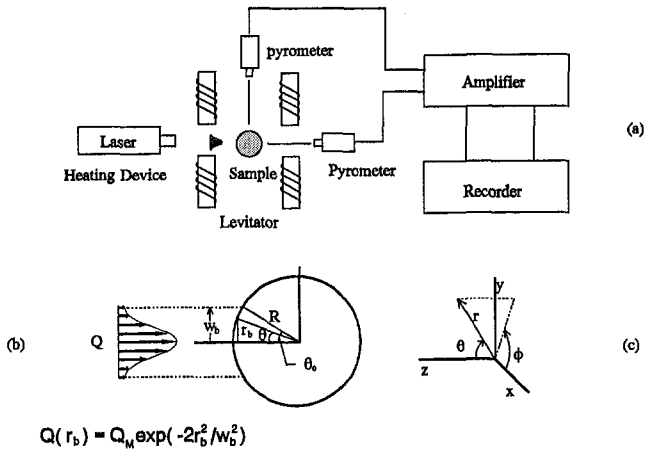

Fig. 1 Schematic diagram of the proposed technique

The details of the ensuing steps will depend on the specific technique employed.

Single-Step Method. For the single-step technique the sample is subjected to a very short burst of high-power radiant energy. The temperature of the irradiated surface area is elevated at once, and transient heat conduction takes place within the sample. Pyrometers are placed to detect the surface temperature rise history at least at two points. The detector signal is fed into the amplifier and filter which have a good time response. Transient temperature rise data are finally collected by using a digital data acquisition system or a digital oscilloscope. The values of the rise time to half-maximum temperature ($t_{1/2}$) can then be read from the temperature rise curves. Thermal diffusivity is then determined using the simple relations proposed in this paper.

Two-Step Method. An appropriately sized spherical sample with the initial temperature (T_i) is allowed to cool down. During the cool down experiments the surface temperature is recorded. The same sample or another one is then heated up in a similar fashion and subjected to a very short burst of high-power radiant energy. The surface temperature rise history along a meridional line ($0 \le \theta \le \pi$) is measured by pyrometers. The surface temperature rise can be fitted by a function $S(\theta, t)$, which will be taken as the new boundary condition replacing the actual nonlinear radiative boundary condition. The temperature field can then be solved either numerically or analytically. Finally, the thermal diffusivity can be evaluated by a minimization scheme.

IV Governing Equation

Both extended flash techniques are modeled as an axisymmetric unsteady heat conduction phenomenon ($T = T(r, \theta, t)$) within the sphere. For solid samples the theoretical formulation of the problem is exact, whereas for liquid samples it is assumed that the convection currents (buoyancy driven and Marangoni) within the sample are negligible due to the very short pulse duration. The recent study of Shen (1996) suggests that under microgravity conditions this assumption is valid if the thermocapillary Reynolds number ($\mathrm{Re} = -\partial\sigma/\partial T Q_M R^2/k\rho\nu^2$) is below 5×10^6. In order to perform the theoretical analysis, the following assumptions are made: (a) the spherical sample is homogeneous and the thermophysical properties are independent of temperature for the given temperature range of interest, and (b) the intensity distribution of the radiation energy flux of the incident beam is known. In cases where a laser is utilized, a Gaussian distribution (Fig. 1) is used:

$$Q(r_b) = Q_M \exp(-2r_b^2/w_b^2) \tag{1}$$

where Q_M is the peak energy flux at the center of the beam, r_b is the radial distance from the center of the beam, and w_b is the e^{-2} radius of the laser beam. Results obtained using both uniform ($Q(r_b)$ = constant) and Gaussian distributions for the single-step method are presented.

Setting the spherical coordinates, as shown in Fig. 1, this phenomenon is governed by the heat conduction equation

$$\frac{1}{r^2}\frac{\partial}{\partial r}\left(r^2\frac{\partial T}{\partial r}\right) + \frac{1}{r^2}\frac{\partial}{\partial \mu}\left[(1-\mu^2)\frac{\partial T}{\partial \mu}\right] = \frac{1}{\alpha}\frac{\partial T}{\partial t}. \tag{2}$$

The solution of Eq. (2) depends on the specific method under consideration. Therefore, the single-step technique is described first, followed by the two-step method.

V Single-Step Method

Boundary and Initial Conditions. Similar to the linearization technique discussed by Clark and Taylor (1975) and in order to obtain a closed-form analytic solution, the radiation boundary condition is linearized. Under this consideration and introducing $\Theta = T - T_{\mathrm{sur}}$, the boundary condition is

$$-k\frac{\partial \Theta}{\partial r}(R, \mu, t) = (4\epsilon_{\mathrm{eff}}\sigma F T_{\mathrm{sur}}^3 + h)\Theta(R, \mu, t) \tag{3}$$

subject to $|\Theta(R, \mu, t)| \ll T_{\mathrm{sur}}$. Alternately, by defining $r^* = r/R$ we can rewrite Eq. (3) as

$$-\frac{\partial \Theta}{\partial r^*}(1, \mu, t) = \mathrm{Bi}\,\Theta(1, \mu, t) \tag{4}$$

with the Biot number (Bi) being a measure of both convective and radiative surface heat losses. In the case of no heat loss, the Biot number equals zero.

The initial condition is specified by assuming that the pulse energy flux is absorbed instantaneously and uniformly in a thin layer of thickness g at the irradiated front surface ($r = R$, $0 \le \theta \le \theta_0$). This assumption is valid since the duration of the radiation burst is negligible compared to the rise time to half-maximum temperature characteristics being sought. Considering the surface curvature effect the initial condition can be written as

$$\Theta(r^*, \mu, 0) = \Theta_i + \frac{Q_M \exp\left[-2\dfrac{(1-\mu^2)}{(1-\mu_0^2)}\right]}{\rho c_p g}\mu$$

$$\left(\left(1 - \frac{g}{R}\right) \le r^* \le 1,\ \mu_0 \le \mu \le 1\right) \tag{5}$$

$$\Theta(r^*, \mu, 0) = \Theta_i \quad \text{rest of the sphere} \tag{6}$$

where g is the thin absorption depth, and $\Theta_i = T_i - T_{\mathrm{sur}}$. The angle θ_0 represents the incidence angle of the beam (also a measure of the relative size of the specimen and beam diameters).

Analytic Solution of the Temperature Field. The solution of the heat conduction Eq. (2), subjected to the boundary condition (4) and initial condition (5, 6), is obtained by applying the classic separation of variables method (Özisik, 1968). The analytic solution can be expressed as

$$\Theta(r^*, \mu, t) = \sum_{n=0}^{\infty}\sum_{p=1}^{\infty} A_{np} e^{-(\alpha t/R^2)\lambda_{np}^2}(\lambda_{np} r^*)^{-(1/2)} J_{n+(1/2)}(\lambda_{np} r^*) P_n(\mu) \tag{7}$$

where $J_{n+1/2}$ is the Bessel function of the first kind of order $(n + \frac{1}{2})$, P_n is the Legendre function of the first kind of order n, and λ_{np}'s are eigenvalues (roots of the transcendental equation)

$$(2Bi - 1)J_{n+(1/2)}(\lambda) + \lambda[J_{n-(1/2)}(\lambda) - J_{n+(3/2)}(\lambda)] = 0, \quad n = 0, 1, 2, \ldots. \quad (8)$$

The coefficient A_{np} in Eq. (7) is determined by applying the initial condition (5, 6), that is

$$A_{np} = \frac{1}{N_\mu N_r} \int_{\mu=-1}^{1} \int_{r^*=0}^{1} \Theta(r^*, \mu, 0) P_n(\mu) r^{*(3/2)} \times J_{n+(1/2)}(\lambda_{np} r^*) dr^* d\mu \quad (9)$$

where $n = 0, 1, 2, \ldots$ and $p = 1, 2, 3, \ldots$. In addition

$$N_\mu = \int_{\mu=-1}^{1} P_n^2(\mu) d\mu = \frac{2}{2n + 1} \quad (10)$$

$$N_r = \int_{r^*=0}^{1} \lambda_{np}^{-(1/2)} J_{n+(1/2)}^2(\lambda_{np} r^*) r^* dr^* = \frac{1}{8\lambda_{np}^{5/2}} \times [(1 - 2\,\mathrm{Bi})^2 + 4\lambda_{np}^2 - 4(n + \tfrac{1}{2})^2] J_{n+(1/2)}^2(\lambda_{np}). \quad (11)$$

In what follows, it is assumed that $\Theta_i = 0$. Then, the analytical expression for the temperature history is obtained by introducing the initial condition into Eq. (7)

$$\Theta(r^*, \mu, t) = \sum_{n=0}^{\infty} \sum_{p=1}^{\infty} \left[\frac{1}{N_\mu N_r} \frac{Q_M}{\rho c_p R} B_n \right] \times \left[\frac{\int_{1-\delta}^{1} r^{*(3/2)} J_{n+(1/2)}(\lambda_{np} r^*) dr^*}{\delta} \right] \times e^{-(\alpha t/R^2)\lambda_{np}^2} (\lambda_{np} r^*)^{-(1/2)} J_{n+(1/2)}(\lambda_{np} r^*) P_n(\mu) \quad (12)$$

where $\delta = g/R$ is the dimensionless absorption thickness. The quantity B_n is defined as

$$B_n = \int_{\mu=\mu_0}^{1} \exp\left[-2 \frac{(1 - \mu^2)}{(1 - \mu_0^2)} \right] \mu P_n(\mu) d\mu \quad (13)$$

for a Gaussian beam. Since the absorption layer is assumed to be very thin, the bracketed term in Eq. (12) can be replaced by its limiting value as δ nears zero, i.e.,

$$\lim_{\delta \to 0} \frac{\int_{1-\delta}^{1} r^{*3/2} J_{n+(1/2)}(\lambda_{np} r^*) dr^*}{\delta} = J_{n+(1/2)}(\lambda_{np}) + O(\delta). \quad (14)$$

Finally, the analytic expression for the dimensionless temperature variation at any point P on the surface is obtained by substituting expressions for N_r and N_μ into Eq. (12) giving

$$\Theta^*(1, \mu_m, t^*) = \sum_{n=0}^{\infty} \sum_{p=1}^{\infty} \frac{4(2n + 1)\lambda_{np}^2}{(1 - 2Bi)^2 + 4\lambda_{np}^2 - 4(n + \frac{1}{2})^2} \times B_n e^{-\lambda_{np}^2 t^*} P_n(\mu_m) \quad (15)$$

where two dimensionless variables for temperature (Θ^*) and time (t^*) are introduced. By examining Eq. (15) it can be concluded that the dimensionless temperature at a chosen point is independent of the incident energy intensity and absorption layer thickness.

Limiting Case of Bi = 0. In evaluating the surface temperature using Eq. (15), the case of zero eigenvalue ($\lambda_{n1} = 0$, $n = 0, 1, 2, \ldots$) needs to be handled in a special manner. It is not difficult to prove that regardless of the value of the Biot number, all the eigenvalues with $p = 1$ are equal to zero, except for $n = 0$ when Bi = 0. For the case of Bi = 0 the first term ($n = 0$, $p = 1$) will be a constant which is equal to the final spatially uniform dimensionless temperature of the sample when $t \to \infty$. This dimensionless temperature, denoted as $[\Theta^*]_\infty$, can be determined from a simple lumped heat balance analysis. For a Gaussian distribution of incident energy (Eq. 1)

$$[\Theta^*]_{\infty G} = \frac{(T - T_i)}{Q_M/\rho c_p R} = \frac{3}{2} \int_0^{\theta_0} \exp\left(-2 \frac{\sin^2 \theta}{\sin^2 \theta_0} \right) \sin \theta \cos \theta d\theta = \frac{3}{8} \left(1 - \frac{1}{e^2} \right) \sin^2 \theta_0. \quad (16)$$

The quantity $[\Theta^*]_{\infty G}$ depends on θ_0 only and its values for several incidence angles θ_0 are given in Table 1. For a uniform distribution of incident energy

$$[\Theta^*]_{\infty U} = \frac{3}{2} \int_0^{\theta_0} \sin \theta \cos \theta d\theta = \tfrac{3}{4} \sin^2 \theta_0. \quad (17)$$

The values of $[\Theta^*]_{\infty U}$ are also given in Table 1. As expected, beams with uniform distribution give rise to higher final temperatures when compared to beams with Gaussian distribution.

Analytic Surface Temperature History. In order to observe the general features of the analytic solution for the surface temperature, the variation of Θ^* versus t^* for three different points are explored. These points are denoted as P180, P135, and P90 and are located at $\theta = 180$ deg, 135 deg, and 90 deg, respectively. The summations of the infinite series were performed for $n = 29$ and $p = 500$. A parametric study showed the adequacy of this combination to guarantee convergence. The dimensionless temperature transient curves were obtained for the Biot number range of 0 to 2 and incidence angle range of 2 deg to 30 deg. The range of the Biot numbers was chosen only for illustrative purposes and no particular recommendation is implied. In realistic experiments, depending on the material being used and the details of the experimental set-up, a new range of Biot number might be appropriate.

A typical set of temperature transient curves are shown in Fig. 2. They correspond to the point P90, with $\theta_0 = 8$ deg and a Gaussian energy flux distribution. The effect of the incident flash ($t^* = 0$) is sensed with a time delay. The dimensionless

Table 1 Values of $[\Theta^*]_{\infty G}$ and $[\Theta^*]_{\infty U}$ for several incidence angles

θ_0	2 deg	4 deg	6 deg	8 deg	10 deg	15 deg	20 deg	25 deg	30 deg
$\Theta^*_{\infty G} \times 10^3$	0.3949	1.578	3.543	6.280	9.777	21.72	37.93	57.91	81.06
$\Theta^*_{\infty U} \times 10^3$	0.9135	3.650	8.195	14.53	22.62	50.24	87.73	134.0	187.5

time delays are of the order of $t^* = 0.05$ at P90 and $t^* = 0.1$ at P180. This is followed by a monotonic rise to a maximum temperature, its value being dependent on the heat loss parameter (Bi). For a given Biot number the characteristic dimensionless time $t^*_{1/2}$, which is defined as the rise time to the half-maximum temperature, is observed to be smaller at P90 when compared to the value at P180. After a long time, due to the heat exchange with the surroundings, the dimensionless temperature goes to zero for all cases with Bi $\neq$ 0. On the other hand temperature at every point in the sphere asymptotically approaches a constant value when there are no heat losses (Bi = 0). These values were in extremely close proximity to those presented in Table 1 and also served as a check for the accuracy of the number of summations mentioned above. The effect of the heat loss on the surface temperature history can be seen clearly in these figures. The bigger the Biot number, the greater the heat loss, and the maximum temperature decreases accordingly. In order to determine how $t^*_{1/2}$ varies with the Biot number, normalized temperature transient curves should be plotted at each point (Θ^*/Θ^*_{max} versus t^*). It is shown that the higher the Biot number, the smaller the value of the dimensionless rise time.

The effect of the relative size of the beam as compared to the sample diameter on the dimensionless temperature at P180 is given in Fig. 3, for Bi = 0.5 and the case of a uniform beam. For a given sample a higher maximum temperature is achieved with a wider beam simply because there is more incident energy absorbed. An interesting feature in this figure is that the rise times to the maximum or half-maximum temperatures are weakly dependent on θ_0, which is a property of the function B_n in Eq. (13). If the curves in Fig. 3 are normalized, it will be found that the normalized curves nearly lie on top of each other. A quantitative discussion of this effect will be presented below.

Temperature Rise Characteristics. Parallel to the work of Parker et al. (1961) the dimensionless rise time to the half-maximum temperature ($t^*_{1/2}$) can be found from the dimensionless temperature transient history. In practical terms, this choice of the half-rise time requires that the flash incidence time is known precisely. The quantity ($t^*_{1/2}$) strongly depends on the Biot number (particularly when Bi is small) and the location of the measurement point (μ_m), and weakly on the incidence angle of the beam (θ_0). The relationship between $t^*_{1/2}$ and the Biot number for the three measurement locations with a Gaussian distribution are given in Fig. 4 for the case of $\theta_0 = 8$ deg. For a fixed measurement point, the rise time to the half-maximum temperature decreases with the increasing of the Biot number. Based on ease of mathematical manipulations and

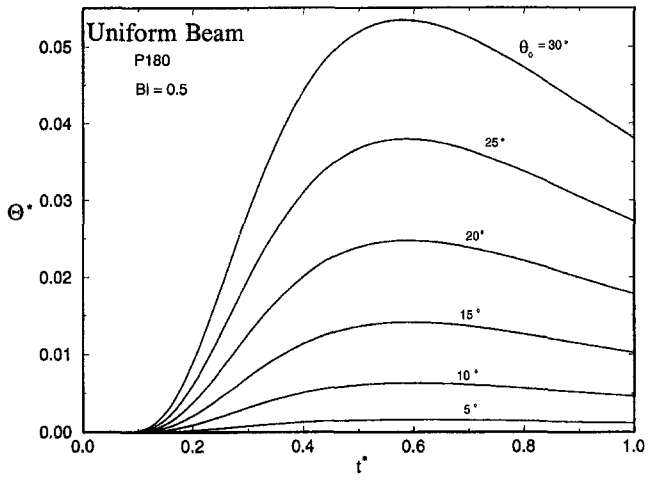

Fig. 3 Dimensionless transient surface temperature curves at P180 for different incidence angles with a uniform distribution (Bi = 0.5)

observed trends, an exponential function was used to fit the variation of $t^*_{1/2}$ with Bi. The fitting function is written as

$$t^*_{1/2} = ae^{-b\sqrt{Bi}}. \tag{18}$$

The values of the positive parameters a and b for different measurement locations and incidence angles are listed in Tables 2 and 3 for both Gaussian and uniform flux distributions. The correlation coefficients ranged from 0.995 to 0.998, suggesting excellent curve fit.

Thermal Diffusivity Determination. Based on the analytic expressions presented above, a simple one-step method to determine the thermal diffusivity is proposed. Suppose the temperature transient curves at points P_1 and P_2 have been recorded. The rise time to the half-maximum temperature $t_{1/2}$ could then be determined. These quantities are denoted as $[t_{1/2}]_1$ and $[t_{1/2}]_2$, respectively, corresponding to points P_1 and P_2. For a given energy distribution and incidence angle, the relationships between $t^*_{1/2}$ and Bi at points P_1 and P_2 are expressed using Eq. (18). Because the Biot number should be the same in both equations, it can be eliminated, leading to

$$\alpha = A\frac{[t_{1/2}]_2^B}{[t_{1/2}]_1^{1+B}}R^2 \tag{19}$$

with the parameters A and B given by

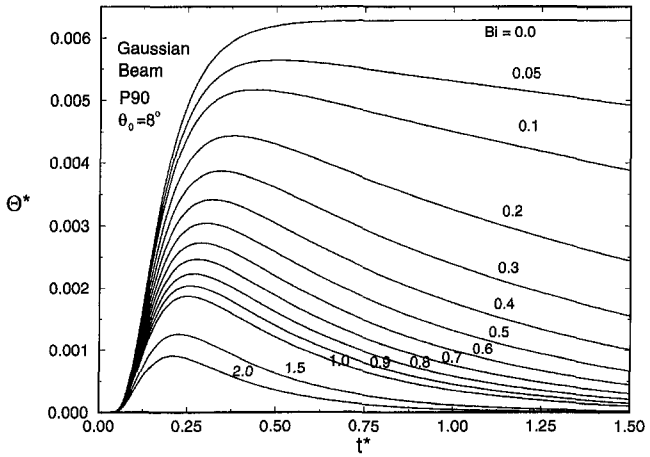

Fig. 2 Dimensionless transient surface temperature curves at P90, with a Gaussian distribution for an incidence angle of $\theta_0 = 8$ deg

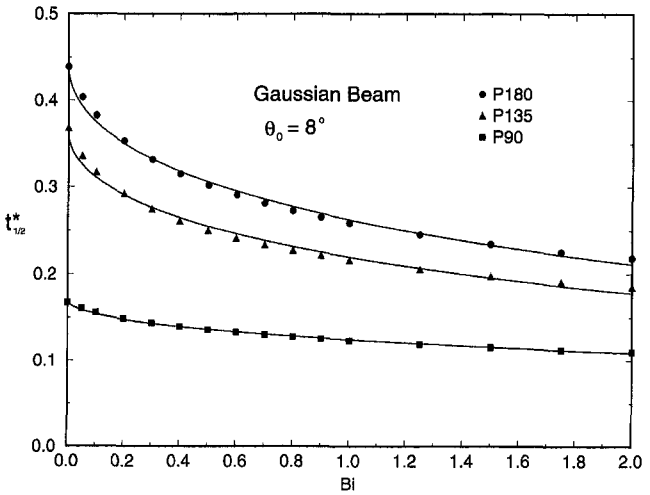

Fig. 4 The relationship between $t^*_{1/2}$ and Bi with a Gaussian distribution ($\theta_0 = 8$ deg)

Table 2 The value of the parameter (a) in the fitting function $t^*_{1/2} = a \exp(-b\sqrt{\text{Bi}})$

Gaussian Energy Flux Distribution						
θ_0	2 deg	4 deg	6 deg	8 deg	10 deg	15 deg
P180	0.44275	0.44259	0.44234	0.44198	0.44152	0.43995
P135	0.36550	0.36535	0.36511	0.36476	0.36432	0.36280
P90	0.17118	0.17101	0.17071	0.17030	0.16977	0.16794
Uniform Energy Flux Distribution						
θ_0	5 deg	10 deg	15 deg	20 deg	25 deg	30 deg
P180	0.44233	0.44094	0.43863	0.43545	0.43139	0.42649
P135	0.36510	0.36376	0.36153	0.35843	0.35450	0.34973
P90	0.17071	0.16909	0.16637	0.16251	0.15763	0.15152

$$A = \left[\frac{a_1^{b_2}}{a_2^{b_1}}\right]^{1/(b_2-b_1)} \qquad B = \frac{b_1}{b_2 - b_1}. \tag{20}$$

The only physical quantities that need to be known in order to determine the thermal diffusivity are the size of the specimen and the simultaneously recorded temperature rise curves at least at two different points on the surface of the sphere.

Initial Nonuniformity of the Temperature Field. In deriving Eq. (19) and the associated constants, it was assumed that the initial temperature field is uniform. Extending the work of Li (1993) to account for realistic induction heating arrangements with multiple coils, Woods (1995) has discussed the relation between the temperature nonuniformities and the variation of the constants A and B in Eq. (19), showing that initial temperature nonuniformities are of little consequence in practical levitation systems.

VI Two-Step Method

For the two-step method Eq. (2) is still valid. The nonlinearity of the radiative boundary condition is avoided by substituting it with a measured surface temperature history of the form

$$T(R, \mu, t) = S(\mu, t) \quad \text{at} \quad r = R. \tag{21}$$

The appropriate initial temperature field within the specimen is given by

$$T(r, \mu, 0) = G(r, \mu) \quad \text{at} \quad t = 0. \tag{22}$$

The numerical and analytical solutions of Eq. (2), in conjunction with the boundary and initial conditions (Eqs. (21) and (22)), are discussed next.

Numerical Solution. The heat conduction problem formulated above can conveniently be solved using a variety of computational techniques. The methodology of these techniques is covered in a number of heat transfer and specialized texts, and only a brief overview is discussed here. In general, the computational domain of the sphere will be covered with a two-dimensional grid system. Grids with fine density will be placed near the surface and in the flash impact area. Given the boundary and initial conditions above, and a value for the thermal diffusivity, the transient temperature field will be determined. The computational techniques are easier to be implemented for a number of reasons. First of all there are a number of software packages that can conveniently be tailored for the problem at hand. The major advantage of using a computational approach is that details of the experimental conditions, such as the finite pulse time duration and two-dimensionality of the heated zone at $t = 0$ can easily be dealt with. The major shortcoming of this approach is that the entire domain of the sphere must be solved for.

Analytic Solution. In order to arrive at an analytic solution of the same problem, it is assumed that the short duration pulse energy is absorbed instantaneously and uniformly within a layer of material which is very thin compared to the radius of the sample. The initial condition, which is based on this assumption, was already presented in Eqs. 5 and 6. It should be noted that with a finite flash time (e.g., Murphy and Bayazitoglu, 1992), a two-dimensional temperature variation will be observed in the absorption layer. The theoretical analysis is still valid for radiation bursts of finite duration, although the problem is analytically more complicated. The solution of this heat diffusion equation subjected to the prescribed boundary and initial conditions is obtained by applying the Bessel-Legendre transformation (Özisik, 1968). The details are not repeated here but have been outlined by Shen (1996). The major advantage of the analytic technique is that the entire domain does not need to be considered and only the surface heat flux values are of interest.

Thermal Diffusivity Determination. The analytic expression $T(r, \mu, t)$ or the numerically obtained temperature field should satisfy the real boundary condition at every point on the sample surface which requires that

$$-k \left.\frac{\partial T}{\partial r}\right|_{r=R} = \epsilon_{\text{eff}} \sigma F (T^4_{r=R} - T^4_{\text{sur}}). \tag{23}$$

Because the surface heat balance Eq. (23) has to be satisfied at every point and at all times, the problem is transformed into a minimization problem of the function Γ that is defined as

$$\Gamma = \sum_{i=1}^{I} \sum_{j=1}^{J} \left[\left.\frac{\partial T}{\partial r}\right|_{r=R} + \frac{M}{\alpha} (T^4_{r=R} - T^4_{\text{sur}}) \right]^2_{ij} \tag{24}$$

where the summation is carried over all the measurement locations ($i = 1$ to I) and discrete time steps ($j = 1$ to J). The radiation parameter ($M = \epsilon_{\text{eff}} \sigma F / \rho c_p$) is introduced in Eq. (24). In order to determine this constant, a cool-down experiment needs to be performed similar to the procedure outlined by Bayazitoglu et al. (1990), and its details are not repeated here.

VII Experimental Validation

In order to validate the merits of the proposed techniques, ground based experiments were performed using solid specimen near their melting temperatures. These experiments can be used to effectively model tests performed on levitated liquid specimen under microgravity conditions. Furthermore, results obtained for solid specimen may be checked against solid phase property data available in the literature.

Experimental Set-Up. A schematic diagram of the apparatus is shown in Fig. 5. Specimens were 12.7 mm and 6.35 mm in diameter spheres of 4N-purity Nickel (ESPI, Agoura, CA) and Inconel-718 (Industrial Techtonics, Ann Arbor, MI). The

Table 3 The value of the parameter (b) in the fitting function $t^*_{1/2} = a \exp(-b\sqrt{\text{Bi}})$

Gaussian Energy Flux Distribution						
θ_0	2 deg	4 deg	6 deg	8 deg	10 deg	15 deg
P180	0.52079	0.52080	0.52080	0.52082	0.52083	0.52090
P135	0.50656	0.50667	0.50685	0.50709	0.50740	0.50848
P90	0.31452	0.31489	0.31551	0.31639	0.31745	0.32133
Uniform Energy Flux Distribution						
θ_0	5 deg	10 deg	15 deg	20 deg	25 deg	30 deg
P180	0.52081	0.52085	0.52092	0.52106	0.52122	0.52135
P135	0.50687	0.50781	0.50936	0.51160	0.51461	0.51819
P90	0.31553	0.31884	0.32434	0.33219	0.34372	0.35794

melting temperature of Nickel is 1728 K, whereas Inconel-718 has a melting range of 1533–1609 K (Inco Alloys Int'l., 1985). All specimen were manufactured with a diameter tolerance of 2.5 μm. The specimen are designated by composition and size as NI06, NI12, IN06, and IN12. A pinpoint hole of one mm in depth was drilled into each specimen which enabled them to be mounted on a one mm in diameter tungsten support wire. The support wire was ground to a fine point at the location of specimen contact in order to retard unwanted heat transfer via conduction down the wire. The specimen were enclosed within a quartz tube containing "commercially pure" argon gas. Heating of the specimen was accomplished using a 451 kHz radio-frequency induction heater with a current of approximately 200 amperes (rms). The induction heating coils were wrapped around the outside of the quartz tube.

Laser Flash Experiments. Multiple laser flash experiments were performed on each of the four specimens. They were heated until they attained a constant bulk temperature, as measured by the optical pyrometer. A line-scan radiometer (LSR) consisting of a 256-element silicon array detector (EG&G Reticon #RL0256TB) was sighted along the vertical diameter of the specimen and used to scan the specimen and record the surface temperature distribution along this vertical length. Each picture element (pixel) of the LSR array recorded temperature independently. The pixel-to-pixel time displacement was 470 μs, giving the entire array an integration time of 0.1205 seconds. After about one second of scanning a pulse of CO_2 laser radiation was focused onto the top of the specimen ($\theta = 0°$). The e^{-2} radius of the Gaussian beam was 0.1 mm and its total power was adjustable up to approximately 100 W. Measurement of the specimen surface temperature continued for about 20 seconds after the end of the laser pulse. Each experiment yielded a large data file containing the temperature transient history of the entire array.

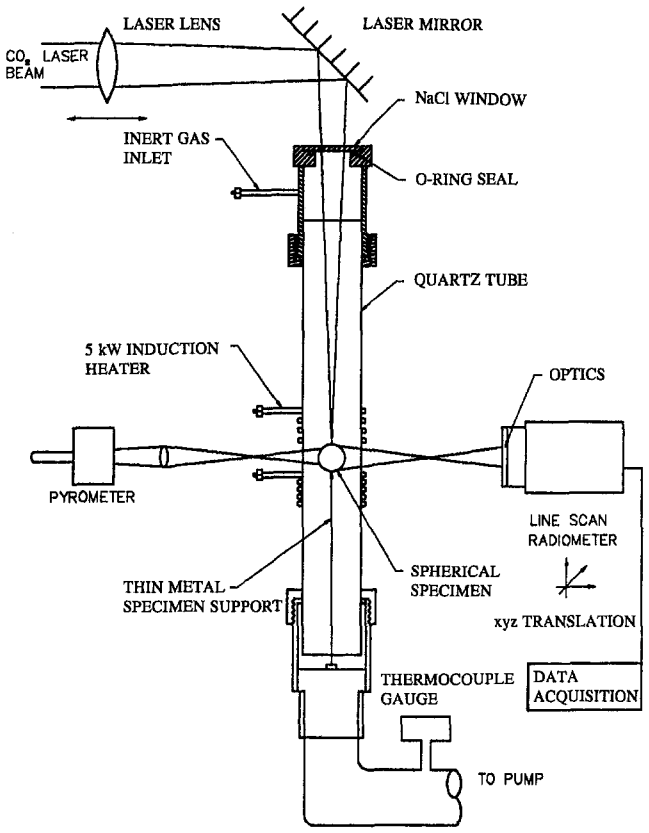

Fig. 5 Schematic diagram of the experimental set-up

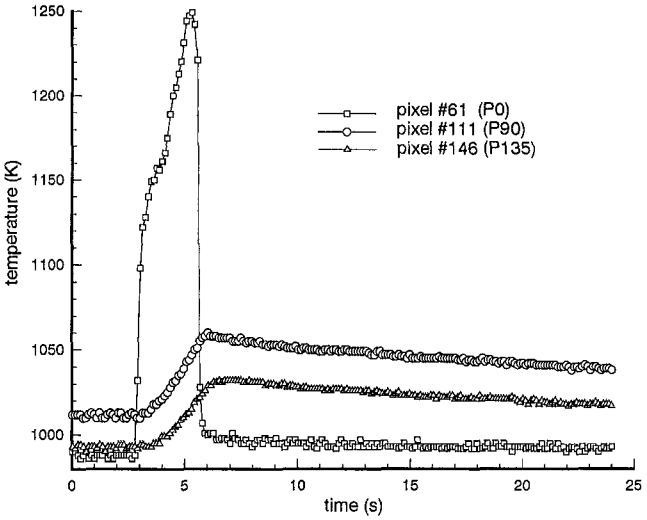

Fig. 6 Temperature rise histories on the surface of the nickel specimen NIO6

Figure 6 is an example of the temperature rise histories at points P0, P90, and P135 on the surface of the NI06 Nickel specimen. The drastic increase and drop of temperature history at P0 ($r = R$, $\theta = 0°$) indicate the instants when the laser heating starts and ends. Therefore, the pulse time duration can be estimated. By examining the temperature rise history at P90 ($r = R$, $\theta = 90°$) and P135 ($r = R$, $\theta = 135°$), shown in Fig. 6, it can be seen straightforwardly that they exhibit the same characteristics as predicted by the theoretical solution presented in Figs. 2 and 3. It should be noted that some nonuniformity at time $t = 0$ was observed although it is generally desirable that the specimen's initial temperature be uniform. This nonuniformity is attributable to two possible causes: (1) the induction heating coil configuration most likely produced a nonuniform temperature distribution in the specimen; and (2) part of the perceived nonuniformity may be due to imprecise temperature readings as a result of imaging limitations.

Modified Data Reduction Methods. In order to tailor the theory of the proposed single-step technique to realistic experimental conditions, two modifications were worked out. Details are given by Shen (1996) and only a brief discussion is presented here.

Two Characteristic Points Method. In applying Eq. (19) the precise measurement of the quantity $t_{1/2}$, which is measured from $t = 0$, is called for. However, the definition of the zero-time is vague. The realistic pulse duration is always finite. Therefore, there are at least two different ways to define the zero-time, i.e., it may be defined as the time when the laser is turned on or turned off. To avoid the uncertainty of zero-time definition and measurement, a two-point data reduction method is presented here. This method is expected to produce more reliable results because it has the advantage of using more information from the temperature rise curves.

Parallel to the above single-step method, the use of characteristic quantity $(t_{3/4} - t_{1/4})$, instead of $t_{1/2}$, is recommended. This is very convenient in the sense that if an error is introduced in measuring $t_{1/2}$, this error will be removed. For a given pulse energy distribution and the incidence angle θ_0, the thermal diffusivity can be determined from the following formula (Shen, 1996):

$$\alpha = A' \frac{[t_{3/4} - t_{1/4}]_2^{B'}}{[t_{3/4} - t_{1/4}]_1^{1+B'}} R^2 \qquad (25)$$

which is similar to Eq. (19). The coefficients A' and B' for this

$(t_{3/4} - t_{1/4})$ single-step method are given in Table 4 assuming P_1 and P_2 are chosen as P90 and P180 (or P135), respectively.

Green's Function Method. In the derivation of the single-step method the pulse duration is assumed to be negligible in comparison with the characteristic rise time for the temperature excursion of the specimen. However, this assumption may not be valid due to the limitation of the experimental setup. In many cases the pulse duration is comparable to the characteristic temperature rise time, therefore, the finite-pulse-time effect is introduced. Since the original flash method was proposed by Parker et al. (1961), the finite-pulse-time effect has been studied by a number of researchers (e.g., Taylor and Cape, 1964) who have provided correction factors for slab and cylinder samples. But these methods are limited to the specific experimental setup and geometry shape of the specimen. To solve this problem more generally a new Green's Function Method is proposed here to resolve the finite-time-pulse duration effect.

This method is based on the Duhamel's Theorem and Green's Function theory. According to Duhamel's Theorem, if a linear system is subjected to a finite square pulse $F(t)$

$$F(t) = Q \quad 0 \le t \le \tau$$
$$= 0 \quad t > \tau \tag{26}$$

in which Q could be a function of spatial coordinates, then the temperature response at any location $\mathbf{x}$ is given by

$$T(\mathbf{x}, t) = \int_0^t F(t')G(\mathbf{x}, t - t')dt'$$
$$= \int_0^t QG(\mathbf{x}, t - t')dt' \tag{27}$$

where $G(\mathbf{x}, t)$ is the Green's function, i.e., the system response function to the instantaneous pulse of unit strength. The physical meaning of $QG(\mathbf{x}, t)$ is no more than that of the solution we derived in Section V. Therefore, for the system under consideration here, $QG(\mathbf{x}, t)$ is just the right side of the Eq. (15), with difference of a constant factor only.

In case of a finite-time-pulse duration the surface temperature signature information of the instantaneous pulse response can be extracted from the temperature response to the finite-time-pulse simply by performing the differential operation on Eq. (27), which produces,

$$Q \cdot G(R, \theta, t) = \frac{dT(R, \theta, t)}{dt} \tag{28}$$

where the generic spatial location $\mathbf{x}$ is replaced by (R, θ) because we are interested in the temperature response on the surface. Once the temperature history is obtained from the above equation, the thermal diffusivity determination formulae (Eqs. (19) and (25)) can be applied. Compared to other techniques this method has provided a more general way to resolve the finite-time-pulse duration problem, and it has no geometry limitation.

Table 4 The values of coefficients A' and B' in Eq. (25) for the $(t_{3/4} - t_{1/4})$ method

Gaussian Energy Flux Distribution, P_1 = P90, P_2 = P180						
θ_0	2 deg	4 deg	6 deg	8 deg	10 deg	15 deg
A'	0.012900	0.012925	0.012975	0.013065	0.013178	0.013504
B'	2.377393	2.375741	2.372081	2.364891	2.356159	2.333248
Gaussian Energy Flux Distribution, P_1 = P90, P_2 = P135						
θ_0	2 deg	4 deg	6 deg	8 deg	10 deg	15 deg
A'	0.021541	0.021558	0.021595	0.021668	0.021753	0.021997
B'	1.983465	1.982886	1.981251	1.977447	1.973245	1.962867

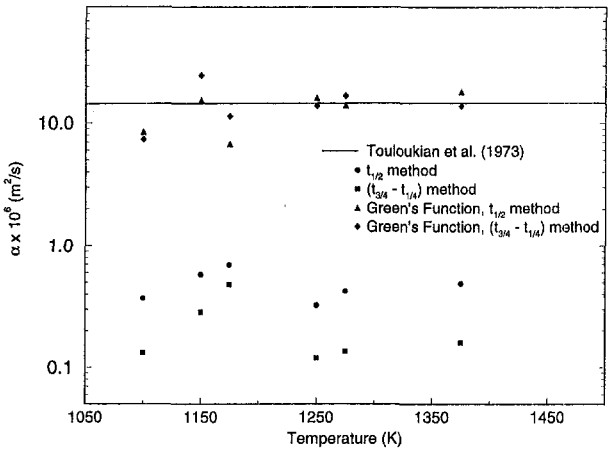

Fig. 7 Experimentally determined thermal diffusivity values for nickel specimen

Evaluation of Thermal Diffusivity Values. Four different methods of rise time extraction were employed to determine the thermal diffusivity of Nickel and Inconel-718 specimen at different temperatures. Extraction Methods 1 and 2 treated the beam as a true energy pulse, i.e., its duration was neglected and all the rise times were measured from the point at which the beam was turned on. From the transient temperature histories of pixels P90 and P135, the rise times $(t_{1/2})$ and $(t_{3/4} - t_{1/4})$ were extracted and the experimental values for thermal diffusivity were calculated using Eqs. (19) and (25). Since in some cases the beam was on for as much as three seconds, these extractions were altogether inaccurate and were employed simply to observe the consequences of neglecting the pulse width. To address the problem associated with finite-time-pulse duration, Extraction Methods 3 and 4 were utilized. These methods employ the Duhamel's Theorem to obtain the system response to a true instantaneous pulse from the data on the system response to a finite pulse. The differentiation was calculated using a five point formula. Then, the $(t_{1/2})$ and the $(t_{3/4} - t_{1/4})$ single-step methods were applied to determine the thermal diffusivity.

The experimentally determined thermal diffusivity values for the Nickel specimen as a function of temperature are shown in Fig. 7. The thermal diffusivity of Nickel, as given by Touloukian et al. (1973), is represented by the solid curve. For the temperature range covered by the flash experiments, the thermal diffusivity of Nickel remains fairly constant at a value of approximately 1.47×10^{-5} m^2/s. The thermal diffusivity values determined by using the technique proposed here for the Inconel-718 specimen are shown in Fig. 8, along with the thermal diffusivity curve calculated from property data provided by Inco Alloys Int'l. (1985). For the indicated temperature range Inconel-718 has a thermal diffusivity of approximately 4.2×10^{-6} m^2/s. As seen in Figs. 7 and 8 Extraction Methods 1 and 2 yielded thermal diffusivity values which were consistently much lower than reference values by more than an order of magnitude. This is consistent with the observation of Taylor and Cape (1964) that the finite-time-pulse results underestimate the thermal diffusivity values. Clearly, in our experiments the laser pulse widths were too long to be ignored. Extraction Methods 3 and 4 yielded thermal diffusivity values which were generally more in line with the accepted thermal diffusivity values of the two materials because the finite-time-pulse duration is taken into account, and the uncertainty of zero-time estimation is removed for Extraction Method 4. The comparison of the thermal diffusivity values among Extraction Methods 1 and 2 and Extraction Methods 3 and 4 proves that the Green's Function method is a good technique to resolve the problem associated

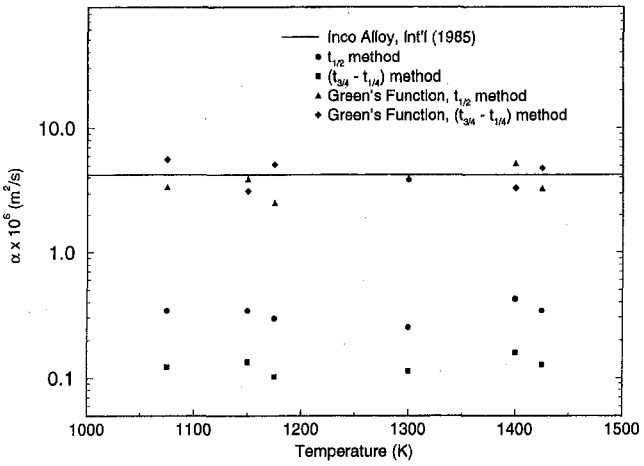

Fig. 8 Experimentally determined thermal diffusivity values for Inconel-718 specimen

with the finite-time-pulse duration. These encouraging results suggest that the proposed single-step methods can prove to be a reliable thermal diffusivity determination method for the containerless measurement environment.

Experimental Uncertainty Analysis. By examining the thermal diffusivity determination formulae (Eqs. 19 and 25), it can be seen that the errors in the measurements of specimen radius, temperature characteristic rise times, and incidence angle will propagate through the equations to produce bias and precision errors. For the sake of convenience the characteristic rise time in Eqs. (19) and (25) is denoted as t_c, i.e., t_c represents $t_{1/2}$ for Eq. (19) and $(t_{3/4} - t_{1/4})$ for Eq. (25). The uncertainty in thermal diffusivity is controlled by the following error propagation equation (Coleman and Steele, 1989):

$$\left[\frac{U_\alpha}{\alpha}\right] = \left[(1+B)^2\left(\frac{U_{t_{c1}}}{t_{c1}}\right)^2 + B^2\left(\frac{U_{t_{c2}}}{t_{c2}}\right)^2 + 2\left(\frac{U_R}{R}\right)^2 + \left(\frac{U_A}{A}\right)^2 + B^2 \ln\left(\frac{t_{c2}}{t_{c1}}\right)\left(\frac{U_B}{B}\right)^2\right]^{1/2}. \quad (29)$$

Equation (29) shows that the uncertainty in α depends not only on the uncertainties in t_{c1}, t_{c2}, R, A, and B, but also on the value of B and $\ln(t_{c2}/t_{c1})$. The uncertainty in α will thus vary with the specific operating conditions, even if the uncertainties in t_{c1}, t_{c2}, R, A, and B are all constant. In a situation such as this, a parametric study of the quantities B and $\ln(t_{c2}/t_{c1})$ is demanded.

The parameter B is dependent on the nature of the beam energy flux distribution and the beam incidence angle θ_0. In all experiments the flux distribution was Gaussian, thus the uncertainty in B will depend only on the incidence angle θ_0. However, we have concluded that the value B is a very weak function of θ_0. Therefore, an error in the incidence angle measurement does not bring about a big variation of the value of parameter B. A parametric study showed that the uncertainty in α does not change much for a reasonable variation range of B.

The quantity $\ln(t_{c2}/t_{c1})$ depends on the specimen material and is always greater than zero (i.e., $t_{c2} > t_{c1}$) if P_1 and P_2 are taken as P90 and P135, as the case is in the present experimental validations. For the materials we used in our validation experiments, i.e., Nickel and Inconel-718, the quantity (t_{c2}/t_{c1}) ranged from 1.65 to 3.82 when the Green's Function Method was applied. For the general case a parametric study of (t_{c2}/t_{c1}) in the range of 1 to 20 was performed. The solid line in Fig. 9 exhibits the variation of the uncertainty in α as a function of the quantity $\ln(t_{c2}/t_{c1})$ for the $(t_{3/4} - t_{1/4})$ method in which all the uncertainties in t_{c1}, t_{c2}, R, A, and B are assumed to be 1 percent. The value of B was chosen for the case of $\theta_0 = 2$ degrees. It can be seen that the uncertainty in α would be higher with the increasing of the quantity $\ln(t_{c2}/t_{c1})$.

In the derivation of Eq. (29) we treated the $(t_{1/2})$ and $(t_{3/4} - t_{1/4})$ single-step methods to be similar for the sake of simplification. However, there exists one additional uncertainty in the measurement of zero-time (t_0) when applying the $(t_{1/2})$ method. This will add another term in the uncertainty transmission equation (Eq. 29), i.e., $[((1+B)^2 + B^2)(U_{t0}/t_0)^2]$. Results of a parametric study of the influence of the uncertainty in t_0 on the uncertainty in α for the range of $(t_{c2}/t_{c1}) = 1$ to 20 is shown in Fig. 9. It is observed that for a given value of (t_{c2}/t_{c1}), the $(t_{3/4} - t_{1/4})$ method will offer more accurate results. The reasoning behind this conclusion is that the uncertainties in t_{c1} and t_{c2} are the uncertainties in the measurement of the characteristic rise time difference for the $(t_{3/4} - t_{1/4})$ method; in other words the systematic measurement error has been removed. On the other hand the uncertainties in t_{c1} and t_{c2} are the uncertainties in the measurement of the characteristic rise time itself for the $(t_{1/2})$ method. Therefore, it is expected that the uncertainties in t_{c1} and t_{c2} are higher for the $(t_{1/2})$ method in comparison to the $(t_{3/4} - t_{1/4})$ method because of nonexistence of the systematic error.

In the validation experiments presented in the previous section, the uncertainties in the measurement of characteristic rise time t_c and the zero-time are assumed to be 2 percent and 4 percent, respectively. The uncertainties in coefficients A and B are estimated as 0.5 percent. The measurement error of the radius is about 25 μm. Thus, the uncertainty in R is taken to be 0.787 percent. Taking the range of (t_{c2}/t_{c1}) to be 1.65 to 3.82 when the Green's Function Method was applied in the experiments, then the uncertainty in the thermal diffusivity is estimated to be 12 percent and 7 percent for the $(t_{1/2})$ and $(t_{3/4} - t_{1/4})$ single-step methods, respectively.

As for the error introduced by the linearization of the surface boundary condition (Eq. 3), it can be kept low by maintaining a small temperature differential between the specimen and the surroundings. In situations where it is difficult to obtain such a hot-wall furnace, the one-step method can serve as an initial estimate and more accurate data can be obtained using the two-step approach. We estimate the error due to taking of the Biot number constant to be small since the specimen's temperature stays within a small range, thus, its thermal conductivity and emissivity should remain constant. Within the low-pressure (20 kPa) test section employed here, the convection contribution was shown to be negligible (Woods, 1995). The temperature of the surroundings would remain fairly constant for such short-

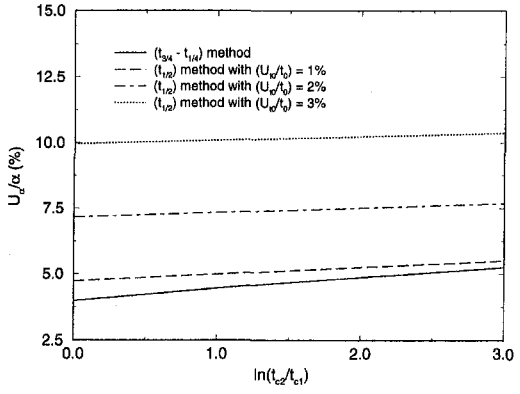

Fig. 9 Uncertainty in thermal diffusivity as a function of the quantity $\ln(t_{c2}/t_{c1})$

duration experiments, thereby making the constant Biot number assumption a well founded one. This, of course, does not mean that the surface heat transfer is constant, as evident from Eq. (4).

VIII Conclusions

In order to determine the thermal diffusivity of high-temperature solid and liquid materials, two extended containerless flash techniques that are applicable to levitated spherical specimen are proposed. Both methods are modeled as an axisymmetric transient conduction heat transfer problem within the sphere. For the single-step method the thermal diffusivity is determined by knowing the sample diameter and recording the temperature rise at least at two different points on the surface of the sphere simultaneously. The main advantage of this method is that the thermal diffusivity can be determined without the necessity of knowing heat losses at the surface and other thermophysical properties of the materials, which are often not available.

For the two-step method the problem of nonlinearity that arises from the radiative heat transfer boundary condition is overcome by replacing it with the measured time-dependent surface temperature data. Upon obtaining the temperature field the determination of the thermal diffusivity turns into a minimization problem, whereby the difference between the actual surface boundary condition and the solution is minimized. Comparison of the experimentally determined thermal diffusivity values to previous data show that the proposed techniques promise to provide reliable data given that accurate temporally resolved temperature rise data are available.

Acknowledgements

The work reported in this paper was supported by the NASA's Office of Commercial Programs under Grant NAGW-1192. The partial support of this work by LEQSF under agreement with NASA/LSU (1991-96)-01 and NASA/LaSPACE under grant NGT-40039 is acknowledged.

References

Bayazitoglu, Y., and Suryanarayana, P. V. R., 1990, "Transient Radiative Heat Transfer From a Sphere Surrounded by a Participating Medium," ASME JOURNAL OF HEAT TRANSFER, Vol. 111, pp. 713–718.

Bayazitoglu, Y., Suryanarayana, P. V. R., and Sathuvalli, U. B., 1990, "High-Temperature Thermal Diffusivity Determination Procedure for Solids and Liquids," *J. Thermophysics and Heat Transfer,* Vol. 4, pp. 462–468.

Clark III, L. M., and Taylor, R. E., 1975, "Radiation Loss in the Flash Method for Thermal Diffusivity," *J. Appl. Phys.,* Vol. 46, pp. 714–719.

Coleman, H. W., and Steele Jr., W. G., 1989, *Experimentation and Uncertainty Analysis for Engineers,* John Wiley & Sons, New York, NY, pp. 40–118.

Inco Alloys International, 1985, "Inconel Alloy 718," 4th ed., Huntington, West Virginia.

Li, B. Q., 1993, "The Magneto-Thermal Phenomenon in EM Levitation Processes," *International Journal of Engineering Science,* Vol. 31, pp. 201–220.

Murphy, J., and Bayazitoglu, Y., 1992, "Laser Flash Thermal Diffusivity Determination Procedure for High-Temperature Liquid Metals," *Numerical Heat Transfer: Part A,* Vol. 22, pp. 109–120.

Özisik, M. N., 1968, *Boundary Value Problems of Heat Conduction,* International Textbook Company, Scranton, Pennsylvania, pp. 223–225 and 228–230.

Parker, W. J., Jenkins, R. J., Butler, C. P., and Abbott, G. L., 1961, "Flash Method of Determining Thermal Diffusivity, Heat Capacity, and Thermal Conductivity," *J. Appl. Phys.,* Vol. 32, pp. 1679–1684.

Schriempf, J. T., 1972, "A Laser Flash Technique for Determining Thermal Diffusivity of Liquid Metals at Elevated Temperatures," *Rev. Sci. Instrum.,* Vol. 43, pp. 781–786.

Shen, F., 1996, "Novel Pulse Techniques for Containerless Thermal Diffusivity Determination: Development of Methods and Numerical Analysis of Thermocapillary and Buoyant Flows," Ph.D. Thesis, Department of Mechanical Engineering, Auburn University.

Taylor, R. E., and Cape, J. A., 1964, "Finite Pulse-Time Effects in the Flash Diffusivity Technique," *Applied Physics Letters,* Vol. 5, pp. 212–213.

Taylor, R. E., and Maglic, K. D., 1984, "Pulse Method for Thermal Diffusivity Measurement," in *Compendium of Thermophysical Property Measurement Methods,* Vol. 1, K. D. Maglic ed., Plenum Publishing Corporation, pp. 305–336.

Touloukian, Y. S., Powell, R. W., Ho, C. Y., and Nicolaou, M. C., 1973, *Thermophysical Properties of Matter; Vol. 10: Thermal Diffusivity,* IFI/Plenum Press, NY.

Woods, M. C., 1995, "Analysis and Evaluation of Extended Laser Flash Methods for Thermal Diffusivity Determination of High-Temperature Materials," MS Thesis, Department of Mechanical Engineering, Auburn University.

Size and Interface Effects on Thermal Conductivity of Superlattices and Periodic Thin-Film Structures

G. Chen
Assistant Professor and
Warren Faculty Scholar
gchen@acpub.duke.edu
Mem. ASME
Department of Mechanical Engineering and
Material Science,
Duke University,
Durham, NC 27708

Superlattices consisting of alternating layers of extremely thin films often demonstrate strong quantum size effects that have been utilized to improve conventional devices and develop new ones. The interfaces in these structures also affect their thermophysical properties through reflection and transmission of heat carriers. This work develops models on the effective thermal conductivity of periodic thin-film structures in the parallel direction based on the Boltzmann transport equation. Different interface conditions including specular, diffuse, and partially specular and partially diffuse interfaces, are considered. Results obtained from the partially specular and partially diffuse interface scattering model are in good agreement with experimental data on GaAs/AlAs superlattices. The study shows that the atomic scale interface roughness is the major cause for the measured reduction in the superlattice thermal conductivity. This work also suggests that by controlling interface roughness, the effective thermal conductivity of superlattices made of bulk materials with high thermal conductivities can be reduced to a level comparable to those of amorphous materials, while maintaining high electrical conductivities. This suggestion opens new possibilities in the search of high efficiency thermoelectric materials.

Introduction

Thermal conductivities of thin-film structures have attracted considerable attention in the last decade. Experimental results on different materials demonstrate that the thermal conductivities of thin films are often smaller than those of their corresponding bulk materials (Decker et al., 1984; Cahill et al., 1989; Lambropoulos et al., 1991; Tien and Chen, 1994). The causes for the reduction of the thin-film thermal conductivity include the microstructural differences between thin films and their bulk media and the boundary and interface effects. Different models have been established for the thermal conductivities of thin films. Similar to the modeling of the thermal conductivities of bulk materials (Callaway, 1959), the Boltzmann transport equation (BTE) is often the starting point for modeling the thermal conductivities of thin films (Tien et al., 1969; Chen and Tien, 1993; Goodson et al., 1993; Kumar and Vradis, 1994). The same approach has been applied extensively in the modeling of the size effects on the electrical conductivities of thin films (Tellier and Tosser, 1982). Majumdar (1993) pointed out the similarity between the BTE and the equation of radiative transfer, and derived the equation of phonon radiative transfer. This analogy between radiation and heat conduction was employed by Chen and Tien (1993) in the study of the thermal conductivities of quantum well structures. Other approaches for the thin-film thermal conductivity modeling include the ray-tracing method based on the heat-carrier mean-free-path (MFP) (Flik and Tien, 1993), and the Wiedemann-Franz law analogy for metallic thin films (Nath and Chopra, 1973; Qiu and Tien, 1993).

Most of the previous work on the thermal conductivities of thin films dealt with a single layer with free-surface types of boundary conditions. In real world applications, thin films are almost always on supporting substrates and/or in multilayer configurations. Chen and Tien (1993) considered the effects of phonon reflection and transmission at interfaces on the effective thermal conductivities of quantum well structures. The interface effect was also included in the study on the thermal conductivities of SiO_2 and chemical-vapor deposited diamond thin films (Goodson et al., 1993; Goodson, 1996). Those studies, however, are still limited to a single layer. It is not clear whether the results obtained for a single layer, either experimental or theoretical, are applicable to the constituting layers in a multilayer structure. Answering this question becomes particularly important for extremely thin-film multilayer structures such as superlattices, which are periodic structures made of several to hundreds of layers of thin films with each layer ranging from a few tens to several hundreds angstroms (Esaki and Tsu, 1970). Studies on the electronic, optical, electrical, and lattice properties on superlattice structures have revealed drastically different properties compared to their corresponding bulk materials due to the quantum size effects (Weisbuch and Vinter, 1991). These properties are being utilized to improve the performance of conventional devices and to invent new ones. Ren and Dow (1982) modeled the thermal conductivity of idealized superlattice structures by combining the classical BTE approach (Callaway, 1959) with a quantum mechanical treatment of the scattering rate and concluded that the thermal conductivities of superlattices are smaller than those of their corresponding bulk media. The predicted maximum reduction in the thermal conductivity for ideal superlattice structures, however, is only about 20 percent. This is in sharp contrast to the significant reduction in thermal conductivity of GaAs/AlAs superlattice structures as experimentally measured at room temperature (Yao, 1987) and cryogenic temperatures (Yu et al., 1995). The detailed mechanism for the observed reduction in thermal conductivity is not understood. In addition to semiconductor superlattices, thermal conductivities on other types of periodic thin film structures have also been

Contributed by the Heat Transfer Division for publication in the JOURNAL OF HEAT TRANSFER. Manuscript received by the Heat Transfer Division August 28, 1995; revision received December 20, 1996; Keywords: Conduction, Thermal Packaging, Thermophysical Properties. Associate Technical Editor: A. Lavine.

reported, such as those used in vertical-cavity surface-emitting lasers (Chen et al., 1994), X-ray mirrors (Wu et al., 1992), and superlattices made of amorphous and metallic materials (Zhang et al., 1990; Clemens et al., 1988).

This work establishes a model to calculate the thermal conductivity of periodic thin-film structures in the parallel direction from the bulk properties of their constituting layers. Different interface conditions are considered for the scattering of phonons. Results from the partially diffuse and partial specular reflecting interfaces are in good agreement with the measured thermal conductivities of GaAs/AlAs superlattices. This study shows that atomic scale interface roughness is the major cause of the experimentally observed significant reduction in the thermal conductivity of GaAs/AlAs superlattice structures. It suggests that by controlling the interface during film growth, the effective thermal conductivity of superlattices and quantum well structures made of good bulk thermal conductors can be engineered to approach those of amorphous materials, while their electrical conductivity can be increased due to quantum size effects. This principle can be utilized in the search of high efficiency thermoelectric materials.

Theoretical Models and Analysis

This work focuses on the thermal conductivities of periodic dielectric and semiconductor thin-film structures in the direction parallel to the film plane as shown in Fig. 1, although an extension of the results to metallic superlattices is straight forward. When the film thickness becomes comparable to the phonon MFP, the interfaces in the composite structure cause reflection and transmission of phonons. It is assumed here that the films are thick enough such that the phonon spectrum in each layer can be represented by that of its bulk form. This assumption implies that the quantum-interference effect on phonons is negligible, which breaks down when the phonon coherence length becomes comparable to the film thickness (Esaki and Tsu, 1970; Narayanamurti et al., 1979; Chen, 1996a). An estimation of the phonon coherence length to be presented in the next section indicates that this approximation is valid for a wide range of superlattice and periodic thin film

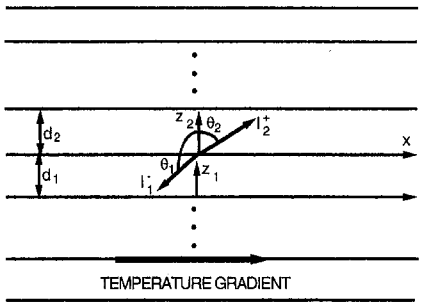

Fig. 1 Model and coordinate system

structures. Under the above assumptions, the BTE is still applicable and can be written as (Majumdar, 1993)

$$\sin\theta_i \cos\varphi_i \frac{\partial I_{\omega i}}{\partial x} + \cos\theta_i \frac{\partial I_{\omega i}}{\partial z_i} = -\frac{I_{\omega i} - I_{\omega oi}}{\Lambda_{\omega i}} \tag{1}$$

where $I_{\omega i}$ is the spectral dependent phonon intensity of the ith layer summed up over all three phonon polarizations (Chen and Tien, 1993),

$$I_{\omega i} = \frac{1}{4\pi} \sum_p v_{pi} f \hbar\omega D_{pi}(\omega). \tag{2}$$

D is the density of state, f the phonon distribution function, v_p the phonon group velocity, θ the polar angle, φ the azimuthal angle, and ω the angular frequency. The equilibrium phonon intensity, $I_{\omega oi}$, is obtained by substituting f in Eq. (2) with the Bose-Einstein distribution.

A formal solution of Eq. (1) can be obtained by introducing a deviation function $i_{\omega i}$ (Tellier and Tosser, 1982):

$$I_{\omega i}(x, z_i) = I_{\omega oi}(x) + i_{\omega i}(x, z_i) \tag{3}$$

and neglecting its derivative in the x-direction. Equation (1) becomes

$$\cos\theta_i \frac{\partial i_{\omega i}}{\partial z_i} + \frac{i_{\omega i}}{\Lambda_{\omega i}} = -\sin\theta_i \cos\varphi_i \frac{dI_{\omega oi}}{dx}. \tag{4}$$

Nomenclature

a = lattice constant of an isotropic medium, Å
A = nondimensional integral functions
C = volumetric specific heat, $JK^{-1}m^{-3}$
d = layer thickness, m
D = density of states, m^{-3}
E = exponential integral function
f = heat-carrier distribution function
F = nondimensional function
G = nondimensional integral functions
h = Planck constant, Js
$\hbar$ = Planck constant divided by 2π, Js
i = deviation from the equilibrium intensity distribution, $Wm^{-2}sr^{-1}$
I = heat-carrier intensity, $Wm^{-2}sr^{-1}$
k = thermal conductivity, $Wm^{-1}K^{-1}$
N = nondimensional function
p = interface scattering parameter
q = wave vector, m^{-1}
Q = heat transfer rate, W
r = reflectivity
S = Seebeck coefficient, VK^{-1}
t = transmissivity
v = phonon group velocity, ms^{-1}
V = volume per base atom or molecule, m^{-3}
x = coordinate parallel to the film
z = coordinate perpendicular to the film
Z = acoustic impedance, figure of merit for thermoelectric effect
α = thermal diffusivity, m^2s^{-1}
β = coefficient
χ = relative layer thickness
Δ = surface roughness, m
κ = Boltzmann constant, JK^{-1}
φ = azimuthal angle, rad
λ = heat-carrier wavelength, m
Λ = heat-carrier mean-free-path, m
μ = directional cosine
ν = phonon frequency, Hz
θ = polar angle, rad; temperature, K
ρ = density, kgm^{-3}
σ = electrical conductivity, $\Omega^{-1}m^{-1}$
ω = angular frequency of heat carriers, Hz
Ω = solid angle, sr
ξ = film thickness normalized to heat-carrier mean-free-path

Subscripts

d = diffuse interface
e = effective value
g = gray medium
L = longitudinal phonons
m = maximum
o = equilibrium
op = optical phonon
p = polarization
s = specular interface
t = transverse phonons
to = low frequency transverse phonons
tu = high frequency transverse phonons
1 = medium one
2 = medium two
12 = from medium one into medium two
21 = from medium two into medium one

Superscripts

ω = spectral quantity
$+$ = in the upper hemisphere direction
$-$ = in the lower hemisphere direction

The solution of the above equation can be represented by well established methods in thermal radiation (Siegel and Howell, 1992):

$$i^+_{\omega i}(\eta_i, \mu_i) = b^+_i(\mu_i)e^{-\eta_i/\mu_i} - \Lambda_{\omega i} \sin\theta_i \cos\varphi_i \frac{dI_{\omega oi}}{dx}$$

$$(\text{for } 0 < \mu_i < 1) \quad (5)$$

$$i^-_{\omega i}(\eta_i, \mu_i) = b^-_i(\mu_i)e^{(\xi_i-\eta_i)/\mu_i} - \Lambda_{\omega i} \sin\theta_i \cos\varphi_i \frac{dI_{\omega oi}}{dx}$$

$$(\text{for } -1 < \mu_i < 0) \quad (6)$$

where μ ($= \cos\theta$) is the directional cosine, η ($= z/\Lambda_\omega$) the nondimensional spectral dependent z-coordinate, and ξ ($= d/\Lambda_\omega$) the nondimensional film thickness. The heat transfer rate in the x-direction carried by two adjacent layers is the sum of that in each layer, $Q = Q_1 + Q_2$, and

$$Q_i = \int_0^{\omega_{mi}} d\omega \int_0^{d_i} dz_i \int_{4\pi} I_{\omega i} \cos\varphi_i \sin\theta_i d\Omega_i$$

$$= \int_0^{d_i} dz_i \int_0^{2\pi} \cos\varphi_i d\varphi_i \int_0^{\omega_{mi}} d\omega \int_0^1 [i^+_{\omega i}(z, \mu_i) + i^-_{\omega i}(z, -\mu_i)] \sin\theta_i d\mu_i. \quad (7)$$

Here Ω is the solid angle. The final expression for the heat transfer rate depends on the interface conditions, which determine the coefficients b^+_i and b^-_i in Eqs. (5) and (6).

Partially Diffuse and Partially Specular Interfaces. A relatively general approach is to assume that the interfaces are partially diffuse and partially specular reflecting for incident phonons. By applying the principle of energy balance to the two interfaces of the first layer, the following equations can be derived:

$$I^+_{\omega 1}(0, \mu_1) = p[r_{12}(\mu_1)I^-_{\omega 1}(0, -\mu_1) + t_{21}(\mu_2)I^+_{\omega 2}(d_2, \mu_2)\mu_2 d\Omega_2/(\mu_1 d\Omega_1)] + (1-p)I_{\omega o1}(T) \quad (8)$$

$$I^-_{\omega 1}(d_1, -\mu_1) = p[r_{12}(\mu_1)I^+_{\omega 1}(d_1, \mu_1) + t_{21}(\mu_2)I^-_{\omega 2}(0, -\mu_2)\mu_2 d\Omega_2/\mu_1 d\Omega_1] + (1-p)I_{\omega o1}(T) \quad (9)$$

where p is the interface scattering parameter—the fraction of specularly reflected phonons at each interface, and is assumed to be the same for incident radiation into both interfaces. Similar boundary conditions can be written out for the two interfaces of the second layer. When $p = 1$, the above interface conditions imply that specular reflection and transmission occur at the interfaces. When $p = 0$, the boundary conditions indicate totally diffuse interface and can be further simplified to $i^+_{\omega 1}(0, \mu_1) = i^-_{\omega 1}(d_1, -\mu_1) = 0$.

The heat-carrier reflectivity and transmissivity, r and t, have been studied extensively in the context of thermal boundary resistance (Little, 1959; Swartz and Pohl, 1989). For phonons going through specular reflection at the interface, the incident and refracted angles obey the Snell law: $v_1/\sin\theta_1 = v_2/\sin\theta_2$ such that $\mu_1 d\Omega_1/(\mu_2 d\Omega_2) = (v_1/v_2)^2$. Strictly speaking, the reflection and transmission at the interface of two crystals are a complicated process because of the change in polarization, i.e., a transverse wave can excite both longitudinal and transverse waves (Auld, 1990; Weis, 1986). This study neglects such polarization change by assuming that thin film materials are isotropic solids and that the incident waves are polarized perpendicular to the plane of incidence. Polarization parallel to the plane of incidence has also been tested, which does not show appreciable difference from the assumed polarization. The spectral-dependent transmissivity and reflectivity can be calculated from (Auld, 1990; Weis, 1986)

$$t_{ij}(\omega, \theta_i) = \frac{Z_i\mu_i}{Z_j\mu_j}\left(\frac{2Z_j\mu_j}{Z_j\mu_j + Z_i\mu_i}\right)^2 \quad (10)$$

$$r_{ij} = 1 - t_{ij} \quad (11)$$

where Z_i ($= \rho_i v_i$) is the specific impedance and ρ_i the density of medium i. The reflectivity and transmissivity depend on frequency through phonon group velocity, as will be discussed later.

The transmissivity and reflectivity given by Eqs. (10) and (11) are valid only when the refracted phonons have the same frequency as the incident ones. For two solids with different phonon spectra, phonons in the layer with frequencies higher than those of its neighboring layers cannot propagate through the interfaces by this elastic scattering process, i.e.,

$$t_{ij} = 0 \quad \text{and} \quad r_{ij} = 1 \quad \text{when} \quad \omega > \min(\omega_{m1}, \omega_{m2}) \quad (12)$$

for each phonon polarization.

Another modification to the transmissivity and reflectivity is for total internal reflection. When the angle of incidence is larger than the critical angle, no phonons can transmit across the interface, i.e., $t_{ij} = 0$ and $r_{ij} = 1$ when $\sin\theta_i > v_i/v_j$. This relation is again assumed for each phonon polarization.

The boundary conditions, Eqs. (8) and (9), together with two similar equations for the two interfaces of the second layer can be employed to solve for the unknown coefficients in Eqs. (5) and (6). Substituting these solutions into Eq. (7) yields the final expression of the effective thermal conductivity of the periodic structure as

$$k_e = \sum_{i=1}^{2} \chi_i \sum_p k_{pi} \quad (13)$$

$$= \sum_{i=1}^{2} \chi_i \sum_p \left\{ k_{bpi} - \frac{1}{2d_i}\int_0^{\omega_{mpi}} v_{pi}C_{\omega pi}\Lambda^2_{\omega pi}[pG_{si}(\xi_1, \xi_2) + (1-p)G_{di}(\xi_1, \xi_2)]d\omega \right\} \quad (14)$$

where k_{bpi} is the contribution to the bulk thermal conductivity due to p-polarized ($p = L, t$) phonons in the ith layer, χ_i [$= d_i/(d_1 + d_2]$] is the relative thickness of the ith layer, and G_{di} and G_{si} are integrals given in Appendix A.

Specular Interface. Results for specular interfaces can be obtained by setting p to 1 in Eqs. (14) and (A6).

$$k_e = \sum_{i=1}^{2} \chi_i \sum_p \left[k_{bpi} - \frac{1}{2d_i}\int_0^{\omega_{mpi}} v_{pi}C_{\omega pi}\Lambda^2_{\omega pi}G_{si}(\xi_1, \xi_2)d\omega \right] \quad (15)$$

Diffuse Interface. For diffuse interfaces, $p = 0$ and the final expression for the effective thermal conductivity becomes

$$k_e = \sum_{i=1}^{2} \chi_i \sum_p \left[k_{bpi} - \frac{1}{2d_i}\int_0^{\omega_{mpi}} v_{pi}C_{\omega pi}\Lambda^2_{\omega pi} \times \left(\frac{1}{4} - E_3(\xi_i) + E_5(\xi_i)\right) d\omega \right] \quad (16)$$

where E_j is the exponential integral function of order j (Siegel and Howell, 1992). Clearly, for diffuse interfaces the effective thermal conductivity in the parallel direction does not depend on the reflectivity and transmissivity. This means that thermophysical properties of multilayer structures can be calculated from their constituting layers in free-standing forms, if the surfaces of the latter scatter heat carriers diffusely. Similar results

were obtained in the study of the thermal conductivities of quantum well structures (Chen and Tien, 1993). For specular or partially specular interfaces, however, this result is no longer valid, as can be seen from the mathematical expressions. Physically, this is due to the transmission and thus the continuation of phonon energy flow from one layer to the next layer.

Relaxation Time and Thermal Conductivity Model

The above obtained expressions are material independent. Further evaluation of the model requires the relaxation time of bulk materials and a model for calculating the thermal conductivity of bulk materials. The rest of this work emphasizes the thermal conductivity of GaAs/AlAs superlattices. The modeling of thermal conductivity has been largely based on the phenomenological approach developed by Callaway (1959). In this approach, the functional form of the frequency and temperature dependence of relaxation time for different processes are obtained from quantum mechanical considerations, and the coefficients of those functions are matched to the experimentally measured temperature dependence of thermal conductivity. Under this general approach, different expressions for the relaxation time have been developed based on the phonon spectra of different materials. Holland (1964) demonstrated that the thermal conductivity of *Si* and *Ge* can be modeled as consisting of three parts:

$$k = k_L + k_{to} + k_{tu} \tag{17}$$

where k_L is longitudinal phonon contribution, and k_{to} and k_{tu} are the contributions of low and high frequency transverse phonons, respectively. Chen and Tien (1993) showed that the bulk thermal conductivity of GaAs can be represented well by this model but also cautioned that the predicted specific heat from this model is four times smaller than the measured values. One possible reason for the underprediction of specific heat is that Holland's model employs two phonon group velocities to approximate the continuously varying transverse phonon group velocity. To better account for the specific heat variation, the phonon dispersion relations of GaAs (Waugh and Dolling, 1963) and AlAs (Giannozzi et al., 1991) are approximated by that of a linear atomic chain (Kittel, 1996)

$$\omega_p = \omega_{mp} \sin(qa/2) \tag{18}$$

where q is the wave vector, ω_{mp} the angular frequency of p-polarized phonons at the boundary of the first Brillouin zone, and a the equivalent atomic separation of an isotropic medium, which can be determined from $a = \pi(6\pi^2/V)^{-1/3}$, as in Debye's model (Kittel, 1996). The volume of a GaAs molecule, V, equals $5.65^3/4$ Å^3 because of its Zincblende lattice structure. Based on the above phonon dispersion relations, the phonon group velocity and specific heat at each frequency can be expressed as

$$v_p = \frac{\omega_{mp} a}{2} \cos\left(\frac{qa}{2}\right) \tag{19}$$

$$C_{\omega p} = \frac{4\hbar^2}{\pi^2 \kappa a^3 T^2 \omega_{mp}} \frac{[\sin^{-1}(\omega/\omega_{mp})]^2}{\cos(qa/2)} \frac{\omega^2 \exp(\hbar\omega/\kappa T)}{[\exp(\hbar\omega/\kappa T) - 1]^2}. \tag{20}$$

Integrating Eq. (20) over all allowable phonon frequencies and summing up three phonon polarizations yield the specific heat of acoustic phonons. For GaAs, the optical phonons also contribute to the specific heat. Since the dispersion in optical phonon is small, its contribution to the specific heat can be approximated by Einstein's model. The final expression for specific heat is

$$C = \sum_p \int_0^{\omega_{mp}} C_{\omega p} d\omega + \frac{3\kappa}{V} \left(\frac{\hbar\omega_{op}}{\kappa T}\right)^2 \frac{e^{\hbar\omega_{op}/\kappa T}}{(e^{\hbar\omega_{op}/\kappa T} - 1)^2} \tag{21}$$

where ω_{op} is the frequency of optical phonons. Figure 2 compares the calculated specific heat of GaAs from the above expression with recommended values, using the averaged acoustic phonon maximum frequencies as given in Table 1. The average is taken in three major directions, i.e., (100), (110), and (111), based on calculated phonon dispersion relations (Giannozzi et al., 1991). The optical phonon temperature of GaAs is taken at 387 K. The contributions from the longitudinal and transverse acoustical phonons, as well as from optical phonons, are also shown in the figure. The major difference of the current approach from the well established Debye model (Kittel, 1996) lies in that the Debye approximation is a best fit to the experimental data on specific heat while the current method does not include any adjustable parameters. This model automatically accounts for different phonon polarizations, which is important for thermal conductivity modeling since the relaxation rates for longitudinal and transverse phonons differ significantly. The figure shows that optical phonons contribute to about half of the room temperature specific heat of GaAs. Since optical phonons have small group velocity, their contribution to thermal conductivity will be neglected such that only Eq. (20) enters into the thermal conductivity expressions. It is worthy pointing out that most previous modeling efforts on thermal conductivity are based on the Debye model while also implicitly neglect optical phonon contributions. The above discussion on specific heat suggests that a conflict may exist in two such assumptions because the Debye model includes specific heat of optical phonons.

Combining the current treatment on phonon dispersion with Holland's model on phonon relaxation time, the corresponding terms to Eq. (17) become

$$k_{Li} = \frac{K\theta_{Li}T}{3} \int_0^{\theta_{Li}/T} \tau_{Li} F(x, \theta_{Li}) \left\{ 1 - \frac{3v_{Li}\tau_{Li}}{2d_i} \times [(1-p)G_{di}(\xi_{L1}, \xi_{L2}) + pG_{si}(\xi_{L1}, \xi_{L2})] \right\} dx \tag{22}$$

$$k_{toi} = \frac{2K\theta_{ti}T}{3} \int_0^{\theta_{tu}/T} \tau_{toi} F(x, \theta_{ti}) \left\{ 1 - \frac{3v_{ti}\tau_{toi}}{2d_i} \times [(1-p)G_{di}(\xi_{to1}, \xi_{to2}) + pG_{si}(\xi_{to1}, \xi_{to2})] \right\} dx \tag{23}$$

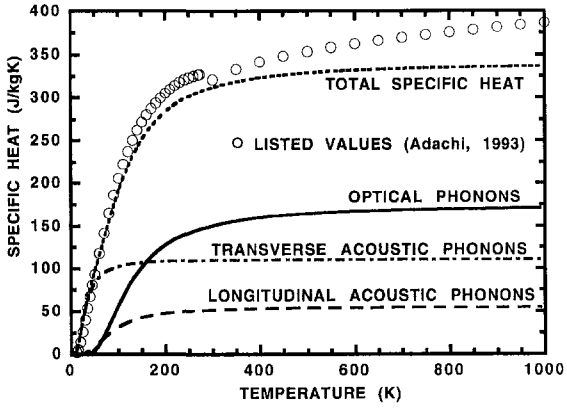

Fig. 2 Specific heat of GaAs based on the model including acoustic phonon dispersion and optical phonon contribution

Table 1 Parameters used in the calculation of thermal conductivity

	θ_L (K)	θ_t (K)	θ_{tu} (K)	α	β_{to}	β_{tu}	β_L	a (Å)
GaAs	303.8	108.6	99	2.0	10.0	16000	0.107	2.87
AlAs	301.4	126.3	103	2.0	10.0	32000	0.022	2.87

$$k_{tui} = \frac{2K\theta_{ti}T}{3}\int_{\theta_{tui}/T}^{\theta_{ti}/T}\tau_{tui}F(x,\theta_{ti})\left\{1-\frac{3v_{ti}\tau_{tui}}{2d_i}\times[(1-p)G_{di}(\xi_{tu1},\xi_{tu2})+pG_{si}(\xi_{tu1},\xi_{tu2})]\right\}dx \quad (24)$$

where $K = \kappa^3/(\pi^2\hbar^2 a)$, $x = \hbar\omega/(\kappa T)$, $\theta_p = \hbar\omega_{mp}/\kappa$, $\Lambda_\omega = v(\omega)\tau(\omega)$, and

$$F(x,\theta) = [\sin^{-1}(xT/\theta)]^2 \times [1-(xT/\theta)^2]^{1/2}x^2e^x/(e^x-1)^2. \quad (25)$$

The bulk relaxation time, τ_{pi} ($p = L, to, tu$), for each type of phonons has the following functional dependence on x:

$$\tau_L^{-1} = \alpha x^4T^4 + \beta_L x^3T^5 \quad (26)$$

$$\tau_{to}^{-1} = \alpha x^4T^4 + \beta_t xT^5 \quad (27)$$

$$\tau_{tu}^{-1} = \alpha x^4T^4 + \beta_{tu}x^2T^2/\sinh x. \quad (28)$$

Values of the unknown coefficients for GaAs have been obtained by matching the bulk thermal conductivity of GaAs and are listed in Table 1. The agreement between the model and experimental results on bulk thermal conductivity of GaAs is comparable to the fit according to Holland's model (Chen and Tien, 1993). Because of the similarity of the phonon spectra of AlAs with those of GaAs (Giannozzi et al., 1991), the above thermal conductivity model is also expected to be valid for AlAs. There exists, however, no measurement on the temperature dependence of the thermal conductivity of AlAs and thus the unknown coefficients cannot be uniquely determined. For most III–V semiconductors it is found that thermal conductivity is inversely proportional to the absolute temperature according to the power law for temperatures higher than the material's Debye temperature (Adachi, 1993; Slack, 1979):

$$k \sim 1/T^n \quad (29)$$

where n is between 1.20 and 1.5. As an approximation, it is assumed that thermal conductivity of AlAs follows the above power law with $n = 1.35$. This allows the determination of β_{tu} and β_L of AlAs. Coefficients due to impurity scattering, α, and low frequency transverse phonons, β_{to}, are assumed to be same as those of GaAs. Because of this assumption the numerical results are not expected to be accurate at low temperatures ($\sim$<50 K).

Comparison With Experimental Results

The results from the above established models will be compared to experimental data on GaAs/AlAs superlattices—the most widely studied semiconductor superlattice structures. Heat conduction in those materials is mainly through phonons. Yao (1987) investigated GaAs/AlAs superlattice structures of different thicknesses at room temperature. Yu et al. (1995) recently studied the temperature dependence of a GaAs/AlAs periodic thin film structure.

Interface Roughness and Scattering Parameter. Atomic scale interface roughness in molecular-beam-epitaxy grown quantum wells and superlattices has been a subject of intense research over the last two decades (Bode and Ourmazd, 1992). Current understanding is that the interfaces consist of terraces with atomic scale roughness fluctuations. Detailed modeling of the effect of such roughness on the interface scattering parameter will not be pursued in this work. Ziman (1960) proposed the following expression for estimating the interface scattering parameter for incidence normal to the interface:

$$p \approx \exp(-16\pi^3\Delta^2/\lambda^2) \quad (30)$$

where λ is the carrier frequency and Δ is the mean interface roughness. At room temperature the dominant phonon wavelength as will be calculated later is $\sim$10–20 Å. The above formula yields the interface scattering parameter to be zero for even a monolayer of roughness ($\Delta \sim 3$ Å). For a perfectly flat interface without atomic level roughness variation, it can be envisioned that phonons will be scattered directionally by the orderly arranged atoms, similar to photons being scattered by an optical grating. On the basis of the above reasoning, a frequency independent scattering parameter will be assumed and used as a fitting parameter.

Comparison with Experiment. Figure 3 shows a comparison of the calculated thermal conductivity of GaAs/AlAs superlattice structures as a function of the layer thickness with reported experimental results at room temperature for different values of the interface scattering parameter p. Both the experiments of Yao (1987) and Yu et al. (1995) employed GaAs/AlAs superlattices of equal thickness for all the layers. The sample of Yu et al. (1995) was doped with *Be* to a concentration of 10^{18} cm^{-3}. No doping of the samples studied by Yao (1987) was reported. Figure 3 suggests that the interface is neither totally specular or totally diffuse. If the interfaces are purely specular, the reduction in thermal conductivity is less than 15 percent. The interface is not totally diffuse possibly because the terrace structures leave atomically flat regions (Bode and Ourmazd, 1992). It can be readily proven that for specular reflection at the surfaces of a free-standing thin film, the thermal conductivity of the thin film equals its bulk value. For a periodic thin film structure with specular interfaces, however, the effective thermal conductivity is no longer equal to its corresponding bulk value. This is because in a free-standing film the specular reflection does not change the energy and the momentum components along the direction of the temperature gradient. In a multilayer structure the refraction alters the x-momentum component of the original heat carriers. Phonons refracted from the

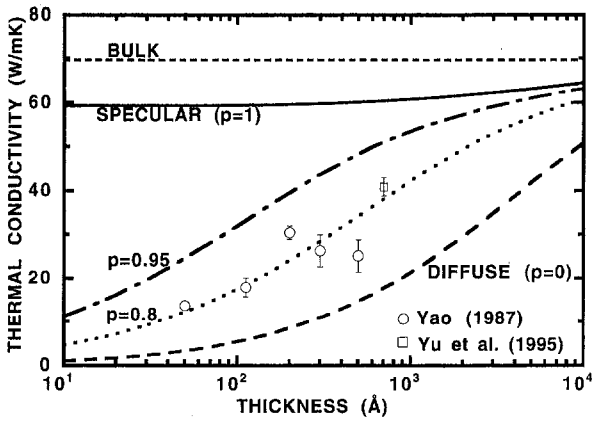

Fig. 3 Thermal conductivity as a function of the layer thickness for GaAs/AlAs superlattices of equal layer thickness at room temperature

layer with the shorter MFP into its neighboring layers will actually have a longer MFP, which increases the effective thermal conductivity of the original layer, and verse versa. The gain of the thermal conductivity in one layer does not cancel the loss in the other layer. A breakdown of the effective thermal conductivity for each layer in GaAs/AlAs superlattices is shown in Fig. 4.

Figure 3 also demonstrates that results for partially specular and partially diffuse cases are not a simple linear superposition of the results from totally specular and totally diffuse cases. A slight imperfection for an otherwise specular interface has a strong effect on the thermophysical properties, particularly as the layers become thinner. This is due to the effect of multiple reflection and/or transmission of heat carriers in a multilayer structure. Although the heat conduction capability loss is small in one collision with the interface, the results of multiple collisions with the interface will pronounce the effect of interface scattering. Mathematically this is manifested in Eq. (A2). The effects of the interface scattering parameter are further demonstrated in Fig. 5.

Figure 6 compares the measured temperature dependence of a GaAs/AlAs (700 Å/700 Å) periodic structure with the calculated results. Again, this figure suggests that diffuse scattering is one major course of the observed reduction in thermal conductivity. The figure also demonstrates that the temperature dependence of the periodic structure is weaker than that of their corresponding bulk materials. The experimentally determined temperature dependence over the whole temperature range is $k \sim 1/T$ (Yu et al., 1995), as compared to bulk thermal conductivity with a T^{-n} ($n = 1.2$–1.5) temperature dependence. The model confirms this trend towards less temperature dependence.

Phonon Coherence Length and Validity of Classical Particle Picture. In their original work on superlattices, Esaki and Tsu (1970) proposed that quantum effects on electron transport should be observable when the layer thickness becomes shorter than its MFP. Although their work broke the ground for the subsequent development of the whole field, the criterion proposed may not be the best. Since quantum effect can be understood as a consequence of interference among particle (electron and phonon) waves, the coherence lengths of these waves should represent more appropriate scales for the observation of interference phenomena. The coherence theory for photons has been well established (Born and Wolf, 1980). Chen and Tien (1992) introduced it to the study of radiative properties of thin films. The coherence length of electrons has also been estimated (Chen, 1996a), and for GaAs it is comparable to their MFP. To estimate the phonon coherence length a simple formulation introduced by Mehta (1963) for blackbody radiation is extended here for phonons due to the similarity in their statistical properties. In the original work of Mehta (1963) two slightly different definitions of the photon coherence length were evaluated. The one yielding a longer coherence length is chosen here, leading to a thicker film limit for observing phonon interference phenomena or quantum effects. The phonon coherence time can be expressed as

$$\Delta\tau = \int_0^{\nu_m} |g(\nu)|^2 d\nu \tag{31}$$

where g is the phonon spectrum density. For a phonon spectrum as given by Eq. (18), g for each phonon polarization is

$$g_p(\nu) = \begin{cases} \dfrac{K_p[\sin^{-1}(\nu/\nu_{mp})]^2\nu}{\sqrt{1-(\nu/\nu_{mp})^2}\,[\exp(h\nu/\kappa T)-1]} & \nu < \nu_{mp} \\ 0 & \nu > \nu_{mp}. \end{cases} \tag{32}$$

The normalization constant K_p can be determined from

$$\int_0^{\nu_m} g_p(\nu) d\nu = 1. \tag{33}$$

Upon the determination of the coherence time, the coherence length can be calculated from

$$L = v\Delta\tau \tag{34}$$

where v is the averaged phonon velocity. Figure 7 shows the coherence length of longitudinal and transverse phonons in bulk GaAs. At room temperature the coherence length is ~10 Å and ~20 Å for the transverse and longitudinal phonons, respectively, which indicates that the BTE can be applied to superlattices of comparable thickness. The exact demarcation line, how-

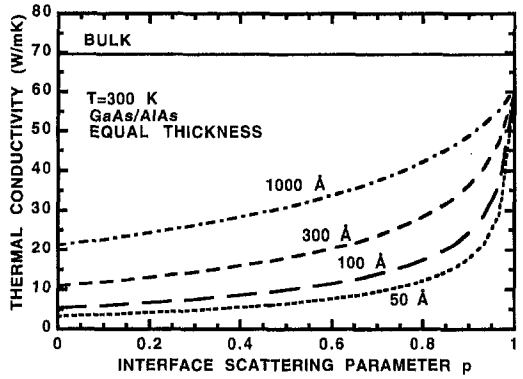

Fig. 5 Thermal conductivity as a function of interface scattering parameter for GaAs/AlAs superlattices of equal layer thickness at room temperature

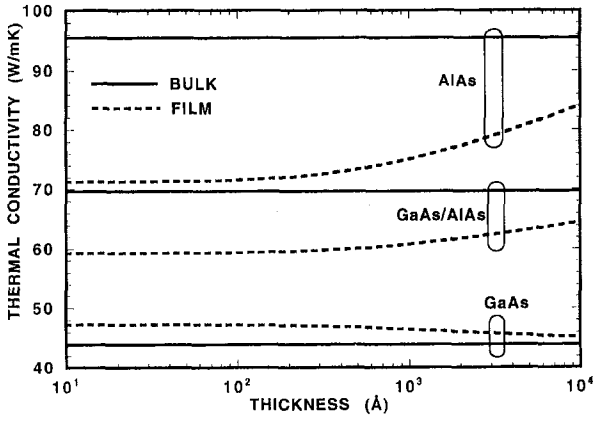

Fig. 4 Thermal conductivity of individual layers in equal thickness superlattices with specular interface conditions

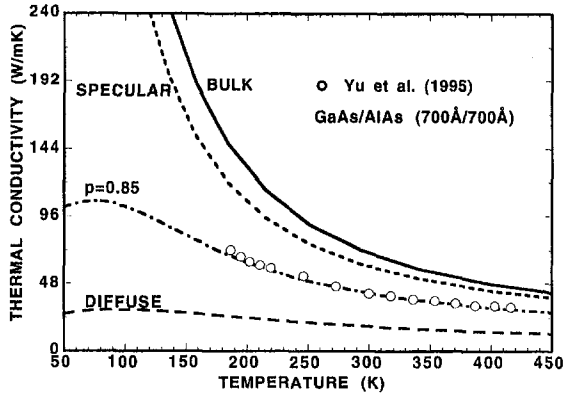

Fig. 6 Thermal conductivity as a function of temperature for a GaAs/AlAs periodic structure

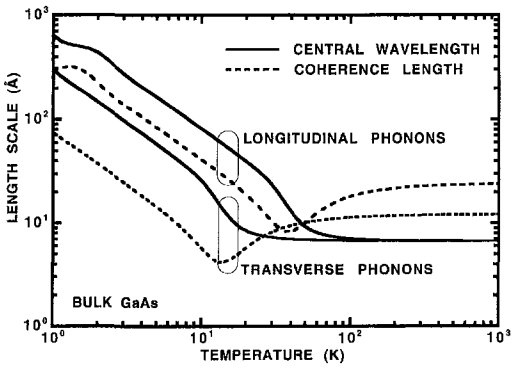

Fig. 7 Phonon coherence properties of bulk GaAs

ever, cannot be determined from such a simple analysis. Also shown in the same figure are the central wavelengths of the transverse and longitudinal phonons. The calculations are based on a straight forward extension of the expressions for phonons (Mehta, 1963).

The above calculation also explains why at least partially diffuse scattering must be assumed to explain the experimentally measured thermal conductivity of GaAs/AlAs superlattices. At molecule-beam-epitaxy grown GaAs/AlGaAs interfaces roughness often extends to one to three atomic layers, or ~3–9 Å. This roughness is comparable to the phonon coherence and will cause diffuse scattering of phonons.

Gray Medium Approximations

Although the above nongray media model has shown good agreement with experimental results, its accuracy is limited by how well the internal scattering rates can be inferred. The determination of the latter is subject to certain arbitrariness because even the bulk thermal conductivity cannot be modeled very well. For example, both the current model, which includes continuous variation of phonon group velocity, and Holland's model (Chen and Tien, 1992) can match the bulk thermal conductivity well, albeit with different values for coefficients in Eqs. (26)–(28). Furthermore, the frequency dependent phonon relaxation time often cannot be inferred due to the lack of temperature dependence of the bulk thermal conductivity data. For those cases, a first order correction to the size effects can be obtained by assuming that the medium is gray, i.e., the MFP is frequency independent. Under this gray medium assumption the effective thermal conductivity of superlattices can be expressed in terms of the bulk properties of each layer as (Chen, 1996b)

$$k_e = \sum_{i=1}^{2} \chi_i k_i [1 - 1.5p(1 - \alpha_j/\alpha_i)A_{si}/\xi_i - 1.5(1 - p)A_{di}/\xi_i] \quad (35)$$

where k_i and α_i are the thermal conductivity and diffusivity of the ith layer, respectively. The nondimensional integral functions A_{si} and A_{di} are given in Appendix A. They depend on the group velocity and MFP in each layer, which can be estimated by the following two methods.

Gray Medium Without Dispersion. The most straight forward approach to estimate phonon MFP is based on the kinetic theory

$$k = Cv\Lambda/3 \quad (36)$$

where v is the average of the long wavelength phonon group velocity, which is 3800 m/s for GaAs and 4540 m/s for AlAs, and C the volumetric specific heat. Phonon MFP calculated from the above expression for GaAs and AlAs are 203 Å and 369 Å, respectively. Figure 8(*a*) compares the effective superlattice thermal conductivity calculated from this approximation. Although the model follows the trend, it underpredicts the actual reduction in the thermal conductivity of superlattices.

Gray Medium With Dispersion. One reason for the overprediction of the effective thermal conductivity is that only the group velocities of long wavelength phonon are used. At room temperature most phonons are populated in the frequency range where their group velocities are much smaller. To compensate for the variation of group velocity the spectral dependent expression for the bulk thermal conductivity, Eq. (A5), can be approximated as

$$k_b \approx \Lambda \sum_p \int_0^{\omega_{mp}} C_p(\omega) v_p(\omega) d\omega/3. \quad (37)$$

The above approximate expression can be combined with Eqs. (19) and (20) to estimate the phonon MFP. Calculations yield the MFP for GaAs and AlAs as 1058 Å and 2248 Å, respectively, at room temperature, clearly due to the smaller phonon group velocities. The average phonon group velocities are obtained from Eq. (36) and are used in the calculation of the interface reflectivity and transmissivity. Based on these new values, the effective thermal conductivities of GaAs/AlAs superlattices are recalculated according to Eq. (35). Results of this approach are shown in Fig. 8(*b*). Agreement with experimental results are closer than the previous approach, although the prediction is still higher than that of the nongray medium approach. This figure shows that the rate of thermal conductivity reduction is smaller when considering frequency dependence than the

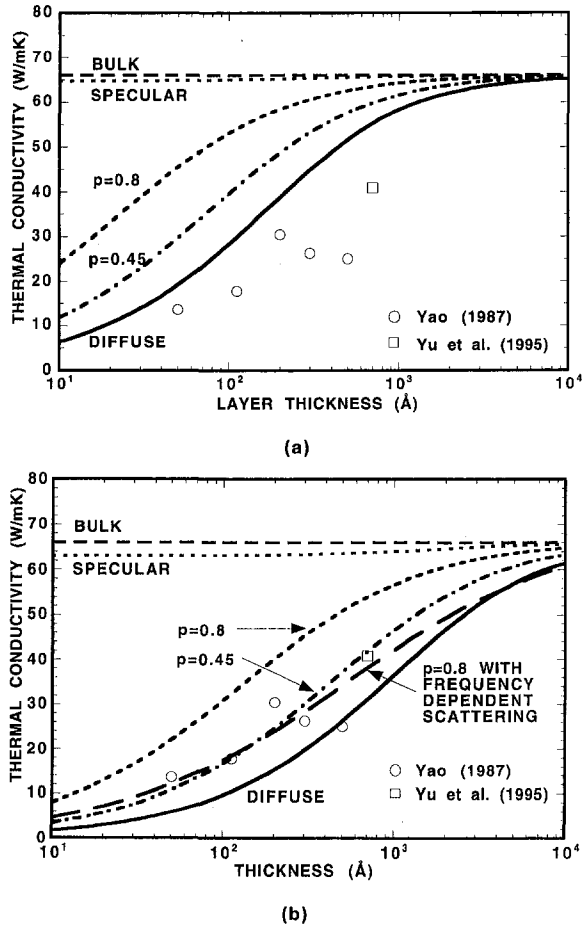

Fig. 8 Gray medium approximations (*a*) without dispersion and (*b*) with dispersion for GaAs/AlAs superlattices of equal layer thickness at room temperature

prediction based on the gray medium approach in the very thin film limit. This is because the relative contribution to thermal conductivity from long wavelength phonons, which is insignificant in bulk materials compared to that of high frequency phonons, increases as the high frequency phonon contribution decreases due to interface scattering. The gray medium approach lumps all phonons together, thus cannot predict this effect.

Phonon-Glass Electron-Crystal Behavior in Superlattices

Although it is well known that thermal conductivities of thin films are usually smaller than their corresponding bulk values, this work demonstrates that the reduction in the effective thermal conductivity of superlattices strongly depends on the interface conditions. By careful control of interfaces, it is possible to further increase or decrease the thermal conductivity of superlattice structures. The increase of thermal conductivity will greatly benefit the reliable operation of electronic and optoelectronic devices. The achievement of a perfect interface, however, is limited by many factors. Significant amount of work exists in improving the interface qualities (Bode and Ourmazd, 1992).

A more significant implication of this work is that the thermal conductivity of superlattice can be greatly reduced by engineering the interfaces. For example, Fig. 3 indicates that thermal conductivity of GaAs/AlAs can be potentially reduced to the level comparable to glass. On the other hand, atomic scale interface roughness does not cause a significant reduction in the electron mobility (which is a measure of the electrical conductivity) along the film direction, except at low temperatures where other scattering mechanisms such as electron-phonon scattering are not effective (Sakaki et al., 1987). This is because the typical electron coherence length in semiconductors is on the order of several hundreds angstroms (Chen, 1996a), much longer than that of phonon, such that electrons can be reflected specularly. The electron wavelength at the Fermi level also depends on the doping concentration and the electron effective mass, and thus can be controlled to a certain extent. The electron mobility in very thin films can actually be further increased by using modulating doping (Weisbuch and Vinter, 1991). These opposite trends in electron and phonon conductivities are ideal for thermoelectric materials because the criterion for a good thermoelectric material is a large figure of merit (Goldsmid, 1964):

$$Z = \frac{S^2\sigma}{k} \tag{38}$$

where S is the Seebeck coefficient, and σ is the electrical conductivity. Recently, there is a strong surge in the study of high efficiency thermoelectric materials in superlattices (Hicks and Dresselhaus, 1993). The search for better thermoelectric materials/structures, however, has been mostly directly at superlattices made of bulk materials with a large Z, which usually have small thermal conductivities. This work suggests that it is possible to control separately the electron and phonon properties in a wide range of superlattice structures by engineering interfaces to obtain ideal phonon-glass electron-crystal properties, and thus opens many new opportunities in the search of high efficiency thermoelectric materials for power generation and cooling.

Conclusions

This work develops models for the effective thermal conductivities of periodic thin-film structures in the direction parallel to the film plane. It shows that interfaces can affect the thermal conductivity differently depending on the interface scattering mechanisms. Specular interfaces do not have a strong effect on the thermal conductivity, while diffuse interfaces decrease the effective thermal conductivity significantly. The model predictions are compared with experimental data on GaAs/AlAs superlattice structures at both room temperature and over an extended temperature range. The model based on the frequency dependent internal scattering rate and partially specular and partially diffuse interfaces shows excellent agreement with experimental data. Although much work has been published on the interface roughness in superlattices and their effects on the electronic and optical properties, this work demonstrates that interface roughness is responsible for the reported reduction in the thermal conductivity of superlattices. Approximate expressions based on the average phonon MFP are also presented. For correcting the size effects on the thermal conductivity three approaches of different levels of complexity are recommended. The gray medium without dispersion is the simplest but least accurate, followed by the gray medium with dispersion. The most accurate method is the nongray medium with dispersion, but the computational demands also increase. This approach also depends on how accurate the bulk thermal conductivity model represents the true physical thermal relaxation processes. The results of this study are applicable for various periodic multilayer structures used in optical coatings and electronic and optoelectronic devices. The models can be readily extended to other types of multilayer structures.

Also developed in this work is a relatively simple model for specific heat. Compared with Debye's model which employs the adjustable Debye temperature to fit experimentally measured specific heat, the current model does not require any fitting parameter. The fact that optical phonons contribute significantly to specific heat points to the contradiction in the popular approach in thermal conductivity modeling, which is based on the Debye model but often neglects optical phonon contributions.

The conclusion that diffuse interface scattering, rather than specular scattering, is the cause of the observed reduction in thermal conductivity of superlattices raises the possibility of controlling thermal and electrical conductivity of superlattices independently. The study on phonon coherence properties suggests that thermal conductivity of superlattices made of bulk good thermal conductors can be reduced to the level comparable to amorphous materials such as glasses while causing minimum effect on the electrical conductivity. In fact, the latter can be greatly enhanced by modulation doping. This principle for creating phonon-glass electron-crystal behavior in superlattice by engineering interface conditions can be a basis for searching a new class of high efficiency thermoelectric materials.

Acknowledgments

After submission of the original manuscript, the author learned of a similar work by Drs. P. Hyldgaard and G. D. Mahan from University of Tennessee that was presented at the 23rd International Conference on Thermal Conductivity. The author acknowledges useful discussion with Dr. Hyldgaard and has benefited from their treatment on the average phonon mean free path in the revision of the manuscript. He also thanks the financial support of a National Science Foundation Young Investigator Award and the Lord Foundation of North Carolina.

References

Adachi, S., ed., 1993, *Properties of Aluminum Gallium Arsenide,* INSPEC, London, United Kingdom.

Auld, B. A., 1990, *Acoustic Fields and Waves in Solids,* 2d ed., Krieger Publishing Company, Malabar, Florida.

Bode, M. H., and Ourmazd, A., 1992, "Interfaces in GaAs/AlAs: Perfection and Applications," *Journal of Vacuum Science and Technology,* B, Vol. 10, pp. 1787–1792.

Born, M., and Wolf, E., 1980, *Principles of Optics,* Pergamon Press Inc., Tarrytown, NY, pp. 491–555.

Cahill, D. G., Fischer, H. E., Klitsner, T., Swartz, E. T., and Pohl, R. O., 1989, "Thermal Conductivity of Thin Films: Measurement and Understanding," *Journal of Vacuum Science and Technology A,* Vol. 7, pp. 1259–12669.

Callaway, J., 1959, "Model for Lattice Thermal Conductivity at Low Temperatures," *Physical Review,* Vol. 113, pp. 1046–1051.

Chen, G., 1996a, "Micro- and Nano-scale Thermal Phenomena in Photonic Devices," *Annual Review of Heat Transfer,* Vol. VII, C. L. Tien, ed., pp. 1–57.

Chen, G., 1996b, "Size and Interface Effects on Thermal Conductivity of Superlattices and Periodic Thin Film Structures," ASME HTD-Vol. 323, pp. 121–129.

Chen, G., and Tien, C. L., 1992, "Partial Coherence Theory of Thin Film Radiative Properties," ASME JOURNAL OF HEAT TRANSFER, Vol. 114, pp. 636–643.

Chen, G. and Tien, C. L., 1993, "Thermal Conductivity of Quantum Well Structures," *AIAA Journal of Thermophysics and Heat Transfer,* Vol. 7, pp. 311–318.

Chen, G., Tien, C. L., Wu, X., and Smith, J. S., 1994, "Measurement of Thermal Diffusivity of GaAs/AlGaAs Thin-Film Structures," ASME JOURNAL OF HEAT TRANSFER, Vol. 116, pp. 325–331.

Clemens, B. M., Eesley, G. L., and Paddock, C. A., 1988, "Time-Resolved Thermal Transport in Compositionally Modulated Metal Films," *Physical Review B,* Vol. 37, pp. 1085–1096.

Colvard, C., Gant, T. A., Klein, M. V., Merlin, R., Fisher, R., Morkoc, H., and Gossard, A. C., 1985, "Folded Acoustic and Quantized Optic Phonons in (GaAL) As Superlattices," *Physical Review B,* Vol. 31, pp. 2080–2091.

Decker, D. L., Koshigoe, L. G., and Ashley, E. J., 1984, "Thermal Properties of Optical Thin Film Materials," NBS Special Publication, 727, Laser Damage in Optical Materials, pp. 291–297.

Esaki, L., and Tsu, R., 1970, "Superlattice and Negative Differential Conductivity in Semiconductors," *IBM Journal of Research and Development,* Vol. 14, pp. 61–65.

Flik, M. I., and Tien, C. L., 1990, "Size Effects on the Thermal Conductivities of High-T_c Thin-Film Superconductors," ASME JOURNAL OF HEAT TRANSFER, Vol. 112, pp. 872–881.

Giannozzi, P, de Gironcolo, S., Pavone, P., Baroni, S., 1991, "Abinitio Calculation of Phonon Dispersions in Semiconductors," *Physical Review B,* Vol. 43, pp. 7231–7242.

Goldsmid, 1964, *Thermoelectric Refrigeration,* Plenum, New York.

Goodson, K. E., 1996, "Thermal Conduction in Nonhomogeneous CVD Diamond Layers in Electronic Microstructure," ASME JOURNAL OF HEAT TRANSFER, Vol. 118, pp. 279–286.

Goodson, K. E., Flik, M. I., Su, L. T., and Antoniads, D. A., 1994, "Prediction and Measurement of the Thermal Conductivity of Amorphous Dielectric Layers," ASME JOURNAL OF HEAT TRANSFER, Vol. 116, pp. 317–324.

Hatta, I., 1990, "Thermal Diffusivity Measurement of Thin Films and Multilayered Composites," *International Journal of Thermophysics,* Vol. 11, pp. 293–302.

Hicks, L. D., and Dresselhaus, M. S., 1993, "Effect of Quantum-Well Structures on the Thermoelectric Figure of Merit," *Physical Review B,* Vol. 47, pp. 12727–12731.

Holland, M. G., 1964, "Phonon Scattering in Semiconductors from Thermal Conductivity Studies," *Physical Review A,* Vol. 134, pp. 471–480.

Johnson, M. B., Maier, U., Meier, H.-P., and Salemink, H. W. M., 1993, "Atomic-Scale View of AlGaAs/GaAs Heterostructures with Cross-Sectional Scanning Tunneling Microscopy," *Applied Physics Letters,* Vol. 63, pp. 1273–1275.

Kittel, C., 1996, *Introductions to Solid State Physics,* Wiley, New York.

Kumar, S., and Vradis, G. C., 1994, "Thermal Conductivity of Thin Metallic Films," ASME JOURNAL OF HEAT TRANSFER, Vol. 116, pp. 28–34.

Lambropoulos, J. C., Jacobs, S. D., Burns, S. J., Shaw-Klein, L., and Hwang, S. S., 1991, "Thermal Conductivity of Thin Films: Measurement and Microstructural Effects," ASME HTD-Vol. 184, pp. 21–32.

Little, W. A., 1959, "The Transport of Heat between Dissimilar Solids at Low Temperatures," *Canadian Journal of Physics,* Vol. 37, pp. 334–349.

Majumdar, A., 1993, "Microscale Heat Conduction in Dielectric Thin Films," ASME JOURNAL OF HEAT TRANSFER, Vol. 115, pp. 7–16.

Mehta, C. L., 1963, "Coherence-Time and Effective Bandwidth of Blackbody Radiation," *IL Nuovo Cimento,* Vol. 18, pp. 402–408.

Narayanamurti, V., Stormer, H. L., Chin, M. A., Gossard, A. C., and Wiegmann, W., 1979, "Selective Transmission of High-Frequency Phonons by a Superlattice: the 'Dielectric' Phonon Filter," *Physical Review Letters,* Vol. 43, pp. 2012–2016.

Nath, P., and Chopra, K. L., 1973, "Experimental Determination of the Thermal Conductivity of Thin Films," *Thin Solid Films,* Vol. 18, pp. 29–37.

Qiu, T. Q., and Tien, C. L., 1993, "Size Effects on Nonequilibrium Laser Heating of Metal Films," ASME JOURNAL OF HEAT TRANSFER, Vol. 115, pp. 842–847.

Ren, S. Y., and Dow, J. D., 1982, "Thermal Conductivity of Superlattice," *Physical Review B,* Vol. 25, pp. 3750–3755.

Ruf, T., Spitzer, J., Sapega, V. F., Belitsky, V. I., Cardona, M., and Ploog, K., 1994, "Interface Roughness and Homogeneous Linewidths in Quantum Wells and Superlattices Studied by Resonant Acoustic-Phonon Raman Scattering," *Physical Review B,* Vol. 50, pp. 1792–1806.

Sakaki, H., Noda, T., Hirakawa, K., Tanaka, M., and Matsusue, T., 1987, "Interface Roughness Scattering in GaAs/AlAs Quantum Wells," *Applied Physics Letters,* pp. 1934–1936.

Siegel, R., and Howell, R., 1992, *Thermal Radiation Heat Transfer,* Hemisphere, Washington, D.C.

Slack, G. A., 1979, "The Thermal Conductivity of Nonmetallic Crystals," *Solid State Physics,* Vol. 34, pp. 1–71.

Smith, A. R., Chao, K.-J., Shih, C. K., Shih, Y. C., and Streetman, B. G., 1994, "Cross-Sectional Scanning Tunneling Microscopy Study of GaAs/AlAs Short Period Superlattices: The Influence of Growth Interrupt on the Interfacial Structure," *Applied Physics Letters,* Vol. 66, pp. 478–480.

Swartz, E. T., and Pohl, R. O., 1989, "Thermal Boundary Resistance," *Review of Modern Physics,* Vol. 61, pp. 605–668.

Tellier, C. R., and Tosser, A. J., 1982, *Size Effects in Thin Films,* Elsevier, Amsterdam.

Tien, C. L., and Chen, G., 1994, "Challenges in Microscale Radiative and Conductive Heat Transfer," ASME JOURNAL OF HEAT TRANSFER, Vol. 116, pp. 799–807.

Tien, C. L., Amarly, B. F., and Jagannathan, P. S., 1969, "Thermal Conductivity of Thin Metallic Films and Wires at Cryogenic Temperatures," *Proceedings of the 8th Thermal Conductivity Conference,* Plenum Press, pp. 13–20.

Waugh, J. L. T., and Dolling, G., 1963, "Crystal Dynamics of Gallium Arsenide," Physical Review, Vol. 132, pp. 2410–2412.

Weis, O., 1986, "Phonon Radiation Across Solid/Solid Interfaces with the Acoustic Mismatch Model," *Nonequilibrium Phonons in Nonmetallic Crystals,* W. Eisenmenger and A. A. Kaplyanski, eds., North-Holland, Amsterdam.

Weisbuch, C., and Vinter, B., 1991, *Quantum Semiconductor Structures,* Academic Press, Boston.

Wu, Z. L., Wei, L. H., and Kuo, P. K., 1992, "Thermal Transport Studies of Nanometric Layer Stacks by Mirage Detection," *SPIE,* Vol. 1848, pp. 361–374.

Yao, T., 1987, "Thermal Properties of AlAs/GaAs Superlattices," *Applied Physics Letters,* Vol. 51, pp. 1798–1800.

Yu, X. Y., Chen, G., Verma, A., and Smith, J. S., 1995, "Temperature Dependence of Thermophysical Properties of GaAs/AlAs Periodic Thin Film Structures," *Applied Physics Letters,* Vol. 67, pp. 3553–3556, Vol. 68, p. 1303.

Zhang, Z. C., Roger, J. P., Fournier, D., Boccara, A. C., et al., 1990, "Thermal Diffusivity of Amorphous Semiconductor Superlattice Films," *Thin Solid Films,* Vol. 186, pp. 361–366.

Ziman, J. M., 1960, *Electrons and Phonons,* Clarendon Press, Oxford.

APPENDIX A

The coefficients in Eqs. (6) and (7) can be determined from the boundary conditions. For the case of partially diffuse and partially specular interfaces without total internal reflection or total reflection due to frequency mismatch, these coefficients are given by

$$b_1^+(\mu_1) = b_1^-(-\mu_1) = \frac{1}{N}\{pt_{12}(1 - pe^{-\xi_2/\mu_2})(\Lambda_{\omega 1}\sin\theta_1 - \Lambda_{\omega 2}\sin\theta_2) + (1-p)[1 - p(r_{21}\Lambda_{\omega 1}\sin\theta_1 - t_{12}\Lambda_{\omega 2}\sin\theta_2)e^{-\xi_2/\mu_2}]\}\cos\varphi\frac{dI_{\omega 1}}{dx} \quad \text{(A1)}$$

where

$$N = 1 - p(r_{12}e^{-\xi_1/\mu_1} + r_{21}e^{-\xi_2/\mu_2}) + p^2(r_{12}r_{21} - t_{12}t_{21})e^{-\xi_1/\mu_1 - \xi_2/\mu_2}. \quad \text{(A2)}$$

For the cases of total internal reflection or total reflection due to frequency mismatch ($t_{ij} = 0$), the coefficients become

$$b_1^+(\mu_1) = b_1^-(-\mu_1) = \frac{(1-p)(1+pe^{-\xi_1/\mu_1})\Lambda_{\omega 1}\cos\varphi\sin\theta_1}{1 - p^2e^{-2\xi_1/\mu_1}}\frac{dI_{\omega 1}}{dx}. \quad \text{(A3)}$$

Coefficients b_2^+ and b_2^- can be obtained by permutations of subscripts in the above expressions.

After substituting Eqs. (5) and (6) into Eq. (7) and performing the integration over z and φ, the heat transfer rate can be expressed as

$$q = -\frac{dT}{dx}\sum_{i=1}^{2} d_i \sum_p \left[k_{bpi} - \frac{1}{2}\int_0^{\omega_{mpi}} v_{pi}C_{\omega pi}\Lambda_{\omega pi}^2[pG_{si}(\xi_1, \xi_2) + (1-p)G_{di}(\xi_1, \xi_2)]d\omega \right] \quad \text{(A4)}$$

where

$$k_{bpi} = \int_0^{\omega_{mpi}} C_{\omega pi}v_{pi}\Lambda_{\omega i}d\omega/3 \quad \text{(A5)}$$

is the bulk thermal conductivity and the subsequent two terms represent roughly contributions due to specular and diffuse interface scattering, respectively. The nondimensional integral functions G are given by

$$G_{s1}(\xi_1, \xi_2) = \left[1 - \frac{\Lambda_{\omega 2} v_2}{\Lambda_{\omega 1} v_1}\right] \int_0^1 t_{12}\mu_1(1 - \mu_1^2) \times (1 - e^{-\xi_1/\mu_1})(1 - pe^{-\xi_2/\mu_2}) \frac{d\mu_1}{N} \quad \text{(A6)}$$

$$G_{d1}(\xi_1, \xi_2) = \int_0^1 \mu_1(1 - \mu_1^2)(1 - e^{-\xi_1/\mu_1}) \times \left[1 - p\left(r_{21} - t_{12}\frac{\Lambda_{\omega 2} v_2}{\Lambda_{\omega 1} v_1}\right) e^{-\xi_2/\mu_2}\right] \frac{d\mu_1}{N} \quad (t_{12} \neq 0) \quad \text{(A7)}$$

$$G_{d1}(\xi_1) = \int_0^1 \frac{\mu_1(1 - \mu_1^2)(1 - e^{-\xi_1/\mu_1})(1 + pe^{-\xi_1/\mu_1})}{1 - p^2 e^{-2\xi_1/\mu_1}} \quad (t_{12} = 0). \quad \text{(A8)}$$

Expressions for G_{s2}, G_{d2} can be obtained by permuting subscripts 1 and 2 in the above equations.

Gray Medium. The integral functions in Eq. (35) are given by

$$A_{s1} = \int_0^1 [t_{12}\mu_1(1 - \mu_1^2)(1 - e^{-\xi_1/\mu_1}) \times (1 - pe^{-\xi_2/\mu_2})/N]d\mu_1 \quad \text{(A9)}$$

$$A_{d1} = \int_0^1 \{\mu_1(1 - \mu_1^2)(1 - e^{-\xi_1/\mu_1}) \times [1 - p(r_{21} - t_{12}\alpha_2/\alpha_1)e^{-\xi_2/\mu_2}]/N\}d\mu_1 \ (t_{12} \neq 0) \quad \text{(A10)}$$

$$A_{d1} = \int_0^1 \{\mu_1(1 - \mu_1^2)(1 - e^{-\xi_1/\mu_1})[1 + pe^{-\xi_1/\mu_1}]/[1 - p^2 e^{-2\xi_1/\mu_1}]\}d\mu_1 \ (t_{12} = 0). \quad \text{(A11)}$$

Refractive Indices at Visible Wavelengths of Soot Emitted From Buoyant Turbulent Diffusion Flames

J.-S. Wu[1]
Research Fellow

S. S. Krishnan
Graduate Student Research Assistant

G. M. Faeth
Prof., Fellow ASME
gmfaeth@umich.edu

Department of Aerospace Engineering,
The University of Michigan,
Ann Arbor, MI 48109-2118

Measurements of the optical properties of soot, emphasizing refractive indices, are reported for visible wavelengths (350–800 nm). The experiments considered soot in the fuel-lean (overfire) region of buoyant turbulent diffusion flames in the long residence time regime where soot properties are relatively independent of position in the overfire region and residence time. Flames fueled with acetylene, propylene, ethylene, and propane that were burning in still air provided a range of soot physical and structure properties. Measurements included soot composition, density, structure, gravimetric volume fraction, and scattering and absorption properties. These data were analyzed to find soot fractal dimensions, refractive indices, refractive index functions, and dimensionless extinction coefficients assuming Rayleigh-Debye-Gans scattering for polydisperse mass fractal aggregates (RDG-PFA theory). RDG-PFA theory was successfully evaluated using measured scattering properties. Soot fractal dimensions were independent of both fuel type and wavelength, yielding a mean value of 1.77 with a standard deviation of 0.04. Refractive indices were independent of fuel type within experimental uncertainties and were in reasonably good agreement with earlier measurements for soot in the fuel-lean region of diffusion flames due to Dalzell and Sarofim (1969). Dimensionless extinction coefficients were independent of both fuel type and wavelength, yielding a mean value of 5.1 with a standard deviation of 0.5, which is lower than earlier measurements for reasons that still must be explained.

Introduction

Information about the structure and optical properties of soot is needed in order to develop reliable nonintrusive (optical) measurements of soot properties and estimates of continuum radiation due to soot in flame environments. Past work has established some information about soot optical properties as follows: (i) soot consists of nearly monodisperse spherical primary particles that collect into mass fractal aggregates having broad size distributions (Faeth and Köylü, 1995; Jullien and Botet, 1987; Medalia and Heckman, 1969); (ii) soot optical properties in the visible can be approximated by Rayleigh-Debye-Gans scattering from polydisperse mass fractal aggregates, called RDG-PFA theory (Dobbins and Megaridis, 1991; Faeth and Köylü, 1995; Farias et al., 1995; Köylü and Faeth, 1994a, b; Martin and Hurd, 1987); and (iii) current estimates of soot optical properties in flame environments are mainly limited by excessive uncertainties about soot refractive indices (Chang and Charalampopoulos, 1990; Faeth and Köylü, 1995; Tien and Lee, 1982; Vaglieco et al., 1990; Viskanta and Mengüc, 1987). Motivated by these observations, the objective of the present investigation was to experimentally determine soot optical properties at visible wavelengths, emphasizing soot refractive indices.

Earlier studies of soot refractive indices in the visible are briefly reviewed in the following, more details can be found in Chang and Charalampopoulos (1990), Charalampopoulos (1992), Lee and Tien (1980), Tien and Lee (1982), Viskanta and Mengüc (1987), and references cited therein. The earliest determinations of soot refractive indices involved ex situ reflectivity measurements of compressed soot samples (Dalzell and Sarofim, 1969; Felske et al., 1984); these results were questioned, however, due to potential changes of soot properties caused by sample collection and compression as well as potential effects of surface irregularities on measured reflectance properties (Charalampopoulos, 1992; Felske et al., 1984; Tien and Lee, 1982). As a result, subsequent work emphasized in situ measurements of extinction and scattering (Chang and Charalampopoulos, 1990; Charalampopoulos, 1992; Habib and Vervisch, 1988; Lee and Tien, 1980; Vaglieco et al., 1990); unfortunately, these studies also involved a number of the following deficiencies: soot structure generally was not characterized adequately; Rayleigh and Mie scattering approximations were used to interpret the measurements, which have not proven to be very effective for soot aggregates; and questionable approximations involving either Drude-Lorentz dispersion models or Kramers-Krönig causality relationships had to be adopted so that soot refractive indices could be found from the measurements (Dobbins and Megaridis, 1991; Faeth and Köylü, 1995; Köylü and Faeth, 1994a, b, 1996).

In view of these considerations, the present experimental study of soot refractive indices and related optical properties was undertaken; this study considered soot emitted from buoyant turbulent diffusion flames in the long residence time regime where soot properties are relatively independent of position in the fuel-lean (overfire) region and the residence time. A range of soot physical and structure properties were studied by considering flames fueled with acetylene, propylene, and ethylene and propane burning in still air. The approach to find optical properties involved ex situ measurements of soot physical and structure properties, gravimetric measurements of soot volume

[1] Now with the National Space Program Office, Hsin-Chu City, Taiwan, Republic of China.

Contributed by the Heat Transfer Division for publication in the JOURNAL OF HEAT TRANSFER. Manuscript received by the Heat Transfer Division February 19, 1996; revision received November 14, 1996; Keywords: Fire/Flames, Radiation, Thermophysical Properties. Associate Technical Editor: S. H. Chan.

fractions, and in situ measurements of soot extinction and scattering properties. Then, after checking that RDG-PFA theory was acceptable, this theory was used to find the fractal dimensions, refractive indices, and dimensionless extinction coefficients of the soot. Present measurements were carried out at visible wavelengths (350–800 nm) because this wavelength range is important for nonintrusive (optional) measurements of soot properties and is accessible for in situ optical techniques due to reasonably large soot scattering levels.

The paper begins with descriptions of experimental and theoretical methods. Results are then considered treating soot scattering properties, fractal dimensions, and optical properties in turn.

Experimental Methods

Apparatus. The apparatus is described by Köylü and Faeth (1994a). Combustion was in still air within a large enclosure to control room disturbances. A 50 mm diameter watercooled burner, injecting fuel gases vertically upward, was used to yield strongly buoyant turbulent diffusion flames. Soot properties were measured by collecting the combustion products in a hood and in a 152 mm diameter sampling duct (both of which were heated to prevent thermophoretic deposition of soot on their surfaces) that discharged into the main exhaust hood of the flame apparatus. Measurements showed that mixing within the collection system was sufficient to yield uniform properties (soot concentrations, gas concentrations, and temperatures) across the exit of the sampling duct where measurements were made. Note: using a collection system in this way does not affect soot structure and optical properties because soot properties are relatively independent of position in the overfire region and residence time within the long residence time regime (Köylü and Faeth, 1994a).

Sampling Measurements. Aside from routine sampling measurements of gas temperatures and compositions at the measuring location, sampling measurements included soot structure, density, composition, and gravimetric volume fractions. Soot structure was found by thermophoretic sampling and analysis using transmission electron microscopy (TEM), following Köylü and Faeth (1992). The sampling surfaces were the carbon-supported copper grids used to hold TEM specimens (3 mm diameter 200 mesh copper grids supported by a 20 nm thick elemental carbon film: SPI Supplies, Philadelphia, PA, Part No. 3520C). When sampling, the grids were parallel to the flow direction (vertical) at the flow axis. The grids were mounted on a double-acting pneumatic probe with sampling times measured using a pair of light-intercepting sensors and controlled so that soot aggregates covered less than 10 percent of the grid surface in order to avoid overlapping aggregates on the grid. Effects of aggregate size on sampling bias for the present soot aggregates are discussed by Köylü and Faeth (1992) and Köylü et al. (1995); approximating aggregates by equivalent spheres suggests sampling velocity variations less than 20 percent over the size range of 95 percent of the aggregates. Similarly, allowing for the branched structure of the aggregates, following Rosner et al. (1991), also suggests sampling velocity variations less than 20 percent over the aggregate size range. The samples were observed using a JEOL 2000 FX analytical electron microscope system with a 1 nm edge-to-edge resolution. Latex spheres having a diameter of 91 nm (5.8 nm standard deviation) were used to calibrate the TEM measurements. Samples of 400 primary particles selected from more than 50 aggregates were used to find the mean value of d_p with an experimental uncertainty less than 2 percent (95 percent confidence). These measurements also established that primary particles were reasonably monodisperse, i.e., standard deviations were typically 17–21 percent of mean values of d_p. Finally, the values of $\bar{N}$, due to Köylü and Faeth (1992), for the same soot were confirmed within experimental uncertainties.

Soot densities were found by thermophoretic sampling at the axis of the measuring location using a finned water-cooled metal plate. Soot was periodically scraped from the plate until a sample weighing roughly 500 mg was obtained. The samples were then compressed into pellets to facilitate density measurements using helium pycnometry with a 1000 mm^3 cell (Micrometrics Inc., Norcross, GA). Experimental uncertainties (95 percent confidence) of density measurements were estimated to be less than one percent. The composition of a portion of the overfire soot was known from Köylü (1992); therefore, these measurements were not repeated.

Gravimetric soot volume fractions were measured at the axis of the measuring location following Choi et al. (1995). This involved sampling the flow and determining the volumes of soot and gas collected. A 13 mm inside diameter water-cooled probe, aligned with the flow direction, was used for sampling. The probe was connected to a modified filter holder that could accommodate a 47 mm diameter filter (Gelman Product 2220, in-line). The filter was connected to a vacuum pump through a flowmeter and valve. The flowmeter had a manometer at its inlet and was calibrated over the required range of inlet pressures and flow rates using a wet test meter. Soot samples were collected for a timed period using two filters (Gelman Part No. 66143, 200 nm, TF200, PTFE membrane filter). One filter was

Nomenclature

C = optical cross section
d_p = primary particle diameter
D_f = mass fractal dimension
$E(m)$ = refractive index function = $Im((m^2 - 1)/(m^2 + 2))$
f_v = soot volume fraction
$F(m)$ = refractive index function = $|(m^2 - 1)/(m^2 + 2)|^2$
$i = (-1)^{1/2}$
I = light intensity
k = wave number = $2\pi/\lambda$
k_e = dimensionless extinction coefficient
k_{eR} = dimensionless extinction coefficient including scattering, Eq. (8)
k_f = fractal prefactor
L = light path length
m = soot refractive index = $n + i\kappa$
n = real part of soot refractive index
n_p = mean number of primary particles per unit volume
N = number of primary particles in an aggregate
q = modulus of scattering vector = $2k \sin(\theta/2)$
Q = volumetric optical cross section
R_g = radius of gyration of an aggregate
x_p = primary particle size parameter = $\pi d_p/\lambda$
θ = angle of scattering from forward direction
κ = imaginary part of soot refractive index
λ = wavelength of radiation
ρ_s = density of soot
ρ_{sa} = ratio of scattering to absorption cross sections
ρ_v = polarization ratio

Subscripts

a = absorption
e = extinction
h = horizontal polarization
ij = incident (i) and scattered (j) polarization directions
s = total scattering
v = vertical polarization

Superscripts

a = aggregate property
p = primary particle property
$\bar{(\ )}$ = mean value over a polydisperse aggregate population

in the filter holder, and the second filter mechanically collected soot from the sampling line and filter assembly. The mass of sampled soot was found by weighing the filters before and after sampling using an electronic balance. Then, given the density of the soot, the mass of soot collected, the volume of gas collected, and gas temperatures at the sampling and volume measuring conditions, the gravimetric soot volume fraction can be calculated in a straightforward manner. Times of sampling for these measurements were adjusted to achieve experimental uncertainties less than 6 percent (95 percent confidence). The exhaust flow was nearly uniform so that sampling rates varying 4:1 around estimated isokinetic sampling rates had negligible effect on the measurements.

Optical Measurements. Scattering and extinction properties of the soot aggregates were found using the same general arrangement as Köylü and Faeth (1994a, b). The light sources used for measurements at various wave lengths were as follows: 351.2, 488.0, and 514.5 nm using an argon-ion laser (4 W Coherent Innova model 90-4); 405.0 nm using a mercury lamp and a 10 nm bandwidth filter (100 W, Oriel model 6333); 632.8 nm using a He-Ne laser (28 mW, Jodon Model HN10G1R); and 800.0 nm using a laser diode (700 mW, SDL-2360-P3). The incident beams were passed through a polarization rotator and a mechanical chopper before being focused on the axis of the sampling duct using a 1000 mm focal length lens. The collecting optics for scattering measurements were mounted on a turntable surrounding the exhaust duct so that scattering angles of 5–160 deg could be considered. The collecting optics consisted of an 85 mm focal length lens (having a collection angle of 0.7 msr), dichroic sheet polarizer filters (1 nm bandwidth for the laser sources and 10 nm bandwidth for the lamp source), neutral density filters (to control the dynamic range), and a photodetector. The extinction measurements employed similar, but rigidly mounted, collecting optics. As noted earlier, concentrations of soot were nearly constant along the optical path for extinction measurements; nevertheless, gravimetric measurements along the optical path allowed correction of the extinction measurements to conditions at the axis where all other measurements were made. An optical system housing and darkroom conditions in the laboratory were used to control optical noise from ambient lighting. The output of the photodetectors was passed through lock-in amplifiers, prior to sampling and storage using a laboratory computer.

The angular light scattering system was calibrated by measuring Rayleigh scattering from propane gas, except at 800 nm where an alternative approach was used, as discussed later. After correcting for the reciprocal sin θ effect caused by the geometry of the measuring volume, the *vv* and *hh* differential cross sections agreed with Rayleigh scattering predictions within 5 percent for $20 \leq \theta \leq 160$ deg. Then, absolute volumetric differential scattering cross sections of soot were found from ratios of the detector signal for soot and propane, after accounting for signal attenuation in the optical path, based on the Rayleigh scattering properties of propane from Rudder and Bach (1968) and Dyer (1979). Total volumetric scattering cross sections were found by integrating volumetric differential scattering cross sections over the whole spherical surface; this required extrapolation to reach $\theta = 0$ and 180 deg, but the effect of these extrapolations was small due to the relatively small solid angles involved. The optical arrangement for the extinction measurements was designed as discussed by Manickavasagam and Mengüc (1993) so that uncertainties due to forward scattering were less than one percent over the present test range. The experimental uncertainties (95 percent confidence) of the angular and total light scattering measurements were comparable and are estimated to be less than 10 percent (they are dominated by calibration uncertainties, finite sampling times, the finite aperture of the collection system, and the angular uncertainty of the collecting optics). The corresponding uncertainties of total extinction and absorption cross sections are smaller, less than 5 percent, due to reduced effects of calibration uncertainties.

Theoretical Methods

Analysis of the scattering measurements to find soot optical properties was based on RDG-PFA theory. The main assumptions of RDG-PFA theory are as follows: individual primary particles satisfy the Rayleigh scattering approximation, soot aggregates satisfy the Rayleigh-Debye-Gans (RDG) scattering approximation, primary particles are spherical and monodisperse, primary particles just touch one another, the number of primary particles per aggregate satisfies a log-normal probability distribution function, and the aggregates are mass fractal-like objects that satisfy the following relationship (Jullien and Botet, 1987):

$$N = k_f (R_g/d_p)^{D_f}. \tag{1}$$

These approximations have proven to be satisfactory during past evaluations for a variety of conditions (Köylü and Faeth, 1992, 1994a, b, 1996); nevertheless, they still were evaluated using present measurements before the theory was used to find soot optical properties.

The first step of the present calculations involve the determination of the mean number of primary particles per unit volume at the measurement location from the gravimetric measurement of soot volume fraction and the TEM measurement of primary particle diameter:

$$n_p = 6 f_v/(\pi d_p^3). \tag{2}$$

Then, noting that $\bar{Q}_a^a = \bar{Q}_e^a - \bar{Q}_s^a$, so that $\bar{Q}_a^a$ can be found from present measurements of $\bar{Q}_e^a$ and $\bar{Q}_s^a$, the refractive index functions, $E(m)$ and $F(m)$ can be computed as follows:

$$E(m) = k^2 \bar{Q}_a^a/(4\pi x_p^3 n_p) \tag{3}$$

$$F(m) = k^2 (qd_p)^{D_f} \bar{Q}_{vv}^a(qd_p)/(k_f x_p^6 n_p) \tag{4}$$

where qd_p must be large enough so that scattering is in the large-angle (power-law) regime where Eq. (4) is appropriate. This requirement was established by noting the behavior of RDG-PFA scattering at the limiting conditions of small-angle (Guinier) and large-angle (power-law) scattering, as follows:

$$\bar{Q}_{vv}^a(qd_p)/Q_{vv}^p = (\bar{N}^2/\bar{N}) \exp(-q^2 \bar{R}_g^2/3), \text{ Guinier regime} \tag{5}$$

$$\bar{Q}_{vv}^a(qd_p)/Q_{vv}^p = k_f (qd_p)^{-D_f}, \text{ power-law regime} \tag{6}$$

where the expression for $\bar{R}_g^2$ in the Guinier regime can be found in Köylü and Faeth (1994a) while the value of $k_f = 8.5$ was adopted from the recent determination of Köylü et al. (1995). The volumetric primary particle Rayleigh scattering cross section used to normalize Eqs. (5) and (6) is given by

$$Q_{vv}^p = n_p x_p^6 F(m)/k^2. \tag{7}$$

From Eqs. (5) and (6) it can be seen that $\bar{Q}_{vv}^a(qd_p)/Q_{vv}^p$ approaches the aggregate size moment, $\bar{N}^2/\bar{N}$, as qd_p approaches zero in the Guinier regime. It is also evident that $\bar{Q}_{vv}^a(qd_p)/Q_{vv}^p$ provides a simple determination of soot fractal dimensions because D_f is the slope of this function in the power-law regime. Finally, $E(m)$ and $F(m)$ provide two nonlinear algebraic equations that can be solved to find the real and imaginary parts of the soot refractive indices.

The dimensionless extinction coefficient is a useful optical property that provides a simple relationship between extinction and soot volume fractions (Dobbins et al., 1994; Choi et al., 1995). This parameter was found for present test conditions by noting that properties were constant along the optical path used for extinction measurements which implies (Choi et al., 1995)

$$k_{eR} = k_e(1 + \rho_{sa}) = -\lambda \ln(I/I_o)/(Lf_v). \quad (8)$$

Results and Discussion

Test Conditions. Flame and soot properties at the test conditions are summarized in Table 1. The flames involved heat release rates in the range 5100–7400 W. The flames are ordered in the table in terms of decreasing propensity to soot, as indicated by progressively decreasing primary particle diameters. Present measurements of soot densities are in the range 1850–1930 kg/m^3, which is typical of earlier measurements in the literature (Jullien and Botet, 1987; Köylü and Faeth, 1992). Primary particle diameters are in the range 30–47 nm and the mean number of primary particles per aggregate is in the range 364–467, both of which are in good agreement with the earlier measurements of Köylü and Faeth (1992) for the same soot. These values of d_p and $\bar{N}$ yield typical aggregate dimensions on the order of 1000–10,000 nm, which is somewhat larger than the visible wavelength range; therefore, present measurements involve significant effects of scattering. Finally, the compositions of this soot, measured earlier by Köylü (1992), exhibit significant variations over the test range, with C/H, C/O, and C/N atomic ratios in the ranges 12–17, 57–107, and 295–411, respectively.

Extinction and Scattering Properties. Measured volumetric extinction and scattering cross sections for the four fuels are plotted in Fig. 1. The values of $\bar{Q}_e^a$ and $\bar{Q}_s^a$ progressively increase with increasing propensity to soot. This effect is caused by both increasing concentrations of soot and increased scattering due to larger primary particle diameters and aggregate sizes as the propensity to soot increases, see Table 1. The values of $\bar{Q}_e^a$ and $\bar{Q}_s^a$ are relatively independent of wavelength over the present test range. It will be seen later that this behavior is caused by increasing refractive indices with increasing wavelength that nearly compensate, fortuitously, for decreasing scattering and extinction cross sections that are expected with increasing wavelength for RDG scattering if refractive indices are constant. The ratio of scattering to absorption cross sections, ρ_{sa}, also remains relatively constant for a particular fuel over the present test range; therefore, single values of ρ_{sa} are given for each fuel in Table 1, while the standard deviations of these values are less than five percent. This effect also follows from the variation of refractive indices which compensates for the greater sensitivity of scattering than absorption to wavelength variations for RDG scattering. Mean values of ρ_{sa} are in the range 0.25–0.43 and tend to increase with increasing propensity to soot. These values of ρ_{sa} are sufficiently large to yield significant effects of aggregate scattering for present conditions; for example, ignoring the contribution of scattering to extinction would overestimate optically-determined soot volume fractions by 25–50 percent. Finally, present values of ρ_{sa} for wavelengths of 350–800 nm agree with the results of Köylü and Faeth (1994a) at 514.5 nm for the same soot within 12 percent, which is well within experimental uncertainties.

Table 1 Test conditions[a]

Fuel	C_2H_2	C_3H_6	C_2H_4	C_3H_8
Heat release rate (W)	6160	6580	5140	7400
f_v (ppm)	0.476	0.247	0.0446	0.0278
n_p (million-part./mm^3)	8.76	6.84	2.60	1.97
Gas temperature (K)	370	420	420	450
ρ_p (kg/m^3)	1870	1850	1930	1900
d_p (mm)	47	41	32	30
$\bar{N}$(-)[b]	417	400	467	364
ρ_{sa}(-)[c]	0.43	0.41	0.32	0.25
D_f(-)[c]	1.74	1.79	1.78	1.78
Atomic ratios:[b]				
C/H	16.8	17.0	---	12.1
C/O	107	57.6	---	---
C/N	295	411	---	331

[a]Soot in overfire region of buoyant turbulent diffusion flames in long residence time regime.
[b]Measured by Köylü (1992) and Köylü and Faeth (1994a).
[c]Effect of wavelength is small compared to experimental uncertainties.

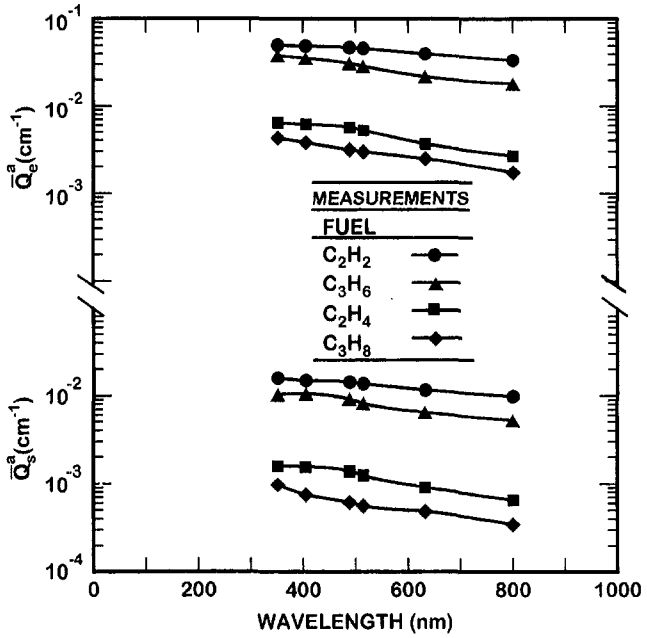

Fig. 1 Measured volumetric extinction and scattering cross sections as a function of wavelength

Scattering Patterns. RDG-PFA scattering theory was evaluated in order to justify the present approach to find soot refractive indices. The smallest wavelengths of the test range were a particular concern because values of x_p become large at these conditions, which raises questions about the RDG scattering approximations (Faeth and Köylü, 1995). Thus, measured and predicted scattering patterns at the worst-case condition for the present test range (acetylene soot at 351.2 nm which yields $x_p = 0.42$) are illustrated in Fig. 2. Similar to past findings at longer wavelength (Köylü and Faeth, 1994b), there is excellent agreement between measurements and predictions, justifying use of RDG-PFA scattering theory over the present test range. The scattering patterns in Fig. 2 exhibit strong scattering at small values of θ in the Guinier regime which is not typical of Rayleigh scattering where $\bar{Q}_{vv}^a$ would be relatively independent of θ. This highlights the importance of considering RDG-PFA scattering theory when interpreting present measurements to find soot optical properties.

The results illustrated in Fig. 2 indicate relatively strong effects of depolarization which must be handled empirically when using RDG-PFA theory. This was done similar to Köylü and Faeth (1994a) by defining a depolarization ratio, ρ_v, as follows:

$$\bar{Q}_{hv}^a = \bar{Q}_{vh}^a = \bar{Q}_{hh}^a(90 \text{ deg}) = \rho_v \bar{Q}_{vv}^a(90 \text{ deg}). \quad (9)$$

This parameter is then used analogous to Rayleigh scattering theory, see Rudder and Bach (1968), to find values of $\bar{Q}_{hh}^a(\theta)$ as follows:

$$\bar{Q}_{hh}^a(\theta) = [(1 - \rho_v)\cos^2\theta + \rho_v]\bar{Q}_{vv}^a(\theta). \quad (10)$$

Present values of ρ_v are summarized as a function of fuel type and wavelength in Table 2, except for C_3H_6, C_2H_4, and C_3H_8 at 800 nm where scattering levels were too small for an accurate determination of ρ_v. Predictions illustrated in Fig. 2 show that the resulting correlation of $\bar{Q}_{hh}^a(\theta)$ is excellent, similar to the

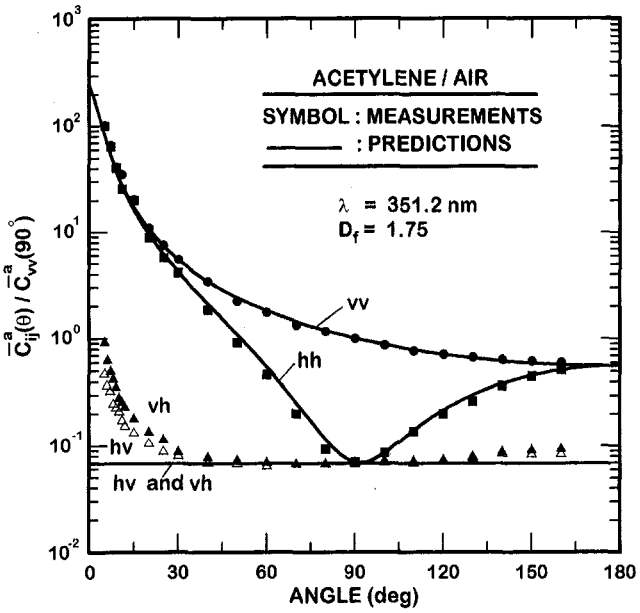

Fig. 2 Measured and predicted angular scattering patterns at 351.2 nm for overfire soot aggregates in buoyant turbulent acetylene/air diffusion flames

predictions of $\bar{Q}^a_{vv}(\theta)$. The values of $\bar{Q}^a_{hv}(\theta)$ and $\bar{Q}^a_{vh}(\theta)$ also are in good agreement with the correlation of Eq. (9), except near the forward scattering direction where measured values increase and the *vh* and *hv* components are no longer equal. Experimental difficulties in the small angle region are thought to be responsible for this behavior because problems of alignment and cross polarization leakage are severe in the forward scattering direction where scattering levels are very high. Scattering behavior at other test conditions was similar to Fig. 2.

The values of ρ_v, summarized in Table 2, are roughly an order of magnitude larger than typical values for Rayleigh scattering from gases, see Rudder and Bach (1968). This behavior is not unexpected because scattering is much stronger for RDG-PFA scattering from soot aggregates than for Rayleigh scattering from gases. Additionally, such trends are supported by the progressive increases of ρ_v with decreasing wavelength and increasing propensity to soot, which also corresponds to changes that increase the effects of scattering. Finally, present values of ρ_v at 514.5 nm agree with the earlier measurements of Köylü and Faeth (1994a) for the same soot within 20 percent, which is well within experimental uncertainties for this variable.

Fractal Properties. Evaluating whether present measurements properly reach the power-law regime, so that Eq. (4) can be used to find refractive indices, and exploiting these conditions to find fractal dimensions, can best be done by plotting $\bar{Q}^a_{vv}(qd_p)/Q^p_{vv}$ as a function of the modulus of the scattering vector, qd_p, as suggested by Eq. (6). These results are illustrated for all four fuels at a wavelength of 632.8 nm in Fig. 3, however, behavior at other wavelengths is similar. The results shown in the figure include the measurements and predictions over the available ranges of qd_p, as well as the extrapolation of power-law behavior based on Eq. (6). As before, the substantial departure of scattering properties from Rayleigh scattering behavior (where $\bar{Q}^a_{vv}(qd_p)/Q^p_{vv}$ would be independent of qd_p) is evident, with forward scattering 100–1000 times larger than back scattering for the present large soot aggregates. The measurements also clearly provide the extended power-law regime where scattering properties are represented by Eq. (6), e.g., roughly, $qd_p > 0.1$ is needed for the current in situ method to find soot refractive indices.

The measurements of $\bar{Q}^a_{vv}(qd_p)/Q^p_{vv}$ in the power-law regime were used to compute fractal dimensions as discussed earlier. It was found that effects of wavelength were small, which is reasonable because fractal properties should only depend on the morphology of the soot aggregates. Thus, only mean values of D_f over the present wavelength range are summarized for each fuel in Table 1. Clearly, the variation of D_f with fuel type is not very significant either, yielding a mean value of $D_f = 1.77$ with a standard deviation of 0.04. These results are in good agreement with earlier determinations of fractal dimensions due to Köylü and Faeth (1994a) for the same soot and with measurements of other soot in flame environments (see Köylü and Faeth

Table 2 Polarization ratios[a]

Wavelength (nm)	Fuel C_2H_2	C_3H_6	C_2H_4	C_3H_8
351.2	0.070	0.065	0.056	0.044
405.0	0.055	0.042	0.041	0.038
488.0	0.042	0.033	0.026	0.022
514.5	0.041	0.030	0.023	0.020
632.8	0.038	0.028	0.022	0.019
800.0	0.032	-------	-------	-------

[a]For overfire soot in buoyant turbulent diffusion flames in the long residence time regime, as summarized in Table 1.

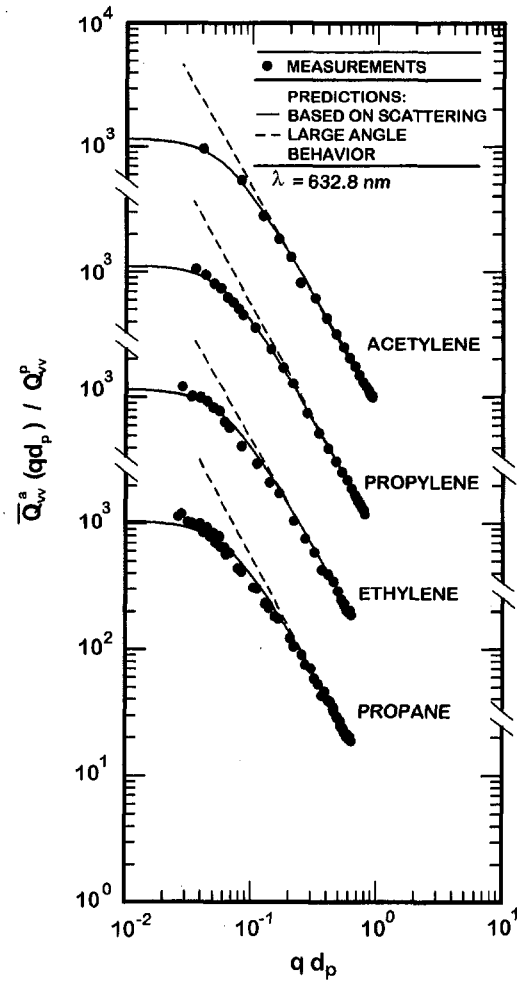

Fig. 3 Measured and predicted volumetric *vv* cross sections at 632.8 nm as functions of the modulus of the scattering vector

(1994a); Faeth and Köylü (1995); references cited therein). This universality of soot fractal dimensions in flames is very helpful for exploiting RDG-PFA scattering theory to find soot properties from scattering measurements and to estimate continuum radiation properties.

Optical Properties. Results, thus far, have shown that RDG-PFA theory performs reasonably well for present conditions, that present scattering measurements are consistent with earlier measurements for the same soot, that present fractal dimensions are in good agreement with earlier work, and that present scattering measurements at large angles ($qd_p > 0.1$) are within the power-law regime. Based on these findings, Eqs. (2)–(8) were used to compute soot optical properties from the present measurements after adopting $k_f = 8.5$ from Köylü et al. (1995), as mentioned earlier. Results at 800.0 nm, however, were analyzed somewhat differently from the rest because signal-to-noise ratios at this wavelength were too low to provide adequate absolute calibrations of scattering levels based on Rayleigh scattering from propane. Thus, since ρ_{sa} was nearly independent of wavelength for each fuel it was exploited, the values summarized in Table 1 were used to define absolute scattering levels at 800 nm from the extinction measurements for each fuel.

The resulting real and imaginary parts of the refractive indices of soot from the present measurements are plotted as a function of wavelength, with fuel type as a parameter, in Fig. 4. Combining all factors, the experimental uncertainties of the real and imaginary parts of the refractive indices of soot (95 percent confidence) are estimated to be less than 20 percent. Refractive index measurements exhibit relatively small effects of fuel type for present test conditions, with standard deviations of n and κ at each wavelength due to variations of fuel type only averaging three and 11 percent of their respective mean values. Thus, no effect of fuel type on refractive indices can be

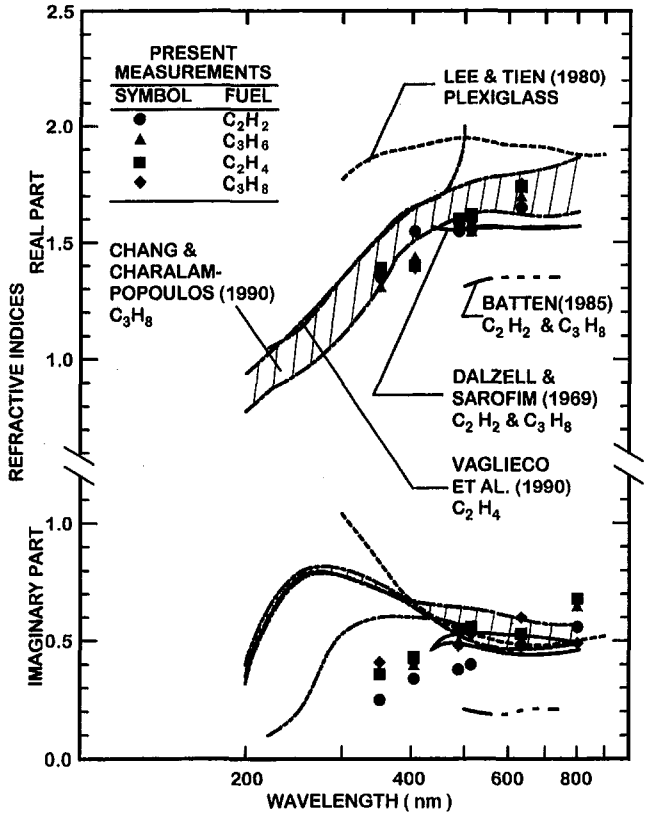

Fig. 4 Measured refractive indices of soot in the ultra-violet and visible portions of the spectrum

Table 3 Soot optical properties[a]

Wavelength (nm)	E(m)	F(m)	n	κ	k_{eR}
351.2	0.19	0.10	1.36	0.35	4.6
405.0	0.21	0.13	1.45	0.40	5.0
488.0	0.22	0.19	1.58	0.48	5.4
514.5	0.24	0.20	1.58	0.51	5.3
632.8	0.22	0.24	1.71	0.53	5.4
800.0[b]	0.23	0.36	-----	0.65	5.1

[a]Average values for overfire soot within buoyant turbulent diffusion flames in the long residence time regime. Measurements consider flames fueled with acetylene, propylene, ethylene and propane burning in still air as summarized in Table 1.
[b]Results at this wavelength were found from extrapolated values of ρ_{sa}.

established for these results within present experimental uncertainties. This behavior generally agrees with past observations of soot refractive indices in diffusion flames (see Köylü and Faeth (1996); Faeth and Köylü (1995); Dalzell and Sarofim (1969); references cited therein). Naturally, functions of n and κ, such as $E(m)$ and $F(m)$, are relatively independent of fuel type as well; therefore, the values of $E(m)$, $F(m)$, n, κ, and k_{eR} (to be discussed later) are summarized as a function of wavelength in Table 3. The experimental uncertainties of $E(m)$ and $F(m)$ (95 percent confidence) are estimated to be less than 19 and 23 percent, respectively. The relatively close agreement between present measurements and the widely-quoted refractive index values of $n = 1.56$ and $\kappa = 0.57$ at 514.5 nm from Dalzell and Sarofim (1969) is quite evident, as discussed next.

Several earlier measurements of soot refractive indices are illustrated in Fig. 4 for comparison with the present results. These measurements include: the classical ex situ reflectometry measurements for soot in the fuel-lean region of acetylene/air and propane/air diffusion flames due to Dalzell and Sarofim (1969); the ex situ measurements for soot in the fuel-lean region of acetylene/air and propane/air diffusion flames due to Batten (1985); the in situ measurements for soot in the fuel-lean region of plexiglass/air diffusion flames due to Lee and Tien (1980); the in situ measurements for soot in the post-flame region of fuel-rich premixed propane/air flames due to Chang and Charalampopoulos (1990); and the in situ measurements for soot in the post-flame region of fuel-rich premixed ethylene/air flames due to Vaglieco et al. (1990). It should be noted that the ex situ measurements of Dalzell and Sarofim (1969) have been criticized by Lee and Tien (1980) for potential problems of soot property changes due to soot collection and sample preparation, and by Felske et al. (1984) for potential problems of diffuse scattering for reflectometry measurements due to surface roughness. On the other hand, the measurements of Lee and Tien (1980), Batten (1985), Chang and Charalampopoulos (1990), and Vaglieco et al. (1990) can be criticized, as noted earlier, because: they all involve questionable models for the optical properties of soot; some involve questionable soot transport properties in cases where dynamic scattering measurements are used to estimate soot aggregate properties; and some involve questionable approximations associated with either Drude-Lorentz dispersion models or Kramers-Krönig causality relationships used to close the procedure to find soot refractive indices. Finally, Chang and Charalampopoulos (1990) observe variations of soot refractive indices with increasing residence time in the post-flame region of premixed flames. This is attributed to an effect of soot aging (or annealing) in a high temperature environment, so that their results are indicated by a band.

The present measurements of soot refractive indices illustrated in Fig. 4 agree best with the findings of Dalzell and Sarofim (1969), as noted earlier, and are similar to the findings of Köylü and Faeth (1994a, 1996) in spite of past criticism of the methodology. Nevertheless, reasons for this behavior and

for the discrepancies among various investigators, as well as adequate definition of effects of fuel type, wavelength, flame conditions, and residence time, clearly merit additional study. Present refractive indices are seen to progressively increase as wavelength is increased. This behavior acts to reduce the variation of extinction, absorption, and scattering cross sections with wavelength, as discussed earlier. Finally, present measurements of soot refractive indices do not exhibit an effect of resonance in the near ultra-violet range of the spectrum that is seen for graphite; instead, the present soot refractive indices progressively decrease as the near ultra-violet is approached, which tends to agree with recent observations of Vaglieco et al. (1990) who observed only a slight effect of resonance near the uv. Naturally, this behavior suggests problems for some past determinations of soot refractive indices where the presence of resonance conditions is assumed, by analogy with graphite, when either Drude-Lorentz dispersion relations or Kramers-Krönig causality relationships were developed.

Present determinations of the dimensionless extinction coefficient, k_{eR}, are plotted as a function of wavelength, with fuel type as a parameter (Fig. 5). The experimental uncertainties of k_{eR} (95 percent confidence) are estimated to be less than 20 percent. Present values of k_{eR} are in the range 4.0–6.2 and really do not exhibit significant variations with wavelength and fuel type. This behavior comes about due to fortuitous cancellation of the effects of scattering, wavelength, and refractive index variations similar to the behavior of $\bar{Q}_e^a$ and $\bar{Q}_s^a$. Values of k_{eR} averaged over the four fuels are summarized as a function of wavelength in Table 3. Averaging over all the present data yields $k_{eR} = 5.1$ with a standard deviation of 0.5; this correlation is also illustrated in Fig. 5.

Other measurements of k_{eR} are plotted in Fig. 5 for comparison with the present measurements. This includes measurements for soot in the fuel-lean region of crude-oil/air diffusion flames, due to Dobbins et al. (1994), and measurements for soot in the post-flame region of premixed fuel-rich acetylene/air flames, due to Choi et al. (1995). These measurements are significantly larger than present measurements with values of k_{eR} in the range 8.1–9.4 reported by Dobbins et al. (1994), and a mean value of $k_{eR} = 8.6$ with a standard deviation of 0.5 reported by Choi et al. (1995). Because present results show that effects of fuel type (and thus degree of aggregation) and wavelength on k_{eR} were not very large, the reasons for this discrepancy are not obvious and clearly merit further study.

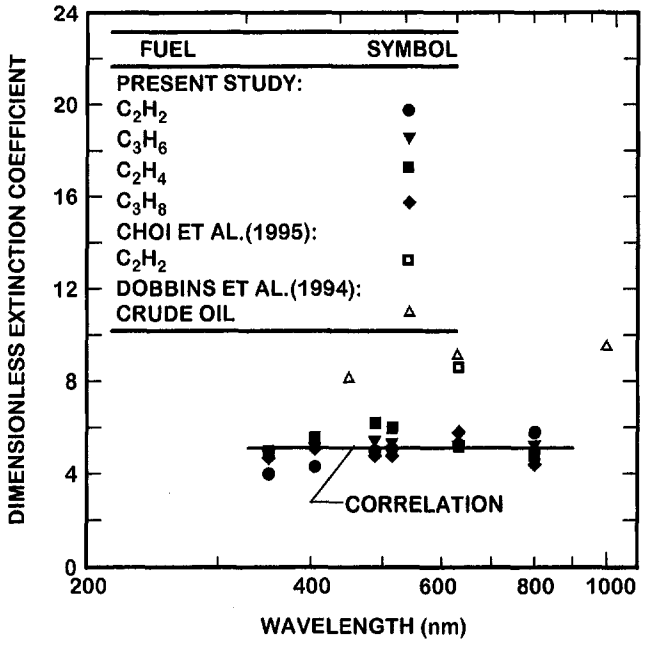

Fig. 5 Measured dimensionless extinction coefficients of soot in the visible and near-infrared portions of the spectrum

Conclusions

The fractal and optical properties of soot were studied experimentally considering soot within the overfire region of buoyant turbulent diffusion flames in the long residence time regime where soot properties are independent of position in the overfire region, and residence time, for a particular fuel. The investigation was limited to soot in flames fueled by acetylene, propylene, ethylene, and propane and burning in still air. They yielded soot having atomic C/H, C/O, and C/N ratios in the ranges 12–17, 57–107, and 295–411, respectively. The investigation was also limited to wavelengths in the visible (350–800 nm). The main conclusions of the study are as follows:

1. Present soot refractive indices did not vary significantly with fuel type and were in reasonably good agreement with earlier measurements for similar conditions due to Dalzell and Sarofim (1969).
2. Present soot refractive indices did not exhibit an approach to a resonance condition in the near uv that is observed for graphite; instead, refractive indices declined continuously as the near uv was approached, similar to the observations of Vaglieco et al. (1990) for amorphous carbon and soot.
3. Present dimensionless extinction coefficients were relatively independent of fuel type and wavelength yielding an average value of 5.1 and a standard deviation of 0.5; however, this value is significantly lower than values in the range 8.1–9.4 reported by Dobbins et al. (1994) and Choi et al. (1995) for reasons that still must be explained.
4. Present fractal dimensions were relatively independent of fuel type and wavelength yielding an average value of 1.77 and a standard deviation of 0.04, which is in reasonably good agreement with the measurements of Köylü and Faeth (1994a) for the same soot at a wavelength of 514.5 nm.
5. The approximate RDG-PFA scattering theory agreed with present measurements within experimental uncertainties; this represents a severe test of the approximate theory because primary particle optical diameters reached values up to 0.42, which represent the largest values considered thus far.

Acknowledgments

This research was supported by the Laboratory for Building and Fire Research of the National Institute of Standards and Technology, Grant Nos. 60NANB1D1175 and 60NANB4D1699, with H. R. Baum and K. C. Smyth serving as scientific officers. The authors also acknowledge the assistance of Ü. Ö. Köylü during the early phases of the work.

References

Batten, C. E., 1985, "Spectral Optical Constants of Soots From Polarized Angular Reflectance Measurements," *Appl. Optics,* Vol. 24, pp. 1193–1199.

Chang, H. Y., and Charalampopoulos, T. T., 1990, "Determination of the Wavelength Dependence of Refractive Indices of Flame Soot," *Proc. R. Soc. London A,* Vol. 430, pp. 577–591.

Charalampopoulis, T. T., 1992, "Morphology and Dynamics of Agglomerated Particulates in Combustion Systems Using Light Scattering Techniques," *Prog. Energy Combust. Sci.* Vol. 18, pp. 13–45.

Choi, M. Y., Mulholland, G. W., Hamins, A., and Kashiwagi, T., 1995, "Comparisons of the Soot Volume Fraction Using Gravimetric and Light Extinction Techniques," *Combust. Flame,* Vol. 102, pp. 161–169.

Dalzell, W. H., and Sarofim, A. F., 1969, "Optical Constants of Soot and Their Application to Heat Flux Calculations," ASME JOURNAL OF HEAT TRANSFER, Vol. 91, pp. 100–104.

Dobbins, R. A., and Megaridis, C. M., 1991, "Absorption and Scattering of Light by Polydisperse Aggregates," *Appl. Optics,* Vol. 30, pp. 4747–4754.

Dobbins, R. A., Mulholland, G. W., and Bryner, N. P., 1994, "Comparison of a Fractal Smoke Optics Model with Light Extinction Measurements," *Atmospheric Environment,* Vol. 28, pp. 889–897.

Dyer, T. M., 1979, "Rayleigh Scattering Measurements of Time-Resolved Concentration in a Turbulent Propane Jet," *AIAA J.,* Vol. 17, pp. 912–914.

Faeth, G. M., and Köylü, Ü. Ö., 1995, "Soot Morphology and Optical Properties in Nonpremixed Turbulent Flame Environments," *Combust. Sci. Tech.,* Vol. 108, pp. 207–229.

Farias, T., Carvalho, M. G., Köylü, Ü. Ö., and Faeth, G. M., 1995, "Computational Evaluation of Approximate Rayleigh-Debye-Gans/Fractal-Aggregate Theory for the Absorption and Scattering Properties of Soot," ASME JOURNAL OF HEAT TRANSFER, Vol. 117, pp. 152–159.

Felske, J. D., Charalampopoulos, T. T., and Hura, H., 1984, "Determination of the Refractive Indices of Soot Particles From the Reflectivities of Compressed Soot Pellets," *Combust. Sci. Tech.,* Vol. 37, pp. 263–284.

Habib, Z. G., and Vervisch, P., 1988, "On the Refractive Index of Soot at Flame Temperature," *Combust. Sci. Tech.,* Vol. 59, pp. 261–274.

Jullien, R., and Botet, R., 1987, *Aggregation and Fractal Aggregates,* World Scientific Publishing Co., Singapore, pp. 45–60.

Köylü, Ü. Ö., 1992, "Emission, Structure and Optical Properties of Overfire Soot From Buoyant Turbulent Diffusion Flames," Ph.D. Thesis, The University of Michigan, Ann Arbor, Michigan.

Köylü, Ü. Ö., and Faeth, G. M., 1992, "Structure of Overfire Soot in Buoyant Turbulent Diffusion Flames at Long Residence Times," *Combust. Flame,* Vol. 89, pp. 140–156.

Köylü, Ü. Ö., and Faeth, G. M., 1994a, "Optical Properties of Overfire Soot in Buoyant Turbulent Diffusion Flames at Long Residence Times," ASME JOURNAL OF HEAT TRANSFER, Vol. 116, pp. 152–159.

Köylü, Ü. Ö., and Faeth, G. M., 1994b, "Optical Properties of Soot in Buoyant Laminar Diffusion Flames," ASME JOURNAL OF HEAT TRANSFER, Vol. 116, pp. 971–979.

Köylü, Ü. Ö., and Faeth, G. M., 1996, "Spectral Extinction Coefficients of Soot Aggregates from Turbulent Diffusion Flames," ASME JOURNAL OF HEAT TRANSFER, Vol. 118, pp. 415–421.

Köylü, Ü. Ö., Faeth, G. M., Farias, T. L., and Carvalho, M. G., 1995, "Fractal and Projected Structure Properties of Soot Aggregates," *Combust. Flame,* Vol. 100, pp. 621–635.

Lee, S. C., and Tien, C. L., 1980, "Optical Constants of Soot in Hydrocarbon Flames," *Eighteenth Symposium (International) on Combustion,* The Combustion Institute, Pittsburgh, PA, pp. 1159–1166.

Manickavasagam, S., and Mengüc, M. P., 1993, "Effective Optical Properties of Coal/Char Particles Determined from FT-IR Spectroscopy Experiments," *Energy and Fuel,* Vol. 7, pp. 860–869.

Martin, J. E., and Hurd, A. J., 1987, "Scattering from Fractals," *J. Appl. Cryst.,* Vol. 20, pp. 61–78.

Medalia, A. I., and Heckman, F. A., 1969, "Morphology of Aggregates—II. Size and Shape Factors of Carbon Black Aggregates from Electron Microscopy," *Carbon,* Vol. 7, pp. 567–582.

Rosner, D. E., Mackowski, D. W., and Garcia-Ybarra, P., 1991, "Size- and Structure-Insensitivity of the Thermophoretic Transport of Aggregated 'Soot' Particles in Gases," *Combust. Sci. Tech.,* Vol. 80, pp. 87–101.

Rudder, R. R., and Bach, D. R., 1968, "Rayleigh Scattering of Ruby-Laser Light by Neutral Gases," *J. Opt. Soc. Amer.,* Vol. 58, pp. 1260–1266.

Tien, C. L., and Lee, S. C., 1982, "Flame Radiation," *Prog. Energy Combust. Sci.,* Vol. 8, pp. 41–59.

Vaglieco, B. M., Beretta, F., and D'Alessio, A., 1990, "In-Situ Evaluation of the Soot Refractive Index in the uv-Visible from the Measurements of Scattering and Extinction Coefficients in Rich Flames," *Combust. Flame,* Vol. 79, pp. 259–271.

Viskanta, R., and Mengüc, M. P., 1987, "Radiation Heat Transfer in Combustion Systems," *Prog. Energy Combust. Sci.,* Vol. 13, pp. 97–160.

Multidimensional Transient Conduction Analysis by Generalized Transfer Functions Tables

L. Laurenti

F. Marcotullio

A. Ponticiello

Dipartimento di Energetica,
Universita' di L'Aquila Monteluco di Roio,
67100 L'Aquila,
Italy

This work provides a general tool for accurate multidimensional transient analysis by means of polynomial heat conduction transfer functions (CTF) which are valid for the whole class of objects having the same geometric shape. With this aim the governing conduction equations were turned into dimensionless variables, such as the well known Biot number (Bi) and Fourier modulus (Fo), and thereafter handled through a finite-element technique to create the CTF with respect to any arbitrary point of the conductive field. In addition, by selecting the nondimensional time interval (ΔFo) according to the sampling theorem, i.e., as a function of Bi, the CTF were scheduled in the form of one-entry tables. The Bi incremental values were furthermore assessed to provide, for any input function, temperature histories within equal percent deviations, say 10 percent. Since for many purposes a five percent tolerance will usually suffice, the CTF tables can be used without the necessity of interpolating. As an example, generalized CTF tables are presented for the central and one of the corner points of a cube.

Introduction

The prediction of temperature history in multidimensional heat conduction problems generally requires a strong computation effort in terms of both time processing and large-scale computer implementation. However, an efficient way to investigate transient heat conduction, especially for those applications that require extensive simulation analysis under various boundary conditions, is to use mathematical output/input formulations, better known as conduction transfer functions (CTF). Such functions are referred to discrete and linear systems in the form of z-transform functions (Jury, 1964):

$$G(z) = \frac{O(z)}{I(z)}. \tag{1}$$

The z-transform is the Laplace transform of sampled functions:

$$O(z) = \sum_{n=0} O(n\Delta\tau)z^{-n}$$
$$I(z) = \sum_{n=0} I(n\Delta\tau)z^{-n}. \tag{2}$$

where $\Delta\tau$ is the sampling time interval and $z = \exp(s\Delta\tau)$. The chief advantage of such transformation is that the CTF, i.e., $G(z)$, can be expressed as the ratio of two polynomials in the argument z^{-1}:

$$G(z) = \frac{N(z)}{D(z)} = \frac{\sum_{n=0} b_n z^{-n}}{\sum_{n=0} d_n z^{-n}} \tag{3}$$

where the polynomial coefficients b and d are characteristic of the system while their values depend upon the sampling interval $\Delta\tau$.

It follows that Eq. (1) may also be written as

$$O(z)D(z) = N(z)I(z)$$

and equating on both sides the coefficients of z^{-n}, we obtain an important relation between the $G(z)$ polynomial coefficients and the time-series of the sampled functions of the output $O(\Delta\tau)$, $O(2\Delta\tau)$, ..., $O(n\Delta\tau)$ and the input $I(\Delta\tau)$, $I(2\Delta\tau)$, ..., $I(n\Delta\tau)$:

$$\sum_{j=0} d_j O[(n-j)\Delta\tau] = \sum_{j=0} b_j I[(n-j)\Delta\tau]. \tag{4}$$

The solution with respect to $O(n\Delta\tau)$ yields the following convolution equation:

$$d_0 O(n\Delta\tau) = b_0 I(n\Delta\tau) + b_1 I[(n-1)\Delta\tau] + b_2 I[(n-2)\Delta\tau] + \ldots - d_1 O[(n-1)\Delta\tau] - d_2 O[(n-2)\Delta\tau] - \ldots \tag{5}$$

Equation (5) relates the output at any time $\tau = n\Delta\tau$ to the input at that time and the values of the input and output at earlier times. Hence, once the characteristic CTF's coefficients are available at any selected point, the convolution Eq. (5) will provide its temperature history, starting from a given initial pattern, for any transient boundary condition.

The transfer function approach has been successfully employed in the past in one-dimensional applications by Stephenson and Mitalas (1971) and in more recent studies it also has been applied to multidimensional fields by Mascheroni et al. (1987) and by Brunello and Nonino (1987). All the referenced authors evaluated the CTF by means of appropriate identification techniques based upon step or ramp input functions or by matching the system frequency response at certain selected frequencies. In multidimensional problems identification was achieved through the response to triangular input signals obtained either by numerical analysis or by experimental procedures in controlled regime chambers. Recently, Marcotullio and Ponticiello (1993) presented an alternative method derived from a finite element analysis that provided drastic reduction of the number of the CTF's coefficients as well as improved accuracy. Although the premise of this procedure is the use of

Contributed by the Heat Transfer Division for publication in the JOURNAL OF HEAT TRANSFER. Manuscript received by the Heat Transfer Division April 22, 1996; revision received December 6, 1996; Keywords: Conduction, Numerical Methods, Transient & Unsteady Heat Transfer. Associate Technical Editor: S. Ramadhyani.

the finite element method, the numerical formulation serves only for resorting to a special recurrence scheme referred to a "lumped" one degree of freedom system and not to carry out numerical solutions for identification purposes.

In the present work the CTF coefficients are provided in a generalized and tabulated form. The use of scheduled CTFs are useful to common practitioners especially for transient simulation since, as it will be shown, only a simple "convolution" is involved and accuracy is consistent with engineering purposes. Generalized CTF tables are proposed, as an example, for the central and one of the corner points of a cube and hold for the entire class of objects having the same geometric shape.

Basic Considerations

The theoretical procedure aimed at the evaluation of the generalized CTF starts from the conduction equation in a uniform thermal conductivity solid free of sources which, in nondimensional variables, can be written as

$$\nabla^2 T(\xi, \eta, \zeta, \mathrm{Fo}) = \frac{\partial T}{\partial \mathrm{Fo}} \tag{6}$$

where $\xi = x/L_c$, $\eta = y/L_c$, $\zeta = z/L_c$ are the dimensionless coordinates with respect to a certain characteristic length L_c and $\mathrm{Fo} = \alpha\tau/L_c^2$ is the Fourier modulus. The Biot number $\mathrm{Bi} = hL_c/k$ arises from the transient boundary condition

$$\mathbf{n} \cdot \nabla T + \mathrm{Bi}(T - T_\infty) = 0. \tag{7}$$

Starting from a known initial condition $T(\xi, \eta, \zeta, 0)$ the analytical solution of the temperature field will be of the form

$$T = T(\xi, \eta, \zeta, \mathrm{Fo}, \mathrm{Bi}). \tag{8}$$

Equation (8) states that two different systems A and B of similar shape have the same thermal behavior at corresponding points provided $\mathrm{Bi}^A = \mathrm{Bi}^B$ and $\mathrm{Fo}^A = \mathrm{Fo}^B$. The same conclusions can be drawn by performing a numerical analysis based, for example, on the finite element method (Marcotullio and Ponticiello, 1994). In this case, the discretization of the whole domain in a certain number of finite elements lead to the matrix equation (Zienkiewicz, 1977)

$$\mathbf{C}\dot{\mathbf{a}} + \mathbf{K}\mathbf{a} - \mathbf{f} = 0 \tag{9}$$

where $\mathbf{a}$ is the vector of the unknown nodal temperatures of the system, $\dot{\mathbf{a}}$ the first time derivative with respect to the Fourier modulus Fo and $\mathbf{f}$ is the vector holding the ambient fluid temperature $\bar{a}$ (forcing term T_∞). By applying the procedure mentioned before (Marcotullio and Ponticiello, 1993) the following recurrence formula at any selected node is obtained:

$$d_1 a_{n+1} = d_0 a_n + d_{-1} a_{n-1} + \ldots + b_1 \bar{a}_{n+1} + b_0 \bar{a}_n + b_{-1} \bar{a}_{n-1} + \ldots. \tag{10}$$

Since Eq. (10) has the same form of Eq. (5), the sets $d_1, d_0, d_{-1}, \ldots b_1, b_0, b_{-1}, \ldots$ can be sought as the CTF coefficients, as they link the time series of the output $(a_{n+1}, a_n, a_{n-1}, \ldots)$ to the time series of the input $(\bar{a}_{n+1}, \bar{a}_n, \bar{a}_{n-1}, \ldots)$. The CTF hold for all the solids of the same geometric shape provided the dimensionless Bi and $\Delta\mathrm{Fo} = (\alpha\Delta\tau)/L_c^2$ are equal.

Bi and ΔFo Selection

To set up a table listing the CTF coefficients for pairs of the independent dimensionless variables Bi and ΔFo, some appropriate criteria should be followed. Firstly, the Fourier modulus discretization ΔFo should not exceed $\lambda_1/15$, λ_1 being the dominant eigenvalue of the matrix $\mathbf{K}^{-1}\mathbf{C}$. The above condition implies that the system frequency response is damped out at approximately two percent of its maximum value. In fact, the transient response to a unitary step function at any arbitrary point may be written as

$$a = 1 - \sum_{i=1} C_i \exp\left(-\frac{\mathrm{Fo}}{\lambda_i}\right) \tag{11}$$

which, as time progresses, can be adequately represented by

$$a \approx 1 - \exp\left(-\frac{\mathrm{Fo}}{\lambda_1}\right).$$

The Laplace transfer function is given by

$$G(s) = \frac{O(s)}{I(s)} = \frac{\dfrac{1}{s} - \dfrac{\lambda_1}{s\lambda_1 + 1}}{\dfrac{1}{s}} = \frac{1}{s\lambda_1 + 1} \tag{12}$$

and by setting the Laplace parameter $s = 2\pi\nu i$ the modulus $|G(s)|$ takes the form

$$|G(2\pi\nu i)| = \frac{1}{\sqrt{(2\pi\nu\lambda_1)^2 + 1}} \tag{13}$$

Nomenclature

$\mathbf{a}$ = vector of nodal temperatures
a = selected nodal temperature
$\bar{a}$ = ambient fluid temperature (T_∞)
$b_1, b_0, b_{-1}, \ldots$ = set of coefficients weighting the time series of the input
Bi = Biot number
c = specific heat
$\mathbf{C}$ = global heat capacity matrix
$d_1, d_0, d_{-1}, \ldots$ = set of coefficients weighting the time series of the output
$\mathbf{f}$ = forcing function vector
Fo = Fourier modulus
$G(s)$ = Laplace transfer function (approximate)
$G(z), I(z), O(z)$ = z-transform of the transfer function, input and output
h = unit surface conductance
k = thermal conductivity
$\mathbf{K}$ = global thermal conductance matrix
L_c = characteristic length
$\mathbf{n}$ = surface normal unit vector
$\nabla\mathbf{T}$ = temperature gradient
s = Laplace parameter
z = polynomial argument (14)

Greek Symbols

α = thermal diffusivity
$\Delta\mathrm{Fo}$ = dimensionless time interval
$\Delta\tau$ = Samplig time interval
ξ, η, ζ = dimensionless coordinates
λ_i = eigenvalues of the matrix $\mathbf{K}^{-1}\mathbf{C}$ (dimensionless)
λ_1 = dominant eigenvalue among λ_i (dimensionless)
ν_c = cut-off frequency (dimensionless)
ρ = density
τ = time

where $i = \sqrt{-1}$. If a cut off frequency ν_c is chosen so as to obtain a two percent attenuation, then $\nu_c \simeq 50/(2\pi\lambda_1)$ and, according to the sampling theorem, $\Delta\text{Fo} = 1/(2\nu_c) \simeq \lambda_1/15$. Since λ_1 depends upon Bi then the above time interval selection criterion allows us to set up the CTF coefficient table with only one entry (Bi). Another useful feature is that interpolation might be unnecessary by selecting the Bi parameter ranges so as to obtain "equal percent" temperature variations, within say ten percent. As an example, a CTF table has been set up for a cubic shape. The central and one of the corner points were chosen as nodes of interest and the corresponding set of coefficients reported in Table 1. The number of coefficients per set ranges from three to twelve according to the solid thermal mass.

Application Example

As an application example, temperature histories in the central and corner points of a 0.3 × 0.3 × 0.3 m homogeneous cube were calculated by the tabulated CTFs and checked against a numerical solution (ANSYS).

The assumed physical quantities are: thermal conductivity k = 1 W/mK, density ρ = 2000 kg/m^3, specific heat c = 963 J/kgK, thermal diffusivity $\alpha = k/\rho c = 1.8692 \times 10^{-3}$ m^2/hr, unit surface conductance h = 18 W/m^{2}K, L_c = 0.3 m. The cube is subject to the following conditions:

- initial condition: uniform temperature of zero
- boundary condition: 3°C/hr linear rise of the ambient fluid temperature

$$T_\infty = \bar{a} = (3\tau)°\text{C}.$$

The temperature evolutions at the selected points involve the following steps: (a) evaluation of the Biot number: Bi = $(hL_c)/k$ = 5.4, (b) selection of the set of coefficients from Table 1 corresponding to Bi = 5.0, (c) evaluation of the Fourier modulus related to Bi = 5.0, $\Delta\text{Fo} = 6.36 \times 10^{-3}$, (d) evaluation of the current time interval $\Delta\tau$ and time instant τ

$$\Delta\tau = \frac{L_c^2}{\alpha}\Delta\text{Fo} = \frac{0.3^2 \times 6.36 \times 10^{-3}}{1.8692 \times 10^{-3}} \simeq 0.31 \text{ hr}$$

$$\tau = (n+1)\Delta\tau = 0.31(n+1),$$

(e) sampling of the ramp input function at equally spaced intervals

$$\Delta\tau = 0.31 \text{ hr}$$

$$\bar{a}_{n+1} = \bar{a}[(n+1)\Delta\tau] = 3(n+1)\Delta\tau = 0.93(n+1)°\text{C},$$

(f) computation for each node of the temperature history a_{n+1} by Eq. (10)

NODE 1

For n = 0, τ = 0.31 hr

$$a_1 = b_1^1\bar{a}_1 = -0.000472 \times 0.93 = -0.000439°\text{C}.$$

For n = 1, τ = 0.62 hr

$$a_2 = d_0 a_1 + b_1^1\bar{a}_2 + b_0^1\bar{a}_1$$

$$= 3.123436 \times (-0.000439) + (-0.000472) \times 1.86 + 0.002997 \times 0.93 = 0.000538°\text{C}.$$

Table 1 CTF coefficients for a cube

Bi	ΔFo x1000		1	0	-1	-2	-3	-4
		b^1	0.025161	0.070001				
0.10	169.44	b^2	0.094130	0.001032			L_c=L	
		d	1	0.904837				
		b^1	0.018432	0.076730				
0.13	130.98	b^2	0.107249	-0.012086				
		d	1	0.904837				
		b^1	0.011808	0.083355				
0.16	106.95	b^2	0.120100	-0.024937				
		d	1	0.904837				
		b^1	0.009442	0.079327	0.003740			
0.20	86.12	b^2	0.114304	-0.000432	-0.021363			
		d	1	0.932727	-0.025235			
		b^1	0.006499	0.077064	0.006978			
0.24	72.23	b^2	0.125243	-0.009645	-0.025057			
		d	1	0.953404	-0.043945			
		b^1	0.004236	0.073993	0.010066			
0.28	62.32	b^2	0.135396	-0.018854	-0.028246			
		d	1	0.977005	-0.065300			
		b^1	0.002515	0.070415	0.012991			
0.32	54.88	b^2	0.144905	-0.028151	-0.030833			
		d	1	1.001949	-0.087870			
		b^1	0.001227	0.066528	0.015767			
0.36	49.09	b^2	0.153886	-0.037566	-0.032798			
		d	1	1.027162	-0.110684			
		b^1	0.001084	0.060036	0.011609	-0.003502		
0.40	44.47	b^2	0.151267	-0.037506	-0.060719	0.016185		
		d	1	1.199020	-0.287824	0.019577		
		b^1	0.000300	0.054985	0.013790	-0.004599		
0.45	39.84	b^2	0.160798	-0.054313	-0.060007	0.017998		
		d	1	1.258583	-0.351367	0.028307		
		b^1	-0.000236	0.050174	0.015918	-0.005705		
0.50	36.14	b^2	0.169891	-0.071559	-0.057793	0.019611		
		d	1	1.314753	-0.412915	0.038010		
		b^1	-0.000664	0.043816	0.018905	-0.007261		
0.57	32.06	b^2	0.182008	-0.096116	-0.052572	0.021477		
		d	1	1.387181	-0.494606	0.052629		
		b^1	-0.000806	0.036202	0.022843	-0.009249		
0.66	28.08	b^2	0.196722	-0.127935	-0.042952	0.023154		
		d	1	1.469853	-0.591058	0.072216		
		b^1	-0.000581	0.028348	0.027373	-0.011424		
0.76	24.76	b^2	0.212154	-0.163155	-0.029361	0.024079		
		d	1	1.549273	-0.686933	0.093944		
		b^1	-0.000008	0.020297	0.032511	-0.013757		
0.87	22.00	b^2	0.228229	-0.201379	-0.011863	0.024055		
		d	1	1.623792	-0.779761	0.116927		
		b^1	0.000965	0.011411	0.038712	-0.016423		
1.00	19.51	b^2	0.246242	-0.245601	0.011204	0.022820		
		d	1	1.697750	-0.874635	0.142220		

Bi	ΔFo x1000		1	0	-1	-2	-3	-4
		b^1	-0.000195	0.011532	0.030305	-0.018431	0.001351	
1.15	17.35	b^2	0.247818	-0.276151	-0.009479	0.084527	-0.022153	
		d	1	1.969098	-1.322794	0.363013	-0.033880	
		b^1	0.000260	0.003670	0.032733	-0.019550	0.001313	
1.35	15.22	b^2	0.269957	-0.345076	0.041183	0.078619	-0.024257	
		d	1	2.081444	-1.508319	0.453901	-0.047451	
		b^1	0.000834	0.000092	0.034983	-0.020234	0.001158	
1.60	13.30	b^2	0.295713	-0.427181	0.108445	0.065552	-0.025696	
		d	1	2.192630	-1.700686	0.555256	-0.064032	
		b^1	0.001450	-0.004766	0.036658	-0.020247	0.000833	
1.90	11.68	b^2	0.324350	-0.519949	0.191380	0.044061	-0.025914	
		d	1	2.295294	-1.885997	0.659162	-0.082386	
		b^1	0.002093	-0.009060	0.037416	-0.019232	0.000201	
2.30	10.17	b^2	0.359435	-0.634795	0.301724	0.009266	-0.024212	
		d	1	2.396688	-2.076218	0.771718	-0.103606	
		b^1	0.002609	-0.012029	0.036490	-0.016770	-0.000828	
2.80	8.90	b^2	0.399298	-0.766064	0.435538	-0.039450	-0.019851	
		d	1	2.486541	-2.250728	0.879863	-0.125148	
		b^1	0.002871	-0.013269	0.033394	-0.012654	-0.002297	
3.40	7.88	b^2	0.442391	-0.908378	0.587395	-0.100760	-0.012603	
		d	1	2.560898	-2.399334	0.975416	-0.145024	
		b^1	0.002816	-0.012713	0.028036	-0.006936	-0.004178	
4.10	7.07	b^2	0.487320	-1.056947	0.751486	-0.172157	0.002678	
		d	1	2.619770	-2.519672	1.055010	-0.162132	
		b^1	-0.000472	0.002997	-0.004218	0.020618	-0.021399	0.005880
5.00	6.36	b^2	0.511145	-1.334375	1.228399	-0.417783	-0.006015	0.022034
		d	1	3.123436	-3.834931	2.315706	-0.688214	0.080597
		b^1	-0.001052	0.006454	-0.014204	0.032191	-0.027433	0.007076
6.00	5.83	b^2	0.558138	-1.517856	1.491470	-0.591153	0.045698	0.016734
		d	1	3.174193	-3.967204	2.442342	-0.741094	0.088732
		b^1	-0.001877	0.011307	-0.027052	0.046671	-0.034821	0.008493
7.50	5.31	b^2	0.618026	-1.751501	1.833594	-0.826733	0.121586	0.007749
		d	1	3.220094	-4.088484	2.560289	-0.791208	0.096588
		b^1	-0.003183	0.018841	-0.045679	0.067054	-0.044922	0.010344
10.50	4.72	b^2	0.709694	-2.109896	2.371356	-1.215013	0.256648	-0.010334
		d	1	3.262593	-4.202147	2.672357	-0.839550	0.104292
		b^1	-0.004405	0.025765	-0.062002	0.084413	-0.053201	0.011761
15.00	4.29	b^2	0.801535	-2.471656	2.928690	-1.636165	0.413280	-0.033353
		d	1	3.283535	-4.258578	2.728469	-0.863981	0.108225
		b^1	-0.005902	0.034122	-0.081057	0.104083	-0.062062	0.013103
30.00	3.79	b^2	0.935997	-3.010642	3.787700	-2.318374	0.684067	-0.076462
		d	1	3.290543	-4.277277	2.746857	-0.871892	0.109483
		b^1	-0.006405	0.036905	-0.087286	0.110353	-0.064687	0.013424
50.00	3.60	b^2	0.988231	-3.225079	4.142083	-2.613266	0.807701	-0.097366
		d	1	3.286990	-4.267426	2.736754	-0.867349	0.108727

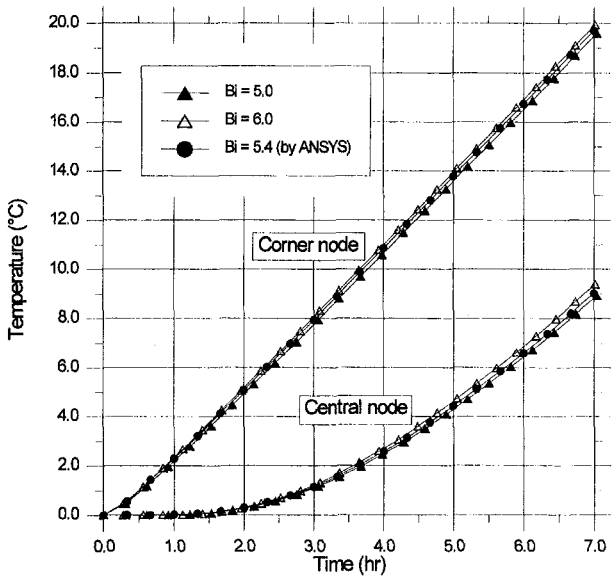

Fig. 1 Temperature histories plots for a cube

For $n = 2$, $\tau = 0.93$ hr

$$a_3 = d_0 a_2 + d_{-1} a_1 + b_1^1 \bar{a}_3 + b_0^1 \bar{a}_2 + b_{-1}^1 \bar{a}_1$$
$$= 3.123436 \times 0.000538 + (-3.834931) \times (-0.000439) + (-0.000472) \times 2.79 + 0.002997 \times 1.86 + (-0.004218) \times 0.93 = 0.003698°C.$$

For $n = 3$, $\tau = 1.24$ hr

$$a_4 = d_0 a_3 + d_{-1} a_2 + d_{-2} a_1 + b_1^1 \bar{a}_4 + b_0^1 \bar{a}_3 + b_{-1}^1 \bar{a}_2 + b_{-2}^1 \bar{a}_1$$
$$= 3.123436 \times 0.003698 + (-3.834931) \times 0.000538 + 2.315706 \times (-0.000439) + (-0.000472) \times 3.72 + 0.002997 \times 2.79 + (-0.004218) \times 1.86 + 0.020618 \times 0.93 = 0.026405°C$$

and so on.

Particular care should be taken in carrying a large number of decimal places in the numerical computations to avoid instability.

Three plots for each node are shown in Fig. 1. The temperature histories were obtained: (1) by a finite element numerical solution (ANSYS), (2) by the set of coefficients corresponding to Bi = 5.0, and (3) by the set of coefficients corresponding to Bi = 6.0.

Apart from the expected convergence of the numerical and transfer function approaches, it is confirmed that the exact temperature histories lie between the upper and lower curves obtained by the CTF, and deviations are within the assumed approximation.

Conclusions

The following conclusions can be emphasized from this work:

1 Polynomial transfer functions (CTF) for any assigned geometry can be scheduled in the form of one-entry tables involving only the Biot dimensionless parameter. The second parameter ΔFo is linked to the former according to the sampling theorem to provide tabulation compactness.
2 As an example, tabulated CTF are given for a cubic shape. Other cases of practical interest are in progress to provide a thorough overview on this subject.
3 The availability of generalized CTF instead of the procedure for their evaluation may be of interest for common practitioners, especially for transient simulation analysis.

References

Brunello, P., and Nonino, C., 1987, "Thermal Response Factors for Heating Panels in Buildings," *Proceedings of the XVII International Congress of Refrigeration,* Vol. E, pp. 115–120.

Jury, E. I., 1964, *Theory and Applications of the z-Transform Method,* John Wiley, NY.

Marcotullio, F., and Ponticiello, A., 1993, "Determination of Transfer Functions in Multidimensional Heat Conduction by Means of a Finite Element Technique," *Numerical Methods in Thermal Problems,* Lewis, R. W. et al., eds., Vol VIII, Part 1, pp. 226–236, Pineridge Press Limited, Swansea, UK.

Marcotullio, F., and Ponticiello, A., 1994, "Generalized Heat Conduction Transfer Functions in Two-Dimensional Linear Systems of Assigned Geometry," *Advanced Computational Methods in Heat Transfer III,* Wrobel, L. C. et al., eds., pp. 35–42, Computational Mechanics Publications, Southampton, Boston.

Mascheroni, R. H., Sanz, O. D., and Dominguez, M., 1987, "A New Way to Predict Thermal Histories in Multidimensional Heat Conduction: the z-Transfer Function Method," *Int. Comm. of Heat & Mass Transfer,* Vol. 14, pp. 81–90.

Stephenson, D. G., and Mitalas, G. P., 1971, "Calculation of Heat Conduction Transfer Function for Multilayer Slabs," *ASHRAE Transactions,* Part 2, pp. 117–126.

Zienkiewicz, O. C., 1977, *The Finite Element Method,* McGraw-Hill, London.

Effect of Unsteady Wake With Trailing Edge Coolant Ejection on Detailed Heat Transfer Coefficient Distributions for a Gas Turbine Blade

H. Du[1]
Research Assistant

S. Ekkad[2]
Research Associate

J.-C. Han
HTRI Professor
Fellow ASME
JCH2187@ACS.TAMU.EDU

Turbine Heat Transfer Laboratory,
Department of Mechanical Engineering,
Texas A&M University,
College Station, Texas 77843-3123

Detailed heat transfer coefficient distributions on a turbine blade under the combined effects of trailing edge jets and unsteady wakes at various free-stream conditions are presented using a transient liquid crystal image method. The exit Reynolds number based on the blade axial chord is varied from 5.3×10^5 to 7.6×10^5 for a five blade linear cascade in a low speed wind tunnel. Unsteady wakes are produced using a spoked wheel-type wake generator upstream of the linear cascade. Upstream trailing edge jets are simulated by air ejection from holes located on the hollow spokes of the wake generator. The mass flux ratio of the jets to free-stream is varied from 0.0 to 1.0. Results show that the surface heat transfer coefficient increases with an increase in Reynolds number and also increases with the addition of unsteady wakes. Adding grid generated turbulence to the unsteady wake further enhances the blade surface heat transfer coefficients. The trailing edge jets compensate the defect in the velocity profile caused by the unsteady passing wakes and give an increase in free-stream velocity and produce a more uniformly disturbed turbulence intensity profile. The net effect is to increase both the front parts of blade suction and pressure surface heat transfer. However, the jet effect diminishes in and after the transition regions on suction surface, or far away from the leading edge on pressure surface.

Introduction

In gas turbine engines the unsteady wakes generated by the trailing edges of the upstream vanes and the blade rotation significantly influence the downstream rotor blade heat transfer. The upstream vanes are internally cooled and hence some coolant is ejected through ejection holes located at the trailing edge. This coolant ejection combined with the unsteady wake further affects heat transfer coefficients on the downstream rotor blade. Heat transfer coefficients on downstream blades under the effects of unsteady wake and trailing edge ejection are important for design considerations.

Many researchers, for example, Abhari et al. (1992), Blair et al. (1989), Blair (1994), Doorly (1988), Dullenkopf et al. (1991), Dullenkopf and Mayle (1994), Dunn et al. (1989, 1994), Han et al. (1993), Liu and Rodi (1992), O'Brien and Capp (1989), Wittig et al. (1987) have studied the effect of unsteady wakes caused by trailing edges of the vanes and the blade rotation on the surface heat transfer coefficient of the downstream blades. Ashworth et al. (1985), Doorly and Oldfield (1985), and Zhang and Han (1995) studied the combined effect of free-stream turbulence and wake passing on turbine blade heat transfer.

Because the upstream vanes are internally cooled the vane trailing edge jet effects on downstream blade heat transfer have to be considered in the gas turbine design. Dunn (1986) measured heat flux for the rotor blade of a Garrett TFE 731-2 hp full stage rotating turbine with upstream nozzle guide vane (NGV) trailing edge injection. They found that the NGV injection effect is to significantly increase the local blade heat transfer up to 20 percent of the streamwise distance from the leading edge on the suction surface and ten percent on the pressure surface. The present study focuses on the measurement of downstream blade surface heat transfer coefficients for the effect of unsteady wake combined with trailing edge ejection under various free-stream conditions.

In recent years, liquid crystal techniques have been used extensively for heat transfer measurements. The two main advantages of this technique over the classical techniques are high spatial resolution and good geometrical adaptability. In addition to those advantages Hippensteele et al. (1983) indicated that, unlike thermocouples, liquid crystal coatings are nonintrusive and cheaper and, therefore, could be a superior alternative to thermocouples for the low temperature tests. Martinez-Botas et al. (1995) presented heat transfer coefficients on transonic gas turbine blades in an annular cascade using a transient liquid crystal technique. Hoffs et al. (1997) used a transient liquid crystal method to study the heat transfer in a linear cascade and compared it to results obtained using the naphthalene sublimation technique. In the present study a transient liquid crystal method is used to measure the detailed heat transfer coefficient distributions on the blade surface under unsteady wakes combined with the effect of the trailing edge jets under various free-stream conditions. The present results are compared with those obtained by Han et al. (1993) using a thin foil-thermocouple technique.

Test Apparatus and Instrumentation

Figure 1 shows the schematic of the test section and camera arrangement. The test apparatus consists of a low speed wind tunnel with an inlet nozzle, a spoked wheel type wake generator,

[1] Current Address: Schlumberger Ltd., SPT Center, Rosharon, TX, 77583-1590.
[2] Current Address: Allison Engines Company, Indianapolis, IN, 46206-0420.

Contributed by the Heat Transfer Division for publication in the JOURNAL OF HEAT TRANSFER. Manuscript received by the Heat Transfer Division May 2, 1996; revision received December 6, 1996; Keywords: Flow Transition, Turbines, Wakes. Associate Technical Editor: T. Rabas.

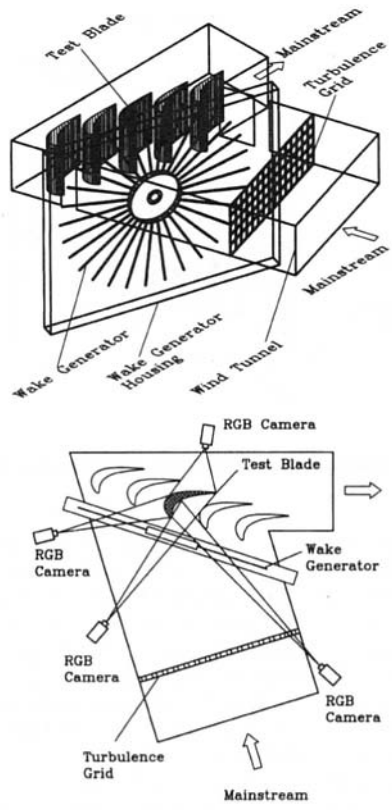

Fig. 1 Schematic of test section and camera arrangement

a linear turbine blade cascade with a test blade at its center, and a suction blower. The wind tunnel has been designed to accommodate the 107.49 deg turning of the blade cascade. The wake generator is covered with a casing to prevent leakage flow, and the center is located below the bottom wall of the wind tunnel. The blade cascade is installed downstream of the wake generator. The test apparatus is described in detail by Han et al. (1993).

A 25-HP AC motor powers the suction blower. The rotation speed of the motor is varied by adjusting a frequency controller to obtain the different Reynolds numbers. The blade cascade is designed to accommodate the wind tunnel facility with an exit air velocity up to 75 m/s for an exit Reynolds number (based on axial chord length of the blade) of 7.6×10^5. The blade configuration is designed to produce a similar velocity ratio (V/V_2) distribution as in a typical advanced high pressure turbine blade cascade. The selected blade has a 107.49 deg turning with relative flow angles of 35 deg and −72.49 deg at the blade inlet and outlet, respectively. A five times scaled up model is used to simulate the engine Reynolds number. The cascade has five blades, each with a axial chord length of 17 cm and radial span of 25.2 cm. The blades are spaced 17.01 cm apart at the cascade inlet. The throat aspect ratio (the span divided by the throat width) is 5. The cascade leading edge is 8.82 cm downstream of the wake generator.

The spoked wheel-type wake generator has 32 hollow rods to simulate the trailing edge of an upstream blade row. Each rod has an outside diameter of 0.63 cm and an inside diameter of 0.32 cm. There are 32 ejection holes opening towards the downstream blade to simulate the trailing edge ejection on each rod. The ejection holes have the diameters of 0.16 cm and are evenly spaced at three hole diameters apart from one another. Figure 2 presents a detailed sketch of the rotating rod. The compressed air source is connected to the rotation union, through which the air is transported to the hub and then to the ejection holes on the hollow rods. The wake generator is driven by 2.2 kW DC motor. The wake Strouhal number is adjusted by controlling the motor speed. The wake generator rotation speed is measured by a DT-36M digital photo tachometer. Figure 3 shows the conceptual view of the unsteady wakes generated by the rotating rods with coolant ejection passing the blade cascade in which the inlet velocity direction of the free-stream and the coolant jet velocity direction are indicated.

A turbulence grid is installed 60 cm upstream of the test blade. A turbulence intensity of five percent at the inlet of the pressure passage of the test blade is obtained without the spokes. The grid is made of hollow brass tubes 1.2 cm square in cross section and 4.8 cm in pitch. The width and the height of the grid are the same as that of the wind tunnel. The open area ratio of the grid is 54 percent.

A calibrated, single hot wire is used to measure the instantaneous velocity from which the time mean turbulence intensity and ensemble-averaged velocity and turbulence intensity can be evaluated. The hot wire sensor is vertically oriented at the inlet of the pressure side passage of the test blade, 8.82 cm downstream of the spokes, and connected to a three-channel TSI IFA 100 Constant Temperature Anemometer (CTA). The analog signal from the anemometer is converted to digital by a 250 kHz Data Translation DT2831G A/D board installed in a PC.

The surface of the center blade is painted black and uniformly coated with liquid crystals (BM/R32C5W/17-10). Liquid crystal color changes from colorless to red, red to green, and green to blue are 31.6°C, 32.7°C, and 37.2°C, respectively. In the experiment the test blade is heated uniformly using a box type

Nomenclature

C_x = blade axial chord length (17 cm)
d = wake simulator rod diameter
d_j = trailing edge jet hole diameter
h = local heat transfer coefficient
k = thermal conductivity of blade material (0.159 w/m°C)
k_{air} = thermal conductivity of air
M = mass flux ratio = $\rho_j V_j / \rho_m V_1$
N = number of rods on wake generator
n = rotating rod speed
Nu = Nusselt number based on chord length, hC_x/k_{air}
$\overline{\text{Nu}}$ = spanwise averaged Nusselt number
PL = streamwise length of the pressure surface (25.6 cm)
Re = Reynolds number based on exit velocity and chord length, $V_2 C_x/\nu$
S = Strouhal number, $2\pi Ndn/(60V_1)$
SL = streamwise length of the suction surface (33.1 cm)
t = color change time recorded by computer
T_i = initial temperature of the blade
T_m = mainstream temperature
T_R = wall temperature when color changes from green to red
Tu = free-stream turbulence intensity
$\tilde{T}u$ = ensemble averaged turbulence intensity
$\bar{T}u$ = mean turbulence intensity
$V(t)$ = instantaneous velocity
$\tilde{V}$ = ensemble averaged mainstream velocity at the cascade inlet
V_1 = mainstream velocity at the cascade inlet
V_2 = mainstream velocity at the cascade outlet
V_j = jet velocity at the ejection hole outlet
X = streamwise distance from blade leading edge
α = thermal diffusivity of the blade (0.135×10^{-6} m^2/s)
ν = viscosity of air
ρ_j = density of trailing edge jet
ρ_m = density of mainstream flow

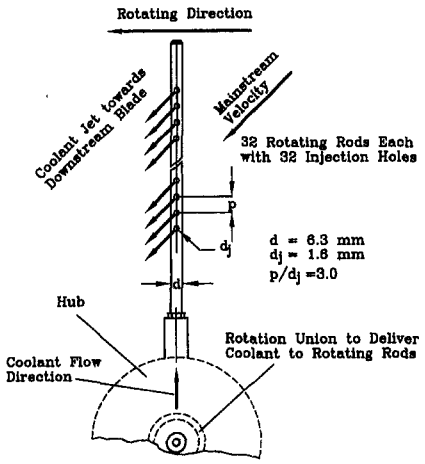

Fig. 2 Sketch of rotating rod with ejection holes

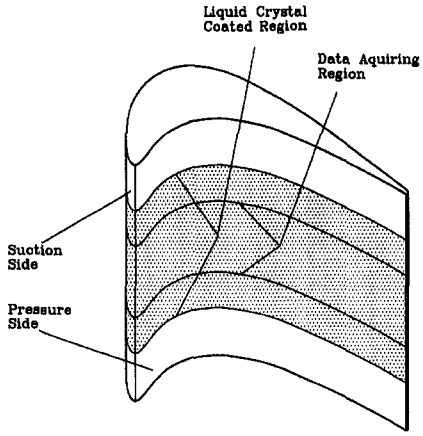

Fig. 4 Measured region on liquid crystal coated blade

heater. A heater box with the same shape and slightly larger size than that of the test blade was designed. The insides of the heater box are instrumented with thin foil heaters and controlled with several variacs to provide a uniform surface temperature. The heater box can be lowered or lifted to cover or expose the installed test blade from the mainstream flow. Once the heater box is lowered there is 0.3 cm clearance between the heated inside surface of the heater box and the test blade surface. The heaters are turned on and the blade is heated by exposing the test blade surface to the foil heaters. The temperature is monitored by embedding thermocouples on the blade surface. The uniformity of the surface temperature in the data acquiring region is within ±1.2°C. In the present study the test blade is heated to a temperature above blue color (37.2°C). The test blade is suddenly exposed to a room temperature flow by removing the heater box within 0.1 s. When the heater box bottom reaches the blade top level, the switch for triggering the data acquiring system is turned on. The liquid crystal coating area is 15.2 cm wide and the data acquiring area is 7.6 cm wide in the midspan region of the blade where the numbers of data taking points are 31,760 on suction surface and 26,000 on pressure surface. Figure 4 shows the blade surface coated with liquid crystals and the measured region. Both the pressure and suction surfaces are shown in the figure.

Test Conditions and Data Analysis

Tests were performed at the chord Reynolds numbers of 5.3 × 10^5 and 7.6 × 10^5 at the cascade exit. The corresponding flow velocities at the cascade exit are 50 m/s and 75 m/s. Unsteady wake strength is defined by wake Strouhal number $S = 2\pi Ndn/(60V_1)$. It can be achieved by the combination of the number of rods (N), diameter of rod (d), and rotation speed of the wake generator (n). The mass flux ratio of the trailing edge jet to the free-stream is defined as $M = \rho_j V_j/\rho_m V_1$. The ensemble-averaged velocity and turbulence intensity were measured at the following two conditions: (1) "grid turbulence and wake without jet" condition for $S = 0.1$, grid turbulence Tu = 5.0 percent (length scale about 1.5 cm) and jet-to-mainstream mass flux ratio $M = 0.0$; and (2) "grid turbulence and wake with jet" condition for $S = 0.1$, grid turbulence $Tu = 5.0$ percent and jet-to-mainstream mass flux ratio $M = 0.5$. The tests for measuring heat transfer coefficients were performed at five different free-stream flow conditions at each Reynolds number. For Re = 5.3 × 10^5 an additional case with an even higher jet mass flux ratio is tested, with $S = 0.1$, grid turbulence Tu = five percent, and $M = 1.0$. Table 1 lists the flow conditions in details.

A vertically oriented single hot wire is used to measure the instantaneous velocity profile under the effect of the grid generated turbulence, passing wakes combined with and without trailing edge jets at the entrance of the blade cascade. The velocity and turbulence intensity are time dependent and periodic. Because of the periodic nature of the wake passing and shedding, the analysis of the unsteady random signal indicates that its behavior cannot be characterized by time averaging only. The ensemble-averaged method was used to obtain the time-dependent periodic velocity and the time-dependent turbulence intensity. The ensemble-averaged velocity is obtained by dividing each rod-passing period into a certain number of bins and entering data from the selected number of the period into each bin. The ensemble-averaged velocity for each bin is then simply the sum of all the entering data for that bin divided by the selected number of the periods. The ensemble-averaged turbulence in-

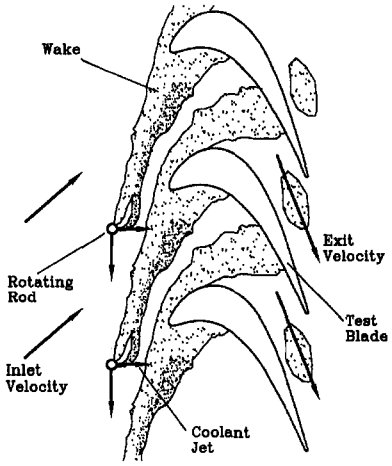

Fig. 3 Conceptual view of effects of unsteady wake with coolant ejection on turbine heat transfer

Table 1 Flow conditions for heat transfer measurement

Case No.	Re	Tu	S	M	$\overline{Tu}$
1	5.3 × 10^5	0.7%	No Wake	0.0	0.7%
2		0.7%	0.1	0.0	10.4%
3		5.0%	0.1	0.0	13.7%
4		5.0%	0.1	0.25	13.4%
5		5.0%	0.1	0.50	13.0%
6		5.0%	0.1	1.00	12.7%
7	7.6 × 10^5	0.7%	No Wake	0.0	0.7%
8		0.7%	0.1	0.0	10.4%
9		5.0%	0.1	0.0	13.7%
10		5.0%	0.1	0.25	13.4%
11		5.0%	0.1	0.50	13.0%

tensity of the flow is obtained with root-mean-square value of the fluctuation of the velocity with respect to ensemble-averaged velocity and divided by the ensemble-averaged velocity. For this study a data set with 16,000 samples is used for measurement of velocity and turbulence intensity. A mean turbulence intensity ($\bar{T}u$) is also used to describe the total turbulence level of the mainstream flow at the inlet of the blade cascade under the conditions of combined grid turbulence and unsteady wake flow with trailing edge ejection. The mean turbulence intensity is obtained by the integration of the ensemble-averaged turbulence intensity over the rod passing period, described in detail by Zhang and Han (1995).

The transient liquid crystal technique is used to measure the heat transfer coefficients on the blade surface. A one-dimensional conduction into a semi-infinite surface with a convective boundary condition at the surface is assumed. The surface temperature response is described by the equation

$$\frac{T_R - T_i}{T_m - T_i} = 1 - \exp\left(\frac{h^2 at}{k^2}\right) erfc\left(\frac{h\sqrt{at}}{k}\right) \qquad (1)$$

where T_R is the wall temperature at which the liquid crystals change color from green to red (32.7°C) at time t, T_i is the initial temperature of the preheated blade, T_m is the free-stream temperature, and α and k are the thermal diffusivity and conductivity of the blade material, respectively. The time t for the actual appearance of red at any location on the test surface is measured during the test. The lab light is used as the main light source. The light intensity in the region covered by each camera must be adjusted uniformly by adding small light sources. If the lighting is uniform over the measured area, then the background intensity of the surface is the same. This ensures that the red color appearance during the test displays the same intensity on the entire measured area. Software in the computer is used to record the time of color change of the liquid crystals on the surface during the transient test. The thermal conductivity (k) and diffusivity (α) of the blade material (low conducting material, Ren Shape) are known. The measured values of time and temperature are input into a computer program which solves for the local heat transfer coefficient using Eq. (1).

The error for the initial wall temperature is estimated as ±1.2°C for the mainstream temperature, ±0.2°C for the wall temperature at time of changing color, ±0.2°C for the time of removing the heater, ±0.1 s for liquid crystal response time, 0.005 s and for the time to catch the color change t (including instrument response time), ±0.5 s. The error in the physical properties ($\sqrt{\alpha}/k$) is estimated to be about three percent. The uncertainty in Nusselt numbers estimated according to the methodology of Kline and McClintock (1953) is found to be about 5.3 percent. On pressure surface trailing part the uncertainty is higher due to the lighting problem which is being studied. The uncertainty in the measurement of velocity is about two percent.

Results and Discussion

Flow Measurement. Ou et al. (1994) described the velocity profiles in the radial direction at the inlet and outlet of the passages adjacent to the instrumented blade. Results from Ou et al. (1994) show that the inlet and outlet velocity profiles in the flow paths are essentially uniform in the midspan region. In addition, the flow direction at the inlet and outlet of both flow paths is uniform. An identical profile blade with static pressure taps was used to measure local mainstream velocity around the blade (Zhang and Han, 1995).

Figures 5(a) and 5(b) present the instantaneous velocity profiles at Reynolds number of Re = 5.3×10^5. In the figure, (a) is for "grid turbulence and wake without jet" condition for S = 0.1, grid turbulence Tu = 5.0 percent and jet mass flux ratio M = 0.0, and (b) is for "grid turbulence and wake with jet" condition for S = 0.1, grid turbulence Tu = 5.0 percent, and jet mass flux ratio M = 0.5. The instantaneous velocity profile shows the periodic unsteady fluctuations caused by the upstream passing wakes. The unsteady wakes are actually the deficiencies in the velocity profiles of the flow fields formed by blocking the free-stream with the rotating rods. Figure 5(a) shows the case without jet effect. The periodic lowest value of the instantaneous velocity caused by the passing wakes is about 12.5 m/sec. Figure 5(b) shows the case with jet effect; the periodic lowest value of the instantaneous velocity is about 15.5 m/sec. This indicates that the trailing edge jets compensate for the deficiency in the velocity fields caused by the rotating rods. In other words, trailing edge jets enhance the mean value of mainstream velocity and at the same time reduce the fluctuations of the flow fields.

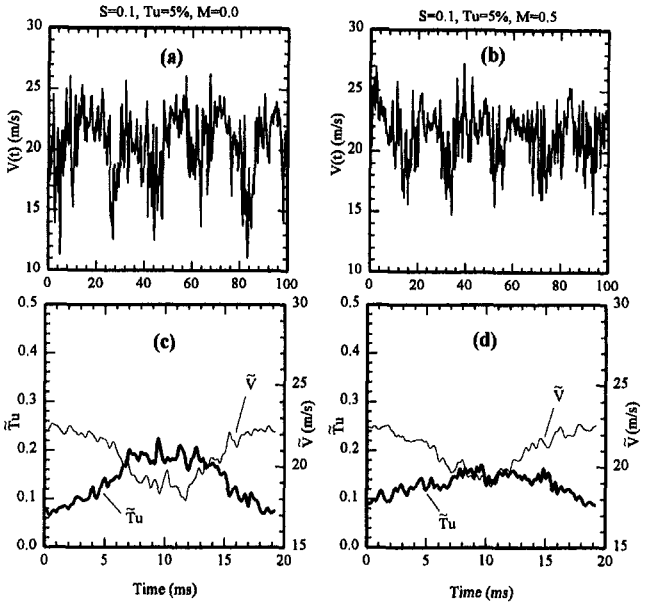

Fig. 5 Instantaneous velocity $V(t)$, ensemble-averaged velocity $\tilde{V}$, and ensemble-averaged turbulence intensity $\tilde{T}u$

Figures 5(c) and 5(d) present the ensemble-averaged velocity and turbulence intensity profile at the inlet of the blade cascade. The conditions for Figs. 5(c) and 5(d) are the same as those in 5(a) and 5(b). The deficiency in velocity profile in the case with jet (Fig. 5(d)) is less than that in the case without jet (Fig. 5(c)). The peak value of the ensemble-averaged turbulence intensity is also reduced by the trailing edge jets (see Figs. 5(c) and 5(d)). However, the turbulence intensity profile with jet is more uniformly disturbed with time as compared to that without jet. Taking the time-averaged values of the ensemble-averaged velocity and turbulence intensity for these two cases, it is found that the time-averaged velocity for "without jet" is V_1 = 20.8 m/s and for "with jet" is V_1 = 21.1 m/s; the time-averaged turbulence intensity for "without jet" is $\bar{T}u$ = 13.7 percent and for "with jet" is $\bar{T}u$ = 13.0 percent.

According to the analysis of the measurements of instantaneous velocity, ensemble-averaged velocity and turbulence intensity, and time-averaged velocity and turbulence intensity the trailing edge jets increase the mainstream velocity and create a slightly reduced but more uniformly disturbed turbulence intensity profile.

Heat Transfer Results. Figure 6 presents the effect of the unsteady wake on the spanwise-averaged Nusselt number distributions on the blade surface for a Re = 5.3×10^5. For Case 1 (no wake) the suction surface Nusselt number decreases monotonically with increasing streamwise distance (X/SL)

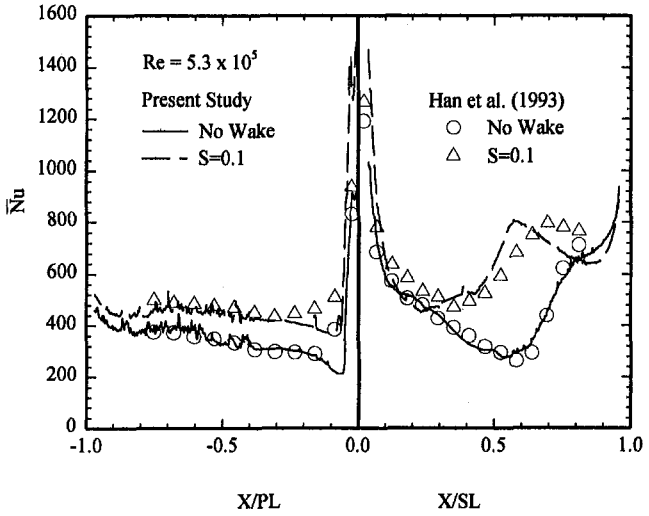

Fig. 6 Effect of unsteady wake on spanwise-averaged Nusselt number for Re = 5.3 × 10^5

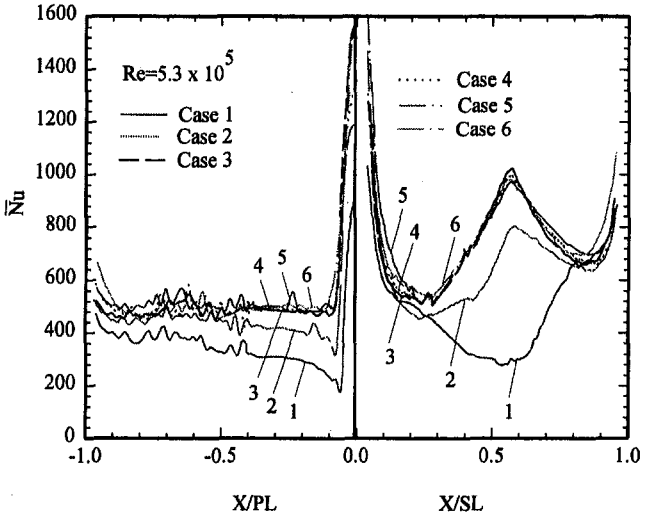

Fig. 7 Combined effect of unsteady wake, free-stream turbulence and coolant ejection on spanwise-averaged Nusselt number for Re = 5.3 × 10^5

from the blade leading edge and then increases sharply due to the transition to turbulent flow around $X/SL = 0.55$. The heat transfer coefficients near the trailing edge on the suction surface are high. This may be attributed to the unsteadiness of the flow near the trailing edge. The pressure surface Nusselt number decreases sharply with increasing streamwise distance from the blade leading edge; it has the lowest at $X/PL = -0.05$ and then increases slightly with increasing streamwise distance. This may be due to the acceleration of the flow on the pressure side. The Nusselt numbers on both the suction and pressure surfaces increase with an increase in the wake Strouhal number from "no wake" (Case 1) to $S = 0.1$ (Case 2). The suction surface boundary layer transition to turbulence starts earlier, with an increase in the Strouhal number. The increase in the suction surface heat transfer coefficients is much higher than that on the pressure surface for increasing wake Strouhal numbers. The present results compare well with results from Han et al. (1993) using a thin foil-thermocouple technique for "no wake" and $S = 0.1$. Their inlet Reynolds number 3×10^5, based on the cascade inlet velocity and the blade geometric chord length, is equivalent to the exit Reynolds number 5.3×10^5 that is based on the cascade exit velocity and the axial chord length used in the present study.

Figure 7 compares the results for the cases with Re = 5.3×10^5 for (1) clear wind tunnel, (2) wake only, (3) grid and wake, (4) grid, wake and jet $M = 0.25$, (5) grid, wake and jet $M = 0.5$, and (6) grid, wake and jet $M = 1.0$. Results show that the blade surface Nusselt numbers increase with adding unsteady wake and free-stream turbulence. Boundary layer transition to turbulence on the suction surface occurs earlier with an increase in mainstream turbulence level. Transition on the suction surface occurs at $X/SL = 0.55$ for Case 1, at $X/SL = 0.3$ for Case 2, and at $X/SL = 0.25$ for Case 3.

For Cases 2 and 3 the Nusselt number increases on the suction surface with the onset of transition and then decreases further downstream after the boundary layer becomes fully turbulent. On the pressure surface Nusselt numbers increase with an increase in mainstream turbulence level. For Case 1 the Nusselt number is lowest at $X/PL = -0.05$. There could be a small separation bubble which causes a very low Nusselt number in that region. Further downstream, Nusselt numbers increase with an increase in streamwise distance. For the higher mainstream turbulence cases the Nusselt numbers are flatter in that region. The increased levels of mainstream turbulence might tend to reduce the flow separation in that region and thus reduces the effect on the heat transfer coefficients. For the cases with trailing edge jets (Cases 4, 5, and 6) the effect of jets on Nusselt number is different at different locations on the blade surface. On the suction side before transition ($X/SL < 0.25$) the jets enhance Nusselt number, and the higher the mass flux ratio of the jets, the greater the magnitude of these effects. The jets can enhance heat transfer up to 25 percent near the leading edge region ($X/SL < 0.2$) for $M = 0.5$ (Case 5). In this region the effect of jet increased mainstream velocity and more uniformly disturbed turbulence intensity profile enhances heat transfer compared to "no jet" (Case 3). Further downstream ($X/SL > 0.25$) there is not much effect of the jets on the heat transfer distributions. This may be because the jet effect decays in the transition and fully turbulent regions. On the pressure side of the blade the Nusselt number shows an increase in the region near the leading edge ($X/PL < -0.1$), but further downstream the effect is negligible. This may be due to the strong pressure gradient diminishing the jet effect. The magnitude of the jet effect on heat transfer is higher on the suction surface compared to the pressure surface.

Figure 8 compares Cases 7 through 11 for Re = 7.6×10^5 for (7) clear wind tunnel, (8) wake only, (9) grid and wake,

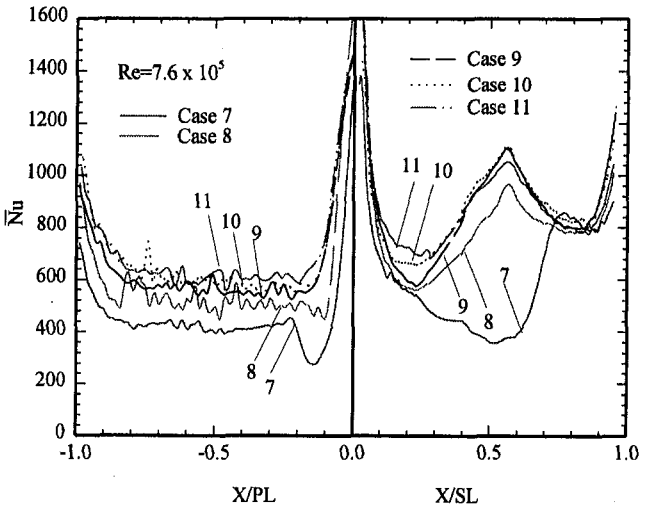

Fig. 8 Combined effect of unsteady wake, free-stream turbulence and coolant ejection on spanwise-averaged Nusselt number for Re = 7.6 × 10^5

(10) grid, wake and jet $M = 0.25$, and (11) grid, wake and jet $M = 0.5$. For this Reynolds number, transition on the suction surface occurs at $X/SL = 0.5$ for Case 7 and at $X/SL = 0.25$ for higher mainstream turbulence cases. The trend for the effect of coolant ejection on heat transfer for $\mathrm{Re} = 7.6 \times 10^5$ is similar to that for $\mathrm{Re} = 5.3 \times 10^5$. The jet effect on the suction side heat transfer before transition can be up to 25 percent, as compared to the case without jet injection. Again, the jet effect diminishes in transition and fully turbulent regions. As explained earlier, heat transfer on the transition and fully turbulent regions is already high, and adding jets to the unsteady wake does not seem to cause any further effect. Therefore, the jet effect (Cases 10 and 11) on suction side heat transfer is limited to the region before the transition location compared with the case without jet injection (Case 9). Also, the jet effect on the pressure surface heat transfer for $\mathrm{Re} = 7.6 \times 10^5$ is significant and can be up to 15 percent, compared with the case without jet (Case 9).

Figures 9(a) to 9(c) shows the detailed distributions of the local Nusselt number for $\mathrm{Re} = 5.3 \times 10^5$. The detailed contour distributions are presented for three flow conditions of (a) "no grid, no wake and no jet", Case 1; (b) combined "grid and wake", Case 3; and (c) combined "grid, wake and jet", Case 5. For the "no grid, no wake" condition ($\bar{T}u = 0.7$ percent) in the region where $X/SL < 0.6$, there is no spanwise variation in the Nusselt number distribution. In transition region ($0.6 < X/SL < 0.8$) the Nusselt number in the spanwise direction shows significant variations. In fully turbulent regions ($X/SL > 0.8$), the Nusselt number is higher, with some spanwise variation. On the pressure surface there is a very small spanwise and streamwise variation on the pressure surface. For the combined "grid and wake", Case 3, and the combined "grid, wake and jet", Case 5, the Nusselt numbers on the blade surfaces are significantly enhanced. The addition of unsteady wake and an elevated free-stream turbulence reduces spanwise variations on the blade surface and promotes earlier transition on the suction side of the blade.

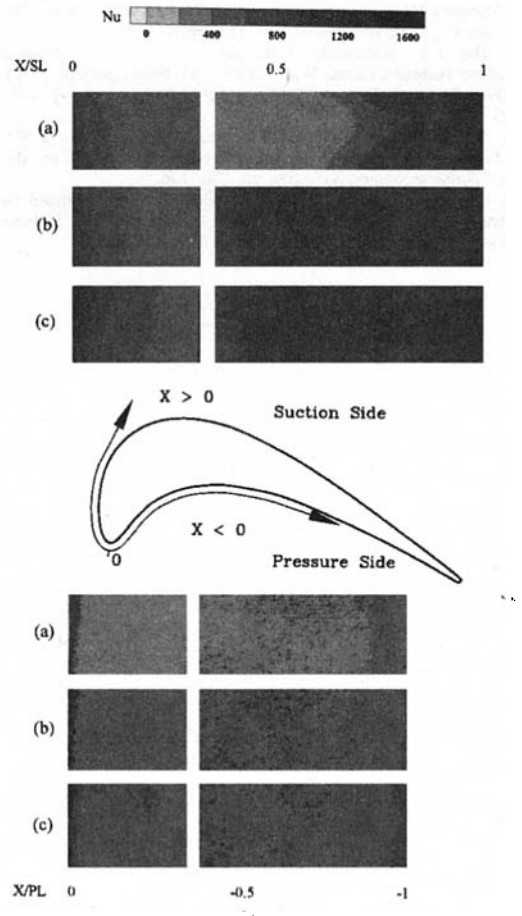

Fig. 9 Detailed Nusselt number distributions for Re = 5.3 × 10⁵: (*a*) Case 1, (*b*) Case 3, and (*c*) Case 5.

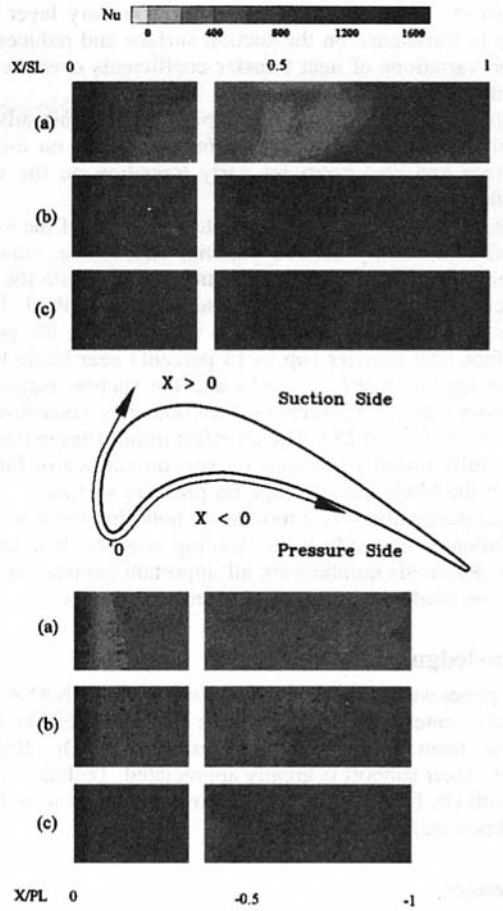

Fig. 10 Detailed Nusselt number distributions for Re = 7.6 × 10⁵: (*a*) Case 7, (*b*) Case 9, and (*c*) Case 11.

Figure 10(a) and 10(c) presents detailed Nusselt number distributions on the blade surface for a $\mathrm{Re} = 7.6 \times 10^5$. The detailed contour distributions are presented for three flow conditions of (a) "no grid, no wake and no jet", Case 7; (b) combined "grid and wake", Case 9; and (c) combined "grid, wake and jet", Case 11. Results show that the Nusselt numbers in general are higher than for $\mathrm{Re} = 5.3 \times 10^5$ on the entire blade surface. There is less spanwise variation and earlier transition for unsteady wake and higher mainstream turbulence cases compared with the low mainstream turbulence case.

Conclusions

Combined effects of unsteady wakes and trailing edge jets on downstream turbine blade heat transfer under various free-stream conditions are studied using a transient liquid crystal technique. The conclusions based on the results are:

1 The transient liquid crystal technique provides detailed distributions on the blade surface midspan region. The detailed heat transfer distributions provide more information about the laminar-turbulent transition behavior under several mainstream turbulence conditions. The present spanwise-averaged results are in good agreement with results obtained for a similar blade using thin foil-thermocouple technique.
2 Unsteady wake promotes mainstream turbulence and thus enhances the heat transfer coefficient on the blade surface.

Unsteady wake also induces earlier boundary layer transition to turbulence on the suction surface and reduces spanwise variations of heat transfer coefficients over the entire blade surface.

3 A grid-generated turbulence imposed on an unsteady wake further enhances the heat transfer coefficient on the blade surface and also promotes early transition on the suction surface.

4 The trailing edge jets compensate the defect of the velocity profile caused by the rod passing, and, hence, velocity is slightly increased for the mainstream flow while the turbulence intensity profile is more uniformly disturbed. The net effect of trailing edge jets is to increase both the pressure surface heat transfer (up to 15 percent) near blade leading edge region ($X/PL < -0.1$) and the suction surface heat transfer (up to 25 percent) before boundary layer flow transition ($X/SL < 0.25$). The jet effect diminishes in transition and fully turbulent regions on suction surface or far away from the blade leading edge on pressure surface.

5 From the results it is important to note that the free-stream turbulence, unsteady wake, trailing edge coolant jets, and flow Reynolds numbers are all important parameters affecting the blade surface heat transfer coefficients.

Acknowledgment

This paper was prepared with the support of the NASA-Lewis Research Center under grant number NAG3-1656. The NASA technical team is Dr. Philip Poinsatte, and Dr. Raymond Gaugler. Their support is greatly appreciated. Technical discussions with Dr. C. Pang Lee of GE Aircraft Engine were helpful and acknowledged.

References

Abhari, R. S., Guenette, G. R., Epstein, A. H., and Giles, M. B., 1992, "Comparison of Time-Resolved Measurements and Numerical Calculations," *ASME Journal of Turbomachinery,* Vol. 114, pp. 818–827.

Ashworth, D. A., LaGraff, J. E., Schultz, D. L., and Grindrod, K. J., 1985, "Unsteady Aerodynamic and Heat Transfer Processes in a Transonic Turbine Stage," *ASME Journal of Engineering for Gas Turbines and Power,* Vol. 107, pp. 1022–1030.

Blair, M. F., 1994, "An Experimental Study of Heat Transfer in a Large-Scale Turbine Rotor Passage," *ASME Journal of Turbomachinery,* Vol. 116, pp. 1–13.

Blair, M. F., Dring, R. P., and Joslyn, H. D., 1989, "The Effects of Turbulence and Stator/Rotor Interactions on Turbine Heat Transfer: Part I—Design Operating Conditions; Part II—Effects of Reynolds Number and Incidence," *ASME Journal of Turbomachinery,* Vol. 111, pp. 87–103.

Doorly, D. J., 1988, "Modeling the Unsteady Flow in a Turbine Rotor Passage," *ASME Journal of Turbomachinery,* Vol. 110, pp. 27–37.

Doorly, D. J., and Oldfield, M. L. G., 1985, "Simulation of the Effects of Shock-Waves Passing on a Turbine Rotor Blade," *ASME Journal of Engineering for Gas Turbines and Power,* Vol. 107, pp. 998–1006.

Dullenkopf, K., and Mayle, R. E., 1994, "The Effect of Incident Turbulence and Moving Wakes on Laminar Heat Transfer in Gas Turbines," *ASME Journal of Turbomachinery,* Vol. 116, pp. 23–28.

Dullenkopf, K., Schulz, A., and Wittig, S., 1991, "The Effect of Incident Wake Conditions on the Mean Heat Transfer on an Airfoil," *ASME Journal of Turbomachinery,* Vol. 113, pp. 412–418.

Dunn, M. G., 1986, "Heat Flux Measurements for the Rotor of a Full-Stage Turbine: Part I—Time Averaged Results," *ASME Journal of Turbomachinery,* Vol. 108, pp. 90–97.

Dunn, M. G., Kim, J., Civiskas, K. C., and Boyle, R. J., 1994, "Time-Averaged Heat Transfer and Pressure Measurements and Comparison with Prediction for a Two-Stage Turbine," *ASME Journal of Turbomachinery,* Vol. 116, pp. 14–22.

Dunn, M. G., Seymour, P. J., Woodward, S. H., George, W. K., and Chupp, R. E., 1989, "Phase-Resolved Heat Flux Measurements on the Blade of a Full-Scale Rotating Turbine," *ASME Journal of Turbomachinery,* Vol. 111, pp. 8–19.

Han, J. C., Zhang, L., and Ou, S., 1993, "Influence of Unsteady Wake on Heat Transfer Coefficient From a Gas Turbine Blade," ASME JOURNAL OF HEAT TRANSFER, Vol. 115, pp. 904–911.

Hippensteele, S. A., Russell, L. M., and Stepka, F. S., 1983, "Evaluation of a Method for Heat Transfer Measurements and Thermal Visualization Using a Composite of a Heater Element and Liquid Crystals," ASME JOURNAL OF HEAT TRANSFER, Vol. 105, pp. 184–189.

Hoffs, A., Bolcs, and Harsagama, S. P., 1997, "Transient Heat Transfer Experiments in a Linear Cascade via an Insertion Mechanism Using the Liquid Crystal Technique," *ASME Journal of Turbomachinery,* Vol. 119, pp. 9–13.

Kline, S. J., and McClintock, F. A., 1953, "Describing Uncertainties in Single-Sample Experiments," *Mechanical Engineering,* Vol. 75, Jan., pp. 3–8.

Liu, X., and Rodi, W., 1992, "Measurements of Unsteady Flow and Heat Transfer in a Linear Turbine Cascade," ASME Paper No. 92-GT-323.

Martinez-Botas, R. F., Lock, G. D., and Jones, T. V., 1995, "Heat Transfer Measurements in an Annular Cascade of Transonic Gas Turbine Blades Using a Transient Liquid Crystal Technique," *ASME Journal of Turbomachinery,* Vol. 117, pp. 425–431.

O'Brien, J. E., and Capp, S. P., 1989, "Two-Component Phase-Averaged Turbulence Statistics Downstream of a Rotating Spoked-Wheel Wake Generator," *ASME Journal of Turbomachinery,* Vol. 111, pp. 475–482.

Ou, S., Han, J. C., Mehendale, A. B., and Lee, C. P., 1994, "Unsteady Wake Over a Linear Turbine Cascade With Air and CO_2 Film Injection: Part I—Effect on Heat Transfer Coefficients," *ASME Journal of Turbomachinery,* Vol. 116, No. 4, pp. 721–729.

Wittig, S., Dullenkopf, K., Schulz, A., and Hestermann, R., 1987, "Laser-Doppler Studies of the Wake-Effected Flow Field in a Turbine Cascade," *ASME Journal of Turbomachinery,* Vol. 109, pp. 170–176.

Zhang, L., and Han, J. C., 1995, "Combined Effect of Free-Stream Turbulence and Unsteady Wake on Heat Transfer Coefficients from a Gas Turbine Blade," ASME JOURNAL OF HEAT TRANSFER, Vol. 117, pp. 296–302.

Heat Transfer in a Thin-Film Flow in the Presence of Squeeze and Shear Thinning: Application to Piston Rings

D. J. Radakovic
U.S. Steel Research,
4000 Tech Center Drive,
Monroeville, PA 15146

M. M. Khonsari
Professor and Chair
Department of Mechanical Engineering,
University of Southern Illinois at Carbondale,
Carbondale, IL 62901

The governing equations and appropriate numerical solutions are presented for the heat transfer and the flow of a shear thinning fluid confined between a curved and plane surface in a thin-film configuration. One surface undergoes a reciprocating motion and the fluid experiences transverse squeeze action, as in a typical piston ring of an internal combustion engine. The effect of viscosity variations with temperature, in conjunction with the non-Newtonian shear thinning behavior of multigrade oils, are included in the analysis. Extensive numerical simulations of the performance of the piston are presented and compared to the isothermal Newtonian solutions. Computations show that shear thinning can have a significant effect on parameters such as film thickness, viscous drag force, and power loss. The thermal effects from viscous dissipation in the clearance space along the piston ring also influence these parameters, but to a lesser degree.

1.0 Introduction

The sliding of a plane surface past another plane or curved surface, with a viscous fluid separating them, leads to the development of hydrodynamic pressure. If the surfaces form a convergent wedge, the hydrodynamic pressure becomes a positive quantity with a load-carrying implication. Known as hydrodynamic lubrication, this mechanism is behind the functionality of slider and journal bearings. The same principle applies to a lubricated piston ring as it rapidly slides past the cylinder wall of an internal combustion engine. In hydrodynamic lubrication, the fluid-film is relatively thick so that the opposing surfaces are prevented from coming into contact. This is the most important form of lubrication, providing very low friction, high resistance to wear, and very little fatigue. Friction develops purely from the shearing action of the viscous lubricant.

The viscosity of most conventional lubricants is dramatically affected by viscous heating. Viscosity drops concomitantly with the rise in fluid temperature. Consequently, film thickness as well as load-carrying capacity can be reduced significantly from thermal effects. This adverse effect is magnified for pseudoplastic fluids, i.e., for lubricants which exhibit shear-thinning behavior common to many multigrade engine oils. Clearly, modeling and performance prediction of such fluids requires consideration of the non-Newtonian characteristics.

Lubrication problems involving thermal behavior are generally known as thermohydrodynamic (THD) analyses. Such problems, particularly dealing with linearly viscous (Newtonian) fluids, have been studied in great depth for many bearing configurations (cf. Khonsari 1987a, b; Pinkus, 1990). The majority of the published works on this subject are limited to steady-state film thicknesses where time-dependent squeeze action is absent. This is true for most steadily loaded lubrication problems where the geometry of the fluid film in the clearance space is known a priori and remains constant during the operation. In the presence of a transverse squeeze action, as in the case of a piston ring, the film thickness must be predicted iteratively. For this reason, the problem is often considered to be in a class of inverse problems (cf. Rhode et al., 1979).

While there exists a number of theoretical models and numerical solutions for piston ring analyses (cf. Ting and Mayer, 1974; Sun, 1990; Jeng, 1991), thermal effects and non-Newtonian characteristics of lubricants have not been considered. In this paper we present the appropriate governing equations and numerical solution procedure for treating thermohydrodynamic problems involving thin-film flows in the presence of transverse squeeze and shear-thinning effects. The procedure is applied to the lubrication of a piston ring. Extensive numerical simulations are presented which elucidate the influence of both thermal and shear-thinning effects on the performance of piston rings.

2.0 Theoretical Model

Figure 1 shows the geometry for the lubrication contact between a piston ring and a cylinder wall. A general off-center parabola represents the profile of the ring surface while the lubricant film thickness between the ring and the cylinder wall is expressed as

$$h(x, t) = h_m(t) + \delta_o\left(\frac{x}{a}\right)^2 \tag{1}$$

where h_m is the minimum film thickness which is a function of time (or crank angle). The variables a and δ_o denote the piston ring half-width and crown height, respectively. It is assumed that the ring does not tilt in its groove, thus it will move only radially as a unit under normal loading.

The piston ring is modeled as a reciprocating slider bearing, with both sliding and squeeze motion present. The ring is subject to cyclic variations in velocity and pressure. As the surfaces are completely separated by a relatively thin film, hydrodynamic lubrication is the predominant mode of lubrication involved in this process. Generally, hydrodynamic lubrication is present over the complete stroke unless the minimum film thickness falls below the composite surface roughness of the piston ring and cylinder wall. If this occurs, boundary lubrication takes place where the surfaces come into intimate contact at the asperity level. As a result, the instantaneous friction force will be affected.

Contributed by the Heat Transfer Division for publication in the Journal of Heat Transfer. Manuscript received by the Heat Transfer Division March 1, 1996; revision received October 30, 1996; Keywords: Non-Newtonian Flows & Systems, Numerical Methods, Thin Film Flow. Associate Technical Editor: M. Kaviany.

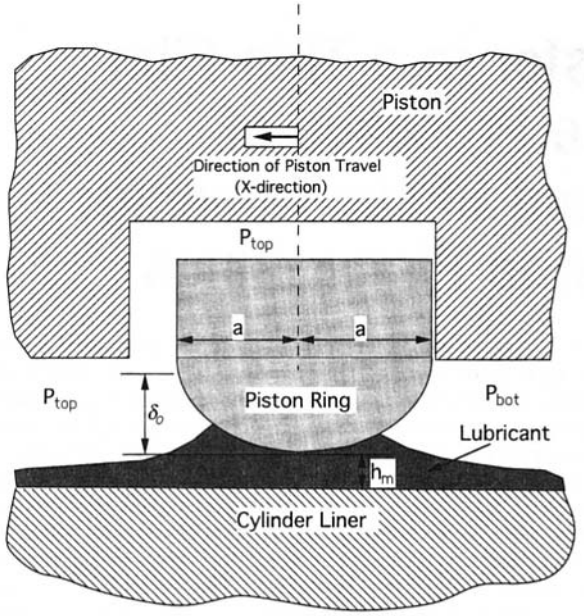

Fig. 1 Piston ring geometry

The equations governing the behavior of the fluid film between the piston ring and the cylinder wall are those representing the conservation of mass, momentum, and energy in the film. Hydrodynamic lubrication is governed by the Reynolds equation which is derived from the continuity and momentum relationships. The integration of the Reynolds equation provides an expression for the pressure distribution between the ring and the cylinder wall which determines the displacement of the ring toward or away from the wall.

Due to shearing action of the lubricant in a thin-film gap, there is the likelihood of temperature rise within the oil film resulting from frictional energy generation in the fluid. The temperature distribution in the film can be described by solving the energy equation. Adding to the complexity of the problem is the shear-thinning action of the multigrade oils, requiring a non-Newtonian treatment of the problem. Thus, the fluid viscosity is influenced by non-Newtonian effects as well as thermal effects. The variations in fluid viscosity become an important part of the solution to the energy and Reynolds equations.

The viscosity of a non-Newtonian fluid μ^* depends strongly on the rate of shear, $\dot{\gamma}$. That is, $\mu^* = \mu^*(\dot{\gamma})$. A generalized constitutive equation therefore takes on the following form:

$$\tau = \mu^*(\dot{\gamma})\dot{\gamma}. \tag{2}$$

It is important to recognize that the viscosity of a non-Newtonian fluid $\mu^* = \mu^*(\dot{\gamma})$ is a scalar quantity and therefore must have the frame-indifference property. That is to say, it must depend only on the invariants of the rate of deformation tensor $\dot{\gamma}$. It can be shown that for the types of fluids that are of interest here, the first and third invariants vanish and thus the viscosity is a function of the second invariant I_2

$$\mu^* = \mu^*(I_2) \tag{3}$$

where I_2 is the second invariant of the strain rate tensor which is defined as

$$I_2 = \dot{\gamma}_{ij}\dot{\gamma}_{ji} = \left(\frac{\partial u}{\partial z}\right)^2 + \left(\frac{\partial w}{\partial z}\right)^2. \tag{4}$$

It can be readily shown that the equation governing the conservation of momentum under the premise of thin-film lubrication approximation and in the absence of inertia effects reduces to

$$\frac{\partial \tau_{xz}}{\partial z} = \frac{\partial p}{\partial x} \tag{5}$$

where

$$\tau_{xz} = \mu^*(I_2)\frac{\partial u}{\partial z}. \tag{6}$$

Next, one can proceed to derive a generalized Reynolds equation for simple non-Newtonian fluids. The result is given as (cf. Khonsari and Hua, 1994)

$$\frac{\partial}{\partial x}\left(F_2\frac{\partial p}{\partial x}\right) = \frac{\partial}{\partial x}\left(\frac{F_1}{F_0}\cdot U\right) + \frac{\partial h}{\partial t} \tag{7}$$

where

$$F_0 = \int_0^h \frac{1}{\mu^*(I_2)}\,dz, \quad F_1 = \int_0^h \frac{z}{\mu^*(I_2)}\,dz,$$
$$F_2 = \int_0^h \frac{z}{\mu^*(I_2)}\left(z - \frac{F_1}{F_0}\right)dz.$$

Nomenclature

a = piston ring half width (mm)
B = cylinder bore diameter (mm)
b = piston ring total width = $2a$ (mm)
c_p = specific heat of lubricant (J/kg/°K)
E = ring modulus (GN/m^2)
F = friction force (N)
f = friction coefficient (Pa·s)
h = film thickness (μm)
h_m = minimum film thickness (μm)
h_{ref} = reference film thickness = 1.0 μm
l_{div} = length of divergent part of piston ring (m)
L = connecting rod length (mm)
p = pressure in the fluid (Pa)
p_{bot} = pressure below piston ring (Pa)
p_{div} = pressure in the divergent gap (Pa)
P = power loss (Watts)
p_m = mean hydrodynamic pressure in fluid film (Pa)
p_{top} = pressure above piston ring (Pa)
q = lubricant flow rate per unit length (m^2/s)
R = crank radius (m)
T = lubricant temperature (°C)
T_i = lubricant inlet temperature (°C)
t_r = ring thickness (mm)
U = piston speed (m/s)
u = velocity component in x direction (m/s)
W = load carrying capacity (N)
w = velocity component in z direction (m/s)
x = coordinate in the direction of piston motion (m)
z = coordinate in the direction normal to piston motion (m)
β_1 = temperature-viscosity coefficient for μ_1 (/°K)
β_2 = temperature-viscosity coefficient for μ_2 (/°K)
β_3 = shear thinning parameter temperature coefficient (/°K)
δ_o = ring crown height (μm)
$\dot{\gamma}$ = shear rate (1/s)
κ = shear thinning parameter (Pa)
ρ = density of lubricant (kg/m^3)
σ = composite roughness (μm)
τ = shear stress (Pa)
μ^* = viscosity of lubricant (Pa·s)
μ_1 = zero shear rate viscosity (Pa·s)
μ_2 = infinite shear rate viscosity (Pa·s)
ω = angular velocity of piston crank (m/s)

The above generalized form of the Reynolds equation possesses the proper components for a thermohydrodynamic solution for non-Newtonian fluids since the variation of viscosity across the film is taken into consideration (cf. Khonsari and Hua, 1984; Paranjape, 1992). The term on the left hand side of Eq. (7) involves the pressure gradient in the film which develops in the direction of sliding motion. The first term on the right-hand-side is the hydrodynamic wedge term that produces pressure in the fluid film allowing for separation of the surfaces. This wedge action is dependent on the shape of the ring face. The second term on the right-hand-side describes the squeeze motion of the piston ring toward or away from the cylinder wall. The piston sliding velocity, U, varies sinusoidally according to the dynamics of a slider-crank mechanism. Figure 2 shows a typical plot of piston speed as a function of crank angle for an engine speed of 2000 rpm. In the figure, the zero degree is defined as the top dead center of the power stroke.

Referring again to Fig. 1, the pressure boundary conditions are

$$p\ (x = -a) = p_{\text{top}}$$
$$p\ (x = +a) = p_{\text{bot}} \tag{8}$$

where p_{top} and p_{bot} represent the upper and lower boundary pressures, respectively. Additionally, it is assumed that $dp/dx = 0$ at the onset of cavitation in the divergent portion of the gap. The pressure above the ring, p_{top}, is assumed to be equal to the combustion chamber pressure and the pressure below is assumed to be half of that pressure. According to Jeng (1992), these pressure values appear to be good approximations for the purpose of lubrication analyses. Figure 3 shows an approximation of a typical gas pressure distribution in the combustion chamber. Again, the zero degree is defined as the start of the engine cycle when the piston is at the top dead center position of the power stroke.

The viscosity of a typical multigrade oil which exhibits shear thinning behavior is characterized as (Gecim, 1990)

$$\mu^* = \mu_1 \left(\frac{\kappa + \mu_2 \left| \frac{\partial u}{\partial z} \right|}{\kappa + \mu_1 \left| \frac{\partial u}{\partial z} \right|} \right) \tag{9}$$

where μ_1 and μ_2 represent the zero and infinite shear-rate viscosities, respectively, and κ is a curve-fitting parameter. For most lubricants the viscosity decreases exponentially with increasing temperature. The viscosities μ_1 and μ_2 and the κ parameter in Eq. (9) vary with temperature according to

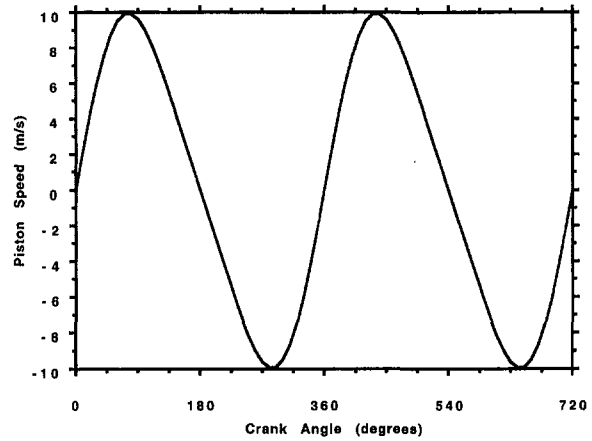

Fig. 2 Piston speed versus crank angle

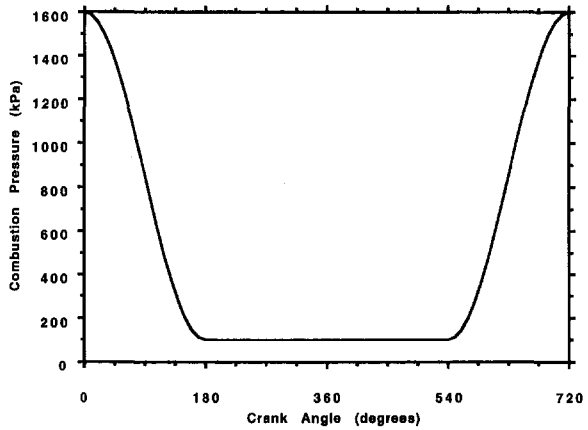

Fig. 3 Combustion chamber pressure versus crank angle

$$\mu_1(T) = \mu_{i,1} e^{-\beta_1 (T - T_i)}$$
$$\mu_2(T) = \mu_{i,2} e^{-\beta_2 (T - T_i)}$$
$$\kappa(T) = \kappa_i e^{+\beta_3 (T - T_i)} \tag{10}$$

where $\mu_{i,1}$ and $\mu_{i,2}$ are the lubricant viscosities evaluated at $T = T_i$, κ_i is the curve-fitting parameter at $T = T_i$, and β_1, β_2, and β_3 are the temperature-viscosity coefficients. The non-Newtonian model in (9) approaches the Newtonian formulation as the curve fitting parameter, κ, becomes very large.

To account for the viscosity variation with temperature, the energy equation must be invoked. For a laminar, incompressible fluid, the steady state energy equation is given by

$$\rho c_p \left(u \frac{\partial T}{\partial x} + w \frac{\partial T}{\partial z} \right) = k \left(\frac{\partial^2 T}{\partial x^2} + \frac{\partial^2 T}{\partial z^2} \right) + \tau \dot{\gamma} \tag{11}$$

where

$$\tau \dot{\gamma} = \mu^* \left(\frac{\partial u}{\partial z} \right)^2.$$

Although conservative, it is reasonable to assume steady-state thermal conditions in the fluid. This assumption is supported by an analysis done by Khonsari and Wang (1992) showing that the steady-state lubricant temperature is reached within milliseconds in a typical journal bearing.

The first term on the left hand side of (11) signifies the energy transported by convection. The terms u and w are the components of velocity in the fluid film in the directions parallel and perpendicular to the cylinder wall. u is determined from the integration of the momentum equation, and the cross film velocity, w, is subsequently determined from continuity. The first term on the right of (11) denotes the heat transfer in the fluid by conduction, and the last term represents the energy generated in the fluid film by internal friction which results from the viscous shearing of the fluid. In this formulation of the energy equation, the temperature varies in both the x and z directions. The x direction is the direction of motion of the piston, and the z direction increases from the cylinder wall across the film thickness. This equation bears the assumption that the lubricant properties, other than viscosity, remain constant, and that the adiabatic compression work in the fluid is negligible. Furthermore, due to the axisymmetric nature of the problem, temperature variation in the circumferential direction is nil. The boundary conditions are

$$T(-a, z) = T_i \tag{12a}$$
$$\frac{dT}{dx}(+a, z) = 0 \tag{12b}$$

$$T(x, 0) = T_i \tag{12c}$$

$$\frac{dT}{dz}(x, h) = 0. \tag{12d}$$

The first condition specifies a uniform temperature at the leading edge corresponding to the lubricant inlet temperature. At the trailing edge the temperature gradient in the flow direction is zero. The third condition specifies that the temperature of the cylinder wall be equal to the inlet temperature. Ezzat and Rhode (1973) have proven the validity of this for typical incline-plane slider bearings. At the oil-ring interface ($z = h$) an adiabatic boundary condition is applied, as the last condition shows. This condition simplifies the problem significantly while it provides a conservative estimate of the maximum temperature in the film (Khonsari and Beaman, 1986).

The system of equations above completely describes the pressure and temperature distribution in the fluid film. The following transformations were used to nondimensionalize the model:

$$\bar{z} = \frac{z}{h}, \quad \bar{h} = \frac{h}{h_{\text{ref}}}, \quad \bar{\mu}^* = \frac{\mu^*}{\mu_{i,1}}, \quad \bar{T} = \frac{T}{T_i}, \quad \bar{x} = \frac{x}{b}$$

$$\bar{u} = \frac{u}{R\omega}, \quad \bar{w} = \frac{w}{R\omega}\left(\frac{b}{h_{\text{ref}}}\right), \quad \bar{t} = t\omega,$$

$$\bar{h}_m = \frac{h_m}{h_{\text{ref}}}, \quad \bar{p} = \frac{p h_{\text{ref}}^2}{\mu_{i,1} R\omega b}. \tag{13}$$

Substituting (13) into the Eq. (7) yields the following nondimensional form of the Reynolds equation:

$$\frac{\partial}{\partial \bar{x}}\left(\bar{F}_2 \bar{h}^3 \frac{\partial \bar{p}}{\partial \bar{x}}\right) = \bar{u}\frac{\partial}{\partial \bar{x}}\left(\bar{h}\frac{\bar{F}_1}{\bar{F}_0}\right) + \frac{b}{R}\frac{\partial \bar{h}}{\partial \bar{t}} \tag{14}$$

where

$$\bar{F}_0 = \int_0^1 \frac{1}{\bar{\mu}^*(I_2)}\, d\bar{z}, \quad \bar{F}_1 = \int_0^1 \frac{\bar{z}}{\bar{\mu}^*(I_2)}\, d\bar{z},$$

$$\bar{F}_2 = \int_0^1 \frac{\bar{z}}{\bar{\mu}^*(I_2)}\left(\bar{z} - \frac{\bar{F}_1}{\bar{F}_0}\right) d\bar{z}$$

and R is the crank radius.

The dimensionless energy equation takes the following form:

$$\bar{u}\frac{\partial \bar{T}}{\partial \xi} + \frac{1}{\lambda_1}\frac{\partial^2 \bar{T}}{\partial \xi^2} + \frac{\bar{w}}{\bar{h}}\frac{\partial \bar{T}}{\partial \bar{z}} = \left(\frac{\lambda_2}{\lambda_1}\right)\frac{1}{\bar{h}^2}\frac{\partial^2 \bar{T}}{\partial \bar{z}^2} + \left(\frac{\lambda_3}{\lambda_1}\right)\frac{\bar{\mu}^*}{\bar{h}^2}\left(\frac{\partial \bar{u}}{\partial \bar{z}}\right)^2 \tag{15}$$

where

$$\frac{\partial}{\partial \xi} = \frac{\partial}{\partial \bar{x}} - \frac{\partial \bar{h}}{\partial \bar{x}}\frac{\bar{z}}{\bar{h}}\frac{\partial}{\partial \bar{z}} \tag{16a}$$

$$\frac{\partial^2}{\partial \xi^2} = \frac{\partial^2}{\partial \bar{x}^2} + \left(\frac{\bar{z}}{\bar{h}}\right)^2\left(\frac{\partial \bar{h}}{\partial \bar{x}}\right)^2\frac{\partial^2}{\partial \bar{z}^2} - 2\frac{\bar{z}}{\bar{h}}\frac{\partial \bar{h}}{\partial \bar{x}}\frac{\partial^2}{\partial \bar{x}\partial \bar{z}} + 2\frac{\bar{z}}{\bar{h}^2}\left(\frac{\partial \bar{h}}{\partial \bar{x}}\right)^2\frac{\partial}{\partial \bar{z}} - \frac{\bar{z}}{\bar{h}}\frac{\partial^2 \bar{h}}{\partial \bar{x}^2}\frac{\partial}{\partial \bar{z}} \tag{16b}$$

$$\lambda_1 = \frac{\rho c_p}{k} R\omega b, \quad \lambda_2 = \left(\frac{b}{h_{\text{ref}}}\right)^2,$$

$$\lambda_3 = \left(\frac{b}{h_{\text{ref}}}\right)^2 \frac{\mu_{i,1}(R\omega)^2}{kT_i}. \tag{17}$$

The expressions in (16) transform the physical domain (x, z), which is a parabolic shape defining the profile of the ring bounded by a cylinder, into a rectangular computational domain $(\xi, \bar{z})$, thus simplifying the numerical solution.

Additional quantities which are readily determined are the lubricant flow rate, the viscous drag force acting on the piston ring, and the power loss. The lubricant flow rate past the ring is defined as

$$q(x, t) = \frac{Uh}{2} - \frac{h^3}{12\mu}\frac{dp}{dx}. \tag{18}$$

The viscous drag acting on the piston ring can be written as

$$F(t) = \int_A \left(\frac{h}{2}\frac{dp}{dx} - \frac{\mu U}{h}\right) dA \tag{19}$$

where A is the area of the lubricated region. If boundary lubrication is present, the friction force is calculated using (Jeng, 1992)

$$F(t) = \mu_c(BW(t))\ \text{sign}\ (-U) \tag{20}$$

where μ_c is the friction coefficient and $W(t)$ is the load carrying capacity of the oil film per unit length represented by

$$W(t) = \int p(x, t)dx. \tag{21}$$

When hydrodynamic lubrication is present between the piston ring and cylinder wall, the power loss is (Jeng, 1992)

$$P(t) = \int_A \left(\frac{\mu}{h}\right)U^2 dA + \int_A \left(\frac{h^3}{12\mu}\right)|\nabla p|^2 dA. \tag{22}$$

This equation automatically includes the power loss due to squeeze motion. In the case where there is boundary lubrication, the power loss is given as

$$P(t) = \mu_c(BW(t))|U|. \tag{23}$$

All of the above parameters can be determined at any instant during the engine cycle.

3.0 Numerical Schemes

3.1 Reynolds Equation. The Reynolds equation is a second-order partial differential equation. The film thickness varies with both position and time. The region representing the fluid film between the piston ring and the cylinder wall was discretized in the direction of the motion of the piston travel (x). Initially, the fluid film in the divergent gap was assumed to be at a constant pressure and therefore did not have to be discretized.

The finite difference form of the Reynolds equation in (14) is given as

$$(\bar{F}_2)_i \bar{h}_i^3\left(\frac{\bar{p}_{i-1} - 2\bar{p}_i + \bar{p}_{i+1}}{\Delta \bar{x}^2}\right) + \left[3(\bar{F}_2)_i \bar{h}_i^2\left(\frac{d\bar{h}}{d\bar{x}}\right)_i + \bar{h}_i^3\left(\frac{d\bar{F}_2}{d\bar{x}}\right)_i\right]\left(\frac{\bar{p}_{i+1} - \bar{p}_{i-1}}{2\Delta \bar{x}}\right) = \bar{u}\left[\bar{h}_i\left(\frac{d\bar{F}_3}{d\bar{x}}\right)_i + (\bar{F}_3)_i\left(\frac{d\bar{h}}{d\bar{x}}\right)_i\right] + \frac{b}{R}\frac{\partial \bar{h}}{\partial \bar{t}} \tag{24}$$

where

$$\bar{F}_0 = \int_0^1 \frac{1}{\bar{\mu}^*(I_2)}\, d\bar{z}, \quad \bar{F}_1 = \int_0^1 \frac{\bar{z}}{\bar{\mu}^*(I_2)}\, d\bar{z},$$

$$\bar{F}_2 = \int_0^1 \frac{\bar{z}}{\bar{\mu}^*(I_2)} \left(\bar{z} - \frac{\bar{F}_1}{\bar{F}_0}\right) d\bar{z}.$$

In this equation the viscosity distribution is available as a known quantity. The film thickness, $\bar{h}_i$, is also known, based on an initial assumption of the minimum film thickness. The unknown quantities are the pressures, $\bar{p}_i$, and the squeeze term, $d\bar{h}_m/d\bar{t}$, which sum to $(n + 1)$ unknowns. Equation (24), however, descries only n equations. The additional equation is obtained from the assumption that the piston ring can be modeled as a thin-walled cylinder subject to internal and external pressure. The equation that describes the deflection of the ring is

$$\overline{Eh}_m = (\bar{p}_m - \bar{p}_{\text{top}}). \tag{25}$$

In this equation all of the variables are dimensionless. $\bar{p}_m$ is the mean external hydrodynamic pressure in the fluid film, $\bar{p}_{\text{top}}$ is the combustion pressure that exists behind the ring, $\bar{h}_m$ describes the deflection of the ring (which is equivalent to the minimum film thickness) and $\bar{E}$ is a dimensionless form of the Young's modulus of the ring. The mean pressure, $\bar{p}_m$, is obtained through integration of the pressure distribution in the film. The value for the mean pressure can be expressed using the trapezoidal integration rule

$$\bar{p}_m = \frac{1}{b}\left[\frac{\Delta x}{2}(\bar{p}_{\text{top}} + 2\sum_i \bar{p}_i + \bar{p}_{\text{bot}}) + \bar{p}_{\text{div}} l_{\text{div}}\right]. \tag{26}$$

Here, b is the total width of the piston ring, Δx is the distance between nodes, and $\bar{p}_{\text{top}}$ and $\bar{p}_{\text{bot}}$ are the known pressures at the boundaries of the region. l_{div} is the length of the divergent portion of the gap between the ring and cylinder liner where the pressure in the lubricant is equal to the pressure at the trailing edge of the ring. $\bar{p}_{\text{div}}$ can be equal to $\bar{p}_{\text{top}}$ or $\bar{p}_{\text{bot}}$ depending on the direction of the motion of the piston. Combining (25) and (26) the unknown pressures in the film can be expressed as

$$\sum_i \bar{p}_i = \frac{1}{\Delta x}[b(\overline{Eh}_m + \bar{p}_{\text{top}}) - \bar{p}_{\text{div}} l_{\text{div}}] - \frac{(\bar{p}_{\text{top}} + \bar{p}_{\text{bot}})}{2}. \tag{27}$$

Upon simplification, Eqs. (24) and (27) can be expressed as

$$\bar{p}_{i+1}B_i + \bar{p}_i A_i + \bar{p}_{i-1}C_i + D_i \frac{\partial \bar{h}}{\partial \bar{t}} = R_i \quad \sum_i \bar{p}_i = \alpha \tag{28a}$$

where

$$A_i = \frac{-2(\bar{F}_2)_i \bar{h}_i^3}{\Delta \bar{x}^2} \quad D_i = \frac{b}{R} \tag{28b}$$

$$B_i = \frac{(\bar{F}_2)_i \bar{h}_i^3}{\Delta \bar{x}^2} + \frac{3(\bar{F}_2)_i \bar{h}_i^2}{2\Delta \bar{x}}\left(\frac{\partial \bar{h}}{\partial \bar{x}}\right)_i + \frac{\bar{h}_i^3}{2\Delta \bar{x}}\left(\frac{d\bar{F}_2}{d\bar{x}}\right)_i \tag{28c}$$

$$C_i = \frac{(\bar{F}_2)_i \bar{h}_i^3}{\Delta \bar{x}^2} - \frac{3(\bar{F}_2)_i \bar{h}_i^2}{2\Delta \bar{x}}\left(\frac{\partial \bar{h}}{\partial \bar{x}}\right)_i - \frac{\bar{h}_i^3}{2\Delta \bar{x}}\left(\frac{d\bar{F}_2}{d\bar{x}}\right)_i \tag{28d}$$

$$R_i = \bar{u}\left[\bar{h}_i\left(\frac{d\bar{F}_3}{d\bar{x}}\right)_i + (\bar{F}_3)_i\left(\frac{d\bar{h}}{d\bar{x}}\right)_i\right] \tag{28e}$$

$$\alpha = \frac{1}{\Delta x}[b(\overline{Eh}_m + \bar{p}_{\text{top}}) - \bar{p}_{\text{div}} l_{\text{div}}] - \frac{(\bar{p}_{\text{top}} + \bar{p}_{\text{bot}})}{2}. \tag{28f}$$

The system of equations (28) completely describes the problem. In matrix form, the problem formulation is

$$\begin{bmatrix} A_1 & C_1 & 0 & 0 & 0 & 0 & 0 & D_1 \\ B_2 & A_2 & C_2 & 0 & 0 & 0 & 0 & D_2 \\ 0 & B_3 & A_3 & C_3 & 0 & 0 & 0 & D_3 \\ 0 & 0 & B_4 & A_4 & C_4 & 0 & 0 & D_4 \\ 0 & 0 & 0 & B_5 & A_5 & C_5 & 0 & D_5 \\ 0 & 0 & 0 & 0 & \ddots & \ddots & \ddots & \vdots \\ 0 & 0 & 0 & 0 & 0 & B_n & A_n & D_n \\ 1 & 1 & 1 & 1 & 1 & \cdots & 1 & 0 \end{bmatrix} \begin{bmatrix} \bar{p}_1 \\ \bar{p}_2 \\ \bar{p}_3 \\ \bar{p}_4 \\ \bar{p}_5 \\ \vdots \\ \bar{p}_n \\ \dot{\bar{h}} \end{bmatrix} = \begin{bmatrix} R_1 - B_1 \bar{p}_a \\ R_2 \\ R_3 \\ R_4 \\ R_5 \\ \vdots \\ R_n - C_n \bar{p}_b \\ \alpha \end{bmatrix} \tag{29}$$

The matrix in (29) is a bordered-band triangular matrix. It was solved using a Gauss Jordan matrix inversion routine. The solution vector contains the pressures at each point in the film, $\bar{p}_i$, as well as the squeeze term $\dot{h}$ ($\dot{h} = \partial \bar{h}/\partial \bar{t}$).

The entire solution procedure described above was based on the assumption that the pressure is constant in the oil in the divergent portion of the gap. It can be seen from Fig. 4 that this assumption forces the pressure distribution to be cut off abruptly at the piston ring half-width location. This constraint on the pressure distribution may not be entirely realistic, especially when the piston velocity is near zero and squeeze action is still occurring in the system. This is indeed the case near the top and bottom dead-center locations. If the transverse squeeze motion of the piston ring were not present in the analysis, it would be desirable to use a different solution scheme to solve the problem such as SOR. This type of iterative solution can be a more efficient means of solving a series of simultaneous equations, and it also allows for positive pressure to develop in the fluid in the divergent gap. Additionally, the SOR technique forces a smooth pressure transition to the boundary pressure in the divergent gap. Figure 4 shows a comparison of the pressure distributions predicted by the two different solution methods. Although the SOR solution is desirable, the presence of the squeeze term as an unknown quantity creates a system of equations that can not be solved directly using SOR.

To resolve this problem an iterative procedure was used in which the results of the above solution scheme were combined with and compared to the results of an SOR solution. To carry this out, the solution procedure described above, using the matrix inversion technique, was performed first. The solution

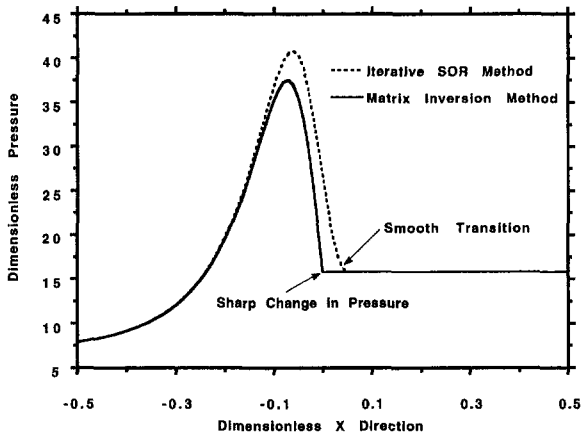

Fig. 4 Pressure distribution for two solutions to the Reynolds equation

yields the pressures at each point in the film, $\bar{p}_i$, as well as the squeeze term, $\partial\bar{h}/\partial\bar{t}$. Now, with a value for the squeeze term known, the SOR iterative scheme may be used to solve for an improved pressure distribution. The new SOR calculated pressure distribution will extend beyond the right half-width location into the divergent gap resulting in a new, smaller value for l_{div}. At this point the matrix inversion solution is performed again using the new value for l_{div}. This process is repeated until there is pressure convergence between the two different solution techniques. Convergence was based on an error tolerance of 0.001. For the SOR algorithm an over-relaxation factor of 1.5 was used and an error tolerance of 0.00001 was imposed.

3.2 Energy Equation. The dimensionless form of the energy equation, Eq. (15), was also solved using the finite difference method. This second-order partial differential equation was discretized in the x and z directions and solved using the Successive Over Relaxation (SOR) method. An over-relaxation factor of 1.5 was used, and an error tolerance of 0.00001 was applied. Either a forward or a backward difference formula was used for the $\partial T/\partial x$ term depending on the sign of the u component of velocity. This was done to assure convergence of the solution when backflow was present in the fluid film. Central difference approximations were used for all other derivatives except on the boundaries where a one-sided, second-order accurate difference representation was used. The overall solution procedure is described next.

3.3 Overall Solution. The region representing the fluid film between the piston ring and the cylinder wall was discretized within 50 nodes in the direction of piston travel and 15 nodes across the film thickness. Further mesh refinement significantly increased the computation time without improving the accuracy of the solution. In fact, doubling the mesh size to 100×30 resulted in an average change in minimum film thickness of only 0.2 percent.

At the onset of the engine cycle (crank angle = 0 deg), a value for the minimum film thickness, $\bar{h}_m$ ($\bar{t} = 0$), the initial temperature field, and the corresponding viscosity distribution are assumed. Then, when the Reynolds equation is solved, the fluid velocities and the shear rates are updated. The reduction in viscosity from the shear effects is then calculated, and the Reynolds equation is solved again until viscosity convergence is achieved. Viscosity convergence was based on an error tolerance of 0.001. An under-relaxation factor of 0.25 was also used in the solution algorithm.

The viscosity distribution and velocity profiles are then fed into the energy equation solution (the Reynolds equation and the energy equation are coupled through the nonlinear temperature-viscosity relationship). The solution to the energy equation yields the temperature and corresponding updated viscosity distribution in the fluid film. If there is no temperature (or viscosity) convergence, the Reynolds equation is again solved and this is repeated until temperature/viscosity convergence is achieved between the Reynolds and energy-equation solutions. Convergence is achieved if the error is within a tolerance of 0.001. An under-relaxation factor of 0.25 was also used in this portion of the analysis.

Once temperature/viscosity convergence in achieved, a time marching technique is used to solve for a new value of the minimum film thickness. The squeeze term, $d\bar{h}_m/d\bar{t}$, which is a product of the solution to the Reynolds equation can be written as

$$\frac{d\bar{h}_m(\bar{t})}{d\bar{t}} = f(\bar{t}, \bar{h}_m). \tag{30}$$

Equation (30) was solved using the Fourth-Order Runge-Kutta method. A time increment corresponding to one half of a degree of crank revolution was used in the analysis. In units of seconds the time step is related to engine speed by: $\Delta\bar{t}$ (sec) = 0.08/Engine Speed (rpm). With the new value for minimum film thickness and the newly calculated viscosity distribution, the time (or crank angle) is incremented by $\Delta\bar{t}$, and the procedure is repeated. It should be noted that convergence of viscosity from the solutions to the Reynolds and the energy equations must be achieved at each increment in time during the entire engine cycle. The minimum film thickness is calculated continuously until a value of $\bar{h}_m$ is found at the end of the engine cycle. This value is compared to the initially assumed value. If the error is less than a prescribed convergence tolerance, the $\bar{h}_m(\bar{t})$ is taken as the solution; otherwise, a new initial guess is made, and the process continues until the solution converges. Typically, the process converges in slightly more than one engine cycle.

Table 1 Relevant engine parameters

Parameters Used by Jeng (1992)

Engine Speed	S = 2000 (rpm)
Cylinder Bore	B = 88.9 (mm)
Bore Radius	r = 44.45 (mm)
Crank Radius	R = 40.0 (mm)
Connecting Rod Length	L = 141.9 (mm)
Composite Roughness	σ = 0.50 (μm)
Piston Ring Width	b = 1.475 (mm)
Ring Thickness	t_r = 3.8 (mm)
Ring Modulus	E = 70.0 (GN/m^2)
Ring Crown Height	δ_o = 14.9 (μm)
Friction Coefficient	f = 0.08
Lubricant Viscosity	μ = 0.00689 (Pa.s)

Lubricant Properties

Low Shear Rate Viscosity

100°C	0.0111	Pa.s

Non-Newtonian Properties

	$\kappa(Pa)$	$\mu_1(Pa.s)$	$\mu_2(Pa.s)$
100°C	1500	0.0111	0.0063

Temperature-Viscosity Coefficients

	$\beta_1(°K^{-1})$	$\beta_2(°K^{-1})$	$\beta_3(°K^{-1})$
100°C	0.0214	0.0214	0.0270

4.0 Discussion of Results

4.1 Validation.

Isothermal/Newtonian Simulations. The results of the present study were compared to those of an isothermal Newtonian analysis performed by Jeng (1992). The current model was modified so that non-Newtonian and thermal effects were negligible. This was done by imposing an artificially high curve-fitting parameter in the non-Newtonian viscosity formulation so that shear-thinning effects were eliminated. Thermal effects were bypassed by imposing a uniform film temperature equivalent to the fluid inlet temperature. The relevant engine parameters used in the analysis are presented in the top section of Table 1. These are the same input parameters used by Jeng. Comparison between the minimum film thickness predictions of the present model and that of Jeng are presented in Fig. 5. It should be noted that Jeng used an analytical integration procedure to solve the Reynolds equation as compared to the numerical SOR technique used in this analysis. Also, the combustion pressure in Jeng's analysis was obtained from actual measurements, whereas the current analysis uses an idealization of Jeng's measured chamber pressure (see Fig. 3). Finally, the present analysis treats the piston ring as a thin ring subject to internal and external pressure which will deflect according to its elastic modulus. Jeng uses a value for tangential ring tension to define the elastic deflection of the ring. Despite the different approaches, the results are in good agreement. The trend of the

results will be presented in section 4.2 with an appropriate comparison, including non-Newtonian effects.

Thermal Simulations. Although thermal effects have not been considered in previous work done on piston ring lubrication, this effect has been considered extensively in slider and journal bearing analyses under steady loading conditions, i.e., when $d\bar{h}/d\bar{t} = 0$. This is a considerably simpler problem since the film thickness does not have to be predicted at each increment in time. To test the validity of the present temperature predictions, the model was modified to represent a slider bearing under steady load by eliminating squeeze motion from the solution and making the proper modifications to the bearing geometry. The thermal model was verified by comparing the predicted thermal trends in the fluid film to those calculated in a similar THD slider bearing analysis done by Ezzat and Rhode (1973).

4.2 Shear Thinning and Thermal Effects. A computer program was developed to implement the algorithm described in previous sections. The main output of the program includes the variation in minimum film thickness between the piston ring and the cylinder wall, the viscous drag force acting on the piston ring, and the power loss resulting from the drag. The variation of these three parameters is determined over one complete engine cycle. In this section, the results of the analysis are presented for engine speeds of 2000 rpm and 3500 rpm. The oil inlet temperature is set to 100°C which is representative of steady-state engine operating temperature. For each case, Newtonian/isothermal, non-Newtonian/isothermal, Newtonian/THD, and non-Newtonian/THD solutions are compared. The non-Newtonian/THD results are most representative of actual operating conditions. The relevant engine parameters used in the analysis (excluding the viscosity of 0.00689 Pa · s) are provided in the top section of Table 1. The viscosity value was used only for model verification purposes with Jeng (1992). The lubricant properties of a 10W40 engine oil were used in the current analysis and are provided in the bottom section of Table 1. The non-Newtonian properties of the oil at 100°C were taken directly from Gecim (1990). The temperature-viscosity coefficients are also listed in the table. It was assumed that the zero and infinite shear-rate viscosities, μ_1 and μ_2, decrease exponentially with temperature and that they have the same temperature-viscosity coefficient. This is because the ratio of μ_1/μ_2 is independent of increasing temperature, meaning that $\beta_1 = \beta_2$ at any temperature. The curve-fitting parameter, κ, increases exponentially with the temperature, according to β_3.

The first case, representing an engine speed of 2000 rpm, is shown in Figs. 6*a*–6*c*. Figure 6*a* shows the minimum film thickness as a function of crank angle. It is evident from Fig. 6*a* that the non-Newtonian effects do indeed influence the variation of minimum film thickness over the engine cycle. At maximum piston velocity locations where hydrodynamic action is the greatest (around crank angle of 90 deg, 270 deg, 450 deg, and 630 deg) the film thickness for the non-Newtonian/isothermal solution is 20 percent less than the results of the Newtonian/isothermal analysis. The thermal effects, however, are virtually indiscernible. For the oil inlet temperature of 100°C, the maximum film temperatures, which occur when piston velocity is greatest, are only 109°C for the Newtonian case and 106°C for the non-Newtonian case. The location of maximum temperature is at the trailing boundary near the piston ring, oil-film interface.

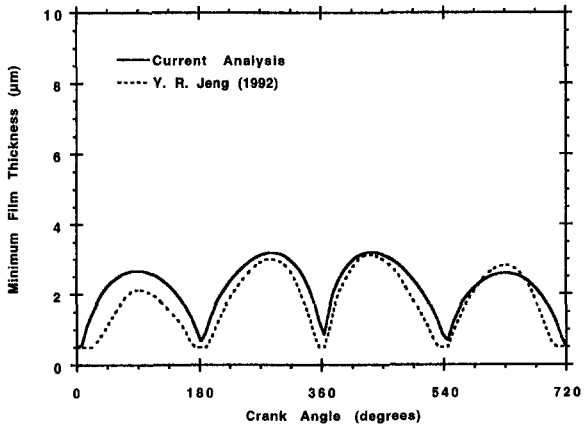

Fig. 5 Comparison of minimum film thickness predictions to those of Y. R. Jeng (1992)

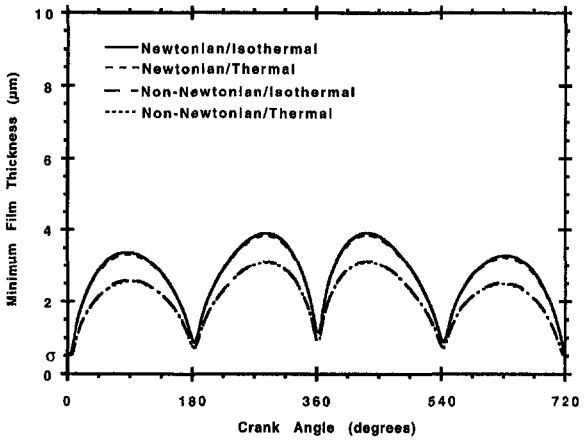

Fig. 6*a* Model predicted minimum film thickness over a complete engine cycle for an engine speed of 2000 rpm

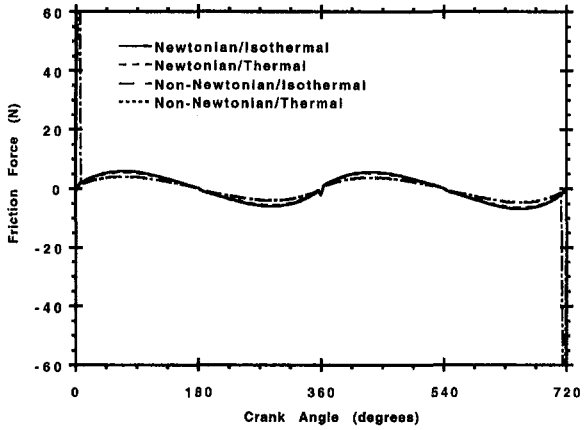

Fig. 6*b* Model predicted friction force over a complete engine cycle for an engine speed of 2000 rpm

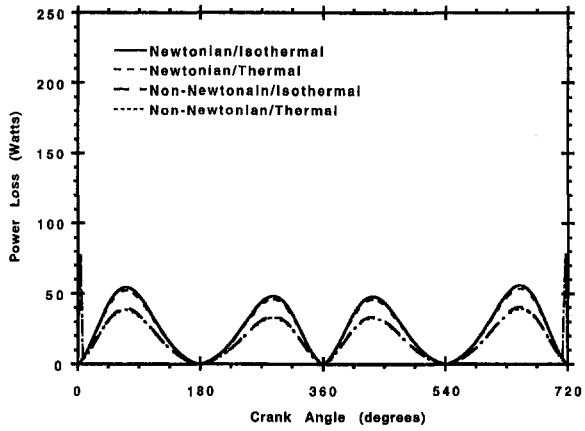

Fig. 6*c* Model predicted power loss over a complete engine cycle for an engine speed of 2000 rpm

These results indicate that viscous dissipation in the thin film is low in the 100°C temperature regime. The thermal effects may also be insignificant because of the small size of the region in question. Compared to a typical three-inch-long bearing, the piston ring is less than 1.5 mm in width. This is a very small dimension over which to develop any significant temperature rise from viscous shearing of the fluid. Moreover, in this temperature range, the viscosity does not vary considerably with temperature so any temperature rise that does occur in the fluid will not translate into a significant reduction in viscosity.

Figures 6*b* and 6*c* show the model predictions for viscous drag force and power loss. Like the minimum film thickness, these values fluctuate with the piston speed as a function of crank angle. Additionally, the figures show that the non-Newtonian behavior of the oil has an effect on the model predictions. The friction force and power loss are reduced when shear thinning effects are included. Again, it is evident that the thermal considerations have a less significant effect on the results.

An important feature of the results in Figs. 6*a*–6*c* is the prediction of the occurrence of boundary lubrication in the non-Newtonian simulations. The Newtonian approach fails to predict this phenomenon under the identical operating conditions. This is evident in Figure 6*a* where, at the zero degree, the minimum film thickness for the non-Newtonian simulations falls below the composite roughness σ of the piston ring and cylinder wall. It is here where wear patterns are most evident on cylinder liners from piston ring scuffing (Ting and Mayer, 1974). At this time during the engine cycle (the onset of the power stroke), the piston velocity approaches zero and there is a loss of hydrodynamic action. This, coupled with the high combustion pressure, increases the possibility of boundary lubrication.

Boundary lubrication is also evident in Figs. 6*b* which shows large spikes in friction force at the zero degree. The friction force resulting from boundary lubrication is significantly higher than the friction force where the ring is hydrodynamically lubricated. Similarly, this effect is evident in Figure 6*c* which shows the power loss during the engine cycle. Again, spikes are predicted for the non-Newtonian solutions when the film thickness falls below the adequate level to completely separate the surfaces. Results attesting to a large friction force at the zero degree have also been reported by Jeng (1992) for isothermal cases. These spikes are predicted using Eqs. (20) and (23) which account for the boundary lubrication effects on friction force and power loss. Generally, the results of the 2000 rpm simulation indicate that the non-Newtonian effects can determine whether or not boundary lubrication is predicted in the analysis.

Simulations were also run for an engine speed of 3500 rpm. The results were similar to the 2000 rpm case. As expected, the minimum film thickness, friction force, and power loss were greater in magnitude for the higher engine speed. It is interesting to note that, in the 3500 rpm case, boundary lubrication was not predicted to occur for any of the simulations. The increased piston velocity resulted in minimum film thickness predictions that were greater than the composite roughness of the piston ring and cylinder wall. These results are presented in Figs. 7*a* and 7*b*.

The non-Newtonian and thermal effects were also similar to those predicted in the 2000 rpm case. The non-Newtonian effects were, again, much more pronounced than the thermal effects. Figure 7*a* shows the minimum film thickness predictions as a function of crank angle and Fig. 7*b* shows the power loss. Although the thermal effects are small, they are more significant than in the 2000 rpm simulations. For the 3500 rpm engine speed, with an oil inlet temperature of 100°C, the maximum film temperatures are predicted to be 120°C for the Newtonian case and 115°C for the non-Newtonian case (vs. 109°C and 106°C for the 2000 rpm case). Again, the location of maximum temperature in the film is at the trailing boundary near the piston ring, oil film interface. Although the thermal effects do not greatly affect the minimum film thickness results, it is interesting that this degree of viscous heating can occur in such a small region.

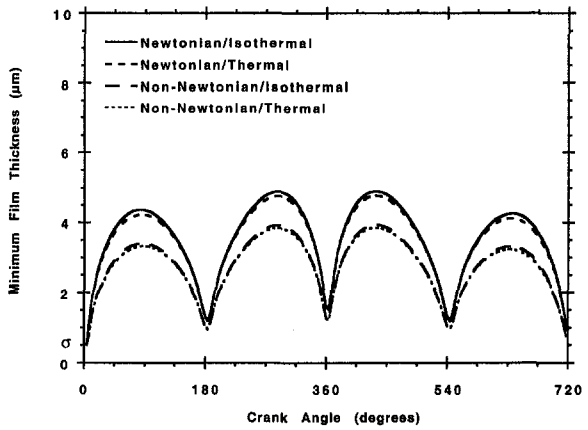

Fig. 7a Model predicted minimum film thickness over a complete engine cycle for an engine speed of 3500 rpm

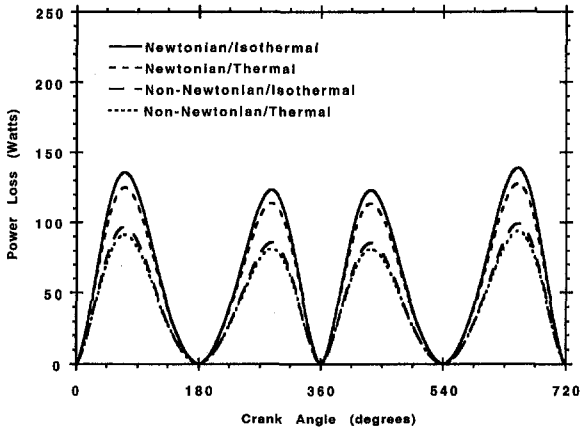

Fig. 7b Model predicted power loss over a complete engine cycle for an engine speed of 3500 rpm

5.0 Concluding Remarks

The appropriate governing equations and the numerical solution procedure have been presented for treating thermohydrodynamic problems involving thin-film flows in the presence of transverse squeeze and shear-thinning effects. The procedure has been applied to a typical piston ring of an internal combustion engine in which the ring reciprocates relative to the cylinder wall, and the separating oil film experiences transverse squeeze action. In the presence of variable squeeze action, the film thickness is not known a priori and must be predicted iteratively. While there exists a number of theoretical models and numerical solutions for piston ring analyses, thermal effects and non-Newtonian characteristics of lubricants have not been considered. In this study, however, the effect of viscosity variations with temperature in conjunction with the non-Newtonian shear-thinning behavior of multigrade oils has been included. The results of the present analysis have shown that a non-Newtonian viscosity formulation can have a significant effect on the solution to the piston ring problem, while thermal effects from viscous dissipation in the fluid film are apparent but less severe. In comparison to piston ring analyses which assume linearly viscous (Newtonian) lubricant properties, the non-Newtonian results show a significant reduction in parameters such as film thickness, viscous drag force, and power loss. Consideration of THD analyses reveal that a piston ring is less sensitive to thermal effects than a typical bearing mainly because of the rather

small size of the lubricated region. Finally, it is shown that for some operating conditions, the non-Newtonian simulations predict the occurrence of boundary lubrication whereas the Newtonian analyses fail to recognize it.

References

Ezzat, H. A., and Rhode, S. M., 1973, "A Study of the Hydrodynamic Performance of Finite Slider Bearings," *ASME Journal of Lubrication Technology,* July, pp. 298–307.

Gecim, B. A., 1990, "Non-Newtonian Effects of Multigrade Oils on Journal Bearing Performance," *Tribology Transactions,* Vol. 33, pp. 384–394.

Jeng, Y. R., 1991, "Theoretical Analysis of Piston Ring Lubrication Part II—Starved Lubrication and Its Application to a Complete Ring Pack," *Tribology Transactions,* Vol. 35, pp. 707–714.

Jeng, Y. R., 1992, "One-Dimensional Analysis of Piston Ring Lubrication: Part I—Fully Flooded Lubrication," *Tribology Transactions,* Vol. 35, pp. 696–705.

Khonsari, M. M., 1987a, "A Review of Thermal Effects in Hydrodynamic Bearings. Part I: Slider and Thrust Bearings," *ASLE Transactions,* Vol. 30, pp. 19–25.

Khonsari, M. M., 1987b, "A Review of Thermal Effects in Hydrodynamic Bearings. Part II: Journal Bearings" *ASLE Transactions,* Vol. 30, pp. 26–33.

Khonsari, M. M., and Beaman, J. J., 1986, "Thermohydrodynamic Analysis of Laminar Incompressible Journal Bearings," *ASLE Transactions,* Vol. 29, No. 2, pp. 141–150.

Khonsari, M. M., and Hua, D. Y., 1994, "Thermal Elastohydrodynamic Analysis Using a Generalized Non-Newtonian Formulation With Application to Bair-Winer Constitutive Equation," *Transactions of the ASME Journal of Tribology,* Vol. 116, pp. 37–46.

Khonsari, M. M., and Wang, S. H., 1991, "On the Maximum Temperature Effects in Double-Layered Journal Bearings," *ASME Journal of Tribology,* Vol. 113, pp. 177–183.

Khonsari, M. M., and Wang, S. H., 1992, "Notes on Transient THD Effects in a Lubricating Film," *Tribology Transactions,* Vol. 35, pp. 177–183.

Paranjape, R. S., 1992, "Analysis of Non-Newtonian Effects in Dynamically Loaded Finite Journal Bearings Includeing Mass Conserving Cavitation," *ASME Journal of Tribology,* Vol. 114, pp. 1–9.

Pinkus, O., 1990, *Thermal Aspects of Fluid-Film Technology,* ASME Press, NY.

Rhode, S. M., Whitaker, K. W., and McAllister, G. T., 1979, "A Study of the Effects of Piston Ring and Engine Design Variables on Piston Ring Friction," *Energy Conservation Through Fluid Film Lubrication Technology: Frontiers in Research and Design,* ASME Press, NY, pp. 117–134.

Sun, D. C., 1990, "A Subroutine Package for Solving Slider Lubrication Problems," *ASME Journal of Tribology,* Vol. 112, pp. 84–92.

Ting, L. L., and Mayer, J. E., 1974 "Piston Ring Lubrication and Cylinder Bore Wear Analysis, Part I—Theory," *ASME Journal of Lubrication Technology,* Vol. 96, pp. 305–314.

Heat Transfer Characteristics of a Radial Jet Reattachment Flame

J. W. Mohr

J. Seyed-Yagoobi

R. H. Page

Drying Research Center,
Department of Mechanical Engineering,
Texas A&M University,
College Station, TX 77843-3123

A Radial Jet Reattachment Combustion (RJRC) nozzle forces primary combustion air to exit radially from the combustion nozzle and to mix with gaseous fuel in a highly turbulent recirculation region generated between the combustion nozzle and impingement surface. High convective heat transfer properties and improved fuel/air mixing characterize this external mixing combustor for use in impingement flame heating processes. To understand the heat transfer characteristics of this new innovative practical RJRC nozzle, statistical design and analysis of experiments was utilized. A regression model was developed which allowed for determination of the total heat transfer to the impingement surface as well as the NO_x emission index over a wide variety of operating conditions. In addition, spatially resolved flame temperatures and impingement surface temperature and heat flux profiles enabled determination of the extent of the combustion process with regards to the impingement surface. Specifically, the relative sizes of the reaction envelope, high temperature reaction zone, and low temperature recirculation zone were all determined. At the impingement surface in the reattachment zone very high local heat flux values were measured. This study provides the first detailed local heat transfer characteristics for the RJRC nozzle.

Introduction

Flame jet impingement is an often utilized method for heat treating processes involving, for example, metals and glass, and it offers several advantages over traditional radiative furnaces. First, since convection heat transfer is significant, very rapid and intense heating is possible. Secondly, direct transfer of the energy from combustion to the surface eliminates the need for radiative refractory materials. Lastly, the process becomes more fuel efficient with the elimination of heat transfer losses associated with the heat-up of radiative furnaces.

A review by Viskanta (1993) of the limited number of investigations involving single round impinging in-line jet (ILJ) flames showed that the major disadvantage of impinging flame jets was the nonuniform surface heat flux and temperature distribution near the jet stagnation point. A novel approach to the solution of these problems involved changing the aerodynamics of the impinging flame jet through an application of Radial Jet Reattachment (RJR) nozzles (Page et al., 1989). Extension of the RJR concept for flame jet impingement applications resulted in a Radial Jet Reattachment Combustion (RJRC) nozzle (Habetz et al., 1994; Mohr et al., 1995, 1996). A typical air flow pattern for either a nonreacting RJR nozzle or a reacting RJRC nozzle is depicted in Fig. 1. The internal air stream of the RJR or RJRC nozzle forces air to exit the nozzle in an outward radial direction. Viscous mixing and mass entrainment causes the exiting air jet to turn toward the impingement surface, where it impinges in a highly turbulent reattachment ring centered about the nozzle. Previous studies have shown that this reattachment region has very high convective heat and mass transport properties (Page et al., 1989). The size of the ring-shaped stagnation region is dependent upon the air exit velocity (V), the air exit angle (θ), and the nozzle-to-plate spacing (X_p/R_o). The air exit velocity at a given flow rate is controlled by the gap width (b/R_o) between the large circular disk and the end of the air pipe. Within the reattachment ring, a subatmospheric pressure recirculation region is created. As shown in Fig. 1, a RJRC nozzle is created from a typical RJR nozzle by introducing gaseous fuel radially into the recirculation region, ensuring that the fuel does not directly impinge upon the surface. The net force exerted on the impingement surface by an RJRC nozzle can be negative, null, or positive depending on the air exit angle of the nozzle. An air exit angle (θ) of 10 deg was machined into the upper disk of the RJRC nozzle, so a slight positive force upon the impingement surface in the reattachment ring was expected.

The present work is a follow-up of the Mohr et al.'s (1996) work, where the combustion characteristics of a large prototype RJRC nozzle were presented. In that work, the RJRC concept was compared to a standard in-line jet (ILJ) flame impingement nozzle. The RJRC nozzle showed slightly higher overall heat transfer to the impingement surface than the ILJ nozzle, with both nozzles operating over a large range of fuel equivalence ratios. In addition, the RJRC nozzle produced a circumferentially symmetric surface temperature distribution and exerted very little force upon the impingement surface. Compared with the RJRC nozzle, the ILJ nozzle produced a nonsymmetric surface temperature distribution and the maximum surface pressure with combustion was more than six times the RJRC nozzle surface pressure. Combustion specie data obtained from a single radial location for the two nozzles revealed lower levels of carbon monoxide and NO_x for the RJRC nozzle. Since this study was based on overall global heat transfer and combustion measurements, no localized data on flame temperature, surface heat flux, or combustion specie concentrations were obtained.

The present work adds to the basic understanding of the RJRC concept through an investigation of a smaller practical RJRC nozzle more suitable for possible implementation into an industrial process. Statistically designed experiments are utilized, and the data from these experiments are used to determine a regression model by which the heat transfer and NO_x formation characteristics of the RJRC nozzle can be predicted. In addition, localized heat transfer data (flame temperatures, impingement surface temperature profile, and impingement surface heat flux distribution) are determined for the RJRC nozzle

Contributed by the Heat Transfer Division for publication in the JOURNAL OF HEAT TRANSFER. Manuscript received by the Heat Transfer Division May 21, 1996; revision received November 14, 1996; Keywords: Combustion, Fire/Flames, Furnaces & Combustors. Associate Technical Editor: S. H. Chan.

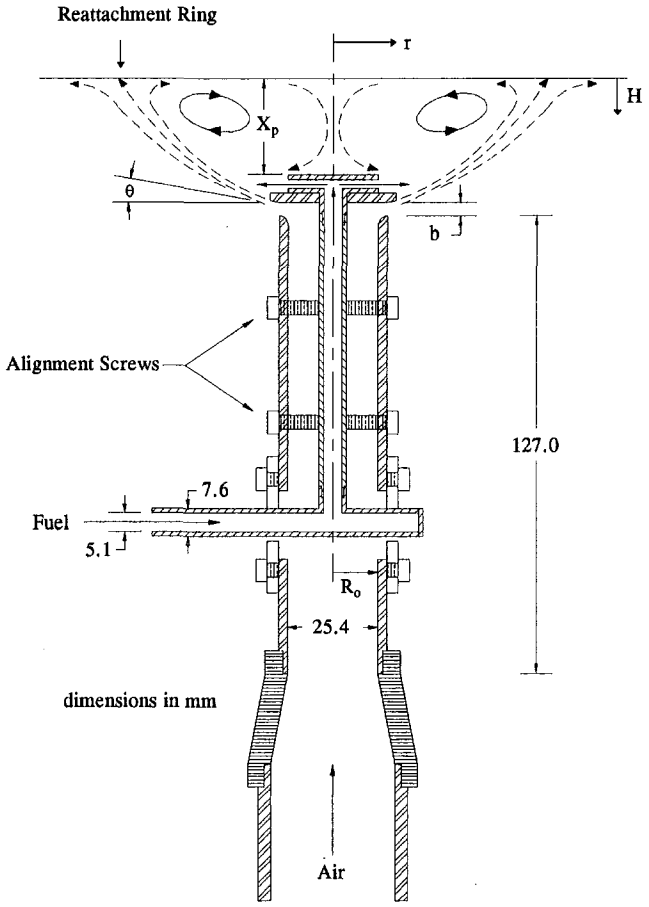

Fig. 1 RJRC nozzle and representative flow field

operating at an ideal condition. These data are utilized to determine the relative sizes of the RJRC reaction, recirculation, and reattachment zones.

Experimental Apparatus and Procedure

The combustion jet impingement facility, consisting of a support structure, combustion nozzle, and impingement surface is shown schematically in Fig. 2. The flame impingement surface is a 6.35 mm thick, 0.836 m^2 copper plate, which is uniformly cooled by a water heat exchanger in contact with the backside of the copper plate. The total heat transfer rate to the surface on an integral basis was determined by measuring the cooling water flow rate and its change in temperature, with the cooling water flow rate held constant at 22.7 liters/min. All measurements were obtained under steady-state, wherein the exit temperature of the cooling water ceased to change following a change in burner operating conditions. The change in temperature (typically about 4.0°C) was measured using thermistor thermometers with an accuracy of ±0.2°C. In order to provide a measure of the efficiency of the combustion process, the rate of heat transfer (q) to the surface was normalized by the rate of energy available from the fuel input to the system (q_f). The resulting variable was designated as the heat transfer ratio, R_t. The total available energy rate was determined by multiplying the heating value of the working gas by its flow rate. The working gas in this study was utility natural gas (90 percent methane) having a heating value of 61,594 kJ/kg.

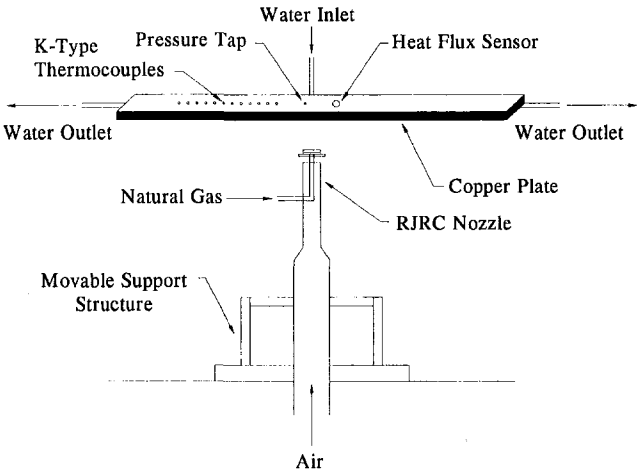

Fig. 2 Combustion jet impingement facility

Impingement surface local heat flux was measured with a single Vatell Corporation factory calibrated HFM-2 heat flux sensor mounted flush with the front side of the impingement surface as shown in Fig. 2. This 0.2 mm wide line sensor is mounted on a 25.4 mm OD, 6.35 mm thick aluminum nitride substrate. The depth of the sensing pattern is 2 μm, making it nearly invisible to any boundary layer flow across the sensor. The HFM-2 sensor is cooled from the backside in an identical manner as the rest of the copper plate. Measurement of the heat flux profile along the impingement surface was possible by moving the RJRC flame horizontally. Each local heat flux measurement was the average of 14,336 data points sampled at a rate of 500 samples/second. Flame temperatures were measured using a 50 μm diameter Type S bare wire thermocouple with an accuracy of ±1.5°C. The measured flame temperatures were corrected for convection and radiation effects according to Bradley and Matthews (1968) and Boyer (1990). Reported mean temperatures represented the average of 12,300 temperature readings recorded at a rate of 2000 samples/second.

Nomenclature

b/R_o = RJR nozzle exit gap width, dimensionless
D_f = fuel pipe inside diameter = 5.1 mm
ENO_x = NO_x emission index, (g NO_x/kg fuel)
H = distance measured from impingement surface, mm
ILJ = in-line jet
MW = molecular weight, g/mol
n = average number of carbon atoms in fuel structure per mole of fuel = 1.05
q = plate heat transfer rate, kW
q_f = fuel heating capability, kW
q'' = local heat flux, W/m^2
q''_{avg} = area averaged heat flux, W/m^2
r = radial location, mm
R_o = air supply pipe inside radius = 12.7 mm
Re = fuel Reynolds number (based on D_f), dimensionless
RJR = radial jet reattachment
RJRC = radial jet reattachment combustion
R_t = heat transfer ratio = q/q_f, percent
V = air exit velocity, m/sec
X_p/R_o = nozzle-to-plate spacing, dimensionless
W = dependent variable
[ ] = concentration, mol/cm^3
θ = air exit angle = 10 deg
Φ = fuel equivalence ratio = (Fuel/Air Ratio)$_{actual}$/(Fuel/Air Ratio)$_{stoichiometric}$

The near-surface temperatures of the impingement surface were measured with K-type thermocouples (20 AWG) with a calibrated accuracy of ±0.5°C. Twelve thermocouples spaced 25.4 mm apart were silver-soldered to the bottom of holes drilled from the rear of the copper plate to within 1.5 mm of the impingement side. A single pressure tap was drilled through the copper plate near the center of the copper plate, as shown in Fig. 2. Surface pressure profiles were possible by moving the support structure, i.e., flame, horizontally while the surface remained stationary. A variable reluctance differential pressure transducer, with an accuracy of ±0.25 percent full scale, was connected to the pressure tap by flexible tubing. The average local gage pressure was calculated from 2048 samples taken at a rate of 200 samples/second.

Combustion specie concentrations were collected from the flame region through a 4.0 mm ID, 6.0 mm OD quartz isokinetic gas sampling probe as outlined by Mohr (1996). The overall emission index of NO_x (ENO_x) was determined from the measured quantities of CO_2 and NO_x ($NO + NO_2$), respectively, and is shown in Eq. 1.

$$ENO_x = \frac{n[NO_x]MW_{NO_2}1000}{[CO_2]MW_{fuel}} \quad (1)$$

This index expresses the grams of NO_x produced per kilogram of fuel burned and best characterizes the emissions from open system diffusion flames (Turns and Lovett, 1989; Junus et al., 1994; Røkke et al., 1994). A complete emissions mapping (Mohr, 1996) with respect to r/R_o at a given value of H/R_o showed the NO_x emission index to be invariant with r/R_o and H/R_o. Therefore, the statistical model emissions data were obtained at $H/R_o = 0.8$ at a nondimensional radial distance of $r/R_o = 36$, just prior to the point where the combustion gases were drawn into the exhaust duct.

Error Analysis. Using the method of Kline and McClintock (1953), the uncertainty in heat transfer ratio was 10.2 percent, while the uncertainty in fuel equivalence ratio (based on the metered air and fuel flow rates) was 4.0 percent. The minimum and maximum uncertainties in the surface heat flux profile were 1.4 and 11.4 percent, respectively. The impingement surface pressure coefficient profile had minimum and maximum uncertainties of 2.6 and 12.8 percent, respectively. The minimum and maximum uncertainties in the surface temperature measurements were 3.0 and 7.4 percent, while the flame temperatures showed an uncertainty range of 0.25–4.0 percent.

Several runs at identical operating conditions were conducted and averaged. The standard deviation of the heat transfer ratio was 1.37 percent. Within the stagnation region, the minimum and maximum standard deviations in local heat flux values were 2.3 and 15.9 percent of the reported mean heat flux values. Repeatability data for the plate surface temperature measurements showed minimum and maximum standard deviations to be 0.7 and 2.8 percent, respectively. Repeatability data for the combustion gas concentrations yielded standard deviations of 0.53, 1.45, 14.6, and 6.0 percent of the mean values for O_2, CO_2, CO, and NO_x measurements, respectively.

RJRC Flame Characterization

In combustion systems utilizing natural gas, a compromise exists between maximizing heat transfer and minimizing pollution formation. Minimum levels of CO are present when flame temperatures are high, since the conversion of CO to CO_2 is enhanced by higher temperatures. However, higher temperatures also promote the formation of thermal NO_x compounds, so one must sacrifice some level of heat transfer (i.e. flame temperature) to attain the desired low levels of NO_x compounds.

Statistical Design. Based on previous studies (Habetz et al., 1994), four major factors affect the heat transfer and pollution formation processes for the RJRC combustion nozzle: (1) fuel Reynolds number (Re), (2) fuel equivalence ratio (Φ), (3) nozzle air exit width (b/R_o), and (4) nozzle-to-plate spacing (X_p/R_o). The primary air flow rate is built into the definition of Φ. Habetz et al. (1994) conducted limited investigations of the effects of each of these factors, but those experiments were conducted by setting all but one of the variables at a constant value and testing over a range of the remaining variable. Utilizing such an experimental method requires a large number of experimental runs and does not give information about the possible interaction between factors. Attempts to use nondimensional analysis in constructing an empirical heat transfer correlation for RJRC performance were not completely successful (Habetz et al., 1994), and there exists great difficulty in numerically modeling the highly turbulent reacting system. Therefore, a statistical model was used to bridge the gap between purely empirical and purely analytical models through a relatively small number of experimental runs. The power of using designed experiments is that one can construct a statistical model that is easy to use and yields valuable performance data useful to a process operator or designer.

Previous investigations (Mohr et al., 1996) showed nonlinear trends in heat transfer and pollution formation as functions of fuel equivalence ratio and fuel Reynolds number, so a traditional 2^k (k factors at 2 different levels) factorial experimental design would be inappropriate in modeling any nonlinear responses. A third level would be required to pick up any quadratic or higher order nonlinear behavior. The difficulty in adding a third level is that 3^4 runs would be required to fully investigate four experimental factors at three different levels. In order to reduce the total number of experimental runs from 81 to 27, a Box-Behnken (Box and Behnken, 1960) experimental design method for four factors was used. This design is similar to a four factor Central Composite Design (Hogg and Ledolter, 1992), but with six fewer experimental runs. One other advantage of a Box-Behnken design is that it lends itself well to fitting higher order quantitative models to experimental data.

Statistical Models. The levels of each of the four main factors were chosen based on several criteria. Lean blow-out data set the lower limits on the fuel Reynolds number (Re) and Φ at 5253 and 1.0, respectively. The upper limits of these two variables were determined based on the limitations of the small RJRC nozzle to safely operate. Within these limits, each variable (Re and Φ) could be varied independently of each other and still maintain a stable flame. The values of nozzle-to-plate spacing, X_p/R_o, were chosen in order to maintain flame stability at the different levels of the other variables. The range of exit gap width, b/R_o, represents the minimum and maximum openings possible with the current RJRC nozzle construction. The levels of each of the four factors are listed in Table 1. Note that the intermediate level of each variable is determined from the arithmetic average of the upper and lower limits, respectively.

Based on the data obtained from the 27 runs in the Box-Behnken design, a second order regression analysis was applied using commercially available statistical software. The resulting

Table 1 Box-Behnken design factor levels

Factor	Low Level	Medium Level	High Level
Φ	1.0	1.5	2.0
Re	5253	8855	12456
X_p/R_o	0.79	1.18	1.57
b/R_o	0.12	0.26	0.40

regression equation for a particular dependent variable, W (R_t or ENO_x), was constructed according to the format of Eq. 2, wherein the first order, interaction, and second order terms are all considered.

$$W = C_1 + C_2\Phi + C_3(X_p/R_o) + C_4 b/R_o + C_5\,\mathrm{Re} + C_6\Phi^2 + C_7(\Phi)(X_p/R_o) + C_8(\Phi)(b/R_o) + C_9(\Phi)(\mathrm{Re}) + C_{10}(X_p/R_o)^2 + C_{11}(X_p/R_o)(b/R_o) + C_{12}(X_p/R_o)(\mathrm{Re}) + C_{13}(b/R_o)^2 + C_{14}(b/R_o)(\mathrm{Re}) + C_{15}\,\mathrm{Re}^2 \quad (2)$$

Statistical analysis revealed that not all of the coefficients in Eq. 2 were statistically significant at a 95 percent confidence level, so it was possible to reduce the number of terms in Eq. 2 considerably. Equations 3 and 4 show the resulting expressions for R_t, and ENO_x, respectively, as well as the correlation coefficients for each expression. The high correlation coefficients (R^2) demonstrate that the models are accurately describing the variability in the data.

$$R_t(\text{percent}) = -86.4 + 51.8\Phi + 194 b/R_o + .00927\,\mathrm{Re} - 11.2\Phi^2 - 266(b/R_o)^2 - 4.8 \times 10^{-7}\,\mathrm{Re}^2 \qquad R^2 = 95.9 \text{ percent} \quad (3)$$

$$ENO_x = 1.36 - 0.448\Phi - 1.87 b/R_o - 1.07 \times 10^{-4}\,\mathrm{Re} + 0.969(\Phi)(b/R_o) + 6.1 \times 10^{-5}(\Phi)(\mathrm{Re}) + 1.73 \times 10^{-4}(b/R_o)(\mathrm{Re}) \qquad R^2 = 93.4 \text{ percent} \quad (4)$$

The statistical analysis revealed that the heat transfer ratio, R_t, was dependent upon the first and second order terms, and independent of the interaction among variables. Some interaction terms were important for ENO_x, while the second order terms were not important. For both response variables, though, the effect of nozzle-to-plate spacing (X_p/R_o) was statistically insignificant. This finding is in contrast to studies with ILJ flame jets where the nozzle-to-plate spacing greatly affected the impingement surface heat transfer (Baukal and Gebhart, 1995a, 1995b; Viskanta, 1993; Rigby and Webb, 1995). Additional experimental data within the range of parameters were obtained in order to test the ability of the model to predict heat transfer and pollution formation with the RJRC nozzle. The differences between all experimental data and the model were less than 7.6 and 11.5 percent for R_t and ENO_x values, respectively. These statistical methods allow for the development of a powerful, yet simple equation which accurately predicts the RJRC nozzle performance.

Heat transfer results from the statistical model are shown in Fig. 3 and indicate that as the air exit gap width, b/R_o, increases, percent heat transfer to the impingement surface increases. One reason for this behavior is that a larger value of b/R_o results in a slower air exit velocity, allowing more time for the fuel and air to fully mix and react. Also, the slower air jet velocity creates a longer residence time for the reacting gasses flowing along the surface following impingement. For larger values of b/R_o, the amount of heat transfer to the impingement surface was quite significant, where up to 50 percent of the available fuel energy was transferred to the impingement surface. The quadratic trend with respect to Re suggests that R_t can be increased by increasing the amount of fuel supplied to the system up to Re = 9656, after which an increase in Re causes a decrease in R_t. A continual increase in Re will lead to an eventual decrease in R_t due the fixed size of the impingement surface. For a constant value of Re, the fuel equivalence ratio was increased by decreasing the air flow rate, and hence, the air velocity. Figure 3 shows that percent heat transfer increases with increasing Φ at a constant value of Re. The lower air flow velocities associated with higher Φ results in the same effect on R_t as increasing b/R_o, as discussed above. Finally, these values of

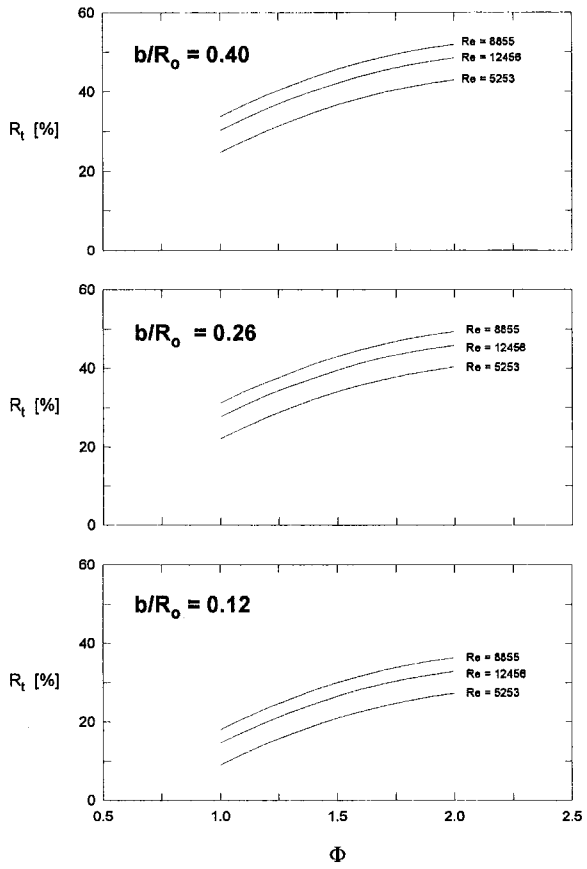

Fig. 3 Percent heat transfer calculated from regression model as a function of Re, Φ, and b/R_o

overall heat transfer compare quite well with other flame jet impingement studies such as Rigby and Webb (1995).

Ideal Condition Results

A procedure outlined by Mohr (1996) was utilized to determine the ideal operating conditions of the RJRC nozzle in terms of maximizing heat transfer and minimizing NO_x emissions. The results of that procedure yielded the following ideal operating conditions: Re = 8855, Φ = 1.0, and b/R_o = 0.29. Since the nozzle-to-plate spacing, X_p/R_o, was not a significant factor in either the heat transfer or ENO_x considerations, the mid-range value of X_p/R_o = 1.18 was selected for further testing. The following results and discussion correspond to the RJRC nozzle operating under these ideal operating conditions.

Flame Temperatures. Figure 4 shows the corrected temperatures for the RJRC flame. These six flame temperature profiles were obtained with the thermocouple probe held at six fixed distances from the impingement surface. The support structure (i.e., the flame) was moved horizontally, corresponding to radial measurement with respect to the flame. Due to the symmetry of the RJRC flame (Mohr et al., 1996), radial measurements were obtained from only one circumferential location. The radial flame temperature profiles for H/R_o = 0.4 and 0.8 were able to reach completely to the nozzle center-line, while the minimum radius for the other profiles was limited by the outer radius of the RJRC nozzle. With the RJRC nozzle, the maximum flame temperature at H/R_o = 0.4 was approximately twice that of the flame centerline temperature. A round flame jet for a methane/air mixture at a fuel Reynolds number of 7000 also resulted in a centerline flame temperature which was about half the maximum temperature (Milson and Chigier, 1973). The nozzle-to-plate spacing used with their round flame

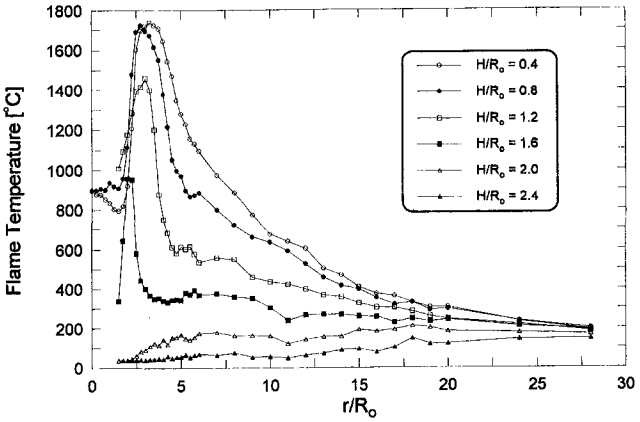

Fig. 4 RJRC flame temperatures at Re = 8855, Φ = 1.0, X_p/R_o = 1.18, b/R_o = 0.29

was 8.5 times larger than the nozzle-to-plate spacing used with the RJRC nozzle. Because of the cool central core of unreacted fuel present in round flame jets, a larger reaction zone (larger X_p/R_o) is required compared with the RJRC nozzle to achieve the same flame temperature at the nozzle centerline. The recirculation region at the centerline of the RJRC nozzle distributes the fuel and air more uniformly, allowing combustion to take place at the nozzle centerline without having to increase the size of the reaction zone by increasing the nozzle-to-plate spacing. The maximum measured flame temperature of Milson and Chigier's (1973) premixed flame was less than 2.0 percent higher than the maximum temperature measured at H/R_o = 0.4 in the present study. This result suggests that this partially premixed RJRC nozzle is operating essentially as a premixed burner.

The location of the reattachment ring is manifested by the steep gradients on both sides of the maximum flame temperatures for profiles where $H/R_o \leq 1.6$. It can be seen that the peak temperature moves radially outward with decreasing H/R_o, due to expansion of the air jet as it leaves the RJRC nozzle. This air jet expansion creates a larger oxygen-rich reaction zone in which combustion can occur, causing the radial width of the reaction zone to increase with decreasing H/R_o. For $H/R_o > 1.6$, the low temperatures indicate that no combustion is occurring, and suggest that the reaction zone is limited to $H/R_o \leq 1.6$. The change in slopes of the flame temperature profiles suggests that the combustion process is nearly complete at $r/R_o \approx 10$.

Surface Heat Flux. The impingement surface local heat flux and the area averaged heat flux defined by Eq. (5) as functions of radial location are shown in Fig. 5.

$$q''_{\text{avg}} = \frac{2\pi \int_0^{r/R_o} q''[r/R_o]d[r/R_o]}{\pi[r/R_o]^2} \tag{5}$$

Also shown in Fig. 5 is the flame temperature profile for H/R_o = 0.4 and the impingement surface temperature distribution. The shape of the local heat flux profile, very closely mirrors the flame temperature profile with the exception that the maximum flame temperature occurs at a slightly smaller radial location than the maximum heat flux. This small difference in radial location is possibly due to the fact that the flame temperature was measured 5 mm from the impingement surface.

The data from Fig. 5 are extremely important. First, the high heat flux ($\approx$140 kW/m^2) within the reattachment region under the given operating conditions shows that very intense heating is possible with the RJRC nozzle. Even higher local heat flux values would be possible if one were to increase the fuel flow rate. The average heat flux profile calculated from Eq. 1 shows a significant drop beyond $r/R_o \approx 10$. This area-averaged heat flux profile is important when considering the optimal spacing between nozzles in an array configuration. The integrated local heat flux values calculated from Eq. 6 were compared to the overall heat transfer to the impingement surface, measured by the sensible heat gain of the cooling water.

$$q = 2\pi \int_0^{r/R_o=28} q''[r/R_o]d[r/R_o] \tag{6}$$

This integrated heat transfer rate was 13 percent lower than the measured overall heat transfer rate. These differences can be attributed to the fact that the heat flux data were possible to be measured up to r/R_o = 28, whereas edge of the water-cooled impingement surface is located at r/R_o = 36. In fact, when the slope of the local heat flux profile is extrapolated out to the edge of the impingement surface (r/R_o = 36), the difference in the integrated and measured heat transfer rates is less than ten percent.

RJRC Flame Map. The characteristics of the RJRC flame have been mapped by combining the data from Figs. 4 and 5 with surface pressure and combustion specie data (Mohr, 1996) for the RJRC nozzle operating under same the ideal conditions. These data are plotted in Fig. 6, where all the nondimensional terms are in relative proportion to each other and the RJRC nozzle. Several distinct features of the RJRC flame are contained within Fig. 6. The reaction envelope, where the gas temperatures are all above 540°C, is located within the boundary of the shaded regions. Glassman (1987) reports that the spontaneous ignition temperature of a methane/air mixture is 540°C. Since the natural gas fuel utilized in this study is over 90 percent methane, it is reasonable to assume that its ignition temperature will be close to the ignition temperature of methane. Hence, any region at or above 540°C is likely to contain reacting combustion gases. It is important to point out the gap between the shaded region and the impingement surface ($0 < H/R_o < 0.4$). No flame temperature measurements were obtained in this region due to spatial limitations and concern in damaging the fine wire thermocouple probe. The same explanation applies to the gap between the shaded region and the top of the RJRC nozzle for $0 < r/R_o < 0.75$.

The main high temperature reaction zone occurs along the boundary of the moving primary air as it exits the RJRC nozzle and contacts the fuel stream. The higher mass flow rate of air

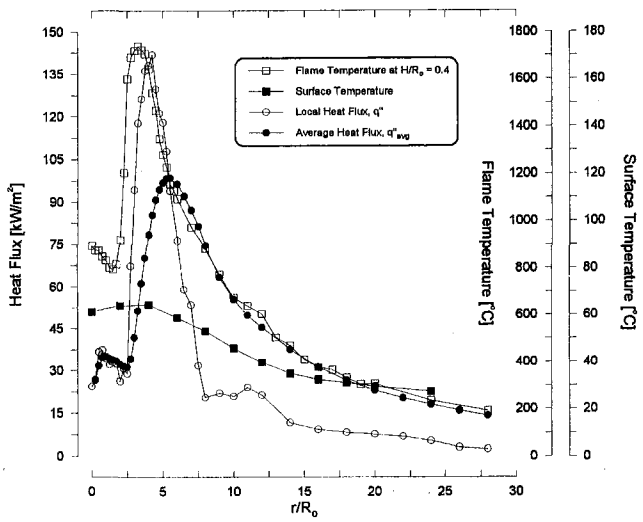

Fig. 5 Impingement surface heat flux and temperature distributions for the RJRC flame operating at Re = 8855, Φ = 1.0, X_p/R_o = 1.18, b/R_o = 0.29; flame temperatures measured at H/R_o = 0.4

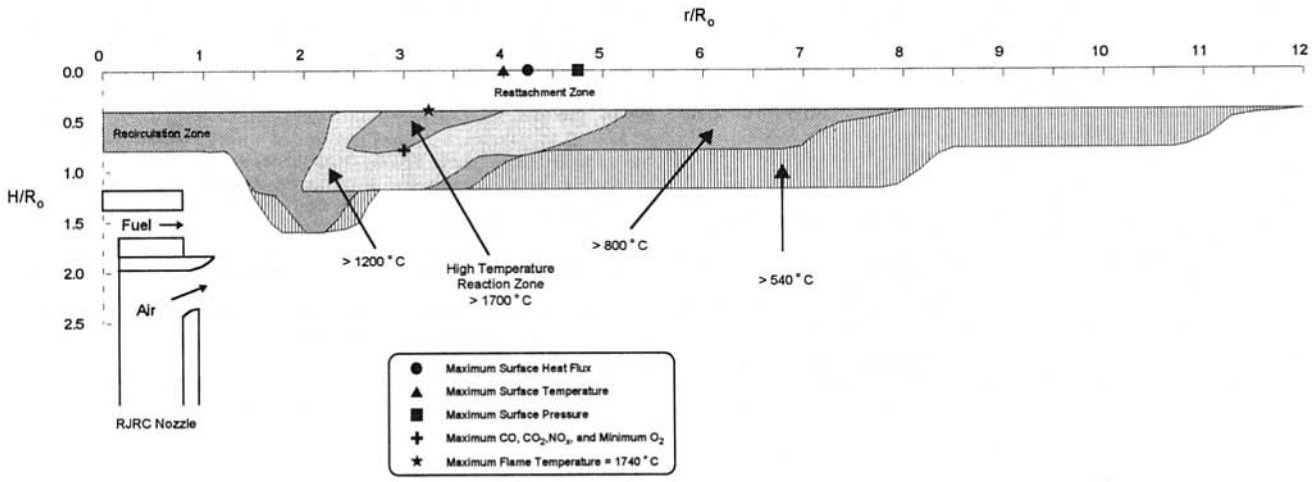

Fig. 6 RJRC flame map for the flame operating at Re = 8855, $\Phi = 1.0$, $X_p/R_o = 1.18$, $b/R_o = 0.29$

relative to the fuel forms the outer boundary of the reaction zone and directs the flame jet toward the impingement surface. As fuel and air react in the small zone between the fuel and air streams, the very high temperature (>1700°C) reaction zone forms over the distance $2.5 < r/R_o < 4.0$ for $0.4 < H/R_o < 0.8$ (see also Fig. 4). The combustion specie profiles (Mohr, 1996) confirmed the location of this high temperature reaction zone. The maximum concentration of CO, CO_2, and NO_x, as well as the minimum concentration of O_2, were all located at a single location in the horizontal plane at $H/R_o = 0.8$, namely $r/R_o = 3.0$. At this location, the high temperatures promoted near-stoichiometric combustion concentrations of CO_2 and O_2, respectively. A lower temperature (>1200°C) reaction zone is also present over the distance $2.00 < r/R_o < 5.25$. Except for a small region in the vicinity of $1.50 < r/R_o < 2.75$, the combustion specie profiles at $H/R_o \geq 1.2$ revealed very little chemical reactions, as also shown by the low (<540°C) flame temperatures in Fig. 6.

The relatively low temperature recirculation zone is located between the nozzle and the impingement surface. This region is identified by the fact that the temperatures were at or above 800°C but less than 1200°C. The reattachment zone on the impingement surface is clearly marked by the maximum values of surface temperature, surface pressure, and surface heat flux. Note that the width of the relatively thin reattachment zone is approximately 0.75 r/R_o, corresponding to 9.5 mm. As discussed above with regard to flame temperatures, the spreading of the flame jet prior to and following reattachment is shown in Fig. 6, as evidenced by the presence of the reaction envelope at radii both smaller and larger than the radial location of the reattachment zone.

Energy Balance. Energy from the RJRC flame is either transferred to the impingement surface, convected out of the system with the spent combustion products, or radiated to the surroundings. The magnitude of each of these losses was determined by Mohr (1996) for the RJRC nozzle operating under the same ideal condition as discussed previously. The results showed that 70 ± 8.5 percent of the fuel input energy was convected out of the impingement system in the form of hot combustion gases. The ±8.5 percent deviation in the convected energy value is a result of the approximate 12.0 percent overall uncertainty of the convected energy measurements and calculations. The total heat transfer to the impingement surface calculated from Eq. 3 was 32 ± 3.0 percent of the fuel input energy. Radiation from the flame to the surroundings was estimated based on a blackbody radiation exchange between the flame and the ambient surroundings. These calculations revealed that the radiation heat transfer from the flame to the surroundings was about 4.0 percent of the fuel input energy supplied to the system. Since the energy convected out of the system and transferred to the surface appear to account for most of the energy available from the fuel input, it can be concluded that radiation from the flame to the surroundings is negligible.

Conclusions

This study was undertaken in order to understand the heat transfer characteristics of a practical RJRC nozzle. Overall heat transfer to the impingement surface depended upon the fuel equivalence ratio, air exit gap width, and fuel Reynolds number. The nozzle-to-plate spacing did not significantly affect the overall heat transfer to the impingement surface. However, for a given nozzle-to-plate spacing, high nozzle centerline flame temperatures were achieved, and the maximum flame temperature and the width of the reaction zone both increased with decreasing distance, H/R_o, from the impingement surface.

Impingement surface heat flux was very high in the reattachment region, while the area averaged heat flux profile identified the possible optimal spacing for future use of RJRC nozzles in array configurations. The relative sizes of the RJRC reaction envelope, high temperature reaction zone, and the reattachment zone were also determined. Calculations revealed the radiation from the flame to the surroundings to be negligible. As a result, the fuel energy was either transferred to the impingement surface or convected out in the combustion product gases. In summary, this study provided the first detailed information regarding the heat transfer characteristics of the RJRC nozzle.

Acknowledgment

This research is partially supported by the Texas Hazardous Waste Research Center and the Texas A&M Drying Research Center. The authors wish to thank Mr. Kai Freudenreich for assistance with the flame temperature measurements.

References

Baukal, C. E., and Gebhart, B., 1995a, "A Review of Flame Impingement Heat Transfer Studies Part 1: Experimental Conditions," *Combustion Science and Technology*, Vol. 104, pp. 339–357.

Baukal, C. E., and Gebhart, B., 1995b, "A Review of Flame Impingement Heat Transfer Studies Part 2: Measurements," *Combustion Science and Technology*, Vol. 104, pp. 359–385.

Boyer, L. M., 1990, "Scalar Dissipation Temperature Measurements in a Lifted Turbulent Diffusion Flame," M.S. Thesis, Brigham Young University, Provo, UT.

Box, G. E. P., and Behnken, D. W., 1960, "Some New Three Level Designs for the Study of Quantitative Variables," *Technometrics*, Vol. 2, No. 4, pp. 455–475.

Bradley, D., and Matthews, K. J., 1968, "Measurement of High Gas Temperatures With Fine Wire Thermocouples," *Journal of Mechanical Engineering Science,* Vol. 10, No. 4., pp. 299–305.

Glassman, I., 1987, *Combustion,* 2nd ed., Academic Press, Inc., Orlando, FL.

Habetz, D. K., Page, R. H., and Seyed-Yagoobi, J., 1994, "Impingement Heat Transfer from a Radial Jet Reattachment Flame," *Proceedings of the 10th International Heat Transfer Conference,* Brighton, England, Vol. 6, pp. 31–36.

Hogg, R. V., and Ledolter, J., 1992, *Applied Statistics for Engineers and Physical Scientists,* Macmillan Publishing Company, New York, NY.

Junus, R., Stubington, J. F., and Sergeant, G. D., 1994, "The Effects of Design Factors on Emissions From Natural Gas Cooktop Burners," *International Journal of Environmental Studies,* Vol. 45, pp. 101–121.

Kline, S. J., and McClintock, F. A., 1953, "Describing Uncertainties in Single Sample Experiments," *Mechanical Engineering,* Vol. 75, pp. 3–8.

Milson, A., and Chigier, N. A., 1973, "Studies of Methane and Methane-Air Flames Impinging on a Cold Plate," *Combustion and Flame,* Vol. 21, pp. 575–586.

Mohr, J. W., 1996, "Studies of Single and Multiple Impinging Radial Jet Reattachment Flames," Ph.D. Thesis, Texas A&M University, College Station, TX.

Mohr, J. W., Seyed-Yagoobi, J., and Page, R. H., 1995, "Optimization of a Practical Radial Jet Reattachment Flame," ASME HTD-Vol. 2, *30th ASME National Heat Transfer Conference,* Portland, OR, pp. 3–10.

Mohr, J. W., Seyed-Yagoobi, J., and Page, R. H., 1996, "Combustion Measurements from an Impinging Radial Jet Reattachment Flame," *Combustion and Flame,* Vol. 106, No. 1–2, pp. 69–80.

Page, R. H., Hadden, L. L., and Ostowari, C., 1989, "Theory for Radial Jet Reattachment Flow," *AIAA Journal,* Vol. 27, No. 11, pp. 1500–1505.

Rigby, J. R., and Webb, B. W., 1995, "An Experimental Investigation of Diffusion Flame Jet Impingement Heat Transfer," *Proceedings of the ASME/JSME Thermal Engineering Joint Conference,* Maui, HI, Vol. 3, pp. 117–126.

Røkke, N. A., Hustad, J. E., and Sønju, O. K., 1994, "A Study of Partially Premixed Unconfined Propane Flames," *Combustion and Flame,* Vol. 97, pp. 88–106.

Turns, S. R., and Lovett, J. A., 1989, "Measurements of Oxides of Nitrogen Emissions from Turbulent Propane Jet Diffusion Flames," *Combustion Science and Technology,* Vol. 66, pp. 233–249.

Viskanta, R., 1993, "Heat Transfer to Impinging Isothermal Gas and Flame Jets," *Experimental Thermal and Fluid Science,* Vol. 6, pp. 111–134.

Enhancement of Heat Transfer Rate by Application of a Static Magnetic Field During Natural Convection of Liquid Metal in a Cube

T. Tagawa
Interdisciplinary Graduate School of Engineering Science

H. Ozoe
Institute of Advanced Material Study, Kyushu University, Kasuga, Fukuoka 816, Japan
ozoe@cm.kyushu-u.ac.jp

Natural convection of liquid metal in a cubical enclosure under an external magnetic field was investigated by three-dimensional numerical analyses. The system parameters were $Ra = 10^5$ and 10^6, $Pr = 0.025$, and $Ha = 0$–1000. One vertical wall of the cubical enclosure was heated, and the opposing vertical wall was cooled, both isothermally; the other four walls were thermally insulated. A uniform horizontal magnetic field was applied parallel to the heated and cooled walls. At $Ra = 10^5$ and $Ha = 50$, the average Nusselt number on the heated wall attained almost the maximum value and was greater than that at $Ha = 0$. The velocity vectors along the vertical walls, and those along the horizontal planes, were rectified in a two-dimensional way at $Ha = 50$ or over, and the average Nusselt number decreased gradually for higher values of the Hartmann number. Similar characteristics were obtained at $Ra = 10^6$. The agreement with our earlier experiments was moderately good.

1 Introduction

The flow of electroconducting fluid under an external magnetic field generates electric currents in the fluid, and the electric currents interact with the external magnetic field to generate Lorentz force. Since external magnetic fields influence the flow of electroconducting fluids, they have been used in various industrial fields. Examples include magnetic suppression of molten semiconducting materials, magnetic control of molten iron flow in the steel industry, liquid metal cooling in nuclear reactors, and plasma flow in magnetic hydrodynamic systems.

It is generally accepted that the flow of liquid metal is suppressed by the Lorentz force under a magnetic field. However, enhancement of heat transfer rate under a weak magnetic field has also been reported.

Fumizawa (1980) studied natural convection of liquid NaK along a vertical heated plate under a transverse magnetic field applied horizontally and parallel to the plate. He found that application of the magnetic field considerably enhanced the heat transfer rate.

Takahashi et al. (1986) reported that the heat transfer rate in mercury decreased with the increase of magnetic intensity. However, for alkali metals, the heat transfer rate showed its maximum value at a certain low magnetic intensity.

Ozoe and Okada (1989) showed by a numerical study that the effect of an external magnetic field on the natural convection of liquid metal in a cubical enclosure depended on the direction of the magnetic field. They then confirmed their numerical prediction in experiments with liquid gallium (Okada and Ozoe, 1992). Their experimental data also suggested the possibility of a slight enhancement of heat transfer under a weak magnetic field, but the exact reasoning was not clarified. The interaction between the magnetic field and the flow of electroconducting fluid has not yet been clarified sufficiently. The present paper tries to clarify the theoretical basis for the enhancement of heat transfer under a static magnetic field by numerical analyses.

2 The System and Model Equations

The modeled regime is the cubical enclosure shown in Fig. 1. One vertical wall is heated, and the opposing vertical wall is cooled isothermally; the other four walls are thermally insulated. A liquid metal whose Prandtl number is 0.025 was assumed to fill the cubical enclosure. A uniform, horizontal magnetic field was assumed to be applied parallel to the heated and cooled walls. To analyze the natural convection of the liquid metal under the magnetic field, the following assumptions were made:

1 The liquid metal is an incompressible Newtonian fluid.
2 Viscous dissipation heating is negligible.
3 The Boussinesq approximation holds.
4 The displacement current can be neglected because high frequency phenomena are not discussed.
5 The liquid metal is not magnetized.
6 Since the convective current $\rho_e \mathbf{u}$ is far less than the conductive current $\sigma(\mathbf{e} + \mathbf{u} \times \mathbf{b})$, $\rho_e \mathbf{u}$ is negligible.
7 The induced magnetic field is negligible due to the small magnetic Prandtl number.
8 Joule heating is negligible for liquid metal.

Then, five basic equations can be obtained in dimensionless form.

Continuity of Mass.

$$\nabla \cdot \boldsymbol{U} = 0 \tag{1}$$

Momentum Equation.

$$\frac{D\boldsymbol{U}}{D\tau} = -\nabla P + \mathrm{Pr}\nabla^2 \boldsymbol{U} + \mathrm{Ha}^2 \mathrm{Pr} \mathrm{Ra}^{-2/3} (\boldsymbol{J} \times \boldsymbol{B}) + [0, 0, \mathrm{Pr}(\Phi - X/L + 0.5)]^T \tag{2}$$

Energy Equation.

$$\frac{D\Phi}{D\tau} = \nabla^2 \Phi + U/L \tag{3}$$

Contributed by the Heat Transfer Division for publication in the JOURNAL OF HEAT TRANSFER. Manuscript received by the Heat Transfer Division June 24, 1996; revision received December 20, 1996; Keywords: Enclosure Flows, Liquid Metals, Natural Convection. Associate Technical Editor: M. Kaviany.

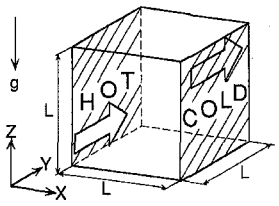

Fig. 1 Schematic of the system. White arrows indicate the uniform external *y*-directional magnetic field.

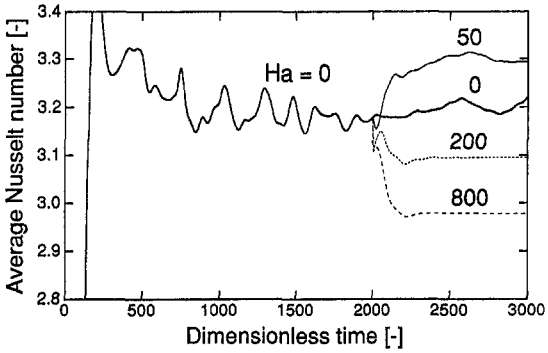

Fig. 2 Transient responses of the average Nusselt number on the heated wall at Ra = 10^5 and Pr = 0.025, with 36 × 36 × 36 grid

Ohm's Law.

$$\boldsymbol{J} = \boldsymbol{E} + \boldsymbol{U} \times \boldsymbol{B} = -\nabla \Psi_e + \boldsymbol{U} \times \boldsymbol{B} \tag{4}$$

Continuity of Electric Current Density.

$$\nabla \cdot \boldsymbol{J} = 0 \tag{5}$$

where Φ indicates the temperature deviation from the conduction temperature profile.

The dimensionless variables are defined as follows:

$$X = x/x_0, \quad Y = y/y_0, \quad Z = z/z_0,$$

$$U = u/u_0, \quad V = v/v_0, \quad W = w/w_0,$$

$$\tau = t/t_0, \quad L = l/x_0 = \mathrm{Ra}^{1/3}, \quad T = (\theta - \theta_0)/(\theta_h - \theta_c),$$

$$\Phi = T - 0.5 + X/L, \quad \boldsymbol{B} = \boldsymbol{b}/b_0,$$

$$\boldsymbol{E} = \boldsymbol{e}/e_0, \quad \boldsymbol{J} = \boldsymbol{j}/j_0, \quad \Psi_e = \psi_e/\psi_{e0},$$

$$\mathrm{Pr} = \nu/\alpha, \quad \mathrm{Ha} = (\sigma/\mu)^{1/2} b_0 l, \quad \mathrm{Ra} = g\beta(\theta_h - \theta_c) l^3/(\alpha\nu),$$

$$x_0 = y_0 = z_0 = \mathrm{Ra}^{-1/3} l, \quad t_0 = x_0^2/\alpha,$$

$$u_0 = v_0 = w_0 = \alpha/x_0, \quad \theta_0 = (\theta_h + \theta_c)/2,$$

$$e_0 = u_0 b_0, \quad j_0 = \sigma u_0 b_0, \quad \psi_{e_0} = \alpha b_0, \quad p_0 = \rho\alpha^2/x_0^2.$$

Initial conditions are as follows:

Temperature.

$$\Phi = T - 0.5 + X/L = 0$$

Velocity.

$$U = V = W = 0$$

Electric Current Density.

$$J_x = J_y = J_z = 0$$

Electric Potential.

$$\Psi_e = 0$$

Nomenclature

b = magnetic flux density (T)
b_0 = uniform external magnetic flux density (T)
B = dimensionless magnetic flux density = $\mathbf{b}/b_0$
e = electric field = $-\nabla\psi_e$ (V/m)
$e_0 = u_0 b_0$ (V/m)
E = dimensionless electric field = $\mathbf{e}/e_0 = -\nabla\Psi_e$
F = the dimensionless Lorentz force = $\mathbf{J} \times \mathbf{B}$
g = acceleration due to gravity (m/s^2)
Gr = Grashof number = $g\beta(\theta_h - \theta_c) l^3/\nu^2$
Ha = Hartmann number = $(\sigma/\mu)^{1/2} b_0 l$
j = electric current density (A/m^2)
$j_0 = \sigma u_0 b_0$ (A/m^2)
J = dimensionless electric current density = $\mathbf{j}/j_0$
l = distance between hot and cold walls (m)
$L = l/x_0$
Nu = Nusselt number = $Q_{\mathrm{conv}}/Q_{\mathrm{cond}}$
Nu_0 = Nusselt number in the absence of magnetic field
Nu_B = Nusselt number under magnetic field
p = pressure (Pa)
$p_0 = \rho\alpha^2/x_0^2$ (Pa)
P = dimensionless pressure = p/p_0
Pr = Prandtl number = ν/α
Q_{cond} = total conduction heat flux ($J/(m^2 \cdot s)$)
Q_{conv} = total convection heat flux ($J/(m^2 \cdot s)$)
Ra = Rayleigh number = $g\beta(\theta_h - \theta_c) l^3/(\alpha\nu) = \mathrm{Gr} \cdot \mathrm{Pr}$
t = time (s)
$t_0 = x_0^2/\alpha$ (s)
T = dimensionless temperature = $(\theta - \theta_0)/(\theta_h - \theta_c)$
u = velocity (u, v, w) (m/s)
$u_0 = v_0 = w_0 = \alpha/x_0$ (m/s)
U = dimensionless velocity (U, V, W) = $\mathbf{u}/u_0$
x = coordinate (m)
$x_0 = \mathrm{Ra}^{-1/3} l$ (m)
$X = x/x_0$
y = coordinate (m)
$y_0 = \mathrm{Ra}^{-1/3} l$ (m)
$Y = y/y_0$
z = coordinate (m)
$z_0 = \mathrm{Ra}^{-1/3} l$ (m)
$Z = z/z_0$

Greek Letters

α = thermal diffusivity of fluid (m^2/s)
β = volumetric coefficient of expansion (1/K)
θ = temperature (K)
θ_c = cold wall temperature (K)
θ_h = hot wall temperature (K)
$\theta_0 = (\theta_h + \theta_c)/2$ (K)
μ = viscosity of fluid (Pa·s)
ν = kinematic viscosity of fluid = μ/ρ (m^2/s)
ρ = density of fluid (kg/m^3)
ρ_e = charge density (C/m^3)
σ = electric conductivity of fluid ($1/(\Omega \cdot m)$)
τ = dimensionless time = t/t_0
Φ = dimensionless temperature deviation = $T - 0.5 + X/L$
ψ_e = electric scalar potential (V)
$\psi_{e0} = \alpha b_0$ (V)
Ψ_e = dimensionless electric scalar potential = ψ_e/ψ_{e0}

Operators

$\nabla = \mathbf{i}\partial/\partial X + \mathbf{j}\partial/\partial Y + \mathbf{k}\partial/\partial Z$
$\nabla^2 = \partial^2/\partial X^2 + \partial^2/\partial Y^2 + \partial^2/\partial Z^2$

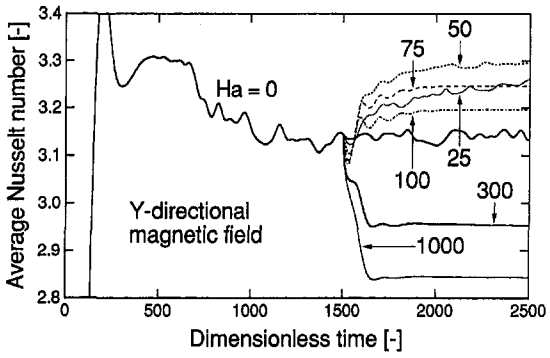

Fig. 3 Transient responses of the average Nusselt number on the heated wall at Ra = 10^5 and Pr = 0.025, with 46 × 46 × 46 grid

Table 1 Coordinates of unequal grid points for half of the regime

0.0000000	0.0089518	0.0185918	0.0289730	0.0401524
0.0521914	0.0651560	0.0791174	0.0941522	0.1103430
0.1277787	0.1465549	0.1667748	0.1885493	0.2119980
0.2372496	0.2644426	0.2937265	0.3252619	0.3592219
0.3957930	0.4351760	0.4775869	0.5000000	

Boundary conditions are as follows:

Temperature.

$$\Phi = 0 \quad \text{at} \quad X = 0, L$$

$$\frac{\partial \Phi}{\partial Y} = 0 \quad \text{at} \quad Y = 0, L$$

$$\frac{\partial \Phi}{\partial Z} = 0 \quad \text{at} \quad Z = 0, L$$

Velocity.

$$U = V = W = 0 \quad \text{at} \quad X = 0, L$$

$$U = V = W = 0 \quad \text{at} \quad Y = 0, L$$

$$U = V = W = 0 \quad \text{at} \quad Z = 0, L$$

Electric Current Density.

$$J_x = 0 \quad \text{at} \quad X = 0, L$$

$$J_y = 0 \quad \text{at} \quad Y = 0, L$$

Table 2 Summary of the computed cases and the results

Pr	Ra	Ha	Nu	Max. velocity
0.025	10^5	0	3.12~3.15	0.78~0.82
		25	3.24~3.26	0.82~0.85
		50	3.28~3.29	0.86~0.87
		75	3.25	0.85
		100	3.20	0.83
		300	2.95	0.70
		1000	2.85	0.64
	10^6	0	5.30~5.70	1.09~1.30
		50	5.75~6.10	1.11~1.19
		100	6.00~6.15	1.17~1.22
		200	5.60~6.30	1.09~1.27
		400	5.60~6.25	1.03~1.23
		800	5.60~6.15	1.00~1.18

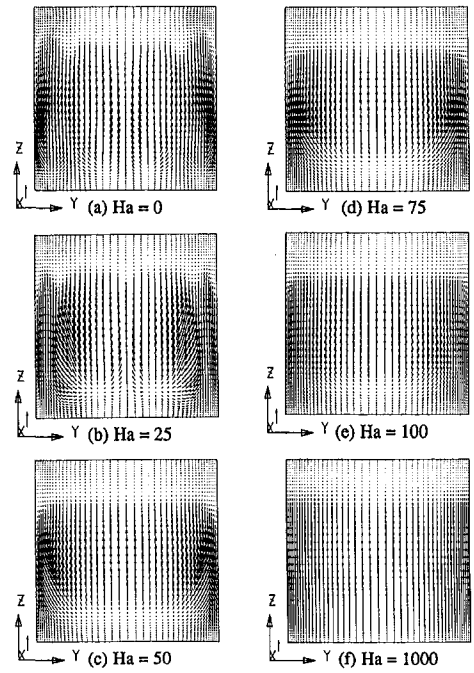

Fig. 4 Velocity vectors near the heated wall (X = 0.024L) at Ra = 10^5, Pr = 0.025, and τ = 2500: (*a*) Ha = 0, (*b*) Ha = 25, (*c*) Ha = 50, (*d*) Ha = 75, (*e*) Ha = 100, and (*f*) Ha = 1000.

$$J_z = 0 \quad \text{at} \quad Z = 0, L$$

These simultaneous equations were approximated by a finite difference method. To satisfy the continuity equation, the staggered grid was employed. The pressure term in the momentum equation was solved by the HSMAC method (Hirt et al., 1975), and the inertial term was approximated by the Utopia scheme (Leonard, 1981; Murakami et al., 1986), which is one of the third-order upwinding schemes. The use of the Utopia scheme

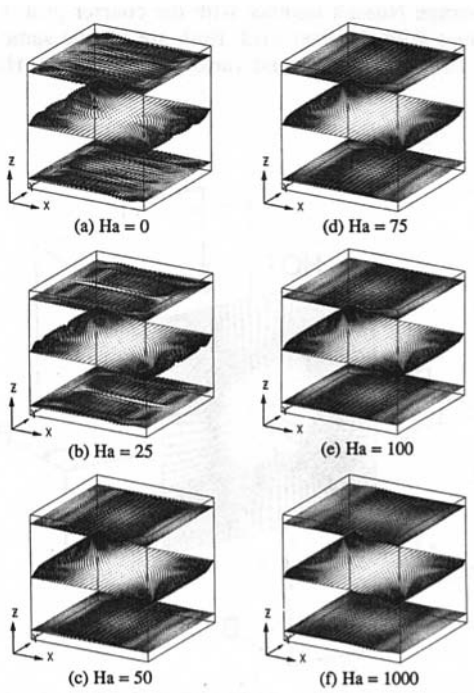

Fig. 5 Perspective velocity vectors at Ra = 10^5, Pr = 0.025, and τ = 2500: (*a*) Ha = 0, (*b*) Ha = 25, (*c*) Ha = 50, (*d*) Ha = 75, (*e*) Ha = 100, and (*f*) Ha = 1000.

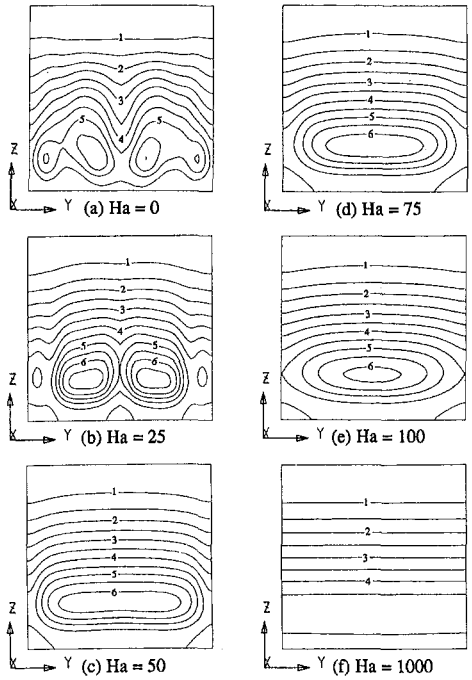

Fig. 6 Contour maps of the local Nusselt number on the heated wall at Ra = 10^5, Pr = 0.025, and τ = 2500: (*a*) Ha = 0, (*b*) Ha = 25, (*c*) Ha = 50, (*d*) Ha = 75, (*e*) Ha = 100, and (*f*) Ha = 1000.

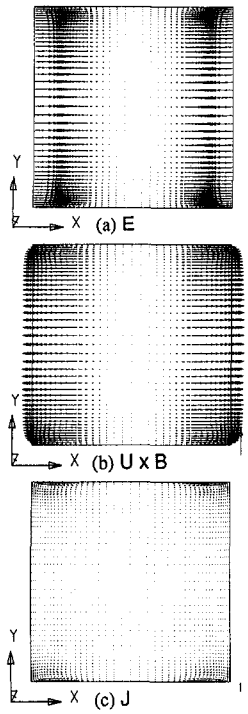

Fig. 8 Top of the electric current density vectors at Ha = 50, Ra = 10^5, Pr = 0.025, *Z* = 0.5*L*, and τ = 2500: (*a*) *E*, (*b*) *U* × *B* and, (c) *J*.

was shown in our previous report (Tagawa and Ozoe, 1996) to be good for the convection of low Prandtl number fluid.

3 Results and Discussion

3.1 Grid Independence. It is well known that the finite difference computation suffers the numerical errors, especially the truncation error. Thus, the computations were carried out with two different grid systems, i.e., a 36 × 36 × 36 grid and a 46 × 46 × 46 grid. Figure 2 shows the transient responses of the average Nusselt number with the coarser grid. Figure 3 shows those with the finer grid. Both are for the same system of Ra = 10^5, Pr = 0.025, and various values of the Hartmann number. The average Nusselt number oscillates by about 3.2 in both Figs. 2 and 3. The enhancement of the average Nusselt number at Ha = 50, and its reduction at higher Hartmann numbers, is also evident. The computational results appear to be sound based upon the effect of the grid size. The detailed results in the remainder of the paper are all from the finer grid computations since they are expected to provide more reliable results.

Table 1 shows grid locations for a 46 × 46 × 46 grid. The same locations were employed for the *X*-, *Y*- and *Z*-directions. The minimum grid is smaller than that of our previous study (Ozoe and Okada, 1989). Table 2 shows the computed cases and some representative results.

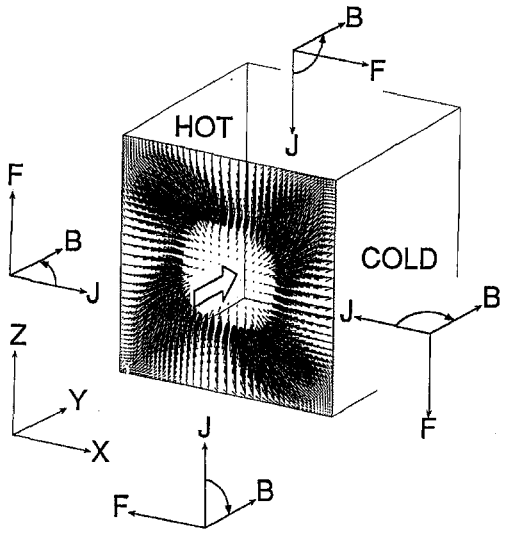

Fig. 7 Perspective view of the electric current density vectors very near the side wall at *Y* = 0.0045*L* for Ha = 50, Ra = 10^5, and Pr = 0.025. The enhancement effect due to the Lorentz force is indicated along the boundaries.

3.2 Computed Results at Ra = 10^5. Figure 3 shows transient responses of the average Nusselt number on the heated wall for various strengths of magnetic field, Ha = 0—1000, at Ra = 10^5, and Pr = 0.025. At dimensionless time τ = 1500 the magnetic field was applied stepwise. At Ha = 50 the heat transfer rate was the most enhanced. The Nusselt number of 3.13 at Ha = 0 was increased to 3.29 at Ha = 50 (about five percent) on average. The convection and the heat transfer rate were suppressed to Nu = 2.85 under the much stronger magnetic field of Ha = 1000.

Figure 4 shows the velocity vectors at $X = 0.024L$ near the vertical heated wall and at τ = 2500. At Ha = 0 and 25, the ascending velocity vectors are not straight, reflecting some nonuniform velocity field in the horizontal *Y*-direction. This means that the ascending fluids do not have the same velocity. However, at Ha = 50 or higher the ascending velocities are almost all in the same direction and of the same magnitude.

Figure 5 shows the perspective view of the velocity vectors at three levels in each graph. Each graph represents a different Hartmann number. For Hartmann numbers of 50 and higher, the velocity fields are all rectified in a straight velocity profile.

Figure 6 shows local Nusselt number profiles at various Hartmann numbers. At Ha = 50 the maximum average Nusselt number was attained due to the widest area of the high local Nusselt numbers.

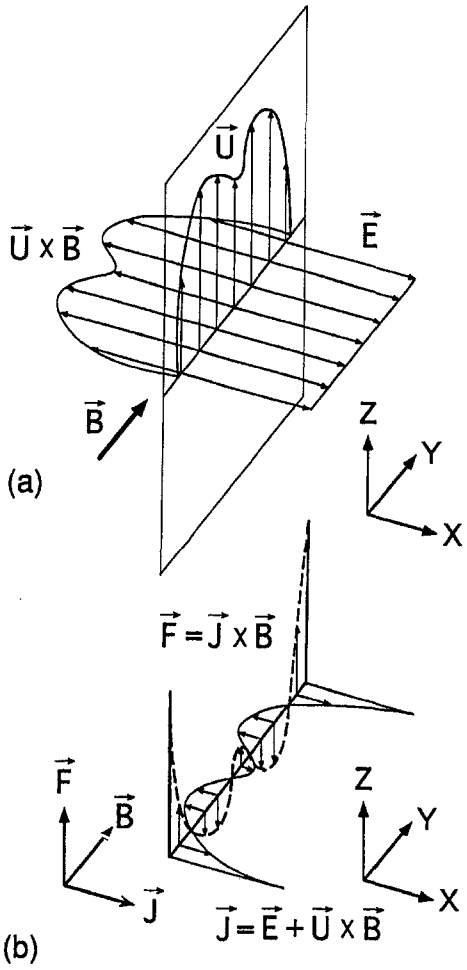

Fig. 9 Flow-rectifying effect due to the Lorentz force: (*a*) $U \times B$ and E, and (*b*) J and F

3.3 Discussion on the Flow Enhancement and Flow Rectifying Effect. The enhancement of heat transfer rate due to the application of a static magnetic field during the natural convection of liquid metal can be explained by considering the electric current and the electric field. Figure 7 shows the electric current density vectors in a vertical plane at $Y = 0.0045L$. The magnetic field is perpendicular to the wall at $Y = 0$. The vector product of the electric current $\boldsymbol{J}$ and the magnetic field $\boldsymbol{B}$ gives the Lorentz force $\boldsymbol{F}$. Near the heated wall this Lorentz force is upward along the heated wall. This assists the ascending natural convection flow near the side wall at $Y = 0$. The rigid wall at $Y = 0$ naturally decreases the convection due to the viscous

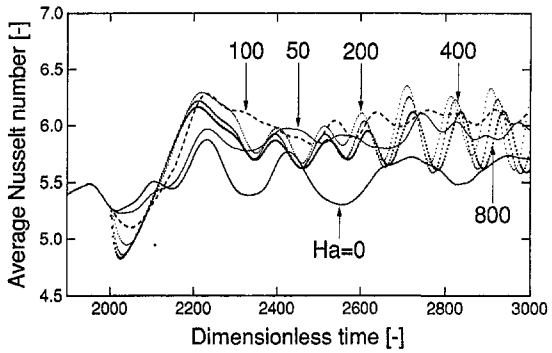

Fig. 10 Transient responses of the average Nusselt number on the heated wall at Ra = 10^6 and Pr = 0.025

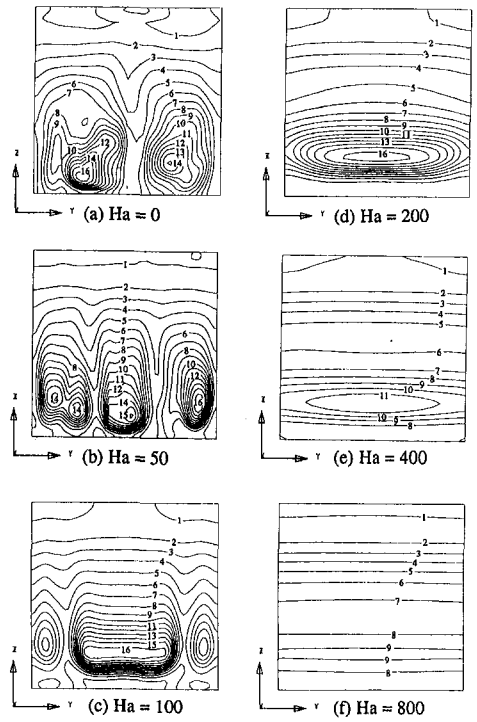

Fig. 11 Contour maps of the local Nusselt number on the heated wall at Ra = 10^6, Pr = 0.025, and τ = 3000: (*a*) Ha = 0, (*b*) Ha = 50, (*c*) Ha = 100, (*d*) Ha = 200, (*e*) Ha = 400, and (*f*) Ha = 800.

force. However, under this Y-directional magnetic field the Lorentz force works to decrease the effect of a rigid wall at $Y = 0$. This flow-enhancement effect also operates for the downward flow on the opposing cooled wall and for the horizontal flow along the top and bottom horizontal boundaries, as shown in Fig. 7. This explains the flow-enhancement effect of the static magnetic field.

Figure 8(a), (b), and (c) show the top views of the electric field vectors $\boldsymbol{E}$, the vector products $\boldsymbol{U} \times \boldsymbol{B}$, and the summation of them that gives the electric current density vectors $\boldsymbol{J} = \boldsymbol{E} + \boldsymbol{U} \times \boldsymbol{B}$ in a horizontal plane at $Z = 0.5L$. The $\boldsymbol{E}$ vectors are large and uniform, for example, near the heated vertical wall at $\boldsymbol{X} = 0$. The ascending velocity vectors W are also dominant. Near this vertical heated wall the vector product, $\boldsymbol{U} \times \boldsymbol{B} \simeq -WB_y$, is almost horizontal and perpendicular to the heated wall for the most domain along the Y-coordinate, as seen in Fig. 8(b). The summation of these two graphs (a) and (b) gives graph (c) for the electric current density vectors $\boldsymbol{J}$, which are almost zero near the heated wall except for very near the side walls at $Y = 0$ and L. These graphs are useful in explaining the flow rectifying effect as follows.

Figure 9 explains the flow-rectifying effect by applying a static magnetic field. If a velocity profile like $\boldsymbol{U}(\simeq W)$ is assumed, the vector product with the magnetic field $\boldsymbol{B}(=B_y)$, $\boldsymbol{U} \times \boldsymbol{B}$, becomes as shown in a horizontal X-Y plain of Fig. 9(a). The electric field $\boldsymbol{E}$ near the heated vertical wall is almost uniform and against $\boldsymbol{U} \times \boldsymbol{B}$, as seen in Fig. 9($a$). The resultant electric current density $\boldsymbol{J}$ becomes alternately positive and negative from the zero magnitude, as shown in Fig. 9(b). This alternation of the electric current density induces a Lorentz force (a hatched line in Fig. 9(b)) in a vertical Y-Z plain toward the opposite direction; in comparison to the original velocity vectors $\boldsymbol{U}$ in Fig. 9(a). In this way, the geometrically fluctuating velocity profiles become almost flat. This explains the flow-rectifying effect seen in Figs. 4 and 5 for Ha of 50 or greater.

The Lorentz force, by applying the Y-directional magnetic field, rectifies the three-dimensional flow and changes it into a two-dimensional one, which increases the heat transfer rate due to the smooth flow. For the lower Hartmann numbers the rectifying effect is superior to the suppressing effect of the convection. On the other hand, for the higher Hartmann numbers than that having a rectified flow, the heat transfer rate decreases because the suppressing effect of flow is superior to the rectifying effect. The maximum enhancement of heat transfer rate occurs at the attainment of this rectified flow by increasing the strength of the magnetic field.

3.4 Computed Results at Ra = 10^6. Figure 10 shows the transient responses of the average Nusselt number at Ra = 10^6 and Pr = 0.025. The average Nusselt number of about 5.6 at Ha = 0 is apparently increased on average over time to the order of 6.1 (about nine percent). This characteristic is similar to that at Ra = 10^5. A quite regular sinusoidal oscillation was found to occur at Ha = 200 to 800. The average Nusselt number was still larger than that at Ha = 0.

Figure 11 shows the contour maps of the local Nusselt number at Ra = 10^6, Pr = 0.025, and at various values of the Hartmann number. The oscillatory flow shows some time-dependent asymmetry at Ha = 0. Furthermore, three or four vortices appeared at Ha = 50, and the maximum average Nusselt number occurred at Ha = 100.

Figure 12 shows top views of the electric current density vectors at Ha = 100, Ra = 10^6, Pr = 0.025, and τ = 3000. These profiles are quite similar to those at Ra = 10^5 in Fig. 8, and the flow rectifying effect should also hold for Ra = 10^6.

The computed results at Ra = 10^6 clarify one more important characteristic of the present subject. In Fig. 10 the transient Nusselt number keeps oscillating even at Ha = 800. We were rather puzzled by this and carried out some additional computations at Ha = 1600 with the present computational grid and with one order finer meshes near the side walls (to decrease the truncation error). However, these gave almost the same results as Fig. 10. These results suggest that the flow suppressing effect due to the Lorentz force does not work for the present system of electrically insulated walls

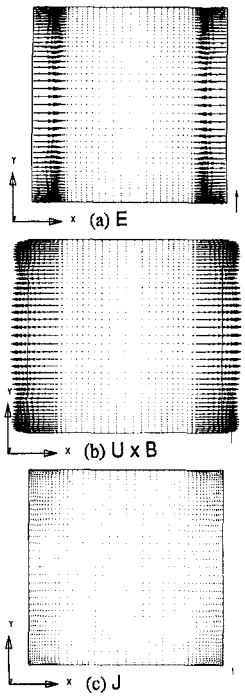

Fig. 12 Electric current density vectors at Ha = 100, Ra = 10^6, Pr = 0.025, Z = 0.5L, and τ = 3000: (*a*) E, (*b*) $U \times B$, and (*c*) J.

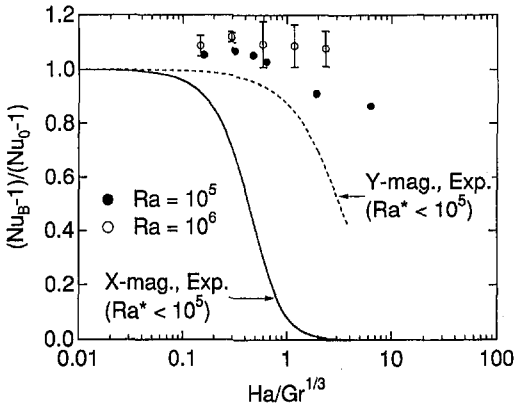

Fig. 13 Comparison between numerical present work and experimental (Okada and Ozoe) average Nusselt number for the magnetic natural convection of gallium (Pr = 0.025)

under the Y-directional magnetic field. This effect could be understood by the electric current density vectors $\boldsymbol{J}$ in Fig. 8(c) and Fig. 12(c). In these graphs $\boldsymbol{J}$ vectors are almost vanishing for most of the regime along the Y-axis. Although they are not shown herein, $\boldsymbol{J}$ vectors are almost zero everywhere in the fluid except very near the side vertical walls at Y = 0, L. ($\boldsymbol{J}$ = 0 is shown in Appendix.) Since $\boldsymbol{J}$ is zero the Lorentz force $\boldsymbol{F} = \boldsymbol{J} \times \boldsymbol{B}$ does not work. This explains that there is no suppressing effect in the present system. At Ra = 10^5 we could see the decrease in the average Nusselt number in Figs. 2 and 3. However, the reduction is not strong: Nu = 2.85 at Ha = 1000 in Fig. 3. These characteristics are quite different from those (Okada and Ozoe, 1992; Ozoe and Okada, 1989) under the X- or Z-directional magnetic field or for the electrically conducting wall system in the Y-directional magnetic field (Tagawa and Ozoe, 1995). The experimental results for molten gallium (Okada and Ozoe, 1992) also did not give an eternal conduction state, even at the highest magnitude of the magnetic field in their apparatus (though it was attained in the X- or Z- magnetic field). For the present system with electrically insulated walls, the electric current density $\boldsymbol{J}$ becomes almost zero everywhere in the fluid except very near the electrically insulated side walls, and the Lorentz force does not work. Near the side walls the electric current density $\boldsymbol{J}$ and the Y-directional magnetic field induces the Lorentz force to enhance the natural convection. The eternal suppression to the conduction state can not be expected in the Y-directional magnetic field.

Figure 13 shows the computed average Nusselt number in comparison to the experimental data reported by Okada & Ozoe (1992) for molten gallium in a 3 cm cube with uniform flux heating. These data were for Rayleigh numbers of 5×10^4 or less, and the effect of enhancement may not be expected. Even so, the agreement is moderately good. The present computation gives the enhancement effect for the range of $Ha/Gr^{1/3}$ between 0.1 and 10. This tendency agrees with the experimental results of Fumizawa (1980).

4 Conclusions

Natural convection of liquid metal in a cube under a uniform static magnetic field applied horizontally and parallel to the heated vertical wall (Y-direction) was numerically studied by using the finite difference method. The Lorentz force induced in the natural convection of liquid metal (Pr = 0.025) heated from one vertical wall and cooled from the opposing vertical wall was found to enhance the heat transfer rate at a weak magnitude of the magnetic field. The average heat transfer rate went from 3.13 at Ha = 0 to 3.29 at Ha = 50 (about five percent) for Ra = 10^5 and from 5.6 at Ha =

0 to 6.1 at Ha = 100 (about nine percent) for Ra = 10^6. These increases in the heat transfer rate appear to explain the experimental finding of the magnetic enhancement reported by Fumizawa (1980), although the systems are not completely the same. Agreement with the experimental data of Okada and Ozoe (1992) is moderately good.

The theoretical reasonings are presented for the flow enhancement effect, flow-rectifying effect, and the almost nonsupressing effect, even under strong magnetic field.

References

Fumizawa, M., 1980, "Natural Convection Experiment With Liquid NaK Under Transverse Magnetic Field," *J. Nuclear Science Technology,* Vol. 17, No. 2, pp. 98–105.

Hirt, C. W., Nichols B. D., and Romero, N. C., 1975, Los Alamos Scientific Laboratory, LA-5852.

B. P. Leonard, 1981, "A Survey of Finite Differences with Upwinding for Numerical Modeling of the Incompressible Convective Diffusion Equation," *Computational Techniques in Transient and Turbulent Flow,* Vol. 2, Pineridge Press, Swansea, U.K.

Murakami, S., Kato, S., and Suyama, Y., 1986, "Study on Diagnostic System for Numerical Simulation of Indoor Turbulent Flow," *Seisan Kenkyu,* (Japan), Vol. 38, No. 12, pp. 44–53.

Okada, K., and Ozoe, H., 1992, "Experimental Heat Transfer Rates of Natural Convection of Molten Gallium Suppressed Under an External Magnetic Field in Either the x-, y-, or z-direction," ASME JOURNAL OF HEAT TRANSFER, Vol. 114, pp. 107–114.

Ozoe, H., and Okada, K., 1989, "The Effect of the Direction of the External Magnetic Field on the Three-Dimensional Natural Convection in a Cubical Enclosure," *Int. J. Heat Mass Transfer,* Vol. 32, pp. 1939–1954.

Tagawa, T., and Ozoe, H., 1995, "Three-Dimensional Numerical Analyses of Natural Convection of Liquid Metal in a Cube With Electro-Conducting Walls Under an External Magnetic Field Either in the x-, y-, or z-directions," *The 14th International Riga Conference on Magnetohydrodynamics,* O. Lielausis, ed., Jurmala, Latvia.

Tagawa, T., and Ozoe, H., 1996, "Effect of Prandtl Number and Computational Schemes on the Oscillatory Natural Convection in an Enclosure," *Numerical Heat Transfer,* Part A, Vol. 30, pp. 271–282.

Takahashi, O., Nagase, N., Michiyoshi I., and Takenaka, N., 1986, "Natural Convection Heat Transfer From a Vertical Cylindrical Heater to Liquid Metals Under Horizontal Magnetic Field," *Eighth Int. Heat Transfer Conference,* San Francisco, Vol. 3, pp. 1317–1322.

APPENDIX

The curl of the Ohm's law becomes as follows:

$$\nabla \times \boldsymbol{J} = \nabla \times (\boldsymbol{E} + \boldsymbol{U} \times \boldsymbol{B}) = \nabla \times \boldsymbol{E} + \nabla \times (\boldsymbol{U} \times \boldsymbol{B})$$

$\nabla \times \boldsymbol{E} = -\partial \boldsymbol{B}/\partial \tau = 0$ for the static magnetic field. $\nabla \cdot \boldsymbol{B} = 0$ and $\nabla \cdot \boldsymbol{U} = 0$. Then,

$$\nabla \times \boldsymbol{J} = (\boldsymbol{B} \cdot \nabla)\mathbf{U} = B_y \frac{\partial \mathbf{U}}{\partial Y}$$

Except near the side walls at $Y = 0, L$, the Y-directional gradient of a velocity $\boldsymbol{U}$ is almost zero due to the flow rectifying effect. Then, $\nabla \cdot \boldsymbol{J} = 0$, $\nabla \times \boldsymbol{J} = 0$ with electrically insulated boundaries give $\boldsymbol{J} = 0$.

Thick-Film Phenomenon in High-Heat-Flux Evaporation From Cylindrical Pores

D. Khrustalev

A. Faghri

Department of Mechanical Engineering,
University of Connecticut,
Storrs, CT 06269

A physical and mathematical model of the evaporating thick liquid film, attached to the liquid-vapor meniscus in a circular micropore, has been developed. The liquid flow has been coupled with the vapor flow along the liquid-vapor interface. The model includes quasi-one-dimensional compressible steady-state momentum conservation for the vapor and also a simplified description of the microfilm at the end of the thick film. The numerical results, obtained for water, demonstrate that formation of extended thick liquid films in micropores can take place due to high-velocity vapor flow under high rates of vaporization. The model has also predicted that the available capillary pressure significantly changes with the wall-vapor superheat and other operational conditions.

Introduction

Heat transfer during evaporation of liquid from cylindrical and/or hemispherical liquid-vapor menisci attached to the heated solid wall (Fig. 1*a*) was considered by Potash and Wayner (1972), Holm and Goplen (1979), Solov'ev and Kovalev (1984), Stephan and Busse (1992), and other investigators due to the importance of this process for operation of capillary driven devices such as heat pipes. More recently, Khrustalev and Faghri (1995a and 1995b) modeled, in detail, the formation of a liquid microfilm attached to an evaporating liquid-vapor meniscus in a capillary groove. They also proposed a simplified model of heat transfer in evaporating menisci with constant curvature of the liquid-vapor interface within the microfilm region. Swanson and Herdt (1992) modeled the evaporating meniscus in a capillary tube. They noted that the local capillary pressure remained constant and equal to $2\sigma/R_{\text{men}}$ regardless of changes in the dimensionless superheat. Khrustalev and Faghri (1996) modeled two-dimensional fluid flow both in the liquid and vapor during evaporation of water from a capillary slot. They reported that in their numerical results the pressure drops in the vapor and liquid were very small compared to the capillary pressure for the wall-vapor temperature difference of up to 10 K at a saturation temperature of 373 K. Therefore, during evaporation from a pore with small wall-liquid temperature drops, the vapor flow does not usually affect the morphology of the liquid-vapor interface, which can be considered of nearly constant curvature except for the microfilm region (Fig. 1(*a*)). Modeling of the extended evaporating meniscus becomes virtually impossible for higher temperature drops between the wall and saturation temperature, $T_w - T_v$, as was noted by Khrustalev and Faghri (1995a). One of the possible reasons for this is a very high peak of curvature of the microfilm free surface (Stephan and Busse, 1992) which increases with the temperature drop (Fig. 1*a*). He and Hallinan (1994) studied thermocapillary effects on the evaporating extended meniscus and concluded that these effects could choke the flow into the evaporating microfilm at higher wall-vapor superheats. Actually, there are no published materials on modeling of evaporating liquid-vapor menisci at room temperatures for $T_w - T_v > 10$ K, especially for low vapor pressures. It should be noted at this point that boiling is a macroscopic phenomena and is anticipated to be different for thin liquid films compared to bulk liquid. Boiling, in its original sense, has not been directly observed in liquid films with thicknesses under 5 μm. Rather than boiling, an important question for vaporization from thin liquid films is if the liquid film will dry out or be stable due to sufficient liquid supply. A physical and mathematical description of this situation is the subject of this paper.

With high wall superheats and low pressures, vapor pressure drops can be of the same order of the magnitude as the capillary pressure. This is especially true for micron-sized pores or channels because evaporation rates are higher for smaller pores and the resulting vapor velocities can be very high. Therefore, it is hypothesized that for extremely high heat fluxes the vapor flow can significantly affect morphology of the extended liquid-vapor interface. For example, existence of extended thick liquid films attached to the evaporating meniscus is possible due to high-velocity vapor flow in spite of the capillary pressure drop between the hemispherical meniscus and nearly flat thick film (Fig. 1(*b*). This hypothesis is considered in the present work for the first time. Thick liquid films (several micrometers thick) were directly observed in the experiment of Belonogov and Kiseev (1995) during evaporation of various liquids from a 0.2 mm inner diameter glass tube. Explanation of their existence by Belonogov and Kiseev (1995) was based on the assumption that the liquid-vapor interface was contaminated by surfactants which resulted in a significant gradient of the surface tension along the observed thick films. These investigators assumed that the surface tension was about two times higher at the beginning of the thick film region compared to the meniscus region allowing for a smooth transition of the meniscus into the thick film. That explanation was, in general, consistent with Wayner et al. (1985) and Volintine and Wayner (1986) who studied mixtures of two liquids with a surface tension gradient along the evaporating liquid film. While Belonogov and Kiseev (1995) and Wayner et al. (1985) made their observations for mixtures of fluids, the present analysis is focused on evaporation of a pure liquid in the vicinity of a hemispherical liquid-vapor meniscus formed within a circular micropore, as shown in Fig. 1(*b*).

The main objectives of the present analysis are: (a) to investigate if high-velocity vapor flows can explain the existence of extended thick liquid films in micropores with high rates of evaporation; and (b) to identify possible mechanisms that can make extended thick liquid films attached to evaporating menisci more stable than a hemispherical meniscus ending with the liquid microfilm.

Contributed by the Heat Transfer Division for publication in the JOURNAL OF HEAT TRANSFER. Manuscript received by the Heat Transfer Division August 16, 1996; revision received January 17, 1996; Keywords: Evaporation, Phase-Change Phenomena, Thin Film Flow. Associate Technical Editor: M. Kaviany.

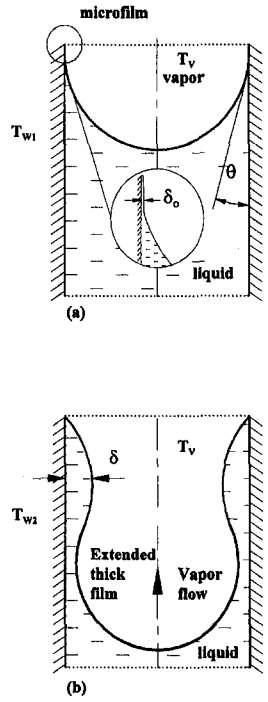

Fig. 1 Evaporation of liquid from cylindrical pores (*a*) at low evaporation rates, and (*b*) at high evaporation rates

A steady state mathematical model developed includes coupled vapor and liquid flows with shear stresses at the liquid free surface due to the vapor-liquid frictional interaction and surface tension gradient. The model is based on the following simplifying assumptions:

1 Local equilibrium exists between the liquid and vapor (saturation conditions)
2 Heat transport in thin liquid films is only due to conduction in the radial direction
3 Viscous flow in the liquid films with low Reynolds numbers

Mathematical Formulation

The cylindrical coordinate system used is shown in Fig. 2. Both the vapor and liquid flow along the z-coordinate. The origin of the coordinate system is fixed with respect to the minimum film thickness. The vapor velocity at $z = 0$ can be high due to extensive evaporation from the liquid-vapor meniscus and affecting the film flow. The physical situation should be described taking into consideration the vapor compressibility and the vapor temperature variation along the channel. Also, the second principal radius of curvature of the liquid-vapor interface should be accounted for (in the equation relating vapor and liquid pressures) while it is usually neglected in modeling of film flows in tubes of larger diameters. Within the assumptions considered above, the mass and energy balances for the liquid film shown in Fig. 2 yields the following:

$$\int_{R-\delta}^{R} r w_l(r) dr = \frac{1}{2\pi\rho_l}\left(\dot{m}_{l,in} - \frac{Q}{h_{fg}}\right). \tag{1}$$

$\dot{m}_{l,in}$ is the liquid mass flow rate in the inner meniscus region at $z = 0$, which supplies the evaporating film with liquid for $z \geq 0$. $Q(z)$ is the heat flow rate through a given cross section due to evaporation from the film for $z \geq 0$ and defined as follows:

$$Q = 2\pi R \int_0^z q_w dz. \tag{2}$$

$q_w(z)$ is the heat flux at the solid-liquid interface due to heat conduction through a cylindrical film with a thickness of δ.

$$q_w = k_l \frac{T_w - T_\delta}{R \ln [R/(R-\delta)]} \tag{3}$$

T_δ is the local temperature of the liquid-vapor interface. From Eqs. (2) and (3) we obtain the following equation:

$$\frac{dQ}{dz} = 2\pi k_l \frac{T_w - T_\delta}{\ln [R/(R-\delta)]}. \tag{4}$$

The momentum conservation for viscous flow in a liquid film is written in the Stokes approximation.

$$\frac{1}{r}\frac{\partial}{\partial r}\left(r\frac{\partial w_l}{\partial r}\right) = \frac{1}{\mu_l}\frac{dp_l}{dz} \tag{5}$$

The boundary conditions for the last equation is non-slip condition at $r = R$ and specified shear stresses at the liquid-vapor interface due to the frictional liquid-vapor interaction and the

Nomenclature

c_p = specific heat at constant pressure, J/(kg-K)
f_v = vapor friction factor
h_{fg} = latent heat of vaporization, J/kg
k = thermal conductivity, W/(m-K)
l_δ = length of the liquid film (Fig. 2), m
K = curvature, m^{-1}
Ma = $\bar{w}_v/\sqrt{\gamma_0 R_g T_v}$, Mach number
$\dot{m}$ = mass flow rate, kg/(s)
p = pressure, Pa
p_d = disjoining pressure, Pa
$Q = 2\pi R \int_0^z q_w dz$, heat flow rate, W
q = heat flux, W/m^2
r = radial coordinate, m
R = inner radius of the channel, m
R_g = gas constant, J/(kg-K)
Re = $2\bar{w}_v(R-\delta)\rho_v/\mu_v$, axial Reynolds number
$\mathrm{Re}_r = 2v_{v,\delta}(R-\delta)\rho_v/\mu_v$, radial Reynolds number
s = coordinate in the meniscus region (see Fig. 2), m
T = temperature, K
$\dot{m}_{l,in}$ = liquid mass flow rate at $z = 0$, kg/s
$\dot{m}_{t,in}$ = total mass flow rate at $z = 0$, kg/s
v = radial velocity, m/s
w = axial velocity, m/s
$\bar{w}$ = area-averaged axial velocity, m/s
z = axial coordinate, m

Greek Symbols

α = accommodation coefficient
β = momentum flux coefficient
$\gamma_0 = c_p/c_v$, ratio of specific heats
$\Delta = d\delta/dz$
$\Delta p_{\mathrm{cap},av} = 2\sigma/(R-\delta_{in}) - (p_{v,in} - p_{v,o})$, available capillary pressure, N/m^2
δ = liquid film thickness, m
θ = contact angle
μ = dynamic viscosity, Pa-s
ρ = density, kg/m^3
σ = surface tension, N/m

Subscripts

ent = entrance
in = at $z = 0$ (inner meniscus)
l = liquid
men = meniscus
mic = microfilm
o = outlet
sat = saturation
v = vapor
w = wall
δ = liquid film free surface

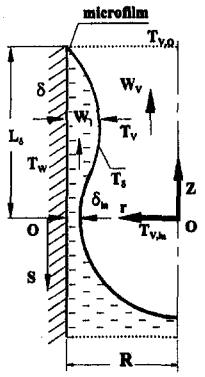

Fig. 2 Schematic of extended thick liquid film in a circular microchannel

surface-tension gradient related to the interfacial temperature gradient along the channel.

$$w_l|_{r=R} = 0 \tag{6}$$

$$\left.\frac{\partial w_l}{\partial r}\right|_{(r=R-\delta)} = \frac{1}{\mu_l}\left(-\frac{f_v}{2}\rho_v \bar{w}_v^2 - \frac{d\sigma}{dT}\frac{dT_\delta}{dz}\right) \equiv E. \tag{7}$$

Solving Eqs. (5–7), the velocity profile is expressed as follows:

$$w_l = -\frac{1}{\mu_l}\frac{dp_l}{dz}\left[\frac{1}{4}(R^2 - r^2) + \frac{(R-\delta)^2}{2}\ln\frac{r}{R}\right] + E(R-\delta)\ln\frac{r}{R}. \tag{8}$$

Substituting Eq. (8) into Eq. (1), we obtain the following equation for the liquid pressure:

$$\frac{dp_l}{dz} = \mu_l\left[\frac{1}{2\pi\rho_l}\left(\frac{Q}{h_{fg}} - \dot{m}_{l,in}\right) + E(R-\delta)F\right] \times \left[\frac{R^4}{16} + \frac{(R-\delta)^2}{2}\left(F + \frac{(R-\delta)^2}{8} - \frac{R^2}{4}\right)\right]^{-1} \tag{9}$$

where

$$F = \frac{(R-\delta)^2}{2}\left(\ln\frac{R}{R-\delta} + \frac{1}{2}\right) - \frac{R^2}{4}. \tag{10}$$

Pressure difference in the vapor and liquid phases is due to capillary and disjoining pressure effects (Faghri, 1995).

$$p_v - p_l = \sigma\left\{\frac{d^2\delta}{dz^2}\left[1 + \left(\frac{d\delta}{dz}\right)^2\right]^{-3/2} + \frac{1}{R-\delta}\cos\left(a\tan\frac{d\delta}{dz}\right)\right\} - p_d \tag{11}$$

The term with cosine in the right-hand side of this equation is due to the second principal radius of the interfacial curvature for a cylindrical film. This term can be important for liquid films in micropores. Introducing an additional variable

$$d\delta/dz = \Delta \tag{12}$$

Eq. (11) can be rewritten as follows:

$$\frac{d\Delta}{dz} = [1 + (\Delta)^2]^{3/2}\left(\frac{p_v - p_l + p_d}{\sigma} - \frac{\cos(\arctan\Delta)}{R-\delta}\right). \tag{13}$$

The integral equation of mass conservation for the vapor flow takes the following form:

$$\rho_v A_v \bar{w}_v(z) = \bar{w}_{v,in}\rho_{v,in}A_{v,in} + Q/h_{fg}. \tag{14}$$

$A_v = \pi(R-\delta)^2$ is the cross-sectional area of the vapor channel. $\bar{w}_{v,in}$ is the area-averaged vapor velocity at $z = 0$ due to evaporation from liquid-vapor meniscus (for $z \le 0$).

The compressible quasi-one-dimensional momentum equation for the vapor flow in the form suggested by Bankston and Smith (1973) is modified to account for inclination of the liquid-vapor interface following Faghri (1995):

$$\frac{dp_v}{dz} = \frac{1}{A_v}\left[\frac{d}{dz}(-\beta_v\rho_v\bar{w}_v^2A_v) - f_v\rho_v\bar{w}_v^2\pi(R-\delta) - 2\pi(R-\delta)\rho_v v_{v,\delta}^2\sin(\arctan\Delta)\right] \tag{15}$$

with $\beta_v = 1.33$ for small radial Reynolds numbers. $v_{v,\delta}$ is the vapor-blowing velocity at the liquid-vapor interface due to evaporation of liquid, defined through the mass flux.

$$v_{v,\delta} = \frac{dQ}{dz}\frac{1}{2\pi(R-\delta)h_{fg}\rho_v} \tag{16}$$

f_v is the vapor friction factor given as follows (Bowman and Hitchcock, 1988; Jang and Faghri, 1991):

$$f_v = 16[1.2337 - 0.2337\exp(-0.0363\,\mathrm{Re}_r)] \times [\exp(1.2\,\mathrm{Ma})]/\mathrm{Re}. \tag{17}$$

The perfect gas law is employed to account for the compressibility of the vapor

$$\rho_v = \frac{p_v}{R_g T_v}. \tag{18}$$

Therefore:

$$\frac{d\rho_v}{dz} = \frac{1}{R_g}\left(\frac{dp_v}{dz}\frac{1}{T_v} - \frac{p_v}{T_v^2}\frac{dT_v}{dz}\right). \tag{19}$$

The saturated vapor temperature and pressure are related by the Clausius-Clapeyron equation which can be written in the following form:

$$\frac{dT_v}{dz} = \frac{dp_v}{dz}\frac{R_g T_v^2}{p_v h_{fg}}. \tag{20}$$

The seven first order differential equations, Eqs. (4), (9), (12), (13), (15), (19), and (20), include the following seven unknown variables: δ, Δ, p_l, Q, p_v, ρ_v, and T_v. Therefore, seven boundary conditions are set forth at $z = 0$:

$$\delta = \delta_{in} \tag{21}$$

$$\Delta = 0 \tag{22}$$

$$p_l = p_{v,in} - \frac{2\sigma}{R-\delta_{in}} + p_d \tag{23}$$

$$Q = 0 \tag{24}$$

$$p_v \equiv p_{v,in} = p_{v,\mathrm{sat}}(T_{v,in}) \tag{25}$$

$$\rho_{v,in} = \frac{p_{v,in}}{R_g T_{v,in}} \tag{26}$$

$$T_v = T_{v,in}. \tag{27}$$

The boundary conditions (22) and (23) follow from the assumptions that the pressure variation in the meniscus liquid is negligible compared to the capillary pressure and that the meniscus smoothly transforms into a liquid film. The boundary condition (24) directly follows from Eq. (2). There are also four parameters δ_{in}, $T_{v,in}$, $\dot{m}_{l,in}$, and $\overline{w}_{v,in}$ and an additional variable T_δ involved in this problem. They will be considered using additional algebraic equations and some constitutive boundary conditions including those at the end of the liquid film, $z = L_\delta$.

The liquid film inevitably ends with a microfilm (Fig. 2); therefore, its thickness at $z = L_\delta$ is very small so that the disjoining pressure is very important in the microfilm region allowing the local interface temperature, T_δ, to approach T_w, suppressing evaporation. On the contrary, δ_{in} is expected to be thick enough for the disjoining pressure to be zero. Following Holm and Goplen (1979), the disjoining pressure for water can be expressed as

$$p_d = \rho_l R_g T_\delta \ln\left[a\left(\frac{\delta}{3.3}\right)^b\right] \tag{28}$$

where $a = 1.5336$ and $b = 0.0243$. The liquid-vapor interface temperature, T_δ, differs from the saturated bulk vapor temperature because of the interfacial resistance and effects of curvature and disjoining pressure on saturation pressure over evaporating films. The interfacial resistance, is defined as (Faghri, 1995):

$$q_\delta = -\left(\frac{2\alpha}{2-\alpha}\right)\frac{h_{fg}}{\sqrt{2\pi R_g}}\left[\frac{p_v}{\sqrt{T_v}} - \frac{(p_{sat})_\delta}{\sqrt{T_\delta}}\right] \tag{29}$$

where p_v and $(p_{sat})_\delta$ are the saturation pressures corresponding to T_v and at the thin liquid film interface, respectively. The following two algebraic equations should be solved to determine T_δ for every point along the z-direction. The relation between the saturation vapor pressure over the thin evaporating film, $(p_{sat})_\delta$, affected by the disjoining pressure, and the normal saturation pressure corresponding to T_δ, $p_{sat}(T_\delta)$, is given by the extended Kelvin equation (Faghri, 1995):

$$(p_{sat})_\delta = p_{sat}(T_\delta)\exp\left[\frac{(p_{sat})_\delta - p_{sat}(T_\delta) + p_d - \sigma K}{\rho_l R_g T_\delta}\right]. \tag{30}$$

Under steady state conditions, $q_\delta(R-\delta)/R = q_w$, and it follows from Eqs. (3) and (29):

$$T_\delta = T_w + \frac{(R-\delta)}{k_l}\ln\frac{R}{R-\delta}\left(\frac{2\alpha}{2-\alpha}\right) \times \frac{h_{fg}}{\sqrt{2\pi R_g}}\left[\frac{p_v}{\sqrt{T_v}} - \frac{(p_{sat})_\delta}{\sqrt{T_\delta}}\right]. \tag{31}$$

Equations (30) and (31) determine the interfacial temperature, T_δ, and pressure, $(p_{sat})_\delta$, for a given vapor pressure, $p_v = p_{v,sat}(T_v)$, temperature of the solid-liquid interface, T_w, and the liquid film thickness, δ. At the end of the microfilm ($z = L_\delta$) the liquid film is nonevaporating ($T_\delta = T_w$) with thickness of δ_0 (Faghri, 1995).

$$\delta_0 = 3.3\left\{\frac{1}{a}\exp\left[\frac{p_{sat}(T_w) - p_v\sqrt{T_w/T_v} + \sigma K}{\rho_l R_g T_w} + \ln\left(\frac{p_v}{p_{sat}(T_w)}\sqrt{\frac{T_w}{T_v}}\right)\right]\right\}^{1/b} \tag{32}$$

where K in Eqs. (30) and (32) is the local curvature of the liquid-vapor interface defined by the term in outer brackets in Eq. (11), $a = 1.5336$ and $b = 0.0243$.

The parameter $\dot{m}_{l,in}$ should be found using a constitutive boundary condition at the end of the microfilm.

$$\dot{m}_{l,in} = \left.\frac{Q}{h_{fg}}\right|_{z=L_\delta} \tag{33}$$

Equation (33) actually states that the liquid mass flow rate at $z = L_\delta$ is zero and is consistent with Eq. (1).

Following the approach by Khrustalev and Faghri (1995b) for prediction of evaporation from a hemispherical liquid-vapor meniscus with a radius of $(R - \delta_{in})$, the vapor mass flow rate at $z = 0$, $\overline{w}_{v,in}$, can be defined as

$$\overline{w}_{v,in} = \frac{2}{h_{fg}\rho_v(R-\delta_{in})}\int_0^{R-\delta_{in}}\frac{T_w - T_\delta}{\delta/k_l} \times \sin\left[\arccos\frac{s}{R-\delta_{in}}\right]ds \tag{34}$$

where s is the coordinate along the solid-liquid interface, shown in Fig. 2, and the liquid film thickness, δ, for $s \geq 0$ is

$$\delta = \delta_{in} - (R - \delta_{in}) + \sqrt{(R-\delta_{in})^2 + s^2}. \tag{35}$$

$T_{v,in}$ should be chosen so that the temperature of the vapor at $z = L_\delta$ is equal to the given $T_{v,o}$ which is usually known from operational conditions. Finally, the condition determining δ_{in} should be considered. δ_{in} should be chosen so as to satisfy the pressure balance requirement in the system containing the evaporating meniscus. This system can be a heat pipe, for example. As a simple case, consider this system to be a capillary tube of the inner radius R and of the total length L_t with the evaporating meniscus at its end. The pressure in the liquid at the entrance of this capillary tube, p_{ent}, is known and can be maintained at a constant. The total pressure drop between the entrance and the outlet of this tube, $p_{ent} - p_{v,o}$, is due to the viscous pressure drops in liquid for $z < 0$ and vapor for $z > 0$, and also due to the capillary pressure.

$$p_{ent} - p_{v,o} = \frac{8\dot{m}_{l,in}(L_t - L_\delta - R + \delta_{in})\mu_l}{R^4\rho_l} + [2\sigma/(R-\delta_{in}) - (p_{v,in} - p_{v,o})]. \tag{36}$$

The term in square brackets is the available capillary pressure and is further denoted as $\Delta p_{cap,av}$. The available capillary pressure is less than capillary pressure by the pressure drop in vapor exiting a liquid-vapor meniscus in a micropore. It can be shown mathematically that the algebraic equation, Eq. (36), is sufficient to determine δ_{in}, while all other variables are completely defined by the set of differential and algebraic equations with the boundary conditions considered above.

Numerical Procedure

Equations (4), (9), (12), (13), (15), (19), and (20) with the boundary conditions (21)–(27) have been solved using the standard Runge-Kutta procedure and the shooting method on parameter $\dot{m}_{l,in}$ to satisfy Eq. (33). Algebraic equations (30) and (31) with two unknowns, $(p_{sat})_\delta$ and T_δ, have been solved numerically for every point on z using a standard numerical procedure (Wegstein's iteration method). All the unknown variables were found with the accuracy of 0.0005 percent. During the numerical procedure, the interval $0 \leq z \leq L_\delta$ was divided into at least 500 parts, and the thermophysical properties of the saturated vapor and liquid were recalculated for each of the parts at the corresponding vapor temperature $T_v(z)$. L_δ was determined by checking if δ was approaching δ_0 at the end of the solution.

It should be noted that direct numerical solution of this one-dimensional problem simultaneously in the thick film region

and the microfilm is difficult to obtain. The focus of our consideration though, is the thick-film region which can be solved using an approximate solution for the microfilm region, provided that the influence of the microfilm on the thick film is not crucial. This influence is basically restricted to the mass flow rate of the liquid evaporating in the microfilm region which contributes to $\dot{m}_{l,in}$. Therefore, the following simplified technique was utilized to accomplish the numerical procedure in the microfilm region:

1 A value of δ_{in} was chosen providing a small thickness of the liquid film, $\delta_{L_\delta-\epsilon}$ approaching L_δ, where the numerical solution broke up. ϵ denotes here an extremely small distance from L_δ on z. This $\delta_{L_\delta-\epsilon}$ was less than 0.1 μm for the results obtained so that the rest of the liquid film was considered to be a microfilm. It should be noted that the liquid-vapor interface was always very steep at that location.

2 For the microfilm region, for the film thicknesses from $\delta_{L_\delta-\epsilon}$ to δ_0, the curvature of the film was assumed to be constant and equal to that at $z = L_\delta - \epsilon$. Furthermore, the vapor pressure was also assumed to be constant and the problem was solved for the microfilm region yielding the total vapor mass flow rate at $z = L_\delta$, $\dot{m}_{l,in}$. The contribution of the microfilm region to the total vapor mass flow rate was negligibly small and did not exceed three percent for the numerical results obtained. Therefore, the assumption of the constant curvature of the microfilm, which is consistent with the simplified model of the microfilm of Khrustalev and Faghri (1995a) and also with the approach of Xu and Carey (1990), was sufficient for this problem focused on the thick film. Finally, a graphical method can be used to find δ_{in} for given operational conditions, as explained by the example given in the next section.

Results and Discussion

Numerical results were obtained for water evaporating from a cylindrical pore with inner radius of 20 μm. The wall temperature was 388 K and the accommodation coefficient, α, was set equal to unity. Examples of thick liquid film configurations are shown in Fig. 3(a) and are similar to those given in the paper by Belonogov and Kiseev (1995). The liquid film thickness initially increases slowly along the z-coordinate and then decreases rapidly approaching the microfilm region, at the end of the film. The film is concave at $z = 0$, where it is attached to hemispherical meniscus, however, it is convex at most of its length. This is due to pressure gradients in the liquid and vapor along the film shown in Fig. 3(b). In general, the vapor pressure is decreasing and the liquid pressure is increasing along the z-coordinate. The liquid flows in the film mainly due to frictional vapor-liquid interaction at the interface. Figure 4(a) demonstrates that the rate of evaporation decreases towards the thickest part of the liquid film and reaches the maximum in the microfilm region. However, the length of the microfilm region is extremely small compared to the case when a hemispherical meniscus ends directly with a microfilm. Therefore, the microfilm region at the end of thick films does not make any significant contribution to the total mass flow rate at a pore outlet, as can be concluded from Fig. 4(a). This is also due to a sharp increase of the temperature of the liquid-vapor interface, T_δ, at the end of the film under the influence of the disjoining pressure, as shown in Fig. 4(b). Note that T_δ is higher than T_v over all of the liquid film due to the interfacial resistance. Influence of δ_{in} on the characteristics of the thick liquid film is given in Figs. 5 and 6. The outlet vapor temperature, $T_{v,o}$, length of the film, L_δ, and the available capillary pressure increase with δ_{in}. The total mass flow rate (or the rate of evaporation from a micropore) decreases with δ_{in} (Fig. 6(a)) because the film thickness increases with δ_{in}. Note that for $\delta_{in} < 0.6$ μm, the total mass flow rate is very high due to the evaporation from the hemispherical meniscus, while the rate of evaporation from the extended liquid films ($\dot{m}_{l,in}$) plays a less significant role in the total mass flow rate. Consequently, thick-film evaporation from micropores can occur at lower rates compared to the case of a hemispherical meniscus ending with the microfilm.

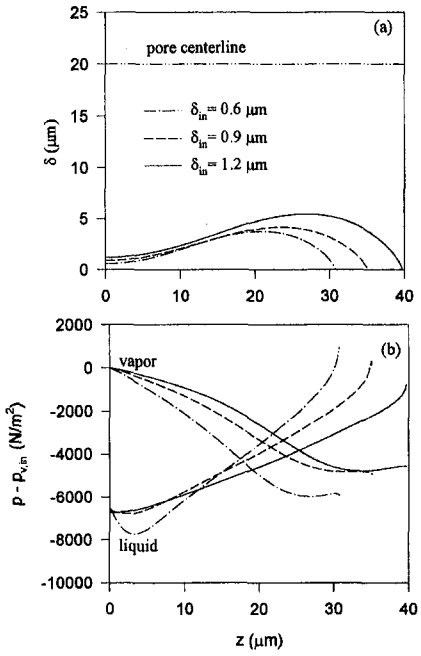

Fig. 3 Variation of characteristics of the liquid-vapor interface along the cylindrical channel (*a*) thickness of the liquid film, and (*b*) pressures in the vapor and liquid phases

The maximum calculated vapor velocities were up to 200 m/s, which resulted in Mach numbers of up to 0.45. Stability of the simulated liquid films was studied. Since no disturbances can arise with a wavelength greater than the length of the liquid-vapor interface, the maximum wavelength of perturbations in the stability analysis was set equal to the film length. The critical vapor velocities causing Kelvin-Helmholtz instability was calculated using expressions available in the literature (for example, Carey, 1992). Maximum vapor velocities that occurred in the calculations never exceeded those critical velocities. Therefore, the simulated liquid films were considered to be stable.

Now consider an example demonstrating that the value of δ_{in} is completely determined by the operational conditions. For a straight capillary tube with the length of L_t = 2.83 mm and inner radius of 20 μm, the vapor outlet saturation temperature is maintained at $T_{v,o}$ = 347.6 K ($p_{v,o}$ = 37933.3 Pa) and the pressure at the entrance is p_{ent} = 44540 Pa. For T_w = 388 K the numerical solution and a graphical analysis of Figs. 5 and 6 give the following parameters of the thick liquid film: $T_{v,in}$ = 350.5 K, L_δ = 36.03 μm, $\dot{m}_{l,in} = 2.3491 \times 10^{-8}$ kg/s, $\dot{m}_{t,in} = 3.2913 \times 10^{-8}$ kg/s, $\Delta p_{cap,av}$ = 1774.1 Pa, and δ_{in} = 0.9 μm. Note that the viscous pressure drop in the liquid is equal to the available capillary pressure in this case. From Figs. 5 and 6, and Eq. (36), it is obvious that this is the only possible value for δ_{in} satisfying all of the equations and boundary conditions written above. If δ_{in} is suddenly increased as a result of disturbances, the rate of evaporation goes down and the length of the liquid films increases. However, the pressure drop in the vapor decreases and the available capillary pressure builds up returning the meniscus to the previous location. The same return mechanism will work if δ_{in} is suddenly decreased.

On the other hand, existence of a hemispherical meniscus ending with the microfilm can also be possible for the situation

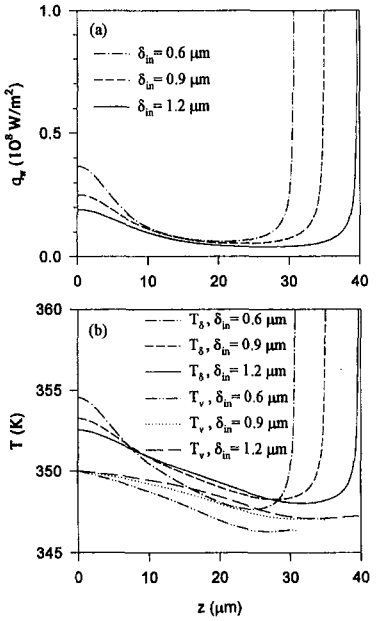

Fig. 4 Variation of characteristics of the liquid-vapor interface along the cylindrical channel (*a*) heat flux at the wall, and (*b*) temperatures of the vapor and liquid-vapor interface

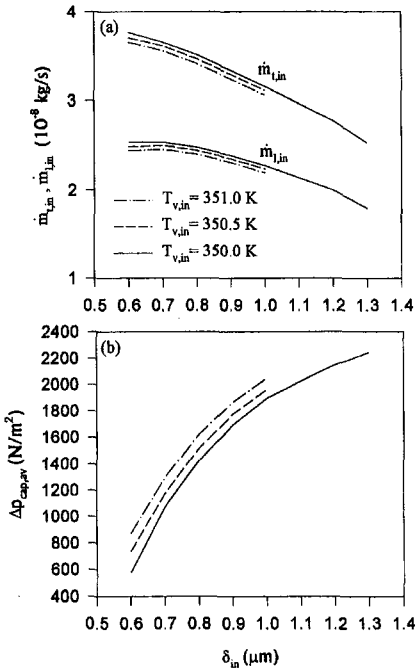

Fig. 6 Influence of the inner meniscus film thickness and vapor temperature on (*a*) total mass flow rate and liquid mass flow rate, and (*b*) available capillary pressure

considered above. This meniscus must be located exactly at the pore outlet (to satisfy the pressure balance requirement), and because of it having a very complicated shape, the apparent contact angle, θ, would have to increase significantly and the microfilm free surface would have a very high curvature. It is possible that the situation with thick liquid films can be more stable compared to the hemispherical meniscus due to the pressure drop in the vapor providing a mechanism for the thick-film meniscus in returning to the stable location on z after occasional disturbances. It should also be noted that the role of thermocapillary phenomena in the thick-film evaporation has been found to be insignificant compared to that of the vapor-liquid frictional interaction. This is quite different from the situation with a hemispherical meniscus ending with the microfilm where thermocapillary shear stresses were found to be the main critical mechanism restricting the meniscus stable existence in the paper by He and Hallinan (1994).

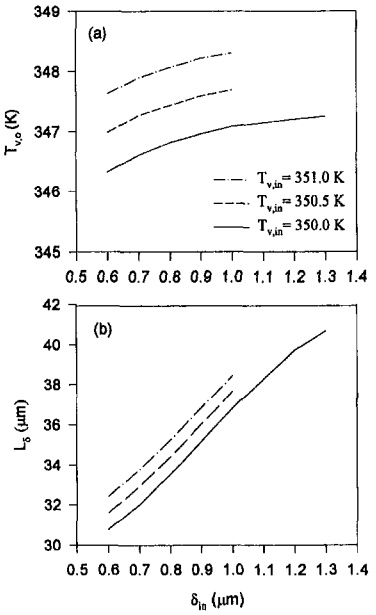

Fig. 5 Influence of the inner meniscus film thickness and vapor temperature on (*a*) vapor temperature at the pore outlet, and (*b*) length of the thick film

The restrictions of the presented mathematical model are recognized and are mainly due to the fact that both the liquid and vapor flows are described using one-dimensional approximation. While this approximation is comparatively easy to solve, it cannot yield valid results for moderate wall-vapor temperature drops but only for high ones. This is related to inaccuracy in calculations of the vapor friction factor, the mass flow rate of the vapor coming from the evaporating meniscus, and other factors. Additionally, the length of the liquid film decreases for smaller temperature drops making the one-dimensional description inaccurate. Therefore, the presented results are for very high wall-vapor temperature drops. The question about the boiling of the liquid in the micropore should be addressed again. There are additional considerations related to this question.

1 The present analysis attempts to answer the question on the existence of the thick liquid films attached to a hemispherical meniscus, in principle. Thick liquid films can exist, for example, for short time periods between the vapor bubbles' blowouts in micropores as described by Gauglitz and Radke (1986).
2 It is anticipated that thick liquid films can exist with the temperature drops significantly smaller than those of the presented results. With smaller temperature drops, the question on boiling would be eliminated. While cases with smaller temperature drops should be considered by a two-dimensional model, the developed model has answered qualitatively some important questions about the thick-film formation in micropores.

Actually, high vapor velocities during evaporation from a micropore do not necessarily have to be related to high wall-vapor temperature drops. Evaporation from the liquid-vapor interface can be induced, for example, by infrared radiation. In the experiment of Belonogov and Kiseev (1995), an axisymmetric electrical heater was positioned off the end of the capillary tube

so that the exit for the vapor coming out of this tube was not blocked. It is possible that infrared radiation could result in direct heating of the liquid-vapor interface in their experiment. In that case, the evaporation rate could be very high with a small wall-vapor temperature difference resulting in thick-film evaporation mode. Therefore, additional experiments on evaporation of ultra pure liquids from restricted capillaries with various heat supplies are needed to further investigate the thick-film phenomenon, which can be important for operation of capillary-driven devices.

Conclusions

The numerical results of the mathematical model, describing the fluid flow and heat transfer in thick liquid films during evaporation of liquid from a micropore, are summarized as follows:

1 High vapor velocities during evaporation of pure liquids in micropores can, in principal, make possible existence of thick liquid films attached to a hemispherical evaporating meniscus.
2 Thick-film evaporation from micropores can occur at lower rates compared to the case of a hemispherical meniscus ending with the microfilm.
3 Available capillary pressure during evaporation from micropores, with high vapor velocities, varies with operational conditions. This can provide a stabilizing mechanism for thick liquid films.

Acknowledgments

Funding for this work was provided by NASA Grant NAG3-1870 and NSF Grant CTS-941458.

References

Bankston, C. A., and Smith, H. J., 1973, "Vapor Flow in Cylindrical Heat Pipes," ASME JOURNAL OF HEAT TRANSFER, Vol. 95, pp. 371–376.

Belonogov, A. G., and Kiseev, V. M., 1995, "Evaporation Problems in Wetting Film Theory," *Proceedings of the 30th National Heat Transfer Conference,* Portland, OR AIChE Symposium Series, Vol. 91, pp. 333–336.

Bowman, W. J., and Hitchcock, J., 1988, "Transient, Compressible Heat-Pipe Vapor Dynamics," *Proceedings of the 25th ASME National Heat Transfer Conference,* Houston, Texas, pp. 329–337.

Carey, V. P., 1992, *Liquid-Vapor Phase-Change Phenomena: An Introduction to the Thermophysics of Vaporization and Condensation Processes in Heat Transfer Equipment,* Hemisphere, New York.

Faghri, A., 1995, *Heat Pipe Science and Technology,* Taylor & Francis, Washington, DC.

Gauglitz, P. A., and Radke, C. J., 1986, "The Role of Wettability in the Breakup of Liquid Films Inside Constricted Capillaries," *Thin Liquid Film Phenomena, AIChE Symposium Series,* Vol. 82, No. 252, pp. 50–63.

He, Q., and Hallinan, K. P., 1994, "Thermocapillary Effects on the Evaporating Extended Meniscus," *Proc. of the 1994 Int. Mechanical Engineering Congress and Exposition,* Chicago, HTD-Vol. 290, pp. 71–82.

Holm, F. W., and Goplen, S. P., 1979, "Heat Transfer in the Meniscus Thin-Film Transition Region," ASME JOURNAL OF HEAT TRANSFER, Vol. 101, No. 3, pp. 543–547.

Jang, J. H., and Faghri, A., 1991, "Analysis of the One-Dimensional Transient Compressible Vapor Flow in Heat Pipes," *Int. J. Heat and Mass Transfer,* Vol. 34, pp. 2029–2037.

Khrustalev, D., and Faghri, A., 1995a, "Heat Transfer During Evaporation on Capillary-Grooved Structures of Heat Pipes," ASME JOURNAL OF HEAT TRANSFER, Vol. 117, No. 3, pp. 740–747.

Khrustalev, D., and Faghri, A., 1995b, "Heat Transfer in the Inverted Meniscus Type Evaporator at High Heat Fluxes," *International Journal of Heat and Mass Transfer,* Vol. 38, No. 16, pp. 3091–3101.

Khrustalev, D., and Faghri, A., 1996, "Fluid Flow Effects in Evaporation from Liquid/Vapor Meniscus," ASME JOURNAL OF HEAT TRANSFER, Vol. 118, pp. 725–730.

Potash, Jr., M., and Wayner, Jr., P. C., 1972, "Evaporation from a Two-Dimensional Extended Meniscus," *Int. J. Heat Mass Transfer,* Vol. 15, pp. 1851–1863.

Solov'ev, S. L., and Kovalev, S. A., 1984, "Mechanism of Evaporation of a Liquid from a Porous Surface," *Proc. 5th Int. Heat Pipe Conf.,* Tsukuba, Japan, Preprints Vol. II, pp. 77–82.

Stephan, P. C., and Busse, C. A., 1992, "Analysis of the Heat Transfer Coefficient of Grooved Heat Pipe Evaporator Walls," *Int. J. Heat Mass Transfer,* Vol. 35, No. 2, pp. 383–391.

Swanson, L. W., and Herdt, G. C., 1992, "Model of the Evaporating Meniscus in a Capillary Tube," ASME JOURNAL OF HEAT TRANSFER, Vol. 114, May, pp. 434–441.

Volintine, B. G., and Wayner, Jr., P. C., 1986, "Fluid Flow and Evaporation in an Ultra-Thin Film of a Binary Mixture," *Thin Liquid Film Phenomena, AIChE Symposium Series,* Vol. 82, No. 252, pp. 157–166.

Wayner, Jr., P. C., Tung, C. Y., Tirumala, M., and Yang, J. H., 1985, "Experimental Study of Evaporation in the Contact Line Region of a Thin Film of Hexane," ASME JOURNAL OF HEAT TRANSFER, Vol. 107, pp. 182–189.

Xu, X., and Carey, V. P., 1990, "Film Evaporation from a Micro-Grooved Surface—An Approximate Heat Transfer Model and Its Comparison with Experimental Data," *J. Thermophysics and Heat Transfer,* Vol. 4, No. 4, pp. 512–520.

Study of Droplet Sprays Prior to Impact on a Heated Horizontal Surface

J. E. González
ASME Assoc. Mem.
Assistant Professor
jo_gonzalez@rumac.upr.clu.edu
Department of Mechanical Engineering,
University of Puerto Rico-Mayagüez,
Mayagüez, Puerto Rico 00680

W. Z. Black
Regents Professor
ASME Fellow
George W. Woodruff School
of Mechanical Engineering,
Georgia Institute of Technology,
Atlanta, GA 30332

This paper concerns a quantitative assessment of the heat and mass transfer behavior of spray droplets, downward oriented prior to their impact on a heated horizontal surface. An experimental and theoretical investigation of the coupling effects between a downward oriented spray and a rising saturated buoyant jet that results from evaporation of the spray on a heated surface has been successfully completed. A model describing the coupled thermal and hydrodynamic behavior of both the spray and the saturated buoyant jet has been developed. An experimental set-up involving a high speed photographic apparatus has been used to observe in-flight monodispersed sprays and to measure the diameter and the velocity of droplets as they approach the heated surface. The theoretical and experimental results indicate that the temperature of the saturated buoyant jet is highly affected by the presence of a subcooled spray and small droplet sprays, vertically projected, experience high condensation rates as they pass through the saturated buoyant jet, reaching the saturation temperature before impacting on the heated surface, as well as experience acceleration as a consequence of an increase in mass due to the condensation.

Introduction

During recent years there has been an increased demand for new techniques capable of removing high heat fluxes and it is expected that this demand will continue to increase in the future. The most commonly used cooling technologies utilize natural and forced single-phase convection mechanisms, while natural and forced two-phase convection and microchannel cooling appear to be the types of techniques used to cool devices which generate high heat fluxes such as in microelectronics and fusion components.

Pool boiling can be achieved by submerging a hot surface in a stagnant liquid column or by injecting the working fluid directly on the surface. For situations which involve a surface temperature close to the saturation temperature of the liquid, the second method is more desirable because of the reduction of the excess liquid. The injection of the liquid can be achieved by using a continuous, single phase jet or by using a mixture of a discrete and a continuous phase. The first case is known as jet impingement cooling and the second one as spray cooling. Researchers (Bonacina et al., 1979; Choi and Yao, 1987; Ghodbane and Hollman, 1991; Pedersen, 1970; Toda, 1974) have shown that heat fluxes in excess of 100 W/cm^2 can be obtained with either technique. Gu et al. (1993) reported spray cooling heat fluxes 50 percent higher than single-phase impingement jet. This increase in heat flux is attributed to the control of uniform thin liquid films that can be obtained with spray cooling.

Because of its potential to remove high heat fluxes, spray cooling has found applications in a wide range of industrial processes including (1) the nuclear industry, to cool the fusion components (Watson, 1990); (2) the medical industry, to cool ion beam targets (Bacon et al., 1984); (3) the metallurgical industry, to achieve fast and control cooling (Hall and Mudawar, 1995); and (4) the ceramic industry, for thermal tempering (Ohkubo and Nishio, 1987).

Contributed by the Heat Transfer Division for publication in the JOURNAL OF HEAT TRANSFER. Manuscript received by the Heat Transfer Division February 6, 1996; revision received November 14, 1996; Keywords: Boiling, Modelling & Scaling, Sprays/Droplets. Associate Technical Editor: B. Webb.

The general study of a liquid spray propelled toward a heated surface can be divided into two subprocesses: the behavior of the droplets prior to impacting on the heated surface, and the dynamics of the drops after they hit the surface. The post-impact process is characterized by the spreading and evaporation of the liquid droplets. On the other hand the pre-impact process is characterized by the bulk convective heat and mass transfer that occur between the spray and surroundings before the drops impact the surface. The majority of the experimental and theoretical works have concentrated on the post-impact spray phenomenon and little effort has gone to studying the pre-impact problem even though the pre-impact behavior will have significance in the overall heat transfer process. The importance of pre-impact effects was first reported by Choi and Yao (1987) and Deb and Yao (1989) in film boiling experiments.

This research investigates the thermal behavior of vertical downward-directed small droplet sprays before they impact on a hot horizontal surface under nucleate boiling condition, and it attempts to fill a void in the full understanding of the spray cooling phenomena. The pre-impact spray cooling problem involves the solution of two coupled sub-problems, namely: (1) evaluation of the thermal behavior of a spray as it approaches the surface after having traveled through a medium with variable thermal and transport properties, and (2) evaluation of the thermodynamic and hydrodynamic states of a mixture of water vapor and air surrounding the surface. The latter includes evaporation from the surface as well as the possibility of both evaporation and condensation in the spray.

The general problem of heat and mass transfer between a gas phase and a discrete liquid phase has been addressed in the combustion gases literature (see for example Zhou, 1993; Liu and Reitz, 1995). However, in spray cooling applications, a mixed convective nonreacting binary gas may result from liquid evaporation at the heated surface that will dynamically and thermally interact with a downward projected spray, making this the problem unique. The primary focus of this paper is to look into the details of this particular coupled problem.

To insure validity of the analysis, the results were compared with measurements made in experiments designed to simulate the behavior of small-droplet sprays projected toward a heated surface. The variables observed in the experiments are the drop-

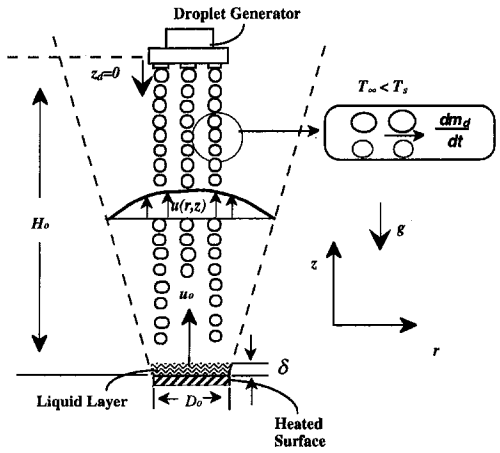

Fig. 1 Schematic of the general problem

let diameters and velocities, as a function of the vertical position. The range of spray properties was limited to nucleate boiling conditions. A monodispersed spray of liquid water at one atmosphere pressure was chosen as the working fluid for these experiments.

Mathematical Formulation

Figure 1 shows a spray of liquid droplets approaching a heated surface. The temperature of the heated plate is high enough to cause evaporation of a liquid film on the surface. The vapor coming from the liquid film will rise and diffuse into the surroundings due to a combination of inertia and buoyancy effects. The thermodynamic state of the resulting buoyant jet will have a strong influence on the temperature and velocity of the droplets as they pass through the gas.

Furthermore, the thermodynamics and physical state of the drops depend upon whether they experience evaporation or condensation with the ambient vapor. Evaporation from the droplets will also have an effect on the buoyant jet due to the heat transfer and mass addition that results from the droplets. Condensation of the vapor may occur on the liquid drops if the partial pressure of the vapor in the buoyant jet is higher than the saturation pressure evaluated at the liquid drop temperature. If the initial temperature of the droplets is lower than the local saturation temperature of the binary gas, the droplets will also experience a sensible heating from the warm jet. Condensation of the vapor in small aerosols, normally present in the ambient, may also occur. The thermal models of the drops and the plume must consider all these factors.

Single Drop Thermal Model. The analysis considers a single drop and utilizes a Lagrangian viewpoint following a single droplet from its injection into the ambient vapor until it approaches the heated surface. Droplets are assumed to be small enough so as to remain spherical with uniform thermal properties. Other assumptions are as follows:

- vapor flow around a drop surface is assumed to be quasi-steady
- vapor and liquid phases are in thermodynamic equilibrium
- the drops do not collide
- radiation heat transfer from the drops is negligible
- buoyancy effects are negligible
- potential and kinetic energy changes of a droplet are small
- the drop moves in a two-dimensional Cartesian space

With these assumptions in mind, the equations for conservation of energy, momentum, and mass of a single droplet are written as a function of time. This is achieved by considering that the thermal state of the droplet is a function of the z and r directions by considering drag, gravity, and Saffman forces and by using a Lagrangian viewpoint so that the control volume always surrounds the moving droplet. The conservation equations then become:

Nomenclature

C_d = drag coefficient
c_p = specific heat
D = diameter of a droplet
D_{ab} = diffusivity of water vapor in air
D_o = heater plate diameter
f = frequency
G = mass flow rate
Gr = Grashoff number = $g(T_o - T_\infty)H_o^3/(\bar{T}\nu^2)$
g = acceleration of gravity
H_o = height between drop generator and heated plate
h = heat transfer coefficient for liquid droplets
h_{fg} = latent heat of vaporization of water
h_m = mass transfer coefficient for liquid droplets
k = thermal conductivity, condensation/evaporation rate
L = spacing between droplets
M = molecular weight
m = mass of single droplet or condensing particle
N_o = density number
p = total pressure
p_a = mean local gas partial pressure between the droplet surface and the buoyant jet
q'' = heat flux
Re = Reynolds number of the droplet = Du_d/ν
Re_H = Reynolds number of the buoyant jet = $H_o u_o/\nu$
r = radial direction
r_c = local radius of the condensation particles
Sc = Schmidt number = ν/D_{ab}
T = temperature
t = time
u = velocity component in the axial direction
v = velocity component in the radial direction
X_A = mass fraction of water vapor = ρ_A/ρ
Z = nondimensional axial coordinate = z/H_o
z = axial direction

Greek Symbols

α = thermal diffusivity = $k/(\rho c_p)$
Δp = water vapor pressure difference at the drop surface = $p_{sd} - p_a$
ν = kinematic viscosity
μ = dynamic viscosity
ρ = total density = $\rho_A + \rho_B$
σ = surface tension
θ = $(T - T_\infty)/(T_o - T_\infty)$

Subscripts

A = water vapor
B = dry air
c = aerosol particles value
cl = value evaluated along the jet centerline
D = drag, diameter
d = droplet value
i = initial value
j = liquid jet out of the droplet generator
m = value of the mixture in the buoyant jet
l = liquid water
o = initial jet value
r = reference value for the drag coefficient
s = surface of the droplet, saturation value
sat = saturated value
v = water vapor
∞ = surroundings

Conservation of Momentum in the Axial Direction.

$$\frac{d(D^3u_d)}{dt} = (D^3g) - \left(\frac{3}{4}\right)\left(\frac{\rho_m}{\rho_l}\right)D^2C_{dz}(u_d - u)|u_d - u| \quad (1)$$

Conservation of Momentum in the Radial Direction.

$$\frac{d(D^3v_d)}{dt} = -\frac{6.46\mu(v_d - v)D^2}{4(\nu)^{1/2}\rho_l}\left(\frac{\partial u}{\partial r}\right)^{1/2} - \left(\frac{3}{4}\right)\left(\frac{\rho_m}{\rho_l}\right)D^2C_{dr}(v_d - v)|v_d - v| \quad (2)$$

Conservation of Energy.

$$\frac{dT_d}{dt} = \frac{3h_{fg}}{c_{pl}}\frac{dln(D)}{dt} - \frac{6h}{D\rho_l c_{pl}}(T_d - T(r, z)) \quad (3)$$

Conservation of Mass.

$$\frac{dD}{dt} = -2\left(\frac{M_v}{M_m}\right)\left(\frac{\rho_m}{\rho_l}\right)\left(\frac{\Delta p}{p_b}\right)\left(\frac{D_{ab}}{D}\right) \times (2.0 + 0.6\,\mathrm{Sc}^{1/3}\,\mathrm{Re}^{1/2}) \quad (4)$$

Initial Conditions.

$$u_d(0) = -u_{di}, \quad v_d(0) = 0; \quad T_d(0) = T_{di}, \quad D(0) = D_i$$

The first term in the right side of Eq. (2) refers to the Saffman force. While this force is usually small, it can be significant in viscous fluids with high velocity gradients, thus creating a force perpendicular to the velocity of the main flow (Saffman, 1965; Saffman, 1968).

Drag Coefficient of Droplets. The drag coefficient for a single evaporating or condensing sphere is obtained from Yuen and Chen (1976) as

$$C_D = C_{Do}\frac{\mu_{m\infty}}{\mu_{mr}} \quad (5)$$

where C_{do} is the drag coefficient of a solid sphere, and μ_{mr} is the viscosity of the water vapor and air mixture. The viscosity μ_m depends on the reference temperature and the reference water vapor concentration, defined by Yuen and Chen (1976) as

$$T_r = T_d + 1/3(T + T_d) \quad X_{Ar} = X_{Ad} + 1/3(X_A + X_{Ad}). \quad (6)$$

The drag coefficient of a solid sphere, C_{do}, corresponds to that of an accelerated particle which can be obtained from Fuchs (1964):

$$C_{Do} = \frac{27}{\mathrm{Re}^{0.84}}. \quad (7)$$

The droplets in this problem may travel at close spacings to each other and their drag coefficient may be affected by the wake formed by the upstream drops. Experimental evidence shows that droplets traveling at close distances from each other may have a drag coefficient that is less than the drag coefficients calculated for an isolated sphere by a factor of four and five (Mullholland, 1988; Poo and Ashgriz, 1991). Mullholland (1988) suggested a drag coefficient model which accounts for the effects of droplet interaction based on the superposition of the drag coefficient of an isolated droplet and that of a long rod:

$$C_D(\mathrm{Re}, L/D)^{-n} = [C_D^{\infty}(\mathrm{Re})]^{-n} + [C_D^0(\mathrm{Re}, L/D)]^{-n}. \quad (8)$$

In Eq. (8), $C_D^{\infty}(\mathrm{Re})$ is the drag coefficient of an evaporating droplet which is given by Eq. (5), a and n are experimental constants and

$$C_D^0(\mathrm{Re}, L/D) = C_{D\text{-rod}}(\mathrm{Re}) + \frac{a}{\mathrm{Re}}(L/D - 1). \quad (9)$$

Here $C_{D\text{-rod}}(\mathrm{Re})$ is the drag coefficient for a cylinder of diameter D. The constants a and n were experimentally determined by Mullholland (1988) to be 0.678 ± 0.07 and 43.0 ± 15.4, respectively, for a range of Reynolds numbers between 1 and 250, and a range of droplet spacing to diameter ratios, L/D, between 10 and 50. The critical value for L/D is defined as the nondimensional droplet spacing for which the droplet drag coefficient starts to be affected by the presence of adjacent droplets.

Solution to Eqs. (1) through (4) for each droplet results in local values for T_d, u_d, v_d, and D as a function of time. The solution to these equations requires a knowledge of the velocity, temperature and density profiles of the surrounding medium. The properties of the surrounding medium are obtained from the thermal model presented in the next subsection.

Thermal Model for the Surroundings. The second part of the thermal model involves solution of the equations representing the thermal behavior of humid air in a buoyant jet rising above a heated, horizontal disk. The liquid film present on the disk is assumed to evaporate at a constant rate, and the analysis also includes the heat and mass transfer effects that result from either the evaporation from, or condensation on, the water droplets. The possibility of condensation of the warm jet due to the presence of aerosols that are commonly present in the ambient is also considered. The spray considered here is a monodispersed one, and it is assumed to be uniformly distributed throughout the gas phase. For dispersed sprays, the hydrodynamic effects that the spray may have on the gas flow can be neglected. In combustion problems, this phenomena is usually referred to as a one-way coupling problem (Zhou and Yao, 1992). In a similar fashion, a one-way momentum coupling is also used for the condensing aerosol particles due to their extremely low inertia. Other assumptions considered in the gas phase formulation are as follows:

- steady state conditions
- the evaporation rate at the surface of the heater is nearly constant
- the air and water vapor are in thermal equilibrium
- the presence of the droplet generator does not affect the properties of the continuous flow
- viscous dissipation, pressure, and Soret effects are negligible as energy terms
- the Dufour effect is negligible
- the gas flow is laminar, two-dimensional, and axisymmetric

The validity of some of these assumptions is expected to diminish in the vicinity of the heater due to the unpredictable bursting of bubbles arising from the liquid film. Furthermore, a typical heat flux value for spray cooling of the order of 100 W/cm^2 was used to characterize the flow. For this case, the ratio of Gr/Re_H^2 is of order one, which implies that the flow is a buoyant jet and gravity effects should be considered in the analysis throughout the entire domain.

By considering an Eulerian point of view and applying the assumptions, the conservation equations for heat, mass, and momentum transfer of a buoyant jet coupled with a droplet spray and condensing particles are written as follows:

Conservation of Mass.

$$\frac{1}{r}\frac{\partial}{\partial r}(rv) + \frac{\partial}{\partial z}(u) = -\frac{N_{oc}}{\rho}\frac{dm_c}{dt} \tag{10}$$

Conservation of Mass for Water Vapor.

$$\frac{1}{r}\frac{\partial}{\partial r}(rX_A v) + \frac{\partial}{\partial z}(X_A u) = \frac{D_{ab}}{r}\frac{\partial}{\partial r}\left(r\frac{\partial X_A}{\partial r}\right) - \frac{N_{oc}}{\rho}\frac{dm_c}{dt} \tag{11}$$

Conservation of Energy.

$$\frac{1}{r}\frac{\partial}{\partial r}(rvT) + \frac{\partial}{\partial z}(uT) = \frac{\alpha}{r}\frac{\partial}{\partial r}\left(r\frac{\partial T}{\partial r}\right) + \frac{N_{od}}{\rho c_{pm}}(hA_s)_d(T_d - T) - \frac{N_{oc}}{\rho c_{pm}}\left(\frac{dm_c}{dt}h_{fg} - (hA_s)_c(T_c - T)\right) \tag{12}$$

Conservation of Momentum.

$$\frac{1}{r}\frac{\partial}{\partial r}(ruv) + \frac{\partial}{\partial z}(u^2) = \frac{\nu}{r}\frac{\partial}{\partial r}\left(r\frac{\partial u}{\partial r}\right) + gf(X_A, T) \tag{13}$$

Equations (10)–(13) satisfy the conditions at the heated surface and outside of the boundary layer. They must also satisfy symmetry at the center of the jet. Thus, the boundary conditions become

$$u\,(z=0) = u_o, \quad X_A\,(z=0) = 1, \quad T\,(z=0) = T_{\text{sat}},$$

$$v = \frac{\partial u}{\partial r} = \frac{\partial T}{\partial r} = \frac{\partial X_A}{\partial r} = 0 \quad (r=0),$$

$$u\,(r\to\infty) = 0, \quad T\,(r\to\infty) = T_\infty, \quad X_A\,(r\to\infty) = X_{A,\infty}. \tag{14}$$

High condensation rates on the nucleation particles and high density numbers are expected to maintain the buoyant jet at saturated conditions. A diffusive mass transfer model has been assumed for the condensation that occurs on the nucleation particles. The sensible heat contribution to both the spray and the condensing particles is retained, and the temperature of the condensing particles is assumed to be equal to the local wet bulb temperature.

The function $f(X_A, T)$ in the momentum equation represents both the concentration and the temperature contribution to the buoyancy force. Assuming ideal gas behavior, this function can be expressed for both water vapor and air as (Gebhart et al., 1988)

$$f(X_A, T) = \left[\frac{1 + X_A(M_B/M_A - 1)}{T_\infty/T} - 1\right]. \tag{15}$$

Numerical Solution

The strategy used to solve the set of equations for the droplet spray and the buoyant jet is now discussed. Initially, the presence of the droplets in the buoyant jet are neglected so that two independent solutions can be determined for the conservation equations applied to the buoyant jet and the droplet spray. Once the first solution for the buoyant jet is known, it is used to solve the equations for each droplet, which are given by Eqs. (1) through (4). The energy and mass contribution of the spray into the buoyant jet can be estimated after the first solution for the velocity and temperature distribution of the buoyant jet. This procedure continues until convergence is reached.

The set of nonlinear, ordinary differential equations describing the behavior of a single droplet, given by Eqs. (1) through (4), is solved by using an initial value Runge-Kutta scheme. The second set of nonlinear partial differential equations which describe the conditions in the buoyant jet, Eqs. (10) through (15), is solved by using a finite difference marching scheme in the axial direction. An implicit approach in the radial direction is used to solve the buoyant jet equations. The resulting set of nonlinear buoyant jet equations is solved using Newton-Raphson method for systems of equations in an unique form. Both sets of equations are eventually combined.

Both the single droplet model and the buoyant jet model were independently compared with previously reported analytical solutions and a limited amount of experimental data. The single droplet model predicts temperatures that are within one percent of temperatures obtained from experimental data for a 2.0 mm condensing droplet falling at a constant velocity in a standard ambient, as reported by Kincaid and Longley (1989). The droplet model also predicted the velocity decrease with an error of less than one percent when compared with the analytical solution obtained for a falling solid sphere with a Reynolds number within the Stoke's flow regime. The buoyant jet model was compared with previous solutions for forced laminar jet (Schlichting, 1979), laminar plumes with linear combination of heat and mass transfer effects (Mollendorf and Gebhart, 1974), and laminar free jets with linear buoyancy terms (Himashekar and Jaluria, 1982). In all cases, the thermal model predicted concentrations, temperatures, and velocities that were within two percent of the established limiting solutions, and the solutions were shown to be independent of the grid size for all cases (for details see González et al., 1995).

Numerical Results

Four independent variables were used to characterize the conditions in the jet and the droplets: initial velocity of the vapor, initial droplet diameter, initial droplet velocity, and droplet density numbers. Table 1 shows values for these four variables for the seven cases considered in this paper. Droplet diameters of 75 and 150 μm were considered because they are typical sizes used in spray cooling applications. The model assumes that the droplets are uniformly generated by a variable frequency monodispersed droplet generator based on the Rayleigh break up phenomenon. Droplet frequencies of 0.5 and 1.0 kHz were selected because they correspond to typical generation rates used during the experiments. The selected values of the droplet frequency determine the number of droplets per unit volume, N_{od}, that were generated. The heat flux and the velocity of the water vapor near the heated surface, u_o, are related to each other by assuming that the heat flux at the surface, q''_o, is used to vaporize the liquid, thus

$$u_o = \frac{q''_o}{h_{fg}\rho_v}. \tag{16}$$

This value of u_o was assumed to remain constant. This assumption is valid under nonfluctuating evaporative conditions at the surface. Although steady-state conditions are assumed in this problem, minor fluctuations in the value of q''_o are expected to occur near the heated surface, due to bursting of bubbles in the thin liquid layer of the heater.

Values of 0.75 and 2.5 m/s for u_o, shown in Table 1, correspond to Jet Reynolds numbers of 300 and 900, and heat fluxes of 100 and 300 W/cm^2, respectively. The numerical results are based on a distance between the droplet generator and the heated surface H_o of 100.0 mm and a diameter of the heated surface D_o of 8.0 mm.

Numerical Results For The Saturated Buoyant Jet. Figure 2 shows the nondimensional buoyant jet centerline temperature for Cases 1 through 3 of Table 1. A significant temperature decrease is observed for Case 1 where large diameter and low velocity water droplets were used. Since the spray is introduced

Table 1 Numerical cases considered

Case	u_o (m/s)	u_{di} (m/s)	D_i (μm)	f (kHz)	T_{di} (°C)	T_o (°C)
1	0.75	5	150	1.0	20	100
2	0.75	15	75	1.0	20	100
3	0.75	15	75	0.5	20	100
4	0.75	10	150	1.0	20	100
5	2.50	5	150	1.0	20	100
6	2.50	5	150	1.0	20	100
7	2.50	18	75	1.0	20	100

into the jet at $Z = 1$ where the temperature is lower than the local jet temperature, the jet experiences a significant cooling for the case of large droplets. For droplets with low velocities, the cooling effect on the jet will be larger due to longer droplet residence times.

Comparison of Cases 2 and 3 shows the effect of the droplet number density, given by the droplet frequency generation rate, on the temperature of a saturated jet. The temperature decrease is larger for large droplet densities (Case 2) than for small droplet densities (Case 3). At intermediate Z values, the jet temperature is higher for cases where the spray is present, due to the fact that at these locations the droplets have reached thermal equilibrium such that their temperature is equal to the local wet bulb temperature of the jet. The wet bulb temperature will be higher than the actual local jet temperature when supersaturation values are present, giving rise to regions where the presence of the drops will actually heat the jet. The jet temperature shows significant changes for all three spray cases considered (Case 1, 2, and 3) when compared with the non-spray solution. Trends in the numerical results for the dimensionless buoyant jet centerline concentration and dimensionless velocity are similar to those obtained for the dimensionless temperature.

Numerical Results For The Spray. Results for the droplet axial velocity, diameter, and temperature for 150 μm droplets that are injected along the jet centerline are shown in Figs. 3 through 5. Droplet initial velocities of 5 and 10 m/s, and jet velocities of 0.75 and 2.5 m/s were considered (see Table 1). From Fig. 3, it can be seen that at small values of Z_d (for the droplet, $Z_d = 0$ is the location of the droplet generator, and $Z_d = 1$ is the location of the heated surface) the droplets experience acceleration. The acceleration is a result of an increase in the droplet mass as condensation occurs on the drop when it is first introduced into the moist jet. The droplet diameter plotted in Fig. 5 shows the increase in droplet size that occurs as long as the droplet has a temperature lower than the local wet bulb temperature of the jet. Once the droplet has reached a maximum diameter, it starts to decelerate. Figure 3 also shows that the velocity decrease is highly affected by the jet velocity, as indicated by the slope of the droplet velocity curves. For higher jet velocities, the droplet experiences larger drag forces resulting in a significant reduction in velocity.

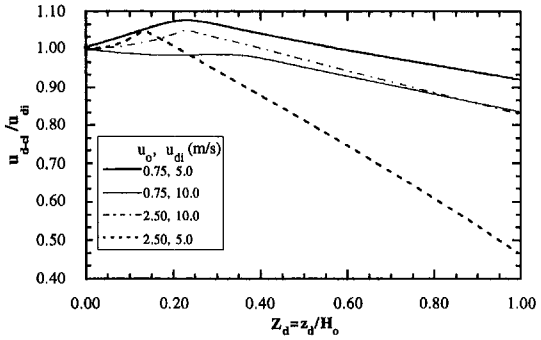

Fig. 3 150 μm droplet velocity at $R = 0$ (centerline)

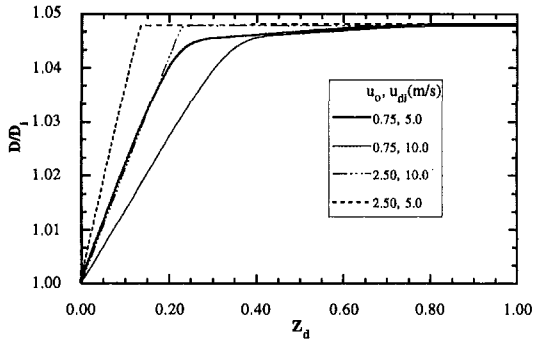

Fig. 4 150 μm droplet diameter at $R = 0$ (centerline)

Condensation stops once the droplet temperature reaches the local wet-bulb temperature in the jet, as seen in Fig. 5. This figure shows that droplets with higher initial velocities reach the wet bulb temperature later than those with lower initial velocities. This figure also shows that the droplets do not experience further heat transfer after they have reached saturation conditions. Figure 5 indicates that the diameter of a rapidly moving droplet in a jet with low velocity increases slower than the diameter of a slowly moving droplet in a high velocity jet.

The radial velocity variation along the axial direction for the case of a 150 μm droplet was also investigated. Results showed that the influence of entrainment and initial droplet momentum dominate the radial momentum balance and that Saffman forces play a small role and do not affect the radial velocity. It was also shown that the maximum radial velocity of the droplets were less than one percent of the minimum axial velocity. This result suggests that for the cases considered here, the droplets do not deviate significantly from their initial, vertical projected path and once they are injected vertically into the jet, they will reach the heated surface.

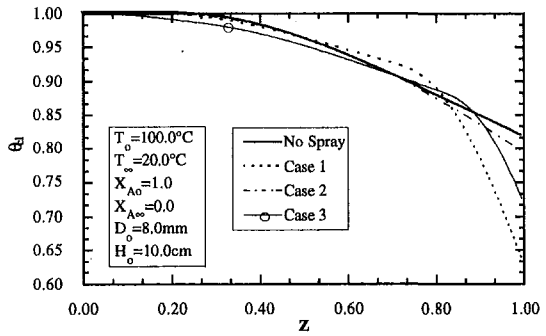

Fig. 2 Saturated jet centerline temperature

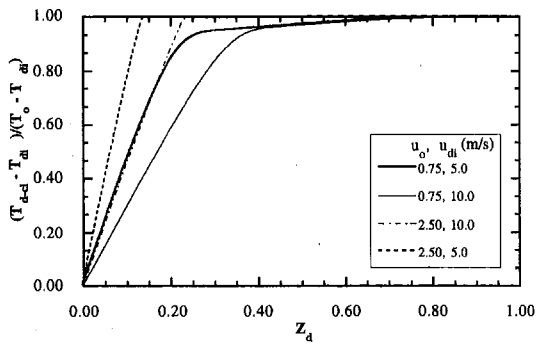

Fig. 5 150 μm droplet temperature at $R = 0$ (centerline)

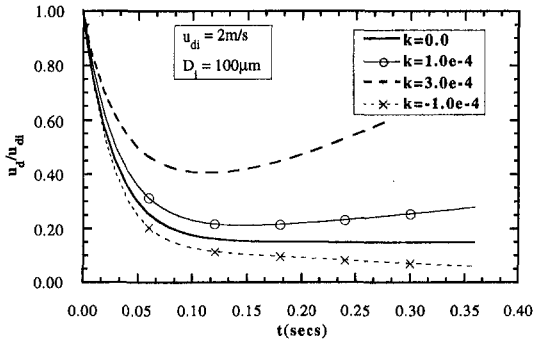

Fig. 6 Condensation/evaporation effects on droplet velocities

Discussion Of Numerical Results. Droplet diameters of 75 and 150 μm at different initial velocities along with jet velocities of 0.75 and 2.5 m/s were considered. These droplet diameters and jet velocities represent typical spray and surface heat fluxes that are encountered in spray cooling applications. A strong dependence between the jet and the spray conditions was shown to exist; that is, the thermal behavior of the jet is highly affected by the spray conditions, while the spray properties are strongly influenced by the initial conditions of the jet.

In most of the cases presented, condensation occurred on the droplets as they approach the heated surface, resulting in initial acceleration until they reach their maximum diameter. The effects of condensation on the velocity of the droplet can be shown by expanding Eq. (1) for a single droplet with constant temperature falling in a quiescent ambient and considering the vapor in the jet moving in the direction opposite to that of the droplet. For this case, Eq. (1) becomes

$$\frac{du_d}{dt} = g + \frac{3u_d}{D}\left[\frac{dD}{dt} - \left(\frac{3}{4}\right)\left(\frac{\rho_m}{\rho_l}\right)C_d u_d\right]. \qquad (17)$$

Equation (17) indicates that acceleration of the drops occurs when the increase in the weight caused by condensation is larger than the opposing drag force. Also note that for evaporating droplets, deceleration will always occur. Equation (17) was solved for the simple linear case in which the evaporation/condensation rate is equal to a constant, or $D = D_i + kt$ (k in m/s), and for low initial droplet velocity so that the Reynolds number was within the Stoke's flow regime. Results of this solution are shown in Fig. 6. The figure shows that an evaporating, or a solid droplet, experience deceleration, i.e., k values less or equal to zero, while a condensing one (positive k values) experience acceleration.

Numerical results show that the thermal behavior of the droplets close to the external region of the boundary layer are less affected than those close to the jet centerline. However, those droplets at the edge of the jet experience jet entrainment effects that tend to drag the droplets toward the centerline. Even though low droplet velocities were considered, in all cases the droplets reached the heated surface for the 100 mm travel distance that was considered in this study. For the case of either larger travel distances or smaller droplets, this might not be the case because these conditions will encourage the migration of the droplets away from the heated surface.

Finally, the numerical results presented in this section show that the droplets reach the plate at fully saturated conditions. The low thermal mass of the droplets considered causes the droplets' temperature to rapidly reach the wet bulb temperature of the saturated jet. Therefore, saturation conditions should be expected for small droplet sprays prior to impact on the heated surface. This interesting result might be an explanation for previous reports by Bonacina et al. (1979) and Toda (1974) where negligible subcooling effects in spray cooling applications were experienced when using small droplet sprays.

Experimental Set-Up

The objective of the experiment was to validate the mathematical formulation for the thermal and hydrodynamic behavior of droplets falling in both a constant and variable-property ambient. The apparatus used during the experiments consisted of a droplet generator, photographic equipment, and a heated surface. A schematic of the experimental set-up is shown in Fig. 7. Water droplets were generated by using the theory of instability of capillary jets first reported by Rayleigh (1878). This theory suggests that a continuous jet of diameter d_j and velocity u_j can be broken into uniform droplets if the jet is disturbed by an optimum frequency f. The liquid must exceed a minimum velocity to form a liquid jet.

A modified ink-jet printer head was used as a droplet generator during the experiments. The printer head had a rectangular plate with 32 orifices and each orifice had a diameter of 50 μm. All orifices were separated by a distance of 1.5 mm. Behind each orifice was a piezoelectric crystal which was driven by a frequency generator as shown in Fig. 7. Frequencies between 100 Hz and 15 kHz were used.

Droplets were generated by activating the piezoelectric crystals at several frequencies causing a disturbance in the continuous jet. The initial diameter of the liquid droplets was calculated from the knowledge of the jet velocity and the optimum disturbance frequency by applying the conservation of mass between the fluid leaving the orifice and an adjacent position after the droplets had been formed. This process yields an expression for the droplet diameter of

$$D = \left(\frac{3}{2} d_j^2 \frac{u_j}{f}\right)^{1/3}. \qquad (18)$$

Several droplet diameters between 125 and 200 μm were generated by varying the liquid pressure and the frequency of the piezoelectric crystals.

The photographic equipment used during the experiments consisted of a microscope with variable magnification and a variable frequency stroboscopic light. The combination of the microscope with the stroboscopic light allowed observation of the magnified stationary droplets. The microscope was attached to a video camera and images of the droplets were stored on a video cassette. The images of the droplets could also be simultaneously observed on a video monitor. The magnification of the photographic system was determined by taking a photograph of a reference scale before and after each test. The uncertainty in the measurements of the droplet diameters was less than two percent, considering the error involved in the magnification.

The heated surface consisted of a large diameter copper cylinder that was tapered to a small horizontal circular area with a diameter of 8.00 mm at the tip. The copper cylinder had a total length of 85 mm. The bottom section of the cylinder was 58 mm high and had a 38 mm diameter. The diameter of the bottom section was reduced to 8.00 mm, forming a cone with length of 14 mm (see Fig. 7).

The energy input to the copper cylinder was provided by a 450 Watt, 240 Volt electrical heater attached to the 38 mm diameter base. The copper cylinder was well insulated to minimize heat losses from the side and bottom surfaces. Heat flux measurements from the cylinder were provided by nine type-K thermocouples placed close to the tip of the copper surface, as shown in Fig. 7. Each axial layer of thermocouples was separated vertically by 3.2 mm, and each of the three thermocouples was equally spaced around the circumference of the top of the copper cylinder. The vertical distance between the surface of the cylinder and the closest set of thermocouples was 6.4 mm. The heat flux was calculated by assuming one-dimensional conduction along the axial direction of the cylinder at the location of the thermocouples. An uncertainty analysis was performed considering errors in thermocouples and distances between them

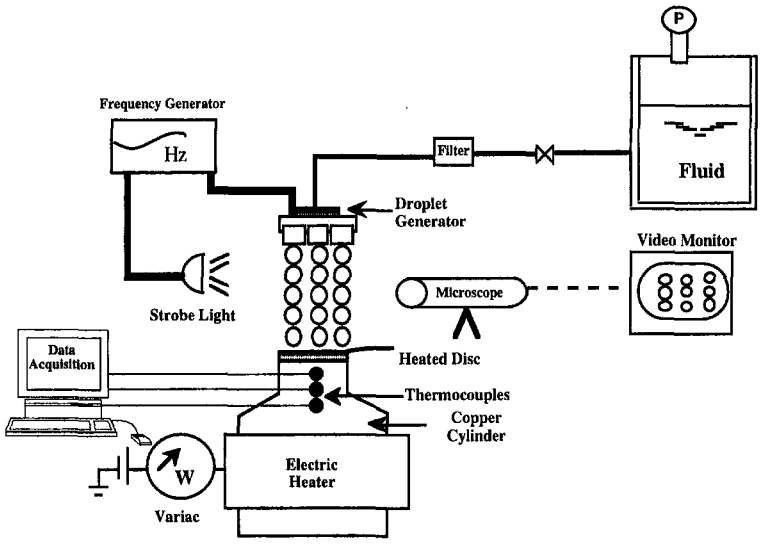

Fig. 7 Experimental apparatus

which resulted in an overall error in the calculated heat flux of less than ten percent. The one-dimensional assumption was verified by estimating heat losses from the heater to the ambient and performing an energy balance under steady-state conditions. This one-dimensional assumption resulted in an error of less than five percent.

Experimental Results

The variables investigated in the experiments included droplet diameters and velocities, as functions of the vertical direction. Two basic experiments were considered: the study of a single stream of water droplets in a constant property ambient, and the study of a stream of water droplets prior to impact on a horizontal heated disc which has an evaporating liquid water film on the surface.

Experiments Without Buoyant Jet. Droplet velocities and diameters were measured at various frequencies when the droplets were injected into a constant property, stagnant ambient air (no heater present). The absence of the heater allowed the study of a stream of droplets at room conditions. Two fluid pressures, 9 kPa and 19 kPa, were chosen.

Photographs of the droplets were taken at several vertical distances by fixing the location of the microscope and varying the height of the droplet generator. Droplet diameters were obtained by photographing the droplets and then a calibrated scale. Velocities were obtained by measuring the distance between droplets at various distances from the print head. The droplet velocity was then calculated from the expression

$$u_j = Lf/M \tag{19}$$

where L is the distance between droplets measured from the photographs, f is the droplet generation frequency, and M is the photographic magnification. The estimated error in predicting droplet velocity from Eq. (19) is within four percent. Photographs were taken up to a vertical position where the monodispersity was lost due to the coalescence of the droplets. This maximum distance varied between 60 and 100 mm. Precautions were taken to avoid air currents in the room. An example of the measured droplet velocity is shown in Fig. 8. Comparison with velocities predicted with the droplet model is also shown for the figure.

By varying the frequency at which the droplets were generated, the drag model used to determine droplet interference effects could be verified. Different values of the critical distance for which adjacent drops influence the drag coefficient, $(L/D)_{crit}$, were used in the droplet hydrodynamic model. For values of L/D greater than the critical value, the drag coefficient was based on a single droplet. For values of L/D less than the critical value, the drag coefficient must be modified to account for the influence of adjacent droplet. The value of $(L/D)_{crit}$ has not been clearly established in the literature. However, Mullholland (1988) suggests a value between four and ten. The results in Fig. 8 are based upon a value of $(L/D)_{crit}$ equal to ten. This value appears to provide the best correlation between the experimental velocity measurements and the velocity values predicted by the hydrodynamic model, with an accuracy within ten percent for all test conditions.

The temperature and relative humidity of the room averaged 25.0°C and 40 percent, respectively, during the tests. For these conditions, the diameter of the droplet was expected to decrease slightly as a result of evaporation to the ambient air. However, the short distances of travel that the droplet experienced caused small variations in droplet diameter, and decreases of less than ten percent were observed. The measured droplet diameters compared within five percent with the value predicted by Eq. (18).

Experiments With Buoyant Jet. The objective of these experiments was to verify the coupled model of droplet sprays prior to impact on a surface that is heated above the saturation temperature of the liquid spray. Spray conditions were fixed at a droplet frequency of 10 kHz, a liquid pressure of 19 kPa, initial droplet temperature of 25°C, and droplet generator height

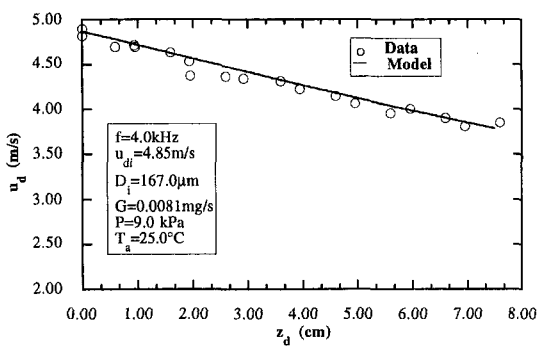

Fig. 8 Comparison of measured and calculated values of droplet velocities

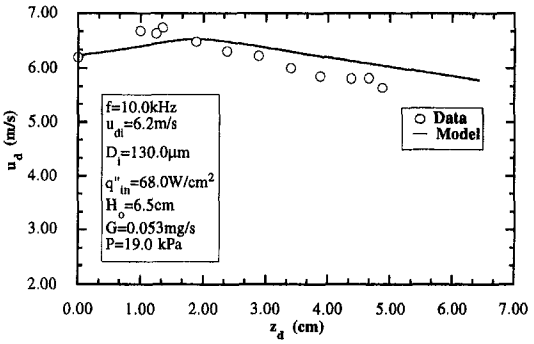

Fig. 9 Experimental and numerical values of the velocity of a stream of droplets in a buoyant jet

above the heated surface, H_o, of 65 mm. This particular set of spray conditions resulted in an average droplet diameter of 130 μm. All heater conditions were fixed at a steady-state heat flux and surface temperature of 68 W/cm^2 and 115°C, respectively. These spray and heater conditions are similar to conditions achieved from commercial nozzles reported by Bonacina et al. (1979). In their case, surface heat fluxes close to 100 W/cm^2 were reported for surface temperatures of 112°C, subcooling of 75°C, and droplet average diameters less than 100 μm.

Five streams of droplets were used to uniformly cover the entire 8.0 mm-diameter heated surface. The distance between the orifices was 1.5 mm. Therefore, the pattern from five orifices provided a fairly uniform coverage on the heated surface. Photographs of the streams of droplets were taken at different vertical distances above the heated surface by fixing the droplet generator at a distance H_o of 65 mm and moving the microscope in the vertical direction. The procedure to measure velocities and diameters was similar to those of the constant ambient experiments. However, for the ambient with variable properties, a lower magnification, on the order of 20 ×, was used because it was extremely difficult to position the microscope close to the heater due to condensation on the microscope lens. Also, data close to the droplet generator exit was difficult to observe with the microscope and the velocity was estimated from a hydrostatic balance.

The data for the droplet velocities in all the experiments were consistently within ten percent for a given vertical location, indicating good repeatability. The heated surface was observed to be fully covered by an evaporating liquid film during most of the tests. However, minor changes in the wetted pattern affected the distribution of the water vapor within the buoyant jet.

A comparison of the droplet velocities predicted by the numerical model and the measured droplet velocities is shown in Fig. 9. The numerical calculations were obtained by solving the conservation equations for the combined spray and saturated buoyant jet models and using input variables shown in the title box of Fig. 9. The agreement between model and experimental data was within 15 percent. However, the deceleration trend predicted by the theoretical model is slightly different from the one indicated by the measured data. The disagreement is mainly due to the assumptions used in the buoyant jet model, namely, negligible presence of the droplet generator and constant vapor velocity at the heater surface. These assumptions are not completely valid for the small distance of 65 mm between the droplet generator and the heated surface. For larger distances, the effects of variations in the vapor velocity due to bursting bubbles are expected to diminish under steady-state boiling conditions. Furthermore, the model assumption of uniform droplet distribution may have affected the results. In the experiments performed, the heated surface was covered by a line of five droplet streams instead of being exactly distributed uniformly across the surface. However, the model does predict the general trend of the condensation and the acceleration followed by deceleration that exists when multiple droplets travel through a saturated medium.

Conclusions

This research reports a comprehensive investigation of the behavior of small droplet sprays that were initially subcooled and downward oriented prior to their impact on a horizontal heated surface. This situation commonly arises in spray cooling applications. An experimental and theoretical investigation of the coupled effects between a downward oriented spray and a rising saturated buoyant jet, which results from a constant evaporation on a heated surface, are reported. A model describing the thermal and hydrodynamic behavior of both the spray and the saturated buoyant jet is developed. A two-dimensional Lagrangian formulation is used to describe the conditions of the spray while the temperature and velocity distribution in the buoyant jet is described by an Eulerian formulation in cylindrical coordinates. An experimental set-up involving a high speed photographic apparatus was used to observe vertically projected monodispersed sprays and measure the diameter and velocity of the droplets as they approached the horizontal heated surface. The theoretical formulation was calibrated against several established theoretical limiting cases and reported data. The full theoretical model was also compared with data gathered in this research; numerical results were within 15 percent of the experimental values. Further theoretical and experimental results indicate that:

- The temperature of the saturated buoyant jet is influenced by the presence of a liquid spray that is initially subcooled.
- The saturated jet experiences high supersaturation levels due to the absence of sufficient condensation nuclei that are needed to maintain saturated thermal equilibrium.
- Vertically projected small droplet sprays in spray cooling applications experience high condensation rates while in contact with a saturated buoyant jet and reach the saturation temperature before impacting the heated surface, thus inhibiting any sub-cooling effects. These droplets may also experience acceleration as a consequence of an increase in mass due to condensation that can occur on the drops.
- The presence of the saturated buoyant jet increases the drag forces on the spray resulting in considerable reduction in droplet velocities. Droplets close to the edge of the jet free boundary experience a "trapping" effect that forces them toward the centerline, as dry ambient fluid is entrained in the jet.
- Closely spaced droplets experience smaller drag coefficients than exist for widely spaced drops.

Finally, this research approach establishes the basis for a unified theory for spray cooling that includes pre-impact and post-impact processes. A unified theory will enable designers to specify spray parameters which will lead to the control of high heat transfer rates in practical applications. The unified spray cooling theory should be a topic of further discussion among researchers.

References

Bacon, F. M., Cowgill, D. F., Hickox, C. E., Walko, R. J., Subia, S. R., and Riedel, A. A., 1984, "High Heat Flux Target for Intense Neutron Source," *Review of Scientific Instruments,* Vol. 55, pp. 42–47.

Bonacina, C., Del Giudice, S., and Comini, G., 1979, "Dropwise Evaporation," ASME JOURNAL OF HEAT TRANSFER, Vol. 101, pp. 441–446.

Choi, K. J., and Yao, S. C., 1987, "Mechanisms of Film Boiling Heat Transfer of Normally Impacting Spray," *International Journal of Heat and Mass Transfer,* Vol. 30, pp. 311–318.

Deb, S., and Yao, S. C., 1989, "Analysis on Film Boiling Heat Transfer of Impacting Sprays," *International Journal of Heat and Mass Transfer,* Vol. 32, pp. 2099–2112.

Fuchs, N. A., 1964, THE MECHANICS OF AEROSOLS, Pergamon Press, New York.

Gebhart, B., Jaluria, Y., Mahajan, R. L., and Sammakia, B., 1988, BUOYANCY INDUCED FLOWS AND TRANSPORT, Hemisphere, New York.

Ghodbane, M., and Hollman, J. P., 1991, "Experimental Study of Spray Cooling with Freon-113," *International Journal of Heat and Mass Transfer,* Vol. 34, pp. 1163–1174.

González, J. E., Black, W. Z., and Desai, P. V., 1995, "Numerical Solution of Saturated Laminar Buoyant Jets," *Proceedings of the ASME Heat Transfer Division,* Vol. 317–1, pp. 321–329.

Gu, C. B., Su, G. S., Chow, L. C., and Pais, M. R., 1993, "Comparison of Spray and Jet Impingement Cooling," ASME Paper 93-HT-20.

Hall, D. D., and Mudawar, I., 1995, "Experimental and Numerical Study of Quenching Complex-Shaped Metallic Alloys with Multiple, Overlapping Sprays," *International Journal of Heat and Mass Transfer,* Vol. 38, pp. 1201–1216.

Himashekar, K., and Jaluria, Y., 1982, "Laminar Buoyancy-Induced Axisymmetric Free Flows in a Thermally Stratified Medium," *International Journal of Heat and Mass Transfer,* Vol. 25, pp. 213–221.

Kincaid, D. C., and Longley, T. S., 1989, "A Water Droplet Evaporation and Temperature Model," *Transaction of the ASAE,* Vol. 32, pp. 457–460.

Liu, Z., and Reitz, R. D., 1995, "Modeling Fuel Spray Impingement and Heat Transfer Between Spray and Wall in Direct Injection Diesel Engines," *Numerical Heat Transfer-Part A: Applications,* Vol. 28, pp. 515–529.

Mollendorf, J. C., and Gebhart, B., 1974, "Axisymmetric Natural Convection Flows Resulting From the Combined Buoyancy Effects of Thermal and Mass Diffusion," *Proceedings of the 5th, International Heat Transfer Conference,* Tokyo, pp. 10–14.

Mullholland, J. A., 1988, "Influence of Droplet Spacing on Drag Coefficient in Nonevaporating, Monodisperse Streams," *AIAA Journal,* Vol. 26, pp. 1231–1237.

Ohkubo, H., and Nishio, S., 1987, "Mist Cooling for Thermal Tempering of Glass," *Proceedings of the ASME-JSME Thermal Engineering Joint Conference,* Vol. 5, pp. 71–78.

Pedersen, C. O., 1970, "An Experimental Study of the Dynamic Behavior and Heat Transfer Characteristics of Water Droplets Impinging Upon a Heated Surface," *International Journal of Heat and Mass Transfer,* Vol. 13, pp. 369–381.

Poo, J. Y., and Ashgriz, N., 1991, "Variation of Drag Coefficients in an Interacting Drop Stream," *Experiments in Fluids,* Vol. 11, pp. 1–8.

Rayleigh, L., 1878, "On the Instability of Jets," *Proceedings of the London Mathematical Society,* Vol. 10, pp. 4–13.

Saffman, P. G., 1965, "The Lift of a Small Sphere in a Slow Shear Flow," *Journal of Fluids Mechanics,* Vol. 22, pp. 385–400.

Saffman, P. G., 1968, "Corrigendum," *Journal of Fluids Mechanics,* Vol. 31, p. 624.

Schlichting, H., 1979, BOUNDARY LAYER THEORY, Seventh Ed., McGraw-Hill, New York, pp. 230–234.

Toda, S., 1974, "A Study of Mist Cooling (2nd Report: Theory of Mist Cooling and Its Fundamental Experiments)," *Heat Transfer: Japanese Research,* Vol. 3, pp. 1–44.

Watson, R. D., 1990, "Structures for Handling High Heat Fluxes," *Journal of Nuclear Materials,* Vol. 176 & 177, pp. 110–121.

Yuen, M. C., and Chen, L. W., 1976, "On Drag of Evaporating Liquid Droplets," *Combustion Science and Publication,* Vol. 14, pp. 146–154.

Zhou, L., 1993, THEORY AND NUMERICAL MODELING OF TURBULENT GAS-PARTICLE FLOWS AND COMBUSTION, CRC Press, Inc., Florida.

Zhou, Q., and Yao, S. C., 1992, "Group Modeling of Impacting Spray Dynamics," *International Journal of Heat and Mass Transfer,* Vol. 35, pp. 121–129.

Evaporation and Growth of Multicomponent Droplets in Random Dense Clusters

T. Elperin
elperin@menix.bgu.ac.il

B. Krasovitov
The Pearlstone Center for Aeronautical Engineering Studies,
Department of Mechanical Engineering,
Ben-Gurion University of the Negev,
P.O. Box 653,
Beer-Sheva 84105,
Israel

Interaction between evaporating (growing) droplets in binary arrays and large random clusters of droplets of different sizes is analyzed in a quasi-steady approximation using the modified method of expansion into irreducible multipoles. Evaporation and condensation of binary arrays and clusters of droplets (i) composed of volatile components and (ii) composed of a volatile and a nonvolatile component was studied. The analytical and numerical results of the investigation are presented in terms of heat and mass correction factors. Solution of the transient problem is obtained, and the evaporation rate is determined. It is shown that for droplets of ideal solution with different compositions, Nusselt and Sherwood numbers depend on the concentration of components inside each droplet. When dense cloud contains both pure droplets and droplets containing soluble nuclei, interactions between temperature and concentration fields causes growth of some droplets in a cluster and evaporation of the other droplets. It is shown that inside an evaporating large cluster of multicomponent droplets composed of volatile components, recondensation occurs whereby evaporating droplets act as mass sources and heat sinks and growing droplets act as mass sink and heat sources. The results of this study are of relevance in the analysis of dynamics of droplet size distribution in clouds, artificial modification of clouds and precipitation, in-cloud pollutants scavenging, and in the analysis of evaporation and combustion of multicomponent (blended) liquid fuels.

1 Introduction

Mass and energy exchange between a dispersed phase and an ambient gas is encountered in numerous atmospheric and industrial processes. The applications include condensation of hydrocarbons and water vapor in stack gases, spray drying, and spray combustion, etc. Condensational droplet growth on nuclei, consisting of hygroscopic substances, is very important in such fields as separation of submicron particles from gases and scavenging of the pollutants (Heidenreich and Ebert, 1995). Single drop evaporation (combustion) models yield the parameters and evaporation (combustion) characteristics of the individual droplets. However, clusters of droplets with high concentration of droplets are encountered in various engineering and environmental applications (see e.g., Bellan and Harstad, 1995). In this case, the droplets behave quite differently from the isolated droplets. The importance of droplet interaction effects has not gone unrecognized in the literature. It is known that interactive problems can be treated by five methods: (i) bispherical coordinates—suitable for two-drop arrays (Carstens et al., 1970; Umemura et al., 1981); (ii) method of images—suitable for arrays less than 20 drops (Labowsky, 1978, 1980a, b); (iii) point sources method—suitable for dilute arrays of 1000 drops (Deutch et al., 1976; Ray and Davis, 1980; Annamalai et al., 1993); (iv) continuum methods—suitable for dilute sprays (Chiu and Liu, 1977; Annamalai et al., 1988; Tsai and Sterling, 1991); (v) method of expansion into irreducible multipoles—suitable for large dense random clusters of droplets (particles) (Elperin and Krasovitov 1994a, 1994b).

State of the art in the above methods was reviewed by Annamalai and Ryan, 1992; Annamalai et al., 1993, 1994; Elperin and Krasovitov 1994a, 1994b. The theoretical methods (1)–(4) deal primarily with droplet evaporation (combustion) in various limiting cases, such as: regular structure of cluster, finite array, dilute clusters, monosized clusters, etc. The method of expansion into irreducible multipoles which was developed in our previous works (Elperin and Krasovitov, 1994a, 1994b) is applicable to more realistic problems and is particularly suitable for dense random clusters of droplets (particles). The droplets that are used in various engineering applications are mainly composed of two or more components. However, in spite of the importance of this field there are only a few works (Labowsky, 1980a; Annamalai et al., 1993) that address evaporation of clusters of multicomponent droplets.

The effects of interactions on the evaporation (combustion) rate are estimated using the correction factor. For an array containing N multicomponent droplets, the correction factor of ith species for the jth droplet is determined as (Annamalai et al., 1993)

$$\eta_{ij} = \frac{(\dot{m}_i)_j}{(\dot{m}_{iso,i})_j} \tag{1}$$

where the isolated droplet has the same composition as the jth droplet in the array.

It is well known that interactive effects could both retard and enhance the rate of evaporation of the interacting droplets. It was shown previously (see e.g., Labowsky, 1980a; Annamalai et al., 1993) that the latter occurs under some restrictive conditions such as buoyant convective effects and when droplets of dissimilar composition are considered. In a case where interactive effects retard the rate of evaporation, the correction factor is less then 1 ($\eta < 1$, "negative" interactions) and in case when the interactive effects enhance the rate of evaporation the correction factor is greater then 1 ($\eta > 1$, "positive" interactions).

However, the above mentioned theoretical results were obtained for constant droplet diameters, compositions, and center-to-center distances. In reality, the compositions and sizes of droplets change with time. The latter implies that the correction factor η depends on time and, therefore, could give rise to the

Contributed by the Heat Transfer Division for publication in the JOURNAL OF HEAT TRANSFER. Manuscript received by the Heat Transfer Division February 26, 1996; revision received January 17, 1997; Keywords: Condensation, Evaporation, Sprays/Droplets. Associate Technical Editor: S. Ramadhyani.

mass and heat sources and sinks inside the cluster. Xiong et al. (1984) conducted evaporation experiments on a two-drop array of pure single component droplets (high volatile heptane drop and low volatile hexadecane drop at an ambient temperature 24°C) and showed that the hexadecane drop acts as a mass sink, and a heat source for the heptane drop. Thus, the diameter of the hexadecane droplet increases as a result of condensation of vapors from the heptane droplet. In this study it is shown that heat and mass sinks and sources within the cluster of multicomponent droplets containing volatile and a nonvolatile components can also occur in a case of condensation on hygroscopic nuclei inside the cluster.

The first theoretical investigation of the transient problem where the sizes of particles inside a random cluster of char/carbon particles change with time was performed by Elperin and Krasovitov (1994b). In the latter work, the results obtained using expansion into irreducible multipoles were validated by comparison with the available experimental data. The purpose of the present study is to develop the theory of evaporation and condensation of dense random clusters of droplets with dissimilar compositions. In the next section some important evaporation characteristics of random clusters of droplets are discussed.

2 Model and Assumptions

2.1 Evaporation of a Single Multicomponent Droplet.

(A) Evaporation of Droplets With a Volatile and Nonvolatile Components. Consider a spherical droplet with high thermal conductivity containing volatile and nonvolatile components immersed in a stagnant binary gas mixture at temperature T_∞, with the concentration of volatile species $C_{1,\infty}$. The influence of convection on the evaporation is neglected. Assume also that the characteristic times of heat and diffusive relaxation are small compared to total time of evaporation so that the steady-state evaporation model is valid.

Under the above assumptions, the system of mass and energy conservation equations is shown in Table 1. Table 2 provides the corresponding boundary conditions that include the boundary conditions (7) – (8) allowing for the occurrence of the temperature and concentration jumps at the surface of a droplet and for the occurrence of the cross effects (see Yalamov et al., 1990). These boundary conditions are supplemented with the condition of continuity of energy flux at the droplet surface (9) and conditions at infinity (10).

Solution of the above system of equations for large-size droplets (without temperature and concentration jumps), in case of a diffusion regime of evaporation, yields the following expressions for the heat and mass fluxes at the droplet surface (Elperin and Krasovitov, 1995):

$$q_T = 4\pi R \int_{T_\infty}^{T_s} k_e dT,$$

$$q_1 = 4\pi R \frac{(C_{1,s}(T_s) - C_{1,\infty})}{\int_{T_\infty}^{T_s} \frac{k_e}{nD} dT} \int_{T_\infty}^{T_s} k_e dT \qquad (11)$$

where q_T and q_1 are integral heat and mass fluxes at the droplet surface, correspondingly, T_∞ is the temperature of the ambient gas and temperature at the droplet surface T_s can be found from the following transcendental algebraic equation:

$$\int_{T_\infty}^{T_s} k_e dT_e \left(1 + m_1 L \frac{(C_{1,s}(T_s) - C_{1,\infty})}{\int_{T_\infty}^{T_s} (k_e/nD) dT_e}\right) + R\gamma\gamma_0(T_s^4 - T_\infty^4) = \frac{q_w}{4\pi R} \qquad (12)$$

where γ and γ_0 are emissivity and Stefan-Boltzmann's constant, correspondingly, q_w is the total power of internal heat sources and $C_{1,s}(T_s)$ is the relative concentration at the droplet surface that is related to the drop temperature through phase equilibrium relations. In case of ideal solutions, the value of the relative concentration $C_{1,s}(T_s)$ is determined by the Raoult's law:

$$C_{1,s}(T_s) = X_{1,w} C_{1,s}^{(0)}(T_s) \qquad (13)$$

and the Clapeyron-Clausius equation:

$$C_{1,s}^{(0)}(T_s) = C_{1,s}(T_0) \exp\left(\frac{L\mu_\nu}{R_g}\left(\frac{1}{T_0} - \frac{1}{T_s}\right)\right) \qquad (14)$$

where $C_{1,s}^{(0)}(T_s)$ is the relative concentration of saturated vapor at the surface of a pure liquid, μ_ν is the molar mass of volatile species and R_g is the universal gas constant. For non-ideal solu-

Nomenclature

$C_k = n_k/n$, dimensionless concentration of k-th specie
D = coefficient of binary diffusion, $m^2 \cdot s^{-1}$
$\mathbf{j}_i$ = mass flux density, $m^{-2} \cdot s^{-1}$
$\mathbf{j}_T$ = heat flux density, $W \cdot m^{-2}$
h = enthalpy, $J \cdot kg^{-1}$
k = coefficient of thermal conductivity, $W \cdot (m \cdot K)^{-1}$
$K_T = D_T(T, C_1)/D$ thermal diffusion ratio
$K_T^{(T)}$, $K_n^{(n)}$ = coefficients of temperature and concentration jumps, m
$K_T^{(n)}$, $K_n^{(T)}$ = cross coefficients, m
L_{ij} = center-to-center distance between droplets, m
L = latent heat of evaporation, $J \cdot kg^{-1}$
m_k = mass of the molecules of k-th species, kg
M' = mass of soluble nucleus, kg
M_d = mass of a droplet, kg
M_j = mass of j-th volatile species, kg
n = molecular number density, m^{-3}
Nu = Nusselt number
q_k = integral mass flux of the molecules of k-th specie, s^{-1}
q_T = integral heat flux, W
q_w = total power of internal sources, W
R_i = radius of i-th droplet, m
R_g = universal gas constant, $J \cdot (mol \cdot K)^{-1}$
r = radius coordinate, m
Sh = Sherwood number
T = temperature, K
X_k = molar fraction of k-th species

Greek

γ = Stefan-Boltzmann constant, $W \cdot m^{-2} \cdot K^{-4}$
γ_0 = integral emissivity
ζ = heat correction factor
η = mass correction factor
μ' = molar mass of soluble hygroscopic nucleus, $kg \cdot mol^{-1}$
μ_v = molar mass of a solvent vapor, $kg \cdot mol^{-1}$
ρ = density, $kg \cdot m^{-3}$
σ = volume fraction
$\tilde{\sigma}$ = surface tension, $N \cdot m^{-1}$

Subscript

i, j = number of a droplet, number of species (Tables 1–3)
β = number of species
s = value at a droplet surface
1, 2 = volatile specie and ambient gas
∞ = value at infinity

Superscript

(e) = value outside a droplet
i = number of a droplet
(s) = value at the surface
(w) = value within a droplet

Table 1 Governing equations

$$\operatorname{div} \Gamma_\phi = 0 \tag{2}$$

Equation	Γ_ϕ: General equations	Γ_ϕ: Linearized equations
Mass conservation	$\mathbf{j}_i$	∇C_i
Energy conservation	$\mathbf{j}_T$	∇T_e

Droplets of a volatile and nonvolatile component

$$\mathbf{j}_i = n_i \mathbf{v} - \frac{m_j n^2}{\rho^{(e)}} D(\nabla C_i + (-1)^{i+1} K_T \nabla \ln T_e) \tag{3}$$

$$\mathbf{j}_T = \sum_i h_i m_i \mathbf{j}_i - k_e \nabla T_e \tag{4}$$

$$(i, j = 1, 2,\ i \neq j)$$

$$C_\nu = n_\nu / \sum_i n_i, \quad C_2 + C_1 = 1$$

Multicomponent droplets of volatile components

$$\mathbf{j}_i = \frac{\sum_k C_k}{\sum_k \frac{C_k}{D_{ik}}} n \nabla C_i + \frac{\sum_k \frac{\mathbf{j}_k}{D_{ik}}}{\sum_k \frac{C_k}{D_{ik}}} C_i \tag{5}$$

$$\mathbf{j}_T = \sum_i h_i m_i \mathbf{j}_i - k_e \nabla T_e \tag{6}$$

$$i, k = \overline{1, \Lambda + 1}, \quad i \neq k, \quad \sum_{i=1}^{\Lambda+1} C_i = 1$$

tions the value of the relative concentration $C_{1,s}(T_s)$ can be found from the following formula (see Mason, 1971, pp. 24–30):

$$C_{1,s}(T_s) = C_{1,s}^{(0)}(T_s)\left(1 + \frac{2\mu_\nu \tilde{\sigma}}{\rho R_g T_s} \frac{1}{R} - \frac{3i\mu_\nu}{4p\rho\mu'} \frac{M'}{R^3}\right) \tag{15}$$

where $\tilde{\sigma}$ is the surface tension, ρ is the density of solvent, μ_ν and μ' are the molar masses of vapor of the solvent and of soluble hygroscopic nucleus, i is van't Hoff's factor which depends on the chemical nature and the degree of dissociation (i.e., on the concentration) of the solute and M' is the mass of a soluble hygroscopic nucleus.

Integrals in expressions (11) and transcendental Eq. (12) can be calculated using dependencies of thermal conductivity and diffusivity on temperature and concentrations of species (see e.g., Lefebvre, 1989, Chapter VIII).

In the case of evaporation of a droplet immersed into a stagnant binary gas mixture with small temperature differences, in the neighborhood of the droplet, the system of Eqs. (2) can be linearized (see Table 1). In the latter system of equations it is taken into account that in a binary gas mixture, the sum of the relative concentrations is equal to unity (i.e., $C_1 + C_2 = 1$).

Finally, the rate of droplet evaporation can be found from the following differential equation:

$$\frac{dM_d}{dt} = -m_1 q_1 \tag{16}$$

where M_d is the mass of a droplet and t is time.

(B) Droplets of Arbitrary Composition. Consider a single multicomponent droplet composed of Λ volatile components immersed into a stagnant mixture of $\Lambda + 1$ components with temperature T_∞. It is assumed that Λ constituent species of the ambient gas mixture are volatile components of the droplet and $\Lambda + 1$th species is an ambient gas. The influence of natural convection on evaporation is neglected. Since the characteristic times of thermal and diffusion relaxation are small, we can consider a steady-state evaporation. Under the above assumptions, the evaporation of a multicomponent droplet can be described by a system of conservation Eqs. (2). However, the densities of energy and mass fluxes in a multicomponent gas mixture are given by Eqs. (5)–(6) (see Table 1).

Using the effective values of velocity and diffusivity (Frank-Kamenetskii, 1969, Chapter IV):

$$\mathbf{v}_i = \frac{1}{n} \frac{\sum_k \frac{\mathbf{j}_k}{D_{ik}}}{\sum_k \frac{C_k}{D_{ik}}}, \quad \bar{D}_i = \frac{\sum_k C_k}{\sum_k \frac{C_k}{D_{ik}}} \tag{17}$$

in the Eq. (6) the mass conservation equation can be written as follows:

$$\operatorname{div}(n_i \mathbf{v}_i + \bar{D}_i n \nabla C_i) = 0 \tag{18}$$

where $\bar{D}_i$ is effective diffusivity that can be calculated using Wilke's rule.

When the temperature differences in the neighborhood of a droplet are small, the Stefan flux can be neglected and transport coefficients are constant. In this case, Eq. (18) can be linearized; one is presented in Table 1.

Finally, the rate of droplet evaporation can be found from the following differential equation:

$$\frac{dM_d}{dt} = -\sum_j m_j q_j. \tag{19}$$

2.2 Modified Method of Expansion into Irreducible Multipoles. A detailed description of the modified method of expansion into irreducible multipoles and its application to the evaporation and combustion of dense random clusters of droplets and particles can be found in Elperin and Krasovitov 1994a, 1994b. For the sake of completeness, a brief discussion of this method is presented below.

Consider a system containing N droplets whose centers are located at $\mathbf{r} = \mathbf{r}_i$ and which have radii R_i, where $i = \overline{1, N}$. The location of each droplet is fixed in a system of coordinate X, Y, Z the origin of which can be located in the center of each droplet. The location of jth droplet can be determined in the system of coordinate X_i, Y_i, Z_i which is connected with the center of each droplet by the vector $\mathbf{L}_{ij}$. Similarly, the location of ith droplet can be determined in the coordinate system X_j, Y_j, Z_j by the vector $\mathbf{L}_{ji} = -\mathbf{L}_{ij}$.

Let U denote concentration or temperature fields which are

Table 2 Boundary conditions and conditions at infinity

The existence of temperature and concentration jumps at the surface of a droplet:

$$(T_e - T_w)|_{r=R} = K_T^{(T)} \left.\frac{\partial T_e}{\partial r}\right|_{r=R} + K_T^{(n)} T_\infty \left.\frac{\partial C_1}{\partial r}\right|_{r=R} \tag{7}$$

$$(C_1 - C_1^{(s)}(T_w))|_{r=R} = K_n^{(n)} \left.\frac{\partial C_1}{\partial r}\right|_{r=R} + \frac{K_n^{(T)}}{T_\infty} \left.\frac{\partial T_e}{\partial r}\right|_{r=R} \tag{8}$$

The continuity of energy flux at the droplet surface:

$$\frac{W_T}{4\pi R^2} = (\sum_i (L_i - h_i) m_i j_{r,i} + j_{r,T} + j_{r,R})|_{r=R} \tag{9}$$

Conditions at infinity:

$$T_e|_{r\to\infty} = T_\infty, \quad C_1|_{r\to\infty} = C_{1\infty} \tag{10}$$

governed by Eq. (2) (see Table 1) where flux Γ_ϕ is determined by the following equation:

$$\Gamma_\phi = \nabla U. \tag{20}$$

Notably, most practical applications involve high temperature differences during evaporation (combustion), and the Stefan's flux must be taken into account. Moreover, the energy and mass conservation equations are nonlinear on the account of dependence of heat and mass transfer coefficients on temperature (see Table 1). However, methods were developed which allow conversion of the Stefan flow (SF) problem into a non-Stefan flow (NSF) problem (Annamalai, 1993) and conversion of the nonlinear problem into the Laplace equation (Elperin and Krasovitov 1994a, 1994b). Therefore, the general problem can reduced to the solution of the Dirichlet, Neumann, or mixed boundary value problem for the Laplace equation in the domain exterior to N arbitrary located droplets.

The boundary condition at the surface of ith droplet and the condition at infinity read:

$$U|_{S_i} = U_i^{(s)} = \text{const}, \quad U|_{|\mathbf{r}-\mathbf{r}_i|\to\infty} \to 0. \tag{21}$$

In case when Eq. (2) is linearized, the solution U in the vicinity of the ith droplet can be represented as a superposition:

$$U = U_i + \delta U_i, \quad \delta U_i = \sum_{\substack{j=1 \\ j\neq i}}^{N} U_j \tag{22}$$

where U_i is the field generated by the ith droplet and δU_i is the perturbation which is caused by the presence of $N-1$ other droplets. Note that in order to simplify notations, hereafter, we omit index i near the solution U in the vicinity of the ith droplet. Note also that the field function in the neighborhood of the ith droplet has singularities at the centers of other $N-1$ droplets.

The field function (e.g., temperature or concentration) can be represented as a tensor expansion suggested by Schmitz and Felderhof (1982):

$$U_i = \sum_{n=0}^{\infty} A^i_{\nu_1\ldots\nu_n} x_i^{-(2n+1)} \overbrace{x^i_{\nu_1}\ldots x^i_{\nu_n}}$$

$$\delta U_i = \sum_{n=0}^{\infty} B^i_{\nu_1\ldots\nu_n} \overbrace{x^i_{\nu_1}\ldots x^i_{\nu_n}} \tag{23}$$

where the tensor $\overbrace{x^i_{\nu_1}\ldots x^i_{\nu_n}}$, defined as follows:

$$\overbrace{x^i_{\nu_1}\ldots x^i_{\nu_n}} = \frac{(-1)^n}{(2n-1)!!}\, x_i^{2n+1} \nabla^i_{\nu_1}\ldots\nabla^i_{\nu_n}\left(\frac{1}{x_i}\right) \tag{24}$$

is a symmetrical tensor with $2n+1$ independent components; $\nabla^i_{\nu_k} = \partial_{x^i_{\nu_k}}$, $x^i_{\nu_k} = (\tilde{x}_{\nu_k} - \tilde{x}^i_{\nu_k})/R_i$, $\tilde{x}_{\nu_k}$ and $\tilde{x}^i_{\nu_k}$ ($\nu_k = \overline{1,3}$, $k = \overline{1,n}$) are current Cartesian coordinates and the Cartesian coordinate of the center of the ith sphere, respectively, and $x_i = \sqrt{\sum_{\nu_k} (x^i_{\nu_k})^2}$ (for details see, e.g., Hess and Köhler, 1980). It is shown below that the latter representation of the solution allows to satisfy the boundary conditions at the surface of each droplet. Since U_i and δU_i are harmonic functions, the coefficients $A^i_{\nu_1\ldots\nu_n}$ and $B^i_{\nu_1\ldots\nu_n}$ are the constant symmetrical tensors that are traceless in any pair of their indices. These tensors must be determined from the boundary conditions.

Using the boundary condition (21) we can express the coefficients $A^i_{\nu_1\ldots\nu_n}$ via the coefficients $B^i_{\nu_1\ldots\nu_n}$:

$$A^i_0 = U_i^{(s)} - B^i_0, \quad \text{for} \quad n = 0$$

$$A^i_{\nu_1\ldots\nu_n} = -B^i_{\nu_1\ldots\nu_n}, \quad \text{for} \quad \forall n \geq 1. \tag{25}$$

Substituting (25) into expansion (23) and using (22) we find that

$$U = U_i^{(s)}(1/x_i) + \sum_{n=0}^{\infty} B^i_{\nu_1\ldots\nu_n}(1 - x_i^{-(2n+1)})\overbrace{x^i_{\nu_1}\ldots x^i_{\nu_n}}. \tag{26}$$

According to (22), the formula for field perturbation in the neighborhood of the ith droplet reads as follows:

$$\delta U_i = \sum_{\substack{j=1 \\ j\neq i}}^{N} \left[U_j^{(s)}(1/x_j) - \sum_{n=0}^{\infty} B^j_{\nu_1\ldots\nu_n} x_j^{-(2n+1)} \overbrace{x^j_{\nu_1}\ldots x^j_{\nu_n}}\right]. \tag{27}$$

Suppose that the origins of the systems of Cartesian coordinates O_k ($k = 1, \ldots, N$) are located at the centers of each droplet. Then, if the axes of these systems are parallel (i.e., $O_1X_1 \| O_2X_2 \| \ldots \| O_NX_N$; $O_1Y_1 \| O_2Y_2 \| \ldots \| O_NY_N$; $O_1Z_1 \| O_2Z_2 \| \ldots \| O_NZ_N$), the Taylor's series expansion of $x_j^{-(2n+1)}\overbrace{x^j_{\nu_1}\ldots x^j_{\nu_n}}$ can be written as follows:

$$x_j^{-(2n+1)}\overbrace{x^j_{\nu_1}\ldots x^j_{\nu_n}} = \sum_{k=0}^{\infty} \omega_{kn}\epsilon_j^{n+1}\epsilon_i^k \Omega_{\nu_1\ldots\nu_n\mu_1\ldots\mu_k}(\mathbf{L}_{ij})\overbrace{x^i_{\mu_1}\ldots x^i_{\mu_k}} \tag{28}$$

where

$$\epsilon_i = \frac{R_i}{|\mathbf{L}_{ij}|}, \ \epsilon_j = \frac{R_j}{|\mathbf{L}_{ij}|},$$

$$\omega_{kn} = \frac{(-1)^{k+n}[2(n+k)-1]!!}{k!(2n-1)!!}, \quad \nabla^{(i,j)}_{\nu_k} = \partial_{L^{(i,j)}_{\nu_k}},$$

$$\Omega_{\nu_1\ldots\nu_n\mu_1\ldots\mu_k}(\mathbf{L}_{ij}) = \frac{(-1)^{k+n}L_{ij}^{k+n+1}}{[2(n+k)-1]!!} \times \left[\nabla^{(i,j)}_{\nu_1}\ldots\nabla^{(i,j)}_{\nu_n}\nabla^{(i,j)}_{\mu_1}\ldots\nabla^{(i,j)}_{\mu_k}\left(\frac{1}{L_{ij}}\right)\right]$$

and $L^{(i,j)}_{\nu_k}$, Cartesian coordinates of the vector $\mathbf{L}_{ij}$.

Substituting expansion (28) into the expression (27), and using expression (23), we can obtain the infinite system of linear algebraic equations for the determination of the coefficients $B^i_{\nu_1\ldots\nu_n}$:

$$B^i_{\nu_1\ldots\nu_n} = B^{i(0)}_{\nu_1\ldots\nu_n} - \sum_{\substack{j=1 \\ j\neq i}}^{N}\sum_{k=0}^{\infty} B^j_{\mu_1\ldots\mu_k}\omega_{nk}\epsilon_j^{k+1}\epsilon_i^n \Omega_{\nu_1\ldots\nu_n\mu_1\ldots\mu_k}(\mathbf{L}_{ij}) \tag{29}$$

where

$$B^{i(0)}_{\nu_1\ldots\nu_n} = \sum_{\substack{j=1 \\ j\neq i}}^{N} U_j^{(s)}\omega_{n0}\epsilon_j\epsilon_i^n \Omega_{\nu_1\ldots\nu_n}(\mathbf{L}_{ij}).$$

The system of Eqs. (29) must be solved by a truncation procedure. Our past experience with the use of expansion into irreducible multipoles showed that convergence characteristics of the system are good, and only a few equations are required to obtain a high accuracy.

2.3 Evaporation of Dense Random Clusters of Multicomponent Droplets.

(A) Interactive Evaporation and Growth of Droplets With Volatile and Nonvolatile Component. Consider a cluster of N spherical droplets composed of volatile and nonvolatile components. It is assumed that there are no internal heat sources inside the droplets and the temperature differences in the neighborhood of each droplet are small. Assume that the characteristical times

of heat and diffusive relaxation are small and we can consider a steady-state evaporation.

Under the above assumptions, the system of mass and energy conservation equations reads:

$$\operatorname{div} \tilde{\Gamma}_\phi = 0 \tag{30}$$

where the flux $\tilde{\Gamma}_\phi$ is determined by equations presented in Table 3. Boundary conditions for conservation Eqs. (30) read:

$$\tilde{C}^{(e)}|_{S_i} = \tilde{C}_i^{(s)}, \quad \tilde{T}^{(e)}|_{S_i} = \tilde{T}_i^{(s)} \tag{31}$$

$$Lm_1 n D^{(e)} (\nabla \tilde{C}^{(e)} \mathbf{n}_r)|_{S_i} + k^{(e)} (\nabla \tilde{T}^{(e)} \mathbf{n}_r)|_{S_i} = k^{(w)} (\nabla \tilde{T}_i^{(w)} \mathbf{n}_r)|_{S_i}. \tag{32}$$

Conditions at infinity read:

$$\tilde{T}^{(e)}|_{|\mathbf{r}-\mathbf{r}_i|\to\infty} \to 0, \quad \tilde{C}^{(e)}|_{|\mathbf{r}-\mathbf{r}_i|\to\infty} \to 0. \tag{33}$$

Note that in case of small temperature differences in the neighborhood of each droplet we can expand the nondimensional vapor concentration at the gas-liquid interface in Taylor series and keep only the linear term:

$$\tilde{C}^{(e)}|_{S_i} = \tilde{C}_i^{(s)} = C_s^i(T_\infty) + \left.\frac{\partial C_s^i}{\partial \tilde{T}_s^i}\right|_{\tilde{T}_s^i=0} \tilde{T}_s^i + \dots$$

where $C_s^i = C_{1,s}^i - C_{1,\infty}$ and $\tilde{T}_s^i = T_{i,s} - T_\infty$. Concentrations $C_{1,s}^i$ can be determined by the Raoult's law (for ideal solutions) and by the formula (15) (for nonideal solutions).

Using the approach discussed in Section 2.2, the temperature and concentration distributions in the neighborhood of the ith droplet can be obtained as follows:

$$\tilde{C}^{(e)} = C^{i(0)} + \sum_{n=0}^{\infty} (B^i_{\nu_1\dots\nu_n}(1 + x_i^{-(2n+1)}\lambda^i_{bn}) + Q^i_{\nu_1\dots\nu_n} x_i^{-(2n+1)}\lambda^i_{qn}) \overline{x^i_{\nu_1} \dots x^i_{\nu_n}} \tag{34}$$

$$\tilde{T}^{(e)} = T_e^{i(0)} + \sum_{n=0}^{\infty} (Q^i_{\nu_1\dots\nu_n}(1 + x_i^{-(2n+1)}\varphi^i_{qn}) + B^i_{\nu_1\dots\nu_n} x_i^{-(2n+1)}\varphi^i_{bn}) \overline{x^i_{\nu_1} \dots x^i_{\nu_n}} \tag{35}$$

where $C^{i(0)} = x_i^{-1}\lambda_n^{i(0)}\delta_{0n}$ and $T_e^{i(0)} = x_i^{-1}\varphi_n^{i(0)}\delta_{0n}$ are nonperturbed fields of concentration and temperature generated by ith droplet.

The temperature distribution inside the ith droplet is determined by the following formula:

$$\tilde{T}_i^{(w)} = \varphi_n^{i(0)}\delta_{0n} + \sum_{n=0}^{\infty} (\varphi^i_{bn} B^i_{\nu_1\dots\nu_n} + (1 + \varphi^i_{qn}) Q^i_{\nu_1\dots\nu_n}) \overline{x^i_{\nu_1} \dots x^i_{\nu_n}}. \tag{36}$$

In (34)–(36)

$$\lambda_n^{i(0)} = \frac{(C_{1,s}^i(T_\infty) - C_{1,\infty})((n+1)k^{(e)} + nk_i^{(w)})}{(n+1)(k^{(e)} + \gamma^i D^{(e)} n^{(e)} Lm_1) + nk_i^{(w)}},$$

$$\lambda^i_{bn} = -\frac{\lambda_n^{i(0)}}{(C_{1,s}^i(T_\infty) - C_{1,\infty})},$$

$$\lambda^i_{qn} = \frac{(2n+1)k^{(e)}\gamma^i}{(n+1)(k^{(e)} + \gamma^i D^{(e)} n^{(e)} Lm_1) + nk_i^{(w)}},$$

$$\gamma^i = C_{1,s}^i(T_\infty)\frac{L\mu_1}{R_g T_\infty^2},$$

$$\varphi_n^{i(0)} = -\frac{(n+1)(C_{1,s}^i(T_\infty) - C_{1,\infty})Lm_1 n^{(e)} D^{(e)}}{(n+1)(k^{(e)} + \gamma^i D^{(e)} n^{(e)} Lm_1) + nk_i^{(w)}},$$

$$\varphi^i_{bn} = -\frac{\varphi_n^{i(0)}}{(C_{1,s}^i(T_\infty) - C_{1,\infty})},$$

$$\varphi^i_{qn} = \frac{-n(k_i^{(w)} - k^{(e)}) - (n+1)Lm_1 n^{(e)} D^{(e)}\gamma^i}{(n+1)(k^{(e)} + \gamma^i D^{(e)} n^{(e)} Lm_1) + nk_i^{(w)}}.$$

As can be seen from above formulas the coefficient of heat conductivity inside the droplet does not enter into the temperature and concentration distributions for $n = 0$. The analysis of these expressions and estimations of the coefficients for $n > 0$ show that for a cluster of droplets with high thermal conductivity the solution of the problem can be carried out in the region outside the droplets only.

Using expansion (28) the unknown coefficients $B^i_{\nu_1\dots\nu_n}$ and $Q^i_{\nu_1\dots\nu_n}$ can be found from the following system of equations:

$$B^i_{\nu_1\dots\nu_n} = B^{i(0)}_{\nu_1\dots\nu_n} + \sum_{\substack{j=1\\ j\neq i}}^{N}\sum_{k=0}^{\infty} (\lambda^j_{bk} B^j_{\mu_1\dots\mu_k} + \lambda^j_{qk} Q^j_{\mu_1\dots\mu_k}) \times \omega_{nk}\epsilon_j^{k+1}\epsilon_i^n \Omega_{\nu_1\dots\nu_n\mu_1\dots\mu_k}(\mathbf{L}_{ij}) \tag{37}$$

$$Q^i_{\nu_1\dots\nu_n} = Q^{i(0)}_{\nu_1\dots\nu_n} + \sum_{\substack{j=1\\ j\neq i}}^{N}\sum_{k=0}^{\infty} (\varphi^j_{bk} B^j_{\mu_1\dots\mu_k} + \varphi^j_{qk} Q^j_{\mu_1\dots\mu_k}) \times \omega_{nk}\epsilon_j^{k+1}\epsilon_i^n \Omega_{\nu_1\dots\nu_n\mu_1\dots\mu_k}(\mathbf{L}_{ij}) \tag{38}$$

where

$$B^{i(0)}_{\nu_1\dots\nu_n} = \sum_{\substack{j=1\\ j\neq i}}^{N} \lambda_0^{j(0)}\omega_{k0}\epsilon_j\epsilon_i^k \Omega_{\nu_1\dots\nu_n}(\mathbf{L}_{ij}) \text{ and}$$

$$Q^{i(0)}_{\nu_1\dots\nu_n} = \sum_{\substack{j=1\\ j\neq i}}^{N} \varphi_0^{j(0)}\omega_{k0}\epsilon_j\epsilon_i^k \Omega_{\nu_1\dots\nu_n}(\mathbf{L}_{ij}).$$

The solution of the above system of coupled linear algebraic equations can be found by Jacobi-Zeidel iterations with successive underrelaxation and can be calculated with any accuracy of the nth power of the small parameter ϵ. All the calculations in this study were performed with the accuracy $O(\epsilon^5)$.

Table 3 Formulation of parameters for the problem of condensation (evaporation) of a cluster of droplets containing a volatile and non volatile component

Conservation equation	$\tilde{\Gamma}_\phi$	Definitions of parameters
Mass (outside droplets)	$\nabla\tilde{C}^{(e)}$	$\tilde{C}^{(e)} = C_1^{(e)} - C_{1,\infty}$, $C_{1,\infty} = \lim_{\lvert\mathbf{r}-\mathbf{r}_i\rvert\to\infty} C_1^{(e)}$, $C_k^{(e)} = n_k^{(e)}/\sum_k n_k^{(e)}$
Energy (outside droplets)	$\nabla\tilde{T}^{(e)}$	$\tilde{T}^{(e)} = T^{(e)} - T_\infty$, $T_\infty = \lim_{\lvert\mathbf{r}-\mathbf{r}_i\rvert\to\infty} T^{(e)}$
Energy (inside droplets)	$\nabla\tilde{T}_i^{(w)}$	$\tilde{T}_i^{(w)} = T_i^{(w)} - T_\infty$, $i = \overline{1, N}$

As was suggested by Labowsky (1980a) for evaporating clusters it is more convenient to represent the obtained results in terms of correction factor. In the notations of the present solution, the heat and mass correction factors could be determined as follows:

$$\zeta_i = -\frac{1}{4\pi R_i \varphi_0^i}\int (\nabla \tilde{T}^{(e)}\mathbf{n}_r)|_{S_i} R_i^2 \sin\vartheta_i\, d\vartheta_i\, d\varphi_i$$

$$\eta_i = -\frac{1}{4\pi R_i \lambda_0^i}\int (\nabla \tilde{C}^{(e)}\mathbf{n}_r)|_{S_i} R_i^2 \sin\vartheta_i\, d\vartheta_i\, d\varphi_i \quad (39)$$

where $\varphi_0^i = \varphi_n^{i(0)}$ $(n = 0)$ and $\lambda_0^i = \lambda_n^{i(0)}$ $(n = 0)$.
Keeping only the first term in expansions (34), (35) we obtain

$$\zeta_i = 1 + \frac{\varphi_{b0}^i}{\varphi_0^i} B_0^i + \frac{\varphi_{q0}^i}{\varphi_0^i} Q_0^i, \quad \eta_i = 1 + \frac{\lambda_{b0}^i}{\lambda_0^i} B_0^i + \frac{\lambda_{q0}^i}{\lambda_0^i} Q_0^i. \quad (40)$$

The expressions for Sherwood and Nusselt numbers read:

$$\mathrm{Sh}_i = 2\,\frac{\lambda_0^i + \lambda_{b0}^i B_0^i + \lambda_{q0}^i Q_0^i}{\lambda_0^i + (1 + \lambda_{b0}^i) B_0^i + \lambda_{q0}^i Q_0^i},$$

$$\mathrm{Nu}_i = 2\,\frac{\varphi_0^i + \varphi_{b0}^i B_0^i + \varphi_{q0}^i Q_0^i}{\varphi_0^i + \varphi_{b0}^i B_0^i + (1 + \varphi_{q0}^i) Q_0^i}. \quad (41)$$

Finally, the rate of evaporation can be found from the Eq. (16) in which the value of mass flux q_1 takes the form

$$q_1^i = \int n D^{(e)} (\nabla \tilde{C}^{(e)}\mathbf{n}_r)|_{S_i} R_i^2 \sin\vartheta_i\, d\vartheta_i\, d\varphi_i. \quad (42)$$

(B) Interactive Evaporation and Growth of Clusters of Multicomponent Droplets With Arbitrary Volatile Components. Similar to the previous section, we consider a system containing N spherical multicomponent droplets immersed into a stagnant mixture of $\Lambda + 1$ components with temperature T_∞. It is assumed that Λ constituent species of the ambient gas mixture are volatile components of the droplet and $\Lambda + 1$th species is an ambient gas. The analysis of evaporation (condensation) of clusters of multicomponent droplets with arbitrary volatile components and small temperature differences in the neighborhood of the droplets will be performed in case of droplets composed of ideal mixtures. Ideal mixtures approximation can be used when mixtures are formed by substances with similar molecular properties (e.g., hexane-heptane, benzene-chlorobenzene, etc.). Since the characteristic times of heat and diffusion relaxation are small, we can consider the steady-state evaporation (condensation). Moreover as it was shown in the previous section when the coefficient of conductivity of droplets is much higher then the coefficient of heat conductivity of the ambient gas, the solution of the problem can be carried out in the domain outside the droplets only. Thus, under the above assumptions the linearized system of mass and energy conservation equations reads:

$$\nabla^2 \tilde{T}^{(e)} = 0, \quad \nabla^2 \tilde{C}_\beta^{(e)} = 0. \quad (43)$$

The boundary conditions for the above system of conservation equations (43) can be written as follows:

$$\tilde{T}^{(e)}|_{S_i} = \tilde{T}_i^{(s)}, \quad \tilde{C}_\beta^{(e)}|_{S_i} = \tilde{C}_{\beta,i}^{(s)} \quad (44)$$

$$k^{(e)}(\nabla \tilde{T}^{(e)}\mathbf{n}_r)|_{S_i} + \sum_{\beta=1}^{\Lambda} L_\beta m_\beta n^{(e)} \bar{D}_\beta (\nabla \tilde{C}_\beta^{(e)}\mathbf{n}_r)|_{S_i} = 0 \quad (45)$$

where the values $\tilde{T}^{(e)}$ and $\tilde{C}_\beta^{(e)}$ are defined similarly to the parameters shown in Table 3, subscript β denotes the number of species, and $\bar{D}_\beta$ is the effective diffusion coefficient.

Conditions at infinity read as

$$\tilde{C}_\beta^{(e)}|_{|\mathbf{r}-\mathbf{r}_i|} \to 0, \quad \tilde{T}^{(e)}|_{|\mathbf{r}-\mathbf{r}_i|} \to 0. \quad (46)$$

Using the approach described in the above sections, the following expressions for the temperature and concentration distributions in the neighborhood of the ith droplet were obtained:

$$\tilde{T}^{(e)} = T^{i(0)} + \sum_{n=0}^{\infty} (x_i^{-(2n+1)} \sum_{\beta=1}^{\Lambda} \alpha_{\beta,gn}^i G_{\beta,\nu_1\ldots\nu_n}^i + (1 + \alpha_{hn}^i x_i^{-(2n+1)}) H_{\nu_1\ldots\nu_n}^i \overline{x_{\nu_1}^i \ldots x_{\nu_n}^i} \quad (47)$$

$$\tilde{C}_\beta^{(e)} = C_\beta^{i(0)} + \sum_{n=0}^{\infty} \left(x_i^{-(2n+1)} \psi_{\beta,hn}^i H_{\nu_1\ldots\nu_n}^i + \left(1 + \gamma_\beta^i \sum_{l=1}^{\Lambda} \left[\alpha_{l,gn}^i - \frac{1}{\gamma_\beta^i}\delta_{l\beta} \right] x_i^{-(2n+1)} \right) G_{\beta,\nu_1\ldots\nu_n}^i \right) \overline{x_{\nu_1}^i \ldots x_{\nu_n}^i} \quad (48)$$

where

$$T_e^{(0)} = \alpha_0^i x_i^{-1}, \quad C_\beta^{i(0)} = \psi_\beta^{i(0)} x_i^{-1},$$

$$\psi_\beta^{i(0)} = C_{\beta,i}^{(s)}(T_\infty)\left(1 + \frac{L_\beta \mu_\beta}{R_g T_\infty^2}\alpha_0^i\right)$$

$$\alpha_{hn}^i = \frac{k^{(e)} n - (n+1)\sum_{\beta=1}^{\Lambda} L_\beta m_\beta n^{(e)} \bar{D}_\beta \gamma_\beta^i}{(n+1)(k^{(e)} + \sum_{\beta=1}^{\Lambda} L_\beta m_\beta n^{(e)} \bar{D}_\beta \gamma_\beta^i)},$$

$$\alpha_{\beta,gn}^i = \frac{(2n+1) L_\beta m_\beta n^{(e)} \bar{D}_\beta}{(n+1)(k^{(e)} + \sum_{\beta=1}^{\Lambda} L_\beta m_\beta n^{(e)} \bar{D}_\beta \gamma_\beta^i)},$$

$$\alpha_0^i = \frac{-\sum_{\beta=1}^{\Lambda} L_\beta m_\beta n^{(e)} \bar{D}_\beta C_{\beta,i}^{(s)}(T_\infty)}{k^{(e)} + \sum_{\beta=1}^{\Lambda} L_\beta m_\beta n^{(e)} \bar{D}_\beta \gamma_\beta^i},$$

$$\gamma_\beta^i = C_{\beta,i}^{(s)}(T_\infty)\frac{L_\beta \mu_\beta}{R_g T_\infty^2}, \quad \psi_{\beta,hn}^i = \gamma_\beta^i (1 + \alpha_{hn}^i),$$

and $\delta_{l\beta}$ is Kronecker's symbol.

Using formula (28), the unknown coefficients $G_{\beta,\nu_1\ldots\nu_n}^i$ and $H_{\nu_1\ldots\nu_n}^i$ can be found from the following system of linear algebraic equations:

$$H_{\nu_1\ldots\nu_n}^i = H_{\nu_1\ldots\nu_n}^{i(0)} + \sum_{\substack{j=1 \\ j\neq i}}^{N} \sum_{k=0}^{\infty} (\alpha_{hk}^j H_{\nu_1\ldots\nu_k}^j + \sum_{\beta=1}^{\Lambda} \alpha_{\beta,gk}^j G_{\beta,\nu_1\ldots\nu_k}^j)\Theta_{nk}^{(i,j)} \quad (49)$$

$$G_{\beta,\nu_1\ldots\nu_n}^i = G_{\beta,\nu_1\ldots\nu_n}^{i(0)} + \sum_{\substack{j=1 \\ j\neq i}}^{N} \sum_{k=0}^{\infty} \left(\psi_{\beta,hk}^j H_{\nu_1\ldots\nu_k}^j + \gamma_\beta^j \sum_{l=1}^{\Lambda} \left[\alpha_{\beta,gl}^j - \frac{1}{\gamma_\beta^j}\delta_{l\beta} \right] G_{\beta,\nu_1\ldots\nu_k}^j \right)\Theta_{nk}^{(i,j)} \quad (50)$$

where

$$\Theta_{nk}^{(i,j)} = \omega_{nk} \epsilon_j^{k+1} \epsilon_i^n \Omega_{\nu_1\ldots\nu_n\mu_1\ldots\mu_k}(\mathbf{L}_{ij}).$$

Similar to previous analysis, the solution of the above system of coupled linear algebraic equations can be found by Jacobi-Zeidel iterations with successive underrelaxation and can be calculated with any accuracy of the nth power of the small parameter ϵ.

In notations of the above solution, the heat and mass correction factors could be determined as follows:

$$\zeta_i = 1 + \frac{1}{\alpha_0^i} \sum_{\beta=1}^{\Lambda} \alpha_{\beta,g0}^i G_{\beta,0}^i + \frac{(1+\alpha_{h0}^i)}{\alpha_0^i} H_0^i$$

$$\eta_{\beta,i} = 1 + \frac{\gamma_\beta^{i(0)}}{\psi_\beta^{i(0)}} \sum_{l=1}^{\Lambda} \left[\alpha_{l,gn}^i - \frac{1}{\gamma_\beta^{i(0)}} \delta_{l\beta} \right] G_{\beta,0}^i + \frac{\psi_{\beta,hn}^i}{\psi_\beta^{i(0)}} H_0^i. \quad (51)$$

For simplicity, we assume that the total droplet volume equals to the sum of the mixing species volumes. The error of the latter approximation is about 2.5 percent. Then, using this approximation, the rate of evaporation can be found from the following system of equations:

$$\frac{dR_i}{dt} = -\sum_{\beta=1}^{\Lambda} \frac{m_\beta}{4\pi R_i^2 \rho_\beta^{(0)}} q_\beta^i(R_i, M_\beta^i)$$

$$\frac{dM_\beta^i}{dt} = -m_\beta q_\beta^i(R_i, M_\beta^i) \quad (52)$$

with the following initial conditions: $R_i = R_{i0}$, $M_\beta^i = M_{\beta,0}^i$ at $t = 0$.

In (52), $\rho_\beta^{(0)}$ is the density of pure βth species, $q_\beta^i(R_i, M_\beta^i)$ is the integral mass flux of βth species, and M_β^i is the mass of the βth species within the ith droplet.

3 Results and Discussion

The solutions derived in the previous sections have been applied to the analysis of interactions between multicomponent droplets and the effect of these interactions on evaporation (condensation) rates for variety configurations of evaporating (growing) clusters. The results were obtained for binary arrays and large clusters of droplets (i) composed of volatile components and (ii) composed of a volatile and a soluble nonvolatile component.

The results of calculation of Nusselt and Sherwood numbers for binary array of droplets consisting of a volatile and a soluble nonvolatile component are shown in Figs. 1 and 2 where two droplets of the same size but with different mole fraction of a volatile species (droplet 1, volatile species: 80 percent; droplet 2, volatile species: 20 percent) are considered. In the calculations it was assumed that the mixture of a volatile component and a soluble nonvolatile component constitutes the ideal solution; octane, heptane, and hexane were considered volatile components. As can be seen from these plots, Nusselt and Sherwood numbers strongly depend on the kind of volatile species and on the distance between droplets. When the relative distance tends to infinity (i.e., $L/R \to \infty$) Sherwood and Nusselt numbers asymptotically approach the value 2, appropriate for a single droplet. In a case when the relative distance decreases, Nusselt and Sherwood numbers of predominantly volatile droplet (droplet 1, with 80 percent volatile species) increase and Nusselt and Sherwood numbers of a droplet with a lower content of volatile component (droplet 2, with 20 percent volatile species) decrease. Therefore, at small distances between droplets, the evaporation rate of a droplet with a higher content of a volatile component increases and a droplet with lower content of a volatile component grows, and its surface temperature increases. Notably, Nusselt and Sherwood numbers increase beyond 2 when octane is the volatile species and the L/R ratio varies in the range from 2 to 3.

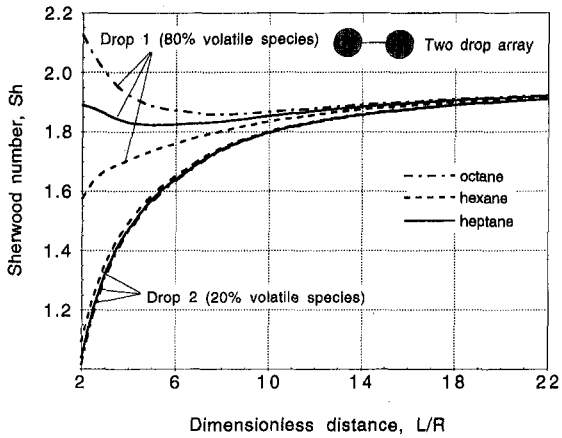

Fig. 2 Sherwood numbers for monosized binary array of droplets with volatile and nonvolatile species (drop 1–80 percent volatile species; drop 2–20 percent volatile species)

Interactive growth of droplets on hygroscopic nuclei is encountered in various environmental applications. In particular, small aerosol soluble particles act as nuclei for droplet condensation in atmospheric clouds. In this case, the mixture of a volatile component and a soluble nonvolatile component constitutes the non-ideal solution. In this connection, the evaporation of a binary array, comprised of a pure droplet and a droplet consisting of volatile and a nonvolatile soluble nucleus, was considered. The results of calculating the evaporation rate of a pure water droplet located in the neighborhood of a droplet consisting of water and a hygroscopic nucleus of NaCl are presented in Fig. 3. The calculations were performed for droplets with the radius 3 μm and for the ambient temperature T_∞ = 278 K, pressure p = 1 atm, mass of soluble nucleus M' =

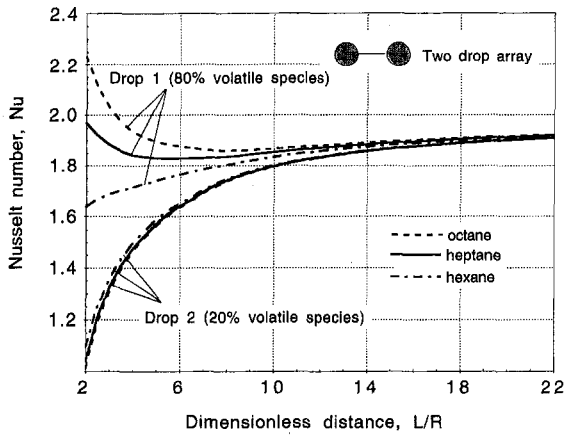

Fig. 1 Nusselt numbers for monosized binary array of droplets with volatile and nonvolatile species (drop 1–80 percent volatile species; drop 2–20 percent volatile species)

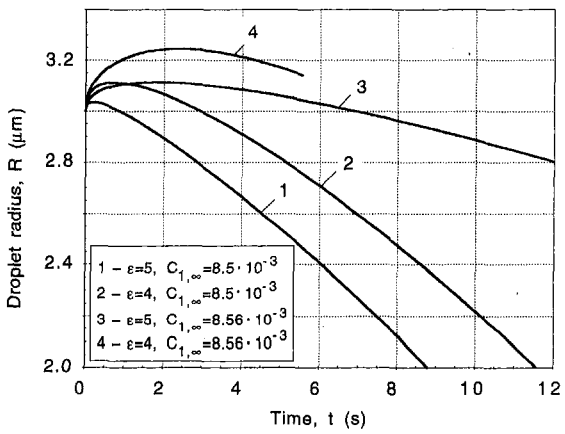

Fig. 3 Evaporation rate of pure water droplet located in the neighborhood of droplet consisting of water and hygroscopic nucleus of NaCl

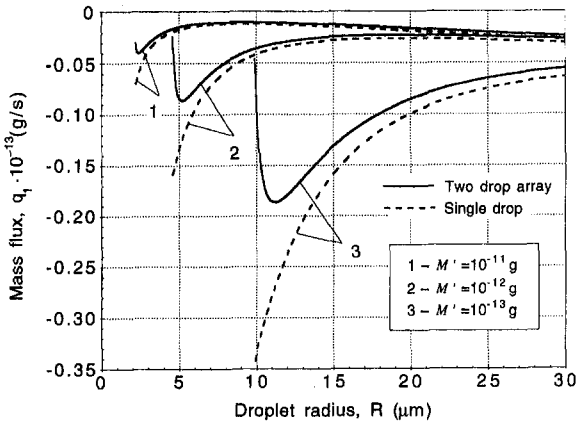

Fig. 4 Mass flux versus radius. Comparison the results obtained for a growing two monosized drop array and single drop contain hygroscopic nuclei NaCl (M'—the mass of hygroscopic nucleus).

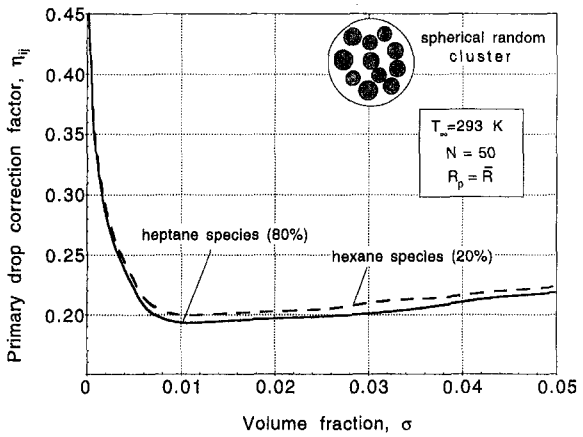

Fig. 6 Average mass correction factor of primary droplet versus volume fraction (radius of the primary droplet is equal to the average radius)

$10^{-10}g$ and various ambient concentrations of volatile species, and center-to-center distances (in this plot ϵ is the L/R ratio). As can be seen from this plot for the considered values of the center-to-center distances and ambient concentrations of volatile species, the pure water droplet grows first and only then the droplet begins to evaporate. In this instance, the droplet containing soluble nucleus (droplet 1) acts as a heat source and a mass sink that causes an increase of vapor concentration in the neighborhood of the droplet. Thus, the pure water droplet (droplet 2) located in the vicinity of droplet 1 grows. When the radii of the pure water droplet and salty droplet increase, the concentration of the solution within the droplet containing a soluble nucleus (droplet 1) decreases. The latter retards the condensation rate at the pure droplet and decreases vapor concentration in the vicinity of the droplets. Thus, inside the dense clusters and clouds containing pure droplets, droplets containing soluble nuclei heat and mass sources and sinks can occur. Therefore, when a dense cloud contains both pure water droplets and droplets containing soluble nuclei, interaction between temperature and concentration fields causes the growth of some droplets in a cluster and evaporation of other droplets. In the case of a finite symmetrical array of compositionally dissimilar interacting droplets this phenomena was originally predicted by Labowsky (1980a) who used the method of images. Later, the theoretical model of recondensation in multicomponent droplet arrays was developed using the point sources method by Annamalai (1993).

The dependence of mass flux on the radius for the array of two identical droplets containing hygroscopic nuclei of NaCl is shown in Fig. 4. In this plot, the solid lines denote the interacting droplets and the dashed lines denote the single droplets. The calculations were performed for the ambient temperature T_∞ = 278 K, ambient pressure p = 1 atm, dimensionless concentration of volatile species $C_{1,\infty}$ = 0.009 and various values of the nuclei's mass. As it can be seen from this plot, the dependence of the mass flux on droplet radius has the minimum in a case of interactive evaporation of droplets. The negative values of mass flux mean that condensation of droplets containing soluble nuclei occurs. Thus, in case of a monosized cluster of droplets the radius of hygroscopic nuclei, which enables the growth of the droplets in the cluster, can be calculated. In clusters with droplet size distribution, the size distribution of hygroscopic nuclei, which enables growth of droplets in a dense cluster, can be determined using the developed theory.

The results of calculation of the average mass correction factor for the primary droplet, $\bar{\eta}_p$, located inside a spherical cluster with log-normal distribution of droplet radii and uniform spatial distribution of droplet are shown in Fig. 5. Notably, the effect of droplet size distribution width on correction factor is small (see Elperin and Krasovitov, 1994b). The calculations were performed for a primary droplet (droplet located in the center of the cloud) with the radii equal to the average radius (solid lines) and 0.5 of average radius (dashed lines). In all calculations presented hereafter, droplet radii and center-to-center distances between droplets are normalized by the average radius. These results are obtained for N = 50 and 100 droplets (N is the number of droplets in the cluster) with octane as

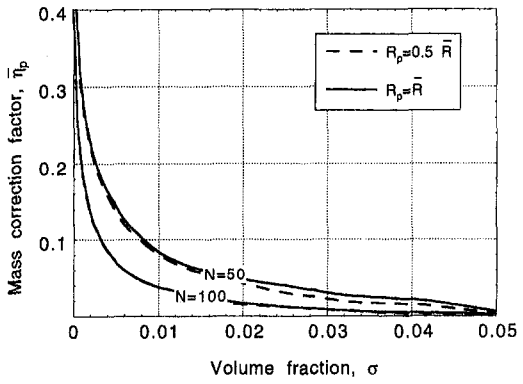

Fig. 5 Variation of average mass correction factor of primary droplet with volatile and nonvolatile component versus volume fraction (N—the number of droplets within the cluster)

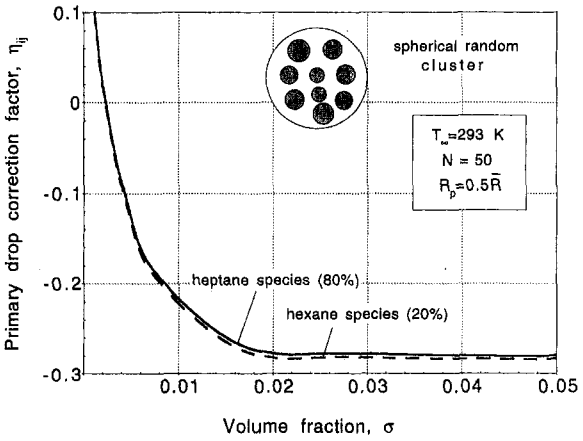

Fig. 7 Average mass correction factor of primary droplet versus volume fraction (radius of the primary droplet is equal to 0.5 of the average radius)

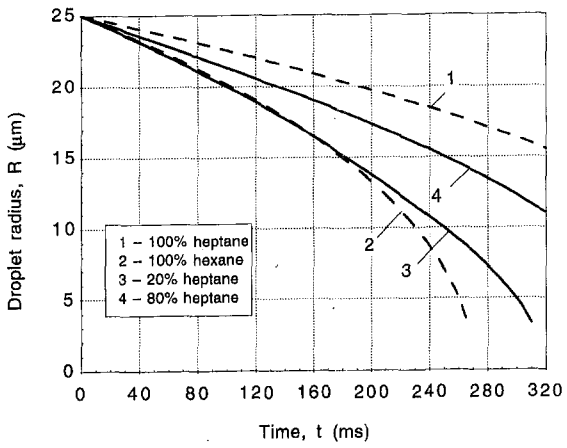

Fig. 8 Droplet radius versus time. Comparison of the results obtained for binary arrays of pure droplets (1—array of heptane droplets; 2—array of hexane droplets) with the results obtained for two drop array of heptane-hexane droplets (4—droplet 1: 80 percent heptane and 20 percent hexane, 3—droplet 2: 20 percent heptane and 80 percent hexane).

a volatile component (octane: 80 percent; soluble nonvolatile component: 20 percent) when the droplet volume fraction is up to five percent inclusive. Note that when droplet volume fraction equals five percent, the average center-to-center dimensionless droplet spacing L_{ij}/R_p (where R_p is the radius of the primary droplet) between neighboring droplets is of order 5, i.e., such clusters are fairly dense. The value of the correction factor for the primary droplet, $\overline{\eta}_p$, was calculated as an average from the calculations of the correction factor $\overline{\eta}_p$ for 100 various randomly sampled configurations of droplets in the cluster.

The results of calculating the average mass correction factor for the primary droplet located inside a spherical random cluster with log-normal distribution of droplet radii and uniform spatial distribution of droplet are shown in Figs. 6 and 7. The calculations were performed for a primary droplet (droplet located in the center of the cloud) with the radii equal to the average radius, Fig. 6, and 0.5 of average radius, Fig. 7. Similar to the previous in the calculations, droplet radii and center-to-center distances between the droplets are normalized by the radius of the primary (trial) droplet. These results are obtained for N = 50 droplets (N is the number of droplets in the cluster) composed of the binary mixture of 80 percent heptane and 20 percent hexane when the droplet volume fraction is up to five percent inclusive. As it can be seen from Fig. 6, the dependence of mass correction factors of heptane and hexane species on volume fraction has a minimum. Remarkably, the increase of the correction factor for more dense clusters occurs due to the phenomena of recondensation whereby evaporating droplets act as mass sources and heat sinks and growing droplets act as mass sink and heat sources. The calculations presented in Fig. 6 were performed for the primary droplet with the radius equal to the average radius of droplets in the cloud. The results of calculations for the primary droplet with 0.5 of the average radius are shown in Fig. 7. As it can be seen from this plot, the primary drop correction factor reverses sign in case of more dense clusters. The latter implies condensation of the primary droplet.

The solution presented above was applied to the analysis of interactions between multicomponent droplets composed of a binary mixture of volatile components. The dependencies of radius on time for an array of two multicomponent droplets is presented in Fig. 8. Droplet 1 has a composition of 80 percent heptane and 20 percent hexane and droplet 2 has a composition of 20 percent heptane and 80 percent hexane. The dashed lines, 1 and 2 in Fig. 8, are plotted for arrays of two heptane and hexane droplets of equal radii correspondingly. The calculations were performed for ambient temperature T_∞ = 283 K, ambient pressure p = 1 atm, and dimensionless concentration of volatile species $C_{\text{Hept},\infty} = 0$ and $C_{\text{Hex},\infty} = 0$.

4 Conclusions

The quasi-steady evaporation of multicomponent drop arrays and random clusters of multicomponent droplets has been studied using the modified method of expansion into irreducible multipoles developed by Elperin and Krasovitov 1994a, 1994b. The evaporation and growth of binary arrays and large random clusters of droplets (i) composed of volatile components and (ii) composed of a volatile and a nonvolatile component were considered. The analytical and numerical results of the investigation are presented in terms of heat and mass correction factors. Transient evaporation and condensation of multicomponent droplet clusters is analyzed, and the evaporation rate is determined. It is shown that for droplets of ideal solution with different compositions, Nusselt and Sherwood numbers depend on the concentration of components inside each droplet. When dense cloud contains both pure droplets and droplets containing soluble nuclei, interactions between temperature and concentration fields causes growth of some droplets in a cluster and evaporation of the other droplets. Remarkably, at a certain stage the growth of the droplets slows down and they begin to evaporate. The developed theory allows to determine the size distribution of hygroscopic nuclei which enables growth of droplets in a dense cloud. It is shown also that inside an evaporating large cluster of multicomponent droplets composed of volatile components, the phenomena of recondensation occurs whereby evaporating droplets act as mass sources and heat sinks and growing droplets act as mass sink and heat sources. The results of this study are of relevance in the analysis of dynamics of droplet size distribution in clouds, artificial modification of clouds and precipitation, in-cloud pollutants scavenging, and in-cloud analysis of evaporation and combustion of multicomponent (blended) fuels.

Acknowledgment

This work was partially supported by the German-Israeli Foundation for Scientific Research (Grant No. I-008-303.06/95).

References

Annamalai, K., Ramalingam, S., Dahdah, T., and Chi, D., 1988, "Group Combustion of a Cylindrical Cloud of Char/Carbon Particles," *Trans. ASME,* Vol. 110, pp. 190–200.

Annamalai, K., and Ryan, W., 1992, "Interactive Processes in Gasification and Combustion. Part I: Liquid Drop Arrays and Clouds," *Prog. Energy Combust. Sci.*, Vol. 18, pp. 221–295.

Annamalai, K., Ryan W., and Chandra, S., 1993, "Evaporation of Multicomponent Drop Arrays," ASME JOURNAL OF HEAT TRANSFER, Vol. 115, pp. 707–716.

Annamalai, K., Ryan, W., and Dhanapalan, S., 1994, "Interactive Processes in Gasification and Combustion—Part III: Coal/Char Particle Arrays, Streams and Clouds," *Prog. Energy Combust. Sci.*, Vol. 20, pp. 487–618.

Bellan, J., and Harstad, K., 1995, "Unsteady Injection of Sequences of Drop Clusters in Vortices Depicting Portions of a Spray," *Atomization and Sprays,* Vol. 5, pp. 17–44.

Carstens, J. C., Williams, A., and J. T. Zung, 1970, "Theory of Droplet Growth in Clouds: II Diffusional Interaction Between Two Growing Droplets," *J. Atmosph. Sci.*, Vol. 27(8), pp. 798–807.

Chiu, H. H., and Liu, T. M., 1977, "Group Combustion of Liquid Droplets," *Comb. Sci. Tech.*, Vol. 17, pp. 127–142.

Deutch, J. M., Felderhof, B. U., and Saxton, M. J., 1976, "Competitive Effects in Diffusion Controlled Reactions," *J. Chem. Phys.*, Vol. 11, pp. 4559–4563.

Eperin, T., and Krasovitov, B., 1994a, "Analysis of Evaporation and Combustion of Random Clusters of Droplets by a Modified Method of Expansion Into Irreducible Multipoles," *Atomization and Sprays,* Vol. 4(1), pp. 79–97.

Elperin, T., and Krasovitov, B., 1994b, "Combustion of Cylindrical and Spherical Random Clusters of Char/Carbon Particles," *Comb. Sci. Tech.*, Vol. 102(1–6), pp. 165–180.

Elperin, T., and Krasovitov, B., 1995, "Radiation, Thermal Diffusion and Kinetic Effects in Evaporation and Combustion of Large and Moderate Size Fuel Droplets," *Int. J. Heat and Mass Transfer,* Vol. 38(3), pp. 409–418.

Frank-Kamenetskii, D. A., 1969, *Diffusion and Heat Transfer in Chemical Kinetics,* Plenum Press, New York.

Heidenreich, S., and Ebert, F., 1995, "Condensatinal Droplet Growth as a Preconditioning Technique for the Separation of Submicron Particles From Gases," *Chem. Eng. Process.,* Vol. 34, pp. 235–244.

Hess, S., und Köhler, W., 1980, *Formeln zur Tensor—Rechnung,* Palm & Enke, Erlangen.

Labowsky, M., and Rosner, D. E., 1978, " 'Group' Combustion of Droplets in the Fuel Clouds: I. Quasi-Steady Predictions," *Adv. Chem. Ser.,* Vol. 166, pp. 63–79.

Labowsky, M., 1980a, "Transfer Rate Calculations for Compositionally Dissimilar Interacting Particles," *Chem. Eng. Sci.,* Vol. 35, pp. 1041–1048.

Labowsky, M., 1980b, "Calculation of the Burning Rates of Interacting Fuel Droplets," *Combust. Sci. Technol.,* Vol. 22, pp. 217–226.

Lefebvre, A. H., 1989, *Atomization and Sprays,* Hemisphere Publishing Co., New York.

Mason, B. J., 1971, *The Physics of Clouds,* 2nd ed., Clarendon Press, Oxford.

Ray, A. K., and Davis, E. J., 1980, "Heat and Mass Transfer With Multiple Particle Interactions: Part I. Droplet Evaporation," *Chem. Eng. Commun.,* Vol. 6, pp. 61–79.

Schmitz, R., and Felderhof, B. U., 1982, "Creeping Flow About a Sphere," *Physica,* Vol. 92A, pp. 423–437.

Tsai, J. T., and Sterling, A. M., 1991, "The Combustion of a Linear Droplet Array in a Convective Coaxial Potential Flow," *Combust. Flame,* Vol. 86, pp. 189–202.

Umemura, A., Ogawa S., and Oshima, N., 1981, "Analysis of Interaction Between Two Burning Fuel Droplets With Different Sizes," *Comb. and Flame,* Vol. 43, pp. 111–119.

Xiong, T. Y., Law, C. K., and Miyasaka, K., 1984, "Interactive Vapoarization and Combustion of Binarydroplet Systems," *20th Symposium (International) on Combustion,* pp. 1781–1787.

Yalamov, Yu. I., Schuckin, E. R., and Alekhin, E. I., 1990, "Calculation of Temperature and Concentration of Discontinuities in a Multicomponent Gas Mixture," *High Temp.,* Vol. 28(2), pp. 184–190.

Optimization of Pulsating Heating in Pool Boiling

J. V. C. Vargas
Assoc. Mem. ASME

A. Bejan
Fellow ASME

Department of Mechanical Engineering
and Materials Science,
Duke University,
Durham, NC 27708-0300

This paper describes an experimental and theoretical study of the periodic on and off heating of water on a horizontal surface. The heat transfer is effected by natural convection and isolated bubbles. The experiments cover the heat flux range 33–154 kW/m^2 and the wall excess temperature range 7–13°C. It is shown experimentally that the cycle-averaged thermal conductance between the surface and the pool can be maximized by properly selecting the time intervals of the on and off heating cycle. The maximum relative augmentation of the thermal conductance is approximately 15 percent. In the second part of the study, an order of magnitude analysis shows that the cycle-averaged thermal conductance can be maximized analytically by considering only the single-phase natural convection effect, and that the optimal time interval when heating is "on" agrees with the experimental results.

Introduction

Several recent studies have shown that pulsating heating can be used to maximize the overall time-averaged thermal conductance between a wall and a flowing fluid (Zumbrunnen, 1992; Kazmierczak and Chinoda, 1992; Lage and Bejan, 1993; Mantle et al., 1994; Antohe and Lage, 1994; Morega et al., 1995; Vargas and Bejan, 1995a, b; Mladin and Zumbrunnen, 1995; Brittingham et al., 1995; Bejan, 1997). The basic idea behind these studies is that the pulsation can be optimally "tuned" to the natural time scale of the flow. There are several ways of inducing pulsations in a convective configuration, for example, in the wall heating pattern, the flow rate, or both.

In the present study we examined the applicability of the pulsating heating process when the heat transfer mechanism is a combination of liquid natural convection and the formation of isolated bubbles. Our objective was to optimize a time-dependent process—a heating strategy—not to design an enhanced heat transfer surface. We used the same surface during the steady state and the many on and off regimes that we studied. We compared these regimes and demonstrated that the on and off regime can be optimized.

A literature survey showed that although there have been many investigations of steady pool boiling, the study of time-dependent pool boiling has attracted very limited attention. For example, Johnson (1971) simulated nuclear reactor excursions by experimenting with water and strips with exponentially increasing heat inputs. His conclusion was that transient nucleate boiling rates for exponential heat inputs are covered reasonably well by steady state nucleate boiling correlation techniques, although large increases in the critical heat flux are possible during highly transient circumstances. Sakurai and Shiotsu (1977a, b) experimented with exponentially heated horizontal wires in a study of reactivity accidents in water cooled nuclear reactors. They found that the transient boiling heat transfer coefficient registered after the commencement of boiling is lower than the steady boiling coefficient at the same heat flux. Bernardin and Mudawar (1994) studied transient boiling during the spray quenching of aluminum parts. Their interest was in achieving faster and more uniform cooling than during bath quenching. They evaluated the temperature-time history of the process and the changes occurring during the quench and concluded that surface roughness enhances the cooling rate significantly. The methods of augmenting nucleate pool boiling heat transfer were reviewed most recently by Thome (1992). Among these, enhanced nucleation, thin film evaporation, and two-phase convection in the reentrant channels (e.g., Nakayama et al., 1980a, b) are recognized as the primary modes for augmenting heat transfer.

A comprehensive review of the literature on quenching phenomena was presented by Nelson and Pasamehmetoglu (1992). This review provides insight into the existing models and covers the fundamental concepts that are relevant to time-dependent boiling. In addition, Pasamehmetoglu and Nelson (1991) documented the effect of site distribution on the nucleate boiling curve. They concluded that as the site distribution becomes less uniform, the average surface temperature and the temperature variations along the boiling surface increase.

In brief, the existing studies of time dependent pool boiling did not consider the optimization of the periodic heating process. The boiling regime considered in this paper is dominated by natural convection with limited bubble generation. The objectives of the present study were to study this phenomenon and to optimize the on and off heating cycle for maximum augmentation effect. In the first part we showed experimentally that the time-averaged heat transfer coefficient for pulsating heating can be greater than for steady heating, and that this augmentation effect can be maximized by properly selecting the pulse period or frequency. In the second part of our study we constructed an order of magnitude analysis, to first explain the existence of an optimal pulse period, and, second, to anticipate analytically the order of magnitude of the optimal pulse period.

Experiments

We began our study with several series of experiments in the natural convection and isolated bubbles regime in a saturated water pool heated from below. The objectives of these experiments were (1) to demonstrate through repeatable measurements the existence of an optimal heat pulse interval for maximum cycle-average thermal conductance, (2) to determine the range of conditions where optimized pulse-heating means "heat transfer augmentation" relative to steady boiling, and (3) to generate a sufficient volume of measurements against which to test the theoretical predictions described in the next section.

Apparatus. The main features of the experimental apparatus are shown in Fig. 1. Water boiled at atmospherical pressure in a well insulated cylindrical vessel made out of aluminum. The wall of the vessel and the heat transfer surface were 1.5

Contributed by the Heat Transfer Division for publication in the JOURNAL OF HEAT TRANSFER. Manuscript received by the Heat Transfer Division August 6, 1996; revision received January 17, 1997; Keywords: Boiling, Natural Convection, Transient & Unsteady Heat Transfer. Associate Technical Editor: R. Nelson.

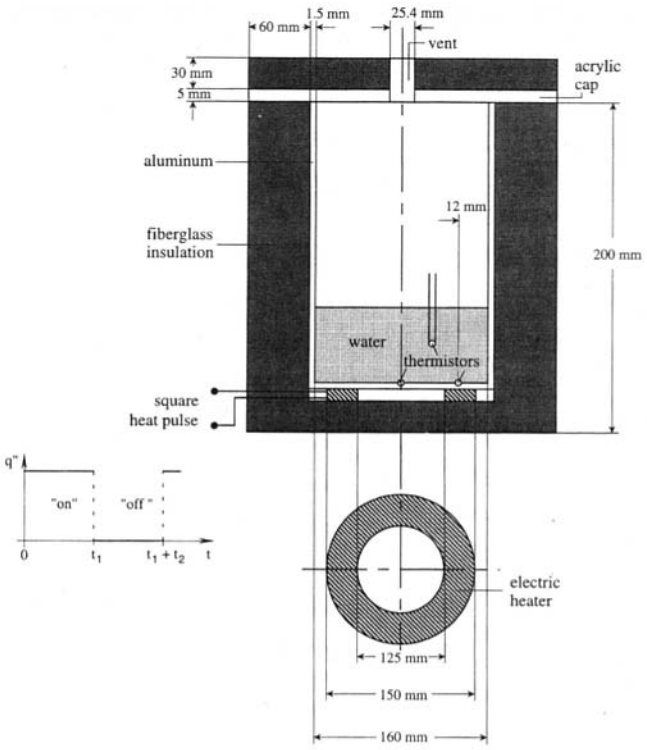

Fig. 1 The main features of the experimental apparatus and the square-wave heat input

mm thick. A flat annular electric heater was attached to the bottom of the aluminum vessel with high conductivity epoxy. The heater has a maximum power of 1200 W at 120 V, and a nominal resistance of 12 Ω. The dimensions of the aluminum vessel and electric heater are indicated directly on Fig. 1. The vessel was covered with an acrylic lid fitted with a boil-off vent. The assembly was wrapped all around with a 6 cm thick layer of fiberglass insulation. It is worth pointing out that the features of the apparatus were selected intentionally to resemble the features of a commercial hot surface for boiling water. We wanted to show that an optimal pulsating boiling regime exists in common (practical) designs, not in idealized laboratory setups. In the experiments we compared steady heating with pulsating heating of several frequencies by using the same heat transfer surface. Therefore, given the process optimization objective of our study, the detailed features and defects (e.g., nucleation sites) did not change from one run to the next. Furthermore, as we shall see in the concluding sections of the paper, the effect of bubble formation was dominated by single-phase convection.

Two high precision thermistors (resistance 2250 Ω at 25°C) were embedded to a depth of 1 mm on the water side of the bottom surface of the aluminum vessel. This thermistor type has a standard Bead I with a 2.4 mm diameter. A layer of heat sink silicone was placed between thermistors and aluminum. One thermistor was placed in the center of the bottom surface and the other above the mid-circle of the ring heater. A third thermistor was lowered to various depths in the water pool. Since in the present experiments natural convection was an important mechanism, the presence of the two thermistors was not expected to influence the heat transfer process. This and other features of the simple apparatus used in these experiments are justified because our objective was to optimize a process: we compared many pulsating heating regimes with the steady-state regime by using the same surface.

As shown on the left side of Fig. 1, the pulse is a step function (on and off), with constant heat flux from $t = 0$ to $t = t_1$, and zero heat flux during the next interval of length t_2. We designed and built the adjustable electronics needed to assemble our own square-wave heat pulse generator. The time intervals of the on and off cycle (t_1, t_2) were controlled by a dual timer integrated circuit, which controls a relay that interrupts the power supply. The time ratio t_1/t_2 can be adjusted: in these experiments we used $t_1/t_2 = 0.5$, 1 and 2. All the time interval settings were adjusted using a chronometer with a bias limit of ±0.01 s. The power input to the electric heater was held constant during each t_1-long interval during every run.

The function of the thermistors was to measure the instantaneous temperature of the bottom surface and to identify the maximum temperature of the bottom surface (T_{max}) during the on and off cycle. The maximum difference between the readings provided by the bottom thermistor placed above the heater and the thermistor placed in the center of the bottom wall was 0.6°C. This suggests that the heat transfer surface corresponded to a sufficiently uniform site distribution: recall that a nonuniform site distribution promotes a large span between the minimum and maximum surface temperatures, cf. Pasamehmetoglu and Nelson (1991). Since the average temperature is the quantity used in plotting the steady-state boiling curve, the results obtained in this study can be compared with previously published results.

The third thermistor monitored the water pool temperature during each run: this temperature was invariably the saturation temperature T_{sat} = 100°C, with deviations less than ±0.1°C. According to the manufacturer (YSI, 1993), the time needed by the thermistor to indicate a newly impressed temperature is less than 1 s when the temperature difference is 200°C. Since in the present experiments the maximum temperature difference was 13°C, we are confident that our temperature measurements were accurate even sooner, for example, after 0.5 s.

The thermistor readings were taken with an ohmmeter capable of measuring resistances as small as 10^{-3} Ω in the temperature range near the saturation temperature, and as small as 10^{-4} Ω in the range near the nominal resistance of the heater. In this way we were able to measure the maximum temperature difference that occurs during steady-periodic heat transfer conditions, $\Delta T_{max} = T_{max} - T_{sat}$. By convention, the steady-periodic

Nomenclature

A = heat transfer area
B = bias limit
g = gravitational acceleration
k = thermal conductivity of liquid water
P = precision limit
q'' = heat flux during t_1 interval
$\bar{q}''$ = cycle-averaged heat flux
R = heater resistance
t = time
t_{th} = time scale of thermal formation
t_1 = time interval when heater is on
t_2 = time interval when heater is off
T = temperature
ΔT = wall excess temperature, $T - T_{sat}$
U = uncertainty limit
V = voltage
α = thermal diffusivity of liquid water
β = coefficient of volumetric thermal expansion
δ = thermal diffusion thickness
ν = kinematic viscosity of liquid water

Subscripts

max = maximum
opt = optimal
sat = saturation
th = thermals

Table 1 Measured times and maximum temperature differences, and the uncertainties in the pulsating heat experiments, each pair of values represents ΔT_{max} (°C)/$U_{\Delta T_{max}}$ (°C)

t_1 (s)	q'' (kW/m^2) = 100			154.3		
	t_1/t_2 = 0.5	1	2	0.5	1	2
0.5		7.922/0.078				
0.7	6.763/0.100				9.336/0.090	
0.8		7.828/0.102		8.460/0.120		
1.0						10.251/0.086
1.5		7.642/0.111				
1.6			8.390/0.150			
1.8					9.108/0.172	
2.0	6.509/0.104			8.150/0.086		
2.3						10.062/0.104
2.6			8.292/0.144			
3.0		7.534/0.072			8.909/0.136	
3.4	6.658/0.144		8.119/0.190			
4.0				8.744/0.112		
4.2					8.862/0.160	
4.4						9.964/0.106
5.0		7.470/0.065	7.820/0.150			10.02/0.160
5.4					9.160/0.170	
6.0		7.520/0.082				
6.5	7.558/0.152					
7.0		7.610/0.093		9.336/0.126		10.17/0.106
7.2			7.876/0.100			
7.4					10.001/0.108	
8.0		7.750/0.081				
8.7	7.899/0.100					
10.0		8.124/0.076				
11.0						10.62/0.174
13.0					10.777/0.150	
14.0		8.520/0.068	9.183/0.200			
15.0				10.921/0.198		11.032/0.138
20.0			9.650/02.00			
23.0	8.882/0.144	9.120/0.128				
30.0					11.537/0.224	
34.0				11.75/0.188		
37.0						12.107/0.172
60.0	9.479/0.246	9.716/0.299	10.08/0.158	11.86/0.268	11.927/0.252	12.323/0.208

regime was reached when the wall temperature history during one on and off cycle matched the history of the next cycle within a specified (small) temperature band, which in this study was set at ±0.5°C. The ±0.5°C deviation occurred either in the very beginning of the cycle or in the final part of the cycle, with little influence on T_{max} and the cycle-averaged temperature. The largest observed deviation of T_{max} (plateau temperature) was ±0.1°C in the steady-periodic regime. The possible influence of the overall water circulation (tank geometry) was investigated by varying the pool depth. Since no significant change in T_{max} was detected, all the runs were conducted by using the same pool depth.

The heat flux generated during the t_1 (''on'') interval q'' was adjusted through a variable resistor the voltage (V) of which was set at 80 and 100 V. The corresponding cycle-averaged heat flux was calculated using

$$\bar{q}'' = \frac{V^2}{RA(1 + t_2/t_1)} = \frac{q''}{1 + t_2/t_1} \tag{1}$$

where R and A are the resistance and the contact surface of the heater, respectively. It is worth noting that the choice of measuring ΔT_{max} (as opposed to the average temperature difference $\overline{\Delta T}$) is conservative since later we are reporting and comparing the values of the heat transfer coefficient $\bar{q}''/\Delta T_{max}$, which is smaller than $\bar{q}''/\overline{\Delta T}$.

Procedure. We performed our own thermistor calibration to determine the bias limits. The thermistor was immersed in a constant temperature bath maintained by a bath circulator, and a total of 64 temperature measurements were made at 80, 90, . . . , 120°C. The bias limit was set at ±0.001°C for all thermistors (Howle et al., 1992; Dally et al., 1993). The precision limits for the heat flux calculated with Eq. (1) were determined using the propagation line of Kline and McClintock (Editorial, 1993):

$$\frac{P_{\bar{q}''}}{\bar{q}''} = 2\frac{P_V}{V} \tag{2}$$

$$\frac{B_{\bar{q}''}}{\bar{q}''} = \frac{[1 + (t_2/t_1)^2]^{1/2}}{1 + t_2/t_1} \cdot \frac{B_{t_1}}{t_1}. \tag{3}$$

The laboratory is a temperature controlled environment without windows, therefore, the variations in room pressure, temperature, and humidity were negligible. In the calculation of the precision limit for the measured $\bar{q}''$, the contributions made by the precision limits of t_1, t_2, R, and A were found to be negligible relative to the precision limit of V. The time measurement contributions were negligible because once the electronic timer was adjusted, the time intervals were reproduced identically in all the runs. In the calculation of the bias limits for $\bar{q}''$, the time bias limit was the most important contribution because the voltage and resistance bias limit provided by the multimeter, $\pm 10^{-6}$ V and $\pm 10^{-4}$ Ω, respectively, were very small in comparison with the time bias limit of the chronometer used in the timer adjustment.

The precision limit for the measured t_1 was negligible relative to the bias limit in the calculation of the uncertainty because an electronic time control method was used. The precision limit for the temperature measurements was calculated as twice the standard deviation of each set (ten values per point) of observations for ΔT_{max}. The uncertainty limits for ΔT_{max}, $\bar{q}''$, and t_1

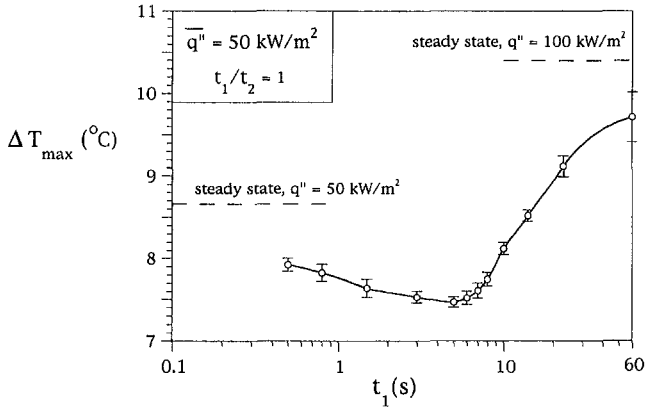

Fig. 2 The effect of the heat pulse interval t_1 on the maximum temperature difference between the wall and the water pool

were calculated using the standard formulas (Editorial, 1993), and the results are summarized in Table 1. In addition, U_{t_1} was equal to 0.01 s in all measurements, and the largest computed $U_{\bar{q}''}/\bar{q}''$ was 0.022.

Results. Figure 2 shows the main features of the measurements collected during one run. The heat flux during the "on" interval was fixed at $q'' = 100$ kW/m^2, and so was the on/off time ratio, $t_1/t_2 = 1$. The corresponding (fixed) cycle-averaged heat flux was $\bar{q}'' = 50$ kW/m^2. Steady-periodic regimes were created for 12 different t_1 values that cover the range 0.5 s–60 s. The bias limit of the chronometer used in the calibration of the electronic timer was 0.01 s, therefore, we found it appropriate to use t_1 intervals greater than 0.5 s to guarantee the accuracy of the measured time intervals. The measured ΔT_{max} values and the calculated precision limits show that ΔT_{max} is minimum when t_1 is approximately 5 s. This means that the thermal conductance $\bar{q}''/\Delta T_{max}$ between the wall and the water pool is maximum at a certain measurable pulse period or frequency.

Figure 2 also shows the ΔT_{max} measurements made in the two t_1 extremes. The $t_1 \to \infty$ limit means that the heater is left "on" forever (at $q'' = 100$ kW/m^2), which is why we wrote "steady state" next to the dashed line, indicating the measured ΔT value. In reality, when t_1 is large but finite, the wall temperature exhibits wide excursions between the $t_1 \to \infty$ asymptote (ΔT_{max}) shown in the figure and the lowest temperature in the system (T_{sat}). The opposite extreme, $t_1 \to 0$, corresponds to steady heating at a q'' value that is equal to the cycle-averaged value, namely, 50 kW/m^2. The measured steady ΔT value is also indicated with a dashed horizontal line: it is with respect to this line that we evaluate the thermal contact augmentation effect achieved by fine-tuning t_1. The minimum ΔT_{max} value registered at $t_1 \cong 5$ s was 14 percent smaller than the steady ΔT measured in the $t_1 \to 0$ limit.

We found that the features of the run presented in Fig. 2 were reproduced by the data collected in all the runs (total runs = 6). Three additional examples are illustrated in Figs. 3(a, b) and 4 where we note that the precision limits on ΔT_{max} are nearly the same as in Fig. 2. Figures 3(a) and 3(b), in association with Fig. 2, show the effect of varying the on/off ratio t_1/t_2 while holding the "on" heat flux q'' fixed. Three changes occur as t_1/t_2 increases: $\bar{q}''$ increases, the steady ΔT value measured in the $t_1 \to 0$ limit increases, and the minimum of the ΔT_{max} versus t_1 curve shifts toward larger optimal t_1 values.

Figure 4 should be compared with Fig. 2 to see what changes occur when the run is repeated at a higher heat flux during the "on" interval. All the ΔT_{max} measurements rise, however, the shape of the ΔT_{max} versus t_1 curve does not change. Even the optimal t_1 interval for minimum ΔT_{max} appears to be insensitive to the increase in q'' from Fig. 2 to Fig. 4.

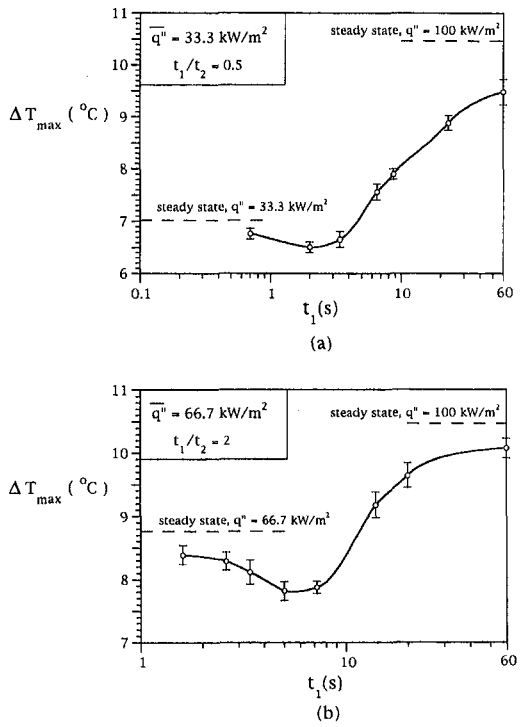

Fig. 3 The effect of changing the time ratio t_1/t_2 relative to the run exhibited in Fig. 2

Figures 5(a) and 5(b), in combination with Fig. 4, show the effect of changing the time ratio t_1/t_2 when the heat flux is high: $q'' = 154.3$ kW/m^2. Once again, the optimal t_1 interval increases as t_1/t_2 increases: this observation reinforces the trend revealed by the runs conducted at the lower heat flux (Figs. 2, 3(a, b)).

To summarize, Figs. 2–5 demonstrate conclusively that an optimal on and off period exists such that the thermal conductance $\bar{q}''/\Delta T_{max}$ is maximized. Figures 6 and 7 summarize the maximum thermal conductance and optimal pulse interval results obtained in the experimental phase of our study. Although the increase in $\bar{q}''/\Delta T_{max}$ registered when t_1 is optimal is generally of the order of 15 percent, the results of Fig. 6 indicate that maximum augmentation occurs when t_1/t_2 is close to 1. Figure 6 also suggests that the augmentation effect becomes stronger as the heat flux decreases: to this effect we return in the next section. Figure 7 summarizes the $t_{1,opt}$ trends noted

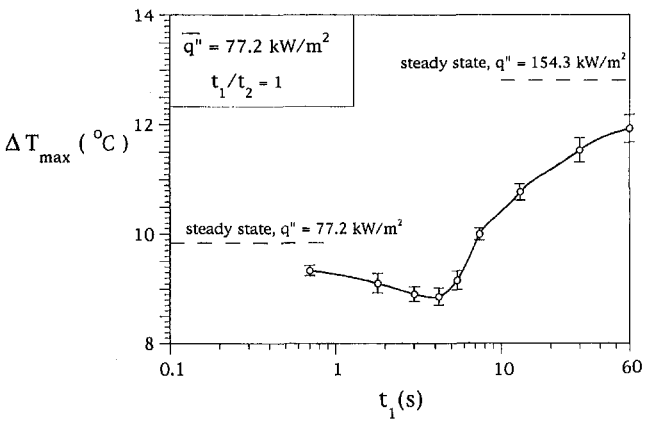

Fig. 4 The effect of increasing the heat flux q'' relative to the run exhibited in Fig. 2

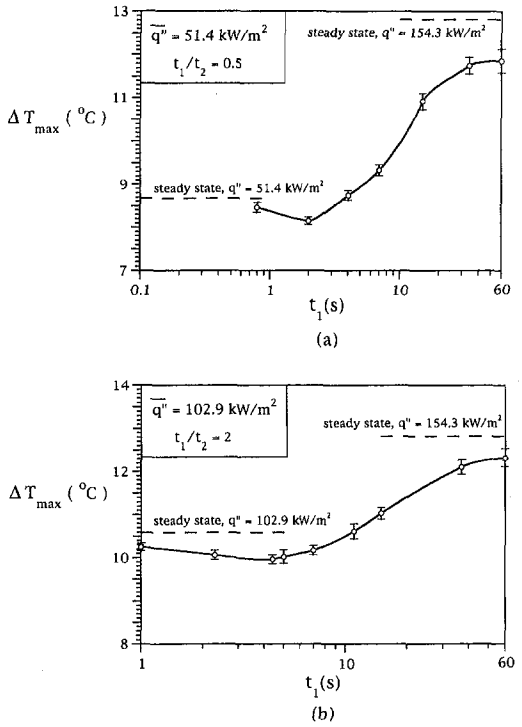

Fig. 5 The effect of changing the time ratio t_1/t_2 relative to the run exhibited in Fig. 4

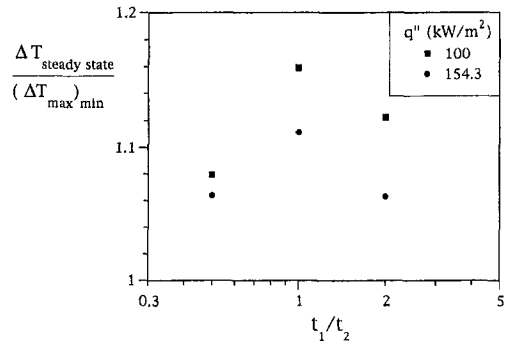

Fig. 6 Summary of the maximum heat transfer augmentation results determined experimentally

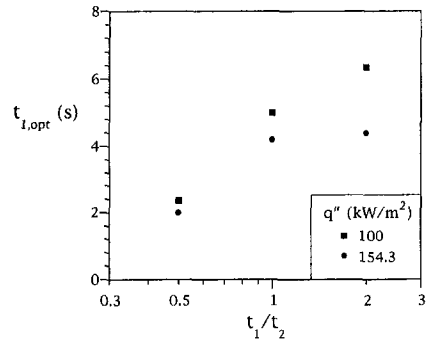

Fig. 7 Summary of the optimal heat-interval results determined experimentally

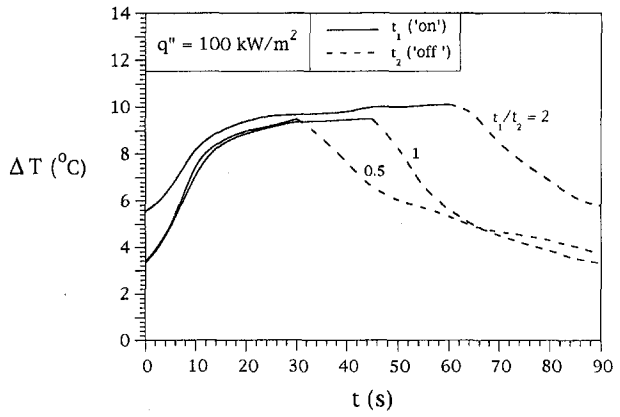

Fig. 8 The wall temperature history during a complete on and off cycle

earlier, namely, that $t_{1,opt}$ increases as t_1/t_2 increases, and that $t_{1,opt}$ is relatively insensitive to increasing the heat flux. The augmentation phenomenon is related to the effect reported by Zumbrunnen and Balasubramanian (1995) in which the air bubbles injected into an impinging liquid jet triggered the renewal of the boundary layer. The augmentation effect maximized in Figs. 2–7 was measured relative to the steady-state regime associated with a heat flux equal to the cycle-averaged heat flux (see the $t_1 \rightarrow 0$ asymptotes in Figs. 2–5).

As an introduction to the theoretical argument constructed in the next section, we end this experimental part with a view of the temperature history of bottom wall surface during a complete on and off cycle after a sufficiently long experiment in which the steady-periodic regime was well established. The three ΔT versus t traces shown in Fig. 8 were recorded with the thermistor placed right above the heater (Fig. 1), and correspond to the $q'' = 100$ kW/m^2 runs seen earlier in Figs. 2, 3(a), and 3(b). One point is exhibited from each one of these figures, as seen in the following table:

	$t_1/t_2 = 0.5$ (Fig. 3a)	$t_1/t_2 = 1$ (Fig. 2)	$t_1/t_2 = 2$ (Fig. 3b)
t_1	30 s	45 s	60 s
$t_1 + t_2$	90 s	90 s	90 s

For example, in Fig. 8 the $t_1/t_2 = 2$ curve shows that the wall temperature increases, reaching a plateau during the "on" time interval. The maximum ΔT recorded during this interval is the ΔT_{max} value presented in Figs. 2–5. The wall temperature decays partially during the "off" time interval. The key message of the periodic variation of ΔT versus t is that the wall thermal inertia plays a role, which, as we show next, is important because it smoothes (tends to hide) the effect of t_1 on the minimization of ΔT_{max}. The wall inertia is also important because it is a permanent feature in the construction of commercial hot surfaces for boiling water.

Theoretical Considerations

The existence of an optimal "on" interval can be anticipated based on a scale analysis of the time-dependent development of natural convection in the liquid phase. Assume that the heating (q'') is turned on at $t = 0$ and that the liquid is motionless. The thickness of the water layer heated by the bottom surface increases in time because of thermal diffusion,

$$\delta \sim (\alpha t)^{1/2}. \tag{4}$$

The temperature difference between the wall and the bulk liquid (ΔT) must also increase as $t^{1/2}$ because q'' is constant:

$$\Delta T \sim \frac{q''}{k}\,\delta. \tag{5}$$

The heated layer (δ) becomes unstable and gives birth to thermals at a time (t_{th}) when the Rayleigh number based on height [$\delta_{th} \sim (\alpha t_{th})^{1/2}$] and vertical temperature difference ($\Delta T_{th} \sim q''\delta_{th}/k$) become comparable with the order of magnitude associated with the onset of Benard convection (Bejan, 1993; p. 372):

$$\frac{g\beta}{\alpha\nu}\,\delta_{th}^3 \Delta T_{th} \sim 2000. \tag{6}$$

Combining Eqs. (4)–(6) we find that the time scale for the formation of thermals is

$$t_{th} \sim \left(2000\,\frac{k\nu}{q''\alpha g\beta}\right)^{1/2}. \tag{7}$$

By substituting $q'' = 10^5$ W/m^2 and the properties of saturated water at 100°C into Eq. (7) we find $t_{th} \sim 2$ s, which in the language of scale analysis means "seconds." This time scale agrees with the time scale of the present experiments and is orders of magnitude greater than the time scale of bubble formation.

The heating process continues until $t = t_1$. We distinguish two scenarios depending on whether t_1 is smaller or greater than t_{th}.

$t_1 < t_{th}$. When thermals do not form while the heating is on, the excess temperature ΔT reaches its highest value at the end of the heating interval:

$$\Delta T_{max} \sim \frac{q''}{k}\,(\alpha t_1)^{1/2}. \tag{8}$$

Equations (1) and (8) show that the overall thermal conductance varies as $t_1^{1/2}/(t_1 + t_2)$:

$$\frac{\overline{q''}}{\Delta T_{max}} \sim \frac{k}{\alpha^{1/2}} \cdot \frac{t_1^{1/2}}{t_1 + t_2}. \tag{9}$$

This quantity has a maximum with respect to t_1 that occurs when

$$t_{1,opt} = t_2. \tag{10}$$

This behavior and the order-of-magnitude conclusion, $t_{1,opt} \sim t_2$, are supported by the minima of the ΔT_{max} curves determined experimentally (Figs. 2–5).

It is worth noting that we reach the same conclusion if, instead of ΔT_{max}, we use the time averaged temperature difference $\overline{\Delta T}$ in the heat transfer coefficient defined in Eq. (9). Specifically, according to Eqs. (4) and (5) the temperature difference averaged over the interval t_1 is simply $\overline{\Delta T} = (\frac{2}{3})\Delta T_{max}$, because ΔT increases as $t^{1/2}$. In other words, the definition of the heat transfer coefficient does not change the analytical form of Eq. (9), which is dictated by the function $t_1^{1/2}/(t_1 + t_2)$.

$t_1 > t_{th}$. When the heating interval extends beyond the departure time of thermals, the time growth of δ and ΔT is terminated at $t \sim t_{th}$. This event is characterized by the maximum temperature difference

$$\Delta T_{max} \sim \frac{q''}{k}\,(\alpha t_{th})^{1/2} \tag{11}$$

which is fixed by t_{th}, i.e., constant, not a function of t_1. If t_1 is considerably greater than t_{th}, then a number ($\sim t_1/t_{th}$) of thermals rise successively from the same region of the wall, and the maximum temperature difference continues to be represented by the ceiling given in Eq. (11). In combination with Eq. (1), this conclusion means that the overall thermal conductance effect due to liquid natural convection,

$$\frac{\overline{q''}}{\Delta T_{max}} \sim \frac{k}{(\alpha t_{th})^{1/2}}\,\frac{t_1}{t_1 + t_2}, \tag{12}$$

does not exhibit a maximum with respect to t_1, in fact it levels off at constant of order $k/(\alpha t_{th})^{1/2}$.

In summary, to search for a conductance maximum we must look in the opposite direction (decreasing t_1) and, according to the first scenario ($t_1 < t_{th}$), the maximum manifests itself first when $t_1 \sim t_{th}$. Combining this with Eq. (10) we conclude that the conductance maximum occurs when the heat pulse matches the time scale of single-phase natural convection:

$$t_{1,opt} \sim t_2 \sim t_{th}. \tag{13}$$

This conclusion is in accord with all our experiments. We saw that the optimal t_1 and t_2 intervals measure several seconds as the t_{th} scale for saturated liquid water.

A more direct alternative to Eq. (13) is to recognize first the natural time scale of single-phase natural convection (thermals), Eq. (7), and to argue that the maximum thermal conductance occurs when the heat pulses are in step with t_{th}. This "resonance" argument is supported by several earlier studies which were reviewed in the introduction. In the present case (significant single-phase natural convection with isolated bubbles) resonance means that the on and off heating administered by the wall has the ability to "organize", in time and space, the formation and departure of thermals. This interaction is similar to the organization displayed by turbulent jets exposed to a lateral loud speaker (e.g., buoyant plume, Kimura and Bejan, 1983).

Next to the time scale of a few seconds, another feature that supports the view that the conductance maximum is governed by the time scale of single-phase natural convection is the fact that the augmentation effect (Figs. 2–5) decreases as q'' and ΔT increase. The opposite direction—a sharper maximum at smaller q'' and ΔT—means that the augmentation effect is a natural convection feature. Further support is provided by the recent study of Ammerman and You (1996): their Fig. 9 shows that at a heat flux of 100 kW/m^2, the heat transfer by boiling (latent heat, bubble generation) is roughly 50 percent, and it increases to about 75 percent when the heat flux is 150 kW/m^2. This means that in the same range, the importance of natural convection diminishes, which agrees with the phenomenological explanation provided in this section.

Conclusion

In this study we showed experimentally that the on and off heating cycle of a surface with pool boiling can be optimized for maximum cycle-averaged thermal conductance. There is an optimal period or frequency of pulse heating (Figs. 2–7), and among these optimal results there is an optimal on/off time ratio, $t_{1,opt} \sim t_2$ (Fig. 6).

The present water experiments covered only the ΔT range associated with the combined effects of liquid natural convection and isolated bubbles. It is quite probable that the augmentation optimization principle demonstrated experimentally can be exploited at other ΔT's along the boiling curve, especially in the direction $\Delta T \to 0$, as well as in single-phase natural convection without boiling.

The maximum relative augmentation effect of approximately 15 percent (Fig. 6) is a realistic indicator of what can be accomplished in practice by fine-tuning the on and off heating cycle. It is realistic because the experimental apparatus had the features of a commercial water heater, namely, wall thermal inertia, and fin conduction along the wall, from heated spots to unheated spots. Such features tend to smooth the $\Delta T(t)$ variation during the on and off cycle and to obscure the optimization with respect

to t_1. It is quite probable that a maximum relative augmentation greater than 15 percent could be achieved with special laboratory apparatuses in which the wall inertia and fin effects are absent. Such a possibility deserves future study, especially now that the on and off optimization principle was demonstrated under conservative conditions.

Regarding the size of the increase in heat transfer coefficient (large or small?) the appropriate design question is quite different: "What is the easiest (cheapest, most robust) way to achieve this increase?" To pulsate the electrical current through the heater is attractive, in comparison with other (e.g., mechanical, invasive) methods. This is why pulsating heat transfer and unsteady heating, in general, are attracting interest across the wide spectrum of heat transfer engineering (Bejan, 1996).

Acknowledgment

This research was supported by a grant from the National Science Foundation.

References

Ammerman, C. N., and You, S. M., 1996, "Determination of the Boiling Enhancement Mechanism Caused by Surfactant Addition to Water," ASME JOURNAL OF HEAT TRANSFER, Vol. 118, pp. 429–435.

Antohe, B. V., and Lage, J. L., 1994, "A Dynamic Thermal Insulator: Inducing Resonance Within a Fluid Saturated Porous Medium Enclosure Heated Periodically from the Side," *International Journal of Heat Mass Transfer,* Vol. 37, pp. 771–782.

Bejan, A., 1993, *Heat Transfer,* John Wiley and Sons, New York, p. 187.

Bejan, A., 1996, "Fundamental Optima in Thermal Science: Time-Dependent (On and Off) Processes," in Manglik, R. M. and Kraus, A. D., eds., *Process, Enhanced, and Multiphase Heat Transfer: A Festschrift for A. E. Bergles,* Begell House, New York, pp. 51–57.

Bejan, A., 1997, "Theory of Organization in Nature: Pulsating Physiological Processes," *International Journal of Heat and Mass Transfer,* Vol. 40, pp. 2097–2104.

Bernardin, J. D., and Mudawar, I., 1994, "An Experimental Investigation into the Relationship Between Temperature-Time History and Surface Roughness in the Spray Quenching of Aluminum Parts," ASME HTD-Vol. 289, pp. 63–71.

Brittingham, R. A., Mladin, E. C., and Zumbrunnen, D. A., 1995, "Heat Transfer Transients in Stagnation Flows Due to Changes in Flow Velocity," *Journal of Thermophysics and Heat Transfer,* Vol. 10, pp. 186–189.

Dally, J. W., Riley, W. F., and McConnell, K. G., 1993, *Instrumentation for Engineering Measurements,* John Wiley and Sons, New York, p. 425.

Editorial, 1993, ASME JOURNAL OF HEAT TRANSFER, Vol. 114, pp. 5–6.

Howle, L., Georgiadis, J., and Behringer, R., 1992, "Shadowgraphic Visualization of Natural Convection in Rectangular-Grid Porous Layers," ASME HTD-Vol. 206-1, pp. 17–24.

Johnson, H. A., 1971, "Transient Boiling Heat Transfer to Water," *International Journal of Heat and Mass Transfer,* Vol. 14, pp. 67–82.

Kazmierczak, M., and Chinoda, Z., 1992, "Buoyancy-Driven Flow in an Enclosure with Time Periodic Boundary Conditions," *International Journal of Heat Mass Transfer,* Vol. 35, pp. 1507–1518.

Kimura, S., and Bejan, A., 1983, "Mechanism for Transition to Turbulence in Buoyant Plume Flow," *Int. J. Heat Mass Transfer,* Vol. 26, pp. 1515–1532.

Lage, J. L., and Bejan, A., 1993, "The Resonance of Natural Convection in an Enclosure Heated Periodically from the Side," *International Journal of Heat Mass Transfer,* Vol. 36, pp. 2027–2038.

Mantle, J., Kazmierczak, M., and Hiawy, B., 1994, "The Effect of Temperature Modulation on Natural Convection in a Horizontal Layer Heated from Below: High-Rayleigh-Number Experiments," ASME JOURNAL OF HEAT TRANSFER, Vol. 116, pp. 614–620.

Mladin, E. C., and Zumbrunnen, D. A., 1995, "Dependence of Heat Transfer to a Pulsating Stagnation Flow on Pulse Characteristics," *Journal of Thermophysics and Heat Transfer,* Vol. 9, pp. 181–190.

Morega, A. M., Vargas, J. V. C., and Bejan, A., 1995, "Optimization of Pulsating Heaters in Forced Convection," *International Journal of Heat and Mass Transfer,* Vol. 38, pp. 2925–2934.

Nakayama, W., Daikoku, T., Kawahara, H., and Nakajima, T., 1980a, "Dynamic Model of Enhanced Boiling Heat Transfer on Porous Surfaces. Part I: Experimental Investigation," ASME JOURNAL OF HEAT TRANSFER, Vol. 102, pp. 445–450.

Nakayama, W., Daikoku, T., Kawahara, H., and Nakajima, T., 1980b, "Dynamic Model of Enhanced Boiling Heat Transfer on Porous Surfaces. Part II: Analytical Modeling," ASME JOURNAL OF HEAT TRANSFER, Vol. 102, pp. 451–456.

Nelson, R. A., and Pasamehmetoglu, K. O., 1992, "Quenching Phenomena," *Post-Dryout Heat Transfer,* G. F. Hewitt, J. M. Delhaye, and N. Zuber, eds., CRC Press, Boca Raton, FL, pp. 39–184.

Pasamehmetoglu, K. O., and Nelson, R. A., 1991, "Cavity-to-Cavity Interaction in Nucleate Boiling: The Effect of Heat Conduction within the Heater," *AIChE Symposium Series, Heat Transfer,* No. 283, Vol. 87, pp. 342–351.

Sakurai, A., and Shiotsu, M., 1977a, "Transient Pool Boiling Heat Transfer. Part 1: Incipient Boiling Superheat," ASME JOURNAL OF HEAT TRANSFER, Vol. 99, pp. 547–553.

Sakurai, A., and Shiotsu, M., 1977b, "Transient Pool Boiling Heat Transfer. Part 2: Boiling Heat Transfer and Burnout," ASME JOURNAL OF HEAT TRANSFER, Vol. 99, pp. 554–560.

Thome, J. R., 1992, "Mechanisms of Enhanced Nucleate Pool Boiling," Engineering Foundation Conference on Pool and External Flow Boiling, ASME, NY, pp. 337–343.

Vachon, R. I., Nix, G. H., and Tanger, G. E., 1968, "Evaluation of Constants for the Rohsenow Pool-Boiling Correlation," ASME JOURNAL OF HEAT TRANSFER, Vol. 90, pp. 239–247.

Vargas, J. V. C., and Bejan, A., 1995a, "Optimization Principle for Natural Convection Pulsating Heating," ASME JOURNAL OF HEAT TRANSFER, Vol. 117, pp. 942–947.

Vargas, J. V. C., and Bejan, A., 1995b, "Fundamentals of Ice Making by Convection Cooling Followed by Contact Melting," *International Journal of Heat and Mass Transfer,* Vol. 38, pp. 2833–2841.

YSI Temperature Sensors & Probes Manual, 1993, YSI Inc., Yellow Springs, OH.

Zumbrunnen, D. A., 1992, "Transient Convective Heat Transfer in Planar Stagnation Flows with Time-Varying Surface Heat Flux and Temperature," ASME JOURNAL OF HEAT TRANSFER, Vol. 114, pp. 85–92.

Zumbrunnen, D. A., and Balasubramanian, M., 1995, "Convective Heat Transfer Enhancement Due to Gas Injection Into an Impinging Liquid Jet," ASME JOURNAL OF HEAT TRANSFER, Vol. 117, pp. 1011–1017.

Quasi-Homogeneous Nucleation in Microgravity at Low Heat Flux: Experiments and Theory

H. Merte, Jr.
merte@engin.umich.edu
Life Fellow ASME

H. S. Lee
Assoc. Mem. ASME

The University of Michigan,
Department of Mechanical Engineering and
Applied Mechanics,
Ann Arbor, MI 48109-2125

Experiments were conducted in the microgravity of space in which a pool of liquid (R-113), initially at a defined pressure and temperature, was subjected to a step imposed heat flux from a semitransparent thin-film heater forming part of one wall of the container such that boiling is initiated and maintained for a defined period of time at a constant pressure level. Measurements of the transient heater surface and fluid temperatures near the surface were made, noting in particular the conditions at the onset of boiling, along with motion photography of the boiling process in two simultaneous views, from beneath the heating surface and from the side. A total of nine tests were conducted at three levels of heat flux and three levels of subcooling. They were repeated under essentially identical circumstances in each of three space experiments. The absence of buoyancy resulted in the onset of boiling at low heat flux levels, with what is defined as quasi-homogeneous nucleation taking place. The influence of these low levels of heat flux and the pressure effect used to produce the bulk liquid subcooling are accounted for by a modification of classical homogeneous nucleation theory.

Introduction

The relatively ready access to the microgravity of space in recent years has generated considerable interest in conducting experiments involving those scientific phenomena where the removal of buoyancy can reveal mechanisms not otherwise evident. This in turn leads to improved understanding and application of such phenomena, both in the presence and absence of buoyancy. The liquid-vapor phase changes associated with boiling or evaporation and condensation are particularly appropriate candidates for such research because of the large density differences involved.

Experiments were conducted in the space environment, $a/g \approx 10^{-4}$, as part of the NASA Get Away Special (GAS) program on the space shuttles (Space Transportation System) STS-47-57-60, designated as the Pool Boiling Experiment (PBE-IA-IB-IC, respectively), in which a stagnant pool of liquid (R-113), initially at a defined pressure and temperature, was subjected to a step imposed constant heat flux from a flat semitransparent thin-film heater such that boiling is initiated and maintained for a specified period of time at a constant pressure level. Measurements of the transient heater surface and fluid temperatures near the surface are made, noting in particular the conditions at the onset of boiling, along with motion photography of the boiling process in two simultaneous views, from beneath the heating surface and from the side.

The absence of buoyancy permitted the onset of boiling to take place at low levels of heat flux, which otherwise would not occur in earth gravity, and also permitted the computation of the temperature distribution in the liquid up to the onset of boiling. The present paper is focused on the explanation behind the unusual behavior noted in connection with the nucleation, or onset, of boiling taking place within the range of parameters used: for a given constant system pressure the mean heater surface superheat at nucleation first increased and then decreased as the heat flux level was increased.

Contributed by the Heat Transfer Division for publication in the JOURNAL OF HEAT TRANSFER. Manuscript received by the Heat Transfer Division January 18, 1996; revision received October 17, 1996; Keywords: Boiling, Microgravity Heat Transfer, Transient & Unsteady Heat Transfer. Associate Technical Editor: M. Sohal.

Experimental Apparatus

Figure 1 is a schematic of the test vessel assembly. The R-113 chamber has internal dimensions of approximately 15 cm diameter by 10 cm high. Thermistors are used to measure the liquid temperatures in the vicinity of the heater surfaces at distances of 1, 5, 10 mm normal to the center of the active heater, with an accuracy of ±0.06°C, while the system pressure is measured and controlled to an accuracy within ±0.35 KPa from the N_2 chamber via flexible stainless bellows. The liquid temperature is maintained constant at a nominal 49°C by heaters attached to the R-113 chamber exterior, while the desired subcooling is established by the system pressure relative to the continuously measured liquid temperature.

Two heater surfaces, 19.05 × 38.1 mm (0.75 in. × 1.50 in.), are placed on a single flat substrate as shown in Fig. 2, with one serving as a back-up. Each heater consists of a 400 Å thick semitransparent gold film sputtered on a polished quartz substrate and serves simultaneously as a heater, with an uncertainty of ±2 percent in the measurement of the heat flux, and as a resistance thermometer, calibrated to an overall uncertainty of ±1.0°C. The general calibration procedures followed are described in Ervin and Merte (1991). The R-113 (trichlorotrifluoroethane, CCl_2FCClF_2) used has a normal boiling point of 47.6°C. It was purified and degassed by a double distillation process and freezing at liquid nitrogen temperature levels while continuously pumping at a low pressure. The degassing was deemed adequate when the measured vapor pressure conformed to the equation of Mastroianni et al. (1978) within the accuracy of the standard laboratory instruments (±0.06°C, ±170 Pa) over the temperature range used.

After the desired uniformity of the liquid temperature and the subcooling are achieved, the specified heat flux is imposed to the heater surface, and the stagnant liquid is subjected to a transient conduction process so that its temperature distribution can be computed at all times up to the moment of nucleation. The parameters varied are the input heat flux, at nominal levels of 8, 4, 2 w/cm^2 in sequence, and initial bulk liquid subcooling, at nominal levels of 11.1, 2.8, 0°C (20, 5, 0°F) in sequence. These constitute the matrix of nine runs conducted for each experiment. The highest heat flux level of 8 w/cm^2 is approximately one half of the estimated critical heat flux for pool

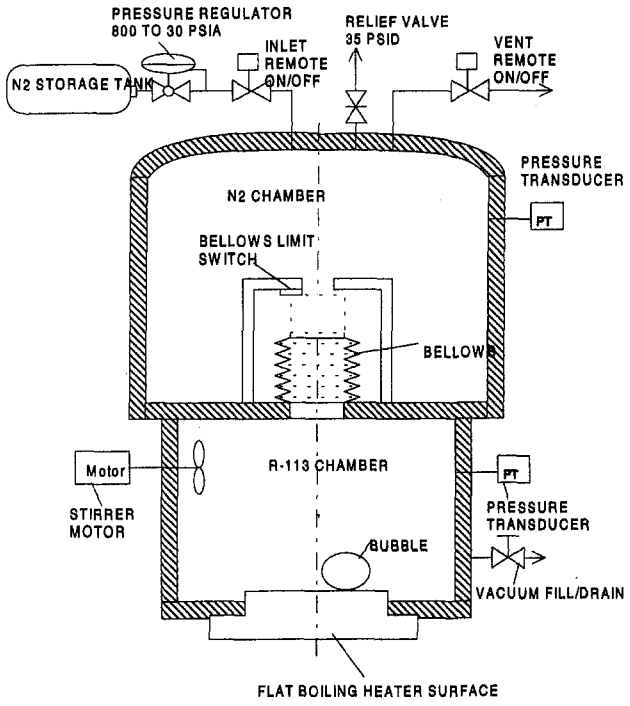

Fig. 1 Schematic of test vessel

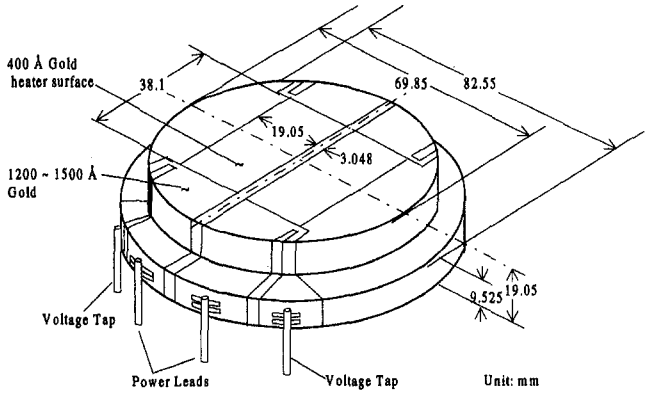

Fig. 2 Layout of gold film heater surfaces on polished quartz substrate

boiling in earth gravity. Each run lasts up to two minutes, during which the system pressure is maintained constant. With a minimum waiting period of 15 minutes between tests, following pressurization of the chamber to condense the vapor formed, normal heat losses to the surroundings are sufficient to compensate for the heat addition during each test.

Experimental Results

The mean heater surface superheat measured at nucleation, or the onset of boiling, as determined visually from the motion picture films and which coincided with the maximum temperatures, are plotted in Fig. 3 for PBE-IA (STS-47). Included here are the results of both the space experiments and pre- and post-flight tests at $a/g = +1$ (facing upward) and $a/g = -1$ (facing downward), and are representative of the behavior in the other two series of experiments on the STS-57-60. Complete results are given in Merte et al. (1995). It is noted that in all cases except for $a/g = +1$, where natural convection is dominant, that a distinct peak exists in the mean heater superheat at nucleation between the high and low levels of heat flux, and is particularly high in microgravity. Upon detailed examination of the motion picture films interesting distinctions were noted in the locations of the nucleation sites, and some attention will be devoted to these here. The major discrepancy between the pre-flight test at $a/g = -1$, labeled B^* in Fig. 3, and the post-flight test occurred the first time that each of the completely assembled hardwares were exercised prior to shipping for installation in the space vehicle. This discrepancy was not present in the case where the complete experiment was repeated, designated as PBE-IC on the STS-60. The other differences between the pre- and post-flight tests at $a/g = -1$ are considered normal in light of the somewhat random nature of nucleation and uncontrollable effects of transient natural convection.

It was originally expected that nucleation and early bubble growth would always occur in that part of the heater having the highest temperature, the central portion, not near the edges where the temperature falls off sharply because of three-dimensional conduction in the substrate. Viewing of the motion films revealed that under certain circumstances nucleation does not take place in the areas of highest surface temperature, but sometimes occurs at locations where the temperatures are lower—near the edges of the heater, depending on the heat flux level. This is illustrated in the upper part of Fig. 4, in which the locations of the nucleation sites are indicated for each Run in the three space flights included here. The correspondence between the run numbers and the input heat flux and subcooling levels are given in the table within Fig. 5. The highest heat flux cases, Run Nos. 1, 4, and 7, nucleated at precisely the identical site near an edge on both the STS-47 and STS-60, identified as (a) in Fig. 4. For the same run numbers 1, 4, and 7 on the STS-57, nucleation also occurred at a single site near an edge, identified as (h). It should be pointed out here that the PBE-IA

Nomenclature

a = thermal diffusivity, acceleration
$b = (P_s - P_l)/P_s$
C = defined in Eqs. (8), (12), (14)
g = acceleration due to earth gravity
G = Gibbs No., Eq. (9)
$G_T = (dG/dT)$
h = Planck constant
h_{fg} = latent heat of vaporization
J = defined in Eq. (8)
k = Boltzmann constant, thermal conductivity
K^* = defined in Eq. (24)
m = mass/molecule
n = number of molecules/liquid volume
n'' = defined in Eq. (15)
P = pressure
q'' = heat flux
R = bubble radius
T = temperature
$\dot{T} = (dT/dt)$
$T_x = (dT/dx)$
t = time
t^* = nucleation delay time (time interval between initiation of heating and nucleation)
v = specific volume
W = work of formation of vapor bubble
x = distance from heater surface
λ_m = latent heat/molecule
ρ = density
σ = surface tension
τ = nucleation time

Subscripts

c = critical
i = initial
l = liquid
s = "normal" saturation state (no surface tension effects)
T = total
v = vapor
w = wall

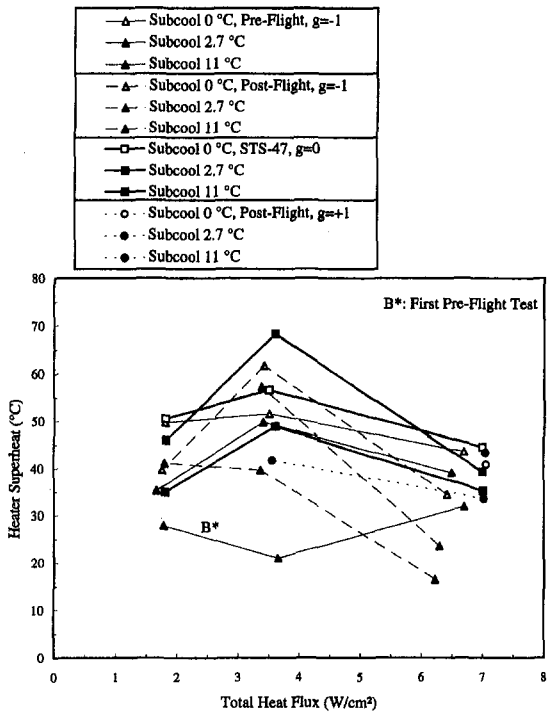

Fig. 3 Mean heater surface superheat at nucleation. Comparisons with ground testing. PBE-IA (STS-47).

(STS-47) and PBE-IC (STS-60) experiments use the identical hardware and heater surface, designated as the primary heater in Fig. 4, while the experimental apparatus for PBE-IC (STS-57) is similar but not identical to the other, and the secondary heater is used. Where the nucleation sites in Fig. 4 are identified as not determined for particular run numbers, this corresponds to the cases where the early vapor bubble growth was quite energetic such that no vapor bubble was visible in one film frame (at 100 pps) but filled the entire heater surface in the next. It is assumed in these cases that nucleation occurred in the central part of the heater, in the highest superheat domain. This is consistent with what took place in run numbers 2 and 5 on STS-47 and -60, point (b) in Fig. 4. Although the four nucleations are shown as taking place at the same site, this is only approximately so, since the bubble growths were too rapid to see the precise locations. In the case of point (f) in Fig. 4, the two nucleating sites also are only approximately at the same location.

In order to illustrate how the liquid superheat distribution at nucleation varied with the nucleation delay times, defined as the time interval between the initiation of heating and nucleation, a three-dimensional transient finite element conduction model was developed for the quartz substrate and R-113 with the plane grid shown in Fig. 4. This led to the conclusion that, since both the thermal conductivity and diffusivity of the quartz are about 20 times that of the liquid R-113, a more accurate computation of the temperature distribution in the R-113 is possible by solving the detailed one-dimensional transient conduction processes in the liquid, using the local heater surface temperatures and liquid heat flux determined by the finite element model as boundary conditions. Numerical computations using measured values tend to degrade the final results. In the present case considerable efforts were expended to minimize this, described in Merte et al. (1995), and the maximum uncertainty in computed local heater surface temperatures is estimated to be less than ±3°C. The liquid superheat distributions, normal to the heater surface at the moment and site of nucleation, are given in Fig. 5 for each of the nine Runs of PBE-IA (STS-47). In addition to the tabulation of the respective levels of heat flux, saturation temperature (corresponding to the system pressure), and initial bulk liquid subcooling, detailed data is given of the nucleation delay time t^*, the local heater surface superheat at the time and place of nucleation, the measured mean heater superheat at nucleation, and the maximum level of the heater surface superheat at the moment of nucleation, which was always at the geometrical center of the heater surface. The difference between the local and maximum heater surface superheat at nucleation provide a measure of edge effects that depend on the heat flux levels and nucleation delay times.

It is noted in Fig. 5 that the runs with the highest heat flux, numbers 1, 4, and 7, have the lowest total superheated liquid content at nucleation, which is related to the subsequent relatively nondynamic bubble growth rates observed. The medium heat flux case, run numbers 2, 5, and 8, have the highest local surface superheat at nucleation, as seen previously in Fig. 3. Of particular note in Fig. 5 are the positions of run numbers 6 and 9, which are low subcooling and saturated, respectively, relative to run number 3, which has a high subcooling. Nucleation thus appears to take place preferentially at a lower heater surface superheat with larger liquid subcoolings, for the same heat flux level.

As was stated earlier in connection with Fig. 4, nucleation in the three run numbers 1, 4, and 7 (the high heat flux level case) of PBE-IA and -IC all occurred at precisely the same location on the heater surface, designated by the letter (a), and for run numbers 1, 4, and 7 of PBE-IB it took place at the location designated by the letter (h). It may be concluded that these nucleations at the highest nominal heat flux level of $q''_T = 8$ w/cm^2 consist of heterogeneous nucleation, since they are associated with specific locations on the solid heater surface, which implies the presence of reproducible nucleation sites. In all the other cases nucleation takes place at different random

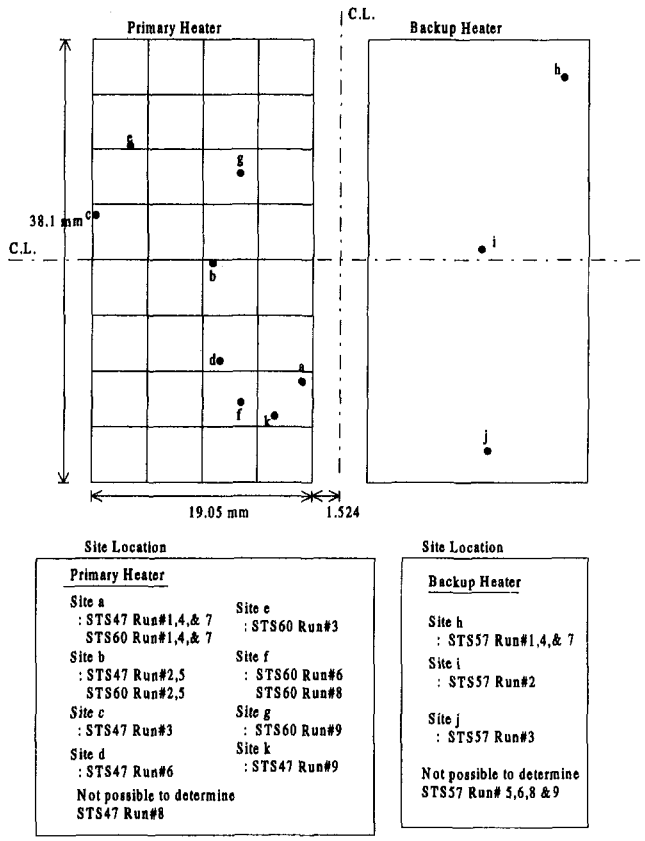

Fig. 4 Layout of heater surfaces from underside, with three-dimensional finite element grid and microgravity nucleation sites superimposed. PBE-IA-IB-IC. (STS-47-57-60).

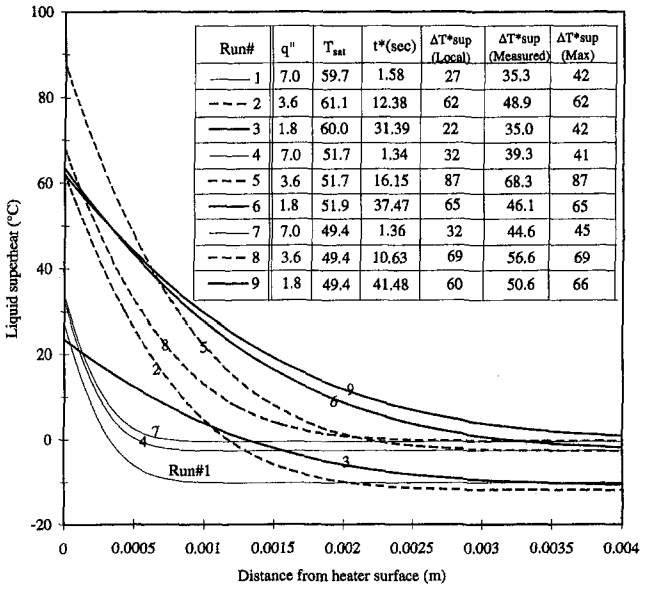

Run#	q"	T_{sat}	t*(sec)	ΔT*sup (Local)	ΔT*sup (Measured)	ΔT*sup (Max)
1	7.0	59.7	1.58	27	35.3	42
2	3.6	61.1	12.38	62	48.9	62
3	1.8	60.0	31.39	22	35.0	42
4	7.0	51.7	1.34	32	39.3	41
5	3.6	51.7	16.15	87	68.3	87
6	1.8	51.9	37.47	65	46.1	65
7	7.0	49.4	1.36	32	44.6	45
8	3.6	49.4	10.63	69	56.6	69
9	1.8	49.4	41.48	60	50.6	66

Fig. 5 Local R-113 temperature distribution at nucleation at heater surface sites indicated on Fig. 4. PBE-IA (STS-47).

locations. It is termed here as a form of homogeneous nucleation, in the sense that these cannot be associated directly with a specific nucleation site.

Heterogeneous nucleation theory considers that vapor bubble growth begins from a cavity at the solid heater surface in which vapor is assumed to be preexisting. Cavities or crevices are present at the surfaces of all solids, differing only in size, number, and distribution of sizes, which depend in turn on how the solid was originally formed and on the subsequent mechanical treatment to which the material was subjected, such as machining, grinding, polishing, etc. Such cavities are filled initially with a gas, such as air, which can later then be expected to be displaced by the vapor of the liquid with which it might be placed in contact.

The possibility is considered here that both heterogeneous and homogeneous nucleation are taking place on the same heater surface, the difference arising with the heat flux, and will be described below. The role of the liquid temperature gradient at the heater surface interface at nucleation, along with bulk liquid subcooling, will be examined. It was demonstrated by Ervin and Merte (1991) that nucleation of R-113 on a large gold film heater can occur at heater surface superheat levels on the order of 6°C if a sufficiently rapid heater surface temperature increase can be instituted. In this latter case approximations to step changes in heater surface temperatures were being attempted, with a surface heating rate of 3000°C/s at nucleation. On the other hand, as reported by Iida et al. (1993), high rates of heating of ethyl alcohol at atmospheric pressure by a small (0.1 mm × 0.25 mm) platinum film 20 Angstroms thick on quartz, to 10^7°C/s, produced nucleation at the theoretical homogeneous nucleation point of 129°C superheat. In this case the liquid subcooling was 53°C, and the formation of the vapor bubbles was described as "caviarwise bubble generation."

Analysis: Heterogeneous Nucleation

The heater surface substrate in the present case is quartz, which was given a final finish by polishing with a material of typical dimensions of 1.4 microns (μ). If a spherical shape is assumed for these particles, the surface cavities remaining after polishing can be expected to have effective radii of 0.7 μ or less. A scanning electron microscope was used to obtain back scattered electron images of a typical gold-film coated quartz surface used for boiling R-113. It was necessary to fracture the surface to a size small enough to fit within the apparatus. Using resolutions down to about 0.1 μ, what appeared to be scratches on the surface could be observed, having a maximum width of 2.5 μ, down to 0.1 μ. The objective of the analysis here is to demonstrate that measurements of the nucleation process taking place are consistent with predictions of heterogeneous nucleation to within an order of magnitude of the size of potential cavities. Heterogeneous nucleation, however, does not account for the observed effects of the heat flux and bulk liquid subcooling, and hence an examination for the possibility of homogeneous nucleation was deemed appropriate and follows below.

A schematic for the development of the expression for the critical size nucleation cavity with heterogeneous nucleation is given in Fig. 6. The cavity is assumed to be circular in opening, and filled with vapor protruding hemispherically into the bulk liquid, with radius R_c. This nucleus will become activated and begin growing when the liquid temperature at the top of the vapor hemisphere equals or exceeds that predicted from liquid-vapor thermodynamic equilibrium on a curved interface. Such a concept is quite well known and was presented by Griffith and Wallis (1960), and later modified and utilized by Hsu (1962).

The condition for mechanical equilibrium of a spherical (or hemispherical) vapor bubble is given by:

$$P_v - P_l = \frac{2\sigma}{R_c}. \tag{1}$$

Equation (1) provides the critical size vapor bubble radius for thermodynamic equilibrium when the thermal state of the liquid is not near the critical state, so that $v_v \gg v_l$ and the related condition of $P_v \cong P_s$ applies. The integration of the Clausius-Clapeyron equation relates the vapor pressure to the bulk liquid superheat:

$$\frac{P_v - P_l}{T - T_s} = \frac{h_{fg}\rho_v}{T_s}. \tag{2}$$

Combining Eq. (1) with Eq. (2) provides the liquid superheat required for equilibrium (albeit unstable) of a spherical vapor bubble:

$$T - T_s = \frac{2\sigma T_s}{\rho_v h_{fg} R_c}. \tag{3}$$

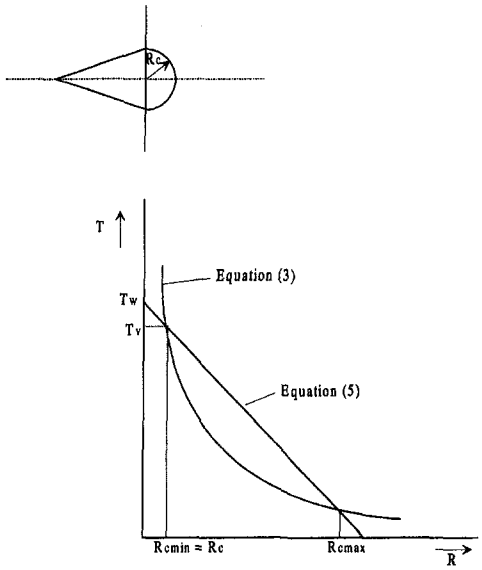

Fig. 6 Schematic for development of heterogeneous nucleation model

Equation (3) can be expressed in terms of heater surface superheat as

$$T_w - T_s = \frac{2\sigma T_s}{\rho_v h_{fg} R_c} + (T_w - T). \quad (4)$$

Equation (3) is plotted in Fig. 6. With an imposed heat flux to the liquid, as is the case in the present experiments, the temperature distribution in the immediate vicinity of the heater surface can be taken to be linear, as given by Eq. (5) and also indicated in Fig. 6, when dealing with bubble dimensions of the order of microns, encountered here

$$q'' = k \frac{T_w - T_v}{R_c}. \quad (5)$$

T in Eq. (4) can be eliminated with the use of $T = T_v$ in Eq. (5):

$$T_w - T_{\text{sat}} = \frac{2\sigma T_s}{\rho_v h_{fg} R_c} + \frac{q'' R_c}{k}. \quad (6)$$

As a practical matter, the difference between T_w and T_v is negligibly small. Equation (6) is solved explicitly for R_c in Eq. (7).

$$R_c = \frac{k(T_w - T_s)}{2q''} \left\{ 1 \pm \left[1 - \frac{8\sigma T_s q''}{\rho_v h_{fg} (T_w - T_s)^2} \right]^{1/2} \right\} \quad (7)$$

The simultaneous solution of Eqs. (3) and (5), given by Eq. (7), is illustrated as their intersection in the sketch of Fig. 6. The last term within the brackets in Eq. (7) has a value on the order of 0.05 for the typical experimental conditions here with R-113. Thus, the resulting value of $R_{c\max}$ becomes so large that the linearity of liquid temperature implicit in Eq. (5) is no longer valid. From the measurement of q'' and T_w at the moment of nucleation, $R_{c\min}$ can be computed, and is plotted as a function of the wall superheat $T_w - T_{\text{sat}}$ in Fig. 7 for each of the three pressure levels used to produce the subcooling in PBE-IA (STS-47). The intersection of the local heater surface superheat at nucleation, with the corresponding pressure level, then provides the theoretical nucleation cavity size for each run number, indicated by the run numbers attached to the points. A band corresponding to the typical radius of the particles used for polishing is included with an arbitrary uncertainty as $R = 0.7\ \mu \pm 0.1\ \mu$. This point at 0°C wall superheat is connected with each run number in order to identify and relate more clearly the corresponding input heat flux levels. It is noted in particular that the three run numbers 1, 4, and 7 at the high heat flux level are clustered at low nucleation wall superheat levels, while the remaining runs are clustered at a high superheat level, except for Run No. 3 which appears to be an anomaly. The nucleation for run numbers 1, 4, and 7 all occurred at precisely the same site on the heater surface, and also with PBE-IC (STS-60), as was shown on Fig. 4. These nucleations are therefore defined as heterogeneous nucleations, since they all took place at a unique location on the heater surface, whereas the other nucleations took place at various scattered locations on the heater surface.

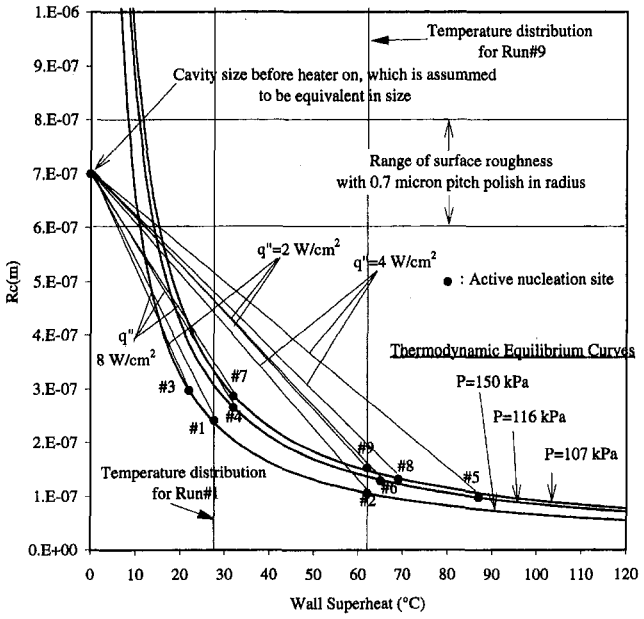

Fig. 7 Relationship between minimum critical size nucleation cavities computed from local heater surface superheat and typical grit size used for polishing the heater surface and liquid temperature distribution at nucleation. PBE-IA (STS-47).

Also plotted on Fig. 7 are the temperature distributions in the liquid for run numbers 1 and 9, corresponding to the highest and lowest levels of heat flux. Over the maximum range of R_c covered here, one micron, the liquid temperature changes are 0.12°C and 0.038°C, respectively, which cannot be detected on the temperature scales used here. Also noteworthy is that the superheated boundary layers are considerably larger in size than the diameters of the critical size nuclei represented in Fig. 7. This means that the possibility for homogeneous nucleation to take place within these superheated boundary layers should be given serious consideration for explaining the seemingly random locations of the nucleation sites, under certain circumstances. If heterogeneous nucleation explains the low level of heater surface superheat at nucleation at the high levels of heat flux in Fig. 3, then what remains is to describe or predict the increase of the heater surface superheat with increase in heat flux, as observed at the lower levels of the imposed heat flux of $q''_T = 2$ w/cm² and 4 w/cm². This will now be examined.

Analysis: Homogeneous Nucleation

In general terms, homogeneous nucleation refers to nucleation taking place in the absence of any other phases or foreign materials. As acknowledged by Skripov (1974), liquids can be superheated even in the presence of so-called artificial centers, provided that the liquid is heated at a sufficiently high rate such that the energy imparted to the liquid exceeds the latent heat of evaporation being absorbed at the active centers. A criteria is developed by Skripov, with sample results for water, for the parameters necessary to obtain "impact" boiling, or homogeneous nucleation. These do not readily lend themselves to computation, requiring for calculation purposes assumptions of pending or available nucleation sites densities such as $\tilde{\Omega} = 10^2$ cm^{-3} within the bulk liquid and $\tilde{\Omega}_A = 10^2$ cm^{-2} at the heating surface for homogeneous nucleation to take place. A construction similar to this will be developed below, except that no arbitrary values will be assumed—only that these quantities required for nucleation remain constant as the other parameters of system pressure and heater surface flux are varied.

The net conclusion of Skripov (1974) in the above is that high levels of heater power are required to produce the necessary conditions for impact boiling or homogeneous nucleation. On the other hand, the space experiments conducted here demonstrate that just the opposite appears to happen in the absence of buoyancy: what appears to be homogeneous nucleation takes place as the heat flux is reduced.

It will be attempted here to predict the behavior of homogeneous nucleation as the heat flux and system pressure are varied, since quasi-homogeneous nucleation has been observed at different levels of both of these parameters. Calculations based on the procedures established by Skripov (1974) were also carried out by Avedisian (1985) to predict homogeneous nucleation as produced by the pulse heating method, using as heater surface nucleation site densities $n'' = 10^3 - 10^6$ cm^{-2}. These resulted in

calculations of volumetric nucleation rates of $J = 10^{15}$–10^{22} nuclei/cm^3-s, producing homogeneous nucleation.

Homogeneous nucleation is viewed by Volmer (1939), among others, as the spontaneous formation and subsequent growth of a vapor bubble associated with random statistical energy fluctuations on a molecular scale within otherwise uniformly superheated liquids. Disturbances associated with the temperature gradients inherent in the pulse heating method, as utilized by Skripov (1974), also arise in the vicinity of rapidly growing vapor bubbles, and also was treated briefly by Skripov (1974). This phenomena may explain the behavior observed in the pool boiling experiments here during certain circumstances of boiling in which bubbles were observed to nucleate and grow in front of the main advancing liquid-vapor interface, and may also explain the phenomena of boiling spread in earth gravity described by Ervin et al. (1992) as the rupture of a smoothly growing liquid-vapor interface.

Classical homogeneous nucleation theory, treated abundantly elsewhere (e.g., Volmer, 1939, Skripov, 1974) and based on statistical treatment of thermal fluctuations, provides an expression for predicting the rate of formation of critical size nuclei per unit volume of the form

$$J = C_e^{-G}. \tag{8}$$

It should be recognized that the formation of a critical size nucleus does not assure that a vapor bubble will subsequently grow from this nucleus, but this J rather constitutes a proportionality or a probability that such growth will take place. Volmer (1939) defines the product of J and a time interval dt as the nucleus formation probability.

The exponent G in Eq. (8) is the Gibbs number, defined as

$$G(T) = W_{cr}/kT \tag{9}$$

where W_{cr} is the work of formation of a critical size bubble nucleus, and kT represents the mean molecular fluctuation energy per degree of freedom. The work of formation in Eq. (9) is given by

$$W_{cr} = 16\pi\sigma^3/3T(P_s - P_l)^2 \tag{10}$$

Substituting Eq. (10) into Eq. (9) and then using Eq. (2) with $P_v = P_s$, the Gibbs number is expressed in terms of the fluid properties, including the bulk liquid temperature, as

$$G(T) = \frac{16\pi\sigma^3}{3k}\left(\frac{T_s}{\rho_v h_{fg}}\right)^2 \frac{1}{T(T - T_s)^2}. \tag{11}$$

Computations demonstrate that as the superheat rises the Gibbs number decreases at a successively increasing rate. If the nucleation probability is given by a form of Eq. (8), the limiting superheat necessary for homogeneous nucleation becomes readily apparent. However, the coefficient C in Eq. (8) remains to be established quantitatively.

According to Volmer (1939), C is proportional to the concentration of elementary vapor bubbles arising from thermal fluctuations, given as

$$C = n\left[\frac{6\sigma}{(3 - b)\pi m}\right]^{1/2} \exp\left(-\frac{\lambda m}{kT}\right). \tag{12}$$

The exponent is the ratio of the latent heat per molecule to the mean fluctuation energy per degree of freedom, which is typically quite small, so that the exponential term may be approximated by unity. In Eq. (12), b is defined as

$$b = (P_s - P_l)/P_s = \frac{P_l h_{fg}}{T_s P_s}(T - T_s). \tag{13}$$

Fisher (1948) estimates the coefficient C in Eq. (8) from the theory of absolute reaction rates as

$$C = \frac{nkT}{h}\exp(-\Delta f_\delta^*/kT) \tag{14}$$

where Δf_δ^* is the free energy of activation for the motion of an individual molecule of liquid past its neighbors into or away from the bubble surface, and may be considered equivalent to the latent heat per molecule, λ_m in Eq. (12).

Cole (1974) cites two additional expressions for C in Eq. (8): one due to Moore (Eq. (62) in Cole) reduces to Eq. (12) above, and the other due to Zeldovich-Kagan (Eq. (64) in Cole) reduces to Eq. (12) with $b = 0$.

The parts of C in Eqs. (12) and (14) excluding the exponentials, which are close to unity, were evaluated for R-113 at atmospheric pressure over the range of liquid superheats of 90°C–150°C. It is obvious from the expressions themselves that these are weak functions of system pressure and are also relatively weak functions of the liquid superheat. However, these two terms differ from one another by two orders of magnitude, being 4.90×10^{38} and 3.43×10^{40}, respectively, at a liquid superheat of 100°C. In computations of the classical isothermal homogeneous nucleation temperatures by Skripov (1974), it is demonstrated that a two order of magnitude difference in J corresponds to a difference in the nucleation temperature between 0.7°C and 5.0°C, depending on the value of b in Eq. (12), and represents a negligible difference in view of other uncertainties in the homogeneous nucleation theories. For R-113 at atmospheric pressure and 100°C superheat b has the value of 0.91, and a difference of 100 in J results in a difference of 5°C in the homogeneous nucleation temperature.

For present purposes it will be assumed that C in Eq. (8) is constant for a given fluid and that J varies only because of the Gibbs number G.

As described earlier, the heater surface for the PBE consists of a flat polished quartz substrate coated with a gold film approximately 400 Angstroms thick, producing a flat heater surface 19.1 mm × 38 mm (0.75 in. × 1.50 in.). Except for a narrow band around the edge of the heater surface, the heat transfer process to the fluid is a transient one-dimensional conduction process. The edge effects will be neglected in the analytical development below, except that a lower heat flux to the liquid is recognized to take place within this narrow band, with its attendant effects on homogeneous nucleation. It was demonstrated in Fig. 7 that the critical size nucleation cavity associated with the heterogeneous nucleation taking place is quite small relative to the corresponding temperature gradients at these levels of heat flux. Since the critical size nuclei with homogeneous nucleation are even smaller, it seems appropriate to consider the homogeneous nucleation taking place during the transient heating process to occur in a quasi-isothermal temperature field near the heater surface. A specific relationship should then exist between the rate of formation of the critical size nuclei per unit volume given by Eq. (8) and the rate of formation of these critical size nuclei per unit heater surface area in the presence of the transient temperature gradient normal to the heater.

In a manner similar to that given by Skripov (1974), the number formed within a time τ and within a distance x from the heater surface is given by

$$n'' = \frac{n}{A} = \int_o^\tau \int_o^x J dx dt \tag{15}$$

where J is given by Eq. (8), and $G(T)$ is given by Eq. (11), and $T(x, t)$. Thus,

$$G(T) = G[T(x, t)]. \tag{16}$$

Successively expanding $T(x, t)$ in a Taylor series about $x = 0$, $t = \tau$, neglecting the higher order terms, and then $G(T)$ about

$T(o, \tau)$, integration of Eq. (15), first with x and then with t, results in

$$n'' = \frac{C \exp(-G(o, \tau))}{G_T^2 T_x \dot{T}} \times (\exp(-xT_x G_T) - 1)(1 - \exp(\tau \dot{T} G_T)). \quad (17)$$

The derivatives in Eq. (17) are evaluated at the moment of nucleation. A detailed development of Eq. (17) is given in Merte et al. (1995). It can be demonstrated that for reasonable values of x and τ the two exponentials in the brackets of Eq. (17) are negligible compared to unity, so Eq. (17) may be written as

$$n'' = \frac{-C \exp(-G(o, \tau))}{G_T^2 T_x \dot{T}}. \quad (18)$$

From Eq. (8), the numerator of Eq. (18) represents J evaluated at the heater surface conditions at the moment of nucleation, or

$$\frac{n''}{J} = -\frac{1}{G_T^2 T_x \dot{T}}. \quad (19)$$

Equation (19) is identical to an expression developed by Skripov (1974) in dealing with liquid temperature perturbations caused by nucleating bubbles resulting from pulse heating.

It is assumed here that, for a given fluid, the left side of Eq. (19) is constant at the moment of nucleation as any other conditions are varied, such as system pressure and/or heat flux in the present case. If true, it thus should be possible to predict the influence of these variables on the temperature at which homogeneous nucleation takes place in the vicinity of a flat heat surface under relatively slowly varying temperatures. It thus becomes unnecessary to assume any specific values for n'' or J in order to compute the homogeneous nucleation temperature, as was necessary to determine the superheat limit, or maximum value arising with large heating rates, termed impulse heating by Skripov (1974).

Using the imposed power input to the thin film gold heater, it is possible to write expressions for the spatial and temporal derivatives in Eq. (19) at the moment of nucleation, in the absence of buoyant effects in microgravity, from the solution for transient conduction in semi-infinite solids

$$T_x = \left(\frac{\partial T}{\partial x}\right)_{x=o} = -\frac{q_l''}{k_l} \quad (20)$$

$$\dot{T} = \left(\frac{\partial T}{\partial t}\right)_{x=o} = \frac{q_l''}{k_l}\left(\frac{a_l}{\pi}\right)^{1/2} \times \frac{1}{t^{1/2}}. \quad (21)$$

The time in Eq. (21) can be expressed in terms of the heater surface temperature, from the analytic solution

$$T(o, t) - T_i = \frac{2q_l''}{k_l}\left(\frac{a_l t}{\pi}\right)^{1/2}. \quad (22)$$

From the solution for a plane heat source at the interface of two semi-infinite solids, the heat flux to the motionless liquid is a constant fraction of the input flux, written here as

$$q_l'' = C_1 \times q_T''. \quad (23)$$

Substituting Eqs. (20) – (23) into Eq. (19) and rearranging with all constants on the left

$$K^* \equiv \frac{J \times k_l^3}{2n'' C_1^3}\left(\frac{\pi}{a_l}\right) = \frac{G_T^2 \times q_T''^3}{T_n - T_i}. \quad (24)$$

T_n is the heater surface temperature at nucleation, while T_i is the initial uniform bulk liquid temperature. The denominator of Eq. (24) can be expressed in terms of the heater surface superheat at nucleation and the bulk liquid subcooling as

$$(T_n - T_i) = (T_n - T_s) + (T_s - T_i) \equiv (T - T_s)^* + \Delta T_{sub}. \quad (25)$$

Substituting Eq. (25) into Eq. (24) and rearranging produces the following:

$$(T - T_s)^* = q_T''^3 \times \frac{G_T^2}{K^*} - \Delta T_{sub}. \quad (26)$$

Equation (26) is plotted in Fig. 8 for R-113 as heater surface superheat at nucleation versus the total heat flux into the gold film for the nominal system pressures used to provide the desired initial bulk liquid subcoolings, evaluating K^* for PBE-IA run number 9, the saturated liquid case. According to the analysis here, subcooling influences the nucleation phenomena only indirectly as to the time required to attain a given heater surface superheat. Figure 8 includes measurements from the PBE-IA and -IC (on the STS-47 and -60), which utilized the identical hardware. The superheats follow the effect of system pressure reasonably well at the low heat flux level of 1.8 w/cm^2, but produce a higher superheat for two of the runs at 3.6 w/cm^2. However, these all follow the influence of the heat flux well, with the heater surface superheat increasing with heat flux. The estimated superheat limits resulting from the classical homogeneous nucleation theory with uniform bulk liquid temperatures are also indicated in Fig. 8 for R-113, given by Eqs. (8) and (14). The decrease in the superheat at nucleation as the heat flux is reduced, as predicted by Eq. (26), can be considered to occur because more time exists for the random thermal fluctuations, always present, to produce such nucleation. This behavior can be observed only in a microgravity environment because convection effects in earth gravity prevail over these fluctuations. Reasonably good qualitative agreement also was present in the results from PBE-IB (STS-57) with respect to the influence of both subcooling and heat flux, given in Merte et al. (1995).

In all cases of the highest heat flux levels included in Fig. 8, the striking behavior arising with the heterogeneous nucleation described earlier is obvious. Also included in Fig. 8 are data obtained from the ground-based testing conducted in the NASA-Lewis 5.1 second drop tower. Because of the short test period these experiments could only be conducted at the higher levels of heat flux. Fifteen drops were conducted with the same surface, with the data given in Appendix A of Ervin and Merte (1991). Of these, four resulted in what is classified as unstable bubble growths, and are plotted in Fig. 8. The remaining eleven tests all resulted in stable vapor bubble growths, with only one representative data point included in Fig. 8 as indicated. These all clustered below the homogeneous nucleation theoretical curves, together with the heterogeneous nucleation data from the space experiments. The theoretical basis for the difference in behavior between the stable and unstable vapor bubble growths and their relationship to the nucleation behavior presented here will be the subject of a subsequent paper. Attempts have been made to account for heterogeneous nucleation behavior by considering the wetting action of the liquid on the heater surface, in terms of the contact angle. A recent example is that of Iida et al. (1994). However, as indicated in Cole (1974), the influence of the contact angle is insufficient to explain the low values of superheat observed in practice: a contact angle of 90 deg reduces the superheat by only approximately 30 percent. For a completely wetting liquid the predicted superheat is the same as for homogeneous nucleation.

Using the empirical value of K^* in Eq. (24) from one run in each physically distinct facility, it is possible to estimate

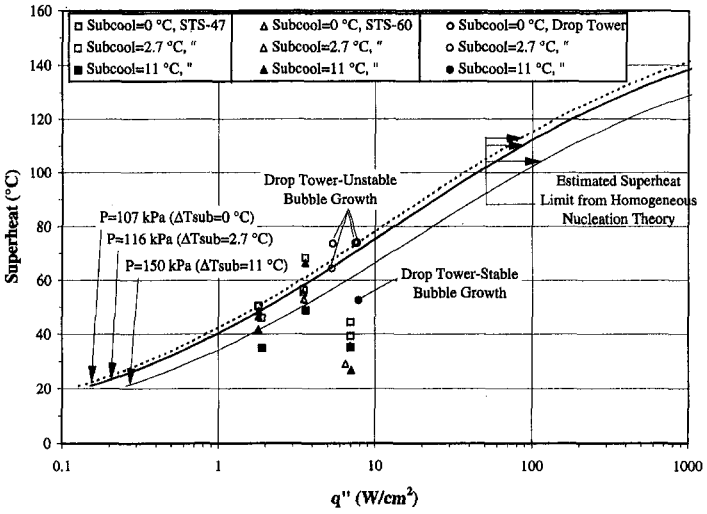

Fig. 8 Homogeneous nucleation model for R-113 with transient heating in microgravity. Measurements with PBE-IA-IC (STS-47-60) and from NASA Lewis 5.1 second drop tower. $K^* = 2.57 \times 10^6$ evaluated for PBE-IA: Run No. 9.

orders of magnitude of J at nucleation. For example, using $K^* = 2.57 \times 10^6$ w^3/°k^3 cm^6 from Fig. 8, together with the properties of R-113, the ratio $J/n'' = 1.22 \times 10^{10}$ (cm-s)$^{-1}$, from Eq. (24). If the minimum value of $n'' = 1$ cm^{-2} is taken as necessary for nucleation, then the rate of formation of the critical size nuclei becomes $J = 1.22 \times 10^{10}$ (cm^3-s)$^{-1}$. If the range of n'' is instead taken as $10^3 < n'' < 10^6$, as used by Avedisian (1985), then from Eq. (24) $1.22 \times 10^{13} < J < 1.22 \times 10^{16}$, which covers the range 10^{15}–10^{22} for many organic liquids and water, as stated by Avedisian (1985).

Conclusions

The absence of buoyancy results in the onset of boiling at low levels of heat flux not otherwise possible in earth gravity. As the heat flux is increased in microgravity, the heater surface superheat at which nucleation occurs first increases and then decreases. On viewing the motion films taken through the semi-transparent heater surface, it is concluded that the decrease in superheat at the highest heat flux used is associated with heterogeneous nucleation, since these nucleations take place at the identical site on the heater surface. At both lower levels of heat flux, on the other hand, nucleation occurs at various random locations, generally followed by vapor bubble growth rates which can be classified as violent, and are believed to represent a special form of homogeneous nucleation, termed quasi-homogeneous nucleation here.

The cavity sizes estimated from the measured heater surface superheats at nucleation, using the heterogeneous nucleation theory involving the activation of a preexisting critical size vapor bubble, agrees reasonably well with the approximate sizes of cavities present on the surface. For what is observed and classified as quasi-homogeneous nucleation here, the influence of heat flux level and system pressure, used to vary the initial bulk liquid subcooling, are explained by a modification of classical homogeneous nucleation theory: The heater surface superheat at nucleation increases as the heat flux increases, and decreases as the system pressure increases.

References

Avedisian, C. T., 1985, "The Homogeneous Nucleation Limits of Liquids," *J. Phys. Chem. Ref. Data,* Vol. 14, No. 3, pp. 695–729.

Cole, R., 1974, "Boiling Nucleation," in *Advances in Heat Transfer,* Vol. 10, J. P. Hartnett and T. F. Irvine, Jr., eds., Academic Press, NY, pp. 85–166.

Ervin, J. S. and Merte, H., Jr., 1991, "A Fundamental Study of Nucleate Pool Boiling Under Microgravity," Report No. UM-MEAM-91-08, Department of Mechanical Engineering and Applied Mechanics, University of Michigan, Ann Arbor, MI, Final Report on NASA Grant NAG3-663.

Ervin, J. S., Merte, H., Keller, R. B., Kirk, K., 1992, "Transient Pool Boiling in Microgravity," *Int. J. Heat Mass Transfer,* Vol. 35, pp. 659–674.

Fisher, J. C., 1948, "The Fracture of Liquids," *J. of Applied Physics,* Vol. 19, November, pp. 1062–1068.

Griffith, P., Wallis, J. D., 1960, "The Role of Surface Conditions in Nucleate Boiling," *Chem. Eng. Prog. Symp.,* Vol. 56, No. 30, pp. 49.

Hsu, Y. Y., 1962, "On the Size Range of Active Nucleation Cavities on a Heating Surface," ASME JOURNAL OF HEAT TRANSFER, 84C, pp. 207.

Iida, Y., Okuyama, K., Sakurai, K., 1993, "Peculiar Bubble Generation on a Film Heater Submerged in Ethyl Alcohol and Imposed a High Heating Rate over 10^7 k/s," *Int. J. Heat Mass Transfer,* Vol. 36, No. 10, pp. 2699–2701.

Iida, Y., Okuyama, K., Sakurai, K., 1994, "Boiling Nucleation on a Very Small Film Heater Subjected to Extremely Rapid Heating," *Int. J. Heat Mass Transfer,* Vol. 37, No. 17, pp. 2771–2780.

Mastroianni, M. J., Stahl, R. F., and Sheldon, P. N., 1978, "Physical and Thermodynamic Properties of 1,1,2-Trifluorotrichloroethane (R-113)," *J. of Chemical and Engineering Data,* Vol. 23, No. 2, pp. 113–118.

Merte, H., Jr., Lee, H. S., Keller, R. B., 1995, "Report on Pool Boiling Experiment Flown on STS-47-57-60 (PBE-IA-IB-IC)," NASA Contract NAS3-25812, Report No. UM-MEAM-95-01, February 1995, Department of Mechanical Engineering and Applied Mechanics, The University of Michigan, Ann Arbor, MI.

Skripov, V. P., 1974, *Metastable Liquids,* Halsted Press, John Wiley & Sons, New York.

Volmer, M., 1939, *Kinetics of Phase Change,* Steinkopff, Dresden, published by J. W. Edwards, Ann Arbor, MI., 1945.

Y. S. Hong
Research Assistant.

C. N. Ammerman
Research Assistant.

S. M. You
Associate Professor.
Mem. ASME

you@uta.edu
Department of Mechanical and
Aerospace Engineering,
The University of Texas at Arlington,
Arlington, TX 76019-0023

Boiling Characteristics of Cylindrical Heaters in Saturated, Gas Saturated, and Pure-Subcooled FC-72

A series of pool boiling experiments are performed in thermodynamically saturated, gas saturated, and pure-subcooled FC-72 using 25-, 50-, 75-, and 390-μm-diameter platinum wires. Comparisons of nucleate boiling characteristics are made between the various fluid-state/wire-size combinations. The effects of dissolved gas concentration on heat transfer are significant and are found to depend on length scale and heat flux. This discovery of a heater size and heat flux impact on dissolved-gas boiling enhancement provides insight into experimental results from previous investigations.

Introduction

The present experimental study was conducted to investigate pool boiling phenomena of a highly wetting liquid (FC-72) in various thermodynamic states. These states are classified as thermodynamically saturated, pure subcooled, and gas saturated. Thermodynamic saturation for a pure substance is achieved when the system temperature is maintained at the substance's saturation temperature for the given system pressure ($T_{sys} = T_{sat}(P_{sys})$). Throughout the remainder of this paper, thermodynamic saturation will be referred to simply as "saturation." For a pure-subcooled liquid, as illustrated in Fig. 1(A), the system temperature is maintained below that of the saturation temperature for the given system pressure ($T_{sys} < T_{sat}(P_{sys})$). The difference between the saturation and system temperature is the level of pure subcooling. A gas-saturated liquid is differentiated from a pure-subcooled liquid by the presence of dissolved gas. The gas-saturated state is what some previous investigators have referred to simply as "subcooled." The gas-saturated state is obtained when noncondensables are dissolved into the liquid substance, resulting in a two-component, two-phase system, as illustrated in Fig. 1(B). The total pressure of the system is the sum of the vapor pressure and the gas pressure ($P_{sys} = P_v + P_g$), using Dalton's law of partial pressures. Since the system is in equilibrium, the system temperature is equal to the saturation temperature at the given vapor pressure ($T_{sys} = T_{sat}(P_v)$). When the system temperature is less than $T_{sat}(P_{sys})$, the difference between T_{sys} and $T_{sat}(P_{sys})$ is the level of "gassy subcooling."

The dissolved gas concentration near a heated surface immersed in a gas-saturated fluid may not be representative of the equilibrium gas content within the bulk liquid. Observations of You et al. (1995) indicate that the dissolved gas content in a boiling fluid is not uniform due to local degassing near the heater surface. They suggest that gas is depleted by being convected away from the surface within the departing bubbles faster than it can be replenished by convection or diffusion. This gas depletion can cause the liquid near the heater surface to approach a pure-subcooled state, thus affecting the boiling heat transfer mechanism.

Previous Investigations. Dissolved gas effects on nucleate boiling were first presented by McAdams et al. in 1949. They studied the heat transfer from an electrically heated surface to water flowing through an annulus. They reported that air-pressurized (gas-saturated) water showed higher heat transfer than steam-pressurized (pure-subcooled) water between incipience and moderate levels of nucleate boiling. They also found that nucleate boiling wall superheats were fairly independent of velocity and level of pure subcooling. You et al. (1990a, 1990b, 1995), using cylindrical heaters immersed in saturated and gas-saturated FC-72, observed reduction of incipient superheat and enhancement in nucleate boiling with increasing dissolved gas concentration.

Carey (1992) reported that the boiling curve usually changes very little with increasing subcooling even though the mechanisms for subcooled boiling are considerably different from those of saturated boiling. Judd and Hwang (1976) observed this independence in wall temperature versus level of subcooling for methylene chloride boiling from a flat glass surface. Mudawar and Anderson (1989) discussed the effects of subcooling in pool boiling of FC-72 using vertically mounted, flat heaters. There was no substantial difference in the wall superheats during nucleate boiling for two different levels of subcooling (ΔT_{sub} = 20 and 35°C).

Carvalho and Bergles (1990), however, showed significant enhancement for subcooled nucleate boiling using a vertically mounted flat heater in FC-72. Levels of enhancement increased with increasing levels of subcooling (ΔT_{sub} = 11 and 31°C). At higher heat fluxes, their data for various subcooling levels merged to an asymptote which could be formed by extrapolation of the saturated boiling curve. Based on their results, it appears that Carvalho and Bergles applied the term "subcooled" in a general sense to refer to a gas-saturated liquid. Ambiguities in definition of thermodynamic state are fairly common in the literature. Zitz and Bergles (1993) tested a vertically oriented multichip array in saturated and subcooled FC-86 (FC-72). Prior to reducing the system temperature, they degassed their test liquid for 30 minutes. Zitz and Bergles saw significant reductions in nucleate boiling wall superheats with increasing levels of subcooling (ΔT_{sub} = 6 to 26°C). It is possible that Zitz and Bergles did not allow sufficient time for degassing or their test apparatus was not able to prevent regassing.

Moreno et al. (1993) introduced a small amount of xenon gas into their sodium-potassium pool boiler solar receiver to prevent large wall temperature overshoots at incipience during hot restarts after cloud transients. They reported that hot restarts were well behaved because some nucleation sites remained active during cloud cover. They suggested that this behavior is a result of gas bubbles that are entrained in the liquid by boiling-

Contributed by the Heat Transfer Division for publication in the JOURNAL OF HEAT TRANSFER. Manuscript received by the Heat Transfer Division August 8, 1995; revision received January 3, 1997; Keywords: Augmentation & Enhancement, Boiling, Phase-Change Phenomena. Associate Technical Editor: V. K. Dhir.

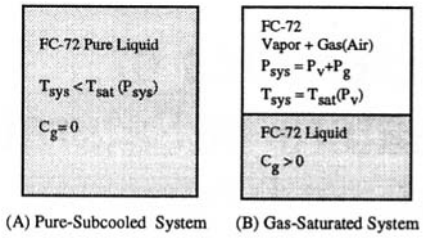

Fig. 1 Thermodynamic states

induced turbulence. However, another explanation may be that their boiling enhancement is instead caused by gas saturation of the sodium-potassium working fluid.

This review of previous investigations indicates that the effect of dissolved gas content on boiling heat transfer is important and is not always well understood. Since some investigators have used the term "subcooled" when referring to gas-saturated liquid, confusion has been introduced in the interpretation of their results. In addition, it should be noted that test vessels vented to atmosphere are unlikely to achieve a pure-subcooled state due to the possibility of noncondensable gases penetrating into the test liquid as the system temperature is decreased. The present study is an ongoing effort of work by You et al. (1990a, 1990b, 1995) to systematically quantify dissolved gas content effects. Their observation that gas-saturated boiling efficiency is affected by local degassing of the fluid near the heated surface is investigated further in the present study with the use of varying cylindrical heater sizes.

Experimental Apparatus and Procedure

The present experiments were conducted using platinum wires as resistance heaters. Platinum wires were chosen because their electrical resistance varies linearly with temperature, enabling wall temperature measurements during experimentation. The 25-, 50- and 75-μm-diameter wires were 2 cm long while the 390-μm-diameter wire was 5 cm long. Each wire was stretched between, and soldered to, the tips of six-gauge (AWG) copper posts which were used as bus bars. Each wire was approximately 15 cm below the surface of the liquid when tested. The test liquid selected for these experiments was FC-72, a highly wetting dielectric liquid used in electronic cooling applications. Liquid FC-72 can absorb 25 times more air than water (48 percent air by volume at 1 atm and 25°C; You et al., 1995).

Tests were conducted at seven different fluid states for each size wire resulting in 28 test cases. The seven fluid states were saturated (56°C), pure subcooled (41, 26, and 11°C), and gas saturated (41, 26, and 11°C)—all at system pressures of 1 atm. For the 75-μm wire, 16°C of pure subcooling was tested instead of 11°C. Table 1 shows a summary of these test conditions. System temperature varied within ±0.6°C at each state. The system temperatures for the pure-subcooled and gas-saturated states resulted in subcooling levels of 15, 30, and 45°C (40 instead of 45°C for the 75-μm wire in the pure-subcooled state).

The test facility used for this investigation was composed of a test vessel and an auxiliary degassing tank (shown in Fig. 2). The 3.5-liter test vessel contained FC-72 and was surrounded

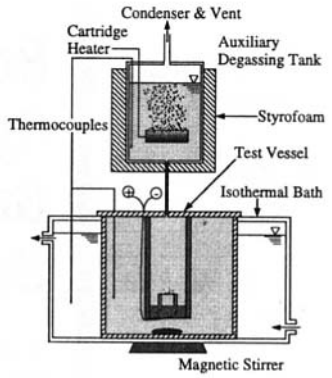

Fig. 2 Experimental apparatus

by an isothermal water bath. A thermovessel allowed precise temperature control of the isothermal bath. The test vessel and isothermal bath were constructed of LEXAN. The top portion of the test vessel was removable to allow access to, and replacement of, the wire heater. This access panel was bolted in place and sealed using a Buna-N gasket. The heater was placed in the test vessel with all electrical and thermocouple wiring exiting through a sealed port.

The test vessel was connected to the auxiliary degassing tank with flexible tubing. The bottom of the tank was elevated 15 cm above the top of the test vessel. The 2.2-liter tank was made from aluminum with LEXAN viewports and was insulated with styrofoam. The auxiliary tank was connected to a condenser which was vented to atmosphere. A 500-W cartridge heater was mounted within the tank to maintain the auxiliary liquid at saturation temperature. Liquid temperatures within the test vessel, auxiliary tank, and isothermal bath were measured using copper-constantan thermocouples which were calibrated with a precision thermometer.

The auxiliary degassing tank was used for both saturated and pure-subcooled tests. For the gas-saturated tests, the test vessel was connected directly to the condenser.

Saturation Test. The test vessel was completely filled with FC-72, and the degassing tank was filled to approximately 80 percent capacity. The cartridge heater was turned on causing the liquid in the degassing tank to boil vigorously for the duration of the experiment. The liquid in the tank was maintained continuously at saturation temperature (56.1 ± 0.1°C), providing a reservoir of degassed FC-72 for the test vessel.

The isothermal bath temperature was initially set at approximately 61°C. A magnetic stirrer inside the test vessel was used to expedite degassing. During degassing, air bubbles rose to the top of the test vessel, traveled through the connecting tubing and auxiliary tank, and were vented to atmosphere through the condenser. After the disappearance of air bubbles within the test vessel, the system was maintained at this condition for at least 48 hours to ensure that the test liquid was free of noncondensable gases. According to You (1990) for FC-72 agitated with a magnetic stirrer, approximately 2 hours of degassing is sufficient to reduce the dissolved gas content from

Nomenclature

C_g = dissolved gas concentration (moles gas/moles liquid)
CHF = critical heat flux (W/cm^2)
h = heat transfer coefficient (W/m^2°C)
P = pressure (kPa)
T = temperature (°C)
$\Delta T_{gas\text{-}sat}$ = level of gassy subcooling (°C)
ΔT_{sub} = level of pure subcooling (°C)

Subscripts

g = gas
gas-sat = gas saturated
sub = pure subcooled
sat = saturation
sys = system property
v = vapor
w = wall

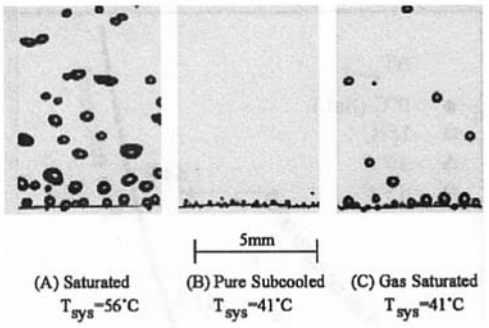

Fig. 3 Nucleate boiling photos at 50 percent of CHF (FC-72, 75-μm-diameter wire)

48 percent to 2 percent. (Likewise, approximately 2 hours of regassing is sufficient to increase the dissolved gas content from 2 percent to 48 percent.)

Pure-Subcooled Test. After conducting the saturation experiments, the isothermal bath temperature was decreased to obtain the desired level of subcooling within the test vessel. The volume of the test liquid decreased as the temperature was reduced (approximately 0.35 liter from 57 to 11°C). This volume deficit was compensated for by a supply of saturated liquid from the auxiliary tank. The magnetic stirrer was activated to accelerate the cooling process. The saturated and pure-subcooled cases were run consecutively so that degassing the test fluid was only required once for each wire size. During the time required to complete a set of saturated/pure-subcooled cases, the total mass of FC-72 liquid within the test facility remained relatively constant, thus no fresh liquid was introduced to "top off" the system.

Gas-Saturated Test. The test liquid was degassed at the saturation state (56°C) for approximately 2 hours. At the end of 2 hours, the system temperature was reduced to, and maintained at, the first level of gassy subcooling. During the temperature reduction, air was allowed to dissolve into the test liquid through the vent. The magnetic stirrer was turned on during this time to promote replenishment of the dissolved gas. The average time duration of a temperature reduction/regassing was 11 hours, with a minimum duration of 5 hours. Upon reaching the desired gas-saturated condition, the magnetic stirrer was turned off and testing was initiated. After completing a series of gas-saturated runs, the temperature was reduced to the next level of gassy subcooling.

Data Acquisition and Visualization. Upon reaching a desired state, five runs for each test condition were conducted with an interval of five minutes between runs. Data were taken only for increasing heat flux. The heater resistance was measured before and after each run to confirm any occurrence of hysteresis in, or damage to the heating element. The uncertainties for the 50-μm-diameter wire, calculated by the methods of Kline and McClintock (1953), are ±2.0 percent and ±1°C for heat flux and wall temperature measurements, respectively.

The test facility, a DC power supply, and a data acquisition board were controlled by a 386 PC. Voltage sensors and the power supply were connected to the wire heater via the copper posts. The power supply was connected in series with the heater and a standard resistor which was used to determine the current passing through the heater. After each power supply increment, the data acquisition program monitored heater temperature (wire resistance) to protect the heater in the event of critical heat flux (CHF). If a temperature difference greater than 20°C occurred between two successive temperature measurements, CHF was presumed. While monitoring temperature for CHF, 1000 temperature data points were collected and averaged over successive 35-second intervals. When the difference between two consecutive average temperatures was less than 0.2°C, steady-state conditions were presumed.

Video imaging equipment was used to record the boiling phenomena. The camera shutter speed was set at 1/10,000th of a second to capture the rapidly moving bubbles. A 30 cm focal-length lens was placed in front of the camera to magnify the image. A high-intensity projection bulb was used to provide background lighting. A more detailed description of the video imaging equipment is given by Ammerman et al. (1996).

Results and Discussion

Representative photos of fully developed nucleate boiling for each thermodynamic state are shown in Fig. 3. These photos are of the 75-μm-diameter wire and are taken at 50 percent of CHF. For the saturated state, shown in Fig. 3(A), the average bubble size appears to be independent of height above the wire, indicating the saturated fluid condition. Figures 3(B) and 3(C) clearly demonstrate differences in nucleate boiling behavior between the pure-subcooled and gas-saturated states, respectively, even though each system is at the same temperature (41°C). Under pure-subcooled conditions, bubbles continuously grow and collapse on the wire. The few bubbles which actually depart from the wire condense rapidly and vanish. For the gas-saturated state, the frequency of bubbles departing the wire is seen to be significantly less than for the saturated state. However, in contrast with the pure-subcooled state, departing bubbles did not vanish. Instead, these bubbles rose to the top of the vessel indicating that they consisted largely of noncondensable gas.

Boiling curves for the 50-μm wire in the saturated and pure-subcooled states are shown in Fig. 4. The saturated data are denoted by closed symbols. The natural convection data (not shown) were within ±2.6 percent of Kuehn and Goldstein's (1976) natural convection prediction for cylinders. The heat flux is plotted against wall superheat ($T_w - T_{sat}(P_{sys})$). With this abscissa, the boiling data for all levels of subcooling merge with the saturated case to form a single, degassed nucleate boiling curve (with a different CHF for each case). This merging of data indicates that nucleate boiling wall temperature is insensitive to level of subcooling for the range of temperatures examined. The result of a single boiling curve for all degassed cases is remarkable considering the differences in the structure

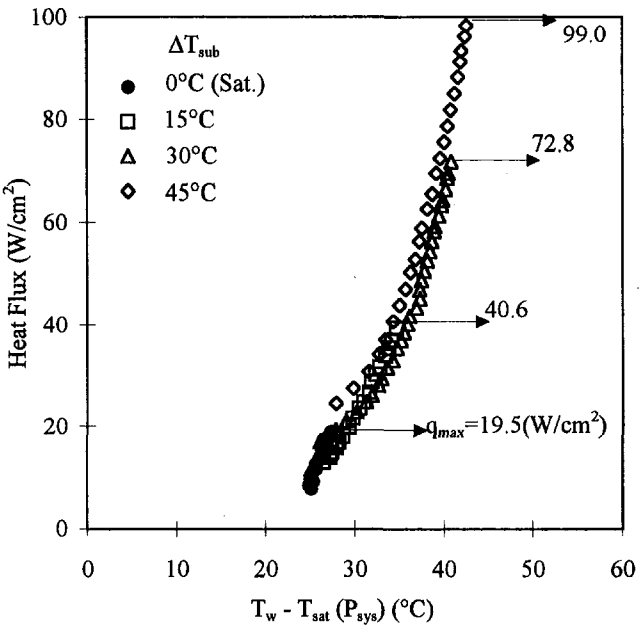

Fig. 4 Pure-subcooled nucleate boiling curves (50-μm-diameter wire)

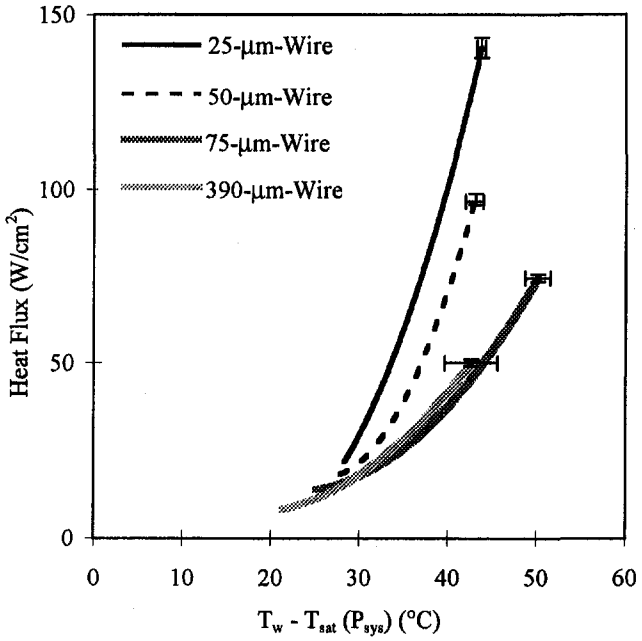

Fig. 5 Pure-subcooled boiling curves (25-, 50-, 75-, and 390-μm-diameter wires)

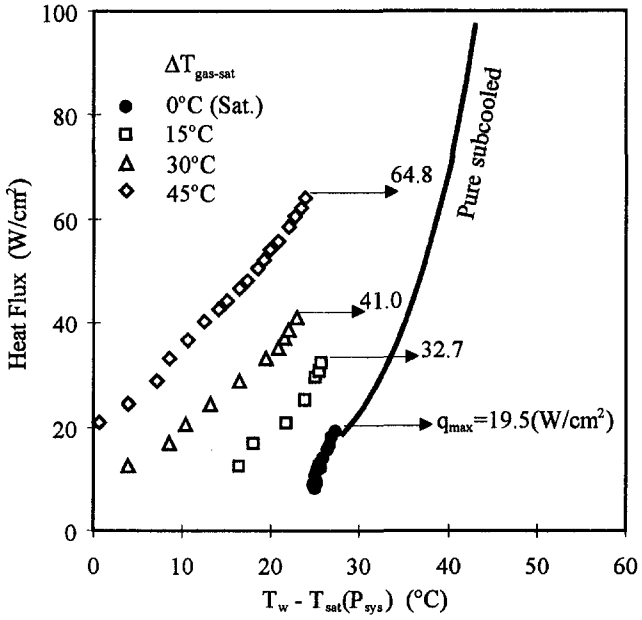

Fig. 6 Gas-saturated boiling curves (50-μm-diameter wire)

of the vapor phase indicated by Figs. 3(A) and 3(B) (i.e., bubbles departing from the wire for the saturated case and collapsing on the wire for the pure-subcooled case). As was mentioned in the introduction, previous investigators have reported on the collapsing of the subcooled nucleate boiling curves.

Figure 5 shows a comparison of the saturated and pure-subcooled boiling curves for all wire sizes tested. The degassed data for each of the wire sizes exhibited a wall temperature independence with level of subcooling. Therefore, a single curve representing each data set is shown with its respective wall temperature and heat flux uncertainty bands (95 percent confidence level). Also clearly demonstrated in this figure is a reduction in nucleate boiling heat transfer coefficient with increasing diameter from the 25- to the 75-μm-diameter wire. The 390-μm boiling curves lie nearly on top of the 75-μm data indicating that nucleate boiling heat transfer may be independent of diameter above the 75-μm-diameter wire size. These trends in heat transfer versus length scale are similar to the trend in saturated CHF versus wire diameter reported by Sun and Lienhard (1970). Sun and Lienhard developed an empirical correlation to predict the CHF of horizontal cylinders immersed in saturated liquids expressed as a function of cylinder radius and fluid properties. Sun and Lienhard's correlation was later expanded by You et al. (1994). This correlation showed a decrease in CHF with increasing cylinder diameter up to a diameter of approximately 3 mm (for FC-72) beyond which CHF was independent of length scale. Relative heater surface roughness is another factor which may contribute to differences in these data sets, however, all wires were obtained from the same manufacturer to minimize this possibility.

Gas-saturated boiling curves are shown in Fig. 6 for the 50-μm-diameter wire. Heat flux is plotted against wall superheat as in Fig.'s 4 and 5. The closed symbols denote the saturated case. Added for comparison is the representative pure-subcooled boiling curve for the 50-μm wire depicted with the solid line. The gas-saturated cases showed enhancement in nucleate boiling compared with the saturated and pure-subcooled cases. This nucleate boiling enhancement increased with decreasing system temperature (increasing gassy subcooling), and thus, increasing dissolved gas content. Table 1 shows the estimated dissolved gas concentration for the levels of gas saturation tested. This gas-saturated enhancement trend was also observed by You et al. (1995). They suggested that higher partial gas pressures promote nucleation and increase the number of active nucleation sites. For a given total pressure, the combined presence of gas and vapor within an embryonic bubble reduces the vapor pressure, and hence, the wall temperature required to activate the cavity. Therefore, more sites are activated at a given wall temperature for the gas-saturated case than for the pure-subcooled or saturated case. The gas-saturated boiling data for the 25-, 75-, and 390-μm wires showed similar trends as the 50-μm data and were therefore omitted.

Although enhancements were seen in both incipience and nucleate boiling, there was a substantial decrease in CHF for the gas-saturated cases compared to their corresponding pure-subcooled cases (Figs. 4 and 6). The authors' suspect that CHF increases for the pure-subcooled condition due to condensation of vapor during bubble growth, delaying the onset of hydrodynamic instability. The presence of gas inhibits this condensation thus causing lower CHF values for the gas-saturated condition. These CHF phenomena are currently being studied in greater detail by the present authors.

The authors propose that the appropriate reference superheat for the gas-saturated data is $T_w - T_{sat}(P_{sys})$, as shown in Fig. 6, even though $T_{sat}(P_v)$ is the saturation temperature of the test liquid. This definition of wall superheat is proposed for two reasons. First, this superheat provides a true measure of the boiling enhancement (reduction in wall temperature) over the saturation and subcooled states due to the presence of dissolved gas. Because of this, the degassed nucleate boiling curve represents the lower limit of gas-saturated enhancement. Secondly,

Table 1 Combinations of tested fluid conditions for 25-, 50-, 75-, and 390-μm-diameter wires

System temperature, subcooling level, and gas concentration [T_{sys} (°C), ΔT (°C), Cg (moles/mole)]		
Saturated	Gas saturated	Pure subcooled
56, 0, 0	41, 15, 2.41×10^{-3}	41, 15, 0
	26, 30, 3.82×10^{-3}	26, 30, 0
	11, 45, 4.55×10^{-3}	11, 45, 0*

* For 75 μm, 16, 40, 0.

due to gas depletion near the heater surface, the local value of gas concentration, and hence the local value of P_v, is unknown. Therefore $T_{sat}(P_v)$ for the liquid near the heater surface is unknown and varies with heat flux as gas depletion rates vary.

As seen in Fig. 6, boiling enhancement due to the presence of dissolved gas decreased with increasing heat flux. This trend is illustrated for the 50-μm wire in Fig. 7 which shows dissolved-gas enhancement versus heat flux for varying levels of gassy subcooling. Dissolved-gas enhancement is defined as $(h_{gas\text{-}sat}/h_{sub}) - 1$. The degree of enhancement increases significantly with increasing dissolved gas concentration (Table 1). Dissolved gas enhancement, however, is clearly seen to decrease with increasing heat flux for a given level of gassy subcooling. The authors attribute this decrease in enhancement to local degassing near the heater surface, as discussed in the introduction. Apparently, as heat flux increases, the volume of gas-depleted liquid near the surface increases creating a fluid barrier which inhibits the convection or diffusion of gas back to the surface.

The effect of heater size on dissolved-gas enhancement is shown in Fig. 8. Included with the present 30°C gas-saturated data are gas-saturated FC-72 boiling data for You et al.'s (1990b) 510-μm-diameter cylinder at 27°C gassy subcooling and O'Connor et al.'s (1996) 8 by 18 mm, flat heater at 20°C gassy subcooling. A clear trend of decreasing enhancement versus increasing heater size can be seen. Furthermore, the data for O'Connor et al.'s rectangular heater (with a characteristic length over 15 times that of the 510-μm cylinder) showed no enhancement over their saturated-state data through most of the fully-developed nucleate boiling regime. This heater size trend is believed to be related to gas depletion near the heater surface also. In the extreme gas-depletion case, fluid near the heater surface becomes pure subcooled resulting in no dissolved-gas enhancement, as in the 20°C gassy subcooled case of O'Connor et al.

The discovery of these heat flux and heater size effects on the gas-enhancement trends provide insight into apparent inconsistencies in previous investigators' experimental results. In addition, some working fluids can absorb large amounts of gas while others may be only minimally affected by the presence of gas. For example, FC-72 can absorb 48 percent air by volume at 1 atm and 25°C, whereas water can only absorb 1.9 percent air by volume at the same conditions (Flourinert Product Manual, 1987). Therefore, special attention to dissolved gases may not be required when testing a relatively large heater immersed in water, and no distinction between pure subcooling and gassy subcooling need be made. However, investigators should be sensitive to the possible effects of noncondensable gases, especially when working with highly wetting liquids.

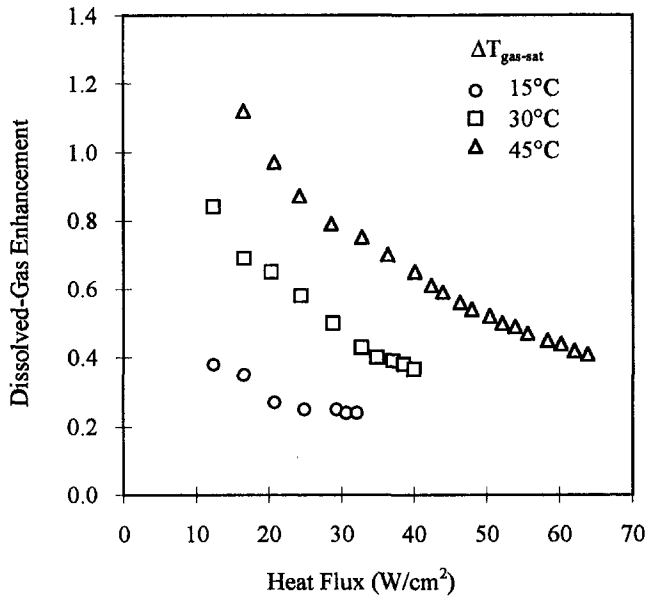

Fig. 7 Effect of heat flux on dissolved-gas enhancement (50-μm wire)

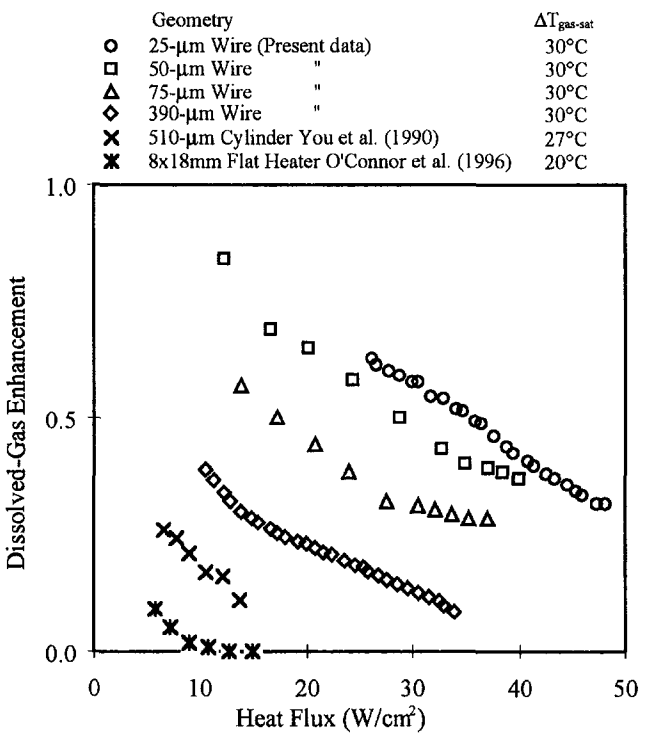

Fig. 8 Heater size effect on dissolved-gas enhancement

Conclusions

An experimental investigation was conducted to examine the heat transfer from 25-, 50-, 75-, and 390-μm-diameter wires immersed in saturated, pure-subcooled, and gas-saturated FC-72. The following conclusions have been reached from this study:

1 The presence of dissolved gas in FC-72 enhanced nucleate boiling heat transfer. For a given wire size, this enhancement increased as the dissolved gas concentration increased.
2 Boiling enhancement due to the presence of dissolved gas decreased with increasing heat flux and increasing heater size. These decreases in enhancement are attributed to local gas depletion within the fluid near the heater surface. Understanding these gas-depletion effects provides insight into apparent inconsistencies in results from previous investigations.
3 Nucleate boiling wall superheats in the pure-subcooled state were observed to be independent of level of subcooling, as reported by other investigators. These subcooled data merged with the saturated boiling data to form a single, degassed nucleate boiling curve (with different values of CHF for each level of subcooling). These data merged despite the obvious differences in vapor-phase structure observed from photos.
4 Nucleate boiling heat transfer in the pure-subcooled state decreased with increasing wire size from the 25- to 75-μm-diameter wire. Data for the 390-μm wire collapsed with the 75-μm wire—this data possibly indicating negligible length-scale effect on heat transfer above 75 μm.

References

Ammerman, C. N., You, S. M., and Hong, Y. S., 1996, "Identification of Pool Boiling Heat Transfer Mechanisms From a Wire Immersed in Saturated FC-72

Using a Single-Photo/LDA Method," ASME JOURNAL OF HEAT TRANSFER, Vol. 118, pp. 117–123.

Carey, V. P., 1992, *Liquid-Vapor Phase-Change Phenomena.* Hemisphere, Washington, pp. 225.

Carvalho, R. D. M., and Bergles, A. E., 1990, "The Influence of Subcooling on the Pool Nucleate Boiling and Critical Heat Flux of Simulated Electronic Chips," *Proceedings of the 9th International Heat Transfer Conference,* Jerusalem, pp. 289–294.

Judd, R. L., and Hwang, K. S., 1976, "A Comprehensive Model for Nucleate Pool Boiling Heat Transfer Including Microlayer Evaporation," ASME JOURNAL OF HEAT TRANSFER, Vol. 98, pp. 623–629.

Kline, S. J., and McClintock, F. A., 1953, "Describing Uncertainties in Single-Sample Experiments," *Mechanical Engineering,* Vol. 75, pp. 3–8.

Kuehn, T. H., and Goldstein, R. J., 1976, "Correlating Equations for Natural Convection Heat Transfer Between Horizontal Circular Cylinders," *International Journal of Heat and Mass Transfer,* Vol. 19, pp. 1127–1134.

McAdams, W. H., Kennel, W. E., Minden, C. S., Carl, R., Picornell, P. M., and Dew, J. E., 1949, "Heat Transfer at High Rates to Water with Surface Boiling," *Industrial and Engineering Chemistry,* Vol. 41, No. 9, pp. 1945–1953.

Moreno, J. B., Andraka, C. E., Mos, T. A., Cordeiro, P. G., Dudley, V. E., and Rawlinson, K. S., 1993, "First On-Sun Test of a NaK-78 Pool-Boiler Solar Receiver," *28th Intersociety Energy Conversion Engineering Conference: Energy Environment Economics,* pp. 2.511–2.518.

Mudawar, I., and Anderson, T. M., 1989, "High Flux Electronic Cooling by Means of Pool Boiling—Part I: Parametric Investigation of the Effects of Coolant Variation, Pressurization, Subcooling, and Surface Augmentation," ASME HTD-Vol. 111, pp. 25–34.

O'Connor, J. P., You, S. M., Chang, J. Y., 1996, "Gas-Saturated Pool Boiling Heat Transfer From Smooth and Micro-Porous Surfaces in FC-72," ASME JOURNAL OF HEAT TRANSFER, Vol. 118, pp. 662–667.

Product Manual, 1987, Fluorinert Electronic Liquids, Commercial Chemical Products Division, 3M Company, St. Paul, Minnesota.

Sun, K. H., and Lienhard, J. H., 1970, "The Peak Pool Boiling Heat Flux on Horizontal Cylinders," *International Journal of Heat and Mass Transfer,* Vol. 13, pp. 1425–1439.

You, S. M., 1990, "Pool Boiling Heat Transfer with Highly-Wetting Dielectric Fluids," Ph.D. thesis, University of Minnesota, Minneapolis, Minnesota.

You, S. M., Hong, Y. S., and O'Connor, J. P., 1994, "The Onset of Film Boiling on Small Cylinders: Local Dryout and Hydrodynamic Critical Heat Flux Mechanisms," *International Journal of Heat and Mass Transfer,* Vol. 37, pp. 2561–2569.

You, S. M., Simon, T. W., and Bar-Cohen, A., 1990a, "Experiments on Boiling Incipience with a Highly-Wetting Dielectric Fluid: Effects of Pressure, Subcooling and Dissolved Gas Content," *Heat Transfer 1990,* Vol. 2, pp. 337–342.

You, S. M., Simon, T. W., and Bar-Cohen, A., 1990b, "Experiments on Nucleate Boiling Heat Transfer with a Highly-Wetting Dielectric Fluid: Effects of Pressure, Subcooling and Dissolved Gas Content," *Cryogenic and Immersion Cooling of Optics and Electronic Equipment,* ASME HTD-Vol. 131, pp. 45–52.

You, S. M., Simon, T. W., Bar-Cohen, A., and Hong, Y. S., 1995, "Effects of Dissolved Gas Content on Pool Boiling of a Highly Wetting Fluid," ASME JOURNAL OF HEAT TRANSFER, Vol. 117, pp. 687–692.

Zitz, J. A., and Bergles, A. E., 1993, "Immersion Cooling of a Multichip Module by Pool Boiling of FC-86," *Advances in Electronic Packaging,* EEP-Vol. 4-2, pp. 917–926.

Enhanced Boiling Heat Transfer From Micro-Porous Cylindrical Surfaces in Saturated FC-87 and R-123

J. Y. Chang
Research Assistant

S. M. You
Associat Professor
Mem. ASME

Department of Mechanical and Aerospace Engineering,
The University of Texas at Arlington,
Arlington, TX 76019-0023

The present research is an experimental study of pool boiling heat transfer from cylindrical heater surfaces immersed in saturated FC-87 and R-123. The baseline heater surfaces tested are plain, integral-fin with 709 fins/m, and commercial enhanced (High-Flux and Turbo-B). In addition, a highly effective micro-scale enhancement coating is applied to the plain and integral-fin surfaces to augment nucleate boiling heat transfer. Experiments are performed to understand the effects of surface micro- and macro-geometries on boiling heat transfer. The boiling performance of the micro-porous enhanced plain and integral-fin surfaces are compared with the High-Flux and the Turbo-B surfaces. At high heat flux conditions, the break down of the bulk liquid feed mechanism reduces boiling enhancement from the cylindrical surfaces.

Introduction

One boiling enhancement method of great interest is to increase the number of micro-scale cavities on a surface through the use of porous coatings, mechanical grooves, or dendrites. The micro-geometries of these enhanced surfaces serve to increase the vapor/gas entrapment volume and the nucleation site density. These increases combine to reduce incipient and nucleate boiling superheats ($T_w - T_{sat}$), resulting in larger boiling heat transfer coefficients.

Considerable endeavors have been undertaken to develop a high-performance nucleate boiling surface. Yilmaz and Westwater (1981) tested five enhanced tube surfaces (ECR-40, GEWA-T, High-Flux, CSBS, and Thermoexcel-E), one integral low-fin tube, and one plain smooth tube with two pure hydrocarbons (isopropyl alcohol and p-xylene). The High-Flux tube showed the best heat transfer rate above 20 kW/m^2. Marto and Lepere (1982) conducted pool boiling heat transfer experiments on a 15.8 mm o.d. copper tube immersed in R-113 and FC-72. They investigated four different surfaces including High-Flux. High-Flux showed the best performance over a range of heat fluxes. Webb (1983) examined a wide variety of pool boiling data for porous coatings composed of nearly spherical particles. He concluded that application of particle diameters between 100–500 μm had little effect on enhancement. He also concluded that the preferred coating thickness is about four particle diameters. The performance benefit of this coating method is thought to be due to an increase in effective boiling surface area within the porous layer. Effective boiling surface area is the vapor-liquid contact surface area which exists within the pores formed between the stacked particles.

Some investigators (Stephan and Mitrovic, 1981; Marto and Hernandez, 1983; Ayub and Bergles, 1987; Sokol et al., 1990) have presented nucleate boiling data for different conditions in an attempt to explain the heat transfer enhancement mechanism of the GEWA-T tube. These studies indicate that the formation of flow channels between neighboring T-shaped fins is important. The liquid/vapor flow within these channels, if properly maintained, causes a significant increase in heat transfer. In a more advanced configuration, composite enhancement techniques were employed to increase the performance of the GEWA-T tube. Marto et al. (1985) wrapped the interfin channels of a GEWA-T tube with 0.1 mm diameter copper wires. Ayub and Bergles (1988) inserted a kitchen sponge material into the lower portions of the channels of the GEWA-T tube. These additional enhancement techniques increased the number of active bubble cavities during decreasing heat flux conditions. Ayub and Bergles (1988) explained that these increases were due to the activation of large, initially inactive nucleation sites during the increasing heat-flux portion of the boiling curve; these larger sites remain active with decreasing heat flux.

McManus et al. (1986) evaluated High-Flux and Turbo-B tubes for use in an R-114 water chiller application. The boiling tubes immersed in the test liquid were heated internally by warm water. The High-Flux tube performed better than the Turbo-B tube. Recently, Webb and Pais (1992) completed a broad comparative study for nucleate pool boiling of five different tube surface geometries: plain, integral-fin with 1024 fins/m, GEWA-TX19, GEWA-SE, and Turbo-B. Five different refrigerants were used with a heat flux range of about 1 to 100 kW/m^2. In nearly all cases, the Turbo-B tube showed the best heat transfer performance.

You et al. (1991), O'Connor and You (1995), O'Connor et al. (1995), and Chang and You (1996) successively developed micro-porous enhancement techniques using various particles: alumina, silver flakes, diamond, copper, and aluminum. The particle sizes ranged from about 1 to 50 μm—at least an order of magnitude smaller than the feature sizes of commercial enhanced surfaces. Their coated flat-heater surface immersed in saturated FC-72 showed about a 330 percent enhancement in the nucleate boiling heat transfer coefficient and about a 100 percent increase in CHF over the non-coated surface.

The present research is an experimental study of pool boiling heat transfer from tubes immersed in FC-87 and R-123. Under increasing heat flux conditions, the following six tube geometries are tested: plain, micro-porous enhanced, integral-fin with 709 fins/m (low fin), micro-porous enhanced low fin, Turbo-B, and High-Flux. Experiments are performed to understand the effects of surface micro- and macro-geometries on boiling heat transfer performance.

Contributed by the Heat Transfer Division for publication in the JOURNAL OF HEAT TRANSFER. Manuscript received by the Heat Transfer Division April 22, 1996; revision received January 22, 1997; Keywords: Augmentation & Enhancement, Boiling, Finned Surfaces. Associate Technical Editor: M. Sohal.

Experimental Apparatus and Procedure

Test Facility. The pool boiling test facility used for this study is shown in Fig. 1. The test liquid was contained within a glass vessel, which was submerged in an isothermal water container. Water temperature was controlled by a 1000-Watt immersion heater/circulator and an immersion cooler. A magnetic stirring bar was located inside the test vessel, and it was used to accelerate the degassing process before each case and to acquire thermal equilibrium before each experimental run. A water-cooled condenser was used during degassing and testing to minimize loss of the test liquid. Atmospheric pressure was maintained by venting the test vessel to ambient. Two copper-constantan thermocouples were placed within the test vessel to measure bulk liquid temperature. The cylindrical test heater was mounted horizontally to an aluminum support assembly and immersed in the test liquid.

Figure 2 shows a cross sectional representation of a typical test heater used during this study. The 76.2-mm-long copper test tube had three thermocouple holes on each end spaced 90 degrees apart. These 1-mm-diameter holes were 25 mm in length and were drilled axially along the tube. The copper tube was fitted to a commercial cartridge heater which was 9.5 mm in diameter and 88.9 mm in length. The incoloy sheath surface of the cartridge heater had been electrochemically plated with a thin copper layer to increase the wettability with molten solder. By heating the copper tube with the cartridge heater, the gap between the components was filled with lead-free silver solder (melting point ≈523 K). The cartridge heater had a 6-mm-long inactive heating zone at each end. The copper tubes used during this study were machined to have the same length with the heated zone of the cartridge heater. The unheated end sections of the cartridge heater were insulated with Teflon blocks and thermally nonconducting epoxy to minimize heat loss. A power supply was connected in series with a shunt resistor and the test heater. Direct current was supplied to the heating element by a DC power supply.

Figure 3 illustrates the representative scatter of measured temperatures from the six thermocouples installed within a single test heater. In this figure, the temperature measurements from initial heat flux up to CHF (256 kW/m^2) were made using the plain-surface cylinder immersed in saturated R-123. The six thermocouple readings fall within a band of ±0.7 K at heat flux values below 95 percent of CHF. The scatter band increased up to ±3.6 K at the heat flux just before CHF. Near the CHF point, three thermocouples at one side showed higher superheats than those at the other side. This surface temperature behavior near CHF is thought to be due to locally developed film boiling on one side of the heater. Localized film boiling is distinctively observed on the hotter side of the test heater, extending axially to the other side. The thermocouple readings in Fig. 3 indicate reliable temperature measurement from the present test heater.

Experimental error analyses for the heat flux and surface superheat measurements were performed using the method of Kline and McClintock (1953). Because the thermocouples were embedded within the copper tube, temperatures measured with them were extrapolated by a one-dimensional, radial heat conduction model to obtain a representative heater surface temperature at each applied heat flux. The correction was less than 1.5 K for the tube tested in Fig. 3. The indicated uncertainties account for calibration error, surface temperature correction, geometric uncertainty, and measurement resolution. For the test in Fig. 3, the uncertainty in the measured average surface superheat was estimated to be ±0.6 K. The calibration error was the major contribution to the uncertainty in the surface superheat measurements. The uncertainty in heat flux measurements was estimated to be ±three percent over the entire range of heat flux.

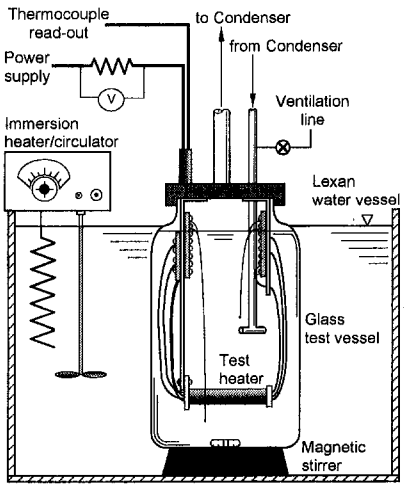

Fig. 1 Schematic of test apparatus

Test Procedure. The immersion heater/circulator was used to heat the water bath to the saturation temperature of the test liquid. Once saturation was reached, the test liquid remained at this temperature for two hours to remove dissolved gases. The magnetic stirrer was used during this process to accelerate dissolved gas removal. After degassing, the magnetic stirrer was turned off and data acquisition was initiated.

Heat flux was controlled by the voltage input of the DC power supply. After each voltage increase (heat flux increment), a 30-second delay was allowed before data acquisition. After the delay, the computer collected and averaged 45 surface temperature data points from each thermocouple, which took about 10 s. This was immediately followed by the acquisition and averaging of an additional 45 data points per thermocouple. A comparison was then made between these two average temperatures for each thermocouple. This procedure was repeated until the temperature differences for all thermocouples were less than 0.2 K. Usually it took about 1-to-2 minutes to reach the steady-state condition after each heat flux increment. After reaching steady state, bulk fluid temperature was measured and heat flux was calculated. For heat flux values greater than ≈80 percent of CHF, the instantaneous surface temperature was monitored for 30 s after each heat flux increment to prevent heater burnout. Each instantaneous surface temperature measurement was compared with the average surface temperature from the previous heat flux. If a temperature difference larger than 20 K at any thermocouple was detected, the data acquisition algorithm assumed CHF and immediately shut down the power supply. The CHF value was computed as the steady-state heat flux value just prior to power supply shutdown, plus half of the increment. If CHF was not detected during the 30 s delay, collecting and averaging of 45 surface temperature data points from each thermocouple was initiated and repeated until the steady-state condition was achieved. At least two consecutive runs were conducted for each surface tested. The time interval allowed be-

Nomenclature

CHF = critical heat flux, W/m^2
Nu_D = Nusselt number based on heater diameter
Pr_f = Prandtl number of liquid
Ra_D = Rayleigh number based on heater diameter
T_{bulk} = bulk fluid temperature, K
T_{sat} = saturation temperature, K
T_w = outside tube wall temperature, K

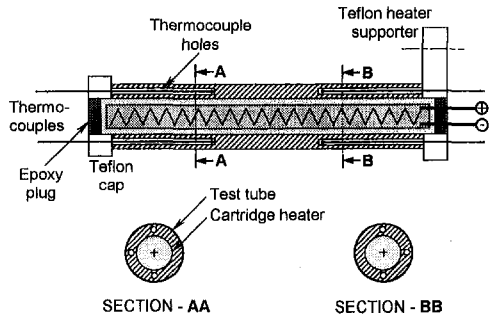

Fig. 2 Cross sectional view of test heater

tween each run was determined by monitoring test section surface temperature. The surface was assumed to reach thermal equilibrium if the surface temperature, averaged over approximately 10 s, was within ±0.1 K of the saturated bulk fluid temperature. In all cases, this time interval between runs was no less than 1 hour.

Results and Discussion

Pool boiling data were taken for six tube heaters with different surface configurations in saturated FC-87 and R-123 at 1 atm. Some selected properties of FC-87 and R-123 are listed in Table 1 for comparison. Both liquids are widely accepted as alternative heat transfer fluids in cooling or refrigeration applications. The six test sections were distinguished by their external surfaces and are summarized in Table 2. The external surfaces tested included a smooth or "plain" surface: the plain surface treated with the micro-porous coating, a low-fin external surface, the low-fin surface treated with the micro-porous coating, a High-Flux surface, and a Turbo-B surface. The micro-porous coating used in this research is the ABM coating developed by Chang and You (1996). The ABM coating was named from the initial letters of the three components: aluminum-brushable ceramic-M.E.K. The mixture of the three components was sprayed over the plain surface and the low-fin surface using a compressed air sprayer. The coated layer resulted in porous micro-structures with aluminum particles (1 to 20 μm) and a binder (Devcon Brushable-Ceramic) having a thickness of ≈50 μm after a carrier (M.E.K.) evaporated. Detailed descriptions of the ABM coating are provided by Chang and You (1996). Cross sectional views of the ABM-coated plain tube, the low-fin tube, the High-Flux tube, and the Turbo-B tube are shown in Fig. 4. For each enhanced tube geometry, the surface area

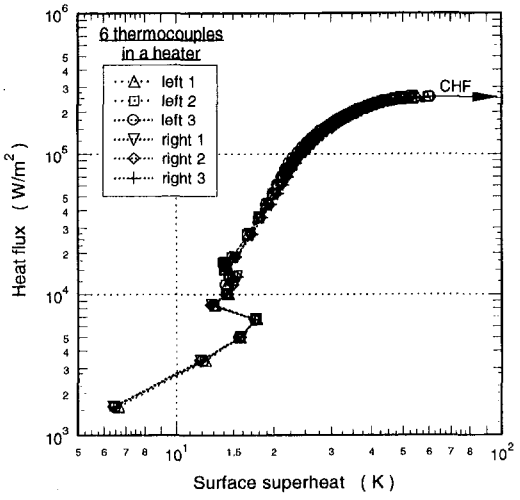

Fig. 3 Typical scatter of measured temperatures

Table 1 Selected properties of saturated FC-87 and R-123 at 1 atm

Property	FC-87	R-123	Ratio
Chemical formula	C_5F_{12}	$CHCl_2CF_3$	—
Boiling point (K)	302.3	301	—
Density: liquid (kg/m^3)	1571.6	1456	0.926
Density: vapor (kg/m^3)	12.38	6.46	0.522
Specific heat: liquid (J/kg · K)	1103	982	0.890
Latent heat (J/kg)	9.897E+4	1.70E+5	1.72
Thermal conductivity: liquid (W/m · K)	5.5E−2	8.0E−2	1.45
Viscosity: liquid (kg/m · sec)	6.69E−4	4.21E−4	0.629
Surface tension (N/m)	8.91E−3	1.483E−2	1.66

used to determine heat flux was based upon the tube outer diameter at the bottom of the fin (or just below the porous layer).

Natural Convection Tests. Natural convection tests were conducted with FC-87 at 1 atm and 283 K to compare with a natural convection correlation. The results of this test are plotted in Fig. 5. The Nu_D of the plain surface copper tube are within 4-to-9 percent of the correlation developed by Churchill & Chu (1975).

Single-phase natural convection curves for the ABM-coated plain tube and the High-Flux tube closely follow the plain surface values. These trends indicate that the effective heat transfer areas are not increased by the application of the micro-porous coating and the High-Flux treatment. The small scale of the pores and the highly viscous fluid layer flowing over the surface prevented area enhancement effects. Natural convection data for the Turbo-B tube show about 11 percent higher heat transfer coefficients than those of the natural convection correlation over the Ra_D values tested. As seen in Fig. 4(d), the Turbo-B tube surface is covered with helical, circumferential tunnels between tiny bent-over fin structures, providing some area enhancement.

Natural convection test results for the low-fin tube are also displayed in Fig. 5. By examining the tube geometry in Figure 4(*b*), the actual area increase of the low-fin tube is approximately 100 percent. By comparing the natural convection data, an area enhancement ratio was calculated. At a given heat flux value, the $(T_w - T_{bulk})$ value ratio was used to estimate the effective area enhancement. From these calculations, the low-fin tube was estimated to have a 67-to-90 percent area enhancement over the unfinned surface.

Plain Tube Tests. The plain surface copper tube was tested first with saturated FC-87 and R-123. The results from these tests are shown in Fig. 6. The natural convection data for the two liquids are in good agreement with the predictions by Churchill and Chu (1975). Boiling incipience was observed at locally activated boiling sites at just under 5 kW/m^2 and boiling over the entire heated surface was observed above 8 kW/m^2 for both cases. Webb and Pais (1992) presented cylindrical nucleate boiling data up to about 62 kW/m^2 with R-123. The current R-123 data are compared with their data in Fig. 6.

As the heat flux approached CHF, the active nucleate boiling sites that produced high vapor generation showed transition to

Table 2 Dimensions of tested tubes

Tested tube	Tube outer diameter	Enhancement thickness
Plain	15.6 mm	
ABM-coated plain	15.6 mm	≈50 μm
Low-fin	13.7 mm	880 μm
ABM-coated low-fin	13.7 mm	≈930 μm
High-flux	12.7 mm	≈400 μm
Turbo-B	17.2 mm	≈600 μm

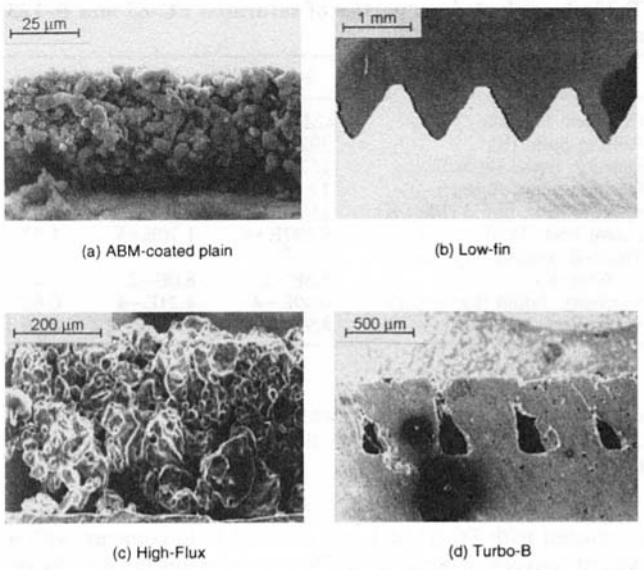

Fig. 4 SEM images of enhanced-surface cross sections

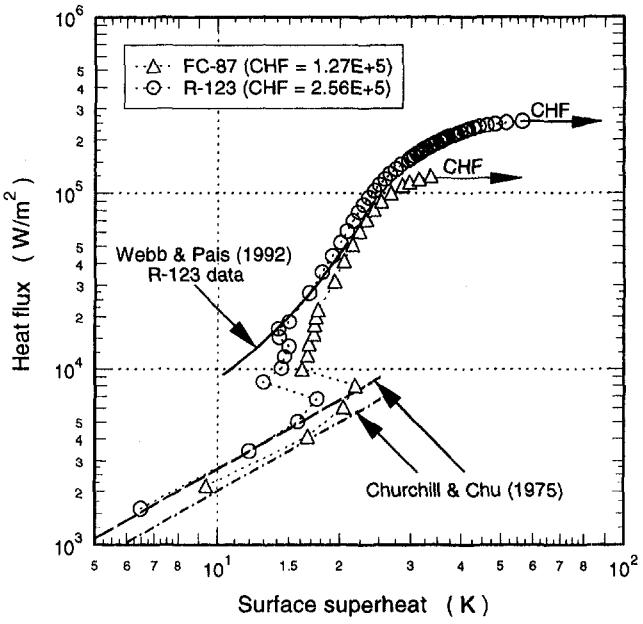

Fig. 6 Plain surface pool boiling data

local film boiling. As already discussed in Fig. 3, uneven surface-temperature behavior near CHF was caused by the localized vapor film on the hotter side of the test heater, which eventually extended axially over the entire heater. The saturated pool boiling curves for the plain tube (Fig. 6) show CHF values of 127 and 256 kW/m^2 for FC-87 and R-123, respectively. Zuber's (1959) CHF correlation predicts 156 and 215 kW/m^2 for saturated FC-87 and R-123, respectively. The plain-tube test results shown in Fig. 6 serve as reference data for the enhanced-tube experiments which follow.

Micro-Porous-Enhanced Tube Tests. Micro-porous enhancement coatings developed by O'Connor and You (1995), O'Connor et al. (1995), and Chang and You (1996) have been proven to augment pool boiling heat transfer. Those coatings effectively produced multi-layered micro-porous structures over the heater surface. In the present study, the ABM coating developed by Chang and You (1996) was applied to the plain tube surface. From Fig. 4(*a*), the ABM-coated plain surface can be seen to form numerous reentrant-type structures whose sizes are on the order of microns.

The pool boiling curves for the ABM-coated plain tube in saturated FC-87 and R-123 are shown in Fig. 7. Heaters immersed in the two liquids show nearly identical nucleate boiling wall superheats. At the initial heat flux values of about 2 kW/m^2, tiny bubbles were observed over the entire heated surface. The natural convection regime was replaced by the nucleate boiling regime. These tiny bubbles in the low heat flux range (<8 kW/m^2) augmented the heat transfer coefficient by up to 610 percent for FC-87 and 410 percent for R-123 compared to the plain surface. This enhancement was a result of the surface micro-porous coating which effectively trapped larger embryonic bubbles, thus dramatically decreasing incipient wall superheat. The observed tiny bubbles performed effectively to in-

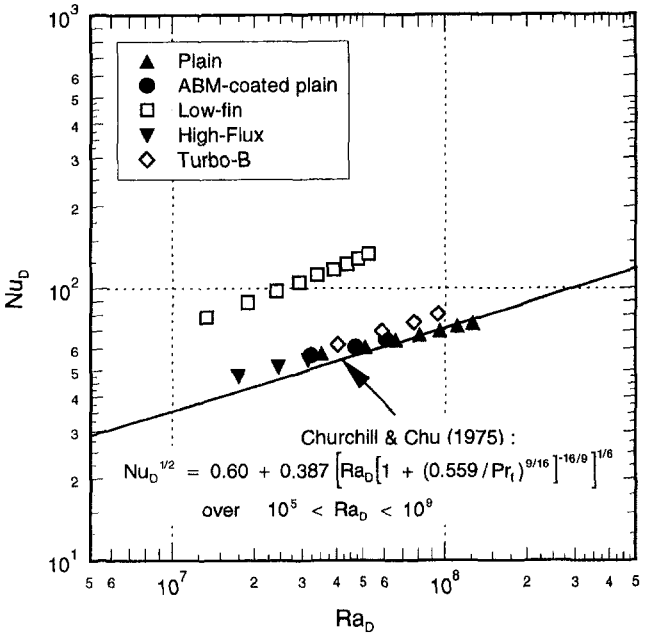

Fig. 5 Natural convection in subcooled FC-87

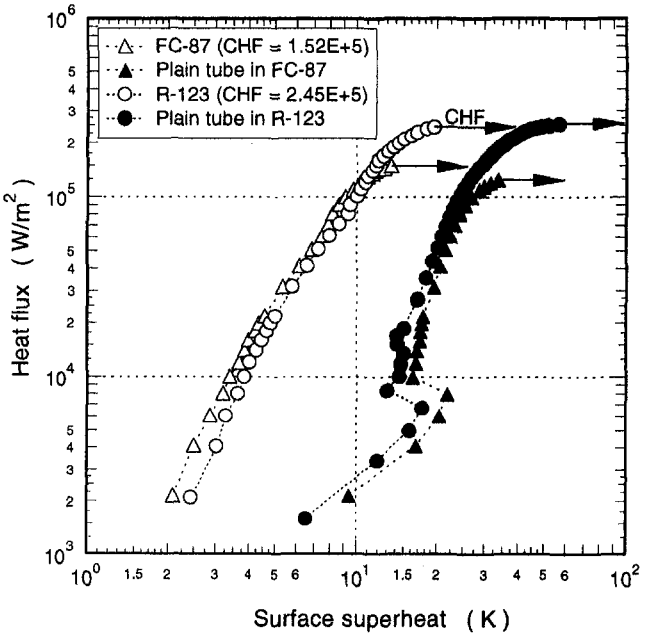

Fig. 7 ABM-coated plain surface pool boiling data

crease heat transfer. As heat flux increased further, bubble departure frequencies and sizes continued to increase. Heat transfer coefficients were 3-to-4.8 times and 2.4-to-3.8 times those of the plain tube for FC-87 and R-123, respectively. During the test with the ABM-coated plain tube, the FC-87 data showed slightly higher heat transfer enhancement than the R-123 data.

In Fig. 7, the ABM-coated plain tube shows CHF values of 152 and 245 kW/m^2 for FC-87 and R-123, respectively. These values are similar to those of the uncoated plain tube. This observation is significantly different from the flat heater test of Chang and You (1996) in which CHF increased significantly with the micro-porous surface enhancement in saturated FC-72. In the present study, the flat heater (10 mm × 10 mm) used by Chang and You (1996) was tested with and without the ABM surface coating in saturated FC-87. In Fig. 8, the boiling curves of the two different heater geometries are compared. At heat flux values greater than 100 kW/m^2, columns of bubbles formed around the cylindrical heater, decreasing the heat transfer rate by reducing the cooler bulk liquid feed mechanism—compare with the uncoated flat and tube heaters. This occurs when vapor bubbles streaming from the bottom side of the cylinder create a barrier which inhibits the feed rate of cool liquid to the sides and top of the cylinder. The vapor content near the sides and top surface of the cylinder increases, resulting in a higher void fraction. This "bubble blanketing" phenomenon over the cylindrical heater surface was dominant enough to produce similar CHF values regardless of the surface treatment. In Fig. 8, the flat heater showed a CHF value of 243 kW/m^2, which is 1.52 times that of the uncoated flat surface (CHF = 160 kW/m^2). The smaller enhancement of CHF for the cylindrical geometry is therefore believed to be due to the failure of the liquid feed mechanism.

For the ABM-coated flat surface data in Fig. 8, the incipient superheat was observed at ≈10 K. Considering the same micro-porous surface characteristics, this similar incipient superheat value is expected for the ABM-coated tube surface. The ABM-coated tube surface already experienced this superheat value at the initial heat flux of about 2 kW/m^2, and hence, boiling incipience was observed from the initial heat flux.

Low-Fin Tube Tests With and Without ABM Coating. A cross sectional view of the low-fin tube was shown in Fig. 4(*b*). The low-fin pitch and height were measured to be 1.39 and 0.88 mm, respectively. Pool boiling test results for this tube in saturated FC-87 are shown in Fig. 9. Boiling incipience occurred at ≈8.8 K superheat, and only a few bubbles were visible prior to a heat flux of 9.8 kW/m^2. At 9.8 kW/m^2, boiling over the entire surface was observed and the superheat shifted to 4.7 K. In the nucleate boiling regime, the low-fin tube showed 170-to-220 percent higher heat transfer coefficients than the plain tube. If the amount of the area increase is considered, this enhancement is higher than expected. In Fig. 9, a predicted nucleate boiling curve of the low-fin surface is plotted, which was based upon the area increase (≈100 percent) estimated from Fig. 4(*b*). It should be noted that the low-fin tube surface was formed by machining, and during the process the surface was roughened. The increased roughness produced more nucleation sites, and hence, higher nucleation performance at incipience and in the nucleate boiling regime. As heat flux approached CHF, the boiling-curve slope decreased, and finally CHF was observed at 236 kW/m^2 which is 1.86 times that of the plain tube.

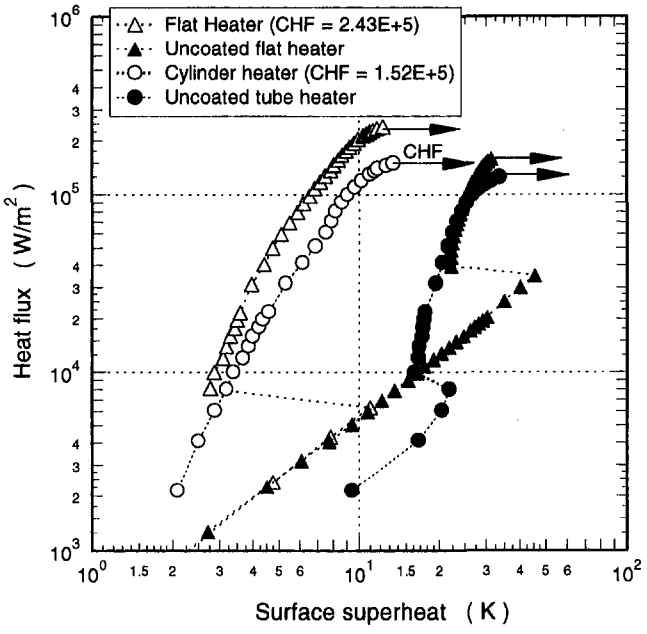

Fig. 8 Pool boiling data of ABM-coated surfaces in saturated FC-87

The ABM coating was applied to the low-fin tube test heater to produce combined enhancement due to increased area and enhanced surface microstructures. Figure 9 shows the boiling test results of the ABM-coated low-fin tube in saturated FC-87. The heat transfer coefficient of the ABM-coated low-fin tube increased up to 50-to-60 percent compared to the uncoated low-fin tube at heat fluxes lower than 50 kW/m^2. At heat fluxes higher than 100 kW/m^2, the enhancement was decreased to 15-to-20 percent. The CHF was measured to be 198 kW/m^2, which is 17 percent smaller than that of the uncoated low-fin tube. The small increase in nucleate boiling heat transfer at higher heat fluxes (>100 kW/m^2) was partially attributed to the bubble blanketing behaviors from the finned surface. Though vapor generation was increased with application of the ABM coating, the amount of vapor trapped between neighboring fins was increased due to a decreased vapor-bubble escape path. The increased thermal resistance due to trapped vapor bubbles produced small heat transfer enhancement and a decreased value of CHF. The boiling crisis mechanism in this case could be described as "dry-out" rather than "hydrodynamic" CHF. The dry-out mechanism is observed when the transition to film boiling is produced by increased void fraction over the heater surface due to geometrical constraints, which also occurs before the formation of hydrodynamic instability. For this reason, an effective bubble removal mechanism (macro-geometry) should be considered for application of the ABM coating to finned tubing to maintain the benefits of the micro-porous coating (micro-geometry).

Commercial Enhanced Tube Tests. Tests were conducted with a High-Flux tube and a Turbo-B tube in saturated FC-87 and R-123 for comparison purposes. Figures 10 and 11 illustrate the test data in FC-87 and R-123, respectively. In both liquids, the High-Flux tube showed incipience over the entire heater surface at the initial heat flux of about 2 kW/m^2. However, the Turbo-B tube in FC-87 showed incipient superheat of 6.8 K at the initial heat flux of about 2 kW/m^2. For the Turbo-B tube incipience data, it can be postulated that the large pores formed by the fin structures in the Turbo-B surface are flooded with FC-87 due to the higher wettability. At incipience, the High-Flux tube showed rapid initiation of boiling across the entire surface. Marto and Lepere (1982) also observed similar incipient behavior from their High-Flux surface. For the Turbo-B tube, the incipient bubbles were generated from sparse sites over the surface and the site density was increased gradually with increasing heat flux.

As seen in Fig. 4(*c*), the High-Flux surface contains cavity structures with nominal sizes ranging from 10 to 100 μm. The High-Flux tube showed the highest performance in the nucleate boiling heat transfer region. At heat fluxes equal to and above 10 kW/m^2, heat transfer coefficients were enhanced by 260 to

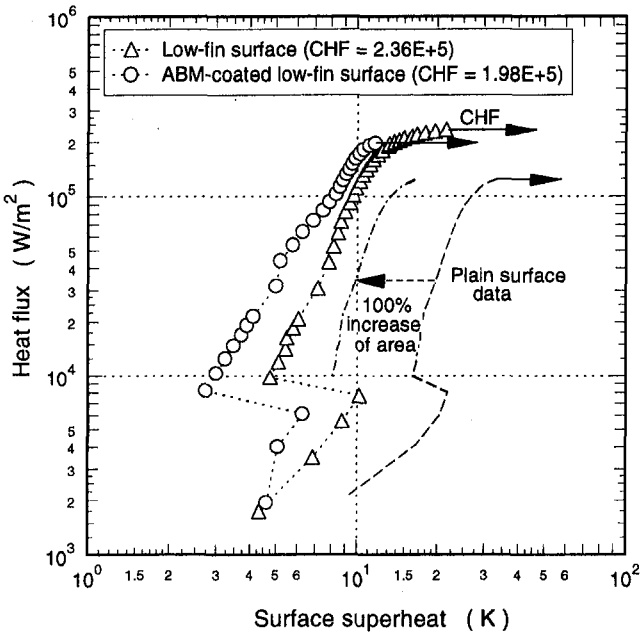

Fig. 9 Low-fin surface pool boiling data in saturated FC-87

810 percent for FC-87 and 460 to 1500 percent for R-123, when compared to the plain surface. From the present test results, it is evident that the amount of heat transfer enhancement tapered off as heat flux approached CHF. As heat flux is increased, enhanced structures are thought to be nearly filled with vapor instead of liquid. This lack of liquid promotes the bubble blanketing effect around the tube, resulting in a lower nucleate boiling enhancement at the higher heat flux values.

In Fig. 4(*d*), the Turbo-B surface is shown to have tiny bent-over fins of ≈600 μm in height, forming reentrant-type tunnels between them. These liquid-and-vapor passages were measured to have a diameter of ≈300 μm. These larger size cavities produced the highest performance in CHF. The Turbo-B tube showed CHF values of 243 kW/m^2 for FC-87 and 376 kW/m^2 for R-123, whereas the High-Flux tube showed 185 and 286 kW/m^2, respectively. The High-Flux surface with its porous structures performed better than the Turbo-B surface in the nucleate boiling regime. However, the Turbo-B surface is more beneficial at CHF. Large-sized tunnel structures in the Turbo-B surface are thought to permit a more effective separation of the vapors, thus retarding the onset of film boiling.

Pool boiling curves for the ABM-coated low-fin tube in FC-87 and R-123 are plotted together in Figs. 10 and 11, respectively. In Fig. 10, the ABM-coated low-fin tube shows comparable performance to the Turbo-B tube in the low heat flux nucleate boiling regime and better nucleate boiling performance above 20 kW/m^2. As heat flux increases to near CHF, the ABM-coated low-fin tube showed comparable heat transfer coefficients to the High-Flux tube. With the tests in R-123 (Fig. 11), the ABM-coated low-fin tube showed comparable performance to the Turbo-B tube above 150 kW/m^2. In the other heat flux ranges, the ABM-coated low-fin tube showed lower nucleate boiling performance than both the High-Flux and the Turbo-B tubes. However, it maintained a steeper slope nucleate-boiling curve up to near CHF.

Pool boiling curves for the ABM-coated plain tube in FC-87 and R-123 are plotted in Figs. 10 and 11, respectively, to compare with those of the ABM-coated low-fin tube. In both liquids, the pool boiling curves for the ABM-coated plain tube showed parallel slopes with those of the ABM-coated low-fin tube. However, the heat transfer coefficients were not enhanced as much as the amount of area increase (≈100 percent) by the low-fin surface. The test results indicate that the number of active nucleation sites was not doubled by applying the ABM coating to the low-fin surface. This was attributed to the superheat required to activate the micro-scale cavities provided by the ABM coating (see Figs. 7 and 8). As the low-fin surface experienced lower superheat due to the increased area (macro-geometry), activation of the micro-scale cavities (micro-geometry) was delayed. For this reason, a porous coating with larger particle sizes should be considered to produce higher nucleate boiling enhancement. From the current test results, surface micro-geometry was proven to be a dominant factor for the nucleate boiling heat transfer performance over the surface area increase. As shown in Figs. 10 and 11, moderate thermal excursions were observed for the ABM-coated low-fin surface.

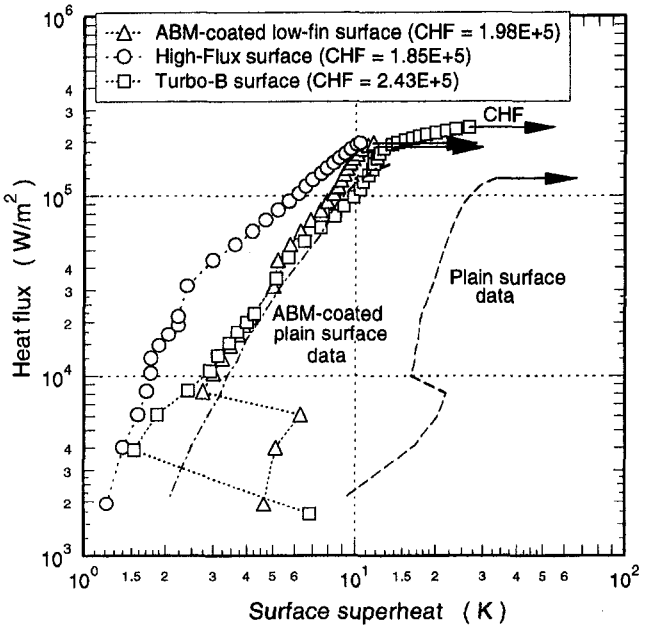

Fig. 10 Pool boiling data of enhanced surfaces in saturated FC-87

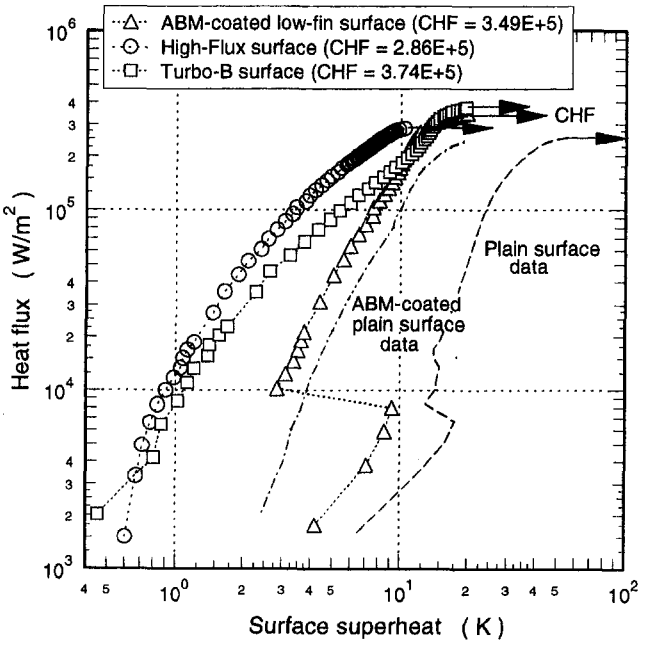

Fig. 11 Pool boiling data of enhanced surfaces in saturated R-123

For the typical heat flux range of industrial vaporizers (10 to 50 kW/m^2), two commercial tubes (High-Flux and Turbo-B tubes) showed highly enhanced boiling performance in the present study. As was shown in Figs. 10 and 11, ABM-coated tubes perform better in FC-87 than R-123. It should be pointed out that since the ABM coating was not optimized for R-123, it is possible that the enhancement with the ABM coating in R-123 can be increased. Also, taking into account its simplicity in application and much lower cost, the micro-porous coating technique has shown the possibility of broad application. The prediction of boiling performance in a tube bundle geometry also has been an important issue in industrial heat exchanger design. Compared to single-tube pool boiling, the boiling in multiple rows of tubes is known to have additional, two-phase convective heat transfer on all but a few bottom rows of the tubes. With theoretical models of tube bundle geometries, the present single-tube nucleate boiling data can be utilized to predict the performance of heat exchanger systems.

Conclusions

Six cylindrical tubes (plain, ABM-coated plain, low-fin, ABM-coated low-fin, High-Flux, and Turbo-B) were tested in pools of saturated FC-87 and R-123 at atmospheric pressure.

1 ABM-coated plain tube showed enhancements of 200-to-380 percent for FC-87 and 140-to-280 percent for R-123 in pool boiling heat transfer. These performance enhancements were due to the creation of micro-porous structures on the heater surface which significantly increased the number of active nucleation sites. Due to the failure of the liquid feed mechanism in the high heat-flux nucleate boiling regime, enhancement of CHF was minimal for cylindrical heaters.

2 The ABM coating was applied to an area-enhanced surface (low-fin tube), generating a doubly enhanced surface. This tube produced an additional 15-to-60 percent enhancement in nucleate boiling heat transfer coefficient over the uncoated low-fin tube. Due to the confined space between neighboring fins, lower enhancement (15-to-20 percent) was observed at higher heat fluxes (>100 kW/m^2). This was attributed to the bubble blanketing behavior from the finned surface.

3 The High-Flux surface with its porous structures performed better than the Turbo-B surface with the bent-over fin structures in the nucleate boiling regime. However, the Turbo-B surface has more benefit at CHF. The Turbo-B tube with its unique surface structure provided the highest CHF enhancements over the plain tube (91 percent for FC-87 and 46 percent for R-123).

4 Nucleate boiling performance of the ABM-coated low-fin tube was compared with that of the ABM-coated plain tube. Due to lower superheat from the ABM-coated low-fin surface, activation of the micro-cavities was delayed. A porous coating with a larger particle size should be considered to produce higher nucleate boiling performance.

5 Even though the ABM-coated and the High-Flux surfaces showed negligible area enhancements in natural convection tests, they showed comparable performance with the area-enhanced surfaces (low-fin and Turbo-B surfaces) in the nucleate boiling regime. From this investigation, it can be concluded that the surface micro-geometry is a dominant factor for the nucleate boiling heat transfer performance over the surface area increase (macro-geometry).

Acknowledgments

This study was supported by the Texas Higher Education Coordinating Board: Advanced Research/Technology Program grant number 003656-014. The authors extend their thanks to the 3M Industrial Chemical Products Division for the donation of FC-87 test liquid and to UOP Process Equipment for providing the High-Flux test surface.

References

Ayub, Z. H., and Bergles, A. E., 1987, "Pool Boiling from GEWA Surfaces in Water and R-113," *Wärme und Stoffübertragung*, Vol. 21, pp. 209–219.

Ayub Z. H., and Bergles, A. E., 1988, "Pool Boiling Enhancement of a Modified GEWA-T Surface in Water," ASME JOURNAL OF HEAT TRANSFER, Vol. 110, pp. 266–268.

Chang, J. Y., and You, S. M., 1996, "Heater Orientation Effects on Pool Boiling of Micro-Porous-Enhanced Surfaces in Saturated FC-72," ASME JOURNAL OF HEAT TRANSFER, Vol. 118, No. 4, pp. 937–943.

Churchill, S. W., and Chu, H. H. S., 1975, "Correlating Equations for Laminar and Turbulent Free Convection from a Horizontal Cylinder," *Int. J. Heat Mass Transfer*, Vol. 18, pp. 1049–1053.

Kline, S. J., and McClintock, F. A., 1953, "Describing Uncertainties in Single-Sample Experiments," ASME *Mechanical Engineering*, Vol. 75, pp. 3–8:

Marto, P. J., and Hernandez, B., 1983, "Nucleate Pool Boiling Characteristics of a GEWA-T Surface in Freon-113," *AIChE Symp. Series*, Vol. 79, No. 225, pp. 1–10.

Marto, P. J., and Lepere, V. J., 1982, "Pool Boiling Heat Transfer from Enhanced Surfaces to Dielectric Fluids," ASME JOURNAL OF HEAT TRANSFER, Vol. 104, pp. 292–299.

Marto, P. J., Wanniarachchi, A. S., and Pulido, R. J., 1985, "Augmenting the Nucleate Pool Boiling Characteristics of GEWA-T Finned Tubes in R-113," ASME HTD-Vol. 52, pp. 67–73.

McManus, S. M., Marto, P. J., and Wanniarachchi, A. S. 1986, "An Evaluation of Enhanced Heat Transfer Tubing for Use in R-114 Water Chillers," ASME HTD-Vol. 65, pp. 11–19.

O'Connor, J. P., and You, S. M., 1995, "A Painting Technique to Enhance Pool Boiling Heat Transfer in Saturated FC-72," ASME JOURNAL OF HEAT TRANSFER, Vol. 117, pp. 387–393.

O'Connor, J. P., You, S. M., and Price, D. C., 1995, "Thermal Management of High Power Microelectronics via Immersion Cooling," IEEE Trans. *CPMT*, Part A, Vol. 18, No. 3, pp. 656–663.

Sokol, P., Blein, P., Gorenflo, D., Rott, W., and Schömann, H., 1990, "Pool Boiling Heat Transfer from Plain and Finned Tubes to Propane and Propylene," IHTC-1990, pp. 75–80.

Stephan, K., and Mitrovic, J., 1981, "Heat Transfer in Natural Convection Boiling on Refrigerant and Refrigerant-Oil Mixtures in Bundles of T-shaped Finned Tubes," ASME HTD-Vol. 18, pp. 131–146.

Webb, R. L., 1983, "Nucleate Boiling on Porous Coated Surfaces," *Heat Transfer Engineering*, Vol. 4, pp. 71–82.

Webb, R. L., and Pais, C., 1992, "Nucleate Boiling Data for Five Refrigerants on Plain, Integral-Fin, and Enhanced Tube Geometries," *Int. J. Heat Mass Transfer*, Vol. 35, pp. 1893–1904.

Yilmaz, S., and Westwater, J. W., 1981, "Effect of Commercially Enhanced Surfaces on the Boiling Heat Transfer Curve," ASME HTD-Vol. 18, pp. 73–91.

You, S. M., Simon, T. W., and Bar-Cohen, A., 1991, "A Technique for Enhancing Boiling Heat Transfer with Application to Cooling of Electronic Equipment," IEEE Trans. *CHMT*, Vol. 15, No. 5, pp. 90–96.

Zuber, N., 1959, "Hydrodynamic Aspects of Boiling Heat Transfer," AEC Report No. AECU-4439, Physics and Mathematics.

Relative Stability Between Nucleate and Film Boiling on a Nonuniformly Heated Plate Surface

W. W. Lin

D. J. Lee
djlee@ccms.ntu.edu.tw

Department of Chemical Engineering,
National Taiwan University,
Taipei, Taiwan, 106,
Republic of China

Flow boiling of methanol over a nonuniform, indirect conduction heating surface is investigated experimentally. An axial (discrete) heat flux distribution corresponding to a neutral stability region where nucleate and film boiling can coexist steadily is identified. Below such a heat flux distribution, nucleate boiling mode is more stable. Above this distribution, film boiling mode becomes more stable. We had employed an equal-area criterion for interpreting the heat flux and wall superheat relationship. Analogy between the wire boiling system is proposed. The differences between average and real transition boiling curves are discussed as well.

Introduction

Under certain conditions, different boiling regimes can coexist on the same heating element. In pool boiling with an electrically heated wire, steady state and unsteady state two-mode boiling (nucleate and film boiling) had been studied (Lu and Lee, 1989, 1991; Lee and Lu, 1992). Some other related researches included Kovalev (1966), Zhukov an Barelko (1983), and Zhukov et al. (1980, 1983). The important conclusions drawn from their works are as follows: (a) there are infinitely many "average" transition boiling curves and one "true" transition curve under a specific heater/fluid combination, with the former being mainly determined by the heating method and the disturbances existing in the boiling processes; (b) an "equilibrium line" exists in each wire boiling system dividing both the nucleate and film boiling, respectively, into stable and metastable regimes; (c) an "equal-area rule" (discussed later) can be employed in determining the equilibrium line, with the two ends of the wire locating at respectively nucleate and film boiling. The intersections between the equilibrium line and the boiling curves denote the separating points dividing the stable and metastable regimes.

The points separating stable and metastable regimes on the boiling curve are important in practice. The critical points, such as the critical heat flux (CHF) and minimum heat flux (MHF) points, indicate the absolutely unstable points at which the system cannot tolerate infinitesimal disturbance. These critical points can be well described by classical hydrodynamic theory (Lienhard and Witte, 1985). On the other hand, a heater under metastable nucleate boiling mode (i.e., the nucleate boiling curve below CHF and above the intersection between equilibrium line and nucleate boiling curve) can tolerate a finite-magnitude disturbance to prevent burnout. If a large enough disturbance is introduced, however, the heater would still transit into film boiling. This is the so-called "nonhydrodynamic" aspect for burnout (Tachibana et al., 1967; Lee, 1989). Furthermore, if the heater is under stable nucleate boiling mode (i.e., the nucleate boiling curve below the intersection between equilibrium line and nucleate boiling curve), no transition to film boiling would occur regardless of the disturbance's magnitude. That is, the system can now tolerate disturbances of infinitely large size. The operation is thereby absolutely stable and safe. Similar conclusions could also be applied to the film boiling curve.

In the forced flow condition, multimode boiling was found to exist in temperature controlled, joule-heating tubes (Passos and Gentile, 1991; Huang and Bartsch, 1993). With a volume-average temperature-controlled, electrically heated tube, when the average temperature is maintained in the transition boiling regime, the boiling surface may actually contain both high temperature film boiling and low temperature nucleate boiling, with a sharp transition region between these two extremes.

To construct the complete boiling curve, an indirect conduction heating method is usually adopted. If the pseudo-steady state criterion is satisfied (Lin and Westwater, 1982), the so-constructed boiling curve is independent of the heating/cooling rate and is reproducible. The transition boiling process thus obtained had been proposed as an alternating process with unstable nucleate and film boiling (Berenson, 1962). With a uniform, indirect conduction heat flux, most portions of the transition boiling curve cannot be controlled steadily.

No comprehensive study of the multimode boiling above an indirect conduction heating surface, such as those observed for electrically heated wire or temperature-controlled heated tube tests discussed above, has been made until recently. In the present work, a nonuniform, indirect conduction heating boiling setup was installed and was employed to investigate the multimode boiling under convective flow condition. The focus is to identify the relative stability between nucleate and film boiling on the same heating surface and to propose an analogy to the wire boiling system.

Experimental

Setup. A schematical drawing of the experimental setup used in this work was shown in Fig. 1a. The operational pressure is atmospheric, and the working liquid is methanol, with a flow rate of 20 kg/m^2-s and a degree of subcooling of 12 K. The flow was driven by the constant head maintained in the storage tank (1) and globe valve (7), that forces methanol to circulate through the heat exchanger (3) and the flow meter (4) to the test section (5). The receiving tank (8) was open to an aspirator (11) through a condenser (10). The used methanol in the receiving tank was then pumped back to the storage tank by a gear pump (9). The boiling dynamics were recorded by a CCD camera (6). A stroboscope was employed to "freeze" the image.

Contributed by the Heat Transfer Division for publication in the JOURNAL OF HEAT TRANSFER. Manuscript received by the Heat Transfer Division May 6, 1996; revision received January 22, 1997; Keywords: Boiling, Conduction, Phase-Change Phenomena. Associate Technical Editor: M. S. Sohal.

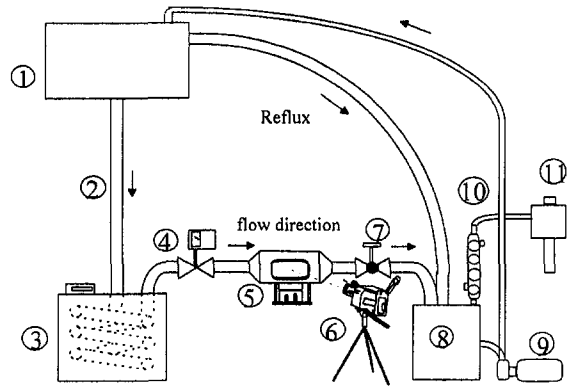

Fig. 1a Schematics of boiling apparatus: (1) storage tank; (2) pipe; (3) heat exchanger; (4) flow meter; (5) testing section; (6) camera; (7) globe valve; (8) receiving tank; (9) gear pump; (10) condenser; and (11) aspirator.

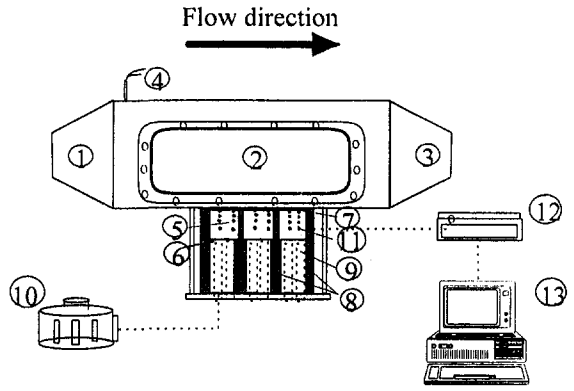

Fig. 1b Schematics of testing block: (1) expanding section; (2) testing chamber; (3) contracting section; (4) thermocouple; (5) heating block; (6) (7) (8) insulation; (9) cartridge heaters; (10) transformer; (11) thermocouples; (12) data acquisition system; and (13) personal computer.

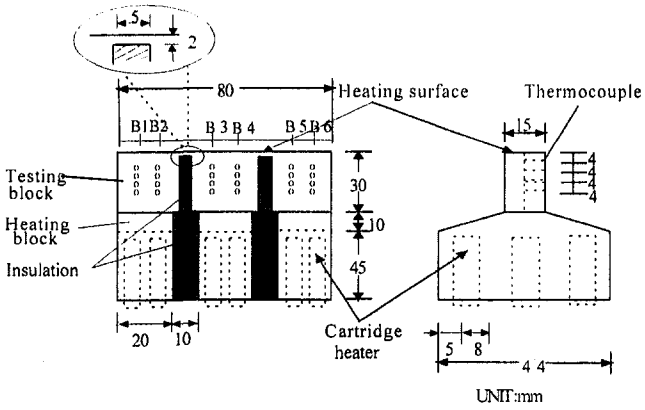

Fig. 1c Schematics of heating assembly

Figure 1b shows the details of the test section. The flow chamber contains an expanding section (1), a test section of dimension (L × W × H) 24 × 8 × 8 cm^3 with front and rear view windows (2), and a contracting section (3). The upper surface of the heating block (5) matches exactly to the lower part of the flow chamber, permitting an undisturbed crossflow without generating secondary flow around the heating surface. The fluid temperature was measured by a thermocouple (4) while the flow mass velocity was calculated by the mass flow rate and the cross section of the test chamber.

Under the testing block (5) there are three independent heating blocks (6) equipped with cartridge heaters (9), whose power is supplied by the transformer (10). The joule heat could generate separately and transit through the testing block to the top surface. The gaps (of a width 10 mm) between these heating blocks were insulated (8) to prevent direct heat conduction among them. Temperatures at 24 positions in the testing block (5) were measured by thermocouples (11), whose readings were sent at a rate of 1 Hz to a data acquisition system (12) connected to a personal computer (13).

Figure 1c shows the details of the heating assembly. In each bottom heating block there were six cartridge heaters, each of 120 W (220 V) capacity, giving out a maximum of 720 W capacity in each block. The testing block was made of pure copper, most of which (93 percent from the bottom) was also divided into three separated parts with a gap of 5 mm in between. Only the top seven percent of the heating block was connected (of 2 mm thickness). Insulation was used to prevent heat conduction from the bottom portions. Axial heat conduction is, therefore, permitted only in the top (or "bridge") connection sections. The joule heat from the bottom cartridge heaters would thereby conduct vertically across most of the testing block to the bridge region, then be dissipated partially by surface boiling, and the rest exchanged among other blocks if a temperature gradient existed.

The upper heating surface is a smooth surface of dimension 80 mm × 15 mm. The positions of the 24 thermocouples were also indicated in Fig. 1c. The corresponding six axial positions above these thermocouples along the flow direction are referred to as B1 to B6, respectively.

To prevent liquid leakage and associated loss, a thin silicon rubber ring (of 2 mm thickness) was used as the seal material between the bridge region of the heating block and the stainless steel test chamber. This, however, limits the time interval and the temperature level at which the film boiling can sustain on the heating surface.

Experimental Procedures. First, the liquid temperature was adjusted by the heat exchanger and by the high heat flux nucleate boiling from the heating surface. After steady state conditions were achieved, all cartridge heaters were set at V_1 to place all heating surfaces in a nucleate boiling mode (phase I). Then the voltage of the cartridge heaters in one of the bottom heating blocks (e.g., the last section along the flow direction) was set at a higher voltage of V_2 (phase II), which would force the top surface to enter the film boiling. Once a visible film boiling was established on the top surface, the voltage of cartridge heaters was decreased from V_2 to V_3 to prevent the burnout of the seal silicon rubber (phase III). (Notably, the heat supplies for the other two blocks always remained at V_1). The higher temperatures created under the film boiling mode would then produce a large axial heat conduction across the bridge connection.

The surface temperature and the surface boiling heat flux (referred to as q_b) from the bottom cartridge heaters can be

Nomenclature

I = integrand defined in Eq. (3), W-K/m^2
k = heater thermal conductivity, W/m-K
q_b = boiling heat flux, W/m^2
q_g = bottom heat flux, W/m^2
T = temperature, K
T_F = film boiling temperature, K
T_N = nucleate boiling temperature, K
ΔT_i = temperature difference, K
V = voltage, volt
x = axial position, m
δ = heater thickness, m

obtained by solving and extrapolating the transient heat conduction equation with the thermocouple readings as the boundary conditions. The local heat fluxes (referred to as q_g) and temperatures at a thickness of 4 mm from the heating surface, where the top six thermocouples are located, can be estimated with a prescribed accuracy. However, especially for the surface boiling heat fluxes q_b, large difference may exist between the real surface quantities and the extrapolated ones if a large axial heat conduction occurs among the blocks.

We had constructed the boiling heat flux versus surface temperature relationship (the boiling curve) by setting all cartridge heaters at the same input voltage. The time evolution of the temperature fields within the three testing blocks, as recorded by the thermocouples readings, are very similar, thereby preventing the axial heat conduction effects. The surface heat flux and wall superheat can then be estimated by extrapolation.

Uncertainty Estimates. The method of Kline and McClintock (1953) had been employed to estimate the uncertainties of the heat flux and temperature measurements. The data acquisition system included three eight-channel thermocouple input modules (ADAM 4018, Advantech Co., Taiwan) and an isolated RS232/RS485 converter (ADAM 4520, Advantech Co., Taiwan), whose bias error is 0.1 percent provided by manufacturer, and an RS232 interface connected to a personal computer. Uncertainties that occurred are mainly attributed to the thermocouple calibration, which is at most 1 K in this study, and the employment of thermal conductivity data, which is estimated to be not higher than two percent. The uncertainties thereby existing in the extrapolated heater surface temperature and the associated heat flux when constructing boiling curves are estimated as ±7 percent and ±11 percent, respectively. The mass flow rates exhibit an uncertainty of approximately ±5 percent, while for fluid temperature measurement, ±1 K. The ripples in voltage outputs from transformer are less than ±4 percent.

Results and Discussion

Time Evolution. The time evolution of extrapolated surface temperature data of a typical run with (V_1, V_2, V_3) = (140, 220, 60) volts are demonstrated in Fig. 2. The photographs for the boiling consequence are depicted in Fig. 3. The time evolution of the boiling modes for the last section (B5 and B6) are nucleate → film → nucleate; while for the central section (B3 and B4), nucleate → transition → nucleate; for the first section (B1 and B2), the boiling is always in nucleate boiling. That is, the film boiling mode set up on the last section cannot sustain, but has made the transition back to the nucleate boiling mode via axial heat conduction.

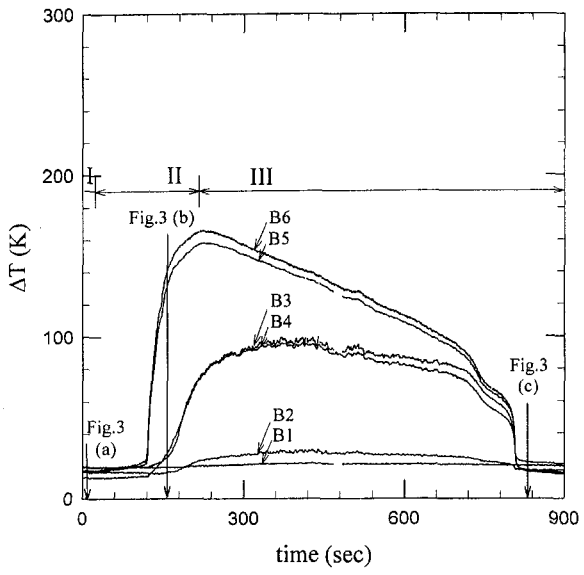

Fig. 2 Time evolution of extrapolated surface temperature data. (V_1, V_2, V_3) = (140, 220, 60) volts; Methanol; Flow rate 20 kg/m²-s; Degree of subcooling 12 K.

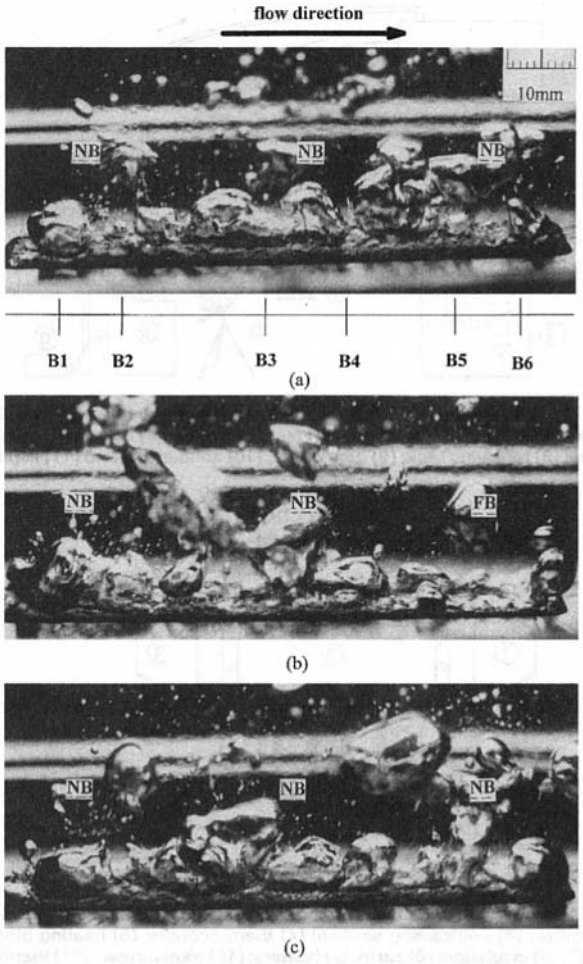

Fig. 3 Photographs for boiling with conditions the same as in Fig. 2: (*a*) Phase I, all in nucleate boiling mode; (*b*) phase II, the last section has enter film boiling mode; and (*c*) phase III, the last section has receded back to nucleate boiling mode.

The time evolution for the extrapolated surface temperature data for an almost identical run, but with a higher V_3 (80 volts), are shown in Fig. 4, where a different pattern results. The corresponding photographs are shown in Fig. 5. For all the three sections, the modes have transited from nucleate to film boiling, following the sequence: B5 and B6, then B4 and B3, and finally B1 and B2. Therefore, the film boiling mode for the last section is now stronger than the nucleate boiling mode in B1 to B4, thereby pushing them into film boiling by axial heat conduction. Since the temperatures become too high, all cartridge heaters are cut off after 500 seconds. This is evidenced by the decreasing temperatures observed in the final phase of the experiment.

The time evolution of the extrapolated surface temperature distribution for the above two runs with a time interval of 20 seconds are demonstrated in Figs. 6a and 6b. At the beginning (V_1), all states are in nucleate boiling mode. In the second stage, as the voltage of the cartridge heaters in the last section has been raised to V_2, the temperatures for B5 and B6 increase quickly, signaling the occurrence of film boiling on the surface. Two subsequently distinct behaviors appear for the third stage.

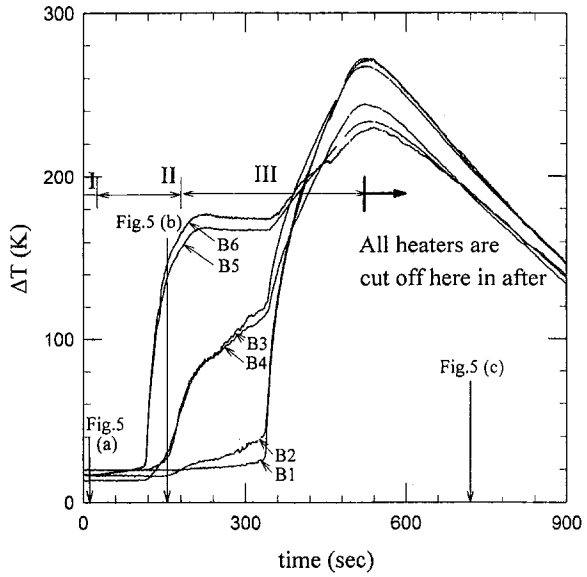

Fig. 4 Time evolution of extrapolated surface temperature data (V_1, V_2, V_3) = (140, 220, 80) volts; Methanol; Flow rate 20 kg/m^2-s; Degree of subcooling 12 K.

For V_3 set to 60 volts, as indicated in Fig. 6a, the extrapolated, axial surface temperature distribution curve moves upwards first (closed symbols), not exceeding the bold curve indicated by N-F, and then recedes back to the nucleate boiling mode (open symbols). When V_3 is increased to 80 volts instead, however, as shown in Fig. 6b, the curve will move and pass over the curve N-F as time progresses. All states will eventually arrive at film boiling state, indicated as the higher surface temperature region in Fig. 6b.

In experiments, when V_1 and V_2 are fixed at 140 and 220 volts, respectively, a critical value exists for V_3 of approximately 70 volts. If V_3 is set above this critical value, all states will be attracted to the film boiling mode, as demonstrated in Fig. 6b. Whereas, below this critical value all final states are in the nucleate boiling mode, as those shown in Fig. 6a. When plotting the time evolution pattern, as in Fig. 6a, the curve N-F can be asymptotically approached to before receding back to the nucleate boiling mode, if V_3 approaches from zero to $V_{3,\text{critical}}$. Once $V_{3,\text{critical}}$ is reached, a steady state coexisting boiling pattern can be found. Further increase in V_3 will bring the curve passing over curve N-F, and all states go to film boiling mode. The curve N-F is therefore a region of neutral stability for the nucleate and film boiling modes (although it is an unstable steady state). The bottom heat fluxes in all phases vary continuously in a test. However, the heat fluxes at point N and F can be found out as approximately 0.70 and 0.33 MW/m^2, respectively.

Figure 7 demonstrates the bottom heat fluxes q_8 at positions B1 and B6. At a V_3 of 60 volts (closed symbols), the bottom heat flux at B6 that remains constant in phase I increases markedly when just entering phase II, where high heat flux nucleate boiling occurs. After passing the critical heat flux point (point A, 1.2 MW/m^2, coincides well with the boiling curve), the transition and film boiling modes incorporate, and largely reduce the heat flux at B6. Owing to the high temperature established at position B6 (consulting Fig. 2), the heat flux at B1 increases slightly, which should be attributed to axial conduction. The heat fluxes for points N and F are depicted in the figure for comparison's sake. Notably, the heat flux at position B1 could not exceed that for point N, while the film boiling heat flux at B6 goes down continuously. While lower than that for point F, finally, the film boiling mode at B6 becomes less stable and recedes back to nucleate boiling mode, as evidenced by the second CHF peak in the figure.

At a V_3 of 80 volts instead (open symbols in Fig. 7), the heat flux at B1 would increase beyond that for point N (point B), where the nucleate boiling becomes less stable. Some hot spots appearing on the surface could push the state at B1 into film boiling mode, as evidenced by the dramatic decrease in the heat flux. Three points are noticeable. First, the bottom heat flux at point B is only 58 percent of the CHF. That is, burnout can occur well below the hydrodynamic limit. Second, the heat flux at B1 would drop to a very low level, which is attributed to the sudden increase (decrease) in surface temperature (boiling heat flux). Third, after this period the heat flux at B1 increases slightly due to the establishment of the stable film boiling. Since its temperature can go beyond that for B6 (consulting Fig. 4), the heat fluxes at B6 increase accordingly.

The $V_{3,\text{critical}}$ values can also be obtained under other conditions via similar experimental procedures. For example, the corresponding $V_{3,\text{critical}}$ value is approximately 30 volts if the first instead of the last section along the flow direction is raised to 220 volts and decreased to V_3. If the heat supply for the last section is still changing, and the initial V_1 is set as 160 rather than 140 volts, the final boiling mode will all be in film boiling, even if V_3 has decreased to zero. No receding back to nucleate boiling will occur.

Equal-Area Criterion. When multiple boiling modes coexist on the same heating surface, a large temperature gradient may appear. The axial heat conduction/boiling equation can be stated as follows:

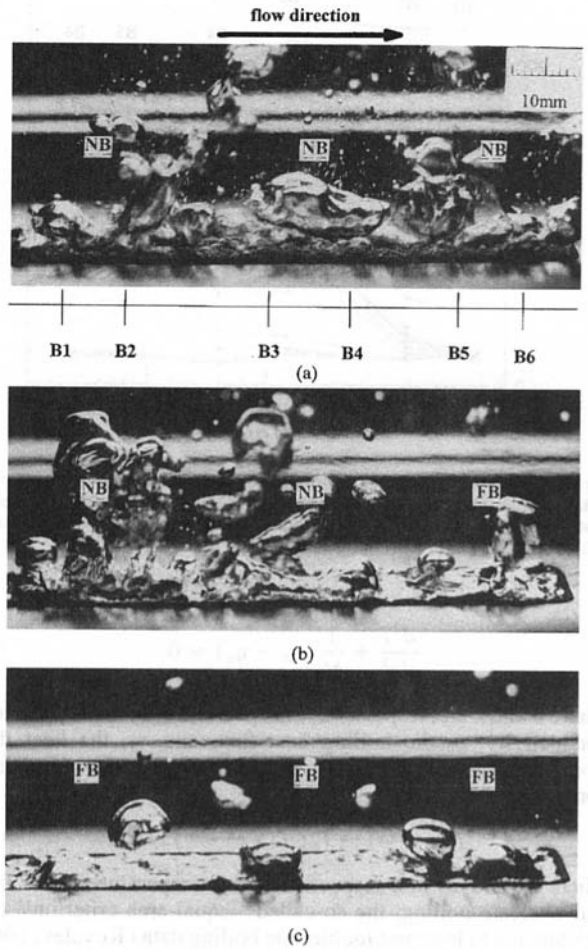

Fig. 5 Photographs for boiling with conditions the same as in Fig. 4: (*a*) phase I, all in nucleate boiling mode; (*b*) phase II, the last section has enter film boiling mode; and (*c*) phase III, the first two sections are pushed into film boiling mode.

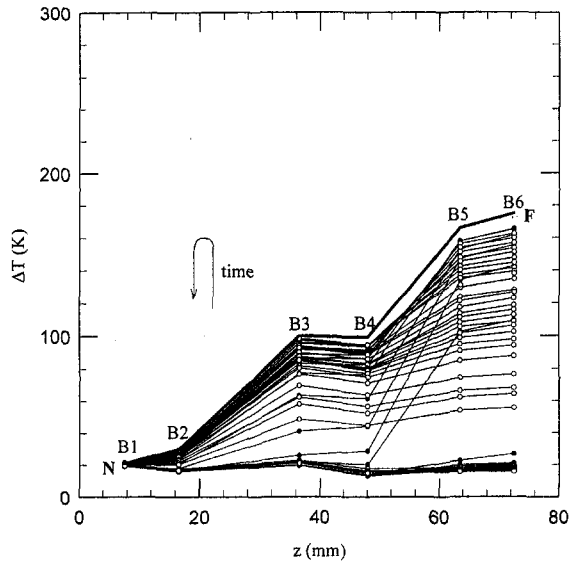

Fig. 6a Time evolution of extrapolated, axial surface temperature distribution. Time interval is 20 seconds. (V_1, V_2, V_3) = (140, 220, 60) volts; Methanol; Flow rate 20 kg/m²-s; Degree of subcooling 12 K; Bold curve NF: coexisting curve with neutral stability; Solid symbols: temperature increasing phase; Open symbols: temperature decreasing phase.

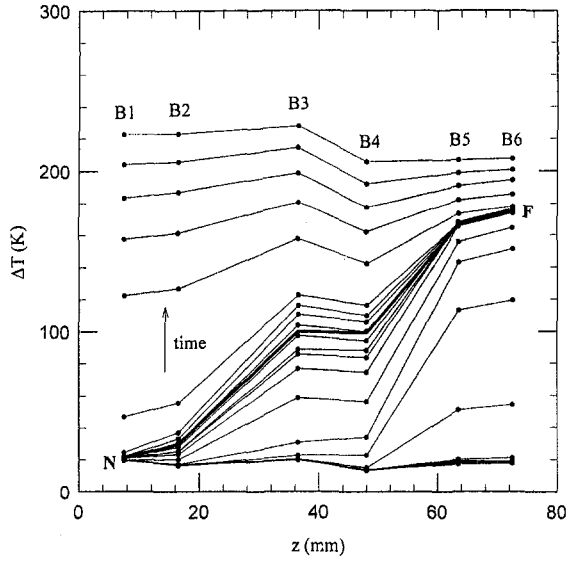

Fig. 6b Time evolution of extrapolated, axial surface temperature distribution. Time interval is 20 seconds. (V_1, V_2, V_3) = (140, 220, 80) volts; Methanol; Flow rate 20 kg/m²-s; Degree of subcooling 12 K; Bold curve NF: coexisting curve with neutral stability.

$$\frac{d^2T}{dx^2} + \frac{1}{\delta k}(q_b - q_g) = 0 \qquad (1)$$

where δ and k are, respectively, the heater thickness and thermal conductivity, q_b the boiling heat flux, and q_g, the heat flux from internal heat supply. If the following no-flux boundary conditions are applied:

$$T(x \to \infty) \to T_N;\ T(x \to -\infty) \to T_F \qquad (2)$$

where T_F and T_N are, respectively, the temperature under film and nucleate boiling, the so-called "equal-area criterion" can be obtained to interpret multimode boiling data (Kovalev, 1966; Passos and Gentile, 1991; Lee and Lu, 1992):

$$I = \int_{T_N}^{T_F} (q_b - q_g)dT = 0. \qquad (3)$$

For an electrically heating wire, q_g can be described by the heater resistance and the electrical current. The electrical current for a heating wire satisfying Eq. (3) is referred to as the "equilibrium current" in Lu and Lee (1991) and Lee and Lu (1992); while the corresponding average q_g versus wall temperature data resemble the equilibrium line.

In the present work, the axial heat conduction is through the connection portion (of 2 mm thickness), while q_g is the bottom heat flux provided by indirect conduction heating. We thereby suggest that the multimode boiling with neutral stability (curve N-F) would satisfy Eq. (3). A first approximation of Eq. (3), according to Trapezoid rule, is as follows:

$$I = \sum_{i=1}^{5} \tfrac{1}{2}((q_b(T_i) - q_{gi}) + (q_b(T_{i+1}) - q_{g,i+1}))\Delta T_i = 0. \qquad (4)$$

T_i and q_{gi} are the extrapolated surface temperature and the bottom heat flux at the axial position Bi, respectively, ΔT_i is the temperature difference $T_{i+1} - T_i$.

There exist only a few studies in the literature that had compared, quantitatively, Eq. (3) with experiments, as was done in Lee and Lu (1992). This arises from the fact that the axial conduction has caused differences between the real surface quantities and the extrapolated ones, whose effect is difficult to estimate. We here make a first estimate for the I value in Eq. (4). First, a finite element program is installed to solve the temperature field within the three testing blocks under various operational conditions. Numerical results reveal that, except near the regions close to the bridge sections, the extrapolated surface temperature based on the calculated values at 4, 8, 12, and 16 mm from the heater surface (the positions of the thermocouples) are found close to the calculated surface temperature, generally with an error less than three percent. This is due to the relatively smaller characteristic length for the gap (2 mm) than that considered for axial heat conduction path (8 cm). Although the surface temperatures might not change much since the extrapolated distance is small (4 mm), however, the corresponding slopes can be 35 percent in difference between the extrapolated ones, especially when a large temperature gradient exists along the axial direction. Therefore, the first approximation for T_i in Eq. (4) is obtained from the thermocouple readings and extrapolation. The boiling heat fluxes $q_{b,i}$ are then read out from the preconstructed boiling curve on the basis of the T_i.

The calculation results for Eq. (4) are shown in Fig. 8. Although the approximation is rather rough owing to the limited

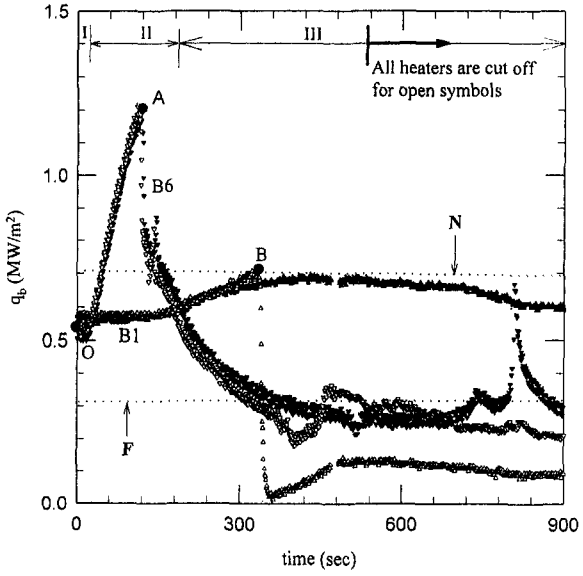

Fig. 7 Time evolution of bottom heat fluxes at positions B1 and B6. Closed symbols: V_3 = 60 volts; Open symbols: V_3 = 80 volts.

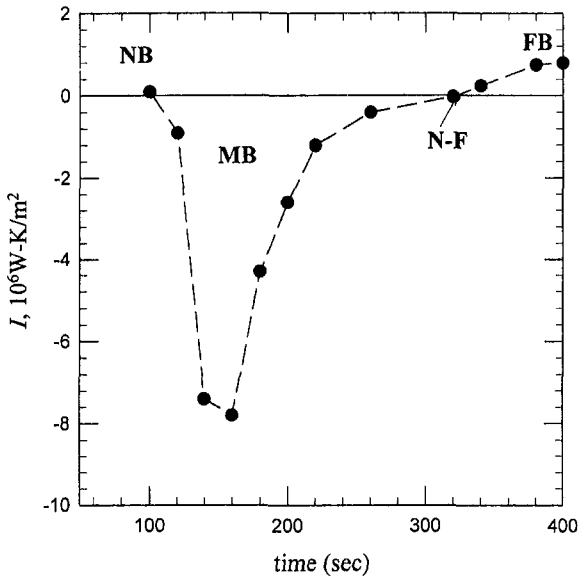

Fig. 8 Time evolution of integrand I in Eq. (4); V_3 = 80 volts; The circles are calculation results at some times during the test; The dashed curve is used to guide the eyes.

number of data points examined along the heating surface (only 6) and the uncertainties existing in the surface quantities estimation, the cross-over of the zero-I axis is still easily identified. Evidently, when $V_3 > V_{3,\text{critical}}$, the integrand will change sign from negative to positive near the time reaching curve N-F (t = 300 seconds).

An analog between the present flow boiling system and the wire boiling system can be proposed. The N-F curve in Figs. 6a and 6b corresponds to the equilibrium line in wire boiling system, which represents a neutral stability region where nucleate and film boiling can steadily coexist. $V_{3,\text{critical}}$ plays a role similar to the equilibrium current in wire boiling. To construct an equal-area cut it is reasonable to find a lowering of the $V_{3,\text{critical}}$ (from 70 to zero volts) in response to an increase in the nucleate boiling heat flux (value of V_1 from 140 to 160 volts). The fact that $V_{3,\text{critical}}$ for the first section (30 volts) is less than that for the last section (70 volts) reflects a weaker relative stability for the corresponding nucleate boiling mode for the former case.

As a result, the present nonuniform heat flux boiling apparatus has provided a flexible and convenient tool for investigating the relative stability and the coexistence of multimode boiling on the same heating element. Since the pseudo-steady state approximation criterion is satisfactorily fulfilled (Lin and Westwater, 1982), the upper surface is continuous and smooth, and the indirect conduction heating method is adopted, the (surface average) boiling curve constructed resembles a so-called "standard" boiling curve. It is also easily obtained from the present study that, although the average heat flux versus surface temperature data may be in the transition boiling region, the real temperature pattern is with a large gradient. We therefore reach the conclusion as suggested by Huang and Bartsch (1993) that the Berenson's definition of transition boiling, as an alternatively existing unstable nucleate and film boiling, occurs only in a limited boiling conditions. In the present experiments, average transition boiling is a combination of nucleate and film boiling with a true transition boiling locating in between, just as those found for wire boiling.

Conclusions

Subcooled flow boiling of methanol over a nonuniform, indirect conduction heating surface is investigated under atmospheric pressure. A discrete bottom heat flux distribution corresponding to a neutral stability region where nucleate and film boiling can coexist steadily is found. Below this heat flux distribution the nucleate boiling mode is more stable, while all surfaces will be attracted to the nucleate boiling mode. Above this distribution, on the contrary, film boiling mode becomes more stable and all final states will be in film boiling mode. The equal-area criterion is employed for interpreting the experimental data. Although the average heat flux versus surface temperature data may be in the transition boiling region, the real temperature pattern is with a large gradient. The analogy with the wire boiling system is proposed.

Acknowledgment

This work is supported by National Science Council, R.O.C.

References

Berenson, P. J., 1962, "Experiments on Pool-Boiling Heat Transfer," *International Journal of Heat and Mass Transfer,* Vol. 5, pp. 985–999.

Huang, X. C., and Bartsch, G., 1993, "About the Second-Order Instability on an Electrically Heated Temperature-Controlled Test Section under Forced Convective Boiling Conditions," *International Journal of Heat and Mass Transfer,* Vol. 36, pp. 2601–2612.

Kline, S. J., and McClintock, F. A., 1953, "Description of Uncertainties in Single Sample Experiments," *Mechanical Engineering,* Vol. 75, Jan., pp. 3–8.

Kovalev, S. A., 1966, "An Investigation of Minimum Heat Fluxes in Pool Boiling," *International Journal of Heat and Mass Transfer,* Vol. 9, pp. 1219–1226.

Lee, D. J., 1989, "Effects of Heater Properties, Heating Methods and Liquid Subcooling on Pool Boiling," Ph.D. dissertation, National Taiwan University, Taipei.

Lee, D. J., and Lu, S. M., 1992, "Two-Mode Boiling on a Horizontal Heating Wire," *AIChE Journal,* Vol. 38, pp. 1115–1128.

Lienhard, J. H., and Witte, L. C., 1985, "A Historical Review of the Hydrodynamic Theory of Boiling," *Chemical Engineering Reviews.* Vol. 3, pp. 187–280.

Lin, D. Y. T., and Westwater, J. W., 1982, "Effects of Metal Properties on Boiling Curves Obtained by the Quenching Method," *7th International Heat Transfer Conference,* PB24, München, Fed. Rep. of Germany.

Lu, S. M., and Lee, D. J., 1989, "Effects of Heater and Heating Methods on Pool Boiling," *AIChE Journal,* Vol. 35, pp. 1742–1744.

Lu, S. M., and Lee, D. J., 1991, "The Effects of Heating Methods on Pool Boiling," *International Journal of Heat and Mass Transfer,* Vol. 34, pp. 127–134.

Passos, J. C., and Gentile, D., 1991, "An Experimental Investigation of Transition Boiling in Subcooled Freon-113 Forced Flow," ASME JOURNAL OF HEAT TRANSFER, Vol. 113, 459–462.

Tachibana, F., Akiyama, M., and Kawamura, H., 1967, "Non-hydrodynamic Aspects of Pool Boiling Burnout," *Journal of Nuclear Science and Technology,* Vol. 4, pp. 121–130.

Zhukov, S. A., and Barelko, V. V., 1983, "Nonuniform Steady States of the Boiling Process in the Transition Region between the Nucleate and Film Regimes," *International Journal of Heat and Mass Transfer,* Vol. 26, pp. 1121–1130.

Zhukov, S. A., Barelko, V. V., and Merzhanov, A. G., 1980, "Wave Processes on Heat Generating Surfaces in Pool Boiling," *International Journal of Heat and Mass Transfer,* Vol. 24, pp. 47–55.

Zhukov, S. A., Bokova, L. F., and Barelko, V. V., 1983, "Certain Aspects of Autowave Transitions From Nucleate to Film Boiling Regimes With a Cylindrical Heat Generating Element Inclined From a Horizontal Position," *International Journal of Heat and Mass Transfer,* Vol. 26, pp. 269–275.

K. Cheung
Naval Center for Space Technology,
Naval Research Laboratory,
Washington, DC

M. M. Ohadi

S. Dessiatoun

Heat Transfer Enhancement Laboratory,
Center for Environmental
Energy Engineering,
Department of Mechanical Engineering,
University of Maryland,
College Park, MD 20742

A. Singh
Advanced Development Center,
Copeland Corporation,
Sidney, OH

EHD-Enhanced Boiling Coefficients and Visualization of R-134a Over Enhanced Tubes

In an earlier study by the authors, the applicability of the EHD technique for augmentation of pool boiling heat transfer of R-134a in a tube bundle was demonstrated. This paper reports additional experiments involving optimization of the electrode/heat transfer surface geometry as well as flow visualization studies that provide improved understanding of the EHD-enhanced pool boiling heat transfer in a tube bundle. Utilizing the flow visualization studies, it is demonstrated that combined electroconvection and improved nucleate boiling dynamics give rise to the augmented heat transfer coefficients.

Introduction

Electrohydrodynamic (EHD) heat transfer augmentation utilizes the effect of secondary motions that are induced when an electric field is coupled with a flow field in a dielectric fluid medium. For the boiling process, application of the EHD field substantially affects the bubble dynamics near the heat transfer surface (Ogata et al., 1993; Kawahira et al., 1990).

Typically, application of the electric field to the heat transfer surface is by an external electrode which surrounds the heat transfer surface and is separated from it with insulating spacers. In most cases, the high voltage is supplied to the electrode, with the heat transfer surface serving as the receiving or grounding electrode. The electric field distribution, and thereby the heat transfer augmentation, critically depends on the electrode orientation and spacing with respect to the heat transfer surface. This issue is discussed in Singh et al. (1993) for external pool boiling over a single tube. Among the electrode configurations that were examined in that study, circular mesh electrode provided the most desirable enhancement performance.

The heat transfer surface also plays a significant role in EHD-enhanced pool boiling. Papar et al. (1993) demonstrated a maximum enhancement of five fold in pool boiling of R-123 over a smooth tube. An improvement was achieved by Singh et al. (1993), where a maximum of 8.5 fold enhancement was reported with a 19 fins per inch (fpi) integral-fin tube. The effect of heat transfer surface in EHD enhancement became prominent when a maximum of 11 fold enhancement was reported for a commercially available 40 fpi integral-fin tube (Kumar 1994). The more pronounced inhomogeneity of the electric field associated with the integral-fin tube was suggested to be the primary reason for the improved EHD enhancement.

The main objective of the present work was to optimize the EHD heat transfer augmentation in a pool boiling regime on a laboratory scale tube bundle. Cheung et al. (1995) had already confirmed the applicability of the EHD technique on the pool boiling heat transfer enhancement on this tube bundle. In that study, the high voltage electric field was applied to the heat transfer surface by a simple straight wire electrode configuration. A maximum enhancement of three fold was achieved. In the present study, two types of mesh electrode configurations (circular and rectangular) were examined with the tube bundle experimentally. Comparisons of the results will be discussed in this paper. Another approach to optimizing the EHD enhancement is by modifying the heat transfer surface. This approach was also addressed in the present study by performing experiments on a single 40 fpi tube which was modified to create additional electric field strength inhomogeneity on the heat transfer surface. The heat transfer performance of this tube was evaluated experimentally for both the base case (no electric field influence) and the EHD case (the electric field effect present).

The present study also attempts to develop an in-depth understanding of the EHD enhancement mechanism on integral-fin geometry. Flow visualization studies, utilizing a high speed camera, were also conducted to capture the changes of the boiling heat transfer mechanism in the fluid field when the electric field is applied.

Experimental Apparatus

The schematic diagram of the experimental setup is shown in Fig. 1. The three major components of the setup are the test section, the boiling chamber, and the cooling unit. The test section (either single tube or tube bundle) was submerged in a pool of liquid refrigerant (R-134a), and boiling took place inside the enclosed boiling chamber. The 40 fpi integral-fin tube used in the present experiments was a commercially available tube (manufactured by Wieland-Werke AG, Germany). A schematic of a typical test section tube and its accessories are shown in Fig. 2. Heating power was supplied by an electrical heater which was surrounded by a copper sleeve and inserted inside the tube. Measurement of the wall temperature was provided by two thermocouples which were mounted approximately 180 deg apart from each other on the inner tube surface. Both ends of the tube were insulated and sealed with stainless steel caps to limit the heat loss. Two electrode configurations (circular and rectangular mesh) were employed in the tube bundles. Their corresponding dimensions and the electrode gap distances are shown in Fig. 3. The wire mesh was made of stainless steel wire with a diameter of 1 mm. The grid size of the mesh was 6.35 mm by 6.35 mm. To ensure a proper gap distance, spacers

Contributed by the Heat Transfer Division for publication in the JOURNAL OF HEAT TRANSFER. Manuscript received by the Heat Transfer Division May 20, 1996; revision received September 30, 1996; Keywords: Boiling, Finned Surfaces, Flow Visualization. Associate Technical Editor: T. Rabas.

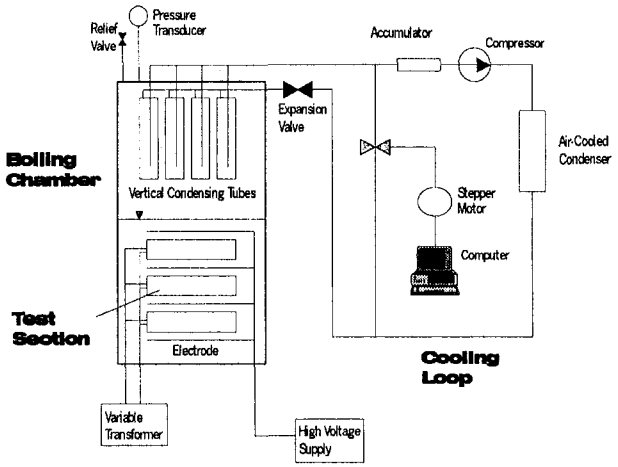

Fig. 1 Schematic diagram of the experimental setup

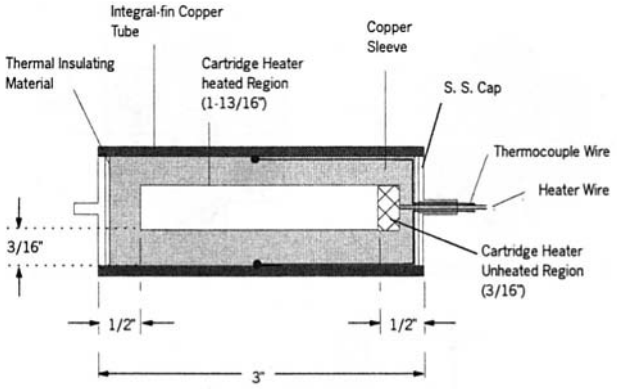

Fig. 2 Schematic of the test section tube

made of electrical insulating material were placed between the electrode and the tube surface.

The saturated pressure in the boiling chamber was maintained by condensing a proper amount of R-134a vapor back to the liquid pool. A separate air-cooled refrigeration unit was installed to remove heat from the vertical condensing tubes (see Fig. 1). In addition, the pressure control was computerized such that precise and continuous monitoring were possible. Further detailed description of the experimental setup can be found in Cheung et al. (1995).

Data Reduction

In general, about 20 readings were collected for each experimental run. These data were then reduced to the parameters of interest, such as the heat transfer coefficient (h), enhancement factor (η), and the EHD power consumption ratio.

Measurement of heater voltage and heater current were used to calculate the heat transfer to the refrigerant as

$$Q = VI. \tag{1}$$

The EHD power consumption was computed as

$$Q_{\text{EHD}} = \phi I_\phi \tag{2}$$

where ϕ and I_ϕ were the applied electric field potential (D.C.) and the corresponding current.

The average wall temperature of the enhanced tubes was taken as the arithmetic mean of n measurement locations.

$$T_{\text{wall}} = \frac{\sum_{i=1}^{n} T_i}{n} \tag{3}$$

Similarly, the pool temperature was taken as the average of the measured refrigerant vapor and liquid pool temperatures.

$$T_{\text{pool}} = \frac{T_{\text{vapor}} + T_{\text{liquid}}}{2} \tag{4}$$

The heat transfer coefficient, h, was then calculated as

$$h = \frac{Q}{A(T_{\text{wall}} - T_{\text{pool}})} \tag{5}$$

where A was the total effective heat transfer surface area of N tubes.

$$A = N\pi DL \tag{6}$$

The enhancement ratio (η) was subsequently calculated as

$$\eta = \frac{h_{\text{EHD}}}{h_0} \tag{7}$$

where subscript '0' represents the base case condition (electrode present but not energized with high voltage).

Finally, the ratio of the EHD power consumption to the total heat transferred to the refrigerant is calculated as

$$\frac{Q_{\text{EHD}}}{Q_{\text{Total}}} = \frac{Q_{\text{EHD}}}{Q + Q_{\text{EHD}}} \tag{8}$$

Results and Discussions

For all the experiments, R-134a was used as the working fluid. The experiments were performed at a saturation pressure of 551.6 kPa (80 psi), which corresponded to a saturation temperature of 18.82°C (66°F).

Experimental Uncertainty Analysis. Table 1 tabulated the precision limit (P) and the bias limit (B) for each variable used in the present study. In order to determine the precision limits,

Nomenclature

A = total surface area of the test section tubes
D = test section tube diameter (O.D.)
$\bar{E}$ = electric field strength
F_e = EHD body force
h = averaged heat transfer coefficient
I = test section heater current
I_ϕ = applied electric field current
L = test section tube length
Nu = Nusselt Number
Q = heat transfer rate
Q_{EHD} = EHD power consumption
q'' = heat flux
T = temperature
ΔT = degree superheat
U = experimental uncertainty
V = test section heater voltage
ϵ = dielectric permittivity
ϵ_0 = dielectric permittivity of vacuum
η = enhancement factor
κ = relative dielectric constant
ρ = fluid mass density
ρ_e = electric charge density
ϕ = applied electric field potential

Subscripts

0 = zero electric field case (base case)
sat = saturation state
w = wall
EHD = Electrohydrodynamics

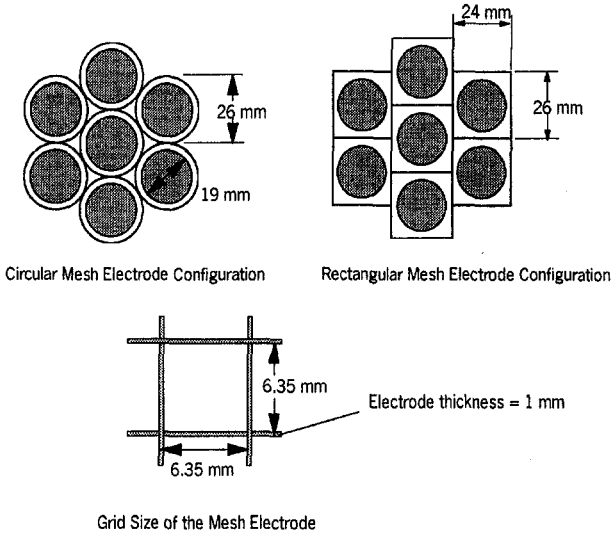

Fig. 3 Electrode configurations and tubes arrangement

50 samples were collected for each variable in a five hour period with normal running condition. The uncertainty analysis for the experimental results was performed with a 95 percent confidence interval, following the guidelines provided by the ASME JOURNAL OF HEAT TRANSFER Editorial Board. The results of the analysis are summarized in Table 2. In some cases, the U_h and U_η can be as high as ±50 percent. It is mainly due to the small superheat (~0.3°C) occurring at low heat flux conditions.

Effect of Electrode Geometry.

Results of the Circular Mesh Electrode. In the experiments, the heat transfer performance of the tube bundle was studied at a heat flux ranging from 8 kW/m^2 (2537 Btu/hr-ft^2) to 20 kW/m^2 (6342 Btu/hr-ft^2). The electrode was charged with positive D.C. voltage, and the test section tubes were grounded. Figure 4 shows the variation of the enhancement factor as a function of applied voltage at three heat flux levels. A maximum enhancement factor of 5.1 was obtained at the heat flux of 8 kW/m^2 (2537 Btu/hr-ft^2). This is a favorable result when compared to an earlier study (Cheung et al. 1995) with the straight wire electrode, where a maximum enhancement factor of three for the same bundle was obtained. The clear advantage of the circular mesh electrode over the straight wire is primarily due to the electric field inhomogeneity provided by the mesh configuration.

As seen in Fig. 4, the enhancement factor decreases as the heat flux increases. At a heat flux of 15 kW/m^2, the maximum enhancement factor is 2.2 (compared to 5.1 at 8 kW/m^2). This observation confirms that at a higher heat flux the boiling process is sufficiently rigorous and, therefore, the additional activities induced by the high-voltage electric field are less pronounced. It additionally shows that in each heat flux level there is an optimum applied electric field potential beyond which additional increases in the applied voltage reduces the heat transfer coefficient. The power consumption throughout the experiments was ranged from two percent to five percent (U_{QEHD} = ±0.14 percent) of the heat transfer rate, depending on the heat flux level applied.

Table 1 Precision and bias limits of the experimental variables

Variables	Precision limit (P)	Bias limit (B)
V	±0.3 %	±0.7%
I	±0.2 %	±1.0%
ϕ	±0.02 %	±0.1%
I_ϕ	±0.02 %	±0.1%
T_{wall}	0.05 °C	0.1 °C
T_{pool}	0.04 °C	0.1 °C

Table 2 Results of the uncertainty analysis

Experiments	U_h (%)		U_η (%)	
Tube bundle with circular mesh electrode	max	±39.3	max	±40.6
	min	±7.8	min	±9.8
Tube bundle with rectangular mesh electrode	max	±44.4	max	±45.1
	min	±8.4	min	±10.2
40 fpi integral-fin tube with circular mesh electrode	max	±28.8	max	±30.5
	min	±7.2	min	±11.4
Modified 40 fpi integral-fin tube with circular mesh electrode	max	±48.5	max	±50.1
	min	±12.5	min	±22.9

Results of the Rectangular Mesh Electrode. The purpose of using a rectangular mesh electrode was to introduce an additional nonuniform electric field distribution along the azimuthal direction. The experimental condition was similar to that of the circular mesh electrode. As shown in Fig. 5, the maximum enhancement factor is about 5.5 and it takes place at a heat flux of 8 kW/m^2 with an EHD voltage of 14 kV. In general, the trends are very similar to those of the circular mesh electrode. Comparison of the two mesh electrodes are shown in Fig. 6. The scatter of data, especially at the low heat flux level, is considered within the range of experimental uncertainty (between ±8.4 percent and ±44.4 percent). It is therefore concluded that the additional nonuniformity created by the rectangular mesh electrode does not have a substantial effect in further improvement of heat transfer. Though not shown here, the power consumption of the rectangular mesh electrode was found to be comparable to that of the circular mesh electrode.

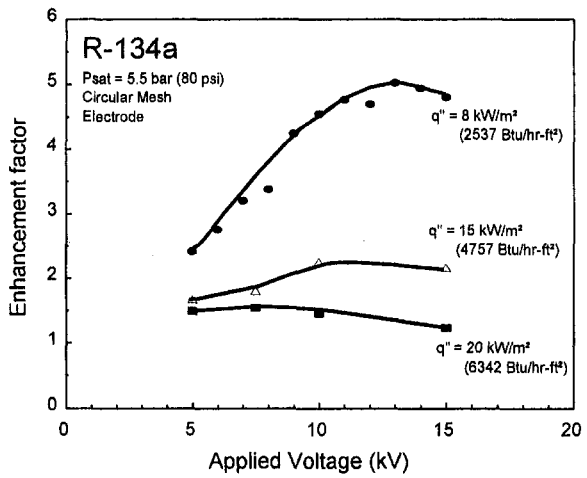

Fig. 4 Enhancement factor versus applied voltage for circular mesh electrode

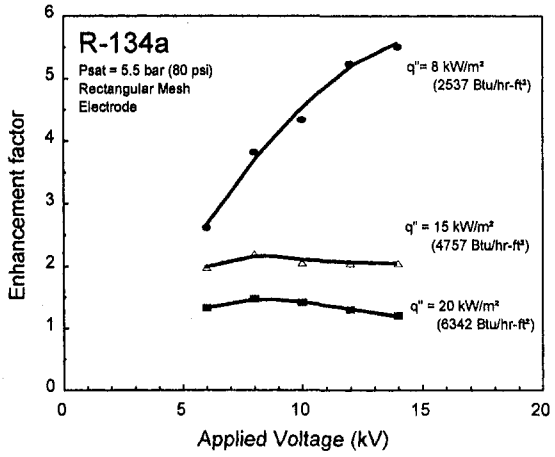

Fig. 5 Enhancement factor versus applied voltage for rectangular mesh electrode

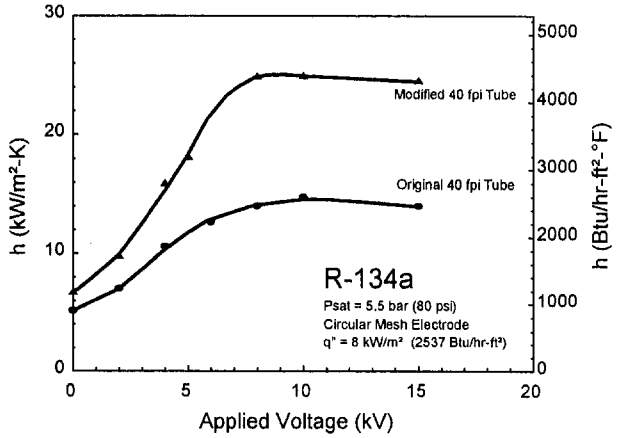

Fig. 7 Variation of h with applied voltage for modified and original 40 fpi integral-fin tubes

Effect of Heat Transfer Surface Modification. The original 40 fpi tube was modified by cutting grooves on the fins along the tube length. The grooves were about 0.7 mm (0.028″) in depth and 0.30 mm (0.012″) in width. A total of 36 grooves were cut with 10 deg intervals. Both the modified and the original 40 fpi tubes were tested with the circular mesh electrode. Figure 7 shows the effect of applied EHD voltage on the heat transfer coefficients at 8 kW/m^2 (2537 Btu/hr-ft^2) for the original and modified 40 fpi tubes; it yielded a maximum enhancement factor of nearly four, which presents an improvement when compared with the maximum enhancement factor of 2.85 for the original 40 fpi tube. Also, note that at the base case condition (no electric field applied but electrode present), the heat transfer coefficient of the modified 40 fpi tube is about 35 percent to 45 percent higher than the original one. The grooves provide additional surface for nucleations, thereby leading to a more dynamic boiling process. In the presence of EHD, the modified 40 fpi tube performs up to nearly 80 percent better than the original 40 fpi tube at the given conditions. This indicates that the increase in spatial gradient of electric field strength on the vicinity of the heat transfer surface creates a substantial improvement in the EHD pool boiling heat transfer enhancement.

EHD-Enhancement Mechanism in Integral Fin Tube. The experimental studies presented here clearly demonstrated that the type of heat transfer surface, the electrode configuration, and the magnitude of applied EHD voltage significantly influence the bubble dynamics as well as the EHD enhancement in nucleate pool boiling. In order to get a better understanding of the mechanism of the EHD-assisted pool boiling on integral-fin tube geometries, a series of flow visualization studies were performed on a 40 fpi tube with a circular wire mesh electrode. The effect of applied EHD voltage on the bubble behavior was investigated and will be described next.

In the absence of the EHD effect, the departure diameter is mainly governed by the surface tension and buoyancy forces (Fig. 8a). Application of high voltage imposes EHD forces on the bubble. The EHD force acting on a dielectric sphere of radius R, with dielectric constant κ_1, in an infinite pool with dielectric constant κ_2, is given by Jones (1978) as

$$\frac{F}{4/3\pi R^3} = \frac{3}{2}\kappa_2\epsilon_0\left(\frac{\kappa_1 - \kappa_2}{\kappa_1 + 2\kappa_2}\right)\nabla E^2. \qquad (9)$$

The above equation indicates that a fluid with higher dielectric constant will tend to move to regions of highest electric field strength. Since the dielectric constant of vapor is always less than that of the liquid, a vapor bubble in a liquid pool (in the absence of gravity) will move to the regions of low electric field strength. This has also been observed in earlier studies (Ogata, 1993b; Ohadi et al., 1992; Kumar, 1994). In EHD-assisted boiling, the heat transfer surface typically serves as the receiving/grounding electrode, and the electrode (here a wire mesh type) is charged with the high voltage. The lowest electric field is at the heat transfer surface because its radius of curvature is highest. Therefore, the EHD forces will act against the buoyancy forces during ebullition as shown in the Fig. 8b, causing the bubble to spread on the heat transfer surface.

Figures 9a–e show changes in boiling behavior with increasing EHD voltage in a 40 fpi integral-fin tube with R-134a. The applied heat flux was 8 kW/m^2, and the saturation pressure was kept at 551.6 kPa (80 psi). Figure 9a shows that in the absence of EHD voltage bubbles grew at the nucleation sites and escaped due to the buoyancy forces.

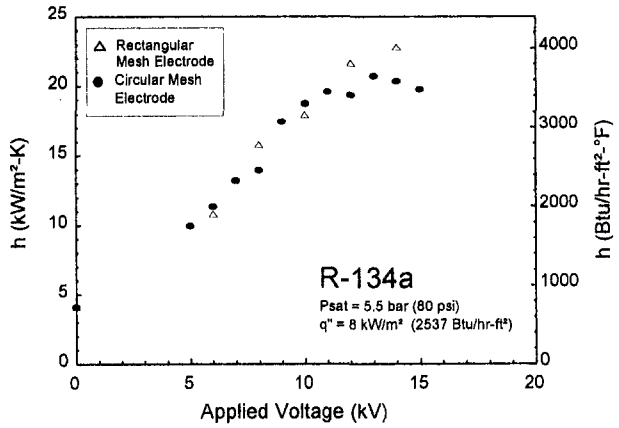

Fig. 6 Comparison of h for both electrodes at 8 kW/m^2

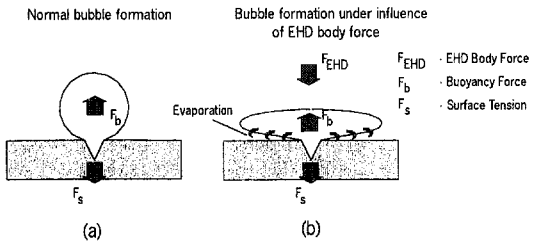

Fig. 8 Forces acting on a growing bubble

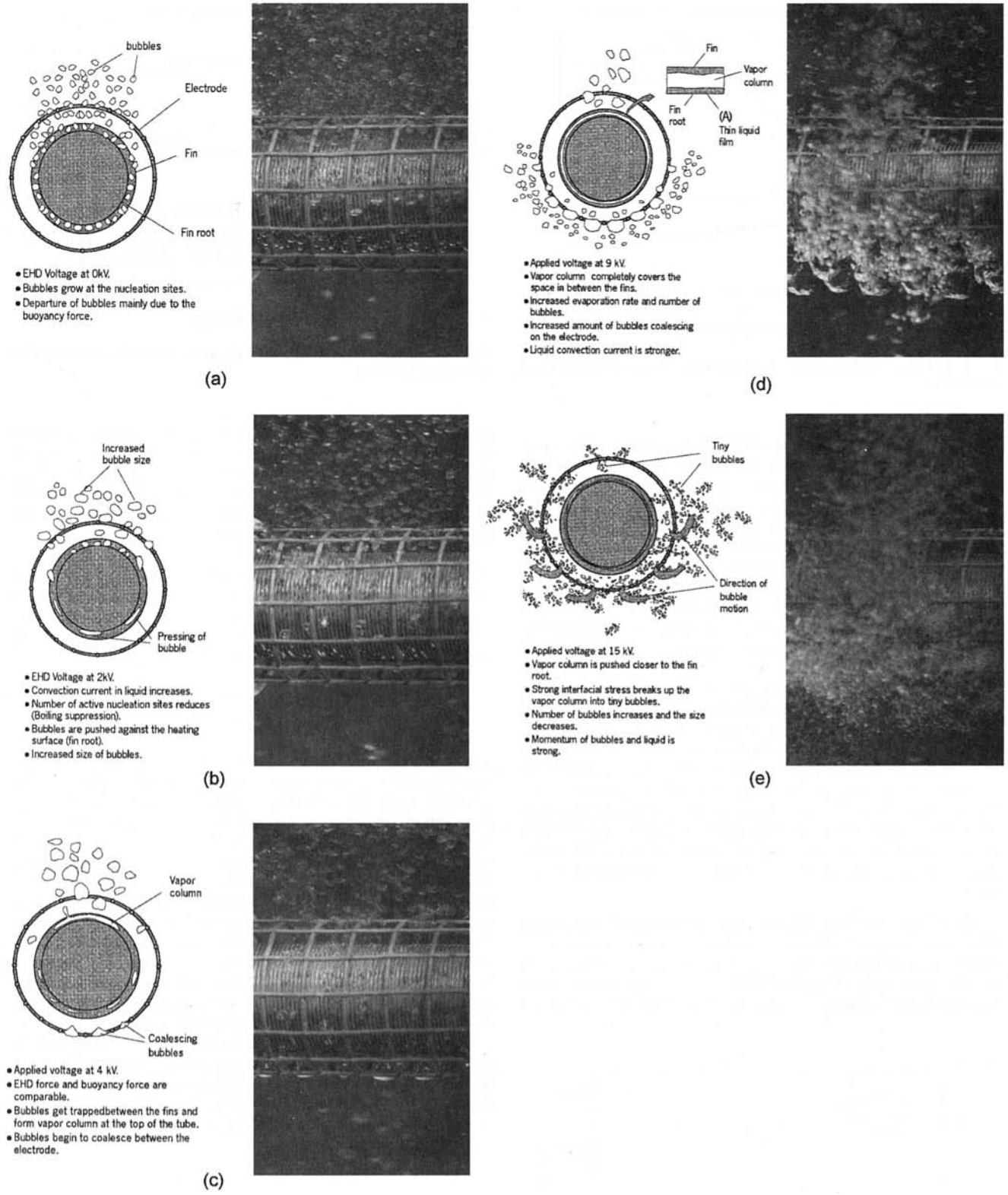

Fig. 9 Bubble behavior in the presence of EHD voltage in an integral-fin tube

When a moderate EHD voltage (0–4 kV) was applied, the liquid convection was augmented, leading to an increase in heat transfer coefficient. However, it was also observed that the number of nucleation sites and generated bubbles were reduced (Fig. 9*b*) as a consequence of the additional EHD induced convection. This phenomenon can be analogous to the one in flow boiling where the active nucleate sites are suppressed by the increased bulk flow. The EHD boiling suppression phenomenon has been observed by others as well as (Ogata and Yabe 1993a; Kawahira et al., 1990). It is believed that at this moderate applied voltage the gain in bulk convection due to EHD is more than the loss associated with EHD boiling suppression, resulting in a net increase in heat transfer coefficient.

The departure sizes of the generated bubbles were generally larger at a moderate applied voltage, since they required a stronger buoyancy effect to overcome the EHD force that pushed them against the heating surface (fin root area). Once they detached from the nucleation site, the majority of the bubbles were forced to travel along the tube circumferentially between the fins until they reached the upper portion of the tube and were released from there. This additional movement of bubbles in-between the fins may further increased the convective heat transfer.

When the EHD voltage increased to around 4 kV, the bubbles began to get trapped between the fins and the electrode, as shown in Fig. 9*c*. At this voltage the EHD force on the bubble became comparable to the buoyancy force. Note that trapping of the bubbles only took place on the top portion of the tube as the EHD force acted directly against the buoyancy forces at this point.

The tube (19 mm O.D.) and electrode (separated by a 3 mm gap from the tube) used in the present study can be approximated as two coaxial circular tubes of radius $r_1 = 9.5$ mm and $r_2 = 9.5 + 3$ mm. By assuming a uniform dielectric constant of the fluid and zero EHD current discharge, the electric field distribution in-between the coaxial tubes is given by

$$E(r) = -\frac{\phi}{r \ln (r_2/r_1)} \tag{10}$$

where ϕ is the applied EHD voltage between the heat transfer surface and the electrode, and r is the radial distance from the tube axis. Thus, by making use of Eqs. (9) and (10), the EHD force acting on a spherical bubble of radius R can be written as

$$\frac{F}{4/3\pi R^3} = \frac{3}{2}\kappa_2\epsilon_0\left(\frac{\kappa_1 - \kappa_2}{\kappa_1 + 2\kappa_2}\right)\left(\frac{2\phi^2}{[\ln (r_2/r_1)]^2}\frac{1}{r^3}\right). \tag{11}$$

The bubble departure diameter can be approximated as 0.5 mm, based on a boiling visualization study of R-134a done by Kedzierski and Kaul (1993). The measurement was obtained with a smooth tube at a saturation pressure of 527 kPa. For refrigerant R-134a, $\kappa_1 \approx 1$ and $\kappa_2 \approx 9.5$ (Fellows et al., 1991). Thus the EHD force acting per unit volume of bubble at an applied voltage V, and radial distance $r = 9.5$ mm, is found to be approximately $0.00045\phi^2$ N/m^3. The buoyancy force acting per unit volume of a bubble is equal to 12,000 N/m^3. Therefore, the EHD voltage at which the buoyancy and EHD forces become comparable is calculated to be 5.2 kV, which is very close to the value observed in the present study.

When the applied EHD voltage increased to more than 4 kV, there was an increase in bubble formation. This phenomenon could be explained as follows: the trapped bubbles on the upper part of the tube deformed into vapor columns due to the stronger electrical stresses. The vapor columns stretched and got closer to the fin root surface. They eventually covered the entire space between the fins as the applied voltage increased (see Fig. 9*d*). The vapor column formation between the fins was also reported by Cooper (1990). The presence of vapor columns in-between the fins (shown by *A* in Fig. 9*d*) caused an increase in the evaporation rate. Ogata and Yabe (1993a) also ascribed the increase in vapor formation to the increase in surface area for evaporation when the bubble spread along the heat transfer surface, leaving a thin liquid film underneath. Each column grew along the circumference, due to the increase in vapor formation, until the buoyancy forces were sufficient to overcome the restraining EHD forces, causing bubbles to be released from the top of the tube. On release of vapor bubbles, the column length decreased. The column again grew due to vaporization until it released other bubbles. This cycle caused the vapor column to oscillate, and contributed to an increase in the liquid convection effect. Also note that when the EHD voltage was more than 4 kV, vapor bubbles coalesced in the center of the wire mesh (where the local electric field strength is zero due to symmetry). The coalescing bubbles were later removed by the buoyancy force and by the surrounding strong convective motions.

When the EHD voltage approached around 9 kV, the vapor columns fully covered the spaces between the fins. They were also pushed deeper between the fins due to the stronger electric force. At this point and beyond ($\geq$9 kV), the oscillating motion of the vapor column stopped, and the liquid replacement was restrained. The fin root area came directly into contact with the vapor, causing an increase in thermal resistance for heat transfer. In addition, the heat transfer by electroconvection decreased as all the spaces between the fins were covered by the vapor. This in turn might lead to a decrease in the heat transfer coefficient at very high applied voltages ($\geq$9 kV).

On the other hand, due to the stronger interfacial stress induced by the electric field at higher voltages, the vapor column and the coalescing bubbles broke down into tiny bubbles, resulting in an increase in the number of bubbles (see Fig. 9*c*). As shown there, the tiny bubbles even passed through the center of the wire mesh as a jet stream. Ogata and Yabe (1993a) also found a sudden increase in the number of bubbles at around 15 kV with boiling of a R-11/ethanol mixture. They attributed the reduction in size of vapor bubbles to breaking of large bubbles by the EHD force. Similarly, Cooper (1990) found that this phenomenon occurred at around 5–8 kV for boiling of R-114. The size of the bubbles formed under such conditions were smaller. With the observation in the present study, it is suggested that the bubble break-up phenomenon destabilized the vapor columns, allowing liquid to reach the areas between the fins and preventing vapor from contacting the surface. The vigorous activities of liquid and bubbles further enhanced convective heat transfer which might lead to an increase in heat transfer coefficient at high applied voltages.

Note that the net effect on the heat transfer coefficient was the combination of the counteracting effects discussed above. Therefore, there was always an optimum EHD voltage at which the EHD enhancement would be maximized or leveled. In Fig. 7, optimum voltage was around 10 kV (8 kW/m^2). The optimum voltage also depended on the operating heat flux levels. In general, this voltage was higher at a lower heat flux. The flow visualization studied and presented here should be valid typically for a low heat flux condition (8 kW/m^2).

Conclusions

Similar to the previous findings for a single tube, the mesh electrode was found to perform better than the straight wire electrode for the tube bundle. Enhancement factors of more than five were obtained with the mesh electrode configurations. The tube bundle experiments confirmed the fact that the EHD effect was more significant at lower heat flux levels. The enhancement factor increased from 1.5 to 5.1 when the heat flux decreased from 20 kW/m^2 to 8 kW/m^2. By varying the applied voltage at a given heat flux level (especially at a high heat flux level), heat transfer coefficient would reach a peak value beyond which additional increase in the voltage would reduce the enhancement. The experimental results demonstrated that the rectangular and the circular mesh electrodes yield comparable enhancements. The EHD power consumption for the two electrode geometries was also comparable and ranged from two percent to five percent of the total heat transfer rate, depending on the magnitude of the applied voltage and the heat flux.

Results also indicate that the modified 40 fpi tube performed better than the original 40 fpi tube, especially in the presence of the EHD field. In the absence of the EHD effect, the modified tube had 35 percent to 45 percent higher heat transfer coefficients than the original one had. When EHD was applied, the modified tube had up to 78 percent higher heat transfer coefficient.

In addition, flow visualization studies were conducted, and the boiling behavior was observed at various applied voltages. It is concluded that the enhancement is a combined result of additional electroconvection and changes in bubble dynamics. Depending on the applied voltage level, one or more of the following phenomena were observed:

- induction of liquid convection current
- suppression of nucleate boiling
- pressed vapor bubbles on the heat transfer surface
- formation of vapor columns between the fins
- increased evaporation rate
- coalescence of bubbles on the electrode
- destabilization and breakage of vapor columns and coalescing bubbles

Additional experiments and a quantified approach to the above observations will contribute to the empirical and/or analytical modeling of EHD-enhanced pool boiling mechanism on tube bundles.

Acknowledgments

The financial support of this work, in part by the U.S. Department of Energy and a consortium of participating companies, is gratefully acknowledged. The 40 fpi integral-fin tubes used in the experiments were provided by Wieland-Werke AG, Germany. The assistants of Mr. Klaus Menze in this regard is greatly acknowledged.

References

Cheung, K., Ohadi, M. and S. Dessiatoun, 1995, "Compound Enhancement of Boiling Heat Transfer of R-134a in a Tube Bundle," *ASHRAE Transactions,* Vol. 101, pt. 1, in press.

Cooper, P., 1990, "EHD Enhancement of Nucleate Boiling," ASME JOURNAL OF HEAT TRANSFER, Vol. 112, May 1990, pp. 458–464.

Fellows, B. R., Richard, R. G., and Shankland, I. R., 1991, "Electrical Characterization of Alternate Refrigerants," *Xvii*th International Congress of Refrigeration, Paper No. 45, Montreal, Quebec, Canada, August 1991.

Jones, T. B., 1978, "Electrohydrodynamically Enhanced Heat Transfer in Liquids—A Review," *Advances in Heat Transfer,* Vol. 14, pp. 107–148.

Kawahira, H., Kubo, Y., Yokoyama, T., and Ogata, J., 1990, "The Effect of an Electric Field on Boiling Heat Transfer of Refrigerant 11—Boiling on a Single Tube," *IEEE Transactions on Industry Applications,* Vol. 26, No. 2, pp. 359–365.

Kedzierski, M. A., and Kaul, M. P., 1993, Technical Report, "Horizontal Nucleate Flow Boiling Heat Transfer Coefficient Measurements and Visual Observations for R-12, R-134a, and R-134a/Ester Lubricant Mixtures," Building and Fire Research Laboratory, NIST, Gaithersburg, Maryland.

Kumar, A., 1994, "Experimental Investigation of Pool Boiling Heat Transfer Augmentation in R-123 Using the Electrohydrodynamic Technique and its Long Term Effects," Master's thesis, University of Maryland, College Park, Maryland.

Ogata, J., and Yaba A., 1993a, "Basic Study on the Enhancement of Nucleate Boiling Heat Transfer by Applying Electric Field," *International Journal of Heat and Mass Transfer,* Vol. 36, No. 3, pp. 775–782.

Ogata, J., and Yabe, A., 1993b, "Augmentation of Boiling Heat Transfer by Utilizing the EHD Effect—EHD Behavior of Boiling Bubbles and Heat Transfer Characteristics," *International Journal of Heat Mass Transfer,* Vol. 36, No. 3, pp. 783–791.

Ohadi, M. M., Papar, R. A., Ansari, A. I., and Kumar, A., 1992, "Some Observations on EHD Enhanced Boiling of R-123 in the Presence of Oil Contamination," *Proceedings of the Engineering Foundation Conference on Pool and External Flow Boiling,* Santa Barbara, CA.

Papar, R. A., Ohadi, M. M., Kumar, A., and Ansari, A. I., 1993, "Effect of Electrode Geometry on EHD-Enhanced Boiling of R-123/Oil Mixture," *ASHRAE Transactions,* Vol. 99, Pt. 1.

Singh, A., Kumar, A., Dessiatoun, S., Faani, M., Ohadi, M., and Ansari, A., 1993, "Compound EHD-Enhanced Pool Boiling of R-123 in a Liquid-to-Refrigerant Heat Exchanger," 93-WA/HT-40, ASME Winter Annual Meeting, New Orleans, Louisiana.

Electrohydrodynamic Enhancement of Falling Film Evaporation Heat Transfer and its Long-Term Effect on Heat Exchangers

K. Yamashita
Heavy Apparatus Engineering Laboratory,
Toshiba Corporation,
2-4 Suehiro-cho, Tsurumi-ku,
Yokohama, 230,
Japan

A. Yabe
Mechanical Engineering Laboratory, AIST,
Ministry of International Trade
and Industry,
1-2 Namiki, Tsukuba, Ibaraki, 305,
Japan

Electrohydrodynamic (EHD) enhancement of vertical falling film evaporation heat transfer has been experimentally studied using HCFC123, which is an alternative working fluid for CFCs. This research verified that EHD enhancement of HCFC123 condensation was as effective as that of conventional working fluids. The electrodes used for EHD enhancement of vertical falling film evaporation utilized the following two EHD phenomena: extracting the liquid by a nonuniform electric field, and surface granulation by a nearly uniform electric field. As a result, an electrode with vertically arrayed offset-slits that is suitable for industrial applications has been developed that showed a six-fold enhancement of evaporation heat transfer over that for a smooth tube. The long-term effects of the high voltages associated with EHD on heat exchanger performance have been evaluated. Operation of EHD heat exchangers for 1000 hours indicates they do not sustain serious damage, and are, therefore, suitable for industrial applications.

Introduction

To improve the performance of compact heat exchangers used in heat pumps, they must operate with as small a temperature difference as possible. One way to achieve this is to exchange heat with a working fluid that undergoes a phase transition, either condensing or boiling. Several studies have been conducted on enhanced boiling, condensation heat transfer by applying electric fields to the heat exchangers. Concerning boiling and evaporation, Cheng and Chaddock (1985) reported the electrohydrodynamic (EHD) effects of bubbles. Allen and Cooper (1987) developed a prototype electrohydrodynamic (EHD) evaporator and showed the potential of EHD evaporators. Ogata and Yabe (1991, 1993) studied the enhancement of nucleate boiling in several working fluids with different electrical properties and found that the relaxation time of the electric charge in boiling liquids affects the enhancement of the boiling heat transfer. Ogata et al. (1992), Ohadi et al. (1992), and Singh and Ohadi (1995) developed a practical evaporator by using EHD boiling enhancement. In space engineering, Pachosa and Chung (1993) reported the EHD boiling in microgravity atmosphere.

Concerning condensation, Didkovsky and Bologa (1982) were first to report the high enhancement of film-wise condensation. Through numerical modeling, Yabe et al. (1987) clarified the extraction phenomena involving a nonuniform electric field and the removal of condensed liquid by a helical wire electrode. Sunada et al. (1991) clarified the liquid surface granulation phenomenon involving a uniform electric field and found that the pseudo-dropwise condensation that is generated on the condensation film enhances the condensation heat transfer over four times. Yamashita et al. (1989, 1991) used EHD condensation heat transfer to enhance the operation of a 50-kW EHD condenser (working fluid was either CFC113, CFC114, or C_6F_{14}). The vertical film condenser had a helical wire electrode inside a lattice electrode. The manufacturing method was improved for a tube-bundle. It was also clarified that the effect of lubricating oil on the condensation heat transfer enhancement was negligible in the EHD condenser. Wawzyniak and Seyed-Yagoobi (1996) reported the enhancement's comparison of Smooth and Tubo C II ® (enhanced tube) and maximum enhancement ratio was up to six times by the coupling effect of EHD and mechanical manufactured tube.

In general, there are three types of evaporators: dry expansion, flooded, and falling film. In dry expansion evaporators, the working fluid flows into the evaporator tube in a two-phase state and then boils and evaporates. Dry expansion evaporators are not suitable for large-scale heat exchangers because of the increasing pressure loss on the working fluid side. Flooded evaporators store the condensed working fluid in vessels, that are needed to achieve high boiling heat performance at low pressure. Many kinds of boiling heat transfer enhancement techniques, which include mechanically manufactured surfaces, have been developed; boiling heat transfer enhancement as much as ten times that for smooth tubes has been achieved. The heat transfer enhancement of these tubes is not applicable to evaporators, however, because the head of liquid above the evaporating working fluid reduces the enhancement effect in evaporators having a lower absolute pressure. Oil contamination also reduces the enhancement effect.

Falling film evaporators, which have been used in chemical distillation processes, have low pressure loss and nonboiling conditions compared to dry expansion and flooded evaporators. The vertical falling film evaporator has high evaporation heat transfer performance if the falling film is thin. Under these conditions, EHD enhancement is possible.

Several studies on vertical falling film evaporation have been reported. Chun and Seban (1971) and Wilke (1962) obtained experimental correlations for the average evaporation heat transfer in laminar and turbulent flow. Brumfield and Theofanous (1976) reported that the correlation derived from the average wave model compared well with the Chun-Seban correlation.

Contributed by the Heat Transfer Division for publication in the JOURNAL OF HEAT TRANSFER. Manuscript received by the Heat Transfer Division December 4, 1995; revision received November 14, 1996; Keywords: Augmentation & enhancement, Condensation, Evaporation, Heat Exchangers, Thin Film Flow. Associate Technical Editor: M. S. Sohal.

Mudawwar and El-Masri (1986) and Shemerler and Mudawwar (1988) proposed the film flow model for the eddy diffusivity and numerically and experimentally the evaporation heat transfer, and compared their results with the Chun-Seban correlation. These papers pursed the correctness of the correlation using Re_f and Pr numbers, and agreed the Chun-Seban correlation relatively well. The Chun-Seban correlation is still then available. But they did not describe the enhancement method of evaporation heat transfer in their system. Rothfus and Newman (1977) described the heat transfer enhancement method with a fluted tube.

CFCs have been used as refrigerants in heat exchangers for many years. CFCs, however, disrupt the ozone layer around the Earth, allowing harmful levels of UV light to reach the Earth's surface. The CFC Restrict Regulation has been enforced, and use of CFCs will thereby be gradually abolished worldwide. Therefore, alternative working fluids for heat transfer systems are under development. At present, there are several candidates. For example, HCFC123, whose boiling point is 27°C, ODP (ozone depleting potential) is 0.02, and GWP (global warming potential) is 0.02. These fluids can be used in large-scale heat pumps and organic Rankine cycles which are in turn used in geothermal binary power plants, ocean thermal energy conversion (OTEC) plants, and solar energy electric power plants. Feasibility studies of using HCFC123 in large-scale heat pumps that currently use CFC11 are underway. There is therefore a need to develop EHD heat exchangers for systems using CFC alternative working fluids.

To verify the effectiveness of vertical EHD condensers using alternative working fluids, and to achieve high-performance vertical EHD falling film evaporators an experimental investigation was carried out using HCFC123. Furthermore, the long term effect of the high electric fields on EHD falling film evaporators and EHD condensers was evaluated; this is important for determining if EHD heat exchangers can be applied to industrial systems.

Experimental Apparatus and Procedure

Figure 1 shows a schematic of our vertical condenser, which is a stainless steel (SUS304) cylindrical vessel, 400 mm in diameter. Cooling water flows through four vertical stainless steel tubes with 19.05 mm o.d., 1.2 mm wall thickness, and 2.04 m length. The total flow is divided evenly among the four tubes by branching T-connectors. The system has two vapor inlets and two condensed liquid outlets. One of these outlets is for the liquid extracted by the electrodes, and the other is for the liquid flowing down along the tubes. The HCFC123 vapor

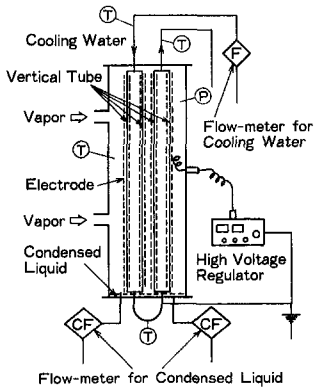

Fig. 1 Experimental apparatus of condenser

condenses on the outer surface of tubes carrying the cooling water because the condensed liquid flows out of the condenser after being separated from the vapor by a U-tube. The lower part of the U-tube is immersed in condensed liquid so vapor can not flow down through it.

The condensed liquid flows down along the outer surface of the tube. The amount of heat exchanged, which is proportional to the quantity of condensed HCFC123, is due to the temperature difference between the HCFC123 vapor and the cooling water. An energy balance of the condenser showed that the amount of energy exchanged, calculated from the temperature difference multiplied by the flow rate of the cooling water, agreed within two percent with that calculated from the latent heat of the condensed liquid.

Figure 2 shows a schematic of our falling film evaporator. It is a cylindrical vessel (shell) made of stainless steel (SUS304), similar to the vertical condenser, and has two vertical stainless steel tubes, (SUS304) with 25.4 mm o.d., 1.2 mm wall thickness, and 2 m length. The length is limited to two m by the tube vibration. This maximum length was selected because EHD enhancement has the potential to realize the thin liquid film for long tubes. This system has a 400 mm deep upper reservoir for storing the liquid HCFC123. The vertical tubes are mounted on a plate that separates the upper reservoir from an evaporation chamber. The gap that feeds the liquid around the periphery of tube has a narrow ring that connects a bowl shaped nozzle and the tube. This nozzle distributes the liquid through a hole that is slightly larger than the outer diameter of the tube. Up to one gap distance the liquid feed rate along the vertical tube is

Nomenclature

A = heat transfer area, m^2
c = electric conductivity, $1/\Omega m$
E = electric field strength, V/m
F = electrostatic force, N/m^2
G = mass flow rate, kg/s
h = heat transfer coefficient, $W/(m^2K)$
k = thermal conductivity, W/(mK)
h_{fg} = latent heat, J/kg
I = current, A
l = tube length, m
Nu* = evaporation number or condensation number, $(=h(\nu^2/g)^{1/3}/k)$
P = pressure, Pa
Pr = Prandtl number
Q = amount of heat exchanged, W
q'' = heat flux, W/m^2
Re_f^* = mean film Reynolds number of evaporation $(=4\Gamma/\mu)$
Re_l^* = film Reynolds number of condensed liquid $(=4q''l/h_{fg}\mu)$
s = distance between electrode and heat transfer surface, m
S = working fluid volumetric flow rate, m^3/s
T = working fluid temperature, K
DT_m = logarithmic mean temperature difference, K
t = water temperature, K
u = velocity, m/s
V = voltage, V
W = electric power consumption, W
ρ = liquid density of working fluid, kg/m^3
ν = kinematic viscosity, m^2/s
μ = dynamic viscosity, kg/ms
k = thermal conductivity, W/(mK)
ϵ_0 = dielectric constant of vacuum, F/m
$\epsilon 1$ = relative dielectric constant of liquid
g = acceleration of gravity, m/s^2
Γ = film flow-rate per unit wetted perimeter, kg/ms, $\{=G/(\pi do)\}$

Subscripts

e = evaporation
c = condensation
in = inside
o = outside
m = tube material
s = saturated working fluid
1 = inlet
2 = outlet

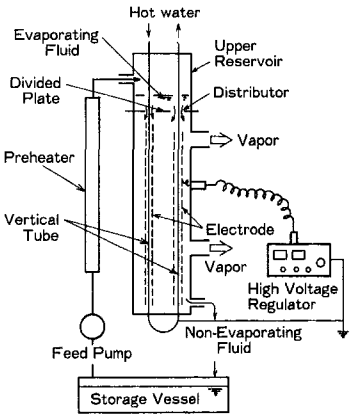

Fig. 2 Experimental apparatus of falling film evaporation

controlled by the liquid head in the upper reservoir. Tubes in the upper reservoir are wrapped in insulation to prevent heat transfer. The thickness of the insulation (PFA, a copolymer of tetrafluoro-ethylene and parafluoroalkyle-vinylether) is 50 mm, and the heat conduction rate is 5.0 W/mK, which is negligible. Hot water is supplied into these tubes from another tank. The amount of heat exchanged, which is proportional to the quantity of the evaporating HCFC123, is due to the temperature difference between the saturated HCFC123 vapor and the hot water. Saturated HCFC123 is supplied by a feed pump to the upper reservoir from a storage vessel through a pre-heater. The non-evaporated HCFC123 is returned to the storage vessel. The flow rate of the returned HCGC123 was measured after separating the vapor by a U-tube. The quality of the vapor flow was 1.0. There was enough space to separate the small liquid drops because the cylindrical evaporator (400 mm i.d.) contained only two vertical tubes of 25.4 mm o.d. each.

Similar to that of the condenser, the energy balance of the falling film evaporator showed that the calculated amount of energy transferred from the hot water agreed within two percent of that calculated from the latent heat of the generated vapor. The amount of generated vapor was calculated from the difference between the supplied and the returned working fluids.

The temperature, flow rate, and pressure measurements in the two heat exchangers were conducted as follows: the flow rate of water was measured by an electromagnetic flowmeter with an accuracy of 0.2 percent F.S (50 L/min); and the flow rate of the working fluid was measured by a positive displacement flowmeter with an accuracy of 0.5 percent F.S (10 L/min).

The temperatures of the cooling water and the condensed working fluid were measured by thermocouples installed inside the tubes. The measurement locations were in areas of agitated flow, for example, in the T-tube header. The measurement locations of the vapor temperature of the working fluid were more than 100 mm from the tube with the electrodes, where the electric field was small enough not to affect the measurement. The saturation temperature corresponding to the gage pressure agreed within ±0.2°C of the measured vapor temperature.

These heat transfer coefficients in the two heat exchangers were calculated from the inlet and outlet temperatures, flow-rates of the water, and the vapor temperature of the HCFC123, after the temperature and pressure had stabilized. The data are the mean values of ten measurements taken over 20 minutes. For P = 100 kPa and 27 < T_s < 30°C, the fluctuation of temperature, flow rate, and pressure were all within ± four percent. The measurement method conformed to the ISO R916 standard. The voltage applied to the electrodes was controlled by a high-voltage dc regulator. The heat transfer tube and the outer shell were electrically grounded.

The condensation and evaporation heat transfer coefficients, h_c and h_e, respectively, were calculated as follows,

Table 1 Error in the heat transfer coefficients

Item	Error (percent)
Heat transfer rate Q	±2.60
Logarithmic mean temperature difference DT_m	±0.70
Heat transfer of water h_w	±0.54
Condensation heat transfer h_c	±3.48
Evaporation heat transfer h_e	±3.48
Rel* Ref*	±3.00
Nu*	±3.48

$$h_c = [(A \cdot DT_m/Q_c) - (1/h_w)\cdot(d_o/d_{in}) - \{d_o/2k_m \cdot \ln(d_o/d_{in})\}]^{-1} \quad (1)$$

$$h_e = [(A \cdot DT_m/Q_e) - (1/h_w)\cdot(d_o/d_{in}) - \{d_o/2k_m \cdot \ln(d_o/d_{in})\}]^{-1} \quad (2)$$

where

$$Q_c = S_c \cdot \rho_s \cdot h_{fg} \quad (3)$$

$$Q_e = S_e \cdot \rho_s \cdot h_{fg} \quad (4)$$

$$DT_m = (t_2 - t_1)/\ln\{(T_s - t_1)/(T_s - t_2)\} \quad (5)$$

$$h_w = k_w/d_i \cdot 0.023 \cdot (u_w d_i/\nu_w)^{0.8} \cdot \mathrm{Pr}_w. \quad (6)$$

The temperature drop of water in the tube was less than 0.5°C, and that is negligible compared with the logarithmic mean temperature difference, which was 5.0°C. Therefore, in this work an assumption of the uniform heat flux was used. The errors in the above quantities were determined by accounting for the accuracy of the thermocouples, flow meters, etc., and are listed in Table 1.

Evaluation of the Heat-Transfer Enhancement of EHD Condensers Using HCFC123

In EHD condensers assembled with helical wires and with lattice electrodes for tube bundles, the heat transfer enhancement (i.e., heat transfer compared with the heat transfer obtained using smooth tubes) already achieved is about four times using C_6F_{14} and about six times using CFC114. The purpose of these experiments was to evaluate the enhancement of the condensation heat transfer in EHD condensers using HCFC123.

Figure 3 shows the helical wire with the lattice electrodes used in the tube bundles. The length of the electrode was about 250 mm. It consisted of the helical wire, four vertical rods, insulating spacers, a condensed-liquid conduit pipe, and lattice-punched curved plates. The lattice-punched curved plates had sufficiently large slits so as not to incur corona discharge by minute splinters and not to accumulate noncondensable gas in warps of the plate. The insulating-spacer material was PFA. The insulating spacers were sandwiched by fixed stainless steel rings. A condensed-liquid conduit pipe was spot-welded on

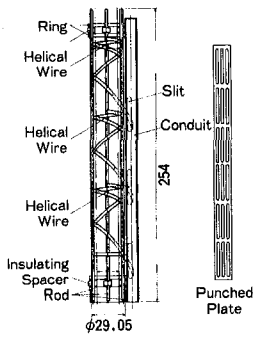

Fig. 3 Electrode of condenser for tube bundle

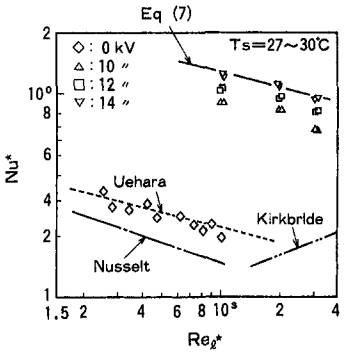

Fig. 4 Condensation heat transfer of HCFC123 with electrode

these rings and the lower edges of the helical wires were inserted into the slits of the conduit pipe.

The condensation performance of this electrode is shown in Fig. 4. The condensation heat transfer was evaluated with the Nu*-Re$_l$* correlation, where Re$_l$* is calculated from the amount of the condensed liquid and is proportional to the heat flux. In Fig. 4, the dash/dot line denotes the Nusselt solution for saturated vapor (Nusselt, 1916) and for the turbulent film flow condensation proposed by Kirkbride (1934). The dotted line denotes the empirical formulas for the wavy film flow condensation proposed by Uehara (1983). When a voltage was applied to the electrode, the condensed liquid was extracted to the helical part of the electrode at 6 kV, and was adequately removed from the tube surface at 10 kV. Pseudo-dropwise condensation on the lattice part was generated at more than 10 kV, and the combination of condensation removal and pseudo-dropwise formation was maximized at 14 kV.

The helical wire with lattice electrodes enhances condensation heat transfer through two EHD effects; the helical wire part decreases the film thickness by shortening the vertical film flow distance, and the lattice part decreases the local film thickness by pseudo-dropwise condensation. The empirical formula for the condensation heat transfer of the helical wire with lattice electrodes is given by Yamashita et al. (1989) as follows

$$\mathrm{Nu}^* = 7.86\ \mathrm{Re}_l^{*-0.25} \text{ for CFC113, CFC114, } V = 14 \text{ kV}$$
$$\text{or } C_6F_{14},\ V = 20 \text{ kV}. \quad (7)$$

The solid lines in Fig. 4 denote Eq. (7). The enhancement ratio of the condensation heat transfer was 5.9 for HCFC123, where the condensation heat transfer coefficient is given by Eq. (7). The Electrohydrodynamics enhancement of condensation using organic working fluids, whose electrical properties were shown in Table 2, was Therefore, two EHD phenomena, extracting the liquid by a nonuniform electric field and surface granulation by a nearly uniform electric field, were effective for $1.6 \times 10^{-11} < \epsilon_0 \cdot \epsilon l < 5.4 \times 10^{-11}$ F/m and $1.0 \times 10^{-15} < c < 1.3 \times 10^{-8}$ 1/Ωm. The electric power consumption using HCFC123 was more than required by the EHD condenser using C_6F_{14} or CFC114, and is probably due to the insulating characteristic of the working fluid (Table 2). The electric power consumption in the experiment was relatively low, only 0.015 percent of the amount of heat exchanged. The performance determined in this work indicates that using EHD heat exchangers for industrial applications should be possible.

Table 2 Electrical properties of the working fluids (T_S = 25°C)

Working fluid	Dielectric permittivity (F/m)	Electric conductivity (1/Ωm)
C_6F_{14}	1.6×10^{-11}	1.0×10^{-15}
CFC113	5.4×10^{-11}	1.3×10^{-8}
CFC114	2.0×10^{-11}	1.5×10^{-13}
HCFC123	4.2×10^{-11}	4.6×10^{-9}

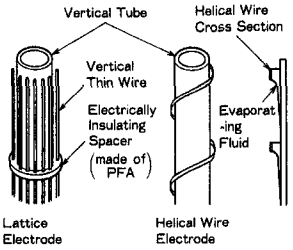

Fig. 5 Electrode's concept for falling film evaporator

EHD Effect of Falling Film Evaporation

The electrode of the condenser is used to extract and remove the falling condensed liquid and to generate a granulated thin film. Liquid extraction occurs because of a dielectrophorotic force exerted by the unequal electric field strength. The nearly uniform electric field imposed on the lattice parts, as Yamashita and Yabe (1991) reported, causes the EHD granulation phenomena on the film surface.

The electrode of the falling film evaporator differs from that of the condenser in that the liquid is not removed. In general, the EHD granulation phenomena on film surfaces is effective for increasing evaporation rates, but this phenomena is not as effective in this system because dry patch formation occurs that decreases the evaporation heat transfer. Dry patches occur because the falling film has transverse waves, which make the electric field unequal, and the dielectrophoretic force then extracts the liquid in the vicinity of the crests of the wave. Either the height of the waves becomes high or liquid poles are generated between the electrode and the tube surface. If the amount of liquid poles becomes excessive, dry patches are easily generated. Therefore, the electrode of the falling film evaporator requires good mixing of the extracted liquid and effective granulation of the film surface.

Prototype Electrodes for Falling Film Evaporators

The evaporation heat transfer enhancement mechanism of the falling film by applying electric fields can be explained as follows. First, the entire tube surface is covered with a falling liquid film. Second, the liquid film becomes thin and is disturbed by the EHD granulation phenomena. Third, the falling liquid is maintained between the electrode and the tube surface. The EHD effects suppress droplets splashing from the liquid film flow caused by the flooding phenomena. Therefore, the two EHD effects create the possibility of enhancing the evaporation heat transfer by making the falling liquid film thin and by retaining the liquid between the electrode and the tube surface.

Considering the above effects, the prototype electrodes are selected as either helical or lattice. Figure 5 shows the shapes and functions of two electrodes.

Helical Wire Electrode. Wire is wound helically around the tube. The wire is separated from the tube surface with four vertical rods penetrating abacus-shaped electrical insulators of PFA (copolymer of tetrafluoro-ethylene and parafluoroalkylevinylether). When a high voltage is applied to the electrode, the liquid is extracted by the helical wire electrode and falls along it. The extracted liquid becomes the main helical stream on the tube surface. Some liquid leaks and falls vertically from the stream, and the leakage rate increases with increasing applied voltage. As the leaking liquid forms a thin film on the tube surface area which does not face the electrode, the evapora-

tion heat transfer is improved. The helix angle is 15–45 deg with respect to the longitudinal axis, the width of the helical wire is 3 mm, the thickness is 0.5 mm, and the distance between the electrode and the tube surface is 3 mm.

Lattice Electrode. Vertical thin wires are installed around the vertical tube, and these wires are prevented from touching the tube surface by electrical insulating ring spacers of PFA. When a high voltage is applied to these wire electrodes, the falling liquid is retained between the electrodes and the tube, disturbing the liquid film flow. Disturbing the liquid film causes many thin parts of the liquid film to be intermittently produced on the tube surface, enhancing the evaporation heat transfer. The electrical insulating ring spacers, which are set at specified intervals along the tube, redistribute the falling liquid and form a relatively uniform film flow over the tube surface.

The electrode configuration is as follows: the maximum number of thin vertical wires is 32 around the tube, the gap between wires is 1.28 ~ 2.28 mm, the distance between the electrode and the tube surface is 3 mm, and the electrical insulating ring spacers are made of PFA and are set at vertical intervals of 250 mm. For determining the heat transfer enhancement of the electrodes, measurements of the evaporation heat transfer coefficients of the smooth tube were done before these prototype electrodes were installed.

The falling film evaporation heat transfer is determined by the falling film state, not by the heat flux, and is evaluated by the Nu^*-Re_f^* correlation. Re_f^* is calculated from the mean falling flow rate along the tube that is calculated from the amount of nonevaporating HCFC123 and the amount of HCFC123 supplied. The evaporation heat transfer coefficient of the smooth tube at $q'' = 10^4$ W/m^2 is defined by the Nu^*-Re_f^* correlation as follows:

$$Re_f^* > 2400,\ Nu^* = 0.0039 \pm 1.36 \times 10^{-4}\, Re_f^{*0.41} Pr^{0.65}. \quad (8)$$

The exponent of Re_f^* is about the same value as used in the Chun-Seban correlation, whereas the exponent of Pr is exactly the same value as used in the Chun-Seban correlation. However, at $q'' = 2 \times 10^4$ W/m^2 and under low flow rate, Nu^* became a little higher than at $q'' = 10^4$ W/m^2 because flow boiling generates and promotes heat transfer in spite of forming dry patches at low flow rates. In these experiments the amount of the supplied liquid compared with that of evaporated liquid was about 2 ~ 6 times.

Figure 6 shows the results of two prototype electrodes. The results of the helical wire electrode and the lattice electrode in this figure are for a 30 deg helix angle and 32 wires, which causes the largest heat transfer enhancement among similar types of electrodes. The solid line in Fig. 6 denotes the empirical formulas of the smooth tube of Chun-Seban, Wilke, and the fluted tube of Rothfus and Newman. The fluted tube is an enhanced tube for falling film evaporation. The dotted line denotes the experimental results of the smooth tube given by Eq. (8).

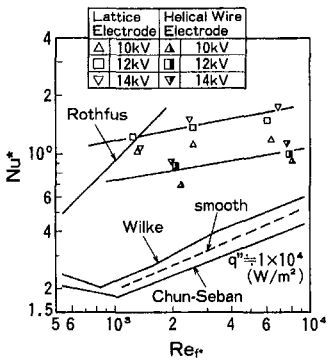

Fig. 6 The evaporation heat transfer coefficient with prototype electrodes

As the applied voltage of the helical wire electrode increased, the falling liquid film began to be extracted at the wire electrode at 6 kV (E = 2 kV/mm) and the falling liquid film on the surface area between helical wires became thin, enhancing the evaporation heat transfer. At more than 14 kV (E = 4.7 kV/mm), however, dry patch formation appeared on the tube surface area between helical wires and the evaporation heat transfer decreased. A helical wire electrode was manufactured to enhance the evaporation heat transfer by the extraction phenomena through the dielectrophoretic force. But the film thickness was not uniform around the tube because the leak liquid flow rate from the electrode was not equal around the periphery. Therefore, the maximum enhancement of the evaporation heat transfer with the helical wire electrode occurred at V = 12 kV and was about three times higher compared with that for a smooth tube.

For the lattice electrode the falling liquid film also began to be extracted at about 6 kV and all of the falling liquid flow was retained between the lattice electrode and the tube surface. As the voltage increased the falling liquid film was disturbed and pseudo-dropwise formation occurred. At more than 12 ~ 14 kV, dry patches appeared on the tube surface in the gap between the thin wires. At $Re_f^* = 10^3$ the applied voltage which caused the maximum evaporation heat transfer was at 12 kV, and at $Re_f^* > 2 \times 10^3$, the voltage causing maximum heat transfer was 14 kV.

The maximum enhancement ratio of the evaporation heat transfer with the lattice electrode was 4.5 times compared with the smooth tube, and was five times using the Chun-Seban correlation.

Practical Punched Electrodes for Falling Film Evaporators

Electrodes of EHD heat exchangers must prevent the electric discharge, therefore, minute slivers on the electrode must be avoided, and electrode warping must also be prevented. To effectively enhance heat transfer, the distance between the electrode and tube surface must be kept constant. But it is also important to be able to manufacture the electrode easily and economically. Therefore, several cylindrical electrodes made from rolled plates with punched slits were evaluated for the falling film evaporator. Three kinds of electrodes were manufactured and tested with this apparatus.

Figure 7 shows the details of three kinds of practical punched-out electrodes. They all had slits 2 mm wide and 30 mm long. The slits did not warp or generate splinters, and the distance between the electrode and the tube surface was 3.05 mm, the same as the prototype lattice electrode. Since these electrodes were installed around the tube, the evaporating vapor passed through these slits of the electrodes. The total area of the electrode's slits was half of the area of the tube surface, and the velocity of the vapor passing through these slits was 0.01 ~ 0.02 m/s for $q'' = 1 \times 10^4 \sim 2 \times 10^4$ W/m^2. The pressure drop was negligible.

Electrode I was similar to the prototype lattice electrode. Electrode II was similar to a shape that combines the prototype helical wire electrode with the lattice electrode. Electrode III was an improvement of Electrode I, whose slits were offset in the horizontal direction.

Electrodes II and III were designed to prevent dry patch formation. With Electrode II the liquid can be supplied to the periphery of the tube, and can prevent discrete rivulets (circumferential partial flow). With Electrode III the liquid can be supplied to the tube surface facing the small stick-shaped slits. The upper liquid pole between the vertical thin wire and the tube surface flows down to the lower surface facing the slits.

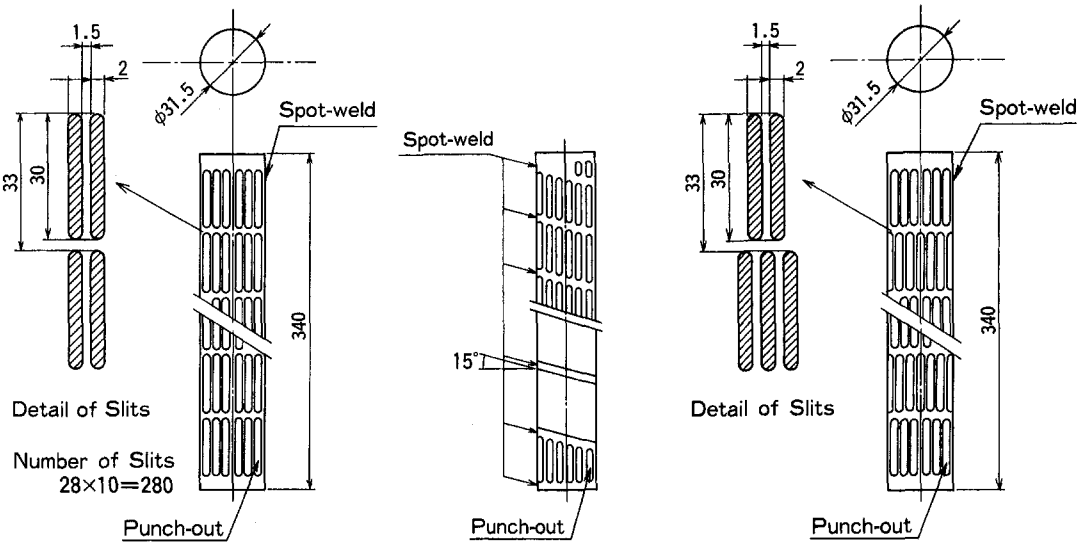

Fig. 7 Practical punched electrodes

We measured the heat transfer enhancement for $2000 < \mathrm{Re}_f^* < 8000$, $0 < V < 18$ kV, and $1 \times 10^4 < q'' < 2 \times 10^4$. Figure 8 shows the enhancement ratio compared with the smooth tube versus the applied voltage of each electrode. We found that the evaporation heat transfer of each electrode increases with increasing V, and there is an optimum voltage for each type of electrode that maximizes the enhancement ratio. These optimum voltages tend to increase with increasing Re_f^*. The cause is that dry patch formation was prevented at high Re_f^* because high flow rates generate thick films. The optimum voltage, V^*, of Electrode II was a function of Re_f^*, that is, $12 < V^* < 14$ kV at $\mathrm{Re}_f^* = 2000$, $12 < V^* < 16$ kV at $\mathrm{Re}_f^* = 4000$, and $14 < V^* < 16$ kV at $\mathrm{Re}_f^* = 6000$. For Electrode I at $\mathrm{Re}_f^* < 3000$, $10 < V^* < 16$ kV. For Electrode III $V^* \approx 16$ kV for $2000 < \mathrm{Re}_f^* < 6000$, and the evaporation heat transfer coefficient was also higher than for the other electrodes in the range of $12 < V < 14$ kV.

Electrode III achieved the maximum evaporation heat transfer. This could be because two rows of offset slits provided liquid continuously to the entire circumference of the tube. As the film falls down the tube, evaporation causes the tube surface to become dry. With the offset slits transverse waves or liquid poles branched off and merged along the electrode, and some leakage flowed down the tube surface in line with the slits. In this way, liquid was continuously supplied to the entire circumference of the tube. With Electrode I there are vertical strips that are not in direct line with the slits, and these strips tend to become dry.

The maximum evaporation heat transfer is expressed by $\mathrm{Nu}_{\max}^*$. The maximum evaporation heat transfer versus falling flow rate, $\mathrm{Nu}_{\max}^*$-Re_f^* of each electrode is shown in Fig. 9. In this figure, the solid lines correspond to the former empirical formulas, which were reported by Chun and Seban (1971), Wilke (1962), and Rothfus and Newman (1977). The dotted line represents the experimental results using the smooth tube (Eq. (8)). All heat transfer data was obtained at $q'' = 1 \times 10^4$ W/m^2. Every maximum evaporation heat transfer was changed by $\mathrm{Re}_f^{*0.4}$ proportionally.

Electrodes I and II achieved about the same performance. The evaporation heat transfer coefficient of Electrode I was lower than that of Electrode II at $\mathrm{Re}_f^* < 3000$ and in the range $10 < V < 16$ kV, the heat transfer coefficient of Electrode I was nearly constant. The reason for the improved performance of Electrode II might be that the helical parts of Electrode II can supply the liquid on the periphery of the tube better than Electrode I.

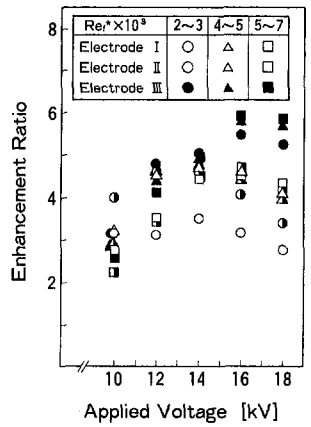

Fig. 8 The evaporation heat transfer coefficient versus applied voltage with practical punched electrodes

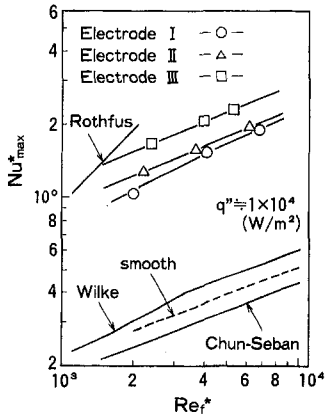

Fig. 9 The evaporation heat transfer coefficient versus film Reynolds with practical punched electrodes

The heat transfer enhancement of Electrodes I and II was about 4.5. Electrode III yielded heat transfer enhancement of about six.

Figure 10 shows the evaporation heat transfer ratio of Electrode III between $1 \times 10^4 < q'' < 2 \times 10^4$ W/m^2. For $V =$ 10 kV, the evaporation heat transfer at $q'' = 2 \times 10^4$ W/m^2 is higher than that at $q'' = 1 \times 10^4$ W/m^2. The cause could be due to film boiling because the smooth tube at $q'' = 2 \times 10^4$ W/m^2 causes film boiling. Ogata and Yabe (1993) reported that HCFC123 boils easily under applied electric fields. When electric fields are applied to boiling films, whether or not boiling is enhanced, depends on the electrical properties of the fluid. There are electroconvection effects on fluids and effects from agitation on the superheated surface by the boiling bubbles. The former effect suppresses boiling, but the latter promotes boiling. The bubble's agitating effect is relevant to the relaxation time of electric charges and the bubble detachment period. If the former time factor is equal to or shorter than the latter time factor, the bubble's agitation generates and promotes boiling. This occurs with HCFC123.

At $V > 12$ kV, the evaporation heat transfer at $q'' = 2 \times 10^4$ W/m^2 was lower than at $q'' = 1 \times 10^4$ W/m^2. This tendency was a strong function of voltage, and the ratio was about half at 16 kV. The cause could be that the bubble growth on tube surface should induce dry patch formation below the bubble in the thin film, and then evaporation heat transfer should deteriorate. But at 10 kV and $4000 < \mathrm{Re}_f^* < 6000$, the evaporation heat transfer at $q'' = 2 \times 10^4$ W/m^2 was higher than that of 1×10^4 W/m^2, because more falling flow rate suppressed the above dry patch formation. The electric power consumption of all electrodes was less than 0.1 percent of the amount of heat exchanged in the falling film evaporator at the voltage achieving the maximum evaporation heat transfer.

Long-Term Effect of Electrohydrodynamics on System Durability

EHD heat exchangers have a high voltage electrode inside that causes low-level electric current flow inside the heat exchanger and across the dielectric working fluid and the tube surface. There is therefore the possibility of corrosion, and EHD heat exchangers must be tested for long term effects. Industrial heat exchangers must be able to operate continuously for at least 9000 hours, because maintenance is generally conducted once a year. To test the system durability, we operated both EHD heat exchangers for about 4 hours per day, Monday through Friday, for one year, for a total of 1000 hours. (Note that during that one year the electrodes were replaced three times.) After 1000 hours of operation the EHD heat exchangers were dismantled and checked thoroughly to determine the effect

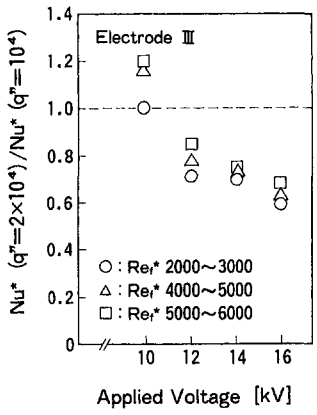

Fig. 10 The evaporation heat transfer coefficient ratio to heat flux with practical punched Electrode III

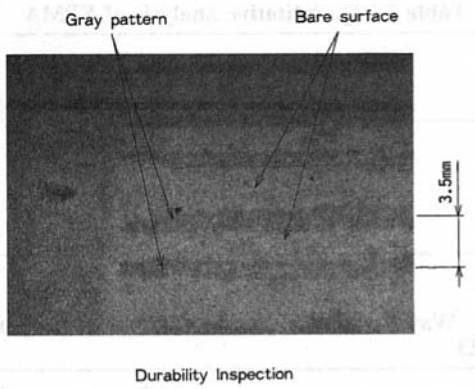

Fig. 11 Pattern on an evaporation tube

of long-term operation. The electrode of the evaporator was replaced, the electrodes were tested, and the duration was about 350 hours between each change. Tubes of the evaporator and condenser, the insulating spacers, and HCFC123 were not changed.

The heat transfer medium, HCFC123, and sections of the heat transfer tubes, electrodes, vessel walls, and electric insulators, were examined. First, the metallic pieces and insulator were checked for corrosion or stain. Then, we inspected each piece by photographing and checking the color of the surface by an optical microscope, checking the electric resistance of the insulator spacer, and checking for treeing breakdown of the surface and the cutting surface of the insulator. If a piece had indications of corrosion or stain, we evaluated it further by qualitatively and quantitatively analyzing the piece by Electron Probe Microanalyzer (EPMA).

This examination revealed that several tube surfaces had patterns similar to the electrode shape. The portion of gray and black pattern were selected after observing the whole tube, and the portion was selected at around the upper part of tube where the gray and black pattern was the clearest. Figure 11 shows the lustrous gray patterns found on the evaporation tube. These patterns were observed as a thin film adhering to the entire tube surface. Spot analysis of this film (using EPMA) indicated aluminum (Al), silicon (Si), and oxygen (O) components. These might be components of the molecular sieves (Al_2O, SiO_2) that dehydrate HCFC123. Small amounts of Cl^- and F^- were also detected, which might be components of HCFC123 and the insulation material. Figure 12 shows the black patterns found on the condensation tube. Such patterns were found near

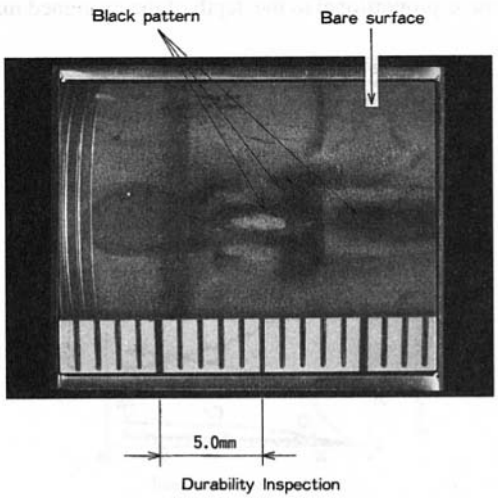

Fig. 12 Pattern on a condensation tube

Table 3 Quantitative analysis of EPMA

Chemical element	Lustrous gray pattern	Black pattern	Clean surface (percent)
C	5.8	14.2	0.8
Cr	14.7	16.5	19.2
Ni	5.6	6.9	8.2
Fe	52.8	57.7	68.6
O	12.3	1.8	<0.5

Table 4 Water concentration and electrical properties of HCFC123

Item/Sample	Fresh HCFC123	Used HCFC123
Water concentration (ppm)	91.3	28.7
Dielectric permittivity (F/m)	4.2×10^{-11}	4.1×10^{-11}
Electric conductivity (l/Ωm)	4.6×10^{-9}	5.9×10^{-10}
Relaxation time for an electric charge (s)	0.0092	0.0696

the surface of the abacus insulator, and a small amount of black powder was found adhering to some of the abacus insulators. Table 3 shows the results of an EPMA analysis of these patterns. Large amounts of carbon (C) were detected compared with the original tube surface. These patterns were probably from the breakdown of HCFC123 due to the high electric field and from electric discharge generated by the higher voltage, over 20 kV. In these black patterns a small amount of oxygen was also detected that might originate from the H_2O and air dissolved in HCFC123. The water solubility for HCFC123 is 662 ppm, which is higher than that for the other CFCs. In this case it is necessary to dehydrate the CFC. Table 4 shows the water concentration and electrical properties for this "used" HCFC123 (which passed through the molecular sieve) and "fresh" HCFC123. The electrical properties, as an insulator, were not deteriorated at all because of low water concentration. Its insulating performance was improved a little because the F^- of the insulating spacer material dissolved a little.

Similar patterns were observed on tubes of actual 50 kW EHD condensers with either CFC113, CFC114, or C_6F_{14} as the working fluid. These patterns were extremely thin, so they could not be analyzed with EPMA. Therefore, we used Auger electron spectroscopy. Figure 3 shows the resulting depth profile of a tube surface. The elements were determined from the Auger electron spectra, and the relative concentration of the surface materials are shown as a function of sputtering time. The sputtering time is proportional to the depth of the examined material

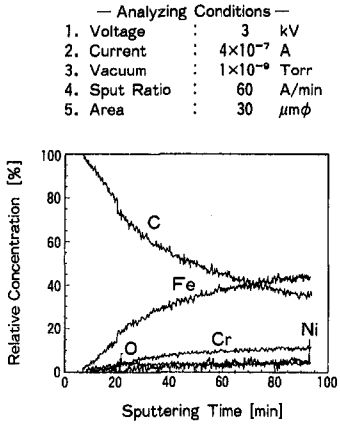

Fig. 13 Depth profile of tube surface with Auger electron spectroscopy

Table 5 Quantitative analysis of the insulator

Sample	Volume resistivity (Ωm)	F^- elution rate (μg)
Used PFA Insulator	$>1 \times 10^{17}$	6.2
New PFA Insulator	1×10^{16}	3.2

and indicates that the thickness of the adhered material (C) was on the order of microns because the amount of C decreased relatively after about 48 μm. The concentration of the deposits was less than 10 ppm, and, therefore, should not hinder the operation of the EHD heat exchanger.

For the insulation materials treeing break down marks on and in the PFA were not found using optic microscopy. Table 5 lists the analysis for these materials and shows that the electric resistance increased (measured using electric conductivity). From ion chromatography we found that the concentration of F^- ions near the surface of the insulator came from the HCFC123, which is better than the original condition.

The result of this analysis indicates that EHD heat exchangers can be used in industrial applications.

Conclusions

The heat transfer characteristics of EHD falling film evaporators and condensers were experimentally investigated using HCFC123 as the working fluid, which will be an alternative to conventional CFC refrigerants in the future. Furthermore, tests of EHD heat exchangers were conducted to determine their suitability for long-term industrial applications. From this study we conclude the following:

- EHD enhancement effects for condensation heat transfer also apply to CFC alternative working fluids, such as HCFC123.
- EHD applied to vertical falling-film evaporation is effective for enhancing heat transfer by retaining the liquid, disturbing the liquid film flow, and thinning the liquid film.
- In EHD falling-film evaporation there is an optimum applied voltage at which the evaporation heat transfer coefficients are maximized. Above this level dry patches form on the tube surface, which then decreases the heat transfer efficiency.
- Evaporation heat transfer is enhanced six-fold over that for smooth tubes by using electrodes made of punched-out plates of vertically arrayed offset fins.
- Small amounts of carbon, aluminum, and silicon adhere to the surface of the heat transfer tube after 1000 hours of operation, but are low enough so that these types of EHD heat exchangers are suitable for industrial applications.

Acknowledgments

This work was an R & D program for the Technology Research Association of Super Heat Pump Energy Accumulation System, entrusted by the New Energy and Industrial Development Organization (NEDO).

We express our sincere gratitude to Mr. S. Nonaka and Dr. Y. Watanabe of Toshiba Co., Ltd. for their assistance, advice, and useful discussions.

References

Allen, P. H. G., and Cooper, P., 1987, "The Potential of Electrically Enhanced Evaporators," *Proceeding of 3rd Int. Symposium on the Large-Scale Application of Heat Pump*, pp. 221–229.

Brumfield, L. K., and Theofanous, T. G., 1976, "On the Prediction of Heat Transfer Across Turbulent Liquid Film," ASME JOURNAL OF HEAT TRANSFER, Vol. 98, 496–502.

Cheng, J. K., and Chaddock, J. B., 1985, "Effect of an Electric Field on Bubble Growth Rate," *Int. Comm. Heat Mass Transfer*, Vol. 12, pp. 259–268.

Chun, K. R., and Seban, R. A., 1971, "Heat Transfer to Evaporating Liquids Film," *Int. J. Heat Mass Transfer,* Vol. 93, pp. 391–396.

Didkovsky, B., and Bologa, M. K., 1982, "Vapor Film Condensation Heat Transfer and Hydrodynamics Under the Influence of an Electric Field," *Int. J. Heat Mass Transfer,* Vol. 24, No. 5, pp. 811–819.

Kirkbride, C. G., 1934, "Heat Transfer by Condensing Vapor on Vertical Tubes," *Ind. Eng. Chem.,* Vol. 26, pp. 425–428.

Mudawwar, I. A., and El-Masri, M. A., 1986, "Momentum and Heat Transfer Across Freely Falling Turbulent Liquid Film," *Int. J. Multiphase Flow,* Vol. 12, No. 5, pp. 771–790.

Nusselt, W., 1916, "Die Oberflachenkondensation des Wasserdampfes," *VDI-Z,* Vol. 60, pp. 541–546 and pp. 569–575.

Ogata, J., and Yabe, A., 1991, "Augmentation of Nucleate Boiling Heat Transfer by Applying Electric Fields (EHD Behavior of Boiling Bubbles)," *Proc. 3rd ASME/JSME Thermal Engineering Joint Conf.,* Vol. 3, pp. 41–46.

Ogata, J., and Yabe, A., 1993, "Augmentation of Boiling Heat Transfer Utilizing EHD Phenomena," *Int. J. of Heat Transfer,* Vol. 36, No. 3, pp. 775–791.

Ogata, J., Iwafuji, Y., Shimada, Y., Yamazaki, T., 1992 "Boiling Heat Transfer Enhancement in Tube-Bundle Evaporators Utilizing Electric Field Effects," *ASHRAE Transaction,* Vol. 98, Part 2, pp. 435–444.

Ohadi, M. M., and Paper, R. A., Faani M. A., and Radermacher, R., 1992, "EHD Enhancement of Shell-Side Boiling Heat Transfer Coefficients of R-123/Oil Mixture," *ASHRAE Transaction,* Vol. 98, Part 2, pp. 427–434.

Pachosa, D. M., and Chung, J. N., 1993, "Dielectrophoresis-Driven Nucleate Boiling in a Simulated Microgravity Environment," ASME JOURNAL OF HEAT TRANSFER, Vol. 115, pp. 495–498.

Rothfus, R. R., and Neuman, C. P., 1977, "The OTEC Program at Carnegie-Mellon Univ., Heat Transfer Research and Power Cycle Transient Modeling," *Proceedings of 4th OTEC Conf.,* pp. VI-55–VI-70.

Shmerler, J. A., and Mudawwar, I. A., 1988, "Local Evaporative Heat Transfer Coefficient in Turbulent Free-Falling Liquid Films," *Int. J. Heat Mass Transfer,* Vol. 31, No. 4, pp. 731–742.

Singh, A., and Ohadi, M. M., 1995, "EHD-Ehanced Boiling of R-123 Over Commercially Available Enhanced Tubes," ASME JOURNAL OF HEAT TRANSFER, Vol. 117, pp. 1170–1073.

Sunada, K., Yabe, A., Taketani, T., and Yoshizawa, Y., 1991, "Experimental Study of EHD Pseudo-Dropwise Condensation," *Proceedings of 3rd ASME/JSME Thermal Engineering Joint Conf.,* Vol. 3, pp. 47–53.

Uehara, H., Kusuda, H., Nakaoka, T., and Yamada, M., 1983, "Wavy Film Flow Condensation of Flat Plate," (in Japanese), *Trans. JSME,* Vol. 49, No. 39, pp. 666–674.

Wawzyniak, M., and Seyed-Yagoobi, J., 1996, "Experimental Study of Electrohydrodynamically Augmented Condensation Heat Transfer on a Smooth and an Enhanced Tube," ASME JOURNAL OF HEAT TRANSFER, Vol. 118, pp. 499–502.

Wilke, W., 1962, "Heat Transfer to Falling Liquid Film," *V.D.I. Forshungsheft 490,* B-28.

Yabe, A., 1991, "Active Heat Transfer Enhancement by Applying Electric Fields," *Proceedings of 3rd ASME/JSME Thermal Engineering Joint Conf.,* Vol. 3, pp. xv–xxi.

Yabe, A., Kikuchi, K., Taketani, T., Mori, Y., and Hijikata, K., 1987, "Augmentation of Condensation Heat Transfer Around Vertical Cooled Tubes Provided With Helical wire Electrodes by Applying Non-uniform Electric Fields," *Int. Heat Transfer Science and Technology,* pp. 812–819.

Yabe, A., Kikuchi, K., Taketani, T., Mori, Y., and Maki, H., 1986, "Enhancement of Condensation Heat Transfer by Applying Electro-Hydro-Dynamical Pseudo-Dropwise Condensation," *Proceedings of 8th Int. Heat Transfer Conf.,* Vol. 6, pp. 2957–2967.

Yamashita, K., Kumagai, M., Watanabe, Y., Yabe, A., Taketani, T., and Kikuchi, K., 1989, "Heat Transfer Characteristics of EHD Condenser," (in Japanese), *Trans. JSME,* Ser. B, Vol. 5, No. 501, pp. 510–516.

Yamashita, K., Kumagai, M., Sekita, S., Yabe, A., Takatani, T., and Kikuchi, K., 1991, "Heat Transfer Characteristics on an EHD Condenser," *Proceedings of 3rd ASME/JSME Thermal Engineering Joint Conf.,* Vol. 3, pp. 61–67.

An Experimental Investigation of Convective Heat Transfer From Wire-On-Tube Heat Exchangers

J. L. Hoke
Graduate Research Assistant.

A. M. Clausing
Professor and Associate Head.
clausing@uiuc.edu

T. D. Swofford
Graduate Research Assistant.

Department of Mechanical and Industrial Engineering,
University of Illinois at Urbana-Champaign,
1206 W. Green St.
Urbana, IL 61801

An experimental investigation of the air-side convective heat transfer from wire-on-tube heat exchangers is described. The study is motivated by the desire to predict the performance, in a forced flow, of the steel wire-on-tube condensers used in most refrigerators. Previous investigations of wire-on-tube heat exchangers in a forced flow have not been reported in the literature. The many geometrical parameters (wire diameter, tube diameter, wire pitch, tube pitch, etc.), the complex conductive paths in the heat exchanger, and the importance of buoyant forces in a portion of the velocity regime of interest make the study a formidable one. A key to the successful correlation of the experimental results is a definition of the convective heat transfer coefficient, h_w, that accounts for the temperature gradients in the wires as well as the vast difference in the two key characteristic lengths—the tube and wire diameters. Although this definition results in the need to solve a transcendental equation in order to obtain h_w from the experimental data, the use of the resulting empirical correlation is straightforward. The complex influence of the mixed convection regime on the heat transfer from wire-on-tube heat exchangers is shown, as well as the effects of air velocity and the angle of attack. The study covers a velocity range of 0 to 2 m/s (the Reynolds number based on wire diameter extends to 200) and angles of attack varying from 0 deg (horizontal coils) to ±90 deg. Heat transfer data from seven different wire-on-tube heat exchangers are correlated so that 95 percent of the data below a Richardson number of 0.004, based on the wire diameter, lie within ±16.7 percent of the proposed correlation.

Introduction

A wire-on-tube heat exchanger consists of solid steel wires that serve as extended surfaces and a single steel tube that carries the fluid. The tube is bent into a serpentine of parallel passes, and the wires are spot welded onto diametrically opposite sides of the tubes, as is illustrated in Fig. 1. Since wire-on-tube heat exchangers are easily manufactured, rugged, and relatively inexpensive, they are used extensively by refrigerator manufacturers as condensers. In this instance, a refrigerant condenses on the inside of the tube, and heat flows from the outer surfaces of the wires and tubes to the surrounding air, predominantly by convection.

One of the largest resistances to the heat flow from wire-on-tube condensers is the air-side resistance. This resistance accounts for as much as 95 percent of the total resistance between the refrigerant and the air when the refrigerant is in the two phase region (Admiraal and Bullard, 1993). In spite of this importance, only studies of the thermal performance of wire-on-tube heat exchangers that are operating under free convection conditions (the industry refers to these condensers as "static" condensers) have been reported. Such studies were performed by Carley (1956), Collicott et al. (1963), Cyphers et al. (1959), Howard (1956), Papanek (1958), Rudy (1956), Witzell and Fontaine (1957a, b), and Witzell et al. (1959). This is surprising since the vast majority of refrigerators manufactured in the United States use condensers that are cooled by forced flow.

The lack of published studies of wire-on-tube heat exchangers in the open literature is probably a consequence of the complexity of the problem. If the dimensions associated with the tube bend region, the gaps in the wire matrix (due to the manufacturing techniques), the contact spot between the wire and tube, etc., are ignored, a single layer wire-on-tube heat exchanger has six characteristic lengths: the wire diameter D_w, the tube diameter D_t, the wire spacing S_w, the tube spacing S_t, the overall wire length L_w, and the length of a tube pass L_t. The problem is further complicated by: (i) the overall heat exchanger geometry, that is, the single coil depicted in Fig. 1 is usually bent into a multilayer stack (these layers may or may not lie in parallel planes); and (ii) the complex, ill defined, nonuniform flow over the condenser that includes, in some cases, a recirculating component. Only unpublished, proprietary studies of wire-on-tube condensers in a forced flow field appear to have been performed. Such studies typically concentrate on the overall performance of the refrigerator and do little to delineate the important parameters and mechanisms. Hence, the results of such studies do not enable the optimization of wire-on-tube heat exchangers.

In order to obtain experimental results that are of general utility and to reduce the investigation into a tractable one, the following simplifications are used:

1. All wire-on-tube heat exchangers are studied in a wind tunnel with a uniform, horizontal flow through a 0.30 m high by 0.91 m wide by 0.76 m long test section.
2. Only single layer, wire-on-tube heat exchangers (see Fig. 1) are studied.
3. Water is employed as the "refrigerant", the heated fluid flowing inside the tube. The use of this fluid: (i) greatly simplifies the instrumentation and installation of the heat exchangers; (ii) results in a relatively small thermal resistance on the inside of the tube that can be accurately estimated; and (iii) enables an accurate experimental determination of the overall rate of heat transfer.

Extensive tests are performed to gain insight into the air-side heat transfer characteristics and the important mechanisms. The

Contributed by the Heat Transfer Division for publication in the JOURNAL OF HEAT TRANSFER. Manuscript received by the Heat Transfer Division March 19, 1996; revision received December 5, 1996; Keywords: Finned Surfaces, Forced Convection, Heat Exchangers. Associate Technical Editor: T. Rabas.

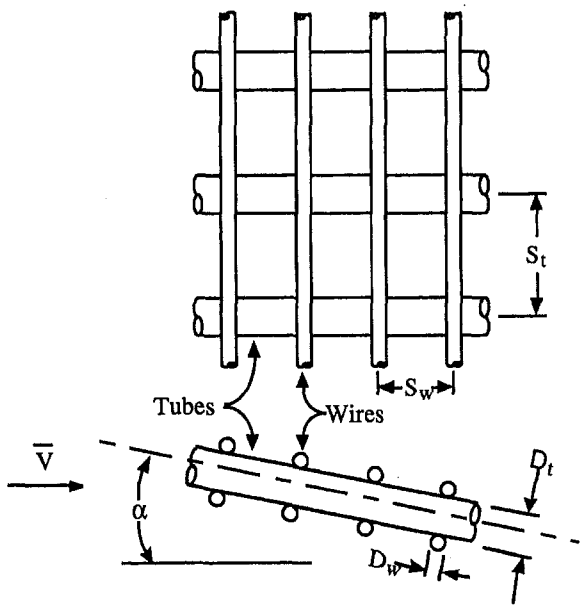

Fig. 1 Schematic diagram of heat exchanger

free stream velocities investigated range from zero (free convection) to two m/s (the Reynolds number based on wire diameter extends to 200). The angle of attack, α, (defined the same way as for an airfoil—α is positive if the leading edge lies above the trailing edge) is varied between −90 deg and 90 deg, see Fig. 1. Two coil yaw angles are investigated: flow perpendicular to the wires, denoted by $\psi = 0$, and flow perpendicular to the tubes, $\psi = \pi/2$. Relevant dimensions of all coils are listed in Table 1. Note that Coil 7 is a wireless coil.

Analysis

Two important and somewhat unique characteristics of wire-on-tube heat exchangers are:

1 The presence of an element (the wires) that can be highly nonisothermal; hence, the fin efficiency of the wires must be taken into account in the definition of h. If this is not done (see, e.g., Collicott et al., 1963), the resulting convective heat transfer coefficient, h, is strongly dependent on the tube spacing (see Figs. 5 and 6 of this reference).
2 The presence of two elements (the wires and tubes) that are both making significant contributions to the total heat transfer. It is unwise to use the same average h for both of these surfaces—as is done in the analysis of plate-fin and circular-fin heat exchangers—because h_w is approximately twice h_t for the tube and wire diameters of interest.

Table 1 Heat exchanger dimensions

Variable	Coil 1	Coil 2	Coil 3	Coil 4	Coil 5	Coil 6	Coil 7	Coil 8
D_w [mm]	1.22	1.24	1.22	1.62	1.21	1.35	N/A	1.58
S_w [mm]	5.34	5.22	5.39	4.57	4.56	5.68	N/A	6.81
N_w	176	168	148	168	166	64	0	150
L_w [mm]	406	446	610	572	383	279	N/A	559
D_t [mm]	4.80	4.73	4.80	4.92	6.21	4.75	4.74	4.76
$D_{t,i}$ [mm]	3.18	3.18	3.18	3.57	5.16	3.18	3.05	3.56
S_t [mm]	25.4	50.8	25.4	31.8	31.8	25.4	31.8	50.8
L_t [mm]	660	679	591	578	575	256	629	483
N_t	16	9	24	18	12	11	10	11
δ_p [mm]	0.06	0.01	0.06	0.01	0.01	0.01	0	0.02
A_w [m^2]	0.274	0.292	0.345	0.489	0.241	0.076	N/A	0.415
A_t [m^2]	0.168	0.100	0.228	0.174	0.145	0.048	0.100	0.091
% A_w	62	74	60	74	62	61	N/A	82

Note: $A_w = \pi * D_w * L_w * N_w$; $A_t = \pi * D_t * L_t * N_t + \pi * D_t * (\pi * S_t/2) * (N_t - 1)$

In correlating the experimental data from wire-on-tube heat exchangers, our first instinct was to derive separate empirical correlations for the wires and the tubes. However, this approach is not viable because of the difficulty of experimentally separating the rate of convective heat transfer, q, into its two components, q_w and q_t.

To find a suitable approach that accounts for the difference in the heat transfer from the two elements and reduces the dependence of the resulting Nusselt number, Nu, on the tube spacing (the fin length), consider the calculation of the rate of heat transfer, q, if h_t and h_w are known. If one assumes that the external tube temperature, T_t, in the region of interest is equal to the temperature of the spot feeding the wire, the rate of heat flow is given by:

$$q = (A_t h_t + \eta A_w h_w)(T_t - T_a) \tag{1}$$

where A_t and A_w are the tube and wire surface areas, respectively; T_a is the air temperature, and η is the fin efficiency of the wire. Assuming h_w is constant along the wire, the fin efficiency of this extended surface can be shown to be

$$\eta \equiv \frac{q_w}{A_w h_w (T_t - T_a)} = \frac{\tanh m}{m} \tag{2}$$

where

$$m^2 = \frac{h_w S_t^2}{k_w D_w}. \tag{3}$$

The dimensionless fin parameter, m, indicates the importance of the temperature gradients in the wires. m^2 is the ratio of

Nomenclature

A = area, m^2
c_p = constant pressure specific heat, J/kg-K
D = diameter, m
h = heat transfer coefficient, W/m^2-K
k = thermal conductivity, W/m-K
L = length, m
$\dot{m}$ = mass flow rate, kg/s
N = number
q = heat flow rate, W
S = centerline-to-centerline spacing, m
T = temperature, K
V = velocity, m/s

Dimensionless Groups

Gr = Grashof Number, $g\beta(T_h - T_c)D^3/\nu^2$
m = fin parameter, $[hS_t^2/kD_w]^{1/2}$
Nu = Nusselt number, hD/k
Ra = Rayleigh number, Gr · Pr
Ri = Richardson number Gr/Re^2
Re = Reynolds number, VD/ν
Pr = Prandtl number, $\mu c_p/k$

Greek Symbols

α = angle of attack, deg
δ = thickness, m
η = fin efficiency, defined by Eq. (2)
ψ = yaw ($\psi = 0$: flow ⊥ to wires, $\psi = \pi/2$: flow ⊥ to tubes)

Subscripts

a = air
i = internal
F = forced convection
N = natural convection
p = paint
r = refrigerant (water)
t = tube
w = wire

Superscripts

* = dimensionless quantity

the internal conductive resistance of the wire to the external convective resistance between the wire and the surrounding air.

Equation (1) can be rearranged to give

$$h_w = \frac{q}{\left(A_t \frac{h_t}{h_w} + \eta A_w\right)(T_t - T_a)}. \quad (4)$$

To reduce Eq. (4) to a useful definition, h_t/h_w needs to be eliminated. It appears possible to do this with sufficient accuracy because:

1 The second term in the denominator of Eq. (4) typically is much larger than the first term. Specifically, the wire area accounts for 60 to 80 percent of the total area in typical wire-on-tube refrigerator condensers in use today. The convective heat transfer coefficients over the wires are generally expected to be much larger than those over the tubes, and most current condenser designs appear to be operating at values of η greater than 0.85.

2 the limits of natural convection from a single horizontal cylinder and forced convection, with flow normal to a single cylinder, both reveal the same dependency on D. Specifically, in the regimes of interest ($10^{-2} < \text{Ra} < 10^2$; $40 < \text{Re} < 4000$), published correlations for both of these limits show that $h \propto D^{-n}$ where n is approximately equal to one half. Thus, if the same correlation is applicable to both surfaces, one obtains

$$\frac{h_t}{h_w} \cong (D_t^*)^{-0.5} \quad (5)$$

where $D_t^* \equiv D_t/D_w$. If Approximation (5) is used in Eq. (4), the definition of h_w used in this study results

$$h_w \equiv \frac{q}{\left(\frac{A_t}{\sqrt{D_t^*}} + \eta A_w\right)(T_t - T_a)}. \quad (6)$$

In assessing the utility of Eq. (6), the following points should be noted: (i) In some regimes, the approximation represented by Eq. (5) is expected to be very accurate. On the other hand, in regimes where Eq. (5) is a poor approximation, it should be remembered that no error has been made. Equation (6) is simply the definition of the convective heat transfer coefficient that is used in this experimental investigation. The ability to correlate the experimental results will speak for the usefulness of this definition; (ii) The tube and wire boundary layers interact extensively, and the geometrical relationship between these two elements determine the flow patterns; thus, h_w would generally be quite different than the corresponding h for flow over a single wire with an identical orientation with respect to the free stream flow. Furthermore, the heat transfer coefficient, h_w, is the average value of h for all of the wires in the coil; and (iii) The determination of h_w from Eq. (6) requires the solution of a transcendental equation since η is a function of h_w. An independent determination of η is not required.

Consider next the dimensionless variables that are to be used in the correlation of the experimental data. First, the characteristic length to be used in the definition of the dimensionless parameters needs to be chosen. Witzell and Fontaine (1957b) and Collicott et al. (1963) use an area weighted average of D_w and D_t. The importance of the wires and the form of the dimensionless fin parameter, m (see Eq. 8), lead us to conclude that D_w is a more meaningful characteristic length. The use of the characteristic length, D_w, also facilitates comparisons with single wire correlations since the Nusselt, Reynolds, Rayleigh, etc. numbers are all consistently defined.

If one assumes that the coil is described by the six geometrical parameters described in the introduction, a dimensional analysis gives

$$\text{Nu}_w \equiv \frac{h_w D_w}{k_a} = f(\text{Re}_w, \text{Ri}_w, \text{Pr}, \alpha, \psi, S_w^*, S_t^*, D_t^*, L_t^*, L_w^*, m). \quad (7)$$

For the low velocities of interest, buoyant forces are known to be of importance in some situations; hence, the Richardson number, $\text{Ri} \equiv \text{Gr}/\text{Re}^2$, is included.

Obviously, experimentally deriving Eq. (7) represents a formidable task. A relationship between 12 dimensionless groups needs to be determined. Therefore, consider the following simplifications:

1 Air is the fluid of interest in this investigation; thus, the influence of the Prandtl number, Pr, need not be resolved.

2 An examination of the expression for the fin efficiency and the fin parameter, m, in which

$$\eta = \frac{\tanh m}{m} \text{ where } m^2 = (S_t^*)^2 \,\text{Nu}_w\left(\frac{k_a}{k_w}\right) \quad (8)$$

reveals that m is not an additional, independent dimensionless variable for the case of interest—steel wires in air—because (k_a/k_w) is a constant.

3 The extent of the coil in the direction perpendicular to the velocity vector has minor influences for the wire and tube lengths of interest. Thus, it is prudent to correlate the following two cases separately: Case I, flow perpendicular to the wires ($\psi = 0$), and Case II, flow perpendicular to the tubes ($\psi = \pi/2$). Only these two values of ψ are studied.

With these three simplifications, Eq. (7) becomes[1]

$$\text{Nu}_w = f(\text{Re}_w, \text{Ri}_w, \alpha, S_w^*, S_t^*, D_t^*, L_t^*); \text{ Case I, } \psi = 0. \quad (9)$$

Thus, the task has been reduced to determining two functional relationships between eight dimensionless parameters.

Although the dimensionless parameters have been reduced from 12 to 8, additional parameters must be eliminated to make the task feasible. Consider first the role of the Richardson number. The results presented in this paper will show that the air-side performance of wire-on-tube heat exchangers is very poor in the mixed convection regime; therefore, it is illogical to operate heat exchangers in this regime. Thus, only the limiting Richardson number, at which our correlations become invalid, is determined in this investigation.

Consider next the influence of S_t^*. As is shown by Eq. (8), S_t^* has a strong influence on the fin efficiency and hence, on the temperature distribution in the wire and the air-side performance of the heat exchanger. Multiplying the wire area by η in the definition of h (see Eq. 6), removes the otherwise strong dependence of Nu_w on S_t^*—a a significant accomplishment. This comes at some expense since a transcendental equation needs to be solved in determining each experimental value of h_w. Unlike the parameter k_a/k_w (see Eq. 8), whose only influence on h_w comes from the indirect influence of η on the thermal boundary layers, S_t^* also influences the flow around and through the coil. However, the range of S_t^* that is of interest is small. The cost of steel wire per kg is much less than that of steel tubing; hence, small values of S_t result in relatively expensive

[1] For brevity, only the relationships for Case 1 will be given in the remainder of this section.

coils. A large tube spacing results in a fin efficiency that is too low. The experimental results show a small secondary influence of S_t^*; hence, this dimensionless group is eliminated from Eq. (9).

Of the three remaining dimensionless lengths, only S_w^* is retained. The parameter D_t^* is not included because the range of tube diameter of interest is small. Most condensers in use today are made with approximately 5 mm diameter tubes. Smaller tubes result in large pressure drops, and the inventory of refrigerant contained in larger diameter tubes is too great.

The influence of the length of typical refrigerator condensers in the direction of the air flow is also not investigated in this study because: (i) the length varies over a relatively small range that is keyed to the depth of the refrigerator, and (ii) tube bank studies and other studies led to the belief that h is a relatively weak function of this length. Hence, the associated dimension parameter, L_t^* or L_w^*, is eliminated from Eq. (9).

With these approximations, Eq. (9) reduces to a function of three dimensionless groups: Re_w, α, and S_w^*. The task is simplified further by assuming that the influence of S_w^* is independent of the influences of Re_w and α. Specifically, the functional form to be used is

$$\mathrm{Nu}_w = f(\mathrm{Re}_w, \alpha) \cdot g(S_w^*); \quad \text{Case I, } \psi = 0. \tag{10}$$

It should be noted that two sets of f and g need to be determined. One set is applicable to flow perpendicular to the wires ($\psi = 0$) and the other to flow perpendicular to the tubes ($\psi = \pi/2$).

Users of Correlation (10) must calculate the rate of heat transfer from the coil using the following equation:

$$q = h_w\left(\frac{A_t}{\sqrt{D_t^*}} + \eta A_w\right)(T_t - T_a). \tag{11}$$

Of course, η must be calculated using Eq. (8) before Eq. (11) can be evaluated. Once Correlation (10) is determined, the calculation of q is straightforward. This is in sharp contrast to the determination of h_w from the experimental measurements.

Unlike an ideal condenser, the temperature of the water flowing through the tube is not constant in this study; hence, the temperature difference in the definition of h_w, $(T_t - T_a)$, must be replaced by an appropriate mean temperature difference. For the conditions of this experimental study, the appropriate quantity is the modified log-mean temperature difference

$$\Delta T_{\mathrm{lm}} \equiv F \frac{(T_{t,\mathrm{in}} - T_a) - (T_{t,\mathrm{out}} - T_a)}{\ln\left[\dfrac{(T_{t,\mathrm{in}} - T_a)}{(T_{t,\mathrm{out}} - T_a)}\right]} \tag{12}$$

where T_a is defined as the temperature of the air entering the test section, and F is a correction factor, $0.5 \le F \le 1$, that shows the degree to which the mean temperature difference is less than the log-mean temperature difference for the counterflow configuration. An examination of the physics of the flow led to the conclusion that a constant air temperature is appropriate in the definition of ΔT_{lm}. Specifically: (i) at large angles of attack, the air entering all sections of the coil is at T_a; (ii) at small angles of attack and small velocities, buoyant forces cause an upward flow of air at T_a through the coil; and (iii) at higher velocities and small angles of attack, a thermal boundary layer envelopes the coil; however, like a flat plate, the ambient temperature at the edge of this boundary layer is T_a. In addition, the change in the water temperature was typically held to a small fraction of ΔT_{lm}. Thus, all heat exchangers are thermally small in our tests. Hence, the heat exchanger performance is independent of the specific configuration of the coil, and F in Eq. (12) is set equal to one for our test conditions.

Experimental Apparatus and Procedure

An induced flow wind tunnel was constructed in order to test the wire-on-tube heat exchangers in a well defined flow field. This tunnel has a test section that is 0.3 m high, 0.91 m wide, and 0.76 m long, a velocity range from 0.15 to 2.0 m/s, a turbulence intensity in the test section that is less than one percent, and a flow field that is uniform and steady to within 2.5 percent of the mean test section velocity. An electronically controlled bath supplies constant temperature hot water to the heat exchanger being studied. Schematic diagrams of the wind tunnel and the hot water supply system as well as additional details of the experimental facilities are given by Hoke et al. (1995).

Under steady-state conditions, the total heat lost by the coil is determined from an energy balance on the water stream

$$q = \dot{m} c_p (T_{r,\mathrm{in}} - T_{r,\mathrm{out}}). \tag{13}$$

The mass flow rate of the water during a test is measured by collecting the water exiting the coil over an accurately timed interval and weighing the output using an electronic balance. The uncertainty in this measurement is ±0.5 percent. Mixing cups at the inlet and outlet of the coil are used to accurately determine $T_{r,\mathrm{in}}$ and $T_{r,\mathrm{out}}$. Each mixing cup contains two calibrated copper-constantan thermocouples. These thermocouples have 1 mm diameter stainless steel grounded sheaths that are inserted into the mixing cup with a 25 mm long wetted area. This long wetted area eliminates conduction errors. The uncertainty in the measurement of the difference between the inlet and outlet temperatures is ±0.08 K.

In order to determine the air-side thermal resistance, the complex heat flow in the tube must be analyzed. As a consequence of the importance of the wires, the bulk of the heat flow from the water is not a radial flow; rather, it must flow along the tube wall and is then constricted to the contact spot before it flows into the wire. This two-dimensional constrictive heat flow is analyzed using finite difference techniques. For the conditions of interest, we found that the additional uncertainty introduced by assuming a purely radial flow is relatively small; hence, this simplification is used in the data reduction. If all the heat flow is radial, the thermal resistance of the tube and the paint on the tube are typically less than 0.2 percent and 1 percent of the total resistance at an air velocity of 1 m/s, respectively.

The convective heat transfer coefficient on the inside of the tube is calculated using the Gnielinski correlation (see Incropera and DeWitt, 1990). Although the uncertainty associated with this calculation is ±20 percent, this internal resistance is always less than 8 percent of the total resistance and is typically less than 3 percent.

The radiative heat transfer must be estimated in order to separate the convective exchange from the total. In the evaluation of the radiative heat transfer rate, the tubes, wires, and surroundings are assumed to form an enclosure of three gray, diffuse, isothermal surfaces. The required view factors are obtained using the assumption that the adjacent wires (or tubes) are uniformly spaced parallel infinite cylinders. Two thermocouples are placed on the surface of the wind tunnel in order to determine the temperature of the surroundings. Errors resulting from uncertainty in the emissivity of the paint, the configuration factors, the temperature gradients in the wires, the temperature of the surroundings, geometrical nonuniformities, etc., result in an overall uncertainty in the radiative exchange of ±27 percent. The radiative heat loss accounts for as much as 40 percent of the total, although at a velocity of 1 m/s, this component is typically less than ten percent of the total rate of heat transfer.

After removing the internal resistance and the radiative contribution, the resulting convective heat transfer coefficient ranges from 5 to 111 $\mathrm{W/m^2\text{-}K}$. The absolute uncertainty ranges from 1 to 3.3 $\mathrm{W/m^2\text{-}K}$ which results in an uncertainty ranging from ±3 percent at the highest rates of convective heat transfer to ±21 percent at the lowest rates. For additional information on the experimental technique and the data reduction procedure, see Hoke et al. (1995).

Results

The test conditions for the 1685 test points presented in this paper varied slightly because they could not be precisely controlled. For example, the inlet air temperature varied from 293 K to 297 K due to annual fluctuations and changes caused by the heat dissipated during previous tests. The change in the water temperature across the coil is typically held between 3 and 5 K; however, it was not possible to obtain sufficient flow with city water pressure to maintain this upper limit for some of the larger coils—coils 3, 4, and 8 at the higher rates of heat transfer. The largest temperature drop is 10 K. The difference between the average refrigerant temperature of the coil and the air temperature ranges between 18 and 24 K.

The first results that will be presented are those for Coil 7, an unpainted, ten pass, serpentine coil without wires (see Table 1 for all dimensions of the coils referred to in this manuscript). This coil is tested at an angle of attack of 90 deg—the classical problem of flow normal to a single cylinder—in order to provide data that can be compared with published results. In Fig. 2, a plot of Nu_t versus Re_t, our experimental data are compared with the correlations of Hilpert (1933) and Zhukauskas (1972). A linear plot is used to clearly show the small differences between our data and these published correlations. The data are taken at velocities ranging from 0.2 to 2.0 m/s; the corresponding Reynolds number range is from 60 to 600. The error bars associated with each data point are indicated. Figure 2 shows an excellent agreement between our data and these two commonly accepted correlations. At $Re_t = 60$, the data lie 1.4 percent above the Zhukauskas' correlation and 14 percent below Hilpert's correlation. At $Re_t = 600$, our data are 7.5 percent above the Zhukauskas' correlation and 1.4 percent below Hilpert's correlation.

Wire-on-tube heat exchangers cooled by forced convection are typically located in a horizontal or nearly horizontal plane. The variation of the heat transfer coefficient with velocity for a typical coil[2] (Coil 6) in a horizontal position with flow perpendicular to the wires is shown in Fig. 3. These results are very surprising, especially at the low velocities. For example, the heat transfer coefficient at 0.25 m/s is less than half of the free convection limit. These data contradict the belief that buoyancy acts to enhance the rate of heat transfer associated with pure forced convection in transverse flows. These results show the futility of using proposed expressions of the form $Nu^n = [Nu_F^n + Nu_N^n]$ where Nu_F and Nu_N are the pure forced and natural convection correlations, to correlate mixed convection heat transfer results (see Incropera and DeWitt, 1990).

On the other hand, the study done by Henderson and Oosthuizen (1989) on tandem cylinders in a horizontal cross flow gives a hint of this result. Their results showed that the heat transfer rate from the downstream cylinder could be significantly less than that of the upstream cylinder at a dimensionless cylinder spacing, S^* (as defined in this paper), less than three. For $S^* = 1.3$, 2.6, and 3.9, their minimums are approximately 0.55 Nu_N, 0.73 Nu_N, and 0.97 Nu_N, respectively; these minimums occurred at $Ri \cong 0.9$. In comparing Henderson and Oosthuizen data with the results given in Fig. 3, note that: (i) the dimensionless wire spacing, S_w/D_w, and tube spacing, S_t/D_t, are 4.21 and 5.35, respectively, for Coil 6; (ii) the minimum shown in Fig. 3 is 0.45 Nu_N; and (iii) the minimum in our data occurred at a $Ri_w = 0.02$. As will become more evident when our results are compared with Correlation (10), the mixed convection regime extends to amazingly low Richardson numbers in a horizontal flow over this wire-on-tube geometry.

The performance of wire-on-tube heat exchangers in a horizontal plane is relatively independent of whether the flow is perpendicular to the wires ($\psi = 0$) or perpendicular to the tubes ($\psi = \pi/2$); hence, the curve in Fig. 3 would remain essentially unchanged if the coil were rotated 90 degrees in the horizontal plane. Quantitative results verifying this statement are presented in Figs. 6 and 7.

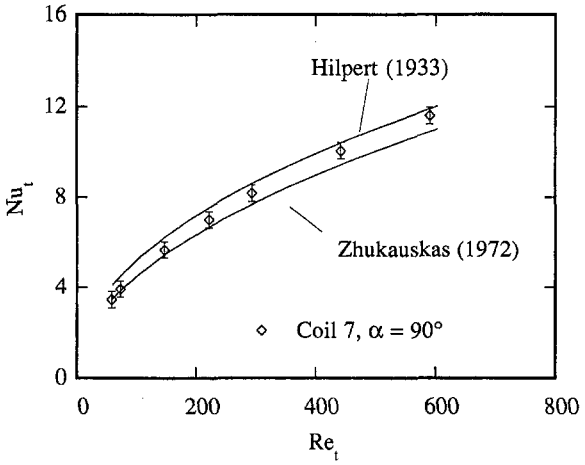

Fig. 2 Nu_t versus Re_t for flow normal to a bare tube serpentine

The variation of h with velocity seen in Fig. 3 is drastically different than that for a cylinder or a flat plate, especially in the velocity range from 0.5 to 1.0 m/s. In this velocity range, the variation of h with velocity is almost linear, whereas h increases as the square root of the velocity in laminar flow over a flat plate. It also varies with the square root of the velocity for a flow in this Reynolds number range that is normal to a cylinder. Comparing h_w with the heat transfer coefficient determined from Hilpert's correlation for a flow at 1 m/s normal to a single wire gives: $h_{\text{single cyl}} = 4.3\ h_w$. This shows the potential air-side capacity of the coil is far from being realized if the coil is in a horizontal position. On the other hand, h_w at 1 m/s is 3.14 times the average h for laminar flow over a flat plate of a length equal to the length of Coil 6.

A key in the successful correlation of air-side convective heat transfer data from wire-on-tube heat exchangers is weighting the wire area by its fin efficiency in the definition of h_w (see Eq. 6). It is hypothesized that this definition removes the strong dependence of h on the tube spacing and reduces the role of this variable to a secondary one. Coils 1 and 2 were chosen to test this hypothesis. Coils 1 and 2 have a tube spacing of 25 mm and 51 mm, respectively; hence, the wire "fins" on Coil 2 are twice as long as those on Coil 1. The wire diameters and the wire spacings are nearly equal. The performance of these two coils are compared in both Fig. 4 and Fig. 5. To increase the magnitude of the gradients in the wires, an angle of attack of 20 deg is used with flow normal to the wires.

The nonisothermal wires are ignored in reducing the data given in Fig. 4 by simply setting the fin efficiency, η, to one. In this case, the heat transfer coefficients on the 25 mm pitch coil are appreciably higher, for example, 31 percent higher at a velocity of 2 m/s. The definition of h_w, Eq. (6), is used in reducing the results presented in Fig. 5. This definition gives appreciably higher heat transfer coefficients on both coils. For example, h on the coil with the 51 mm tube pitch at 2 m/s increased by 64 percent; that is, the artificially low heat transfer coefficient has been eliminated by properly accounting for the relatively small driving temperature difference over the center portion of the wires.

The small but significant difference between the heat transfer coefficients that remains in the results presented in Fig. 5 is believed to be predominately a consequence of the poor quality of the welds in Coil 1. This problem was discovered using liquid crystal thermography (LCT) to study the temperature distribution over the coil. Approximately 25 percent of the

[2] The test results presented in the balance of this paper are for typical wire-and-tube heat exchangers that were supplied to us by various manufacturers.

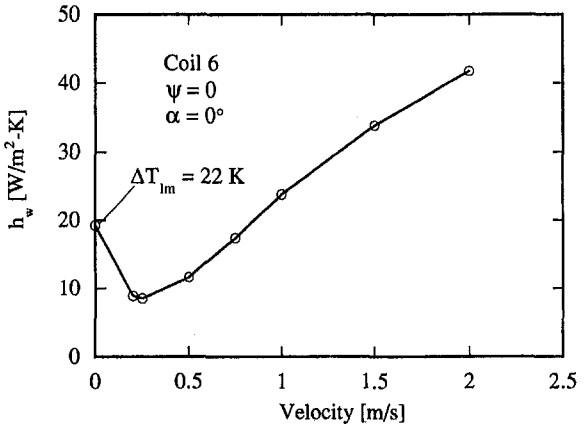

Fig. 3 Influence of velocity on h_w; horizontal heat exchanger

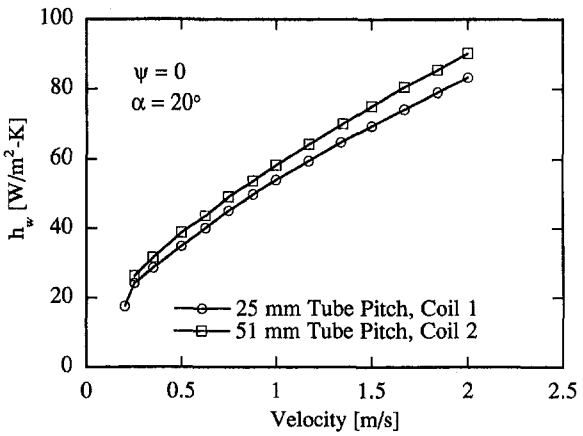

Fig. 5 Effect of tube pitch and velocity on h_w

welds over the portion of the coil that was studied with LCT were bad. This coil is the only coil used in this study made by this manufacturer and is the only coil that showed evidence of poor weld quality.

LCT studies were conducted under a variety of conditions and coil orientations including both natural and forced convection. These studies were even used to quantitatively determine fin efficiencies, η. However, the complexity and nonuniformity revealed with LCT led us to conclude that LCT was not a viable tool for determining h_w and η. There is simply too much variation between wire segments. Specifically, the LCT studies revealed the following: (i) In natural convection from a horizontal or nearly horizontal coil, the heat transfer coefficients over the lower wire segments are significantly greater than those over the wire segments on the upper side of the tubes; (ii) With forced convective flow normal to the wires of a horizontal or nearly horizontal coil, the wire segments near the leading edge, whose interior channel is not blocked by a tube bend, are significantly more effective than those between the adjacent passes where the interior channels are blocked by tube bends; (iii) If two wire segments are spaced irregularly, due to a manufacturing imperfection, an anomaly in the heat transfer from the respective wire segments is evident; (iv) For horizontal or nearly horizontal coils with flow perpendicular to the wires or tubes, the heat transfer from wire segments at the edges of a wire mat, even downstream edges, perform considerably better than the segments in the interior portion of the mat at all velocities studied, including free convection. The variation in the fin efficiency across these mats often results in a "barrel" shape color pattern; and (v) With flow perpendicular to the tubes and $\alpha \cong 0°$, the wire segments between the first two tube passes performed significantly better than those between subsequent passes. There was no evident change downstream of the second set of wire segments.

As the data given in Fig. 3 show, horizontal wire-on-tube heat exchangers perform poorly, especially at velocities around 0.5 m/s. The drastic improvement that occurs if the coil is at an angle of attack, α, is considered next. Although current condenser designs do not employ high angles of attack, sawtooth configurations could take advantage of the improvement gained by large angles of attack without changing significantly the volume occupied by the condenser. Coil 6 is used to show the influence of α because this coil is small enough to enable positioning it normal to the flow. The results with flow perpendicular to the wires are given in Fig. 6. As the angle of attack increases from 0 deg, the heat transfer coefficient rises rapidly and is almost double that of the horizontal coil at an angle of only 20 deg. Between angles of 50 deg and 80 deg, h_w is relatively constant at a value that is almost three times the corresponding value of h_w for the horizontal coil. There is a small but significant drop when the angle is increased from 80 deg to 90 deg. The wires are in tandem at α = 90 deg. At 2 m/s, Re_w = 170; hence, a single cylinder would shed Karman vortex streets at this Reynolds number. The dimensionless wire spacing in the direction normal to the plane of the wires for Coil 6 is 4.5. At this Reynolds number, Henderson and Oosthuizen (1989) data show slightly higher values of h on the downstream cylinder for dimensionless spacing of 3.9 and 6.5; however, their data were taken at much higher Grashof numbers. Tube bank data also show higher values of h on the second row of

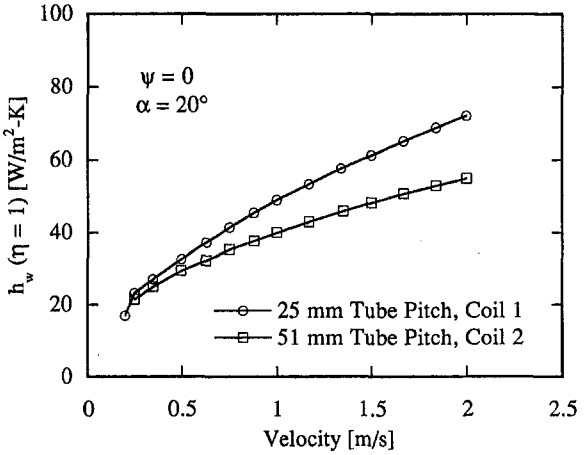

Fig. 4 Effect of tube pitch and velocity on h_w with η = 1

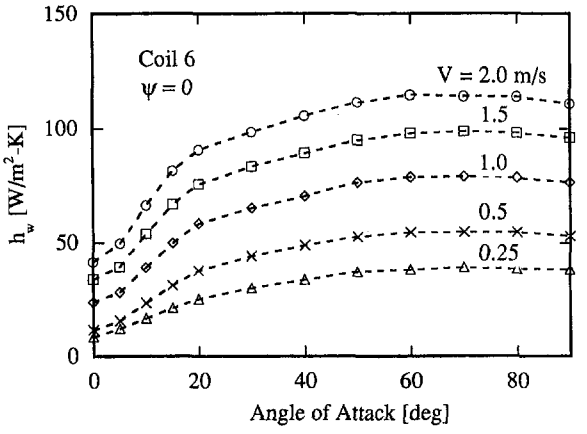

Fig. 6 Influence of angle of attack and velocity on h_w; flow normal to wires

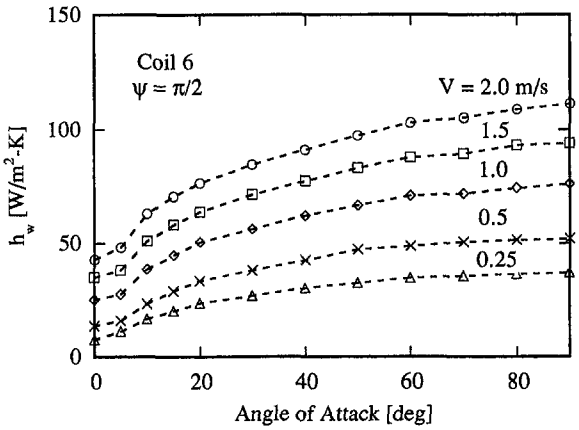

Fig. 7 Influence of angle of attack and velocity on h_w; flow normal to tubes

cylinders; however, tube bank correlations are not valid for such low Reynolds numbers. The decrease in h_w as the angle is changed from 80 deg to 90 deg, demonstrated in Fig. 6, may point to a stabilizing influence of the neighboring wires.

For a coil located perpendicular to the flow, $\alpha = 90$ deg, the influences of the boundary layer interactions and tandemly located wires can be deduced by comparing h_w with h for flow normal to a single cylinder. For example, Hilpert's Correlation

$$\mathrm{Nu} = 0.683\ \mathrm{Re}^{0.466}\mathrm{Pr}^{1/3}$$

for an air flow of 2 m/s normal to a cylinder with a diameter equal to the wire diameter of Coil 6 gives $h = 126$ W/m^2-K. In comparison, the $\psi = 0$ and $\psi = \pi/2$ data given in Figs. 6 and 7, respectively, both give $h_w = 111$ W/m^2-K. If the temperature gradients in the wires and the difference between the tubes and wires were ignored in the definition of h, that is if h were defined as $q/[A_{\mathrm{tot}}(T_t - T_a)]$, h would be 77 W/m^2-K for these two data points.

In the regime dominated by inertia forces ($V > 0.5$ m/s), the performance of Coil 6 at angles of attack between 15 deg and 45 deg is significantly better if the flow is perpendicular to the wires, as can be seen by comparing the results given in Figs. 6 and 7. The maximum percentage difference between the $\psi = 0$ and $\pi/2$ cases occurs at 20 deg and is approximately 18 percent. This is an expected result. For example, Vornehm's (1936) data for flow over an inclined cylinder at a Reynolds number of 3000 show that h with flow parallel to a cylinder is 0.63 times the corresponding h with flow normal to the cylinder.

Interestingly, when the coil is horizontal, the $\psi = 0$ orientation gives nearly identical results to the $\psi = \pi/2$ orientation at all velocities. At an angle of attack of 90 deg, the $\psi = 0$ and $\pi/2$ orientations are identical problems in the inertia dominated regime. The differences in the experimental results between these two orientations are less than 1 percent at velocities greater than 1 m/s. Thus, orientation is not a significant design parameter at angles of attack of 0 deg and 90 deg; however, the coil should be oriented with the wires perpendicular to the air flow if positioned at intermediate angles of attack.

Correlation of Experimental Results

In correlating the experimental data, that is, in deducing Correlation (10), the following points should be noted: (i) Only two yaw angles, $\psi = 0$ and $\pi/2$, are being investigated, and a separate correlation needs to be derived for each orientation; and (ii) Only the forced convection regime is targeted; hence, the Richardson number at which the correlations cease to be valid is to be determined.

Since Coil 6 is the only coil that can be tested at angles of attack greater than 40 deg, a correlation unique to this coil is derived first. In this case, the function $g(S_w^*)$, need not be determined since S_w^* is a constant. The form chosen for the function $f(\mathrm{Re}_w, \alpha)$ is

$$\mathrm{Nu}_w = C\mathrm{Re}_w^n \tag{14}$$

where C and n are functions of α and ψ. This correlation is derived for each value of ψ by: (i) determining sets of C and n for each α from a least squares fit of the Nu_w versus Re_w data for each α; (ii) generating a least squares curve fit of the n versus α data; and (iii) determining new values of C from a least squares fit of the Nu_w versus Re_w data for each α using the functional relationship for n determined in Step (ii); and (iv) generating a least squares curve fit for C from the C versus α data. This process had to be repeated several times in order to determine, and then discard, those points in the mixed convection regime. The final curve fits are based on all points in the inertia dominated regime. The experimental results showed that this regime lies below a Richardson number of 0.004 ($V > 0.5$ m/s). The resulting equations are:

Case I Flow perpendicular to the wires; $\psi = 0$, $0° \le \alpha \le 90°$, $\mathrm{Ri}_w < 0.004$.

$$C = 0.385 - 0.350\cos(\alpha)\exp(-0.00102\alpha^2) \tag{15}$$

$$n = 0.531 + 0.267\cos(\alpha)\exp(-0.00181\alpha^2) \tag{16}$$

Case II Flow perpendicular to the tubes; $\psi = \pi/2$, $0° \le \alpha \le 90°$, $\mathrm{Ri}_w < 0.004$.

$$C = 0.339 - 0.290\cos(\alpha)\exp(-0.00121\alpha^2) \tag{17}$$

$$n = 0.540 + 0.241\cos(\alpha)\exp(-0.00344\alpha^2) \tag{18}$$

where α is in degrees.

The functional relationships between C and α, and n and α are shown graphically in Figs. 8 and 9. The exponent n for both orientations approaches 0.55 as the angle of attack approaches 90°. If $\mathrm{Ri}_w < 0.004$ ($\mathrm{Re}_w > 50$), 95 percent of the data lie within ±14 percent of the correlation.

Consider next the generation of a more general correlation. The seven representative wire-on-tube heat exchanges described in Table 1 were chosen for this task. The range of S_w^* represented by these coils, $2.82 \le S_w^* \le 4.43$, is less than ideal for the deduction of the function $g(S_w^*)$, and special coils are to be constructed for more thoroughly studying the influence of S_w^* in future work. Equation (14) was again chosen for the form of the function $f(\mathrm{Re}_w, \alpha)$, and the function $g(S_w^*)$ was chosen to be

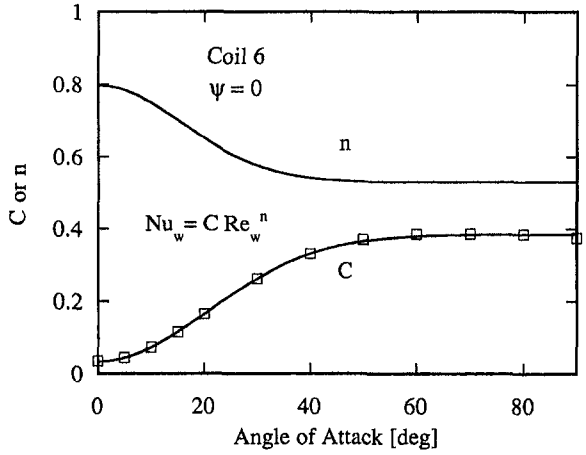

Fig. 8 C and n as a function of angle of attack; flow normal to wires

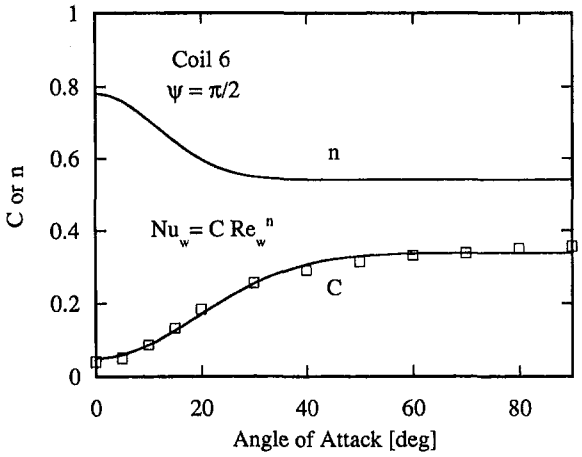

Fig. 9 C and *n* as a function of angle of attack; flow normal to tubes

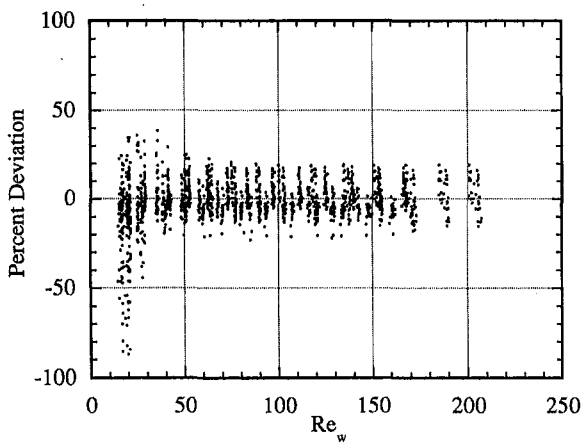

Fig. 10 Comparison between correlation and experimental data, all α's

$$g(S_w^*) = 1 - C_2\{e^{(-C_3 S_w^*)}\} \quad (19)$$

where C_2 and C_3 are constants to be determined from the experimental data. The form of this function was chosen to give an asymptotic value of 1 as S_w^* approaches infinity. The resulting form of Correlation (10) is:

$$\mathrm{Nu}_w = C\,\mathrm{Re}^n[1 - C_2\{e^{(-C_3 S_w^*)}\}]. \quad (20)$$

Using only the data from two coils with similar values of S_w^*, the functions $C = f(\alpha)$ and $n = f(\alpha)$ are derived using the same procedure used to obtain Eqs. (15)–(18). Then, all of the experimental values of Nu_w are divided by the resulting function $f(\mathrm{Re}_w, \alpha)$. A least squares fit of $\mathrm{Nu}_w/f(\mathrm{Re}_w, \alpha)$ versus S_w^*, gives C_2 and C_3. The resulting relations are given by Eqs. (21)–(24).

Case I Flow perpendicular to the wires, $\psi = 0$; $-20° \le \alpha \le 20°$.

$$C = 0.270 - 0.243\cos(\mathrm{abs}(\alpha) - 4.87) \times \exp(-0.00234(\alpha + 0.902)^2) \quad (21)$$

$$n = 0.585 + 0.249\cos(\mathrm{abs}(\alpha) + 20.0) \times \exp(-0.00441(\alpha + 1.66)^2) \quad (22)$$

Case II Flow perpendicular to the tubes, $\psi = \pi/2$; $-40° \le \alpha \le 40°$.

$$C = 0.259 - 0.232\cos(\alpha)\exp(-0.00289\alpha^2) \quad (23)$$

$$n = 0.55 + 0.269\cos(\alpha)\exp(-0.00597\alpha^2) \quad (24)$$

where α is in degrees and for both cases $C_2 = 100$ and $C_3 = 2.32$. The range of α was dictated by the size of the coils relative to the height of the test section. Six of the coils tested were limited to angles of attack of either 20 deg or 40 deg.

A comparison is given in Fig. 10 between Correlation (20) and the 1685 data points from the seven wire-on-tube heat exchangers studied. Even the data in the mixed convection regime are included in this comparison; hence, large deviations are present in the regime $\mathrm{Re}_w < 50$ where Correlation (20) is not applicable if the angle of attack is small. The test points given in Fig. 10 include both $\psi = 0$ and $\pi/2$ data for both positive and negative angles of attack. For $\mathrm{Re}_w > 50$ ($\mathrm{Ri}_w < 0.004$), 95 percent of the data lie within ±16.7 percent of Correlation (20).

A second comparison is given in Fig. 11 between Correlation (20) and the results from the seven wire-on-tube heat exchangers, although only the 433 data points that lie in the regime 20 deg $\le |\alpha| \le$ 40 deg are plotted. In this case, the maximum and average absolute deviations are only 18.2 percent and 5.0 percent, respectively, and there is no evidence of a mixed convection regime. These data extend to Richardson numbers as large as 0.03.

Conclusions

The following conclusions are drawn from the results of this investigation of the air-side convective heat transfer from wire-on-tube heat exchangers:

1 The definition of the convective heat transfer coefficient, h_w, introduced in this investigation has great utility. Although one needs to solve a transcendental equation in order to determine each experimental value of h_w, the definition adequately accounts for highly nonisothermal wires, if present, as well as the large differences between h_w and h_t that are always present. The definition reduces the role of the tube spacing to a secondary one as is evidenced by the data being successfully correlated assuming $\mathrm{Nu} \neq f(S_t^*)$.
2 Single cylinder correlations vastly overestimate the air-side heat transfer coefficient in the forced convection regime if the wire-on-tube heat exchanger is horizontal or nearly horizontal. Single cylinder correlations give values of the convective heat transfer coefficient, h_w, that are approximately four times too large.
3 When the coil is horizontal, the heat exchanger orientation (flow perpendicular to the wires, $\psi = 0$, or flow perpendicular to the tubes, $\psi = \pi/2$) is inconsequential. At an

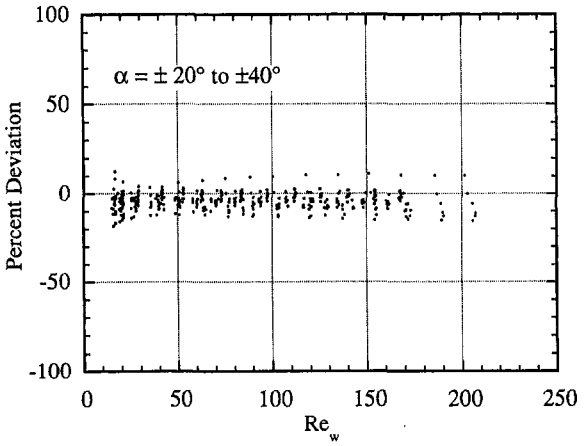

Fig. 11 Comparison between correlation and experimental data, 20 deg $\le |\alpha| \le$ 40 deg

angle of attack of 90 deg, the $\psi = 0$ and $\pi/2$ orientations are identical problems in the inertia dominated regime. Thus, orientation is not a significant design parameter at angles of attack of 0 deg and 90 deg; however, the coil should be oriented with the wires perpendicular to the air flow if positioned at intermediate angles of attack.

4 If the wire-on-tube heat exchanger is horizontal, the mixed convection regime extends to extremely low Richardson numbers, $\mathrm{Ri}_w \cong 0.004$, and uncommonly small values of h_w occur in this regime. For example, Coil 6 at a Grashof number of 7.8 has a value of h_w at $\mathrm{Re}_w = 21$ ($V = 0.25$ m/s) that is less than half of the corresponding h_w for the natural convection case.

5 Wire-on-tube heat exchangers that are cooled by forced convection should be designed such that they can be located at a significant angle of attack. For example, in the forced convection regime with flow perpendicular to the wires, the heat transfer coefficients over wire-on-tube heat exchangers at an angle of attack of 20 deg are nearly twice as large as corresponding values for horizontal coils.

6 Equation (20) does an excellent job of correlating all of the experimental data obtained from the seven wire-on-tube heat exchangers studied, as long as the data lie in the forced convection regime. The agreement is especially good if the angle of attack of the wire-on-tube heat exchanger lies in the range 20 deg $\leq |\alpha| \leq$ 40 deg. At these angles there is no evidence of the importance of buoyancy even at the lowest velocities studied ($V = 0.2$ m/s with a Richardson number as large as 0.03). The maximum and average absolute percentage deviations from Correlation (20) are only 18.2 percent and 5.0 percent, respectively, if 20 deg $\leq |\alpha| \leq$ 40 deg.

Some of the extensions of this investigation currently being pursued are: (i) heat exchanger designs, such as saw tooth configurations, that minimize space and fan-power requirements while keeping the coil at high angles of attack; (ii) heat exchanger performance in ducts that tightly confine the flow; (iii) multilayer heat exchangers; and (iv) the effects of dust on wire-on-tube heat exchangers.

Acknowledgment

The authors gratefully acknowledge the financial support of the Air Conditioning and Refrigeration Center at the University of Illinois at Urbana-Champaign. This center is funded by a consortium of 17 industrial sponsors and the National Science Foundation.

References

Admiraal, D. M., and Bullard, C. W., 1993, "Heat Transfer in Refrigerator Condenser and Evaporators," ACRC TR-48, University of Illinois at Urbana-Champaign, IL., pp. 34–35.

Carley, H. J., 1956, "A Study of Wire and Tube Heat Exchangers," M.S. Thesis, Purdue University, Lafayette, Indiana.

Collicott, H. E., Fontaine, W. E., and Witzell, O. W., 1963, "Radiation and Free Convection Heat Transfer from Wire and Tube Heat Exchangers," *ASHRAE Journal,* Vol. 5, pp. 79–83.

Cyphers, J. A., Cess, R. D., and Somers, E. V., 1959, "Heat Transfer Character of Wire-and-Tube Heat Exchangers," *ASHRAE Journal,* Vol. 1, pp. 86–90, 110.

Henderson, C., and Oosthuizen, P. H., 1989, "Experimental Study of Combined Convective Heat Transfer From Tandem Cylinders in a Horizontal Air Flow," *Heat Transfer in Convective Flows,* HTD-Vol. 107, pp. 221–229.

Hoke, J. L., Swofford, T. D., and Clausing, A. M., 1995, "An Experimental Investigation of the Air-Side Convective Heat Transfer Coefficient on Wire and Tube Refrigerator Condenser Coils," ACRC TR-86, University of Illinois at Urbana-Champaign, IL.

Howard, W. H., 1956, "A Study of Wire and Tube Heat Exchangers," M.S. Thesis, Purdue University, Lafayette, Indiana.

Hilpert, R., 1933, "Wärmeabgabe von geheizten Drähten und Rohren im Luftstrom," *Forsch. Gebiete Ingenieurw.,* Vol. 4, p. 215.

Incropera, F. P., and DeWitt, D. P., 1990, *Fundamentals of Heat and Mass Transfer,* 3rd ed., John Wiley & Sons, New York, NY.

Papanek, W. J., 1958, "Convective Film Coefficients for a Wire and Tube Heat Exchanger," M.S. Thesis, Purdue University, Lafayette, Indiana.

Rudy, W. J., 1956, "A Study of Wire and Tube Heat Exchangers," M.S. Thesis, Purdue University, Lafayette, Indiana.

Vornehm, L., 1936, "Einfluss der Anstromrichtung auf den Warmeubergang," *Zeitschrift des Vereines Deutscher Ingenieure,* Vol. 80, pp. 702–703.

Witzell, O. W., and Fontaine, W. E., 1957a, "Design of Wire and Tube Condensers," *Refrigerating Engineering,* Vol. 65, pp. 41–44.

Witzell, O. W., and Fontaine, W. E., 1957b, "What are the Heat Transfer Characteristics of Wire and Tube Condensers?" *Refrigerating Engineering,* Vol. 65, pp. 33–37, 127.

Witzell, O. W., Fontaine, W. E., and Papanek, W. J., 1959, "Convective Films Evaluated for Wire and Tube Heat Exchangers," *ASHRAE Journal,* Vol. 1, pp. 35–37, 127.

Zhukauskas, A., 1972, "Heat Transfer From Tubes in Cross Flow," J. P. Hartnett and T. F. Irvines, Jr., eds., *Advances in Heat Transfer,* Vol. 8, Academic Press, New York, NY.

Impact of Manifold Design on Heat Exchanger Efficiency

D. K. Harris

D. G. Warren[1]

V. W. Goldschmidt

Herrick Laboratories,
School of Mechanical Engineering,
Purdue University,
West Lafayette, IN 47906

The impact of manifold design on single-phase heat exchanger effectiveness is studied using the NTU-Effectiveness method. Manifolds are devices that redistribute the internal flow stream of a heat exchanger from one to several passages. Two manifold types are identified: collector box and direct split designs. The particular application considered is that of a gas fired forced air heating system. A general enhancement analysis is performed which covers four different combinations of performance and objective criteria. Three cases involve increasing the heat exchanger effectiveness while constraining either the internal flow head loss, the internal mass flow rate, or their product. The other case involves reducing the required heat exchanger flow length while constraining the heat transfer rate. Familiar convection correlations are then incorporated into the enhancement analysis to predict general trends and behavior when the main tube is split into several smaller tubes. Analytical estimates of improved effectiveness are presented for three operating conditions of an actual heat exchanger which possesses a manifold. Experimental data acquired from the gas-to-gas heat exchanger are compared to numerical predictions of its performance without a manifold (baseline design). The analytical equations developed closely predict the improvement in heat exchanger effectiveness.

Introduction

Many heat exchanger designs involve redistributing the internal flow stream into several (usually smaller) passages. The transition can occur anywhere along the flow length and is usually associated with an increase in the heat transfer surface area. These manifolds are typically reserved for locations where the overall heat transfer coefficient (U) is relatively small. The effect is to increase the overall heat transfer coefficient and surface area and hence the heat exchanger performance. Two different types of manifolds can be encountered in typical heat exchanger designs. One method involves using a collector box to assemble and redistribute the flow, while the other type simply splits the flow into several smaller passages. See Fig. 1 where the collector box design manifold has expansion, turning, and contraction head losses while the direct split type has only contraction head losses for the internal flow stream. Either type of manifold design can be viewed as a passive heat transfer enhancement device.

Heat transfer enhancements, particularly in heat exchangers, have interested many researchers. A recent overview of single-phase tube enhancements is reported by Ravigururajan and Rabas (1993). Many passive techniques have been reported to enhance the internal convection of annular channels such as those discussed by Joye and Cote (1995). Webb (1982) provides a general overview of the single-phase Performance Evaluation Criteria (PEC) which gives a systematic approach to quantifying the performance of an enhancement device under given constraints and objectives. A more exhaustive description is found in Webb (1994). Most enhancement studies concentrate on ribs, indentations, spiral flutes, coil insets, and internal fins as passive devices to enhance the inner convection coefficient. While many techniques are identified, the enhancement created by manifolds has not been reported. In fact, there is very little mention in the heat transfer enhancement literature of flow-splitting which involves the branching of a heat exchanger tube into several (usually smaller) passages. The open literature contains no general design criteria for the optimum number and size of smaller tubes or where the manifold should occur along the heat exchanger flow length for optimum performance. The focus of this paper is to provide such guidelines by describing the influence of manifold designs on heat exchanger performance.

General Heat Transfer Analysis

Several different flow arrangements are used for heat exchangers used in industry. Most of these heat exchanger designs contain many complicating features such as multiple passes. However, for purposes of generality a first order analysis on a single pass tubular heat exchanger is considered. Clearly a simplified model will not accurately predict the behavior of an actual complex heat exchanger. However, the behavior of a manifold with this simplified geometry gives general trends that apply to most exchanger designs as long as the underlying assumptions made in this analysis are reasonable approximations. Trends and not predictions are pursued here.

The geometry is shown in Fig. 2 where an internal hot gas stream that is being cooled by a external gas stream at some ambient temperature (T_∞) encounters a flow split (at $x = 0$). The one-dimensional steady energy equation with negligible radiation and constant properties for a single tube heat exchanger is shown below. Buoyancy induced flows are assumed negligible and no sources (such as combustion) are present.

$$\dot{m} \cdot C_p \cdot \left.\frac{dT_g}{dx}\right|_x + h_i \cdot P \cdot (T_{g_x} - T_{w_i}) = 0 \qquad (1)$$

For most heat exchangers the temperature drop through the thin tube wall is negligible compared to the temperature drops experienced between the inner and outer fluids. Equation (1) can therefore be rewritten in terms of the outer ambient temperature instead of the wall temperature.

$$\dot{m} \cdot C_p \cdot \left.\frac{dT_g}{dx}\right|_x + \frac{h_o h_i}{h_o + \frac{r_i}{r_o} h_i} \cdot P \cdot (T_{g_x} - T_\infty) = 0 \qquad (2)$$

[1] Currently with Nordyne Corporation, 1801 Park, 270 Drive, Box 46911, St. Louis, MO 63146.

Contributed by the Heat Transfer Division for publication in the JOURNAL OF HEAT TRANSFER. Manuscript received by the Heat Transfer Division May 24, 1996; revision received December 6, 1996; Keywords: Augmentation & Enhancement, Forced Convection, Heat Exchangers. Associate Technical Editor: T. Rabas.

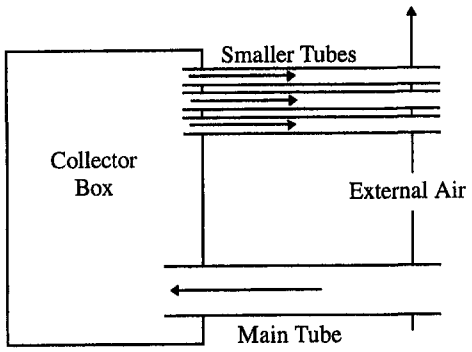

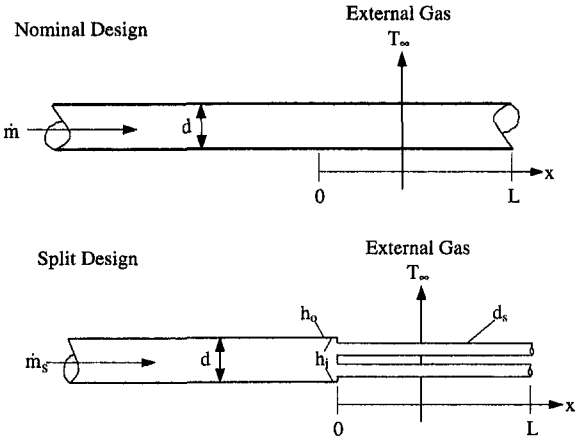

Fig. 2 Heat exchanger geometry and nomenclature

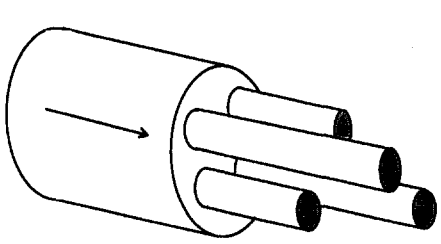

Fig. 1 Manifold design types; collector box and direct split

The solution to Eq. (2) is given below in dimensionless form,

$$\Theta_x = \exp(-\mathrm{NTU}) \tag{3}$$

$$\Theta_x \equiv \frac{T_{g_x} - T_\infty}{T_{g_0} - T_\infty},$$

$$\mathrm{NTU} \equiv \frac{UA}{C_{\min}} = \frac{U \cdot P \cdot L}{(\dot{m} \cdot c_p)_i}, \quad \text{where} \quad U \equiv \frac{h_o h_i}{h_o + \rho h_i}$$

and $C_{\min}$ designates the minimum heat capacity rate. For this analysis we consider those cases where the heat capacity rate of the inner flow stream is sufficiently less than that of the outer stream. Therefore, C_r, which is defined as the minimum to maximum heat capacity rate ($C_{\min}/C_{\max}$), is very small. Additionally, the ratio of inner to outer pipe diameters is represented by ρ. This term can be ignored for analyses that include a negligible tube wall thickness. Equation (3) can now be used to compute the actual heat transfer rate using $\dot{Q} = \dot{m}c_p\Delta T$. Dividing this quantity by the maximum possible heat transfer rate, under given flow conditions and a given environment, gives the familiar heat exchanger effectiveness, ϵ.

$$\epsilon \equiv \frac{\dot{Q}}{\dot{m}c_p \cdot (T_{g_0} - T_\infty)} = 1 - \exp(-\mathrm{NTU}) \tag{4}$$

This result is valid for all heat exchangers where $C_r \sim 0$ regardless of the heat exchanger flow arrangement. Equation (4) can now be used to find the heat transfer rate in the presence of a manifold over the heat transfer rate with no manifold,

$$\frac{\epsilon_s}{\epsilon} = \frac{M \cdot (1 - \exp(-\mathrm{NTU}_s))}{1 - \exp(-\mathrm{NTU})} \tag{5}$$

where

$$M \equiv \frac{\dot{m}_s}{\dot{m}}$$

and s designates the tube split design. The inner mass flow rate for the baseline design is $\dot{m}$ while that in the presence of a manifold is $\dot{m}_s$. This ratio (M) is required in order to evaluate

Nomenclature

A = area
C = fluid heat capacity rate
c_p = constant pressure specific heat
$C_{1,2,\ldots}$ = arbitrary constants
d = pipe diameter
f = Moody friction factor
Gz = Graetz number $\mathrm{RePr}/(x/d)$
h = convection coefficient
k = fluid thermal conductivity
L = total flow length after the flow split
m = mass flow
N = ratio of smaller diameter tubes to larger diameter tubes
NTU = Number of Thermal Units
Nu = Nusselt number
p = pipe perimeter or pressure
P = pump power
Pr = Prandtl number
Q = heat transfer
Re = Reynolds number
T = temperature
u = internal fluid velocity
U = overall heat transfer coefficient
x = flow length coordinate

Greek

α = smaller to larger pipe inner diameter ratio d_s/d
X = manifold enhancement term
ϵ = heat exchanger effectiveness
Γ = ratio of thermally developing Nusselt number to fully developed Nusselt number
$\hbar$ = head loss
κ = equivalent flow length
Λ = cross sectional area ratio A/A_s
ρ = ratio of inner to outer pipe diameter
Θ = dimensionless temperature
M = ratio of mass flow rates
ξ = dimensionless flow length L/d
Ξ = ratio of internal to external convection coefficients at $x = 0$

Subscripts

g = gas
i = internal
lam = laminar
o = external
r = ratio min/max
s = split
turb = turbulent
w = wall
x = at flow location x
∞ = ambient
0 = location of manifold inlet

the manifold case effectiveness with respect to the maximum possible heat transfer in the baseline (no split) case. Equation (5) can be rearranged into a more convenient form by using properties and values upstream of the split for scaling,

$$\frac{\epsilon_s}{\epsilon} = \frac{M \cdot (1 - \exp(-\mathrm{NTU} \cdot X/M))}{1 - \exp(-\mathrm{NTU})} \tag{6}$$

where

$$X = N\alpha \cdot \frac{\left(\frac{h}{h_s}\right)_o \cdot \left(\frac{h}{h_s}\right)_i \cdot (1 + \rho\Xi) \cdot \Gamma}{\left(\frac{h}{h_s}\right)_o + \left(\frac{h}{h_s}\right)_i \cdot \rho_s \cdot \Xi \cdot \Gamma}. \tag{7}$$

The effects of the redeveloping thermal boundary layers downstream of the split are represented by Γ, and Ξ is the ratio of internal to external convection coefficients just upstream of the split location. The number of smaller diameter tubes per larger tube upstream of the split is represented by N. Additionally, α is the ratio of the tube diameter downstream of the split to the diameter upstream of the split. The desirable design range for manifolds is $N\alpha > 1$, where the surface area available for heat transfer is increased.

Equation (6) gives two insights into the design criteria of any manifold. First is that any manifold design that allows a reduction of internal mass flow rate could actually reduce the heat exchanger effectiveness. The condition that ϵ_s/ϵ be greater than unity gives the following condition for the required heat exchanger flow length:

$$\mathrm{NTU} \geq \frac{M}{X} \ln\left\{\frac{\exp(-\mathrm{NTU}) + (M - 1)}{M}\right\}. \tag{8}$$

Figure 3 shows the general behavior of heat exchanger effectiveness for given manifold design parameters. As seen in the figure, as the heat exchanger flow length becomes large, all performance curves approach unity.

Secondly, for certain combinations of design parameters and flow conditions there exists an optimum heat exchanger flow length. That is, there are combinations of X and M that give the heat exchanger an optimum effectiveness for a given flow length downstream of the manifold. Figure 4 illustrates this for $X = 5$. The steep gradient of the curves show the sensitivity of the heat exchanger performance to the flow length. As X increases these gradients become steeper. To evaluate this optimum it is necessary to differentiate the term X. Referring to Eq. (7) the general form of X is $C_1\Gamma/(C_2 + C_3\Gamma)$. Therefore,

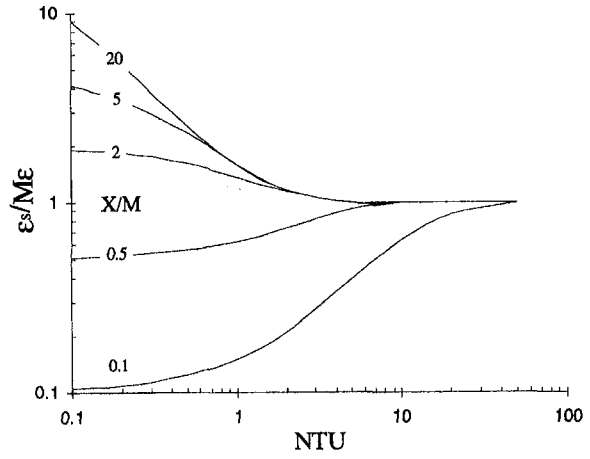

Fig. 3 General manifold behavior

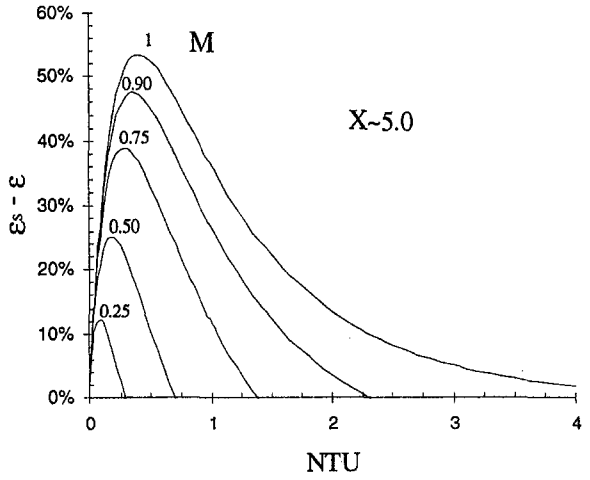

Fig. 4 Manifold behavior for $X = 5$

the optimum flow length for the case where M is not constant is as shown here:

$$\mathrm{NTU}|^{\mathrm{opt}} = \frac{M}{X} \ln\left[\frac{\mathrm{NTU}}{M'L}\left(\exp\left(-\mathrm{NTU}\left(\frac{X}{M} - 1\right)\right)\right.\right.$$
$$\left.\left. - X - \frac{LC_1C_2\Gamma'}{(C_2 + C_3\Gamma)^2} + \frac{LX}{M}M'\right) + 1\right]. \tag{9}$$

The primes indicate differentiation with respect to L, and clearly, the equation is implicit in L. The general form of Γ which depends on the internal flow regime is needed for evaluation of the optimum flow length. The thermal entry Nusselt parameter for laminar flow (Γ_{lam}) in a circular duct has been reported by Shah and London (1978) as $1 + 0.036\ \mathrm{Gz}/(1 + 0.011\ \mathrm{Gz})$. The thermal entry Nusselt parameter for turbulent flow (Γ_{turb}) was reported by Notter and Sleicher (1972) as having the general form of $1 + C_4/\xi_s$. Therefore, the Γ' terms needed are as shown below for the laminar and turbulent flow regimes, respectively:

$$\Gamma'_{\mathrm{lam}} = \frac{1 - \Gamma_{\mathrm{lam}}}{L(1 + 0.011\ \mathrm{Gz})} \quad \Gamma'_{\mathrm{turb}} = \frac{1 - \Gamma_{\mathrm{turb}}}{L}. \tag{10}$$

Enhancement Analysis

Now that the general behavior of manifolds has been described, an enhancement analysis similar to Webb (1982) can be performed. This type of analysis will help identify the impact of manifold designs on heat exchanger performance for given system constraints and objectives. Four different enhancement scenarios are analyzed as described in Table 1.

Table 1 Enhancement performance objectives

	Constraints			Objectives	
	$\frac{\dot{m}_s}{\dot{m}}$	$\frac{\hbar_s}{\hbar}$	$\frac{P_s}{P}$	$\frac{L_s}{L}$	$\frac{\varepsilon_s}{\varepsilon}$
Case I	1	>1	>1	1	>1
Case II	1	>1	>1	<1	1
Case III	<1	1	<1	1	>1
Case IV	<1	>1	1	1	>1

Both X and M need to be evaluated for each case identified in Table 1. To evaluate X, the convection coefficients need to be estimated with correlations. Since all manifold designs considered assume a circular cross-section for the tubes, the external convection coefficient ratio can always be based on the same correlation. The external correlation chosen for this analysis for flow around a circular cylinder is that of Churchill and Berstein (1977). Their correlation has been verified for $1 < \mathrm{Re}_d < 10^6$ and $\mathrm{Re}_d\mathrm{Pr} > 0.2$. The internal heat transfer correlations are dependent on the internal flow regime. The solutions for fully developed laminar flow in a circular duct ($\mathrm{Re} < 2300$) can be retrieved from any text on fundamentals and are known to be a constant independent of Reynolds number. See Burmeister (1993) for a detailed description. For turbulent channel flow ($\mathrm{Re} > 10{,}000$) the correlation for uniform wall flux as described by Kays and Crawford (1993) can be used. For confined flows in the transition regime, the Gneilinski (1976) correlation can be employed.

Case I. The first case considered allows for an increase in the internal pressure head loss by constraining the mass flow rate moving through the manifolded exchanger as identical with that which would flow through a baseline exchanger with the same flow length. This would have to be accompanied with an increase in the pump power, $P = \dot{m}\hbar g$. Because the mass flow rates in the baseline and manifolded designs are the same, the ratio of the flow velocities (u_s/u) is $1/N\alpha^2$ and the corresponding Reynolds number ratio ($\mathrm{Re}_s/\mathrm{Re}$) is given as $1/N\alpha$.

There are several effects on the streamwise pressure drop as the confined gas moves through the manifold. There are contraction head losses associated with the abrupt expansion and contraction and turning within a collector box, and other losses associated with the increased friction head loss in the smaller tube section. The increased pressure losses for the manifold above the losses expected if no split occurred for a given flow length are:

$$\hbar_s - \hbar = \frac{u^2}{2g}\cdot\left[\frac{(f\xi/\alpha + \kappa)}{\Lambda^2} - f\xi\right]. \tag{11}$$

In Equation (11) all flow losses except the friction losses incurred in the smaller tubes are lumped as an equivalent flow length in κ. $X^{\mathrm{I}}_{\mathrm{lam}}$ can now be computed where the superscript denotes the case number.

$$X^{\mathrm{I}}_{\mathrm{lam}} = \frac{N(1 + \Xi)\Gamma_{\mathrm{lam}}}{1 + \alpha^{-1/2}\Gamma_{\mathrm{lam}}\Xi} \tag{12}$$

Likewise, using the turbulent internal convection ratio $X^{\mathrm{I}}_{\mathrm{turb}}$ can be evaluated.

$$X^{\mathrm{I}}_{\mathrm{turb}} = \frac{(N\alpha)^{1/5}(1 + \Xi)\Gamma_{\mathrm{turb}}}{\alpha + \sqrt{\alpha}(N\alpha)^{-4/5}\Gamma_{\mathrm{turb}}\Xi} \tag{13}$$

Evaluation of Eq. (6) using Eq. (13) shows that for there to be a noticeable enhancement to the heat transfer, the term $X^{\mathrm{I}}_{\mathrm{turb}}$ needs a value of at least two for the manifold to have any noticeable impact on the heat exchanger effectiveness.

Case II. This case requires the heat transfer rate to remain unchanged while the manifolded exchanger flow length is reduced from that which is needed in a baseline exchanger. Duplicating the analysis shown for Case I,

$$\Delta\epsilon^{\mathrm{II}} = \exp(-\mathrm{NTU}) - \exp\left(-\mathrm{NTU}\,\frac{L_s}{L}X^{\mathrm{I}}\right) = 0 \tag{14}$$

where the mass flow rate is held constant. The baseline heat exchanger flow length is designated by L, whereas the manifolded heat exchanger flow length is designated as L_s. Note that X^{II} is identical to X^{I} since the performance constraints are identical between the two cases. Therefore, the flow length reduction achieved using a given manifold design is given as follows:

$$\frac{L_s}{L} = \frac{1}{X^{\mathrm{I}}}. \tag{15}$$

The head loss for a given manifold design can be found using Eq. (11) where κ depends on the manifold design type.

$$\hbar_s - \hbar = \frac{u^2}{2g} f\xi\left\{\frac{1}{\alpha\Lambda^2 X^{\mathrm{I}}} + \frac{\kappa}{f\xi} - 1\right\} \tag{16}$$

Case III. This next case considered allows for a decrease in the mass flow rate while maintaining the same internal pressure head loss for the manifolded exchanger as that experienced by the baseline exchanger with the same flow length. This change would be accompanied with a decrease in the pump power. The requirement of unaltered head loss for a given heat exchanger flow length gives the relative (internal) mass flow rates,

$$\frac{\dot{m}_s}{\dot{m}} = \sqrt{\frac{\Lambda^2 f\xi}{f\xi/\alpha + \kappa}}. \tag{17}$$

Using this relationship for X^{III}, both inner laminar and inner turbulent flow conditions can be found.

$$X^{\mathrm{III}} = X^{\mathrm{I}}\cdot\sqrt{\frac{f\xi/\alpha + \kappa}{\Lambda^2 f\xi}} \tag{18}$$

Using $X^{\mathrm{III}}_{\mathrm{turb}}$ along with Eq. (17) the heat exchanger effectiveness can be estimated for the turbulent case as is shown here:

$$\Delta\epsilon^{\mathrm{III}}_{\mathrm{turb}} = \exp(-\mathrm{NTU}) - \sqrt{\frac{\Lambda^2 f\xi}{f\xi/\alpha + \kappa}} \times\left(1 - \exp\left(-\mathrm{NTU}\cdot\sqrt{\frac{f\xi/\alpha + \kappa}{\Lambda^2 f\xi}}\cdot X^{\mathrm{I}}_{\mathrm{turb}}\right)\right) - 1. \tag{19}$$

This design option can actually reduce the heat transfer rate, as can be seen if $\Delta\epsilon^{\mathrm{III}} < 0$. A designer must be cautious when the incorporation of a manifold reduces the internal mass flow rate. For manifold designs that do not significantly alter the mass flow rate, the requirement needed for increased heat transfer is independent of the flow length. That is, since M is approximately unity the heat exchanger effectiveness is increased as long as $X^{\mathrm{III}} > 1$.

Case IV. This last case considers constant pump power while increasing the heat transfer rate. This is the most realistic case for most heat exchangers where the manifold is included but the pump power is not increased. The requirement of constant pump power for a given heat exchanger flow length gives the relative (internal) mass flow rates.

$$\frac{\dot{m}_s}{\dot{m}} = \sqrt[3]{\frac{\Lambda^2 f\xi}{f\xi/\alpha + \kappa}} \tag{20}$$

Since the pump power is assumed constant, the relative head loss is as shown:

$$\hbar_s - \hbar = \frac{u^2}{2g} f\xi\cdot\left(\sqrt[3]{\frac{f\xi/\alpha + \kappa}{\Lambda^2 f\xi}} - 1\right). \tag{21}$$

Using these relationships for X^{IV}, both laminar and turbulent internal flow conditions can be found.

$$X^{\mathrm{IV}} = X^{\mathrm{I}}\cdot\sqrt[3]{\frac{f\xi/\alpha + \kappa}{\Lambda^2 f\xi}} \tag{22}$$

Using X^{IV} along with Eq. (20), the heat transfer enhancement can be estimated for the turbulent case as is shown here. This design option can also reduce the heat transfer rate, as can be seen if $\Delta\epsilon^{IV} < 0$.

$$\Delta\epsilon^{IV}_{turb} = \exp(-NTU) - \sqrt[3]{\frac{\Lambda^2 f\xi}{f\xi/\alpha + \kappa}} \times \left(1 - \exp\left(-NTU \sqrt[3]{\frac{f\xi/\alpha + \kappa}{\Lambda^2 f\xi}} \cdot X^{I}_{turb}\right)\right) - 1 \quad (23)$$

The relative flow parameters for all four cases are summarized in Table 2.

Empirical Verification

The equations developed were used to estimate the improved performance of an actual heat exchanger possessing a manifold over its predicted performance without any flow splits. The internal gases were heated via combustion of natural gas and cooled by forced convection of ambient air. The heat exchanger has a cross flow arrangement with four passes of the internal gas stream where the internal gases are unmixed and the external gases are mixed. After the second pass each larger tube is split into four smaller tubes with an α of 0.291. See Fig. 5. The fan inducing internal gas flow is assumed to operate at the same power level regardless of the heat exchanger flow arrangement, and hence the improved effectiveness is best estimated using Case IV equations. The values of C_{min} and C_{max} were 4.8×10^{-5} and 3.4×10^{-4}, respectively, giving a value of C_r for this exchanger of 0.14. The internal flow regime was almost fully turbulent (Re = 9300). The manifold design parameters for this heat exchanger are $M = 0.30$ and X approximately 2.8. Radiation accounted for only one percent of the total heat transfer in the third and fourth passes.

In addition to the measured heat exchanger effectiveness, predictions of effectiveness without the manifold present were needed. The difference between these two values gives the predicted influence the manifold has on the heat exchanger performance. A computer model was created to predict the performance of this type of heat exchanger under any environmental and flow conditions. The numerical model is one-dimensional and uses correlations for its convective heat transfer coefficients. Therefore, the accuracy of the numerical predictions is limited by that of the correlations, (10–20 percent). The numerically simulated geometry is identical to Fig. 5 except that the larger diameter tube continues for all four passes.

The amount of combustion excess air was varied from 60.8 percent (nominal operation) to 44.6 percent, so as to compare the heat exchanger performance under varying conditions. The measured heat exchanger effectiveness was found to be unaffected by the moderate variation in excess air. The measured effectiveness increased by 1.8 percent as the excess combustion air was reduced. The estimated increase in effectiveness was also found to be relatively independent of this variation (increasing 1.3 percent). Although the predicted increase in effectiveness is within one percent of the measured effectiveness for all three tests, the overall uncertainty in the measurements is relatively high. The propagation of bias and precision errors in the data reduction of the heat exchanger effectiveness for a single measurement is 8.9 percent with a 95 percent level of confidence. An analysis revealed that the uncertainty in temperature measurements is responsible for most of the overall uncertainty. This is primarily due to the measurement of high temperatures, which yields a large range of expected (95 percent confidence) temperatures. The reliance of fluid properties on temperature makes the accuracy in temperature measurement all the more critical.

Therefore, multiple tests were repeated (ten in all) to mitigate the high level of overall uncertainty to a level of 4.9 percent. These multiple tests were during nominal operation (60.8 percent excess combustion air). The numerical predictions of the heat exchanger effectiveness (without any splits) was 68.0 percent. The equations developed in the analysis presented earlier predict an improvement in the effectiveness of 8.4 percent, giving an estimated effectiveness of 76.4 percent. The measured effectiveness during nominal operation was 75.6 ± 4.2 percent. The estimated increase in heat exchanger effectiveness is considerably close to that measured in spite of all the assumptions made in the derivation of Eq. (6). Therefore, the estimates made correctly predict that the heat exchanger effectiveness increases with the inclusion of the manifold.

Final Comments

The general trends developed for the impact of manifold designs on heat exchanger performance are based on the results of a simplified first-order analysis. Various simplifications were made in an effort to obtain a general model applicable to a wide range of heat exchanger designs. These assumptions were as follows: one-dimensional and steady heat transfer, negligible radiative heat transmission, negligible conduction in the tube material, buoyancy induced flows insignificant, no internal energy generation (combustion), single pass geometry, and constant fluid properties. Most heat exchangers can be accurately modeled assuming one-dimensional and steady operation. As

Table 2 Summary of flow parameters for manifolds

	$\frac{U_s}{U}$	$\frac{Re_s}{Re}$	$\frac{\dot{m}_s}{\dot{m}}$	$\frac{\hbar_s}{\hbar}$	$\frac{L_s}{L}$
Case I	Λ^{-1}	$1/(N\alpha)$	1	$\left(\frac{f\xi}{\alpha}+\frac{\kappa}{f\xi}\right)\frac{1}{\Lambda^2}$	1
Case II	Λ^{-1}	$1/(N\alpha)$	1	$\left(\frac{f\xi}{\alpha}+\frac{\kappa}{f\xi}\right)\frac{1}{\Lambda^2}$	$\frac{1}{X}$
Case III	$\sqrt{\frac{f\xi}{f\xi/\alpha+\kappa}}$	$\sqrt{\frac{\alpha^2 f\xi}{f\xi/\alpha+\kappa}}$	$\sqrt{\frac{\Lambda^2 f\xi}{f\xi/\alpha+\kappa}}$	1	1
Case IV	$\sqrt[3]{\frac{f\xi}{\Lambda(f\xi/\alpha+\kappa)}}$	$\sqrt[3]{\frac{\alpha^3 f\xi}{\Lambda(f\xi/\alpha+\kappa)}}$	$\sqrt[3]{\frac{\Lambda^2 f\xi}{f\xi/\alpha+\kappa}}$	$\sqrt[3]{\frac{f\xi/\alpha+\kappa}{\Lambda^2 f\xi}}$	1

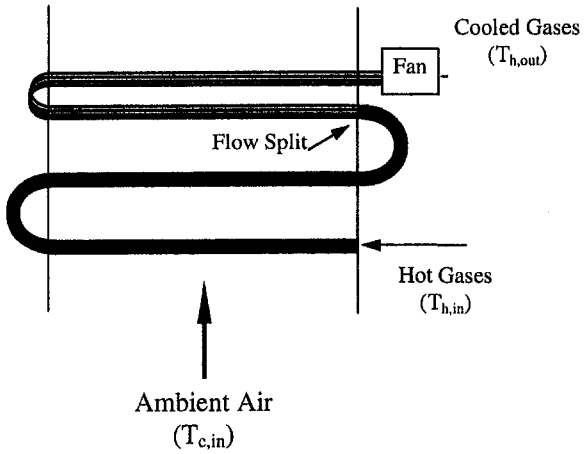

Fig. 5 Test specimen configuration

long as the internal gas temperatures are moderate, radiation is usually not significant. Of course, this analysis is not appropriate in the portion of an exchanger where combustion is occurring. Also, most exchangers are designed such that conduction within the tube walls is insignificant. Although this analysis was generated assuming a single pass geometry, the results are applicable to any heat exchanger design with C_r vanishingly small.

Finally, the assumption of constant properties is the most treacherous. Significant temperature variations are typical in most single-phase heat exchangers. The thermal conductivity, density, and dynamic viscosity vary significantly with temperature for most gases. For example, the internal combustion products during testing cooled from 1110 K at the split to 527 K at the heat exchanger exit. Over this range the thermal conductivity, dynamic viscosity, and specific heat all decreased by 35.0 percent, 31.3 percent, and 6.7 percent, respectively. Additionally, the density and Prandtl number both increased by 110.8 percent and 5.8 percent, respectively. The convection coefficient depends linearly on k, and the Reynolds number varies inversely with viscosity. Therefore, the variation in these two parameters cannot be ignored if the gas temperature drop along the given flow length is significant. However, in lieu of a computational model the analytical results presented here appear to give reasonable estimates of the impact a manifold will impose on a heat exchanger.

Detailed numerical models or measured performance data of heat exchangers are usually developed for a given heat exchanger type and arrangement. To accurately predict the performance of any heat exchanger, such information would be needed. The modeling approach is usually cumbersome in the early stages of a design, and performance curves cannot be generated until the exchanger is built. However, during the design phase first order estimates of system components are usually very helpful. It is intended that these general trends presented here would assist designers in identifying the impact a manifold would have on the heat exchanger performance and help achieve an optimum design. These equations could also be helpful in retrofit decisions when contemplating a tube count and tube size change.

Acknowledgments

The authors would like to express their gratitude to Nordyne Corporation for their generous funding of this research project and the approval to publish these findings.

References

Burmeister, L., 1993, *Convective Heat Transfer,* second ed, John Wiley & Sons, New York, NY, pp. 111–115.

Churchill, S. W., and Berstein, M., 1977, "A Correlating Equation for Forced Convection From Gases and Liquids to a Circular Cylinder in Cross Flow," ASME JOURNAL OF HEAT TRANSFER, Vol. 99, pp. 300–306.

Gnielinski, V., 1976, "New Equations for Heat and Mass Transfer in Turbulent Pipe and Channel Flow," *International Chemical Engineering,* Vol. 16, pp. 359–368.

Joye, D. D., and Cote, A. S., 1995, "Heat Transfer Enhancement in Annular Channels With Helical and Longitudinal Fins," *Heat Transfer Engineering,* Vol. 16, No. 2, pp. 29–34.

Kays and Crawford, 1993, *Convective Heat and Mass Transfer,* second ed., McGraw-Hill, Hightstown, NJ, pp. 316.

Notter, R. H., and Sleicher, C. H., 1972, "A Solution to the Turbulent Graetz Problem-III," *Chemical Engineering Science,* Vol. 27, pp. 2073–2093.

Ravigururajan, T. S., and Rabas, T. J., 1993, "An Overview of Single-Phase In-Tube Enhancements: Part 1—Data-Base Development," ASME 93-WA/HT-38, pp. 1–8.

Shah, R. K., and London, A. L., 1978, "Laminar Flow in Forced Convection Ducts," *Advances in Heat Transfer,* Academic Press, New York, NY.

Webb, R., 1982, "Performance Evaluation Criteria for Use of Enhanced Heat Transfer Surfaces in Heat Exchanger Design," *International Journal of Heat and Mass Transfer,* Vol. 24, pp. 715–726.

Webb, R., 1994, *Principles of Enhanced Heat Transfer,* John Wiley & Sons, New York, NY.

(Contents continued)

DISCUSSION

ANNOUNCEMENTS

Journal of Heat Transfer

Technical Briefs

Thermal Contact Conductance of a Paper/Elastomer Interface

J. W. Mohr[1], J. Seyed-Yagoobi[1], and D. C. Price[2]

Introduction

Several parameters greatly affect the heat transfer in printing, copying, and paper making processes. Fully understanding these parameters will allow for greater accuracy in design, manufacturing, and control of the processes. The thermal contact conductance at the interface of the paper is one of these key parameters. Limited experimental information (Asensio et al., 1993; Kerekes, 1980; Seyed-Yagoobi et al., 1992) focuses on the contact conductance of a paper/metal interface, as commonly found in paper production applications. In general, it is well documented that the thermal contact conductance increases with increasing interface pressure and sheet moisture content, as well as decreasing basis weight (Asensio et al., 1993). Basis weight describes the weight of an air dry paper sheet divided by the sheet surface area.

This paper deals with a second common interface involving paper and rubber elastomer surfaces. This situation is typically found in printing, copying, and calendering operations, wherein the thermal contact conductance plays a critical role in the transfer of heat into the paper sheet. Two types of elastomers are considered in this work, and the operating conditions explored are representative of printing and copying processes.

Experimental Program

An existing contact conductance apparatus was modified for use in this study. The apparatus consists of two aluminum flux meters, a spring system to control interface loading conditions, a 1 kW band heater acting as a heat source, a constant temperature bath and coolant lines acting as a heat sink, a load cell, and a linear variable differential transformer for measuring interface deflection. A detailed description of the apparatus can be found in Seyed-Yagoobi et al. (1992). Modifications to this apparatus shown in Fig. 1 included improving the loading and deflection measurement systems for more accurate determination of paper sample deflection, to within 1×10^{-4} mm. The length of the flux meters and the heavy insulation ensured that the heat flux through each flux meter was one-dimensional.

A series of experiments was conducted to investigate the thermal contact conductance of a paper and elastomer interface. The thermal contact conductance of a paper and aluminum interface was also investigated for comparison purposes. The circular paper samples used in this study were 7.62 cm in diameter, 0.104 mm thick plain laser printer sheets with a dry basis weight of 77.2 g/m^2. The measured moisture content of the samples was five percent. The elastomer pieces on either side of the paper sheet were 1.78 mm thick and 7.62 cm in diameter. A thin coating of silicone heat sink compound was applied to both the top and bottom heat flux meters. This compound helped secure the elastomer to the flux meter as well as significantly reducing the contact resistance between the flux meter and the elastomer.

Both of the elastomers utilized in this study are silicone polymers (polydimethylsiloxane) manufactured by American Roller Company. Elastomer A contains a titanium dioxide filler and carbon black, giving the elastomer a gray color. Elastomer B contains an aluminum oxide filler with iron oxide, resulting in a red color. The elastomer properties, measured surface characteristics, and measured thermal conductivity values are shown in Table 1.

Experiments were conducted in order to investigate whether or not these particular elastomers would exhibit the unique thermal characteristics found in some synthetic rubbers, such as a high negative coefficient of thermal expansion and "shape memory" (Whitby, 1954). First, the elastomer samples were heated to the operating temperature both with and without the applied load. In both cases, no shrinkage or shape change of the elastomers was observed over the entire range of pressures ($0 < P < 350$ kPa) and temperatures (300 K $< T < 440$ K) used in this study. In fact, the total measured reduction in the thickness of each elastomer was less than three percent over the entire range of pressures and temperatures used in this study. Furthermore, the thermal conductivity of the two elastomers (Table 1) was measured at an interface pressure of 104 kPa over the temperature range of 300 K $< T < 440$ K, in order to simulate typical copying and printing conditions. These thermal conductivity measurements were repeated three times for different sample thicknesses and negligible differences between tests were observed.

Based on the durometer readings in Table 1, it can be seen that Elastomer B is about 50 percent harder than Elastomer A. However, the difference in the deformation of both elastomers over the range of pressures used in this study was very small. This result suggests that material hardness is not a distinguishing property of the two elastomers in this study. The surface characteristics of each elastomer sample are described by three

[1] Drying Research Center, Department of Mechanical Engineering, Texas A&M University, College Station, TX 77843-3123.

[2] Aero/Thermal Technology Branch, Defense Systems & Electronics Groups, Texas Instruments, Plano, TX 75086.

Contributed by the Heat Transfer Division of THE AMERICAN SOCIETY OF MECHANICAL ENGINEERS. Manuscript received by the Heat Transfer Division July 25, 1996; revision received January 8, 1997; Keywords: Conduction, Direct-Contact Heat Transfer, Mat'ls Processing & Manufacturing Process. Associate Technical Editor: T. Bergman.

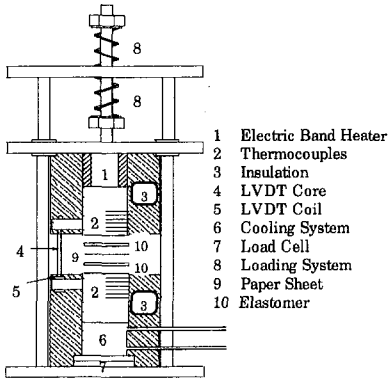

Fig. 1 Schematic of the contact conductance measurement apparatus

variables: surface roughness, surface waviness, and surface total indicator reading. Whereas surface roughness (or tool mark) is caused by the helix pattern formed as material is cut, surface waviness is caused by vibration of the milling equipment or lathe. The wavelength of this vibration component is much greater than the wavelength of the surface roughness. Over the entire surface, the straightness of the surface (error of form) measures the total distance between the largest "peak" and smallest "valley" along the surface. This error of form is called the surface total indicator reading. To place the surface roughness, surface waviness, and surface total indicator reading in perspective, one can view these surface indicators in terms of increasing size. The small surface roughness is imposed on top of the longer wavelength surface waviness variable which in turn, causes the large "peaks" and "valleys," which determine the surface total indicator reading (Federal Products Corporation, 1991).

Approximately 4–6 hours were required for the apparatus to reach initial steady state. Following a change in interface pressure (applied loading), approximately 15–30 min of continual monitoring were required for a new steady state to be achieved. For each new test, the load cell was zeroed with the peripheral equipment (i.e., band heater, insulation, etc.) attached to the apparatus. Steady state measurements were recorded during each experiment and included applied load, temperature profiles in the upper and lower aluminum flux meters, and interface thickness. For the aluminum/paper case, the interface thickness consisted of only the paper sample. For the elastomer/paper case, the total joint thickness consisted of the upper and lower elastomers and the paper sheet. Calculated results included heat fluxes for the upper and lower flux meters, the temperature drop across the interface, and overall joint conductance. The average sheet temperature was also calculated by averaging the temperatures of the surfaces (aluminum or elastomer) in contact with either side of the paper sample. All experiments were conducted at calculated average paper sheet temperatures in the range 400 K–425 K and a pressure range of 34.5 to 350 kPa. Over the range of pressures considered, the effects of using a range of average paper sheet temperatures on the overall conductance with the elastomers were negligible and were within the experimental uncertainty. Following each experiment, the paper sample was removed from the experimental apparatus and placed in storage, and the silicone heat sink compound was cleaned from the elastomer pieces and aluminum flux meters. Before each new test, a new paper sample was obtained and a fresh coating of heat sink compound was applied to the aluminum flux meters.

The measured thermal conductivity of the aluminum flux meters, Eq. (1), was used to calculate the upper and lower heat fluxes. The difference in the calculated heat flux of the upper and lower meters were less than ten percent.

$$k_{\text{aluminum}}(\text{W/mK}) = -267.9 + 3.72T - 0.011T^2 + 1.04 \times 10^{-5}T^3 \quad 300\ \text{K} < T < 450\ \text{K} \quad (1)$$

The overall joint conductance was calculated by dividing the average heat flux of the upper and lower aluminum flux meters by the temperature drop across the paper sheet; this temperature drop was defined as the difference between the surface temperatures of the upper and lower flux meters in contact with the paper sheet. For the elastomer/paper interface, the temperature drop across the paper sheet was defined as the difference of the surface temperatures of the upper and lower elastomers in contact with the paper sheet. Since the actual temperatures within the elastomers were not possible to measure, the temperature difference across the thin elastomer sample was determined from the calculated one-dimensional heat flux in each flux meter and by knowing the elastomer conductivity and thickness at a given pressure.

Data showed negligible paper sheet compression with the elastomer interface, while the thickness of the paper sample in the bare aluminum interface varied with pressure P, according to Eq. (2):

$$t(\text{mm}) = -0.0039 \ln (P) + 0.0675; \quad 34.5\ \text{kPa} \le P \le 344.7\ \text{kPa}. \quad (2)$$

Because of the silicone heat sink compound, the resistance at the interface of the aluminum flux meter and elastomer was considered negligible. In fact, the overall joint conductance determined by including the contact resistance between the aluminum and elastomer differed from the overall joint conductance without these contact resistances by less than one percent.

Knowing the overall joint conductance, the interface contact conductance was determined from Eq. (3), where h_o, h_c, t_{sheet}, and k_{sheet} are the overall conductance, contact conductance, pa-

Table 1 Elastomer properties and surface characteristics at room temperature and thermal conductivity as a function of temperature

	Elastomer A	Elastomer B
color	gray	red
filler	titanium dioxide/carbon black	aluminum oxide/iron oxide
specific gravity	1.14	2.26
tensile strength (kPa)	4689	4482
hardness, durometer (Shore A*)	50	70–73
roughness arithmetic mean (μm)	0.6	1.4
roughness root mean square (μm)	0.8	1.8
surface waviness (μm)	106.3	7.1
surface total indicator reading (μm)	346.4	49.8
thermal conductivity (W/mK)	$k = 1.71–0.0019\ T$	$k = 0.50–0.00048\ T$
(T in Kelvin)	$300\ \text{K} < T < 420\ \text{K}$	$300\ \text{K} < T < 440\ \text{K}$

* Shore A corresponds to the "A" range for the durometer manufactured by Shore Inc.

per sheet thickness, and paper sheet thermal conductivity, respectively.

$$\frac{1}{h_o} = \frac{2}{h_c} + \frac{t_{\text{sheet}}}{k_{\text{sheet}}} \tag{3}$$

Because of identical surface characteristics in Eq. (3), the contact conductance in the upper and lower interfaces were assumed to be equal. The thermal conductivity in W/mK of the paper sheet is calculated from Eq. (4), where the contribution of the moisture in the sheet was neglected since the paper samples considered in this study had moisture contents below five percent.

$$k_{\text{sheet}} = k_{\text{fiber}}*(1 - \epsilon_{\text{sheet}}) + k_{\text{air}}*\epsilon_{\text{sheet}} \tag{4}$$

The value of the thermal conductivity of paper fiber, k_{fiber}, was assumed to be 0.15 W/mK (Kerekes, 1980; Asensio, 1992). The thermal conductivity of air was determined from the available literature at the given paper sheet average temperature, and the measured sheet porosity, ϵ_{sheet}, was 0.6.

Assuming a negligible contribution of $t_{\text{sheet}}/k_{\text{sheet}}$ in Eq. (3) results in the minimum thermal contact conductance values which are equal to twice the overall joint conductance values. These minimum contact conductance values are also reported in this paper and are compared to actual calculated contact conductance values described above.

Error Analysis

A Kline and McClintock (1953) error analysis was performed for the relations used to calculate the overall joint thermal conductance and thermal contact conductance. The minimum and maximum uncertainties in the overall joint conductance were 10.2 and 11.1 percent, while the corresponding minimum and maximum uncertainties for the thermal contact conductance were 11.5 and 13.2 percent, respectively.

The data from three repeated experiments for the elastomer/paper interface case using Elastomer A were averaged at each pressure. The minimum and maximum standard deviations from the calculated mean in the overall conductance data were 1.3 and 9.7 percent, respectively. The minimum and maximum deviations from the mean of the contact conductance values were 2.7 and 13.3 percent, respectively.

Results

The effect of the interface pressure on the overall joint conductance for the three cases considered is shown in Fig. 2. For

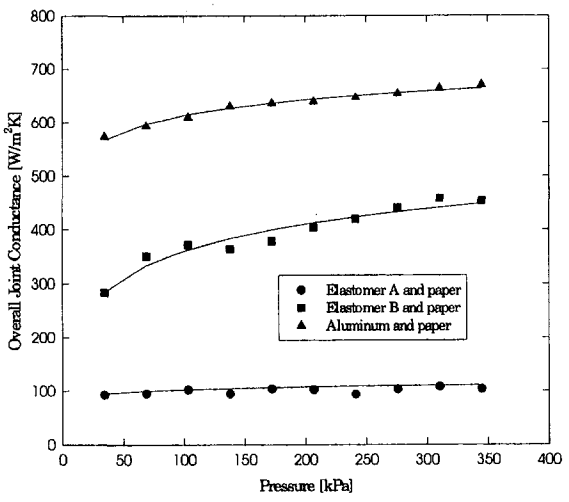

Fig. 2 Overall thermal joint conductance as a function of applied pressure for three interfaces

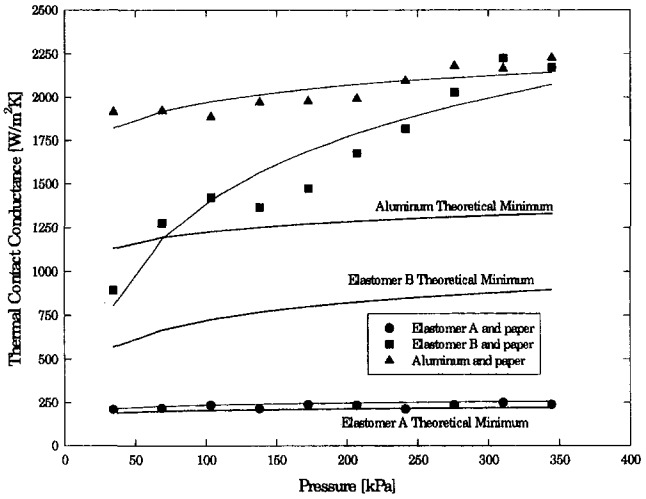

Fig. 3 Thermal contact conductance as a function of applied pressure for three interfaces

all three interfaces, the magnitude of the overall conductance increases with increasing pressure. This trend is largely caused by interface compression, wherein the voids at the interface decrease in size and the sample conforms effectively to the surface in contact. This interface compression causes an increase in the overall contact conductance surface area, resulting in higher conductance values.

The calculated contact conductance using Eq. (3) for the aluminum/paper interface are shown in Fig. 3 as a function of interface pressure. Equation (5) is the regression equation describing the aluminum/paper interface data.

$$h_{c\text{Al}}(\text{W/m}^2\text{K}) = 140.0 \ln (P) + 1326.4 \tag{5}$$

The calculated contact conductance for the elastomer/paper interfaces are also shown in Fig. 3 and represented by Eqs. (6) and (7) for the two elastomers.

$$h_{c\text{A}}(\text{W/m}^2\text{K}) = 17.9 \ln (P) + 153.8 \tag{6}$$

$$h_{c\text{B}}(\text{W/m}^2\text{K}) = 551.4 \ln (P) - 1149.0 \tag{7}$$

Equations (5–7) are valid for the paper sheet average temperature range of 400 K to 425 K and the pressure range of 34.5 kPa $\leq P \leq$ 344.7 kPa.

The contact conductance values for Elastomer A were approximately an order of magnitude lower than the contact conductance values for the aluminum/paper interface, as shown in Fig. 3. With Elastomer B, the contact conductance approached the value for the aluminum/paper interface at the highest values of pressure used in this study. When the contact conductance for the two elastomers is compared, the values with Elastomer B are 3.7 times higher than Elastomer A at the lowest interface pressure, and 8.0 times higher at the highest interface pressure. One main reason for such higher thermal contact conductance values for Elastomer B in comparison to Elastomer A is the fact that the thermal conductivity of Elastomer B is 2.7 times higher than the thermal conductivity of Elastomer A in the range of 400 K to 425 K (see Table 1). The thermal conductivity of the elastomer directly affects the thermal contact conductance because, at the contact interface, heat is conducted through the contact points.

Because the thermal contact conductance values with Elastomer B are higher than Elastomer A by an amount greater than that which can be attributed solely to the differences in thermal conductivity, the surface properties of the elastomers must also influence the contact conductance values. The major differences between the two elastomers (Table 1) are in the values of surface roughness and surface flatness (surface waviness and

total indicator reading). Since the Elastomer A has smaller mean and RMS roughness heights than Elastomer B, one would believe that the Elastomer A would possibly produce a larger contact conductance. However, these roughness scales are at least an order of magnitude smaller than the diameter range (10–45 μm) for typical pulp fibers (Smook, 1982). Because of the relative sizes of the fiber diameter and elastomer roughness scales, the surface of each elastomer (A and B) appears smooth to the paper sample.

In terms of the larger scale surface flatness characteristics (waviness and total indicator reading), Elastomer B is a much more uniform surface. Whereas the waviness of Elastomer B (7.1 μm) is of the same scale as the paper fiber diameter, the waviness of Elastomer A is almost 15 times greater than the waviness of Elastomer B. The 106.3 μm value of waviness for Elastomer A is also more than twice the size of typical paper fiber diameter. In addition, whereas the total indicator reading for Elastomer B (49.8 μm) continues to be of nearly the same scale as the paper fiber diameter, the total indicator reading for Elastomer A (346.4 μm) is seven times greater than Elastomer B. These larger scale surface flatness characteristics (waviness and total indicator reading), relative to the paper fiber diameter, suggest that the paper sample will see a "smooth" surface with Elastomer B and a relatively "rough" surface with Elastomer A. Therefore, better contact with the paper sample will occur with Elastomer B than Elastomer A. The effects of surface flatness properties is especially evident at higher pressures, where the differences in contact conductance between the two elastomers are even more pronounced. These data suggest that for relatively soft materials, such as the elastomers used in this study, the surface flatness characteristics are important parameters for thermal contact conductance.

As described previously, the minimum thermal contact conductance is equal to twice the overall joint conductance, when the resistance to heat transfer through the paper sample is ignored. These minimum curves are also shown in Fig. 3 for both interfaces. Note the proximity of the contact conductance curve for Elastomer A to the theoretical minimum, whereas, the theoretical curves for Elastomer B and the bare aluminum/paper cases deviate greatly from the theoretical minimum. For the bare aluminum/paper interface, the theoretical minimum is clearly a poor representation of the actual physics of the process. The resistance to heat transfer through the paper sample is of the same order of magnitude as the contact resistance with the aluminum flux meters on either side of the paper sample. Because of the effective contact between Elastomer B and the paper sample, the resistance to heat transfer through the paper sample is also of the same order of magnitude as the contact resistances at the elastomer paper interfaces. Therefore, the theoretical minimum is also a poor indicator of the actual process using Elastomer B. However, because the contact between Elastomer A and the paper sample is relatively poor, the contact resistance on either side of the paper sample is relatively greater than the resistance to heat transfer through the paper sample. Therefore, the theoretical minimum is a very good indicator of the thermal contact conductance for Elastomer A.

Acknowledgments

The authors thank Professor L. S. Fletcher and his research group for determining the thermal conductivity values and Mr. Jeff Wirtz for gathering much of the data. Financial support for this work was provided by Texas Instruments and the Drying Research Center at Texas A&M University.

References

Asensio, M. C., 1992, "Simulation of Paper Drying Systems With Incorporation of an Experimental Drum/Paper Thermal Contact Conductance Relationship," M. S. Thesis, Texas A&M University, College Station, TX.

Asensio, M. C., Seyed-Yagoobi, J., and Fletcher, L. S., 1993, "Thermal Contact Conductance of a Moist Paper Handsheet/Metal Interface for Paper Drying Applications," ASME JOURNAL OF HEAT TRANSFER, Vol. 115, pp. 1051–1053.

Federal Products Corporation, 1991, "Instruction Manual for Surfanalyzer 5000-400," Providence, RI.

Kerekes, R. J., 1980, "A Simple Method for Determining the Thermal Conductivity and Contact Resistance of Paper," TAPPI Journal, Vol. 63, No. 9, pp. 137–140.

Kline, S. J., and McClintock, F. A., 1953, "Describing Uncertainties in Single Sample Experiments," *Mechanical Engineering*, Vol. 75, pp. 3–8.

Ng, K., 1990, "Thermal Contact Conductance of a Paper Handsheet/Metal Interface," M.S. Thesis, Texas A&M University, College Station, TX.

Seyed-Yagoobi, J., Ng, K. H., and Fletcher, L. S., 1992, "Thermal Contact Conductance of a Bone-Dry Paper Handsheet/Metal Interface," ASME JOURNAL OF HEAT TRANSFER, Vol. 114, pp. 326–330.

Smook, G. A., 1982, "Handbook for Pulp and Paper Technologists," Technical Association of the Pulp and Paper Industry, Atlanta, GA.

Whitby, G. S., 1954, *Synthetic Rubber*, John Wiley & Sons, New York, NY.

Convection in a Porous Medium Induced by an Inclined Temperature Gradient With Mass Flow

Z. Qiao[1] and P. N. Kaloni[1]

Nomenclature

a = dimensionless overall horizontal wave number
D = differential operator, d/dz
g = gravitational acceleration
H = layer height
$\mathbf{i}, \mathbf{j}, \mathbf{k}$ = unit vectors in the x, y and z-directions, respectively
K = permeability
l = dimensionless wave number in the y-direction
P, p = dimensionless pressure/perturbation pressure
p_s = dimensionless basic-state pressure
q = horizontal mass flow rate
Q = dimensionless horizontal mass flow rate
R_E = critical vertical Rayleigh number in energy stability analysis
R_H = horizontal Rayleigh number
R_L = critical vertical Rayleigh number in linear stability analysis
R_V = vertical Rayleigh number
T = dimensionless temperature
T_s = dimensionless basic-state temperature
t = dimensionless time
$\mathbf{u}, \mathbf{v}$ = dimensionless perturbation velocity vector/velocity vector
$\mathbf{u}_s$ = dimensionless basic-state velocity vector
x, y, z = dimensionless Cartesian coordinates

Greek symbols

α_m = thermal diffusivity
β_T = horizontal temperature gradient
γ_T = coefficient of volume expansion
θ = dimensionless perturbation temperature
κ = thermal diffusivity
μ = dynamic viscosity
ρ_0 = density at the reference temperature

[1] Department of Mathematics and Statistics, University of Windsor, Windsor, Ontario, Canada N9B 3P4.

Contributed by the Heat Transfer Division of THE AMERICAN SOCIETY OF MECHANICAL ENGINEERS. Manuscript received by the Heat Transfer Division June 12, 1996; revision received November 5, 1996; Keywords: Flow Instability, Natural Convection, Porous Media. Associate Technical Editor: P. Simpkins.

total indicator reading). Since the Elastomer A has smaller mean and RMS roughness heights than Elastomer B, one would believe that the Elastomer A would possibly produce a larger contact conductance. However, these roughness scales are at least an order of magnitude smaller than the diameter range (10–45 μm) for typical pulp fibers (Smook, 1982). Because of the relative sizes of the fiber diameter and elastomer roughness scales, the surface of each elastomer (A and B) appears smooth to the paper sample.

In terms of the larger scale surface flatness characteristics (waviness and total indicator reading), Elastomer B is a much more uniform surface. Whereas the waviness of Elastomer B (7.1 μm) is of the same scale as the paper fiber diameter, the waviness of Elastomer A is almost 15 times greater than the waviness of Elastomer B. The 106.3 μm value of waviness for Elastomer A is also more than twice the size of typical paper fiber diameter. In addition, whereas the total indicator reading for Elastomer B (49.8 μm) continues to be of nearly the same scale as the paper fiber diameter, the total indicator reading for Elastomer A (346.4 μm) is seven times greater than Elastomer B. These larger scale surface flatness characteristics (waviness and total indicator reading), relative to the paper fiber diameter, suggest that the paper sample will see a "smooth" surface with Elastomer B and a relatively "rough" surface with Elastomer A. Therefore, better contact with the paper sample will occur with Elastomer B than Elastomer A. The effects of surface flatness properties is especially evident at higher pressures, where the differences in contact conductance between the two elastomers are even more pronounced. These data suggest that for relatively soft materials, such as the elastomers used in this study, the surface flatness characteristics are important parameters for thermal contact conductance.

As described previously, the minimum thermal contact conductance is equal to twice the overall joint conductance, when the resistance to heat transfer through the paper sample is ignored. These minimum curves are also shown in Fig. 3 for both interfaces. Note the proximity of the contact conductance curve for Elastomer A to the theoretical minimum, whereas, the theoretical curves for Elastomer B and the bare aluminum/paper cases deviate greatly from the theoretical minimum. For the bare aluminum/paper interface, the theoretical minimum is clearly a poor representation of the actual physics of the process. The resistance to heat transfer through the paper sample is of the same order of magnitude as the contact resistance with the aluminum flux meters on either side of the paper sample. Because of the effective contact between Elastomer B and the paper sample, the resistance to heat transfer through the paper sample is also of the same order of magnitude as the contact resistances at the elastomer paper interfaces. Therefore, the theoretical minimum is also a poor indicator of the actual process using Elastomer B. However, because the contact between Elastomer A and the paper sample is relatively poor, the contact resistance on either side of the paper sample is relatively greater than the resistance to heat transfer through the paper sample. Therefore, the theoretical minimum is a very good indicator of the thermal contact conductance for Elastomer A.

Acknowledgments

The authors thank Professor L. S. Fletcher and his research group for determining the thermal conductivity values and Mr. Jeff Wirtz for gathering much of the data. Financial support for this work was provided by Texas Instruments and the Drying Research Center at Texas A&M University.

References

Asensio, M. C., 1992, "Simulation of Paper Drying Systems With Incorporation of an Experimental Drum/Paper Thermal Contact Conductance Relationship," M. S. Thesis, Texas A&M University, College Station, TX.

Asensio, M. C., Seyed-Yagoobi, J., and Fletcher, L. S., 1993, "Thermal Contact Conductance of a Moist Paper Handsheet/Metal Interface for Paper Drying Applications," ASME JOURNAL OF HEAT TRANSFER, Vol. 115, pp. 1051–1053.

Federal Products Corporation, 1991, "Instruction Manual for Surfanalyzer 5000-400," Providence, RI.

Kerekes, R. J., 1980, "A Simple Method for Determining the Thermal Conductivity and Contact Resistance of Paper," TAPPI Journal, Vol. 63, No. 9, pp. 137–140.

Kline, S. J., and McClintock, F. A., 1953, "Describing Uncertainties in Single Sample Experiments," *Mechanical Engineering*, Vol. 75, pp. 3–8.

Ng, K., 1990, "Thermal Contact Conductance of a Paper Handsheet/Metal Interface," M.S. Thesis, Texas A&M University, College Station, TX.

Seyed-Yagoobi, J., Ng, K. H., and Fletcher, L. S., 1992, "Thermal Contact Conductance of a Bone-Dry Paper Handsheet/Metal Interface," ASME JOURNAL OF HEAT TRANSFER, Vol. 114, pp. 326–330.

Smook, G. A., 1982, "Handbook for Pulp and Paper Technologists," Technical Association of the Pulp and Paper Industry, Atlanta, GA.

Whitby, G. S., 1954, *Synthetic Rubber*, John Wiley & Sons, New York, NY.

Convection in a Porous Medium Induced by an Inclined Temperature Gradient With Mass Flow

Z. Qiao[1] and P. N. Kaloni[1]

Nomenclature

a = dimensionless overall horizontal wave number
D = differential operator, d/dz
g = gravitational acceleration
H = layer height
$\mathbf{i}, \mathbf{j}, \mathbf{k}$ = unit vectors in the x, y and z-directions, respectively
K = permeability
l = dimensionless wave number in the y-direction
P, p = dimensionless pressure/perturbation pressure
p_s = dimensionless basic-state pressure
q = horizontal mass flow rate
Q = dimensionless horizontal mass flow rate
R_E = critical vertical Rayleigh number in energy stability analysis
R_H = horizontal Rayleigh number
R_L = critical vertical Rayleigh number in linear stability analysis
R_V = vertical Rayleigh number
T = dimensionless temperature
T_s = dimensionless basic-state temperature
t = dimensionless time
$\mathbf{u}, \mathbf{v}$ = dimensionless perturbation velocity vector/velocity vector
$\mathbf{u}_s$ = dimensionless basic-state velocity vector
x, y, z = dimensionless Cartesian coordinates

Greek symbols

α_m = thermal diffusivity
β_T = horizontal temperature gradient
γ_T = coefficient of volume expansion
θ = dimensionless perturbation temperature
κ = thermal diffusivity
μ = dynamic viscosity
ρ_0 = density at the reference temperature

[1] Department of Mathematics and Statistics, University of Windsor, Windsor, Ontario, Canada N9B 3P4.

Contributed by the Heat Transfer Division of THE AMERICAN SOCIETY OF MECHANICAL ENGINEERS. Manuscript received by the Heat Transfer Division June 12, 1996; revision received November 5, 1996; Keywords: Flow Instability, Natural Convection, Porous Media. Associate Technical Editor: P. Simpkins.

Introduction

The linear stability of convective flow in a porous medium, which is induced by an inclined temperature gradient in a shallow horizontal layer, was first studied by Weber (1974) and then by Nield (1991). The effect of nonzero horizontal mass flow rate was included by Nield (1990). Nield et al. (1993) and Manole et al. (1994) have investigated the linear stability problems for convection in a porous medium induced by inclined thermal and solutal gradients without/with nonzero horizontal mass flow rate. All of these studies are based on low-order Galerkin approximations. However, in a recent paper Nield (1994) noted that his earlier treatment of the problem (Nield, 1991), based upon a low-order Galerkin approximation, was not satisfactory, particularly as the horizontal temperature gradient increased. Nield (1994) then used a higher order Galerkin approximation and found considerably different results. In particular, he noted that the values of the critical vertical Rayleigh number, rather than increasing indefinitely with the increase of the horizontal Rayleigh number, reached a maximum and then decreased to zero. That is to say, beyond a certain value the effect of horizontal Rayleigh number is changed from stabilizing to destabilizing. We note that Manole et al. (1994), in their calculations of the double diffusive case, have also speculated on the deficiency of low-order Galerkin approximations. Kaloni and Qiao (1997) have presented a nonlinear stability analysis for the title problem in the absence of mass flow via the energy method. These authors have used the compound matrix method to solve the associated eigenvalue problem and the golden-section search method to carry out the maximum and the minimum routines (cf. Lindsay and Straughan, 1992). They have also carried out the linear stability calculations and their findings compare reasonably well with Nield's (1994) results. For the nonlinear stability problem, Kaloni and Qiao (1997) establish the possibility of subcritical instability.

Our purpose in this note is to generalize the discussion of Kaloni and Qiao (1997) by including the effect of a nonzero horizontal mass flow rate. We again employ the energy method for a nonlinear stability analysis. For the purpose of comparison, the calculations for linear stability are also carried out. We find that Nield's (1990) results are good only for lower values of the horizontal Rayleigh number and the mass flow rate, and that our linear stability results supplement those of Nield (1990) for a wide spectrum of the horizontal Rayleigh number and mass flow rate. The energy stability results are, however, new and they predict the possibility and range of subcritical instabilities.

Basic Equations

The model to be studied is the same as that considered by Nield (1990), and we follow the notation and scaling of Nield (1994). The porous medium occupies a layer of height H. The vertical temperature difference across the boundaries is ΔT, and there is also a nonzero mass flow rate q along the x-direction. We assume that the flow in the porous medium is governed by Darcy's law. For the density variation the Boussinesq approximation is assumed to be valid. Accordingly, following the nondimensionalization scheme of Nield (1994), the governing equations take the form of

$$\nabla \cdot \mathbf{v} = 0 \tag{1}$$

$$\mathbf{v} + \nabla P = T\mathbf{k} \tag{2}$$

$$\frac{\partial T}{\partial t} + (\mathbf{v}\cdot\nabla)T = \nabla^2 T \tag{3}$$

where $\mathbf{v}$, P, and T are the nondimensionalized seepage velocity, pressure, and temperature, respectively, and $\mathbf{k}$ is the unit vector in the z-direction. For rigid boundaries the nondimensional boundary conditions are

$$w = 0 \quad \text{and} \quad T = -(\pm \mathrm{R}_V/2) - \mathrm{R}_H x \quad \text{at} \quad z = \pm\tfrac{1}{2} \tag{4}$$

where R_V and R_H are vertical and horizontal Rayleigh numbers, respectively, and are defined as

$$\mathrm{R}_V = \rho_0 g \gamma_T K H \Delta T/\mu\alpha_m$$

and

$$\mathrm{R}_H = \rho_0 g \gamma_T K H^2 \beta_T/\mu\alpha_m. \tag{5}$$

Here ρ_0 is the density at the reference temperature, g is the gravitational acceleration, γ_T is the thermal expansion coefficient, K is the permeability of the medium, β_T is the horizontal temperature gradient, μ is the dynamic viscosity, and α_m is the thermal diffusivity. The basic steady-state solution $(\mathbf{u}_s, T_s, p_s)$ of Eqs. (1)–(3), satisfying the boundary condition (4), is (cf. Nield, 1990)

$$u_s = \mathrm{R}_H z + Q, \quad v_s = 0, \quad w_s = 0$$

$$T_s = -\mathrm{R}_H x - \mathrm{R}_V z + \mathrm{R}_H^2 f(z) + \mathrm{R}_H Q s(z)$$

$$\nabla p_s = T_s\mathbf{k} - \mathbf{u}_s \tag{6}$$

where

$$f(z) = \tfrac{1}{24}(z - 4z^3), \quad s(z) = \tfrac{1}{8}(1 - 4z^2) \tag{7}$$

and we have imposed the requirements that there is a nondimensional net mass flow rate Q in the x-direction, and there is no mass flow in the y-direction:

$$\int_{-1/2}^{1/2} u_s dz = Q, \quad \int_{-1/2}^{1/2} v_s dz = 0. \tag{8}$$

We now perturb the basic state solution as follows:

$$\mathbf{v} = \mathbf{u}_s + \mathbf{u}, \quad T = T_s + \theta, \quad P = p_s + p. \tag{9}$$

The perturbation equations then take the form

$$\nabla \cdot \mathbf{u} = 0 \tag{10}$$

$$\mathbf{u} + \nabla p = \theta\mathbf{k} \tag{11}$$

$$\frac{\partial \theta}{\partial t} + (\mathbf{u}\cdot\nabla)\theta = \nabla^2\theta - \mathbf{u}_s\cdot\nabla\theta - \mathbf{u}\cdot\nabla T_s \tag{12}$$

where $\mathbf{u}_s$ and T_s are given by (6). The corresponding boundary conditions become

$$w = 0 \quad \text{and} \quad \theta = 0 \quad \text{at} \quad z = \pm\tfrac{1}{2}. \tag{13}$$

Energy-Stability Analysis

A quick look at the system of Eqs. (10)–(12) tells us that the linearized system is not symmetric (self-adjoint) and hence the energy method will give a different result than the linear stability method. We define an energy functional as

$$E(t) = \frac{\xi}{2}\|\theta\|^2 \tag{14}$$

where ξ is a positive coupling parameter. We remark that the choice of this parameter is to make R_E, the critical vertical Rayleigh number in energy stability analysis, as large as possible. On multiplying (11) by $\mathbf{u}$, (12) by θ and integrating over V, using the boundary conditions and divergence theorem, we find

$$\frac{1}{2}\frac{d}{dt}\|\theta\|^2 = -\|\nabla\theta\|^2 - \langle(\mathbf{u}\cdot\nabla T_s)\theta\rangle, \tag{15}$$

$$\|\mathbf{u}\|^2 = \langle\theta w\rangle. \tag{16}$$

Here V denotes a typical periodic cell, i.e., $V = [0, a_x] \times [0, a_y] \times [-\frac{1}{2}, \frac{1}{2}]$, where a_x and a_y are the periods of the periodic functions in x- and y-directions, respectively, $\langle \cdot \rangle$ denotes the integration over V, and $\| \cdot \|$ denotes the $L^2(V)$ norm. The system of Eq. (15) and (16), along with (14), can be put in the form (cf. Straughan, 1992)

$$\frac{dE}{dt} = \mathcal{I} - \mathcal{D} \tag{17}$$

where

$$\mathcal{I} = -\xi \langle (\mathbf{u} \cdot \nabla T_s)\theta \rangle + \langle \theta w \rangle \tag{18}$$

$$\mathcal{D} = \xi \|\nabla \theta\|^2 + \|\mathbf{u}\|^2. \tag{19}$$

We now define

$$m = \max_{\mathcal{H}} \frac{\mathcal{I}}{\mathcal{D}} \tag{20}$$

where $\mathcal{H}$ is the space of admissible solutions. On combining (17) with (18)–(20), and by using Poincaré inequality, we can infer, for $0 < m < 1$, that

$$\frac{dE}{dt} \leq -2\pi^2(1 - m)E. \tag{21}$$

Inequality (21) clearly indicates that for $0 < m < 1$, $E(t) \to 0$, at least exponentially as $t \to \infty$. Since $E(t)$ in (14) does not contain the term $\|\mathbf{u}\|^2$, the kinetic energy term for the velocity, it is worthwhile checking into what happens to $\|\mathbf{u}\|^2$ as $t \to \infty$. A use of Cauchy-Schwartz inequality on (16) implies that

$$\|\mathbf{u}\|^2 \leq \|\theta\|^2. \tag{22}$$

Thus (14) and (22) clearly indicate that decay of $E(t)$ ensures the decay of $\|\mathbf{u}\|^2$.

We now return to (20) and consider the maximum problem at the critical argument $m = 1$. The associated Euler-Lagrange equations become

$$-\xi \nabla T_s \cdot \mathbf{u} + w + 2\xi \nabla^2 \theta = 0 \tag{23}$$

$$\xi \nabla T_s \theta - \theta \mathbf{k} + 2\mathbf{u} = \nabla \omega \tag{24}$$

where ω is a Lagrange multiplier introduced since $\mathbf{u}$ is solenoidal. On taking curlcurl of (24), and then taking the third component of resulting equation we find

$$2\nabla^2 w - \nabla_1^2(h\theta) + \xi \mathrm{R}_H \frac{\partial^2 \theta}{\partial x \partial z} = 0 \tag{25}$$

where $\nabla_1^2 = \partial^2/\partial x^2 + \partial^2/\partial y^2$ and

$$h = 1 + \xi(\mathrm{R}_V - \mathrm{R}_H^2 f_1 + \mathrm{R}_H Q z), \quad f_1 = \tfrac{1}{24}(1 - 12z^2). \tag{26}$$

Also (23) and (24) can be written as

$$\xi \mathrm{R}_H u + hw + 2\xi \nabla^2 \theta = 0 \tag{27}$$

$$-\xi \mathrm{R}_H \theta + 2u = \frac{\partial \omega}{\partial x}. \tag{28}$$

Nield (1990) has pointed out that the longitudinal mode is the most favorable mode of disturbances for this problem. Our calculations for linear stability also confirm that the most unstable mode is the steady longitudinal mode. We thus, from now on restrict our attention to this situation. We perform the standard normal mode analysis and look for the solution of (25), (27), and (28) in the form

$$[u, w, \theta, \omega] = [u(z), w(z), \theta(z), \omega(z)] \exp[ily].$$

The corresponding eigenvalue problem can, after some rearrangement of terms, be written as

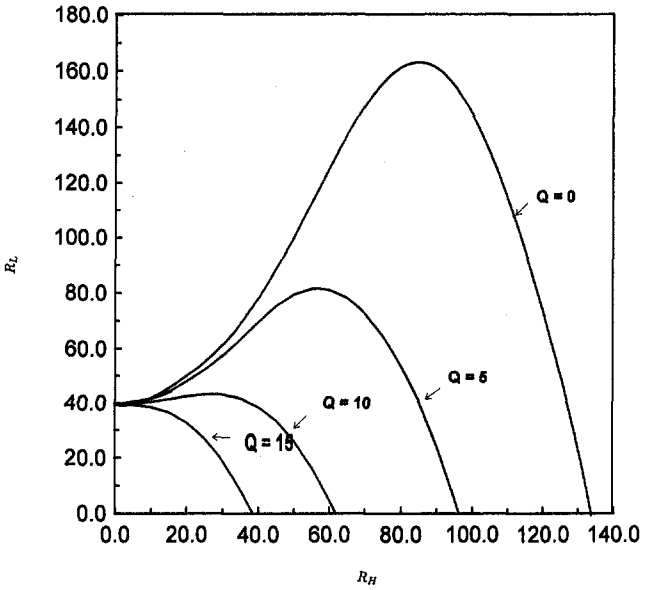

Fig. 1 Linear stability results

$$D^2 w = h_1 w + h_2 \theta \tag{29}$$

$$D^2 \theta = h_3 w + h_4 \theta \tag{30}$$

where $D = d/dz$, $a^2 = l^2$. The variables $h_1, \ldots, h_4$, which are function of z, are given as

$$h_1 = a^2, \quad h_2 = -\frac{a^2}{2} h$$

$$h_3 = -\frac{h}{2\xi}, \quad h_4 = a^2 - \frac{\xi}{4} \mathrm{R}_H^2 \tag{31}$$

and in which h is defined in (26). The relevant boundary conditions are

$$w = \theta = 0 \quad \text{at} \quad z = \pm \tfrac{1}{2}. \tag{32}$$

We consider R_V as the eigenvalue with the remaining variables as parameters. The critical vertical Rayleigh number is defined by

$$\mathrm{R}_E = \max_{\xi} \min_{a^2} \mathrm{R}_V(R_H, a^2, \xi, Q). \tag{33}$$

On letting $x_1 = w$, $x_2 = Dw$, $x_3 = \theta$, and $x_4 = D\theta$ the system (29)–(30) can be written in the matrix form as

$$\dot{\mathbf{X}} = \mathbf{A}\mathbf{X} \tag{34}$$

where $\mathbf{X} = (x_1, x_2, x_3, x_4)^{\perp}$ and $\mathbf{A}$ is the coefficient matrix defined by

$$\mathbf{A} = \begin{bmatrix} 0 & 1 & 0 & 0 \\ h_1 & 0 & h_2 & 0 \\ 0 & 0 & 0 & 1 \\ h_3 & 0 & h_4 & 0 \end{bmatrix}.$$

The boundary conditions now take the form

$$x_1 = x_3 = 0, \quad \text{at} \quad z = \pm \tfrac{1}{2}. \tag{36}$$

We next employ the compound matrix method and carry out the maximization and minimization by the golden-section search method (cf. Lindsay and Straughan, 1992).

Numerical Results and Discussions

The numerical calculations are carried out for determining the critical values of vertical Rayleigh number R_V in both linear stability and energy stability theories. These are denoted by R_L and R_E, respectively. Figure 1 displays the results for linear

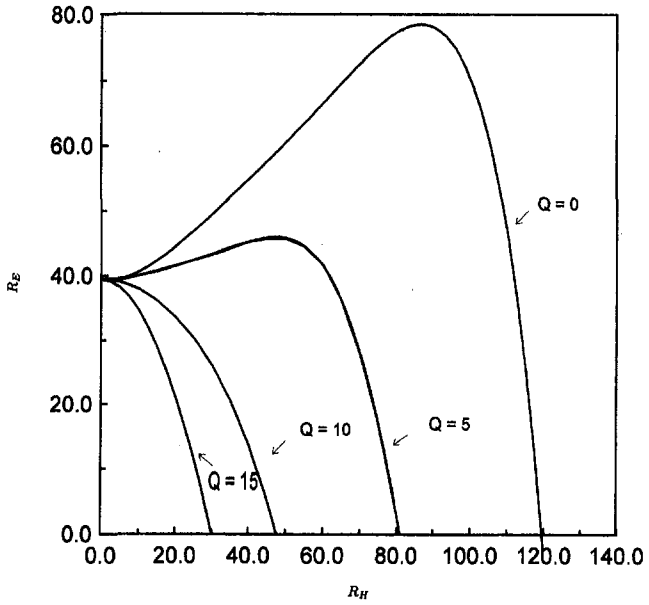

Fig. 2 Energy stability results

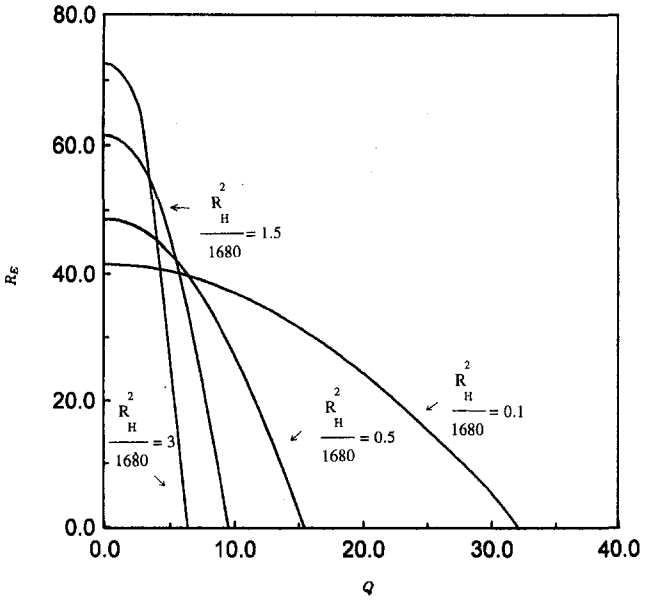

Fig. 4 Energy stability results

theory and gives the plot of R_L against the horizontal Rayleigh number R_H for various values of the mass flow rate Q. We note that as Q increases the instability also increases. For low values of Q we find that instability depends upon the R_H values. A smaller value of R_H has a stabilizing effect, whereas a higher value has a destabilizing effect. For higher values of Q the effect of R_H, however, is immaterial; in fact, for $Q > 15$ we note that the effect is always destabilizing. Figure 2 shows the corresponding energy stability results. Here, in comparison to the linear case we find that for comparative values of R_H and Q, the stability regions are much smaller. We also observe that for very high values of Q, instability is possible even in the absence of a vertical temperature gradient.

Figure 3 and Figure 4 show the effect of varying R_H on R_L and R_E, respectively. Figure 3 presents the plots of R_L against Q for varying R_H from a linear stability analysis. We have chosen the values of R_H so as to match Nield's calculations. A comparison with Nield's (1990) results clearly indicates the limitation of low-order Galerkin approximations. We note the similarity in the values of our calculations with Nield's calculations for low values of Q, but only our calculations give the complete spectrum of results. We also find that our results are very close to those of Nield at lower values of R_H. For higher values of R_H the difference between the two methods of calculation becomes quite apparent. We find that when R_H increases, its stabilizing effect decreases with an increase in Q. As expected the corresponding range of values from the energy method are much smaller even though the overall pattern is similar. This is clearly seen in Fig. 4.

To sum up, we conclude that increasing the mass flow rate Q has a destabilizing effect on R_L and R_E and that, at lower values of Q, the effect of R_H on R_L and R_E changes from stabilizing to destabilizing as R_H values are increased. We also find that the calculated stability limits from energy theory are smaller than the instability limits of linear stability values and hence there is the possibility of subcritical instability, which needs to be further analyzed. This behavior is observed in all the cases considered.

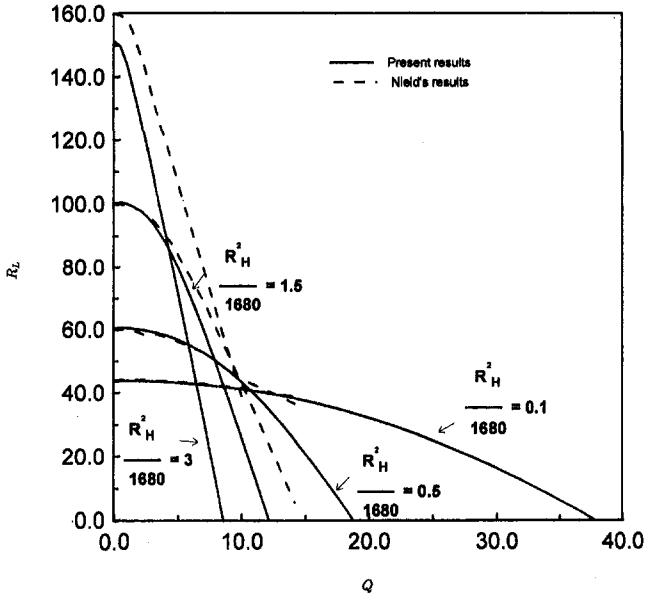

Fig. 3 Linear stability results and comparison with Nield's results (1990)

Acknowledgement

The work reported in this paper has been supported by Grant No. A7728 of NSERC of Canada. The authors gratefully acknowledge the support thus received.

References

Kaloni, P. N., and Qiao, Z. C., 1997, "Nonlinear Stability of Convection in a Porous Medium With Inclined Temperature Gradient," *Int. J. Heat and Mass Transfer*, Vol. 40(7), pp. 1611–1615.

Lindsay, K. A., and Straughan, B., 1992, "Penetrative Convection in a Micropolar Fluid," *Int. J. Engng. Sci.*, Vol. 30 (12), pp. 1683–1702.

Manole, D. M., Lage, J. L., and Nield, D. A., 1994, "Convection Induced by Inclined Thermal and Solutal Gradients, With Horizontal Mass Flow, in a Shallow Horizontal Layer of a Porous Medium," *Int. J. Heat Mass Transfer*, Vol. 37 (14), pp. 2047–2057.

Nield, D. A., 1990, "Convection in a Porous Medium With Inclined Temperature Gradient and Horizontal Mass Flow," *Heat Transfer 1990: Proceedings of the Ninth International Heat Transfer Conference, Jerusalem*, G. Hetsroni, ed., Hemisphere, New York, Vol. 5, pp. 153–158.

Nield, D. A., 1991, "Convection in a Porous Medium With Inclined Temperature Gradient," *Int. J. Heat Mass Transfer*, Vol. 34 (1), pp. 87–92.

Nield, D. A., Manole, D. M., and Lage, J. L., 1993, "Convection Induced by Inclined Thermal and Solutal Gradients in a Shallow Horizontal Layer of a Porous Medium," *J. Fluid Mech.*, Vol. 257, pp. 559–574.

Nield, D. A., 1994, "Convection in a Porous Medium With Inclined Temperature Gradient: Additional Results," *Int. J. Heat Mass Transfer*, Vol. 37 (18), pp. 3021–3025.

Straughan, B., 1992, *The Energy Method, Stability, and Nonlinear Convection*, Springer-Verlag, Berlin-Heidelberg-New York.

Weber, J. E., 1974, "Convection in a Porous Medium With Horizontal and Vertical Temperature Gradients," *Int. J. Heat Mass Transfer*, Vol. 17, pp. 241–248.

Free Convection Heat Transfer From Wire-and-Tube Heat Exchangers

G. Tanda[1] and L. Tagliafico[1]

Nomenclature

c_p = constant-pressure specific heat, J kg^{-1} K^{-1}
d = outer diameter, m
g = acceleration of gravity, m s^{-2}
H = exchanger height, m
h = average heat transfer coefficient, Wm^{-2} K^{-1}
k = thermal conductivity, W m^{-1} K^{-1}
M = mass flow rate, kg s^{-1}
Nu = $(=hH/k_a)$, Nusselt number
p = pitch, m
q = heat transfer rate, W
Ra = $((\beta\rho^2 c_p/\mu k)_a g(T_t - T_\infty)H^3)$, Rayleigh number
S = heat transfer surface area, m^2
s = $(p - d)/d$, spacing-to-diameter ratio
T = temperature, K

Greek symbols

β = thermal expansion coefficient, K^{-1}
η = fin efficiency
μ = dynamic viscosity, kg m^{-1} s^{-1}
ρ = density, kg m^{-3}

Subscripts

a = denoting physical properties of air, to be evaluated at $(T_t + T_\infty)/2$
c = free convection
ex = exchanger
f = fluid (water)
r = radiation
t = tube
tot = total (tubes + wires)
w = wire
∞ = ambient air

Introduction

Extended-surface heat exchangers consisting of wires attached to tubes are widely used, especially in small, air-cooled refrigeration appliances (e.g., domestic food refrigeration and supermarket display cabinets). In these fields the device is used to condense the refrigerant flowing inside the tubes.

Despite the widespread use of these exchangers, only a few early works dealing with heat transfer characteristics are available in the literature. Witzell and Fontaine (1957a, b) were among the first to experimentally investigate heat transfer from wire-and-tube heat exchangers. Further contributions were made by Cyphers et al. (1959), Witzell et al. (1959), Collicott et al. (1963), and Cavallini and Trapanese (1970). To the authors' knowledge, a heat transfer relationship including the effects of the numerous geometrical and operating parameters affecting the phenomenon has not yet been developed.

The purpose of this note is to present a correlation giving the natural-convection heat transfer from the external surface of the heat exchanger to the ambient air.

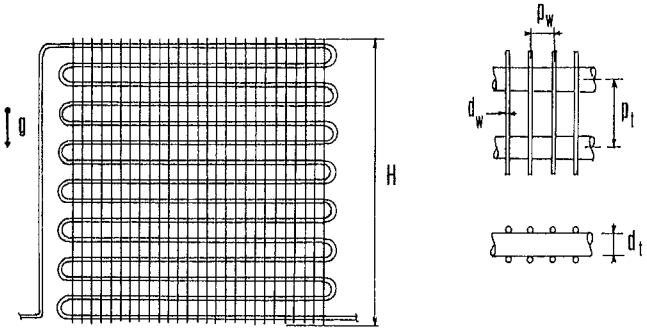

Fig. 1 Sketch of the wire-and-tube heat exchanger

Analysis

The heat exchanger considered here consists of a tube, wound in a serpentine manner, with wires welded to both sides in a direction normal to the tubes, as shown in Fig. 1. The wires act as extended surfaces that increase the heat transfer from the wall to the external environment. The geometry is defined by the overall height H of the exchanger, the external diameters d_t and d_w of tube and wires, the tube pitch p_t, and the wire pitch p_w. Further geometric parameters could be introduced, such as the angle of inclination of the exchanger and the distances between the exchanger and confining parallel plates on one or both sides. In this study, the heat exchanger was vertically oriented without confining walls (free-standing configuration). The operating conditions of the heat exchanger are defined by the mean temperature difference between the wall and the ambient air.

When a hot fluid circulates inside the tube, heat transfer between the fluid and the external environment takes place. The heat is transferred from the tube wall to the external environment by natural convection and radiation. From the practical standpoint, the main interest is the combined-mode heat transfer coefficient. However, for a better understanding of the complex physical phenomena involved, the combined-mode heat transfer must be subdivided into its convective and radiant components.

The total heat transfer rate q_{tot} from the external walls of the exchanger to the surroundings is given by

$$q_{tot} = q_c + q_r \tag{1}$$

where subscripts c and r denote convective and radiant components, respectively. The convective heat transfer rate may be expressed as

$$q_c = hS_{tot}(T_{ex} - T_\infty). \tag{2}$$

In Eq. (2) h is the average heat transfer coefficient, S_{tot} is the total heat transfer surface area, T_∞ is the ambient air temperature, and T_{ex} represents the weighted average of the surface temperature on the external side of the exchanger, which can be evaluated as follows:

$$T_{ex} = (S_t T_t + S_w T_w)/S_{tot} \tag{3}$$

where T_t, S_t and T_w, S_w are the mean external surface tempera-

[1] Dipartimento di Termoenergetica e Condizionamento Ambientale, Università di Genova, via all'Opera Pia 15a, I-16145 Genova, Italy; E-mail: ditec@unige.it

Contributed by the Heat Transfer Division of THE AMERICAN SOCIETY OF MECHANICAL ENGINEERS. Manuscript received by the Heat Transfer Division February 6, 1996; revision received January 17, 1997; Keywords: Heat Exchangers, Natural Convection, Refrigeration. Associate Technical Editor: T. Rabas.

Nield, D. A., 1994, "Convection in a Porous Medium With Inclined Temperature Gradient: Additional Results," *Int. J. Heat Mass Transfer*, Vol. 37 (18), pp. 3021–3025.

Straughan, B., 1992, *The Energy Method, Stability, and Nonlinear Convection*, Springer-Verlag, Berlin-Heidelberg-New York.

Weber, J. E., 1974, "Convection in a Porous Medium With Horizontal and Vertical Temperature Gradients," *Int. J. Heat Mass Transfer*, Vol. 17, pp. 241–248.

Free Convection Heat Transfer From Wire-and-Tube Heat Exchangers

G. Tanda[1] and L. Tagliafico[1]

Nomenclature

c_p = constant-pressure specific heat, J kg^{-1} K^{-1}
d = outer diameter, m
g = acceleration of gravity, m s^{-2}
H = exchanger height, m
h = average heat transfer coefficient, Wm^{-2} K^{-1}
k = thermal conductivity, W m^{-1} K^{-1}
M = mass flow rate, kg s^{-1}
Nu = $(=hH/k_a)$, Nusselt number
p = pitch, m
q = heat transfer rate, W
Ra = $((\beta\rho^2 c_p/\mu k)_a g(T_t - T_\infty)H^3)$, Rayleigh number
S = heat transfer surface area, m^2
s = $(p - d)/d$, spacing-to-diameter ratio
T = temperature, K

Greek symbols

β = thermal expansion coefficient, K^{-1}
η = fin efficiency
μ = dynamic viscosity, kg m^{-1} s^{-1}
ρ = density, kg m^{-3}

Subscripts

a = denoting physical properties of air, to be evaluated at $(T_t + T_\infty)/2$
c = free convection
ex = exchanger
f = fluid (water)
r = radiation
t = tube
tot = total (tubes + wires)
w = wire
∞ = ambient air

Introduction

Extended-surface heat exchangers consisting of wires attached to tubes are widely used, especially in small, air-cooled refrigeration appliances (e.g., domestic food refrigeration and supermarket display cabinets). In these fields the device is used to condense the refrigerant flowing inside the tubes.

Despite the widespread use of these exchangers, only a few early works dealing with heat transfer characteristics are available in the literature. Witzell and Fontaine (1957a, b) were among the first to experimentally investigate heat transfer from wire-and-tube heat exchangers. Further contributions were made by Cyphers et al. (1959), Witzell et al. (1959), Collicott et al. (1963), and Cavallini and Trapanese (1970). To the authors' knowledge, a heat transfer relationship including the effects of the numerous geometrical and operating parameters affecting the phenomenon has not yet been developed.

The purpose of this note is to present a correlation giving the natural-convection heat transfer from the external surface of the heat exchanger to the ambient air.

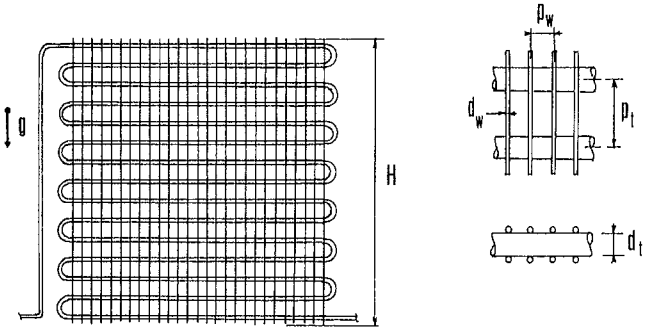

Fig. 1 Sketch of the wire-and-tube heat exchanger

Analysis

The heat exchanger considered here consists of a tube, wound in a serpentine manner, with wires welded to both sides in a direction normal to the tubes, as shown in Fig. 1. The wires act as extended surfaces that increase the heat transfer from the wall to the external environment. The geometry is defined by the overall height H of the exchanger, the external diameters d_t and d_w of tube and wires, the tube pitch p_t, and the wire pitch p_w. Further geometric parameters could be introduced, such as the angle of inclination of the exchanger and the distances between the exchanger and confining parallel plates on one or both sides. In this study, the heat exchanger was vertically oriented without confining walls (free-standing configuration). The operating conditions of the heat exchanger are defined by the mean temperature difference between the wall and the ambient air.

When a hot fluid circulates inside the tube, heat transfer between the fluid and the external environment takes place. The heat is transferred from the tube wall to the external environment by natural convection and radiation. From the practical standpoint, the main interest is the combined-mode heat transfer coefficient. However, for a better understanding of the complex physical phenomena involved, the combined-mode heat transfer must be subdivided into its convective and radiant components.

The total heat transfer rate q_{tot} from the external walls of the exchanger to the surroundings is given by

$$q_{tot} = q_c + q_r \tag{1}$$

where subscripts c and r denote convective and radiant components, respectively. The convective heat transfer rate may be expressed as

$$q_c = hS_{tot}(T_{ex} - T_\infty). \tag{2}$$

In Eq. (2) h is the average heat transfer coefficient, S_{tot} is the total heat transfer surface area, T_∞ is the ambient air temperature, and T_{ex} represents the weighted average of the surface temperature on the external side of the exchanger, which can be evaluated as follows:

$$T_{ex} = (S_t T_t + S_w T_w)/S_{tot} \tag{3}$$

where T_t, S_t and T_w, S_w are the mean external surface tempera-

[1] Dipartimento di Termoenergetica e Condizionamento Ambientale, Università di Genova, via all'Opera Pia 15a, I-16145 Genova, Italy; E-mail: ditec@unige.it

Contributed by the Heat Transfer Division of THE AMERICAN SOCIETY OF MECHANICAL ENGINEERS. Manuscript received by the Heat Transfer Division February 6, 1996; revision received January 17, 1997; Keywords: Heat Exchangers, Natural Convection, Refrigeration. Associate Technical Editor: T. Rabas.

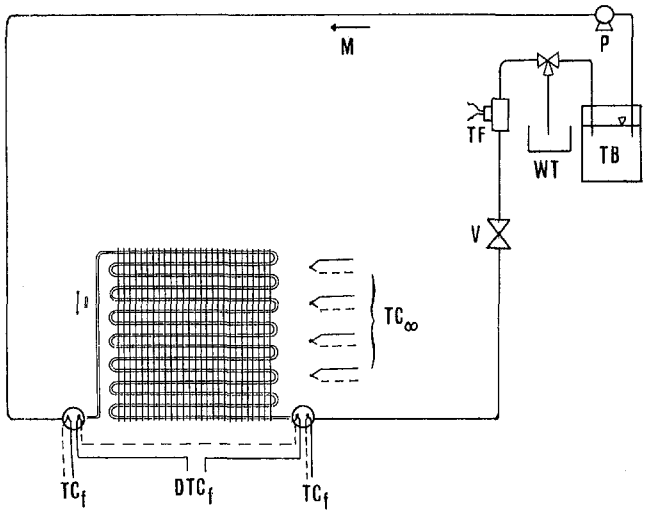

Fig. 2 Schematic drawing of the experimental apparatus where: *P* = water pump; *TB* = thermostatic bath; *TF* = turbine flow meter; *WT* = weigh tank; *V* = valve; *TC* = thermocouple; *DTC* = differential thermocouple.

ture and the heat transfer surface area of the tube and wires, respectively. If the fin efficiency η_w is introduced under the assumption of uniform heat transfer coefficient along the wire surface, one obtains

$$\eta_w = (T_w - T_\infty)/(T_t - T_\infty). \tag{4}$$

Equations (2–4) lead to

$$q_c = h(T_t - T_\infty)(S_t + \eta_w S_w). \tag{5}$$

Experiments

Experiments were performed in order to obtain a relationship for the convective heat transfer coefficient as a function of the geometric and operating parameters. The apparatus is sketched in Fig. 2. A hot water flow coming from a thermostatic bath circulates steadily inside the heat exchanger tube. From an overall energy balance for the heat exchanger, it follows that

$$q_{\text{tot}} = Mc_{p,f}(T_{f,\text{in}} - T_{f,\text{out}}) \tag{6}$$

where $T_{f,\text{in}}$ and $T_{f,\text{out}}$ are the fluid temperatures at the inlet and outlet of the exchanger, respectively, while M is the water mass flow rate. The heat exchangers tested were coated with a low-emissivity paint in order to minimize the radiant heat transfer. The emissivity of the paint, measured by a radiometric apparatus (Misale et al., 1989), was found to be 0.35. A simple model based on the configuration factor algebra under the assumptions of gray, diffuse, and isothermal surfaces has been developed in order to calculate the radiant component q_r and to subtract it from the overall heat transfer. According to Eqs. (5–6), the convective heat transfer rate from the outside walls of the exchanger to the environment is given by

$$q_c = Mc_{p,f}(T_{f,\text{in}} - T_{f,\text{out}}) - q_r = h(T_t - T_\infty)(S_t + \eta_w S_w). \tag{7}$$

Errors in the q_r calculation were estimated to be within 15 percent. Taking into account the relative role played by radiation heat transfer (12–35 percent of q_{tot}), the resulting error in the evaluated convective heat transfer rate q_c is about 5 percent in the worst case (2.5 percent on average).

Since the thermal resistances associated with the forced convection of water inside the tube and with the conduction through the tube wall are typically two to three orders of magnitude lower than the air-side thermal resistance, the tube temperature can be assumed equal to the water temperature; with reference to the entire exchanger, the mean external surface temperature of the tube T_t can be estimated as the mean between $T_{f,\text{in}}$ and $T_{f,\text{out}}$. In conclusion, the average heat transfer coefficient of the exchanger can be expressed as

$$h = \frac{Mc_{p,f}(T_{f,\text{in}} - T_{f,\text{out}}) - q_r}{\left[\dfrac{(T_{f,\text{in}} + T_{f,\text{out}})}{2} - T_\infty\right](S_t + \eta_w S_w)}. \tag{8}$$

Equation (8) has been used to evaluate the average heat transfer coefficient for each experimental run.

The mass flow rate M has been measured by means of a precalibrated (within ± 1 percent) turbine flow meter. Inlet and outlet water temperatures were measured by means of two independent thermocouples (calibrated to ±0.1 K), while their difference was also measured directly by means of a differential thermocouple. These thermocouples were placed inside tube segments thermally insulated on the outside in order to prevent significant water temperature gradients in the radial direction, and thus to minimize the influence of the radial location of the probe on the detected water temperature. Furthermore, the leads were run about 30 mm along the flow direction in the tube in order to reduce conduction errors. The temperature of ambient air T_∞ was evaluated as the average of the values measured by four shielded, calibrated (to ±0.1 K) thermocouples located at different elevations. The fin efficiency η_w was carefully determined by mapping the surface thermal field by means of infrared thermography in order to obtain the average surface temperature of wires by integration of local values. In particular, the η_w values for the heat exchangers tested were found to be in the range from 0.65 to 1.

The laboratory in which the experiments were performed was a large isolated room. All instrumentation was located in an adjacent room. For each experiment, the temperature difference $(T_{f,\text{in}} - T_{f,\text{out}})$ was kept within a small percentage of the mean wall-to-air temperature difference (generally lower than 15 percent) by properly adjusting a flow control valve. This procedure assures the best compromise between the desired condition of quasi-isothermal tube wall (as occurs when a fluid condenses inside the tube) and the accuracy requirements in the heat transfer rate measurement (greater accuracy can be obtained at higher water temperature drops). The experimental uncertainty in h values, evaluated according to the procedure outlined by Moffat (1988), turned out to be ±7 percent.

Heat Transfer Correlation

The authors have developed a mathematical relationship for the free convection heat transfer from the heat exchanger to the ambient air that exhibits the proper behavior for both very tightly and very sparse vertical wires attached to the array of horizontal tubes. The relationship, expressed as the Nusselt number $\text{Nu}_H = hH/k_a$, has the following form:

$$\text{Nu}_H = 0.66(\text{Ra}_H H/d_t)^{0.25} \times \{1 - [1 - 0.45(d_t/H)^{0.25}] \exp(-s_w/\varphi)\} \tag{9}$$

where

$$\text{Ra}_H = \left(\frac{\beta\rho^2 c_p}{\mu k}\right)_a g(T_t - T_\infty)H^3$$

is the Rayleigh number, and

$$\varphi = (A/H)^{0.4} s_w^{0.9} s_t^{-1.0} + (A/H)^{0.8}[B/(T_t - T_\infty)]^{0.5} s_w^{-1.5} s_t^{-0.5}$$

where $s_t = (p_t - d_t)/d_t$, $s_w = (p_w - d_w)/d_w$, $A = 28.2$ m, and $B = 264$ K.

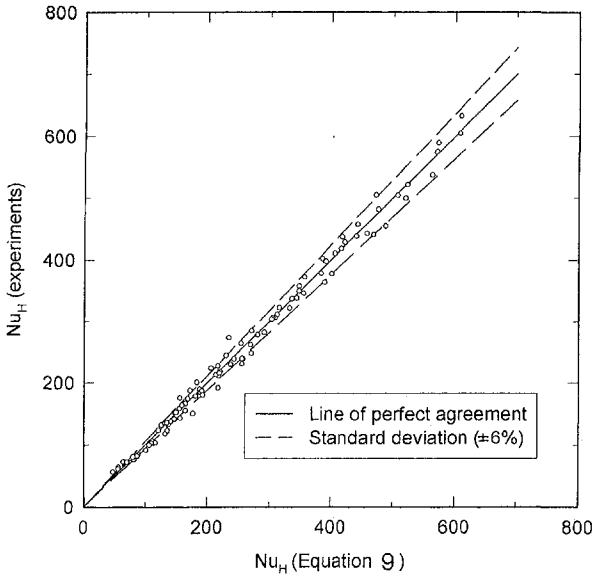

Fig. 3 Experimental Nusselt number versus Nusselt number given by Eq. (9)

The heat transfer coefficient given by Eq. (9) fits the experimental data with a standard deviation of ±6 percent, as shown in Fig. 3.

The relationship respects the limiting solutions for large and small values of the parameter s_w, which is the most important factor affecting the heat transfer performance. As s_w approaches zero, the condenser becomes a double array of vertical wires attached to one another, with the tube sandwiched in between. In this condition the thermal behavior of the external side is similar to that of a constant-temperature flat plate, while heat transfer from internal sides is completely inhibited. Therefore, the resulting Nusselt number is given by

$$\mathrm{Nu}_H = 0.297\ \mathrm{Ra}_H^{0.25} \tag{10}$$

which corresponds, within 1 percent, to half of the Nusselt number for a constant temperature flat plate (Mc Adams, 1954). As s_w tends to infinity, the geometry degenerates into a vertical array of horizontal tubes. The resulting Nusselt number is given by

$$\mathrm{Nu}_{d_t} = 0.66\ \mathrm{Ra}_{d_t}^{0.25} \tag{11}$$

where the tube diameter d_t is the characteristic length. Equation (11) has been determined experimentally on the basis of 27 tests conducted on nine heat exchangers without wires and with s_t ranging from 4.3 to 14.6, and H ranging from 0.45 m to 1.1 m.

The empirical expression for φ has been introduced to correlate the heat transfer coefficient with the main parameters in the intermediate range of s_w values. Exponents and coefficients have been adjusted on the basis of 99 tests on 33 wire-and-tube heat exchangers with different geometric characteristics.

All air physical properties are to be evaluated at the reference temperature here defined as $(T_t + T_\infty)/2$. The parameter ranges in which the proposed relationship has been derived are the following: $4.3 < s_t < 14.6$; $1.7 < s_w < 7.8$; $0.45\ \mathrm{m} < H < 1.1\ \mathrm{m}$; and $17\ \mathrm{K} < (T_t - T_\infty) < 48\ \mathrm{K}$.

Practical Usefulness of Results

Equation (5), combined with the relationship (9) for the Nusselt number, enables the convective heat transfer rate from tube-and-wire heat exchangers to be evaluated. The proposed analysis is particularly suitable for determining either the heat transfer performance of an existing (already sized) exchanger (rating problem) or the geometrical characteristics of a new exchanger with specified heat transfer performance (sizing problem). Therefore, it constitutes a powerful tool for the design of wire-and-tube heat exchangers.

It should be pointed out that the use of Eq. (5) requires the knowledge of η_w, which depends on the temperature distribution along the wire. A simplified approach can be employed to evaluate η_w without the availability of detailed local temperature measurements along the wire surface. In fact, according to the conventional one-dimensional fin model, η_w can be expressed as

$$\eta_w = \{\tanh\,(mp_t/2)\}/(mp_t/2) \tag{12}$$

where $m = \{4h_w/(k_w d_w)\}^{1/2}$ and subscripts w and t refer to wires and tubes, respectively.

Experiments showed that replacing h_w by the estimated h values, η_w values calculated from Eq. (12) were in close agreement with those reconstructed by means of the infrared thermographic measurements (Eq. 4). In particular, typical differences of 4 percent between the calculated and the reconstructed (by means of thermography) η_w values were found. This demonstrates the suitability of the one-dimensional fin model assumption for the evaluation of η_w.

Conclusions

A Nusselt number correlation to predict free-convection heat transfer from a vertical wire-and-tube heat exchanger to ambient air is presented. The relationship takes into account the effects of the most important geometric and operating parameters: the spacing-to-diameter ratios of tubes and wires, the overall height of the exchanger, and the mean tube-to-air temperature difference. Owing to the form of the mathematical expression, the limiting cases of very tightly and very sparse vertical wires attached to the tubes (very low s_w and very high s_w) are successfully correlated. In the intermediate range of s_w values, an empirical expression (φ) has been developed in order to fit the experimental data obtained on numerous heat exchangers with a standard deviation of ±6 percent.

Acknowledgements

This work has been supported by the Italian Government (grant on refrigeration appliances, MURST 60 percent) and by Bundy S.P.A in Busalla, Genova (DITEC contract n.121/94).

References

Cavallini, A., and Trapanese, G., 1970, "Convezione naturale in aria per i condensatori a tubo e fili," *La Termotecnica,* Vol. 24, No. 4, pp. 184–187.

Collicott, H. E., Fontaine, W. E., and Witzell, O. W., 1963, "Radiation and Free Convection Heat Transfer From Wire and Tube Heat Exchangers," *ASHRAE Journal,* Vol. 5, No. 12, pp. 79–83.

Cyphers, J. A., Cess, R. D., and Somers E. V., 1959, "Heat Transfer Character of Wire-and-Tube Heat Exchangers," *ASHRAE Journal,* Vol. 1, No. 5, pp. 86–110.

McAdams, W. H., 1954, *Heat Transmission,* McGraw-Hill Book Co., New York.

Misale, M., Pisoni C., and Tanda G., 1989, "Investigation of Total Emittance of Metals and Steels Subjected to Mechanical Surface Treatments," *High Temperatures—High Pressures,* Vol. 21, No. 3, pp. 311–315.

Moffat, R. J., 1988, "Describing the Uncertainties in Experimental Results," *Experimental Thermal and Fluid Science,* Vol. 1, pp. 3–17.

Witzell, O. W., and Fontaine, W. E., 1957a, "What are the Heat Transfer Characteristics of Wire-and-Tube Condensers?," *Refrigerating Engineering,* Vol. 65, No. 3, pp. 33–37 and p. 127.

Witzell, O. W., and Fontaine, W. E., 1957b, "Design of Wire-and-Tube Condensers," *Refrigerating Engineering,* Vol. 65, No. 9, pp. 41–44.

Witzell, O. W., Fontaine, W. E., and Papanek, W. J., 1959, "Convective Films Evaluated for Wire-and-Tube Heat Exchangers," *ASHRAE Journal,* Vol. 1, No. 6, pp. 35–37.

On Modeling of Turbulent Vapor Condensation With Noncondensable Gases

S. M. Ghiaasiaan[1] and D. A. Eghbali[2]

Nomenclature

C = total molar concentration (k-mole/m^3)
C_c = scale factor for condensation heat transfer coefficient
C_p = specific heat (J/kgK)
C_s = scale factor for sensible heat transfer coefficient
$\mathcal{D}$ = vapor-noncondensable binary mass diffusivity (m^2/s)
Gr = Grashof number
h = convective sensible heat transfer coefficient in the limit of zero mass transfer (W/m^{2}K)
h_c, h_p = condensation and sensible heat transfer coefficient (W/m^{2}K)
K = mass transfer coefficient in the limit of zero mass transfer (k-mole/m^{2}s)
k_c = effective condensation thermal conductivity (W/mK)
L = length scale (m)
M = molar mass (kg/k-mole)
N_c'' = condensation flux (k-mole/m^{2}s)
Nu = Nusselt number
P = pressure (N/m^2)
Pr = gas Prandtl number = ν/α
q'' = heat flux (W/m^2)
$\mathcal{R}$ = universal gas constant (J/k-mole K)
Re = Reynolds number
Sc = Schmidt number = $\nu/\mathcal{D}$
Sh = Sherwood number
X = mole fraction

Greek Letters

α = gas thermal diffusivity (m^2/s)
β, β' = dimensionless parameters defined in Eqs (3) and (4)
δ_G = stagnant film (diffusion layer) thickness (m)
ν = gas kinematic viscosity (m^2/s)
ρ = density (kg/m^3)

Subscripts

av = average
b = gas bulk
G = gas
i = liquid-gas interface
L = liquid
n = noncondensable
t = total
v = vapor
w = wall

Superscripts

s = saturation
$\cdot$ = in the presence of high mass transfer

1 Introduction

The adverse effect of noncondensables on the condensation process is well known, and the mechanism responsible for it, i.e., the formation of a noncondensable-rich gas film adjacent to the liquid-vapor interphase, is qualitatively well understood. Condensation in the presence of noncondensables is a combined heat and mass transfer process for which rigorous analytical and numerical solutions are available only for simple and idealized situations. Simple methods for condenser design have been available for some time (Bell and Ghaly, 1972; Price and Bell, 1974; Butterworth, 1983). Recently, condensation in the presence of noncondensables in two-phase flow has attracted considerable attention due to its occurrence during the operation of the safety coolant injection systems of advanced nuclear reactors, and several experimental (Vierow, 1990; Ogg, 1991; Siddique, 1992) and analytical studies (Kageyama et al., 1993; Siddique et al., 1994; Ghiaasiaan et al., 1995; Hassan and Banerjee, 1996, Muñoz-Cobo et al., 1996) have been reported.

A simple and proven engineering method for modeling condensation in the presence of noncondensables is the stagnant film model (SFM), or Couette flow model, described in detail in several textbooks (Bird et al., 1960; Edwards et al., 1979; Kays and Crawford, 1993). SFM has been successfully applied, among others, by Corradini (1984) and Kim and Corradini (1990) to experimental data relevant to condensation in nuclear reactor containments and by Panchal and Bell (1984) to Open-Cycle Ocean-Thermal Energy Conversion (OC-OTEC) condensers. It has also been recently applied, along with the two-fluid modeling technique, to condensing two-phase channel flows (Ghiaasiaan et al., 1995). Application of SFM requires that several coupled nonlinear algebraic equations be iteratively solved in order to obtain the gas-liquid interphase temperature. This makes direct incorporation of the model in two-phase numerical solution schemes problematic. It has been shown, however, that with some mathematical manipulations, SFM can be incorporated in three important numerical algorithms (Yao and Ghiaasiaan, 1996; Yao et al., 1996).

Recently, Peterson et al. (1993) developed a model for turbulent vapor condensation with noncondensables, referred to as the diffusion layer model (DLM), which, unlike SFM, does not require an iterative solution for the interphase temperature when the interphase heat and mass transfer coefficients representing the limit of zero condensation mass flux are assumed constant. Kageyama et al. (1993) and Peterson (1996) subsequently applied DLM to the experimental data of Uchida et al. (1965) for condensation in natural convection. Peterson (1996) provided a theoretical basis for the form of Uchida's correlation, and showed that the accuracy of Uchida's correlation was an artifact of the experimental data which all had noncondensable partial pressures around 1 atm. The same data, as well as the natural convection condensation data of Tagami (1965), had previously been shown to be well predicted by SFM (Corradini, 1984). DLM has also been recently used by Muñoz-Cobo et al. (1996) in their model for condensation in vertical channels. There has even been an attempt to incorporate DLM in the RELAP5/MOD3 computer code (Hassan and Banerjee, 1996).

The objectives of this technical note are to review the formulation of DLM, assess the express and implied assumptions leading to its derivation, and compare it with SFM.

2 Stagnant Film Model (SFM)

SFM is briefly described here to facilitate the discussion in the next section. The derivation of SFM is based on the assump-

[1] G. W. Woodruff School of Mechanical Engineering, Georgia Institute of Technology, Atlanta, GA 30332-0405; seyed.ghiaasiaan@me.gatech.edu
[2] G. W. Woodruff School of Mechanical Engineering, Georgia Institute of Technology, Atlanta, GA 30332-0405.

Contributed by the Heat Transfer Division of THE AMERICAN SOCIETY OF MECHANICAL ENGINEERS. Manuscript received by the Heat Transfer Division August 23, 1996; revision received January 17, 1997; Keywords: Condensation, Direct-Contact Heat Transfer, Multiphase Flows, Phase-Change Phenomena. Technical Editor: J. R. Howell.

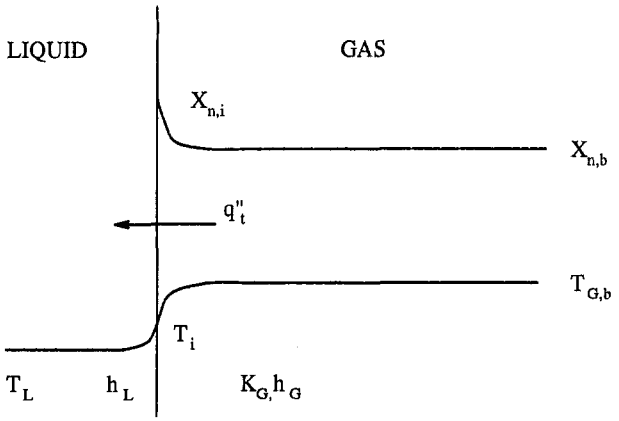

Fig. 1 The liquid-vapor interphase

tion that a quasi-steady stagnant (or Couette flow) gas-vapor film resides adjacent to the gas-liquid interphase. SFM can be formulated in the following two ways: (1) based on assumed constant molar fluxes of vapor and noncondensable; or (2) based on assumed constant mass fluxes of vapor and noncondensable in the stagnant film. The molar flux-based formulation also assumes that the product of molar concentration and mass diffusivity $C\mathcal{D}$ = constant in the film, while the mass flux based formulation is based on the poorer assumption that $\rho\mathcal{D}$ = constant in the film. Kuhn et al. (1995) recently showed that the mass flux-based method provided a better prediction of the experimental data they modeled. Both formulations are frequently used, however. Since DFM is based on molar fluxes, the molar flux based formulation of SFM will be used in the following discussion.

Figure 1 is a schematic of the interphase between the liquid (condensate) and the vapor-noncondensable gas mixture, where consistent with the stagnant film model, one-dimensional and quasi-steady state heat and mass transfer are assumed in the depicted liquid- and gas-side films adjacent to the interphase. An energy balance on the interphase leads to

$$q''_t = h^*_L(T_i - T_L) = q''_s + q''_c \tag{1}$$

where

$$q''_s = h^*_G(T_{G,b} - T_i) \tag{2}$$

$$q''_c = M_v N''_c h_{fg} \tag{3}$$

where the condensation molar flux, accounting for the suction effect of mass transfer, can be written as

$$N''_c = -K_G \ln \frac{X_{n,b}}{X_{n,i}}. \tag{4}$$

Parameters h^*_L and h^*_G also must account for the effect of high mass transfer (the Ackermann correction), e.g., according to

$$h^*_L = \frac{\beta}{\exp\left(\frac{\beta}{h_L}\right) - 1}, \quad \beta = N''_c M_v C_{pL} \tag{5}$$

$$h^*_G = \frac{-\beta'}{\exp\left(-\frac{\beta'}{h_G}\right) - 1}, \quad \beta' = N''_c M_v C_{pv}. \tag{6}$$

The interphase temperature is related to the local vapor partial pressure and mole fraction (assuming that vapor and noncondensable both act as ideal gases) according to

$$X_{v,i} = 1 - X_{n,i} = P^S(T_i)/P_t. \tag{7}$$

Knowing h_L, h_G, and K_G, Eqs. (1)–(7) generally need an iterative solution.

3 Diffusion Layer Model (DLM)

The molar flux-based formulation of SFM is now simplified, leading to the DLM of Peterson et al. (1993), everywhere using assumptions applied by the latter authors:

1 Neglect the effect of high mass transfer on both liquid and gas-side sensible heat transfer coefficients; therefore, replace h^*_L and h^*_G with h_L and h_G, respectively.
2 Define $X_{n,av}$ as

$$X_{n,av} = \frac{X_{n,b} - X_{n,i}}{\ln \frac{X_{n,b}}{X_{n,i}}} = \frac{X_{v,i} - X_{v,b}}{\ln \frac{X_{n,b}}{X_{n,i}}}. \tag{8}$$

With the above definition, and utilizing Eq. (4), Eq. (3) becomes

$$q''_c = -K_G \frac{M_v h_{fg}}{X_{n,av}} (X_{v,i} - X_{v,b}). \tag{9}$$

3 Apply the Clausius-Clapeyron relation, assuming that $\rho_v \ll \rho_L$, and assuming that the vapor acts as an ideal gas, to get the following:

$$X_{v,i} - X_{v,b} = \left(\frac{P_{v,i} - P_{v,b}}{P_t}\right)\left(\frac{X_{v,av}}{X_{v,av}}\right) \approx \frac{h_{fg}(T_i - T^s_b)X_{v,av}}{\frac{\mathcal{R}}{M_v} T^2_{av}} \tag{10}$$

where

$$T^s_b = T^s(P_{v,b}). \tag{11}$$

Combining Eqs. (9) and (10), one obtains

$$q''_c = h_c(T^s_b - T_i) \tag{12}$$

where

$$h_c = K_G\left(\frac{X_{v,av}}{X_{n,av}}\right)\frac{h^2_{fg} M^2_v}{\mathcal{R} T^2_{av}}. \tag{13}$$

Consistent with the stagnant film model, one can write (Edwards et al., 1979)

$$K_G = \frac{C\mathcal{D}}{\delta_G} = \frac{P_t\mathcal{D}}{\mathcal{R} T_{av}\delta_G} \tag{14}$$

where the ideal gas law has been utilized to eliminate C.

Eq. (1) can now be written as

$$q''_t = h_L(T_i - T_L) = h_G(T_{G,b} - T_i) + h_c(T^s_b - T_i) \tag{15}$$

where, from Eqs. (13) and (14),

$$h_c = \left(\frac{X_{v,av}}{X_{n,av}}\right)\frac{h^2_{fg} P_t M^2_v \mathcal{D}}{\mathcal{R}^2 T^3_{av}\delta_G}. \tag{16}$$

By eliminating T_i from the two equations represented by Eq. (15), the latter equation can be solved for q''_t to get:

$$q''_t = \frac{h_c(T^s_b - T_L) + h_G(T_{G,b} - T_L)}{1 + \frac{h_G + h_c}{h_L}}. \tag{17}$$

Note that for a laminar condensate film the heat flux through the film can be represented as

$$q_t'' = h_L(T_i - T_w) \tag{18}$$

with h_L^{-1} now representing the total thermal resistance of the liquid film.

Equation (17) above is identical to Eq. (15) of Peterson et al. (1993). Also Eq. (13), or equivalently Eq. (16), is identical to the first term on the right side of Eq. (1) of Peterson et al. (1993) when it is combined with Eq. (8) of the latter authors, and the ideal gas equation of state is applied to eliminate C.

Peterson et al. (1993) further manipulated Eq. (16) based on the approximate functional dependence of $\mathcal{D}$ on temperature, defined an effective condensation thermal conductivity, and so on. The details of these definitions and manipulations are unimportant when one notes what they lead to. Peterson et al. define

$$\mathrm{Sh} = \frac{h_c L}{k_c} \tag{19}$$

where

$$k_c = \left(\frac{X_{v,av}}{X_{n,av}}\right)\frac{h_{fg}^2 P_t M_v^2 \mathcal{D}}{\mathcal{R}^2 T_{av}^3}. \tag{20}$$

Peterson et al. (1993) subsequently obtained Sh based on the analogy between heat and mass transfer. For forced convection, for example

$$\mathrm{Nu} = h_G L/k_G = f(\mathrm{Re}, \mathrm{Pr}) \tag{21}$$

$$\mathrm{Sh} = f(\mathrm{Re}, \mathrm{Sc}). \tag{22}$$

Now, substituting for h_c from Eq. (13), which is equivalent to Eq. (16), and substituting for k_c from Eq. (20), in Eq. (19), one gets

$$\mathrm{Sh} = \frac{K_G L}{\mathcal{D}}\frac{\mathcal{R}T_{av}}{P_t} = \frac{K_G L}{C\mathcal{D}} \tag{23}$$

where, once again, the ideal gas law has been applied. Clearly, therefore, Sh as defined and applied in DLM is identical to the one defined and applied in low mass transfer correlations (Edwards et al., 1979). Eqs. (12), (16), (19), and (20), which are used in DLM, are thus equivalent to Eqs. (3), (4) and (23) used in SFM. Thus DLM is similar to SFM, except that the effect of mass transfer on the sensible heat transfer coefficients has been left out in the former.

The model validation calculations performed on DLM (Peterson et al., 1993; Peterson, 1996) clearly indicate the consequences of neglection of the effect of mass transfer on heat transfer coefficients. In these calculations for forced and natural convection, which deal with condensation on flat surfaces, values of Nu are found respectively from

$$\mathrm{Nu} = C_s\,\mathrm{Re}^m\,\mathrm{Pr}^n \tag{24}$$

$$\mathrm{Nu} = C_s(\mathrm{Gr}\,\mathrm{Pr})^{m'}. \tag{25}$$

For mass transfer, the same relations are used, where Nu, Pr, and C_s are replaced with Sh, Sc, and C_c, respectively, and C_s and C_c are empirically adjusted scale factors. To obtain agreement with forced convection experimental data, C_s and C_c are both found to be larger than the corresponding coefficients in the original heat transfer correlations (which represent sensible heat transfer in the limit of zero mass transfer). Furthermore, $C_s \gg C_c$ is needed for natural convection, which the latter authors attributed to fog formation. These adjustments are evidently required to compensate for the neglection of the augmenting effect of condensation mass flux on the gas-side heat transfer. Recently, Brouwers (1996) used his earlier model for laminar free and forced flow convection condensation (Brouwers, 1992), and pointed out that the effects of fog formation and sensible heat transfer enhancement due to condensation mass flux may be comparable in the data analyzed by Peterson et al. (1993).

3 Concluding Remarks

The diffusion layer model (Peterson et al., 1993) is similar to the molar flux formulation of the stagnant film (Couette flow) model, where in the derivation of the former model the Clausius-Clapeyron relation and the ideal gas assumption are applied. Most importantly, the effects of mass flux on convective sensible heat transfer coefficients are left out. Instead the gas-side convective mass transfer coefficient representing the limit of zero mass transfer is utilized, and the gas-side heat transfer coefficient representing the limit of zero mass transfer is applied using an empirically-adjusted scale factor C_s as the coefficient in the corresponding correlations.

4 References

Bell, K. J., and Ghaly, M. A., 1972, "An Approximate Generalized Design Method for Multicomponent/Partial Condensers," AIChE Symp., Ser. No. 131, Vol. 69, pp. 72–79.

Bird, R. B., Stewart, W. C., and Lightfoot, E. N., 1960, *Transport Phenomena*, John Wiley and Sons, New York.

Brouwers, H. J. H., 1992, "A Film Model for Heat and Mass Transfer With Fog Formation," *Chemical Engineering Science*, Vol. 47, pp. 3023–3036.

Brouwers, H. J. H., 1996, "Effect of Fog Formation on Turbulent Vapor Condensation With Noncondensable Gases," ASME JOURNAL OF HEAT TRANSFER, Vol. 118, pp. 243–245.

Butterworth, D., 1983, "Condensation in Vapor Mixtures," *Heat Exchanger Design Handbook*, E. U. Schlunder ed., Hemisphere, Washington, D.C., Vol. 2, pp. 2.6.3-1–2.6.3-10.

Corradini, M. L., 1984, "Turbulent Condensation on a Cold Wall in the Presence of a Noncondensable Gas," *Nuclear Technology*, Vol. 64, pp. 186–195.

Edwards, D. K., Denny, V. E., and Mills, A. F., 1979, *Transfer Processes*, 2nd. ed., Hemisphere, New York.

Ghiaasiaan, S. M., Kamboj, B. K., and Abdel-Khalik, S. I., 1995, "Two-Fluid Modeling of Condensation in the Presence of Noncondensables in Two-Phase Channel Flows," *Nuclear Science and Engineering*, Vol. 119, pp. 1–17.

Hassan, Y. A., and Banerjee, S., 1996, "Implementation of a Non-Condensable Model in RELAP5/MOD3," *Nuclear Engineering and Design*, Vol. 162, pp. 281–300.

Kageyama, T., Peterson, P. F., and Schrock, V. E., 1993, "Diffusion Layer Modeling for Condensation in Vertical Tubes with Noncondensable Gases," *Nuclear Engineering and Design*, Vol. 141, pp. 289–302.

Kays, M. K., and Crawford, M. E., 1993, *Convective Heat and Mass Transfer*, 3rd ed., McGraw-Hill, New York.

Kim, M. H., and Corradini, M. L., 1990, "Modeling of Condensation Heat Transfer," *Nuclear Engineering and Design*, Vol. 118, pp. 193–212.

Kuhn, Z. S., Schrock, V. E., and Peterson, P. F., 1995, "An Investigation of Condensation From Steam-Gas Mixtures Flowing Downward Inside a Vertical Tube," presented at the Seventh Int. Topical Meeting on Nuclear Reactor Thermal-Hydraulics (NURETH-7), Saratoga Springs, New York.

Muñoz-Cobo, J. L., Herranz, L., Sancho, J., Tkachenko, I. and Verdú, G., 1996, "Turbulent Vapor Condensation with Noncondensable Gases in Vertical Tubes," *International Journal of Heat and Mass Transfer*, Vol. 39, pp. 3249–3260.

Ogg, D. G., 1991, "Vertical Downflow Condensation Heat Transfer in Gas-Steam Mixtures," M.S. thesis, University of California at Berkeley, Berkeley, CA.

Panchal, C. B., and Bell, K. J., 1984, "Theoretical Analysis of Condensation in the Presence of Noncondensable Gases as Applied to Open-Cycle OTEC Condensers," ASME Paper 84-WA/Sol-27.

Peterson, P. F., 1996, "Theoretical Basis for the Uchida Correlation for Condensation in Reactor Containments," *Nuclear Engineering and Design*, Vol. 162, pp. 301–306.

Peterson, P. F., Schrock, V. E., and Kageyama, T., 1993, "Diffusion Layer Theory for Turbulent Vapor Condensation with Noncondensable Gases," ASME JOURNAL OF HEAT TRANSFER, Vol. 115, pp. 998–1003.

Price, B. C., and Bell, K. J., 1974, "Design of Binary Vapor Condensers Using the Colburn-Drew Equations," AIChE Sym., Ser. No. 138, Vol. 70, pp. 163–171.

Siddique, M., 1992, "The Effects of Noncondensable Gases on Steam Condensation Under Forced Convection Conditions," Ph.D. thesis, Massachusetts Institute of Technology, Boston, MA.

Siddique, M., Golay, M. W., and Kazimi, M. S., 1994, "Theoretical Modeling of Forced Convection Condensation in a Vertical Tube in the Presence of Noncondensable Gas," *Nucl. Technology*, Vol. 106, pp. 202–215.

Tagami, T., 1965, "Interim Report on Safety Assessments and Facilities Establishment Project for June 1965," No. 1 Japanese Atomic Energy Research Agency, unpublished work (see Corradini, 1984).

Uchida, H., Oyama, A., and Togo, Y., 1965, "Evaluation of Post-Incident Cooling Systems of Light-Water Power Reactors," *Proceedings of the Third International Conference on the Peaceful Uses of Atomic Energy,* Geneva, Vol. 13, pp. 93–104, United Nations, New York.

Vierow, K. M., 1990, "Behavior of Steam-Air Systems Condensing in Cocurrent Vertical Downflow," M.S. thesis, University of California at Berkeley, Berkeley, CA.

Yao, G. F., and Ghiaasiaan, S. M., 1996, "Numerical Modeling of Condensing Two-Phase Flows," *Numerical Heat Transfer, Part B: Fundamentals,* Vol. 30, pp. 137–159.

Yao, G. F., Ghiaasiaan, S. M., and Eghbali, D. A., 1996, "Semi-Implicit Modeling of Condensation in the Presence of Noncondensables in the RELAP5/MOD3 Computer Code," *Nuclear Engineering and Design,* Vol. 166, pp. 277–291.

Simple Model of Boiling Heat Transfer on Tubes in Large Pools

Y. Parlatan[1] and U. S. Rohatgi[2]

A simple method has been developed to model boiling heat transfer from a heat exchanger to pools using the experimental data available in the literature without modeling the flow dynamics of the pool. In this approach the heat flux outside vertical tubes is expressed as a function of outside wall temperature of the tubes and saturation temperature of the pool at or near atmospheric pressure.

Nomenclature

h = heat transfer coefficient, W/m^{2}K
h_{fg} = specific latent heat of vaporization, J/kg
k = thermal conductivity, W/mK
L = tube length, m
Nu = Nusselt number, hL/k
q'' = heat flux, W/m^2
$q''_{max,Z}$ = Zuber's maximum heat flux, W/m^2
q''_{min} = minimum heat flux, W/m^2
R = Pearson's r-value for curve-fitting
Ra = Raleigh number, $g\beta TL^3/\nu\alpha$
T = temperature, K
ΔT_{sat} = difference between wall and saturation temperature of liquid, K
α = thermal diffussivity, m^2/s
β = thermal expansion coefficient, 1/K
ρ = density, kg/m^3
σ = surface tension, N/m
ν = kinematic viscosity, m^2/s
sat = saturation
w = wall
b = bulk
f = liquid
g = vapor

Introduction

Many applications require tube-and-shell type heat exchangers residing in a pool of water as a heat sink. Advanced Light Water Reactors (ALWR) are a class of applications which extensively use this type of heat exchangers. The Simplified Boiling Water Reactor (SBWR) and Passive Pressurized Water Reactor (AP-600) are two reactors which have passive safety systems consisting of heat exchangers connected to containment and to reactor vessels. The heat transfer on the outside of the tubes is crucial in determining the performance of the passive system. A simple method is developed for use with system codes for ALWRs. This model is general enough to be used for other applications. The heat flux and/or heat transfer coefficient is expressed only as a function of outside wall temperature of the tubes and the saturation temperature of the pool.

Pool Boiling

Pool boiling occurs when a heater is immersed in a large stagnant pool filled with liquid and the surface temperature of the heater is above the saturation temperature of the liquid. This type of boiling process is encountered in a number of applications, including the proposed tube-and-shell type heat exchangers for ALWRs. The regimes of pool boiling can be analyzed using a pool boiling curve where heat flux is plotted against the wall superheat ΔT_{sat}, the difference between the wall, and saturation temperature of the pool. A complete pool boiling curve can be divided into four regimes: (1) natural convection; (2) nucleate boiling; (3) transition film boiling; and (4) stable film boiling.

Most passive heat exchangers are designed to operate under nucleate pool boiling conditions. However, for the sake of completeness, all four regimes are included in this study. In the following sections these modes of heat transfer will be analyzed separately for saturated pool boiling of water in the following range: $0 < \Delta T_{sat} < 400$ K. The assumption of saturated pool for nucleate boiling is not needed since the heat transfer rate in this regime depends only on the wall superheat and not on the actual water temperature. However, in the natural convection and film boiling regimes, guidance is provided for subcooled pools.

The correlations presented here are valid for vertical plates and tubes at or near atmospheric pressure. Some guidance is provided at the end of each section for higher pressures and other fluids.

Natural Convection

This mode of heat transfer occurs when the wall temperature is higher than the pool temperature at very low wall superheat levels without phase change. The onset of nucleate boiling depends on the geometry, subcooling surface orientation, and heat transfer coefficient. Natural convection is assumed to be the dominant heat transfer regime when ΔT_{sat} is less than ~3 K in this analysis. This limit is chosen since the heat flux deviates from a straight line below this temperature for a vertically heated surface (Nishikawa et al., 1983), with water at atmospheric pressure as shown in Fig. 1.

The heat transfer regime for most heat exchanger tubes in water is turbulent even for low wall superheats. The following turbulent natural convection correlation on a vertical isothermal wall is then selected (Jaluria, 1987):

$$\mathrm{Nu} = 0.1\ \mathrm{Ra}^{1/3} \qquad (1a)$$

where Nu = hL/k. For turbulent natural convection, the heat transfer coefficient is independent of the tube length as can be seen in Eq. (1). After some algebraic manipulation the heat transfer coefficient and heat flux for water are obtained as follows:

$$h = 365.0\Delta T_{sat}^{0.333}\ \mathrm{W/m^2K} \qquad (1b)$$

and

$$q'' = 365.0\Delta T_{sat}^{1.333}\ \mathrm{W/m^2} \quad \text{for} \quad \Delta T_{sat} \le 3\ \mathrm{K} \qquad (1c)$$

[1] Atomic Energy Canada Ltd., Mississauga, Ontario, Canada, L5K 1B2.
[2] Dept. of Advanced Technologies, Brookhaven National Laboratory, Upton, NY 11973.

Contributed by the Heat Transfer Division of THE AMERICAN SOCIETY OF MECHANICAL ENGINEERS. Manuscript received by the Heat Transfer Division January 5, 1996; revision received December 6, 1996; Keywords: Boiling, Heat Exchangers, Natural Convection. Associate Technical Editor: J. R. Howell.

Uchida, H., Oyama, A., and Togo, Y., 1965, "Evaluation of Post-Incident Cooling Systems of Light-Water Power Reactors," *Proceedings of the Third International Conference on the Peaceful Uses of Atomic Energy,* Geneva, Vol. 13, pp. 93–104, United Nations, New York.

Vierow, K. M., 1990, "Behavior of Steam-Air Systems Condensing in Cocurrent Vertical Downflow," M.S. thesis, University of California at Berkeley, Berkeley, CA.

Yao, G. F., and Ghiaasiaan, S. M., 1996, "Numerical Modeling of Condensing Two-Phase Flows," *Numerical Heat Transfer, Part B: Fundamentals,* Vol. 30, pp. 137–159.

Yao, G. F., Ghiaasiaan, S. M., and Eghbali, D. A., 1996, "Semi-Implicit Modeling of Condensation in the Presence of Noncondensables in the RELAP5/MOD3 Computer Code," *Nuclear Engineering and Design,* Vol. 166, pp. 277–291.

Simple Model of Boiling Heat Transfer on Tubes in Large Pools

Y. Parlatan[1] and U. S. Rohatgi[2]

A simple method has been developed to model boiling heat transfer from a heat exchanger to pools using the experimental data available in the literature without modeling the flow dynamics of the pool. In this approach the heat flux outside vertical tubes is expressed as a function of outside wall temperature of the tubes and saturation temperature of the pool at or near atmospheric pressure.

Nomenclature

h = heat transfer coefficient, W/m^{2}K
h_{fg} = specific latent heat of vaporization, J/kg
k = thermal conductivity, W/mK
L = tube length, m
Nu = Nusselt number, hL/k
q'' = heat flux, W/m^2
$q''_{max,Z}$ = Zuber's maximum heat flux, W/m^2
q''_{min} = minimum heat flux, W/m^2
R = Pearson's r-value for curve-fitting
Ra = Raleigh number, $g\beta TL^3/\nu\alpha$
T = temperature, K
ΔT_{sat} = difference between wall and saturation temperature of liquid, K
α = thermal diffussivity, m^2/s
β = thermal expansion coefficient, 1/K
ρ = density, kg/m^3
σ = surface tension, N/m
ν = kinematic viscosity, m^2/s
sat = saturation
w = wall
b = bulk
f = liquid
g = vapor

Introduction

Many applications require tube-and-shell type heat exchangers residing in a pool of water as a heat sink. Advanced Light Water Reactors (ALWR) are a class of applications which extensively use this type of heat exchangers. The Simplified Boiling Water Reactor (SBWR) and Passive Pressurized Water Reactor (AP-600) are two reactors which have passive safety systems consisting of heat exchangers connected to containment and to reactor vessels. The heat transfer on the outside of the tubes is crucial in determining the performance of the passive system. A simple method is developed for use with system codes for ALWRs. This model is general enough to be used for other applications. The heat flux and/or heat transfer coefficient is expressed only as a function of outside wall temperature of the tubes and the saturation temperature of the pool.

Pool Boiling

Pool boiling occurs when a heater is immersed in a large stagnant pool filled with liquid and the surface temperature of the heater is above the saturation temperature of the liquid. This type of boiling process is encountered in a number of applications, including the proposed tube-and-shell type heat exchangers for ALWRs. The regimes of pool boiling can be analyzed using a pool boiling curve where heat flux is plotted against the wall superheat ΔT_{sat}, the difference between the wall, and saturation temperature of the pool. A complete pool boiling curve can be divided into four regimes: (1) natural convection; (2) nucleate boiling; (3) transition film boiling; and (4) stable film boiling.

Most passive heat exchangers are designed to operate under nucleate pool boiling conditions. However, for the sake of completeness, all four regimes are included in this study. In the following sections these modes of heat transfer will be analyzed separately for saturated pool boiling of water in the following range: $0 < \Delta T_{sat} < 400$ K. The assumption of saturated pool for nucleate boiling is not needed since the heat transfer rate in this regime depends only on the wall superheat and not on the actual water temperature. However, in the natural convection and film boiling regimes, guidance is provided for subcooled pools.

The correlations presented here are valid for vertical plates and tubes at or near atmospheric pressure. Some guidance is provided at the end of each section for higher pressures and other fluids.

Natural Convection

This mode of heat transfer occurs when the wall temperature is higher than the pool temperature at very low wall superheat levels without phase change. The onset of nucleate boiling depends on the geometry, subcooling surface orientation, and heat transfer coefficient. Natural convection is assumed to be the dominant heat transfer regime when ΔT_{sat} is less than ~3 K in this analysis. This limit is chosen since the heat flux deviates from a straight line below this temperature for a vertically heated surface (Nishikawa et al., 1983), with water at atmospheric pressure as shown in Fig. 1.

The heat transfer regime for most heat exchanger tubes in water is turbulent even for low wall superheats. The following turbulent natural convection correlation on a vertical isothermal wall is then selected (Jaluria, 1987):

$$\mathrm{Nu} = 0.1\ \mathrm{Ra}^{1/3} \qquad (1a)$$

where Nu = hL/k. For turbulent natural convection, the heat transfer coefficient is independent of the tube length as can be seen in Eq. (1). After some algebraic manipulation the heat transfer coefficient and heat flux for water are obtained as follows:

$$h = 365.0\Delta T_{sat}^{0.333}\ \mathrm{W/m^2K} \qquad (1b)$$

and

$$q'' = 365.0\Delta T_{sat}^{1.333}\ \mathrm{W/m^2} \quad \text{for} \quad \Delta T_{sat} \le 3\ \mathrm{K} \qquad (1c)$$

[1] Atomic Energy Canada Ltd., Mississauga, Ontario, Canada, L5K 1B2.
[2] Dept. of Advanced Technologies, Brookhaven National Laboratory, Upton, NY 11973.

Contributed by the Heat Transfer Division of THE AMERICAN SOCIETY OF MECHANICAL ENGINEERS. Manuscript received by the Heat Transfer Division January 5, 1996; revision received December 6, 1996; Keywords: Boiling, Heat Exchangers, Natural Convection. Associate Technical Editor: J. R. Howell.

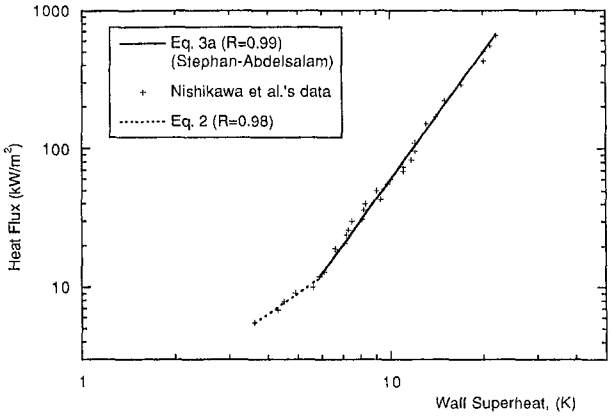

Fig. 1 Nucleate boiling regime data and curve fits

where the physical properties are evaluated at saturation temperature at atmospheric pressure.

At higher pressures the coefficients in Eqs. (1*b–c*) should be evaluated using the physical properties at the corresponding saturation temperature. For example, the coefficient in Eq. (1*b*) at saturation temperature of 120°C, is 400.8, which indicates that the heat transfer will increase with pressure. Similarly, Eq. (1*a*) can be used for other fluids. In case of natural convection in a subcooled pool, ΔT_{sat} in Eq. (1) should be replaced with $(T_w - T_b)$, and the properties should be evaluated at the average film temperature.

Nucleate Boiling

When the level of wall superheat is increased, nucleation is initiated in some of the cavities on the surface of the heat exchanger. At low superheats, the number of active nucleation sites are few and widely separated. At higher superheat levels, the number of active nucleation sites and the bubble departure frequency from these sites increase, resulting in a very effective heat transfer mechanism. (The Nusselt number is proportional to ΔT_{sat}^3). Pool subcooling has negligible effect on the heat transfer in this regime. However, it may significantly increase the value of the critical heat flux, thereby extending the upper range of nucleate boiling regime.

Heater surface orientation has no effect at higher wall temperatures, but may have a pronounced effect at wall superheats of less than 15 K (Nishikawa et al., 1983). Data from recent experiments (Nishikawa et al., 1983) with water at atmospheric pressure, and with varying surface orientation on a flat copper plate, is used to assess several correlations available in the literature. These include: (1) Rohsenow correlation; (2) Forster-Zuber correlation; (3) Stephan-Abdelsalam correlation; and (4) Borishansky correlation. These correlations were compared with relatively good agreement for pool boiling of water at atmospheric pressure (Carey, 1992). We have compared these correlations with the experimental data of Nishikawa et al. for vertically heated surfaces. The best agreement is observed with Stephan-Abdelsalam correlation in the following range: $6 < \Delta T_{sat} < 22$ K, as shown in Fig. 1. Therefore, this correlation is recommended for the above temperature range on vertical surfaces.

The experimental data of Nishikawa et al. for wall heat flux is also used for wall superheat temperatures between 3 and 6 K. In this region, the experimental data deviates from Stephan-Abdelsalam's correlation, possibly due to the contribution of a natural convection term that is not negligible below a wall superheat of about 6 K. The following correlation is obtained from data (Nishikawa et al., 1983) in this temperature range, as shown in Fig. 1:

$$q'' = 775 * T_{sat}^{1.52} \text{ W/m}^2 \quad \text{for} \quad 3 < \Delta T_{sat} < 6 \text{ K}. \qquad (2)$$

The Stephan-Abdelsalam correlation is as follows (Stephan and Abdelsalam, 1980):

$$q'' = \{C_1[T_w - T_{sat}(P_f)]\}^{1/0.327} \text{ W/m}^2 \qquad (3a)$$

where the coefficient C_1 depends on pressure (for water $C_1 = 3.65\,P^{0.13}$ for $1 \le P \le 2$ and P in bar). After some manipulation one obtains

$$q'' = 52.4\Delta T_{sat}^{3.058} \text{ W/m}^2\text{K} \quad \text{for} \quad 6 < \Delta T_{sat} < 22 \text{ K}. \qquad (3b)$$

In the case of subcooled pool conditions Eqs. (3*a–b*) are still valid since the subcooling does not change the heat flux significantly. Equation (3*a*) can be used for different fluids and for pressures higher than 2 bars by changing the coefficient and the exponent appropriately (Carey, 1992). For example, the coefficient in Eq. (3b) at saturation temperature of 120°C is 69.1, indicating an increase in heat transfer coefficient with temperature. For horizontal and inclined surface configurations where wall superheat is less than 15 K, Eqs. (2) and (3) should be modified using appropriate data, e.g., see Nishikawa et al. (1983).

CHF Point

Near the critical heat flux point, the nucleate pool boiling heat flux reaches a peak and then starts to decrease with increasing wall superheat. Here, the slope of the boiling curve levels off. The maximum heat transfer can be calculated in terms of $q''_{max,Z}$ (Zuber's maximum heat flux):

$$q''_{max,Z} = \frac{\pi}{4}\,\rho_g^{0.5} h_{fg}[\sigma g(\rho_f - \rho_g)]^{0.25}. \qquad (4a)$$

For vertically oriented surfaces, Lienhard and Dhir (1973) suggested the following correlation:

$$q''_{CHF} = 0.90 q''_{max,Z} = 1.044 \text{ MW/m}^2 \text{ at } \Delta T_{sat} = 30 \text{ K} \qquad (4b)$$

where $q''_{max,Z} \approx 1.16$ MW/m^2 for water near atmospheric pressure. The critical heat flux at other pressures can be evaluated from Eq. (4*a–b*).

The temperature where the CHF occurs also depends on fluid properties as well as fluid-surface combination. For example, for a water-steel combination CHF occurs at a wall superheat of about 30 K, while for a water, copper-chrome plated combination, it occurs at 23–28 K (Vachon et al., 1968). We have selected 30 K as a representative value for CHF point here, but a different value can be used for different combination of fluid and metal. Furthermore, for subcooled pool boiling conditions, the value of the maximum heat flux, and the wall superheat at which it occurs, need to be adjusted (Zuber et al., 1961).

To represent the boiling curve behavior near the CHF point where the heat flux slightly increases with wall superheat, the heat transfer coefficient is ramped from 34.3 kW/m^{2}K to 34.8 kW/m^{2}K (equivalent to 1.044 MW/m^2 at $\Delta T_{sat} = 30$ K) on a log-log plot:

$$q'' = 7800\ \Delta T_{sat}^{1.44} \text{ W/m}^2\text{K} \quad \text{for} \quad 22 < \Delta T_{sat} < 30 \text{ K}. \qquad (5)$$

Zuber's maximum heat flux (Eq. (4*a*)) is valid at higher pressures and for different fluids. For different geometry and orientation configurations, an extensive list is provided (Carey, 1992).

Transition Film Boiling

When the wall temperature increases beyond CHF temperature, the mean overall heat flux decreases with increasing wall superheat. There are large fluctuations in the local heat flux and/or temperature; therefore, heat transfer is difficult to correlate. This regime is called the transition film boiling regime. The experimental data found in the literature show a significant scatter, and the agreement between various experimental results

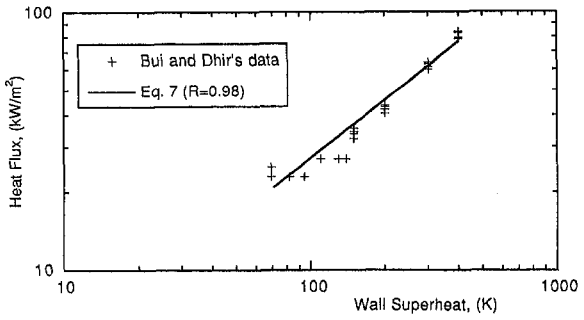

Fig. 2 Curve fit to the transition and film boiling data of Bui and Dhir (1985a, 1985b)

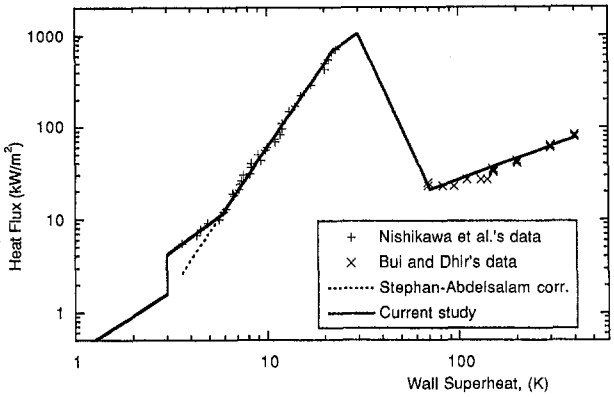

Fig. 3 Heat flux in saturated pool boiling of water near atmospheric pressure in the natural convection, nucleate boiling, transition, and film boiling regimes

is generally not good. Transition film boiling also depends on the fluid properties and surface characteristics of the wall (material, finish, cleanliness, and aging). Witte and Lienhard (1983) have suggested that there are two distinctly different transition boiling curves (1) when the transition region is entered from film boiling side (quenching), and (2) when it is entered from the nucleate boiling side (heating up).

The heat transfer in the transition boiling region has been generally represented in the literature by a straight line connecting the maximum point in nucleate boiling (CHF) and the minimum point in film boiling on a log-log plot (Bui and Dhir, 1985a). This approach is also taken in this analysis. The maximum and minimum points determined from relevant experimental data and correlations are explained below.

Transition film boiling is assumed to occur in the following range: $30 < \Delta T_{sat} < 70$ K. The lower value of this range was discussed in the previous section. The upper value is taken from quasi-steady state transition film boiling experiments of Bui and Dhir (1985a), with water at atmospheric pressure and boiling on a vertical surface. The minimum heat transfer point also depends on surface conditions and the history of the process (heating or cooling). However, the minimum heat flux point falls generally between 60 and 90 K superheat. The value of minimum heat flux changes slightly with the surface condition, but the following value represents the general behavior:

$$q''_{min} = 22.0 \text{ kW/m}^2 \quad \text{at} \quad \Delta T_{sat} = 70 \text{ K} \qquad (6)$$

Note that this value is 16 percent higher than that to sustain minimum stable film boiling for an infinite surface at atmospheric pressure; namely, Leidenfrost point. Figure 2 shows the transient film boiling data of Bui and Dhir (1985a).

Heat transfer in transition film boiling is represented by a straight line connecting the maximum point in the nucleate boiling and the minimum point in film boiling on a log-log plot. The following results are obtained:

$$q'' = 5.58 \times 10^{12} \Delta T_{sat}^{-4.555} \text{ W/m}^2 \ (30 < T_{sat} < 70 \text{ K}). \qquad (7)$$

For subcooled boiling conditions, the value of heat flux is expected to be higher than that for saturated boiling. However, there is virtually no quantitative information on its effect (Carey, 1992). At higher pressures and for other fluids, a correlation similar to Eq. 7 can be developed by calculating the maximum and minimum heat flux values and interpolating on a log-log scale.

Stable Film Boiling

The heat transfer coefficient in the stable film boiling is determined from stable film boiling experiments of Bui and Dhir (1985b) with boiling water at atmospheric pressure on an isothermal vertical surface. They found that the heat transfer coefficient decreases slightly with increasing wall superheat in this regime ($h \sim \Delta T_{sat}^{-0.25}$). Figure 2 shows the following correlation fitted to their experimental data:

$$q'' = 857 \Delta T_{sat}^{0.75} \text{ W/m}^2\text{K for } 150 \text{ K} < \Delta T_{sat} < 400 \text{ K}. \qquad (8)$$

For subcooled film boiling, the heat transfer is enhanced, but this enhancement diminishes as the heat flux and wall superheat increase. Therefore, adjustment is needed for subcooled pool conditions; see, e.g., Sparrow and Cess (1962) for an analysis of subcooled film boiling. For different geometry and orientation configuration, and for different fluids, the above equation is not valid, and relevant experimental data and correlations should be used.

Summary and Conclusions

The behavior of heat flux and heat transfer coefficient as a function of wall superheat temperature for water boiling on a vertical surface near atmospheric pressure is summarized in the natural convection, nucleate boiling, transition film boiling, and stable film boiling regimes. Figure 3 shows pool boiling curve for vertical tubes in a water pool at atmospheric pressure. A similar approach can be developed for other geometries, pressure and subcooling conditions, and a combination of fluid and metal. Figures 1–3 show the quality of the correlations through a factor of R. The value of R is greater than 0.98, indicating a good fit.

The approach described here is useful; where one needs only the heat transfer from heat exchanger tubes and is not interested in the flow behavior in the pool itself. It can be also used in

Table 1 Summary of pool boiling correlations: coefficient A and exponent b of Eq. 9

Flow regime	Wall superheat (K)	A (W/m^{2}K^b)	b	Remark
Natural Convection	$\Delta T_{sat} \leq 3$	365	1.333	Eq. 1c
Nuc. Boil. and Nat. Conv.	$3 \leq \Delta T_{sat} \leq 6$	775	1.52	Eq. 2
Nucleate Boiling	$6 \leq \Delta T_{sat} \leq 22$	52.4	3.058	Eq. 3b
Nucleate Boiling	$22 \leq \Delta T_{sat} \leq 30$	7800	1.44	Eq. 5
Transition Boiling	$30 \leq \Delta T_{sat} \leq 70$	5.58E12	−4.555	Eq. 7
Film Boiling	$70 \leq \Delta T_{sat} \leq 400$	857	0.75	Eq. 8

applications such as the passive heat exchangers in SBWR and AP-600. Furthermore, this approach can be extended for the steam generators provided that the forced convection contribution is small compared to the boiling heat transfer. The heat transfer coefficient and heat flux are tabulated against wall superheat temperature for a saturated pool near atmospheric pressure and with a stainless steel-water combination.

After a thorough literature survey, Table 1 has been developed to model the heat transfer rate from vertical tubes in large pools of water. This table shows the correlation to be used for a given wall superheat. All correlations have the following form:

$$q'' = A * \Delta T_{\text{sat}}^{b} \tag{9}$$

The coefficient A and exponent b have different values for different heat transfer regimes and they are shown in this table. This method has been used in modeling of SBWR and several related test facilities with a system code. The heat transfer coefficient on the outside surface of the passive heat exchanger tubes was calculated using this table.

References

Bui, T. D., and Dhir, V. K., 1985a, "Transition Boiling Heat Transfer on a Vertical Surface," ASME JOURNAL OF HEAT TRANSFER, Vol. 107, No. 4, pp. 756–763.

Bui, T. D., and Dhir, V. K., 1985b, "Film Boiling Heat Transfer on an Isothermal Vertical Surface," ASME JOURNAL OF HEAT TRANSFER, Vol. 107, No. 4, pp. 764–771.

Carey, V. P., 1992, *Liquid-Vapor Phase-Change Phenomena: An Introduction to the Thermophysics of Vaporization and Condensation Processes in Heat Transfer Equipment,* pp. 239–243, 252, 299, 301. Hemisphere, Washington, DC.

Jaluria, Y., 1987, "Basics of Natural Convection," *Handbook of Single-Phase Convective Heat Transfer,* S. Kakaç et al., eds., pp. 12–24, John Wiley and Sons, New York.

Lienhard, J. H., and Dhir, V. K., 1973, "Hydrodynamic Prediction of Peak Pool-boiling Heat Fluxes from Finite Bodies," ASME JOURNAL OF HEAT TRANSFER, Vol. 95, No. 2, pp. 152–158.

Nishikawa, K. et al., 1983, "Effect of Heating Surface Orientation on Nucleate Boiling Heat Transfer," *Proc. ASME-JSME Thermal Eng. Joint Conf.,* Honolulu, HI.

Sparrow, E. M., and Cess, R. D., 1962, "The Effect of Subcooled Liquid on Laminar Film Boiling," ASME JOURNAL OF HEAT TRANSFER, Vol. 84, pp. 149–156.

Stephan, K., and Abdelsalam, M., 1980, "Heat-Transfer Correlations for Natural Convection Boiling," *Int. J. Heat Mass Transfer,* Vol. 23, pp. 73–87.

Vachon, R. I., et al., 1968, "Evaluation of Constants for the Rohsenow Pool Boiling Correlation," ASME JOURNAL OF HEAT TRANSFER, Vol. 90, pp. 239–247.

Witte, L. C., and Lienhard, J. H., 1983, "On the Existence of Two 'Transition' Boiling Curves," *Int. J. Heat Mass Transfer,* Vol. 26, pp. 1103–1104.

Zuber, N., Tribus, M., and Westwater, J. W., 1961, "The Hydrodynamic Crisis in Pool Boiling of Saturated and Subcooled Liquid," *Proc. Int. Heat Transfer Conference,* Paper No. 27, p. 230, Denver, Colorado.

Geometric Mean Beam Lengths Between Two Concentrical Spheres

F. M. B. Andersen[1]

1 Introduction

Geometric mean beam lengths are applied in engineering radiative heat transfer calculations when the radiative absorption coefficient and temperature are constant within the absorbing/emitting medium. Using geometric mean beam lengths in the optically thin limit gives exact results for the radiative heat transfer. For other optical thicknesses, the so-called mean beam lengths are applied; they are obtained from the geometric mean beam lengths by using correction factors. Since only average values of the correction factors are known and not their exact values, the results for the radiative heat transfer are approximate.

Two types of geometric mean beam lengths are described in the literature. One type is used for the radiative transmission between surfaces i and j and denoted by L_{ij}, and the other type is used for the radiative emission from a gas to a surface j and is denoted by L_{gj}. The two types of geometric mean beam lengths are calculated from integral equations as follows:

$$L_{ij} = \frac{1}{A_i \cdot F_{ij}} \cdot \int_{A_i} \int_{A_j} \frac{\cos \beta_j \cdot \cos \beta_i}{\pi \cdot l} \, dA_j dA_i \tag{1}$$

$$L_{gj} = \frac{1}{A_j} \cdot \int_{A_j} \int_{\omega=2\pi} \frac{l \cdot \cos \beta_j}{\pi} \, d\omega dA_j, \tag{2}$$

where the angles β_i and β_j are the angles from the normal of the surfaces i and j to the line between the infinitesimal elements dA_i and dA_j; l is the length between the infinitesimal elements; A_i and A_j are the areas of surface i and j, respectively; F_{ij} is the view factor from surface i to surface j; and $d\omega$ is an infinitesimal solid angle.

Due to the complexity of the integrations in Eq. (1) and (2), only a few geometric mean beam lengths are given in the literature. Andersen and Hadvig (1989) obtained analytically the geometric mean beam lengths of the space between two infinitely long concentrical circular cylinders. Dunkle (1964) gives the geometric mean beam lengths for the transmission between two rectangles which in one case are equal, parallel, and directly opposed and in another case are orthogonal with a common edge. Other simple cases solved analytically (Siegel and Howell, 1992) are: parallel layer of gas, sphere, hemisphere to an infinitesimal element in center, finite and semi-infinite circular cylinders radiating to the center of base, and infinite circular cylinders. An equation for the common geometric mean beam length for the radiative emission in an enclosure is $L_g = 4V/A$, where V is the volume and A is the surface area of the enclosure. This equation gives the geometric mean beam lengths in many elementary cases (parallel layer, sphere, infinitely long circular cylinder, cube, etc.) but may also be applied in more sophisticated cases such as infinite tube bundles (Andersen and Denev, 1996).

The geometric mean beam lengths may also be used in the optically thin limit for calculating the direct exchange areas in the Hottel Zone method for detailed numerical analyses of radiative heat transfer (Hottel and Sarofim, 1967).

For other cases that are not optically thin, the mean beam lengths must be applied to obtain the gas emissivities and transmissivities. These lengths, called L_{ij}^{*} and L_{gj}^{*}, are obtained using correction factors C_{ij} and C_{gj} so that $L_{ij}^{*} = C_{ij} \cdot L_{ij}$ and $L_{gj}^{*} = C_{gj} \cdot L_{gj}$. The correction factors can be obtained in cases where the exact solution of the radiation problem is known either from analytical or numerical integration. Average correction factors for some cases are given by Siegel and Howell (1992).

Yuen and Ma (1992) and Yuen (1990) investigate and apply the absorption mean beam lengths and extinction mean beam length, which are identical to mean beam lengths in cases where the single scatter albedo is zero. Yuen (1981, 1982) obtains geometric mean transmissivities and absorptivities using advanced methods.

It appears that the geometric mean beam lengths of the absorbing/emitting space between two concentrical spheres have not been derived previously.

The work is relevant to modeling furnaces which are near spherical with a spherical load, or source, in the center where

[1] Associate Research Professor, Department of Energy Engineering, Building 402, Technical University of Denmark, DK-2800 Lyngby, Denmark; vklfa@ws1.vk.dtu.dk

Contributed by the Heat Transfer Division of THE AMERICAN SOCIETY OF MECHANICAL ENGINEERS. Manuscript received by the Heat Transfer Division May 15, 1996; revision received December 9, 1996; Keywords: Radiation. Associate Technical Editor: B. Webb.

applications such as the passive heat exchangers in SBWR and AP-600. Furthermore, this approach can be extended for the steam generators provided that the forced convection contribution is small compared to the boiling heat transfer. The heat transfer coefficient and heat flux are tabulated against wall superheat temperature for a saturated pool near atmospheric pressure and with a stainless steel-water combination.

After a thorough literature survey, Table 1 has been developed to model the heat transfer rate from vertical tubes in large pools of water. This table shows the correlation to be used for a given wall superheat. All correlations have the following form:

$$q'' = A * \Delta T_{\text{sat}}^{b} \tag{9}$$

The coefficient A and exponent b have different values for different heat transfer regimes and they are shown in this table. This method has been used in modeling of SBWR and several related test facilities with a system code. The heat transfer coefficient on the outside surface of the passive heat exchanger tubes was calculated using this table.

References

Bui, T. D., and Dhir, V. K., 1985a, "Transition Boiling Heat Transfer on a Vertical Surface," ASME JOURNAL OF HEAT TRANSFER, Vol. 107, No. 4, pp. 756–763.

Bui, T. D., and Dhir, V. K., 1985b, "Film Boiling Heat Transfer on an Isothermal Vertical Surface," ASME JOURNAL OF HEAT TRANSFER, Vol. 107, No. 4, pp. 764–771.

Carey, V. P., 1992, *Liquid-Vapor Phase-Change Phenomena: An Introduction to the Thermophysics of Vaporization and Condensation Processes in Heat Transfer Equipment,* pp. 239–243, 252, 299, 301. Hemisphere, Washington, DC.

Jaluria, Y., 1987, "Basics of Natural Convection," *Handbook of Single-Phase Convective Heat Transfer,* S. Kakaç et al., eds., pp. 12–24, John Wiley and Sons, New York.

Lienhard, J. H., and Dhir, V. K., 1973, "Hydrodynamic Prediction of Peak Pool-boiling Heat Fluxes from Finite Bodies," ASME JOURNAL OF HEAT TRANSFER, Vol. 95, No. 2, pp. 152–158.

Nishikawa, K. et al., 1983, "Effect of Heating Surface Orientation on Nucleate Boiling Heat Transfer," *Proc. ASME-JSME Thermal Eng. Joint Conf.,* Honolulu, HI.

Sparrow, E. M., and Cess, R. D., 1962, "The Effect of Subcooled Liquid on Laminar Film Boiling," ASME JOURNAL OF HEAT TRANSFER, Vol. 84, pp. 149–156.

Stephan, K., and Abdelsalam, M., 1980, "Heat-Transfer Correlations for Natural Convection Boiling," *Int. J. Heat Mass Transfer,* Vol. 23, pp. 73–87.

Vachon, R. I., et al., 1968, "Evaluation of Constants for the Rohsenow Pool Boiling Correlation," ASME JOURNAL OF HEAT TRANSFER, Vol. 90, pp. 239–247.

Witte, L. C., and Lienhard, J. H., 1983, "On the Existence of Two 'Transition' Boiling Curves," *Int. J. Heat Mass Transfer,* Vol. 26, pp. 1103–1104.

Zuber, N., Tribus, M., and Westwater, J. W., 1961, "The Hydrodynamic Crisis in Pool Boiling of Saturated and Subcooled Liquid," *Proc. Int. Heat Transfer Conference,* Paper No. 27, p. 230, Denver, Colorado.

Geometric Mean Beam Lengths Between Two Concentrical Spheres

F. M. B. Andersen[1]

1 Introduction

Geometric mean beam lengths are applied in engineering radiative heat transfer calculations when the radiative absorption coefficient and temperature are constant within the absorbing/emitting medium. Using geometric mean beam lengths in the optically thin limit gives exact results for the radiative heat transfer. For other optical thicknesses, the so-called mean beam lengths are applied; they are obtained from the geometric mean beam lengths by using correction factors. Since only average values of the correction factors are known and not their exact values, the results for the radiative heat transfer are approximate.

Two types of geometric mean beam lengths are described in the literature. One type is used for the radiative transmission between surfaces i and j and denoted by L_{ij}, and the other type is used for the radiative emission from a gas to a surface j and is denoted by L_{gj}. The two types of geometric mean beam lengths are calculated from integral equations as follows:

$$L_{ij} = \frac{1}{A_i \cdot F_{ij}} \cdot \int_{A_i} \int_{A_j} \frac{\cos \beta_j \cdot \cos \beta_i}{\pi \cdot l} \, dA_j dA_i \tag{1}$$

$$L_{gj} = \frac{1}{A_j} \cdot \int_{A_j} \int_{\omega=2\pi} \frac{l \cdot \cos \beta_j}{\pi} \, d\omega dA_j, \tag{2}$$

where the angles β_i and β_j are the angles from the normal of the surfaces i and j to the line between the infinitesimal elements dA_i and dA_j; l is the length between the infinitesimal elements; A_i and A_j are the areas of surface i and j, respectively; F_{ij} is the view factor from surface i to surface j; and $d\omega$ is an infinitesimal solid angle.

Due to the complexity of the integrations in Eq. (1) and (2), only a few geometric mean beam lengths are given in the literature. Andersen and Hadvig (1989) obtained analytically the geometric mean beam lengths of the space between two infinitely long concentrical circular cylinders. Dunkle (1964) gives the geometric mean beam lengths for the transmission between two rectangles which in one case are equal, parallel, and directly opposed and in another case are orthogonal with a common edge. Other simple cases solved analytically (Siegel and Howell, 1992) are: parallel layer of gas, sphere, hemisphere to an infinitesimal element in center, finite and semi-infinite circular cylinders radiating to the center of base, and infinite circular cylinders. An equation for the common geometric mean beam length for the radiative emission in an enclosure is $L_g = 4V/A$, where V is the volume and A is the surface area of the enclosure. This equation gives the geometric mean beam lengths in many elementary cases (parallel layer, sphere, infinitely long circular cylinder, cube, etc.) but may also be applied in more sophisticated cases such as infinite tube bundles (Andersen and Denev, 1996).

The geometric mean beam lengths may also be used in the optically thin limit for calculating the direct exchange areas in the Hottel Zone method for detailed numerical analyses of radiative heat transfer (Hottel and Sarofim, 1967).

For other cases that are not optically thin, the mean beam lengths must be applied to obtain the gas emissivities and transmissivities. These lengths, called L_{ij}^{*} and L_{gj}^{*}, are obtained using correction factors C_{ij} and C_{gj} so that $L_{ij}^{*} = C_{ij} \cdot L_{ij}$ and $L_{gj}^{*} = C_{gj} \cdot L_{gj}$. The correction factors can be obtained in cases where the exact solution of the radiation problem is known either from analytical or numerical integration. Average correction factors for some cases are given by Siegel and Howell (1992).

Yuen and Ma (1992) and Yuen (1990) investigate and apply the absorption mean beam lengths and extinction mean beam length, which are identical to mean beam lengths in cases where the single scatter albedo is zero. Yuen (1981, 1982) obtains geometric mean transmissivities and absorptivities using advanced methods.

It appears that the geometric mean beam lengths of the absorbing/emitting space between two concentrical spheres have not been derived previously.

The work is relevant to modeling furnaces which are near spherical with a spherical load, or source, in the center where

[1] Associate Research Professor, Department of Energy Engineering, Building 402, Technical University of Denmark, DK-2800 Lyngby, Denmark; vklfa@ws1.vk.dtu.dk

Contributed by the Heat Transfer Division of THE AMERICAN SOCIETY OF MECHANICAL ENGINEERS. Manuscript received by the Heat Transfer Division May 15, 1996; revision received December 9, 1996; Keywords: Radiation. Associate Technical Editor: B. Webb.

Table 1 The correction factor and its standard deviation for all the geometric mean beam lengths. The ratio of the radii is constant $\lambda = r_1/r_2 = 0.5$ in all cases. "a" is the absorption coefficient of the gas between the spheres

$a \cdot r_2$	$C_{g1} = C_{12} = C_{21}$	C_{22}	C_{g2}
0.1	0.99940/0.00029	0.99270/0.00062	0.990964/0.000055
0.5	0.99716/0.00015	0.96261/0.00017	0.955081/0.000084
1.0	0.99499/0.00037	0.92225/0.00037	0.91213/0.00030
5.0	0.976200/0.000098	0.62813/0.00013	0.66960/0.00044
10.0	0.95816/0.00070	0.43388/0.00036	0.50729/0.00033

the source could be a spherical surface gas burners. Furthermore, the mean beam lengths can also be applied in simpler models for spherical celestrial gas bodies.

2 Analysis

The values connected to the inner and outer spheres are indexed "1" and "2", respectively, and the gas is indexed g. Five geometric mean beam lengths have to be considered for the case with two concentrical spheres, namely: L_{12}, L_{21}, L_{22}, L_{g1} and L_{g2}. Fortunately, three of these are identical: $L_{g1} = L_{12} = L_{21}$. In the following, the three unknown geometric mean beam lengths $L_{g1} = L_{12} = L_{21}$, L_{22} and L_{g2} are to be found.

2.1 Case: $L_{g1} = L_{12} = L_{21}$. Of the three geometric mean beam lengths only L_{21} is considered. Integration of Eq. (1) gives the dimensionless geometric mean beam length

$$\frac{L_{21}}{r_2} = \frac{2}{3\lambda^2}[1 - \lambda^3 - (1 - \lambda^2)^{3/2}] \tag{3}$$

where r_1 and r_2 are the radii of the inner and outer spheres respectively and $\lambda \equiv r_1/r_2$.

2.2 Case L_{22}. Equation (1) gives

$$L_{22}/r_2 = \frac{4}{3} \cdot \sqrt{1 - \lambda^2}. \tag{4}$$

2.3 Case L_{g2}. Equation (2) is expressed as the sum of two integrals over two solid angles where one covers the solid angle in which the outer sphere is visible, and the other covers the solid angle in which the inner sphere is visible. These integrals are expressed by the already calculated geometric mean beam lengths giving the result

$$\frac{L_{g2}}{r_2} = \frac{2}{3} \cdot [1 - \lambda^3 + (1 - \lambda^2)^{3/2}]. \tag{5}$$

2.4 Correction Factors. The classic Monte Carlo method, as described in Siegel and Howell (1992), is used to obtain numerical solutions of the radiative transfer between the two concentrical spheres and from the gas to the spheres. Three Monte Carlo computer programs were made: one where the energy bundles are emitted from the inner sphere, one where the energy bundles are emitted from the outer sphere, and one where the energy bundles are emitted from the gas volume between the spheres. In all three cases the bundles were tracked until they hit a surface. The correction factors were calculated from the number of hits on the two spheres, the total number of emitted energy bundles, the product of the absorption coefficient and the radius of the outer sphere $a \cdot r_2$, and the equation for the geometric mean beam lengths. Ten Monte Carlo calculations of each case were then made and the mean value of the correction factor and its standard deviation was calculated. If the standard deviation is too high, the number of emitted bundles should be increased. Further details for calculating the correction factors using the Monte Carlo method are given in Andersen and Denev (1996) for another geometry. The correction factors and their standard deviations are shown in Table 1.

References

Andersen, F. M. B., and Denev J., 1996, "Mean Beam Lengths of Gas Radiation in Tube Bundles," submitted to *Heat Transfer Engineering* for possible publication.

Andersen, K. M., and Hadvig, S., 1989, "Geometric Mean Beam Lengths for a Space Between Two Coaxial Cylinders," ASME JOURNAL OF HEAT TRANSFER, Vol. 111, No. 3, pp. 811–813.

Dunkle, R. V., 1964, "Geometric Mean Beam Lengths for Radiant Heat Transfer Calculations," ASME JOURNAL OF HEAT TRANSFER, Vol. 86, No. 1, pp. 75–80.

Hottel, H. C., and Sarofim, A. F., 1967, *Radiative Transfer,* McGraw-Hill, New York.

Siegel, R., and Howell, J. R., 1992, *Thermal Radiation Heat Transfer,* Hemisphere, Washington, DC.

Yuen, W. W., 1981, "A Simplified Approach to the Evaluation of the Geometric-Mean Transmittance and Absorptance for Gas Enclosure," ASME JOURNAL OF HEAT TRANSFER, Vol. 103, pp. 808–813.

Yuen, W. W., 1982, "Evaluation of the Geometric Mean Transmittance and the Total Absorptance for Two-Dimensional Systems," *Int. J. Heat Mass Transfer,* Vol. 25, No. 7, pp. 1069–1071.

Yuen, W. W., 1990, "Development of a Network Analogy and Evaluation of Mean Beam Lengths for Multidimensional Absorbing/Isotropically Scattering Media," ASME JOURNAL OF HEAT TRANSFER, Vol. 112, pp. 408–414.

Yuen, W. W., and Ma, A., 1992, "Evaluation of Total Emittance of an Isothermal Nongray Absorbing, Scattering Gas-Particle Mixture Based on the Concept of Absorption Mean Beam Length," ASME JOURNAL OF HEAT TRANSFER, Vol. 114, pp. 653–658.

Shape Optimization of Cooling Channels Using Genetic Algorithms

Jens von Wolfersdorf,[1] E. Achermann,[2] and B. Weigand[3]

A shape optimization method for convective cooling channels within a two-dimensional heat conduction region is presented. This method combines genetic algorithms with a point heat sink approach that is used to model the heat removal of the cooling channels during the optimization process. The method can be easily combined with the Finite Element Method (FEM) for the calculation of the optimized temperature field distribution.

Nomenclature

B_G = gas Biot number, $(\alpha_G R_0/\lambda)$
B_C = coolant Biot number, $(\alpha_C R_0/\lambda)$
G = domain
m = number of point heat sinks
n = population size
$\vec{\mathbf{n}}$ = normal vector at a surface
q = point heat sink strength in (W/m)
r, ϕ = polar coordinates
R = radius
R_0 = disk radius
S = surface
T = temperature
x, y = Cartesian coordinates
α = heat transfer coefficient
∇ = Nabla operator

[1] ABB, Corporate Research Center, 5405, Baden, Switzerland.
[2] ETH, Institute of Scientific Computing, 8000, Zürich, Switzerland.
[3] ABB, Power Generation Ltd., 5401, Baden, Switzerland.

Contributed by the Heat Transfer Division of THE AMERICAN SOCIETY OF MECHANICAL ENGINEERS. Manuscript received by the Heat Transfer Division September 25, 1995; revision received December 20, 1996; Keywords: Computer Codes, Conduction, Numerical Methods. Associate Technical Editor: S. Ramadhyani.

Table 1 The correction factor and its standard deviation for all the geometric mean beam lengths. The ratio of the radii is constant $\lambda = r_1/r_2 = 0.5$ in all cases. "a" is the absorption coefficient of the gas between the spheres

$a \cdot r_2$	$C_{g1} = C_{12} = C_{21}$	C_{22}	C_{g2}
0.1	0.99940/0.00029	0.99270/0.00062	0.990964/0.000055
0.5	0.99716/0.00015	0.96261/0.00017	0.955081/0.000084
1.0	0.99499/0.00037	0.92225/0.00037	0.91213/0.00030
5.0	0.976200/0.000098	0.62813/0.00013	0.66960/0.00044
10.0	0.95816/0.00070	0.43388/0.00036	0.50729/0.00033

the source could be a spherical surface gas burners. Furthermore, the mean beam lengths can also be applied in simpler models for spherical celestrial gas bodies.

2 Analysis

The values connected to the inner and outer spheres are indexed "1" and "2", respectively, and the gas is indexed g. Five geometric mean beam lengths have to be considered for the case with two concentrical spheres, namely: L_{12}, L_{21}, L_{22}, L_{g1} and L_{g2}. Fortunately, three of these are identical: $L_{g1} = L_{12} = L_{21}$. In the following, the three unknown geometric mean beam lengths $L_{g1} = L_{12} = L_{21}$, L_{22} and L_{g2} are to be found.

2.1 Case: $L_{g1} = L_{12} = L_{21}$. Of the three geometric mean beam lengths only L_{21} is considered. Integration of Eq. (1) gives the dimensionless geometric mean beam length

$$\frac{L_{21}}{r_2} = \frac{2}{3\lambda^2}[1 - \lambda^3 - (1 - \lambda^2)^{3/2}] \tag{3}$$

where r_1 and r_2 are the radii of the inner and outer spheres respectively and $\lambda \equiv r_1/r_2$.

2.2 Case L_{22}. Equation (1) gives

$$L_{22}/r_2 = \frac{4}{3} \cdot \sqrt{1 - \lambda^2}. \tag{4}$$

2.3 Case L_{g2}. Equation (2) is expressed as the sum of two integrals over two solid angles where one covers the solid angle in which the outer sphere is visible, and the other covers the solid angle in which the inner sphere is visible. These integrals are expressed by the already calculated geometric mean beam lengths giving the result

$$\frac{L_{g2}}{r_2} = \frac{2}{3} \cdot [1 - \lambda^3 + (1 - \lambda^2)^{3/2}]. \tag{5}$$

2.4 Correction Factors. The classic Monte Carlo method, as described in Siegel and Howell (1992), is used to obtain numerical solutions of the radiative transfer between the two concentrical spheres and from the gas to the spheres. Three Monte Carlo computer programs were made: one where the energy bundles are emitted from the inner sphere, one where the energy bundles are emitted from the outer sphere, and one where the energy bundles are emitted from the gas volume between the spheres. In all three cases the bundles were tracked until they hit a surface. The correction factors were calculated from the number of hits on the two spheres, the total number of emitted energy bundles, the product of the absorption coefficient and the radius of the outer sphere $a \cdot r_2$, and the equation for the geometric mean beam lengths. Ten Monte Carlo calculations of each case were then made and the mean value of the correction factor and its standard deviation was calculated. If the standard deviation is too high, the number of emitted bundles should be increased. Further details for calculating the correction factors using the Monte Carlo method are given in Andersen and Denev (1996) for another geometry. The correction factors and their standard deviations are shown in Table 1.

References

Andersen, F. M. B., and Denev J., 1996, "Mean Beam Lengths of Gas Radiation in Tube Bundles," submitted to *Heat Transfer Engineering* for possible publication.

Andersen, K. M., and Hadvig, S., 1989, "Geometric Mean Beam Lengths for a Space Between Two Coaxial Cylinders," ASME JOURNAL OF HEAT TRANSFER, Vol. 111, No. 3, pp. 811–813.

Dunkle, R. V., 1964, "Geometric Mean Beam Lengths for Radiant Heat Transfer Calculations," ASME JOURNAL OF HEAT TRANSFER, Vol. 86, No. 1, pp. 75–80.

Hottel, H. C., and Sarofim, A. F., 1967, *Radiative Transfer,* McGraw-Hill, New York.

Siegel, R., and Howell, J. R., 1992, *Thermal Radiation Heat Transfer,* Hemisphere, Washington, DC.

Yuen, W. W., 1981, "A Simplified Approach to the Evaluation of the Geometric-Mean Transmittance and Absorptance for Gas Enclosure," ASME JOURNAL OF HEAT TRANSFER, Vol. 103, pp. 808–813.

Yuen, W. W., 1982, "Evaluation of the Geometric Mean Transmittance and the Total Absorptance for Two-Dimensional Systems," *Int. J. Heat Mass Transfer,* Vol. 25, No. 7, pp. 1069–1071.

Yuen, W. W., 1990, "Development of a Network Analogy and Evaluation of Mean Beam Lengths for Multidimensional Absorbing/Isotropically Scattering Media," ASME JOURNAL OF HEAT TRANSFER, Vol. 112, pp. 408–414.

Yuen, W. W., and Ma, A., 1992, "Evaluation of Total Emittance of an Isothermal Nongray Absorbing, Scattering Gas-Particle Mixture Based on the Concept of Absorption Mean Beam Length," ASME JOURNAL OF HEAT TRANSFER, Vol. 114, pp. 653–658.

Shape Optimization of Cooling Channels Using Genetic Algorithms

Jens von Wolfersdorf,[1] E. Achermann,[2] and B. Weigand[3]

A shape optimization method for convective cooling channels within a two-dimensional heat conduction region is presented. This method combines genetic algorithms with a point heat sink approach that is used to model the heat removal of the cooling channels during the optimization process. The method can be easily combined with the Finite Element Method (FEM) for the calculation of the optimized temperature field distribution.

Nomenclature

B_G = gas Biot number, $(\alpha_G R_0/\lambda)$
B_C = coolant Biot number, $(\alpha_C R_0/\lambda)$
G = domain
m = number of point heat sinks
n = population size
$\vec{\mathbf{n}}$ = normal vector at a surface
q = point heat sink strength in (W/m)
r, ϕ = polar coordinates
R = radius
R_0 = disk radius
S = surface
T = temperature
x, y = Cartesian coordinates
α = heat transfer coefficient
∇ = Nabla operator

[1] ABB, Corporate Research Center, 5405, Baden, Switzerland.
[2] ETH, Institute of Scientific Computing, 8000, Zürich, Switzerland.
[3] ABB, Power Generation Ltd., 5401, Baden, Switzerland.

Contributed by the Heat Transfer Division of THE AMERICAN SOCIETY OF MECHANICAL ENGINEERS. Manuscript received by the Heat Transfer Division September 25, 1995; revision received December 20, 1996; Keywords: Computer Codes, Conduction, Numerical Methods. Associate Technical Editor: S. Ramadhyani.

δ = Dirac distribution
λ = thermal conductivity
p_c = probability with which an individual undergoes crossover
p_m = probability with which a single point undergoes mutation
θ = temperature difference at cooling channel, $T - T_C$
Θ = nondimensional temperature, (T/T_W)

Subscripts

G = gas
C = coolant
max = maximum
min = minimum
W = wall

Introduction

Shape optimization problems arise in many areas of engineering and have received increasing attention in the recent literature. In many heat transfer problems, the temperature or the heat flux distribution on the outer boundary of the structure under consideration is of interest. The objective of the optimization is to locate and shape cooling channels with related cooling conditions within the structure to balance the imposed heat load while maintaining a desired outer temperature distribution. Several approaches using the Boundary Element Method (BEM) have been developed for this purpose.

Barone and Caulk (1982) developed a special boundary integral method for optimal positioning of isothermal circular holes in a two-dimensional heat conduction region. In this method the integrals around the circular interior boundaries were calculated analytically using a finite sum of circular harmonics with unknown coefficients. This method was extended by Parang et al. (1987) to include various heat flux distributions at the cooling holes and to increase accuracy. A general approach to the problem using the BEM was given by Kennon and Dulikravich (1985) that determined the shape of the inner boundary. This method has been applied to minimize the number of cooling holes (Dulikravich and Kosovic, 1991) and to regions with multiple materials (Dulikravich and Martin, 1994; Shau et al., 1990).

More recently genetic algorithms have been applied to the optimization of heat transfer problems. An approach to optimize cooling of electronic components using genetic algorithms has been given by Queipo et al. (1994).

The presented method uses genetic algorithms in connection with a point heat sink method that allows one to optimize cooling channel locations and shapes having convective boundary conditions. Additionally, the present method does not prescribe a priori the shape of the cooling channel. The shapes are calculated during the solution process and are part of the solution algorithm. This method can be easily combined with the Finite Element Method (FEM) for the temperature field computation.

Point Heat Sink Method

Consider a two-dimensional region G as shown in Fig. 1a. The temperature field within this region is described by the heat conduction equation. Under the assumption of steady state conditions, this equation can be written in the following form:

$$\frac{\partial}{\partial x}\left(\lambda \frac{\partial T}{\partial x}\right) + \frac{\partial}{\partial y}\left(\lambda \frac{\partial T}{\partial y}\right) = 0. \quad (1)$$

The convective boundary conditions at the outer boundary S_1 and at the inner boundary S_2 are given by

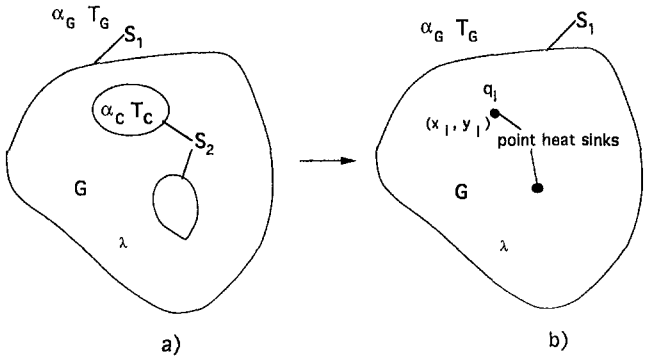

Fig. 1 Point heat sink approach

$$-\lambda \frac{\partial T}{\partial \vec{n}} = \alpha_G(T_G - T) \quad \text{on } S_1 \quad (2)$$

$$-\lambda \frac{\partial T}{\partial \vec{n}} = \alpha_C(T - T_C) \quad \text{on } S_2. \quad (3)$$

During a geometry optimization process the shape of the cooling channels, and thereby the geometry of the boundary S_2, will change. This makes the application of numerical methods—especially the Finite Element Method (FEM)—difficult, since for every iteration step a new FEM-model has to be generated. To avoid these difficulties, a different method—the point heat sink method—is applied. Its purpose is to model the heat removing channels by point heat sinks rather than by actual cooling channels (see Fig. 1b). The number, locations, and strengths of the point heat sinks are free parameters which can obtain a prescribed temperature distribution along the outer surface. Having found a proposal for the temperature field by a genetic algorithm, the related cooling channel geometries for given inner convective boundary conditions have to be determined afterwards. The problem to be solved is then given by

$$\frac{\partial}{\partial x}\left(\lambda \frac{\partial T}{\partial x}\right) + \frac{\partial}{\partial y}\left(\lambda \frac{\partial T}{\partial y}\right) = \sum_{i=1}^{m} q_i \delta(x - x_i)\delta(y - y_i) \quad (4)$$

with the boundary condition from Eq. (2).

When combining this concept with the FEM, the modification of the structure, and therefore the need to generate a new mesh at each optimization step, is eliminated. The full structure (without cooling channels or even with some fixed cooling channels, which are not subject to the optimization) is discretized only once, and the resulting nodes within the structure provide possible heat sink locations. In a similar fashion regions with various material properties can be included.

Determination of Cooling Channel Geometries

Within the optimization procedure, temperature fields induced by different point heat sink distributions are calculated and assessed. Cooling channel geometries have to be found for these temperature fields in such a way that these cooling channels with given cooling conditions will produce the same temperature field. Around each point heat sink, a cooling channel has to be determined to fulfill the Laplace equation in the remaining outer structure. It is possible that one cooling channel includes more than one point heat sink.

For the determination of the cooling channel geometry an arbitrary curve in a local polar coordinate system (see Fig. 2) is investigated. This coordinate system has its origin in the point sink location. The boundary condition, to be fulfilled on the channel boundary, is given by Eq. (3).

Defining the curve of the cooling channel by

$$C = r - R(\phi) = 0, \quad (5)$$

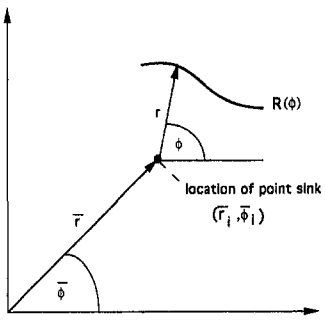

Fig. 2 Local coordinate system for cooling channel geometry determination

the normal vector is given by

$$\vec{\mathbf{n}} = \frac{\nabla C}{|\nabla C|} = \frac{1}{\sqrt{1 + \frac{R'^2}{r^2}}} \left(1, -\frac{R'}{r}\right) \tag{6}$$

where $R' = (dR/d\phi)$. Therefore, the normal temperature gradient on the curve $R(\phi)$ can be rewritten using Eq. (3) as

$$\nabla T \cdot \vec{\mathbf{n}} = \frac{1}{\sqrt{1 + \frac{R'^2}{r^2}}} \left(T_r - \frac{R'}{r^2} T_\phi\right) = \beta(T - T_C) = \beta\theta \tag{7}$$

where $\beta = (\alpha_C/\lambda)$. Equation (7) is an ordinary differential equation in cylindrical coordinates with the periodic boundary condition $R(0) = R(2\pi)$. Problems in solving Eq. (7) arise for two reasons. First, the periodic boundary condition does not allow a simple stepwise integration, and an iterative procedure to fulfill the boundary condition is required. Second, if Eq. (7) is written in explicit form for R' one obtains

$$R' = -\frac{r^2 T_r T_\phi}{r^2\beta^2\theta^2 - T_\phi^2} \pm \frac{r^2\beta\theta}{r^2\beta^2\theta^2 - T_\phi^2} \sqrt{r^2 T_r^2 + T_\phi^2 - r^2\beta^2\theta^2}, \tag{8}$$

which indicates that at every point of the solution two possible tangential directions R' exist. A unique integration over the full period $0 \le \phi \le 2\pi$ is therefore difficult.

Nevertheless, it is possible to derive an approximation to the solution of Eq. (8) in the following way: the differential equation in general implicit form is

$$F(\phi, r, R') = T_r - \frac{R'}{r^2} T_\phi - \sqrt{1 + \frac{R'^2}{r^2}}\,\beta\theta = 0. \tag{9}$$

If the partial derivative with respect to R' is taken to be zero

$$\frac{\partial F}{\partial R'} = 0, \tag{10}$$

a possible singular solution in form of an envelope to all solution curves can be obtained. For more detailed information on this subject the reader is referred to special textbooks about solution of implicit differential equations (e.g., Collatz, 1981; Kamke, 1956). Eliminating R' by combining Eqs. (9) and (10) results in the following approximation for the radius of the cooling channel:

$$r(\sqrt{\beta^2\theta^2 - T_r^2}) = T_\phi. \tag{11}$$

This is the condition for the discriminant in Eq. (8) being zero and therefore gives the real limit. Hence, the nonlinear Eq. (11) has to be solved in a pointwise manner (for every ϕ). The curve obtained can be a partial or even a full solution of the original differential equation. For instance, in a pure radial (one-dimensional) case ($T_\phi = 0$, $R' = 0$) Eq. (11) gives

$$\beta\theta = T_r \tag{12}$$

from which the radius has to be determined. This is the boundary condition to be fulfilled in the pure radial case. In every case, Eq. (11) will give a cooling channel which produces at least the desired local temperature distribution since Eq. (11) describes the envelope of all possible real solutions, as was mentioned above. Thus, the generated cooling channel might locally be bigger than necessary, leading to a lower temperature there.

It should be noted that for the computation of the partial derivatives with respect to T, the relationship between the local r, ϕ coordinate system, and the global $\bar{r}$, $\bar{\phi}$ system (see Fig. 2) has to be taken into account, where

$$\bar{r} = \sqrt{(\bar{r}_i \cos\bar{\phi}_i + r\cos\phi)^2 + (\bar{r}_i \sin\bar{\phi}_i + r\sin\phi)^2} \tag{13}$$

$$\bar{\phi} = \arctan\left(\frac{\bar{r}_i \sin\bar{\phi}_i + r\sin\phi}{\bar{r}_i \cos\bar{\phi}_i + r\cos\phi}\right). \tag{14}$$

Since the solution for the temperature field will generally be given in Cartesian coordinates, Eq. (11) is translated into x, y coordinates. Using $x = r\cos\phi$ and $y = r\sin\phi$ one obtains the following:

$$\sqrt{T_x^2 + T_y^2} = \beta\theta \tag{15}$$

Equation (15) provides a simple method for the numerical determination of the cooling channel geometry after a numerical temperature field computation. The zero isoline of the two-dimensional function $f = \sqrt{T_x^2 + T_y^2} - \beta\theta$ provides the approximate channel contour. In Appendix A an example is given which shows how accurately the cooling channel geometry can be calculated using the envelope solution discussed above.

Genetic Algorithm

Genetic algorithms are a class of very powerful nondeterministic search methods. Their concept is inspired by nature, and they work according to Darwin's theory on evolution which is premised on the notion that the most fit or adaptable members of a population have higher chances of successful reproduction and, therefore, of perpetuation (Davis, 1991).

Consider a fitness function f: $X \mapsto \mathbb{R}$. One wants to find an $x \in X$ such that $f(x)$ is minimized. By coding each x into a string, the search space X is transformed into a search space over chromosomes, each consisting of genes. The genetic algorithm works on these genes like nature does its evolutionary work on the genes of each species.

The structure of a genetic algorithm can be outlined as follows:

1 Initialization: initialize the population as a subset of all possible genes.
2 Evaluation: each individual of this population is evaluated by the fitness function $f(x)$, where x is an individual represented by its genes.
3 Selection: individuals with high fitness (i.e., low values) are selected more often into the new population, the average may remain and the worst die off.
4 Crossover: each individual (in the new population) undergoes with probability p_c the crossover operation; the selected individuals are randomly mated.
5 Mutation: each of the smallest information units has an equal chance to undergo mutation, so it is altered with probability p_m, which is normally very small.
6 Iteration: proceed at Step 2.

After a number of such iterations it is expected that the population contains better individuals with respect to the fitness function.

To understand why this simple algorithm works, suppose that a good property is coded somewhere in the right section of the first gene, and another good property is coded somewhere in the left section of the second gene. The crossover operation then combines these good properties to a single new gene. Such subsections of a gene are called building blocks (BB). Building blocks refer to partial solutions of the initial optimization problem. The mutation provides the possibility of altering the building blocks to restore lost information or gain new information.

Theoretical investigations on genetic algorithm have shown that a genetic algorithm seeks (near) optimal solutions through the juxtaposition of small, compact building blocks, which are used for information exchange during crossover.

The coding function which transforms individuals (solutions of the initial optimization problem) into a genetic algorithm's internal representation has to be designed very carefully. The coding is critical for the genetic algorithms performance. The following conditions must be fulfilled:

- partial solutions in terms of building blocks
- allow for combining building blocks
- possibility of altering building blocks

Coding. Different research on GAs has shown (Goldberg, 1989; Davis, 1991; Holland, 1992; Michalewicz, 1992) that the coding of individuals can be done in different ways. Although the theoretical foundation relies on binary string codings, it is not necessary to represent individuals as binary strings. One can instead use floating point representations or even more complex codings. A systematic comparison is done in Michalewicz (1992) between a GA relying on a binary representation and one relying on a floating point representation. Michalewicz (1992) concludes that "floating point representation is faster, more consistent from run to run, and provides a higher precision. Especially on large domains, which would require prohibitively long binary representations, the accuracy as well as the performance can be enhanced by special operators. The floating point representation is intuitively closer to the problem space, which makes it easier to design other operators incorporating problem specific knowledge. This is essential in handling nontrivial, problem specific constraints." In high level representations, such constraints can be applied already during crossover and mutation. In our case for example the sum of cooling strengths over all points must equal the total amount of heat to be removed Q_{tot}. So prior to each evaluation, the coded cooling strengths s_i have to be scaled in the following way:

$$\tilde{s}_i := \frac{s_i}{\sum_i s_i} = \frac{q_i}{Q_{\text{tot}}}. \tag{16}$$

This made us code the heat sinks as what they are: simple points in a plane represented by a triplet of floating point numbers, two for the position and one for its relative strength $\tilde{s}_i$.

Fitness Function. To verify the combination of the discussed point heat-sink method with a GA, a simple circular disk with radius R_0 is chosen. The disk is heated by an outer temperature distribution $T_G(\phi)$, and a constant heat transfer coefficient α_G is assumed. The goal of the optimization is to minimize the variation of the temperature at the border $T_W(s) = T(R_0, \phi)$ around a given value $\bar{T}_W$ by positioning point heat sinks within the disk with a GA. A good measure of this variation is

$$\text{fitness} = \int_s (T_W(s) - \bar{T}_W)^2 ds. \tag{17}$$

Equation (17) provides a fitness function for each individual. The total amount of heat removed by the point heat sinks is constant and given by

$$Q_{\text{tot}} := \sum_{i=1}^{m} q_i = \int_0^{2\pi} \alpha_G R_0 (T_G(\phi) - \bar{T}_W) d\phi. \tag{18}$$

Hence, the average wall temperature $\bar{T}_W$ is determined by Q_{tot} and is, therefore, constant as well. Another measure for the temperature variation at the boundary is

$$\text{fitness} = \max (T_W(\phi)) - \bar{T}_W. \tag{19}$$

This fitness function is much faster to approximate than Eq. (17). Both fitness functions rate the temperature distribution by means of a flat distribution at the boundary. Since preliminary experiments with different fitness functions produced similar solutions (Achermann, 1995) and Eq. (19) is fast to calculate, we exclusively used Eq. (19).

To find the temperature distribution $T(r, \phi)$, the problem as described by Eq. (4) has to be solved. This is given in cylindrical coordinates by

$$\frac{1}{r}\frac{\partial}{\partial r}\left(\lambda \frac{\partial T}{\partial r}\right) + \frac{1}{r^2}\frac{\partial}{\partial \phi}\left(\lambda \frac{\partial T}{\partial \phi}\right) = \frac{1}{r}\sum_{i=1}^{m} q_i \delta(r - r_i)\delta(\phi - \phi_i) \tag{20}$$

with the boundary condition

$$-\lambda \frac{\partial T}{\partial r} = \alpha_G (T_G(\phi) - T) \quad \text{at } r = R_0. \tag{21}$$

The outer temperature $T_G(\phi)$ is prescribed by a Fourier series expansion

$$T_G(\phi) = \frac{a_0}{2} + \sum_{n=1}^{\infty} (a_n \cos(n\phi) + b_n \sin(n\phi)). \tag{22}$$

The analytical solution to this problem can be obtained using the Green's Function approach (Beck et al., 1992) and is given by

$$T(r, \phi) = \sum_{i=1}^{m} \frac{q_i}{2\pi\lambda} \left\{ \frac{1}{B_G} + \frac{1}{2} \ln \left(\frac{R_0^2 + \left(\frac{r_i r}{R_0}\right)^2 - 2 r_i r \cos(\phi - \phi_i)}{r^2 + r_i^2 - 2 r_i r \cos(\phi - \phi_i)} \right) + 2 \sum_{n=1}^{\infty} \frac{1}{B_G + n} \left(\frac{r_i r}{R_0^2}\right)^n \cos(n(\phi - \phi_i)) \right\} + \frac{a_0}{2} + \sum_{n=1}^{\infty} \left(\frac{r}{R_0}\right)^n \frac{B_G}{B_G + n} (a_n \cos(n\phi) + b_n \sin(n\phi)). \tag{23}$$

Equation (23) involves some numerical problems by evaluating the second sum because the oscillating cosine term may lead to numerical cancellation. The accuracy of the temperature field $T(r, \phi)$ determines the accuracy of the fitness function, which is crucial for the genetic algorithm in the selection phase. It was found that using another representation of the second sum leads to the needed accuracy for the fitness function. The reader is referred to Appendix B for details.

Selection. The standard roulette wheel selection (see Goldberg, 1989) is used in the present application. Additionally, an elitist strategy was applied which ensures that the best individual is always selected.

Crossover. Because a high level representation is used, the crossover operation can be formulated very problem specifically. It has to be ensured that the sum of cooling strengths stays constant. The crossover operation is designed to make sure that good regions are possibly combined in one new indi-

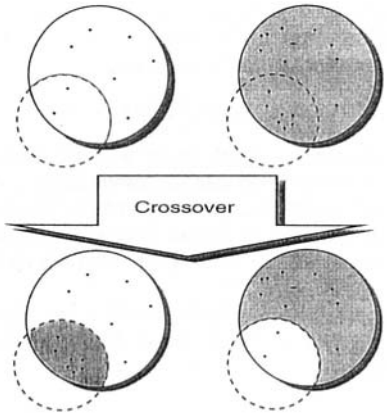

Fig. 3 Crossover on a circle shaped area

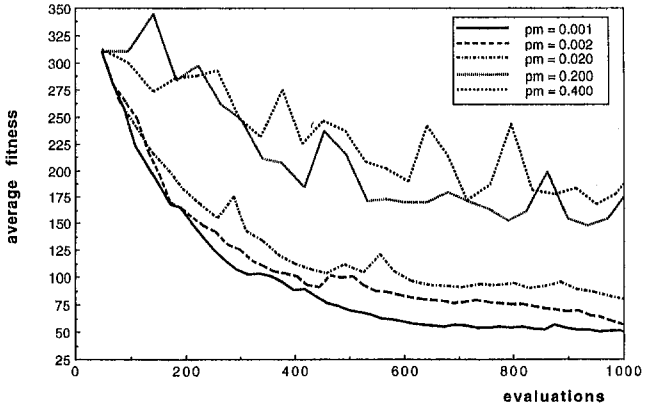

Fig. 6 Different convergences by varying the mutation rate

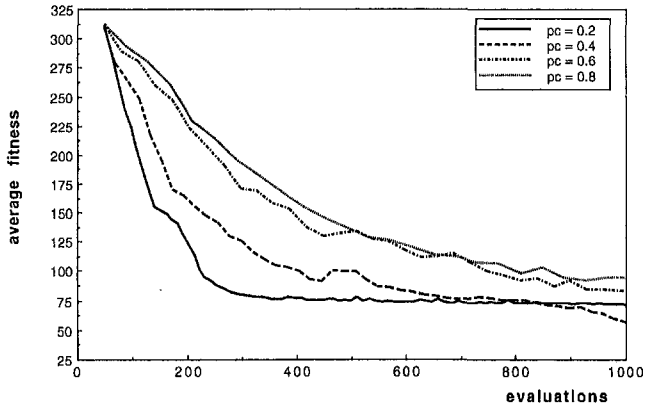

Fig. 4 Different convergences by varying the crossover rate

vidual. This is done by exchanging randomly selected regions (see Fig. 3), i.e., the crossing areas.

Let Q_A denote the strength of an area A, i.e., the sum of cooling strengths in that area ($Q_A = \Sigma_{P_i \in A}\, q_i$, where P_i are the heat sink points in the crossing area A). Since this strength is usually different for different crossing areas, simply swapping the crossing areas would result in an implicit scaling of the unchanged area. Thus, every time two crossing areas are swapped, their sink strengths must be rescaled. As a consequence, heat sinks with small cooling strengths may evolve that do not contribute significantly to the final solution. The high level coding allows us to delete all these useless sinks before the evaluation, thus saving considerable calculation time.

Mutation. The classical mutation changes only one bit, the smallest information unit. An analogous mutation of one sink in the two-dimensional plane is to split it into several sinks with the same cooling strength within a small circle around the original sink, merge several sinks within a small circle into one new sink, move it by a small amount in a random direction, or change its cooling strength by a small amount; a small amount is in the order of one per cent of the original value. Good results were obtained with a mixture of these four mutations, i.e., when-

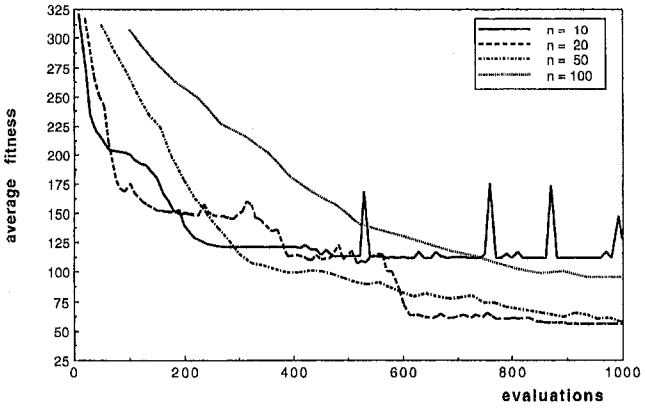

Fig. 7 Different convergences due to varying the population size

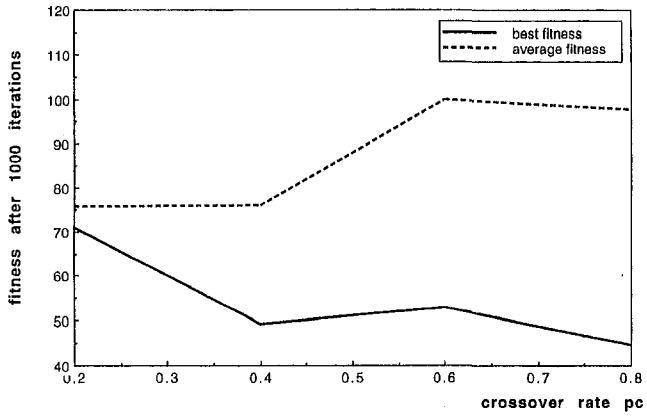

Fig. 5 Effect of different crossover rates on the fitness after 1000 generations

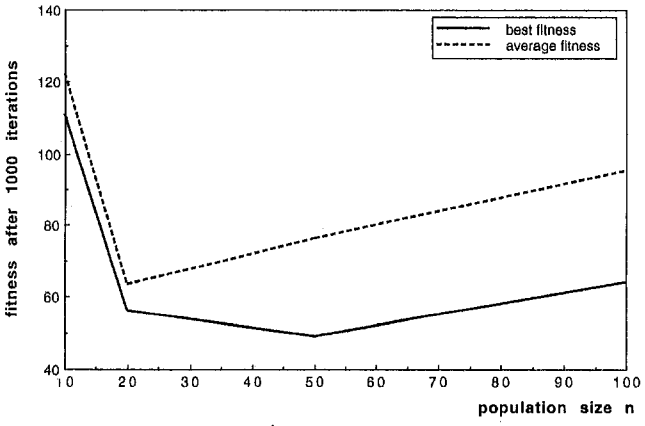

Fig. 8 Effect of varying the population size on the fitness after 1000 generations

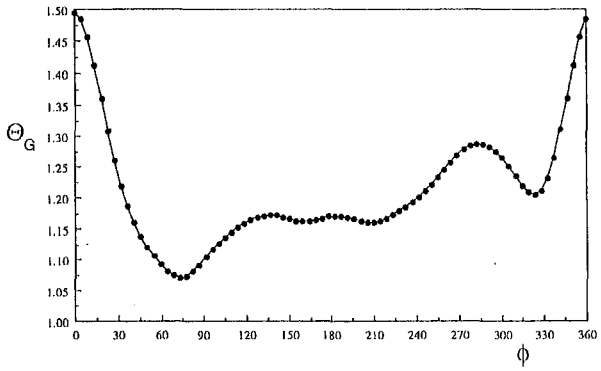

Fig. 9 Prescribed outer gas temperature distribution

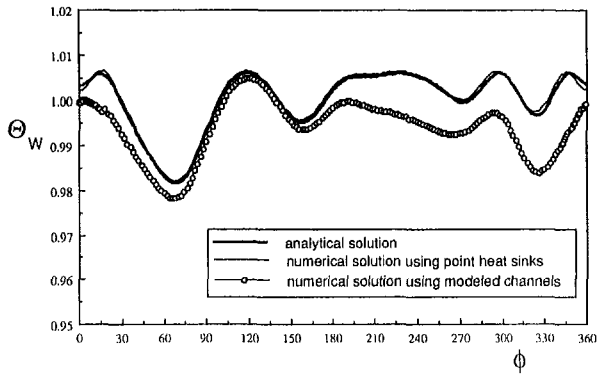

Fig. 11 Wall temperature distributions

ever a sink undergoes a mutation, one of these four operations is with equal probability applied.

Tuning the GA Parameters

GA research has stressed the importance of finding effective combinations of crossover rate, mutation rate, and population size. Some have even implemented a meta GA to look for the best parameters (Grefenstette, 1986). The essential conclusions from these works are (a) good GA parameters affect the convergence of a GA very strongly, and (b) good GA parameters are problem specific.

Each genetic algorithm depends on the choice of parameters leading to quick and stable convergence. In the present case, the GA's properties were analyzed by varying a single parameter. After a number of iterations the performances of the GA's were compared. Figure 4 shows that small crossover rates (in this example $p_c = 0.2$) lead to fast convergence, but the GA is trapped in a local optimum; whereas larger crossover rates lead to more continuous convergence. Crossover rates between $0.4 \leq p_c \leq 0.8$ show similar convergence behavior (Fig. 5) with respect to best fitness. A value of $p_c = 0.6$ was used for subsequent computations. Varying the mutation rate has a strong influence on the GA's performance. If the mutation rate is too high, the GA approximates a random search with typically poor performance (Fig. 6). If the mutation rate is too low (below $p_m = 0.001$), the GA will get trapped in a local optimum.

In Fig. 7 it is obvious that a small population size often leads to premature convergence: with a population size of 10, after 450 generations the GA stops improving the best individuals. The solution found is not as good as the other GA's solutions. Figure 8 shows that there exists an optimal population size, but there is also a wide range of reasonably good population sizes between $20 \leq n \leq 100$. In summary, a GA parameter set of $p_c \approx 0.6$, $p_m \approx 0.002$, and $n \approx 50$ gives good results for the present application.

Example

A disk with radius R_0 is heated by the gas temperature distribution shown in Fig. 9, the Biot number is assumed to be $B_G = 2$ for the following example. The goal of the optimization is to achieve a uniform wall temperature by distributing the point heat sinks with given total sink strength Q_{tot}. For this example we used the fitness function from Eq. (19) and used Eq. (23) to compute the temperature field.

It is clear that the genetic algorithm cannot find a unique solution for the problem given by Eqs. (20)–(22) because this problem is not fully specified. The idea behind the genetic optimization process for the present application is basically that a class of solutions will be found which might be further constrained by several additional relations and rules. The "set of optimal solutions" can be taken as a starting point for further optimization, perhaps another GA.

A very good solution which was found has four point heat sinks with different sink strengths that produce the temperature field shown in Fig. 10, and the wall temperature distribution shown in Fig. 11 (note the scale of the figure). The difference between the determined wall temperature and the goal value is

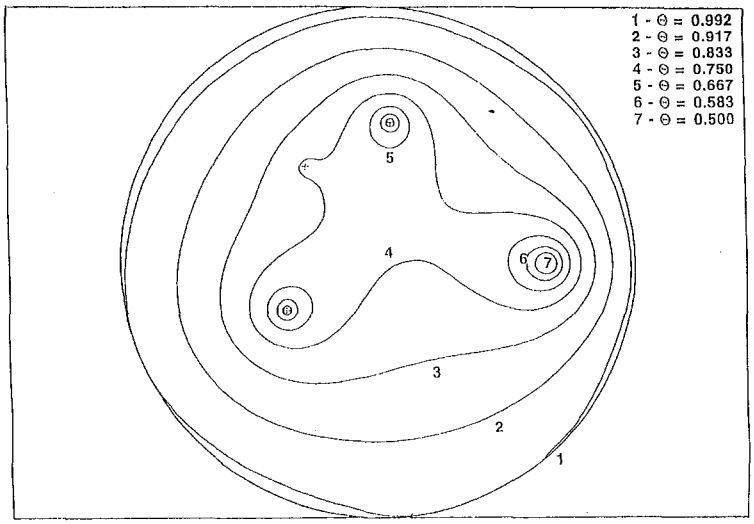

Fig. 10 Temperature field from analytical solution

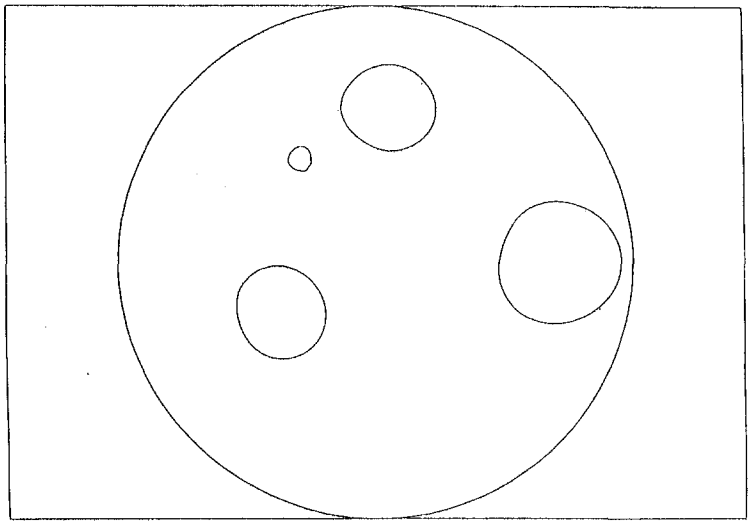

Fig. 12 Cooling channel geometries

less than two per cent. In comparison to the above analytical results, the numerical solution for the given point heat sinks using a two-dimensional finite element solver is shown in Fig. 11. Having found this solution for the optimization goal, cooling channels (cooling conditions $B_C = 2.5$, $\Theta_C = 0.4167$) are determined using Eq. (15) (Fig. 12). Modeling these cooling channels with the finite element solver gives the temperature distribution shown in Fig. 11, which is close to the analytical solution. The differences in the wall temperature distributions are small, and the cooling channel solution gives always lower temperatures as expected from the previous discussion on determination of cooling channel geometry. These optimization were done on a Sparc 20. A typical run lasted about 18 hours.

Conclusions

Combining the point heat sink approach with genetic algorithm optimization is shown to be a promising method to solve the complex problem of convective cooling channel shape optimization. Since this combination is rather new, there remain several open questions (e.g., irregular geometries) which might be subject of future work. The given method does not determine a unique optimum but gives a class of useful solutions to the problem. Additional constraints will further limit the number of possible solutions. Such constraints may include a minimum wall thickness and minimum mass flow requirements (using correlations for the pressure drop and the heat transfer). Also, further fitness requirements (mean temperature of the structure, thermal gradients, etc.) may be set to narrow possible solutions.

Acknowledgment

The authors would like to thank Dr. S. P. Harasgama of ABB Power Generation Ltd., Dr. H. Sugaya of the ABB Corporate Research Computer Science department, and R. Strebel of the ETH Institute of Scientific Computing for initiating the concepts discussion and their helpful comments and advice. Additionally the authors would like to thank ABB Power Generation Ltd. and ABB Corporate Research for permission to publish this paper.

References

Achermann, E., 1995, "Optimierung der Kühlkanalgeometrie mit Hilfe Genetischer Algorithmen," Diploma Thesis, ETH Zürich, Switzerland.

Barone, M. R., Caulk, D. A., 1982, "Optimal Arrangement of Holes in a Two-Dimensional Heat Conductor by a Special Boundary Integral Method," *Int. J. Num. Meth. Eng.*, Vol. 18, 675–685.

Beck, J. V., Cole, K. D., Haji-Sheikh, A., Litkouhi, B., 1992, "Heat Conduction Using Green's Function," Series in computational and physical processes in mechanics and thermal sciences, Hemisphere.

Collatz, L., 1981, "Differentialgleichungen," Teubner, Stuttgart, Germany.

Davis, L., ed., 1991, *Handbook of Genetic Algorithms,* Van Norstrand Reinhold, New York.

Dulikravich, G. S., Kosovic, B., 1991, "Minimization of the Number of Cooling Holes in Internally Cooled Turbine Blades," ASME Paper 91-GT-52.

Dulikravich, G. S., Martin, T. J., 1994, "Inverse Design of Super-Elliptic Cooling Passages in Coated Turbine Blade Airfoils," *Jornal of Thermophysics and Heat Transfer,* Vol. 8, No. 2, 288–294.

Goldberg, D. E., 1989, *Genetic Algorithms in Search, Optimization, and Machine Learning,* Addison-Wesley, New York.

Grefenstette, J. J., 1986, "Optimization of Control Parameters for Genetic Algorithms," *IEEE Trans. on Systems, Man and Cybernetics,* Vol. 16, No. 1, 122–128.

Holland, J. H., 1992, *Adaption in Natural and Artifical Systems,* The University of Michigan, 1992 ed., MIT Press, Cambridge, MA.

Kamke, E., 1956, *Differentialgleichungen reeller Funktionen,* 3d ed., Leipzig, Germany.

Kennon, S. R., Dulikravich, G. S., 1985, "The Inverse Design of Internally Cooled Turbine Blades," *ASME Journal of Engineering for Gas Turbines and Power,* Vol. 107, 123–126.

Michalewicz, Z., ed., 1992, *Genetic Algorithms + Datastructures = Evolution Programs,* Springer.

Parang, M., Arimilli, R. V., Ketkar, S. P., 1987, "Optimal Positioning of Tubes in Arbitrary Two-Dimensional Regions Using a Special Boundary Integral Method," ASME JOURNAL OF HEAT TRANSFER, Vol. 109, 826–830.

Prudnikov, A. P., Brychkov, Y. A., Marichev, O. I., 1988, *Integrals and Series, Vol. 1,* 2nd ed., Gordon and Breach Science Publishers.

Shau, R., Batista, J., Carey, G. F., 1990, "An Improved Algorithm for Inverse Design of Thermal Problems With Multiple Materials," ASME JOURNAL OF HEAT TRANSFER, Vol. 112, 274–279.

Queipo, N., Devarakonda, R., Humphrey, J. A. C., 1994, "Genetic Algorithms for Thermosciences Research: Application to the Optimized Cooling of Electronic Components," *Int. J. Heat Mass Transfer,* Vol. 37, No. 6, 893–908.

Appendix A: Example

As an example for the accuracy of Eq. (15) a unit circle with a constant wall temperature $\bar{T}_W$ is chosen. Two point sinks are located at $(r_1/R_0) = 0$, $\phi_1 = 0°$ with $Q_1 = q_1/(\lambda(\bar{T}_W - T_C)) = -1$ and at $(r_2/R_0) = 0.5$, $\phi_2 = 45$ deg with $Q_2 = q_2/(\lambda(\bar{T}_W - T_C)) = -1.5$. Equation (23) with $B_G \to \infty$ is used for computation of the temperature field. The resulting temperature field is given in Fig. A.1. The cooling geometry is determined for the cooling conditions $B_C = 1.4$, $\Theta_C = 0$. The resulting channel shape is shown in Fig. A.2. Calculating the temperature field with the modeled cooling channel using the Finite Element mesh shown in Fig. A.2, the temperature distribution in Fig. A.3 is obtained. The accuracy of the determined cooling channel geometry can be estimated by comparing the temperature distributions along the contour of the channel (Fig. A.4). It can be seen that the agreement between both distributions is good in

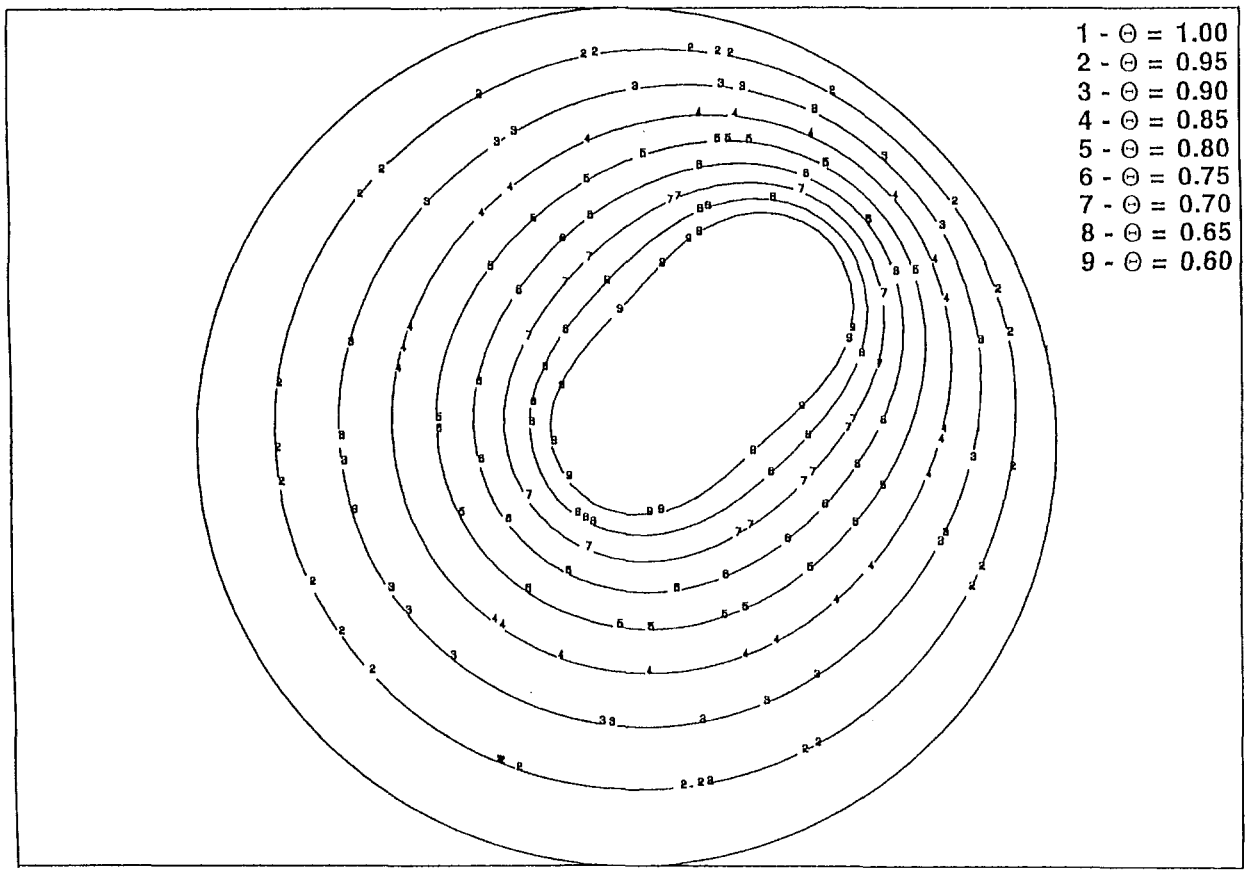

Fig. A.1 Temperature field from point heat sink solution

general, thus showing the accuracy of the approximative envelope solution Eq. (15). Differences are observed at the points where the cooling channel is tied up. At these locations the numerical solution gives somewhat lower temperatures.

Appendix B: Numerical Problems

During the optimization with the genetic algorithm we observed that the second sum of Eq. (23)

$$S(r, \phi) := \sum_{n=1}^{\infty} \frac{1}{B_G + n} \left(\frac{r_i r}{R_0^2} \right)^n \cos\left(n(\phi - \phi_i)\right) \quad \text{(B.1)}$$

where r_i and ϕ_i indicate the locations of the point sinks, gave rise to numerical inaccuracy of the solution because of poor convergence. In order to avoid this problem a closed form solution to this expression was obtained in the following way. Equation (B.1) can be rewritten using complex variables as

$$S(\hat{r}, \hat{\phi}) = \Re\left(\sum_{n=1}^{\infty} \frac{1}{B_G + n} x^n \right) = \Re(f(x))$$

$$= \sum_{n=1}^{\infty} \frac{1}{B_G + n} \hat{r}^n \cos\left(n\hat{\phi}\right) \quad \text{(B.2)}$$

where $\Re(\cdot)$ indicates the real operator. The variable x is defined by

$$x := \hat{r} \exp\left(i\hat{\phi}\right) \quad \text{with} \quad \hat{r} = \frac{r_i r}{R_0^2} \quad \text{and} \quad \hat{\phi} = \phi - \phi_i. \quad \text{(B.3)}$$

If B_G is an integer ($B_G = m$), the series

$$S(\hat{r}, \hat{\phi}) = \sum_{n=1}^{\infty} \frac{1}{B_G + n} \hat{r}^n \cos\left(n\hat{\phi}\right) \quad \text{(B.4)}$$

can be rewritten (see Prudnikov et al., p. 737, note a typographical error there)

$$S(\hat{r}, \hat{\phi}) = \sum_{k=0}^{m-1} \frac{-1}{m - k} \frac{\cos\left(k\hat{\phi}\right)}{\hat{r}^k}$$

$$- \frac{\cos\left(m\hat{\phi}\right)}{2\hat{r}^m} \ln\left(1 - 2\hat{r}\cos\left(\hat{\phi}\right) + \hat{r}^2\right)$$

$$+ \frac{\sin\left(m\hat{\phi}\right)}{\hat{r}^m} \arctan\left(\frac{\hat{r}\sin\left(\hat{\phi}\right)}{1 - \hat{r}\cos\left(\hat{\phi}\right)} \right). \quad \text{(B.5)}$$

where $k = n - 1$.

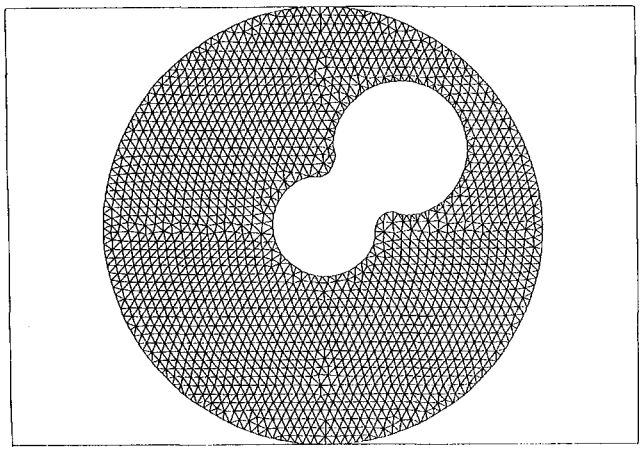

Fig. A.2 Determined cooling channel with finite element mesh

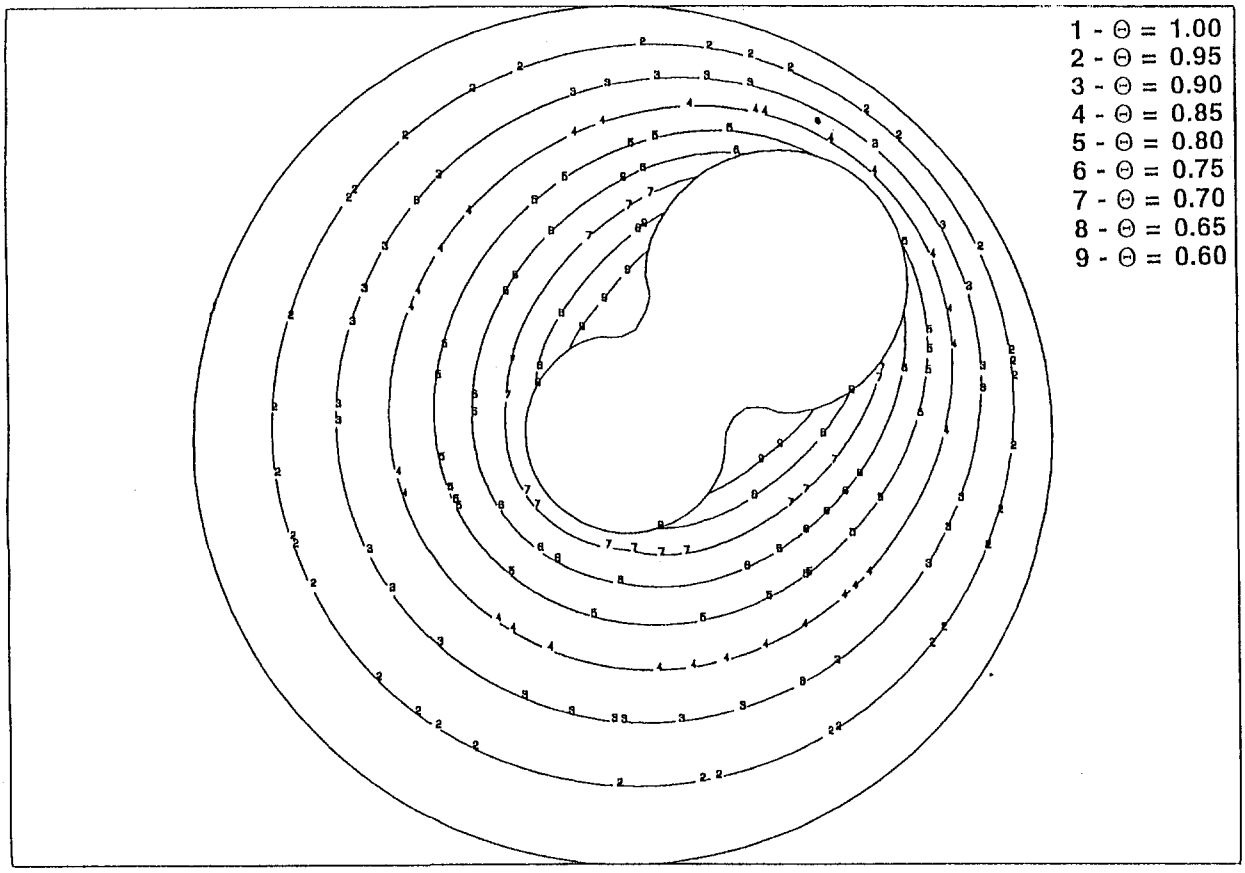

Fig. A.3 Temperature field from finite element computation

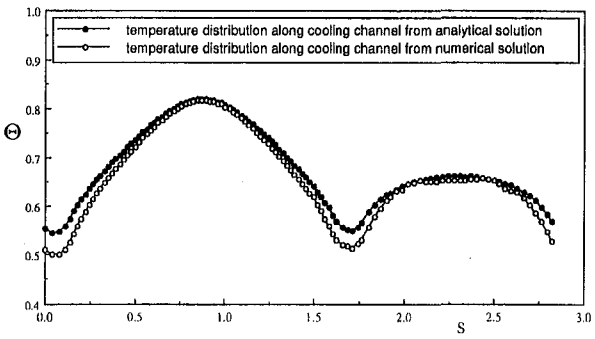

Fig. A.4 Temperature distributions along the cooling channel

For general $B_G > 0$ an improvement of convergence of the series equation (B.2) can be obtained in the following way:

$$\sum_{n=1}^{\infty} \frac{1}{B_G + n} x^n = \sum_{n=1}^{\infty} \frac{x^n}{n} + \sum_{n=1}^{\infty} \left(\frac{1}{B_G + n} - \frac{1}{n} \right) x^n$$

$$= -\ln (1 - x) - B_G \sum_{n=1}^{\infty} \frac{1}{n(n + B_G)} x^n \quad \text{(B.6)}$$

where the last series converges uniformly in $|x| < 1$.

Temperature Measurements of a Transient Thermal Plume in a Confined Space

C.-H. Hsu,[1] C.-F. Hsieh,[2] and J.-T. Teng[3]

Experiments are performed by measuring a developing thermal plume in an enclosure, that is generated by a constant heat flux annular cylinder heater, with six T-type thermocouples. An empirical correlation obtained among local Nusselt number, Fourier number, and modified Rayleigh number is $Nu_x/Ra_x^{*1/4} = 0.00422Fo_L^{-0.893}$.

Introduction

Transient natural convective phenomena of a confined thermal plume are of practical importance in fields such as the formation process of material, cooling of electronic parts, design of solar collectors, cooling of fins, physics of space, fire plume in a compartment, movement of ocean current, etc. Many previous works are focused on the study of steady characteristics. Based on needs in practical fields, unsteady phenomena have draw more attention in recent years. Patterson and Imberger (1980) provided in-depth research on the unsteady natural convection in an enclosure through the scale analysis, and they used three-dimensionless numbers, Rayleigh number, Prandtl number, and aspect ratio, respectively, to divide the flow field into six transient patterns. Yewell et al. (1982) verified Patterson's results by their experimental data. Ivey (1984) used thermocouple and flow visualization methods to perform measurements and observations of high frequency temperature-fluctuation phenomena in a cavity. Schladow (1989) used numerical methods to simulate Ivey's experiments, and showed a close agreement of results.

Studies of natural convective phenomena in confined spaces with complex geometries are also reported in literature. Sparrow and Faghi (1980) studied the natural convective phenomenon of a flow between two parallel, separated constant-temperature rectangular heaters. Jaluria (1982a, 1982b) studied the same heat transfer problem with more heaters. Jularia also applied numerical and experimental methods to study the heat transfer problem for the case of a heater with a line heat source. Zinnes (1970) and Carey and Mollendrof (1977) compared heat transfer results with heat sources at various locations on a vertical plate. Park and Bergles (1987) conducted tests for natural convective phenomenon with several heaters at various locations on the plate. Chu et al. (1976) studied effects of localized heat sources in a confined space. Moffat and Ortega (1986) and Ortega and Moffat (1985, 1986) performed a series of studies on the heat dissipation of electronic components using a bank of square heat emitting components placed on a vertical plate.

The objective of the present study is to obtain a correlation formula relating heat transfer and buoyancy of a developing thermal plume in a confined space. The formula is served as a part of model equations to simulate a fire plume in a compartment, and can also be used to simulate heat transfer of annular-cylindrical packed electronic chips, or computers, in a confined space.

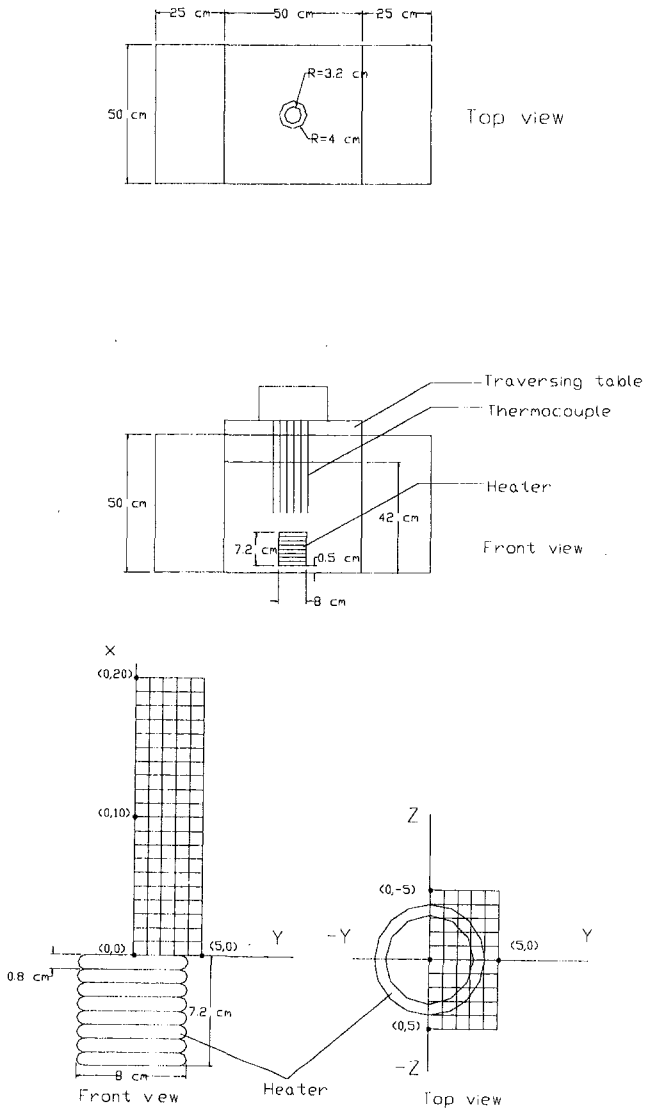

Fig. 1 Schematic diagram of the apparatus and measurement range

Apparatus and Procedures

The experimental apparatus used includes a water table, an annular-cylinder heater, a set of thermocouples assembly, a three-axis precision traversing system, and a data acquisition system. The schematic diagram of the apparatus, dimensions of equipment, and the measurement range are shown in Fig. 1. The enclosure is in the center portion of the water table. The longitudinal walls of the water table are made of two 1.2 cm-thick glass plates, the lateral and top walls are made of five 1.3 cm-thick plexiglass plates, and the bottom wall is made of a 1.0 cm-thick aluminum plate. An annular-cylinder heater is located 0.5 cm above the center of the bottom plate of the enclosure, and water used for the experiments is pre-filtered.

The power of the heater is controlled by a current regulating controller, including a heater break alarm and a temperature monitor/readout device (RKC model REX-C900). The rated error of the controller is ±0.05°C. The maximum output power of the heater is 4840W, and the rated averaged error of the power output is ±2.25 percent.

[1] Associate Professor, Mechanical Engineering Department, Chung Yuan Christian University, Taiwan 32023, Republic of China.

[2] Graduate Student, Mechanical Engineering Department, Chung Yuan Christian University, Taiwan 32023, Republic of China.

[3] Professor, Mechanical Engineering Department, Chung Yuan Christian University, Taiwan 32023, Republic of China.

Contributed by the Heat Transfer Division of THE AMERICAN SOCIETY OF MECHANICAL ENGINEERS. Manuscript received by the Heat Transfer Division October 9, 1995; revision received December 20, 1996; Keywords: Enclosure Flows, Plumes, Transient & Unsteady Heat Transfer. Associate Technical Editor: Y. Jaluria.

A three-axis computer-controlled traversing system is mounted above the water table to locate measurement points. The rated error is ±0.05 mm/300 mm. Spans for three axes are 300 mm, 300 mm, and 1000 mm, respectively. Six 1.0 mm outer-diameter, sheathed, and ungrounded T-type thermocouples are mounted on the traversing system. Measurement joints (hot joints) are extended vertically down into the enclosure to measure temperature profiles of the plume. The separation distance between adjacent hot joints is 10.0 mm. Six 1.5 m-long precision compensation wires are used to connect thermocouples to an ice bath (reference joints or cold joints), which has the datum within 0.05°C.

Each emf voltage produced in the thermocouples is filtered, amplified 200 times, and digitized by a PCLD-779 plug-in card and an AD/DA PCL-818 card, and is stored in a 386 personal computer. Voltage-temperature transfer functions of each thermocouple were calibrated by the monitor/readout device. The uncertainty of the slope of the voltage-temperature relation is within ±0.6 percent, the correlation coefficient is about 0.9995, and the sensitivity of the correlated formula is about 114.

At the beginning of each experiment, the water in the enclosure is preheated up to 31°C; then, turn off the heater until the water cools down to 30°C (about 20 min), restart the heater and keep the power at 3300 W, and begin to measure. Six thermocouples were located at six adjacent points, and each point was 10 mm apart. Each run lasted 200 minutes. The water temperature raised from 30°C to about 80°C, and 201 sets of samples were taken. The laboratory temperature was around 26 to 28°C. Several trial runs were conducted with 30 s, one min, two min, and five min time steps; a one min time step was chosen due to limitations of the facilities. The sampling rate is 50 Hz (maximum frequency response of the amplifier), and each channel collected and average of seven samples in one measurement. Temperature histories at measurement points were calculated by calibration curves. After finishing all of the measurements at these points, thermocouples were moved to the other six measurement points to begin a new test run when the water temperature reduced to 30°C.

Results and Discussions

Measurements of a developing plume in an enclosure were performed. Due to the transient nature of the plume, thermocouples were fixed in each run. Theoretically speaking, portions of the plume that are lower than tips of the thermocouples should not be disturbed by the presence of thermocouples. Therefore, if the plume generation is stable, then a combination of all measurements can build up full temperature profiles of the plume; even measurements were performed in different test runs.

The stability of the heat generation and the effect due to the variation of room temperature are examined by checking the repeatability of the temperature-time histroy at a reference point. Results of three different full-time runs indicated that the uncertainty is within ±1.9 percent (±1 standard deviation). Three other full-time runs were also performed to examine the symmetry of temperature profiles, and the results were with satisfaction. Due to high specific heat of water, from trial runs, the averaged temperature raise at measurement points is within 0.4°C per minute. Estimated error of temperature raising in the sampling period (0.84 s for 42 samples) is less than 0.01°C, and is still within the uncertainty of the equipment. Therefore, averaging seven samples to obtain the temperature at each minute is adequate.

Initial temperature (T_{in} = 30°C) and measured temperature at each point are chosen as references to compute related local dimensionless parameters. Fluid properties, such as the density, the viscosity, and the thermal diffusivity at each measurement point were computed from property tables according to the temperature measured at each minute. (Properties used are varied with water temperature at each point and each minute.) The local Nusselt number, the modified local Grashof number, and the modified local Rayleigh number are defined as

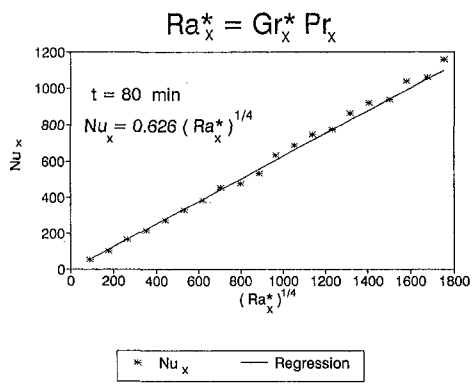

Fig. 2 The correlated curve of Nu_x versus Ra_x^* at 80 min

$$\mathrm{Nu}_x = \frac{hx}{k_x} = \frac{q_w x}{k_x(T_x - T_{in})} \tag{1}$$

$$\mathrm{Gr}_x^* = \mathrm{Gr}_x\,\mathrm{Nu}_x = \frac{g\beta q_w x^4}{k_x \nu^2}, \quad \mathrm{Ra}_x^* = \mathrm{Gr}_x^* \cdot \mathrm{Pr}_x \tag{2}$$

where x, h, k_x, g, β, ν, Pr and Gr_x are the vertical displacement, the heat transfer coefficient, the conductivity, the gravitation, the thermal expansion coefficient, the kinematic viscosity, the Prandtl number, and the Grashof number, respectively. A correlation equation is assumed as

$$\mathrm{Nu}_x = C(\mathrm{Fo}_L)\mathrm{Ra}_x^{*1/4}, \quad \mathrm{Fo}_L = \frac{\alpha t}{L^2} \tag{3}$$

where Fo_L, α and L are the averaged Fourier number at each measuring time, the thermal diffusivity and the characteristic length (height of the enclosure), respectively. Regression results for the Nusselt number versus the modified Rayleigh number at 80 min is shown in Fig. 2, which indicate that the assumed function related the Nusselt number and the modified Rayleigh number is well correlated. Finally, a correlation between the constant C at each time step and the Fourier number is obtained as

$$C = 0.00422\mathrm{Fo}_L^{-0.893}. \tag{4}$$

Conclusions

Temperature profiles of a transient thermal plume, which is generated by a constant heat flux annular cylinder heater at the bottom of an enclosure filled with water, were measured. Experiments were well designed and proceeded, and an empirical correlation among local Nusselt number, averaged Fourier number and modified local Rayleigh number is obtained as $\mathrm{Nu}_x/\mathrm{Ra}_x^{*1/4} = 0.00422\mathrm{Fo}_L^{-0.893}$.

References

Carey, V. P., and Mollendrof, J. C., 1977, "The Temperature Field Above a Concentrated Heat Source on a Vertical Adiabatic Surface," *Int. J. Heat and Mass Transfer*, Vol. 20, pp. 1059–1067.

Chu, H. S., Churchill, S. W., and Patterson, C. V. S., 1976, "The Effects of Heater Size, Location, Aspect Ratio, and Boundary Conditions on Two-Dimensional, Laminar, Natural Convection in Rectangular Channels," ASME JOURNAL OF HEAT TRANSFER, Vol. 98, pp. 194–201.

Ivey, G. N., 1984, "Experiments on Transient Naturnal Convection in a Cavity," *Journal of Fluid Mechanics*, Vol. 144, pp. 389–401.

Jaluria, Y., 1982a, "Buoyancy-Induced Flow Due to Isolated Thermal Sources on a Vertical Surface," ASME JOURNAL OF HEAT TRANSFER, Vol. 124, pp. 223–227.

Jaluria, Y., 1982b, "Natural Convection Flow Due to Line Thermal Sources on a Vertical Adiabatic Surface," *Heat Transfer-1982, Proceedings of the Seventh International Heat Transfer Conference*, Vol. 2, Hemisphere, Washington, DC, pp. 147–152.

List, E. J., 1982, "Turbulent Jets and Plumes," *Ann. Rev. Fluid Mech.*, Vol. 14, pp. 189–212.

Moffat, R. J., and Ortega, A., 1986, "Buoyancy Induced Forced Convection," *Heat Transfer in Electric Equipment—1986*, ASME HTD, Vol. 57, pp. 135–144.

Ortega, A., and Moffat, R. J., 1985, "Heat Transfer from an Array of Simulated Electronic Components: Experimental Results for Free Convection With and Without a Shrouding Wall," *Heat Transfer in Electronic Equipment—1985*, ASME HTD, Vol. 48, pp. 5–15.

Ortega, A., and Moffat, R. J., 1986, "Buoyancy-Induced Convection in Nonuniformly Heated Array of Cubical Elements on a Vertical Channel Wall," *Heat Transfer in Electronic Equipment—1986*, ASME HTD, Vol. 57, pp. 123–134.

Park, K. A., and Bergles, A. E., 1987, "Natural Convection Heta Transfer Characteristics of Simulated Microelectric Chips," ASME JOURNAL OF HEAT TRANSFER, Vol. 109, pp. 90–96.

Patterson, J. C., and Imberger, J., 1980, "Unsteady Natural Convection in a Rectangular Cavity," *Journal of Fluid Mechanics*, Vol. 100, pp. 65–86.

Schladow, S. G., Patterson, J. C., and Street, R. L., 1989, "Transient Flow in a Side-Heated Cavity at High Rayleigh Number: Numerical Study," *Journal of Fluid Mechanics*, Vol. 200, pp. 121–148.

Sparrow, E. M., and Faghi, M., 1980, "Natural Convection Heat Transfer From the Upper Plate of a Colinear, Separated Pair of Vertical Plates," ASME JOURNAL OF HEAT TRANSFER, Vol. 122, pp. 623–629.

Yewell, R., Poulikakos, D., and Bejan, A., 1982, "Transient Natural Convection Experiments in Shallow Enclosures," ASME JOURNAL OF HEAT TRANSFER, Vol. 104, pp. 533–538.

Zinnes, A. E., 1970, "The Coupling of Conduction With Laminar Natural Convection From a Vertical Flate Plate with Arbitrary Surface Heating," ASME JOURNAL OF HEAT TRANSFER, Vol. 92, pp. 528–535.

Journal of Heat Transfer

Discussion

Elastoplastic Contact Conductance Model for Isotropic Conforming Rough Surfaces and Comparison With Experiments[1]

C. V. Madhusudana[2] and Y. Z. Li.[2] The authors are to be complimented on presenting an interesting paper on this important topic. However, we feel that several aspects of the paper need further clarification. The authors have used an elastoplastic deformation model to solve the thermal contact conductance problem. This model tries to combine Mikic's elastic model (1974) and CMY's geometric plastic model (1964) and predict the contact radius and displacement without assuming the type of deformation.

1. Equation Relating Mean Contact Radius a to Curvature Radius β and Contact Displacement δ. Hertz derived Eq. (1) for a, β, and δ in his elastic contact model between a flat and a sphere (see Johnson, 1985):

$$a^2 = \beta\delta. \tag{1}$$

For the CMY geometric plastic model the relation between the three variables is shown to be $a^2 = 2\beta\delta$.

As the load between a flat and a sphere increases, the deformation of contact changes from elastic to elastoplastic and then to the plastic range. In the elastoplastic contact conductance model one would expect an equation for a, β, and δ, which is different from both elastic and geometric plastic models and reflects the true relation between above three parameters.

The authors used Eq. (1) to derive the following equation:

$$\varepsilon^*_{c,a} = \varepsilon^*_{c,\delta} = \varepsilon^*_c \tag{2}$$

where $\varepsilon^*_{c,a} = E'a/(S_f\beta)$ and $\varepsilon^*_{c,\delta} = E' \cdot \sqrt{\delta/\beta}/S_f$.

Equation (2) is valid only in the elastic deformation range, but the authors have used this result as the cornerstone to develop the elastoplastic contact conductance model to predict the contact radius and deformation in the elastoplastic and the fully plastic range.

2. "Blending" Parameter n. The relative elastoplastic constraint parameter C_{ep} is defined as

$$C_{ep} = [(C_e)^{-n} + (C_p)^{-n}]^{-1/n}$$

where n is the "blending" parameter.

From Hertz's solution to the contact problem of a flat and a sphere, we have

$$a = \left(\frac{3P\beta}{4E'}\right)^{1/3}.$$

In Eq. (3) the authors defined the nondimensional elastic hardness as

$$C_{e,a} = \frac{H_{e,a}}{S_f} = \frac{4}{3\pi}\cdot\frac{E'}{S_f}\cdot\frac{a}{\beta} = \frac{4}{3\pi}\cdot\varepsilon^*_{c,a}. \tag{3}$$

It can be seen in $C_{e,a}$, being dependent on a, is a function of $P^{1/3}$. However, the nondimensional plastic hardness, as defined by the authors in Eq. (4), is a constant.

$$C_{p,a} = \frac{H_{p,a}}{S_f} = 2.76 \tag{4}$$

Thus the validity of assuming a single "blending" parameter n for both C_e (a function of $P^{1/3}$) and C_p (a constant) is doubtful.

3. The Contact Radius. Mikic (1974) defined the elastic hardness as $H_e = E' \cdot m/\sqrt{2}$. For a given contact, therefore, H_e is a constant independent of load and contact radius. Equating this to their definition of the elastic hardness,

$$H_{e,a} = \frac{4}{3\pi}\cdot E'\cdot\frac{a}{\beta}$$

the authors found that $a = 1.67\beta m$.

This leads to the conclusion that contact radius is only a function of the surface characteristics, namely, the radius of curvature β and effective mean absolute surface slope m. In particular it implies that the contact radius is independent of the load. According to Eqs. (33) and (34) in the authors' paper, however, the contact radius is a function of the load.

Which of these statements is true? Which one has a physical basis? Since the iterative procedure to determine P/H_{ep} is based on the nondimensional elastic strain ε^*_c, which was found by the authors to be independent of the load, this procedure is also open to question.

Finally, the discussers notice that the "brief review" of deformation models contains no less than eight separate references to the Ph.D. thesis of one of the authors. Since Ph.D. theses are not generally readily accessible to the international reader of this journal, this makes the review harder to understand.

Author's Closure

Response to Question No. 1

The ratio $a_e^2/a_p^2 = \frac{1}{2}$ (i.e., $\beta = \delta/(2\beta\delta)$). The relationships $a_e^2 = \beta\delta$ and $a_p^2 = 2\beta\delta$ relate two output variables, i.e., size a and displacement δ. The load does not appear in this relationship. If the same ratio is expressed as a_{ep}^2/a_p^2, then the right hand side of

[1] By M. R. Sridhar and M. M. Yovanovich, published in the February 1996 issue of the ASME JOURNAL OF HEAT TRANSFER, Vol. 118, pp. 3–9.

[2] School of Mechanical and Manufacturing Engineering, University of New South Wales, Australia, 2052.

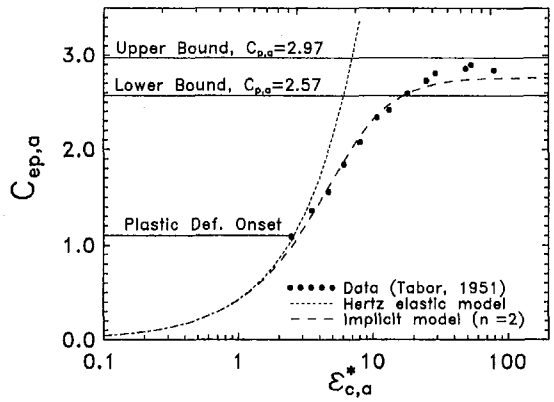

Fig. 1 Comparison of implicit elastoplastic contact radius model with data and the elastic and fully plastic asymptotes

this equation would have changed from $\frac{1}{2}$ (when $a_{ep} \to a_e$) to 1.0 (when $a_{ep} \to a_p$). This true relationship is given by the expression for f_{ep} (Eq. (18)) in the paper. Since load does not appear in this relationship, f_{ep} is a function of only the index ϵ_c^*.

The blending method proposed by Churchill and Usagi (1972) has been used to obtain the elastoplastic solution. In the blending method both the elastic and the plastic solutions are used to obtain the elastoplastic solution. The index ϵ_c^* (nondimensional contact strain) is part of the elastic solution. Hence the derivation $\epsilon_{c,a}^* = \epsilon_{c,\delta}^* = \epsilon_c^*$ is based on the elastic solution.

Response to Question No. 2

The relative elastoplastic constraint parameter is $C_{ep} = [(C_e)^{-n} + (C_p)^{-n}]^{1/n}$, where the blending parameter is a constant, $n = 2$. This can be seen in the comparison with the Tabor (1951) data in Fig. 1 (From Sridhar and Yovanovich, 1995).

Response to Question No. 3

The ratio $\tilde{A}_{ep}/\tilde{A}_p = f_{ep}(\epsilon_c^*)$ in Eq. (18) was derived for a single sphere in contact with a flat. The index ϵ_c^* in Eq. (18) represents the nondimensional contact strain for sphere-flat contact (i.e., $\epsilon_c^* = E'/S_f a/\beta$). In order to incorporate function f_{ep} into the surface roughness model one needs to translate the index $\epsilon_c^* = E'/S_f a/\beta$ to an elastoplastic index for a rough surface. A simple way to accomplish this was to equate the elastic hardness derived by Mikic (1974) for a rough-interface with the Hertz elastic hardness expression for a sphere-flat.

Therefore, the equation $a/\beta = 1.67m$ represents the translation of the contact strain for single sphere-flat contact (i.e., $E'/S_f a/\beta$) to an elastoplastic index for a rough surface (i.e., $E'/S_f\, 1.67m$). Equations (33) and (34) refer to the mean contact radius for a rough interface. Therefore, the question of comparison of these equations to Eq. (25) does not arise.

Finally, it is unfortunate that we could not clarify these questions properly in the paper due to space limitations. The section of the Ph.D. thesis which Madhusudana and Li are interested in is available in the form of a technical report (Sridhar and Yovanovich, 1995).

References

Churchill, S. W., and Usagi, R., 1972, "A General Expression for the Correlations of Rates and Other Phenomena," *A.I.Ch.E. Journal*, Vol. 18, pp. 1121–1132.

Mikic, B. B., 1974, "Thermal Contact Conductance; Theoretical Considerations," *Int. J. Heat Mass Transfer*, Vol. 17, pp. 205–214.

Sridhar, M. R., and Yovanovich, M. M., 1995, "Elastoplastic Hardness Models for Sphere-Flat Contacts," UW/MHTL Technical Report #9504-G47.

Tabor, D., 1951, *The Hardness of Metals*, Oxford University Press, London.

Optimum Design of Radiating Rectangular Plate Fin Array Extending From a Plane Wall[1]

C. Balaji.[2] In the above mentioned article, the author has numerically investigated the effect of various parameters on the heat transfer performance of a fin array consisting of vertical fins standing on a horizontal base, losing heat to outer space by radiation alone. The study is one-dimensional, uses the radiosity-irradiation method of analysis, and is for gray-diffuse surfaces. The study concludes that the heat transfer enhancement with the use of fins is limited, and for a typical case of emissivity (ϵ) of 0.9, the enhancement is about 7.8 percent.

However, there are a few basic and crucial points which seem to have been overlooked by the author.

1 The mathematical formulation is incomplete as there is no mention of the two end fins. The end fins receive irradiation only on one side as opposed to all the other intermediate fins which receive irradiation from both the sides. In view of this, the governing equation itself is different for the end fins. Also, it must be borne in mind that since the two end fins receive irradiation only on one side, they will dissipate more heat than any other intermediate fin. Therefore, the total heat transfer from the fin system, as calculated in the paper, does not represent the actual heat transfer occurring in the fin array (any fin array has to have end fins). This being the case, the definition of the dimensionless heat quantity, ϕ, is again not correct. So, if ϕ is now redefined as the ratio of actual heat transfer (including end fins) to the heat transfer from a black isothermal base, its value can indeed exceed unity.

2 Even so, from the above arguments it does not necessarily mean that adding fins on a horizontal base is an advantage. If one considers the physics of the heat transfer mechanism in the problem under consideration, the so-called "enhancement" depends on two competing factors at work: (a) increase in apparent emissivity because of multiple reflections, which is also known as the "cavity effect," and (b) increase in thermal resistance due to both conduction resistance and irradiation. When one is interested in maximizing the heat transfer from the fin system, the emissivity of the surfaces will be necessarily high (typically 0.9 and above). Under these conditions, the increase in apparent emissivity by the use of fins will be more than offset by the increase in conduction resistance, and most importantly, the mass of the system increases tremendously as more and more fins are added. Under these conditions it is intuitively apparent that the system of a horizontal base with two end fins will give the maximum value of heat transferred/system mass. In fact, there can also be a few cases, as for example fins with low thermal conductivity and high emissivity, where the absolute value of the heat transfer itself will be more for the case of a base with two edge fins. This leads one to redefine the dimensionless heat transfer quantity, ϕ, as the ratio of actual heat transfer from a fin array of several fins to the heat transfer from a fin array of the same material with just two end fins of the same height and emissivity. It needs to be examined whether this ratio exceeds unity at all. Even so irrespective of whether there can be cases where ϕ can exceed unity, it is very clear that if the mass of the system is also taken into account, adding anything more than two fins can actually be disastrous!

[1] By C. K. Krishnaprakas, published in the May 1996 issue of the ASME JOURNAL OF HEAT TRANSFER, Vol. 118, pp. 490–493.

[2] Senior Project Manager, National Institute of Ocean Technology, Indian Institute of Technology, Campus, Madras 600 036, India: balaji@niot.ernet.in

3 Better still, for the problem under consideration, for a given volume of material with emissivity being 0.9 and above, the best configuration would be just a long, horizontal base with no fins at all. With no irradiations and no conduction resistance, this simple configuration would be radiatively losing the maximum amount of heat. The only geometries where adding fins result in superior thermal performance, in space radiators like the one considered in the present study, are the cases of longitudinal/circumferential fins on circular tubes and pipes where again the actual enhancement is very much due to the increased apparent area, also otherwise known as the "area effect." For plane geometries like vertical fins on a horizontal base, there is no area effect. In fact, there is a blockage of the base surface area because of the fins.

Author's Closure

The author wishes to thank Dr. Balaji for his discussion on the paper. The responses to his comments are as follows:

1 End fin effect was not considered in the analysis because in the case of large area radiators, the end fins have only local cooling and their impact on the total radiator performance will be small.
2 The finding from the present paper coincides with the statement "it does not necessarily mean that adding fins on a horizontal base is an advantage."
3 It is true that longitudinal/circumferential fins on circular tubes are likely to be more useful. However, that was not the object of the analysis in this work. Separate analysis has to be done for such finned radiators in the presence of external loads such as solar, albedo, and earthshine.

3 Better still, for the problem under consideration, for a given volume of material with emissivity being 0.9 and above, the best configuration would be just a long, horizontal base with no fins at all. With no irradiations and no conduction resistance, this simple configuration would be radiatively losing the maximum amount of heat. The only geometries where adding fins result in superior thermal performance, in space radiators like the one considered in the present study, are the cases of longitudinal/circumferential fins on circular tubes and pipes where again the actual enhancement is very much due to the increased apparent area, also otherwise known as the "area effect." For plane geometries like vertical fins on a horizontal base, there is no area effect. In fact, there is a blockage of the base surface area because of the fins.

Author's Closure

The author wishes to thank Dr. Balaji for his discussion on the paper. The responses to his comments are as follows:

1 End fin effect was not considered in the analysis because in the case of large area radiators, the end fins have only local cooling and their impact on the total radiator performance will be small.
2 The finding from the present paper coincides with the statement "it does not necessarily mean that adding fins on a horizontal base is an advantage."
3 It is true that longitudinal/circumferential fins on circular tubes are likely to be more useful. However, that was not the object of the analysis in this work. Separate analysis has to be done for such finned radiators in the presence of external loads such as solar, albedo, and earthshine.